



NOAA PROFESSIONAL PAPER SERIES
National Ocean Service 1

AIRBORNE LASER HYDROGRAPHY

System Design and Performance Factors

Gary C. Guenther

Charting and Geodetic Services
National Ocean Service
Rockville, Md 20852

March 1985

U.S. DEPARTMENT OF COMMERCE

Malcolm Baldrige, Secretary

National Oceanic and Atmospheric Administration

Anthony J. Calio, Acting Administrator

National Ocean Service

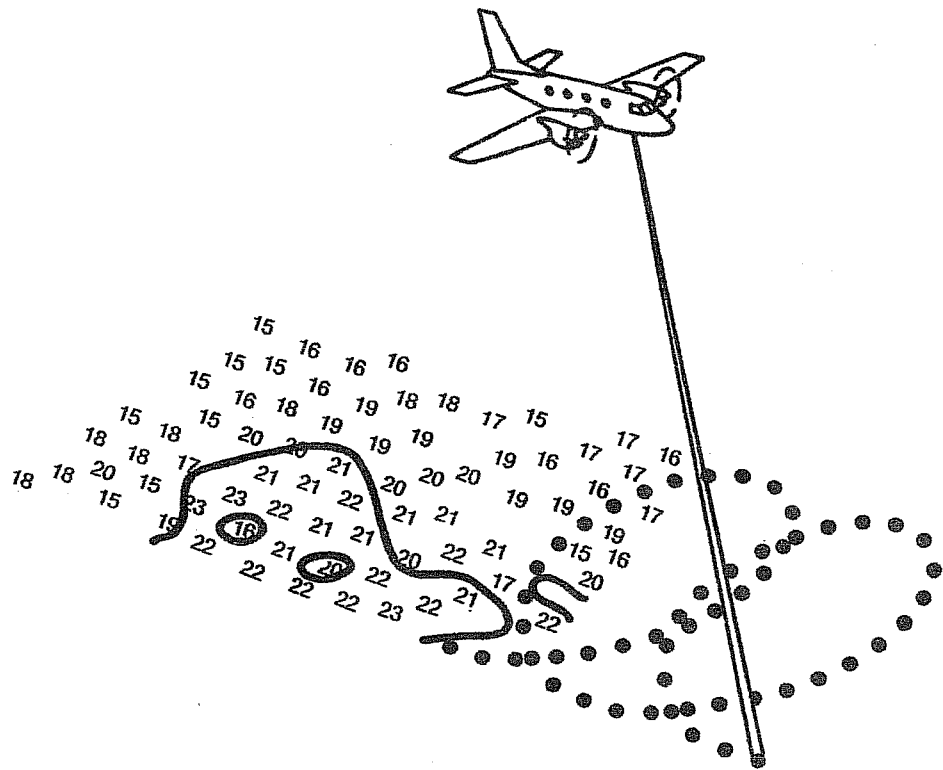
Paul Wolff, Assistant Administrator

Charting and Geodetic Services

John D. Bossler, Director

Report Documentation Page			Form Approved OMB No. 0704-0188	
<p>Public reporting burden for the collection of information is estimated to average 1 hour per response, including the time for reviewing instructions, searching existing data sources, gathering and maintaining the data needed, and completing and reviewing the collection of information. Send comments regarding this burden estimate or any other aspect of this collection of information, including suggestions for reducing this burden, to Washington Headquarters Services, Directorate for Information Operations and Reports, 1215 Jefferson Davis Highway, Suite 1204, Arlington VA 22202-4302. Respondents should be aware that notwithstanding any other provision of law, no person shall be subject to a penalty for failing to comply with a collection of information if it does not display a currently valid OMB control number.</p>				
1. REPORT DATE MAR 1995	2. REPORT TYPE	3. DATES COVERED 00-00-1995 to 00-00-1995		
4. TITLE AND SUBTITLE Airborne Laser Hydrography System Design and Performance Factors			5a. CONTRACT NUMBER	
			5b. GRANT NUMBER	
			5c. PROGRAM ELEMENT NUMBER	
6. AUTHOR(S)			5d. PROJECT NUMBER	
			5e. TASK NUMBER	
			5f. WORK UNIT NUMBER	
7. PERFORMING ORGANIZATION NAME(S) AND ADDRESS(ES) National Ocean Service, Charting and Geodetic Services, Rockville, MD, 20852			8. PERFORMING ORGANIZATION REPORT NUMBER	
9. SPONSORING/MONITORING AGENCY NAME(S) AND ADDRESS(ES)			10. SPONSOR/MONITOR'S ACRONYM(S)	
			11. SPONSOR/MONITOR'S REPORT NUMBER(S)	
12. DISTRIBUTION/AVAILABILITY STATEMENT Approved for public release; distribution unlimited				
13. SUPPLEMENTARY NOTES				
14. ABSTRACT				
15. SUBJECT TERMS				
16. SECURITY CLASSIFICATION OF:			17. LIMITATION OF ABSTRACT Same as Report (SAR)	18. NUMBER OF PAGES 396
a. REPORT unclassified	b. ABSTRACT unclassified	c. THIS PAGE unclassified	19a. NAME OF RESPONSIBLE PERSON	

AIRBORNE LASER HYDROGRAPHY



System Design and Performance Factors

Library of Congress Catalog number 85-600602

Mention of a commercial company or product does not constitute an endorsement by NOAA (NOS). Use for publicity or advertising purposes of information from this publication concerning proprietary products or the tests of such products is not authorized.

For sale by the National Technical Information Service, 5285 Port Royal Road, Springfield, VA 22161

Printed in the United States of America

To the Pioneers,
and to those
who kept the Faith.

PREFACE

This report has been organized to permit several different modes of use. If the sections are read in order, the narrative provides an orderly, logical sequence from the historical perspective, through the basic physics and terminology, to the detailed technical results and their ramifications. On the other hand, specific areas of research and technical results may be accessed directly by referencing the appropriate section. To this end, each section is largely self-contained, and associated concepts are thoroughly cross referenced. In order to make each section stand alone as much as possible, a certain amount of repetition has been included where necessary.

It is recommended that sections 3 and 4 be scanned before referencing specific results in following sections in order to become accustomed with the basic concepts and terminology.

Section 2 outlines the history of research and development efforts pertinent to airborne laser hydrography from its inception in the early 1960's and presents a detailed, chronological reference guide which describes the major milestones and their meaning. Section 3 describes conceptually the pertinent optical properties of the water which will be extensively utilized in later sections. Section 4 introduces the basic terminology, system parameterization, propagation geometry, and return waveform characteristics. Section 5 documents in detail test results from the 1977 NOAA/NORDA/NASA bathymetric flight experiments with the NASA Airborne Oceanographic Lidar.

The remainder of the volume is dedicated to detailed analyses of the physical interactions affecting penetration depth, measurement accuracy, and system and operational parameters. Section 6 introduces the Monte Carlo propagation simulation whose results play vital roles in succeeding sections. Section 7 describes studies of wind/wave, water clarity, and nadir angle effects on the "surface" return (which may come either from the interface reflection or from volume backscattering). Section 8 describes bottom return characteristics and introduces new peak power and penetration calculations for propagation-stretched pulses. Section 9 reviews error sources and depth measurement accuracy with special emphasis on random errors,

propagation-induced biases, non-linear processing, and environmental effects such as surface uncertainty, beam steering, and wave correction. Section 10 discusses the highly critical and interdependent nature of major system design parameters with special emphasis on scanner nadir angle, aircraft altitude, pulse repetition rate, transmitter beam divergence, pulse energy, pulse width, peak power, receiver field of view, receiver bandwidth and resolution, pulse location algorithms, and amplitude dynamic range limitations.

I gratefully acknowledge the management staff of the Engineering Development Office and the National Ocean Service for providing the resources necessary to perform this work. I would like to recognize Lowell Goodman who inspired the program and directed the early phases. I owe a special debt of gratitude to my collaborator, Robert Thomas, whose immense contributions are manifest throughout many of the analyses. This volume could not have been completed without his imaginative and tireless efforts. I thank the Defense Mapping Agency and the Naval Ocean Research and Development Activity for their generous support, and NASA/Wallops Flight Center for their cooperation and resources associated with the AOL experiment. Finally, I applaud Carol Hurley, who diligently typed this manuscript, and James Moore, who cleared the way for printing through considerable red tape.

G.C.G.
March 1985

CONTENTS

PREFACE.....	iii
1.0 INTRODUCTION.....	1
References.....	3
2.0 HISTORY AND REFERENCE GUIDE.....	4
References.....	10
3.0 OPTICAL PROPERTIES OF THE WATER.....	23
3.1 Secchi Depth.....	23
3.2 Diffuse Attenuation Coefficient.....	23
3.3 Beam Attenuation Coefficient.....	26
3.4 Scattering Phase Function.....	29
3.5 Single-Scattering Albedo.....	30
3.6 Interrelationships of Parameters.....	30
3.7 References.....	39
4.0 BASIC CONCEPTS AND SYSTEM DESIGN.....	41
4.1 Basic Physical Concepts.....	41
4.1.1 Propagation Geometry.....	41
4.1.2 Return Waveform.....	55
4.2 System Design and Parameterization.....	59
4.3 References.....	73
5.0 BATHYMETRIC FIELD TESTS OF THE "AIRBORNE OCEANOGRAPHIC LIDAR".....	76
5.1 Introduction.....	76
5.2 Background.....	76
5.3 System Description.....	81
5.4 Field Test Program.....	87
5.4.1 Site Selection.....	87
5.4.2 Support Data.....	89
5.4.3 Test Plans.....	97
5.4.4 Data Processing.....	101

CONTENTS (cont.)

5.5	Flight Acceptance Tests.....	101
5.5.1	Hardware Problems.....	101
5.5.2	Deep-Water Calibration.....	108
5.6	Engineering Results from "User" Flight Tests.....	111
5.6.1	General.....	111
5.6.2	Surface Return.....	112
5.6.3	Bottom Return.....	116
5.7	Bathymetric Performance.....	121
5.7.1	Controls.....	121
5.7.2	Precision and Wave Correction.....	122
5.7.3	Depth Measurement Accuracy.....	147
5.8	Conclusions.....	158
5.9	Acknowledgements.....	159
5.10	References.....	160
6.0	MONTE CARLO PROPAGATION SIMULATION.....	163
6.1	Background.....	163
6.2	Simulation Mechanics.....	165
6.2.1	Definitions.....	166
6.2.2	Downwelling Distributions.....	168
6.2.3	Impulse Response at a Distant Receiver.....	169
6.2.4	Inhomogeneous Media.....	172
6.3	Outputs.....	172
6.4	Acknowledgements.....	175
6.5	References.....	175
7.0	INTERFACE REFLECTION AND VOLUME BACKSCATTER CHARACTERISTICS.....	178
7.1	Background.....	178
7.2	Interface Return.....	178
7.3	Volume Backscatter Return.....	192
7.4	Volume to Interface Peak Power Ratio.....	196
7.5	Acknowledgements.....	201
7.6	References.....	201

CONTENTS (cont.)

8.0	BOTTOM RETURN SIGNAL AND PENETRATION.....	203
8.1	Introduction.....	203
8.2	Signal Equation.....	204
8.2.1	Bottom Return Pulse Energy.....	204
8.2.2	Bottom Return Peak Power.....	207
8.2.3	Incremental Power Sensitivity.....	214
8.2.4	Implications of Eye-Safety Requirement and.....	214
Wave Correction Techniques		
8.2.5	Receiver Field-of-View Effects.....	216
8.2.5.1	Spatial Distributions.....	216
8.2.5.2	Temporal Effects.....	220
8.2.5.3	System Design.....	222
8.2.6	Nadir Angle Effect for Constant Swath Width.....	227
8.3	Noise Sources.....	228
8.3.1	Daytime.....	228
8.3.2	Nighttime.....	230
8.3.3	Electronics.....	231
8.4	Waveform Model.....	231
8.5	Penetration Predictions.....	233
8.5.1	AOL Flight Test Extrapolation.....	233
8.5.2	Australian Results.....	236
8.5.3	Waveform Model Predictions.....	237
8.6	Conclusions.....	240
8.7	Acknowledgements.....	240
8.8	References	
9.0	DEPTH MEASUREMENT ACCURACY.....	243
9.1	Introduction.....	243
9.1.1	Background.....	243
9.1.2	Error Handling Procedures.....	244
9.1.3	Outline.....	246

CONTENTS (cont.)

9.2 Environmental-Based Errors.....	246
9.2.1 Biases from Propagation-Induced Bottom Return.....	246
Stretching and Geometry	
9.2.1.1 Background.....	246
9.2.1.2 Bias Computation.....	253
9.2.1.3 Bias Sensitivities.....	257
9.2.1.4 Bias Variation.....	273
9.2.1.5 Bias Correction.....	283
9.2.1.5.1 Active Bias Correction.....	283
9.2.1.5.2 Passive Bias Correction.....	286
9.2.1.5.3 Bias Correction Conclusions.....	287
9.2.1.6 Conclusions.....	288
9.2.1.7 Acknowledgements.....	290
9.2.2 Interface/Volume Backscatter Uncertainty.....	290
9.2.3 Beam Steering at the Air/Water Interface.....	296
9.2.4 Surface Return Geometric Pulse Stretching.....	301
9.2.5 Wave Correction.....	304
9.3 Hardware-Based Error.....	308
9.3.1 Pulse Location Estimation.....	308
9.3.1.1 Introduction.....	308
9.3.1.2 Description of the Simulation.....	310
9.3.1.2.1 Concept.....	310
9.3.1.2.2 Data Synthesis.....	312
9.3.1.2.3 Pulse Location Estimators.....	315
9.3.1.3 Results.....	316
9.3.1.3.1 Prediction of AOL Performance.....	316
9.3.1.3.2 Sensitivity Studies.....	317
<u>Low Signal Rates</u>	317
<u>High Signal Rates</u>	331
9.3.1.4 Conclusions.....	342
9.3.1.5 Acknowledgements.....	344
9.3.2 Non-Linear Signal Processing Effect on Detection Time.....	344
9.3.2.1 Background.....	344
9.3.2.2 Formalism.....	345

CONTENTS (cont.)

9.3.2.3 Results.....	349
9.3.2.4 Conclusions.....	354
9.3.2.5 Acknowledgement.....	354
9.3.3 Miscellaneous.....	355
9.3.3.1 Timing.....	355
9.3.3.2 Other Non-Linear Processing Effects (HALS).....	355
9.3.3.3 Spurious Responses.....	356
9.4 Summary.....	356
9.4.1 Random Errors.....	356
9.4.2 Variable Biases.....	357
9.5 References.....	357
Appendix 9A.....	360
 10.0 SYSTEM DESIGN TRADEOFFS.....	370
10.1 Background.....	370
10.2 Scanner Nadir Angle, Aircraft Altitude, and.....	372
Pulse Repetition Rate	
10.3 Transmitter Beam Divergence, Pulse Energy,.....	376
Pulse Width, and Peak Power	
10.4 Receiver Field of View and Optical Bandwidth.....	378
10.5 Receiver Resolution and Pulse Location Algorithm.....	379
10.6 Dynamic Range Limitation.....	381
10.7 Summary.....	382
 EPILOG.....	383

1.0 INTRODUCTION

The National Ocean Service (NOS) within NOAA is the agency responsible for charting U.S. coastal waters and the Great Lakes. Methods are being sought to improve the efficiency of shallow-water hydrography. In 1980, NOS spent \$10 million to operate a fleet of hydrographic survey vessels which use sonar to acquire shallow-water data for the production of nautical charts. The cost of hydrographic surveys for charting purposes has increased steadily as a result of inflationary pressures, the increased amount of surveying performed, and the need for more thorough surveys. Ways are sought to counter this trend by pursuing means for reducing cost, manpower, and data collection time while simultaneously improving sounding distribution and increasing productivity to satisfy growing user requirements. Such improvements are acceptable, however, only as long as the resulting data continues to meet the stringent accuracy standards established by the International Hydrographic Bureau (IHB).

The airborne, scanning laser bathymetry concept represents a new generation in shallow-water hydrographic technology. It is as far beyond launch-acoustic techniques as they are beyond the venerable lead line. The payoffs are a significant decrease in survey costs per unit area, increases in coverage rate and yearly coverage area, a rapid response reconnaissance capability, and an improved spatial distribution of soundings. Through a program of analysis, field testing, simulation, and modeling, NOS has critically evaluated airborne laser hydrography as a new technique for performing low-cost hydrographic surveys in shallow waters where present costs are highest. It has been estimated that airborne laser hydrography has the potential for performing surveys at about one-fifth the cost and manpower of conventional, launch-based sonar systems (Enabnit et al. 1978). One laser system can easily survey 2000 square nautical miles annually (Enabnit 1982), an area equal to that now being surveyed by 20 hydrographic launches. Using actual data on the optical properties of water in ten typical areas, it was determined that large tracts on East and Gulf Coasts where national survey requirements now exist could be surveyed by laser (Enabnit et al. 1981).

The critical performance factor is depth measurement accuracy. The airborne lidar technique is prone to a number of depth measurement errors which could exceed IHB standards if not constrained by carefully restricting system design and operational parameters. Examples include multiple-scattering propagation geometry, air/water interface reflection and volume backscatter uncertainty, beam steering and geometric stretching at the air/water interface, wave correction, hardware quantization, non-linear signal processing and detection algorithms, and spurious responses. Each of these errors has been estimated through either analytic or Monte Carlo modeling for a full range of operating conditions. The error functionalities are entwined with system and environmental parameters such as scan angle, altitude, receiver field of view and optical bandwidth, transmitter pulse characteristics, pulse location algorithms, wind speed, and water clarity in a complex web which requires careful compromises in system design and operation to minimize the resulting errors. All of these error sources and relationships are discussed in this volume.

Airborne laser hydrography is slowly coming of age. The problems posed by this evolving technology are numerous and complex, but great strides have been taken. The benefits of the technique are recognized world wide in government and private industry alike. Second generation airborne laser hydrography test systems in various stages of development have been flying in the U.S., Australia, and Canada, and interest has been expressed by many other nations including Mexico, Sweden, Norway, England, Finland, and France. An operational system is currently being tested by the Canadian Hydrographic Service. Australian and U. S. Navy operational systems are approaching the contract stage. This fact, however, must not lead to complacency! Each system has been designed to meet a unique set of individual requirements, and none have been proven in the field. System design and performance parameters are highly interdependent, and the many trade-offs required for each specific system design must be carefully balanced in order for the performance to meet accepted standards and user needs.

Studies of the technical and operational feasibility of airborne laser hydrography were begun in NOAA in 1972. These have involved numerous investigations of physical phenomena as well as detailed models of impact in

areas of economy, efficiency, data processing, positioning, and surveyability. For the most part, the end of the "physical studies" phase of the NOAA program has been reached, and satisfactory results have been obtained. This report is a compendium of technical accomplishments with results and references encompassing all the major areas of system design and performance. It brings together, under one cover, a detailed description of the problems, results, and tradeoffs for the broad spectrum of physical studies which were conducted by the Engineering Development Office and the National Ocean Service under NOAA's Laser Hydrography Development Project from 1975 to the present.

References

Enabnit, D.B., Goodman, L.R., Young, G.K., and Shaughnessy, W.J., 1978: The Cost Effectiveness of Airborne Laser Hydrography. NOAA Technical Memorandum, NOS 26, National Oceanic and Atmospheric Administration, U.S. Department of Commerce, Washington, D.C., 56 pp.

Enabnit, D.B., Guenther, G.C., Williams, J., and Skove, F.A., 1981: An Estimate of the Area Surveyable with an Airborne Laser Hydrography System at Ten U.S. Sites. NOAA Technical Report OTES 05, National Oceanic and Atmospheric Administration, U.S. Department of Commerce, Washington, D.C., 46 pp.

Enabnit, D.B., 1982: FY 1983 Issue Paper -- Airborne Laser Hydrography. NOAA Technical Memorandum OTES 04, National Oceanic and Atmospheric Administration, U.S. Department of Commerce, Washington, D.C., 86 pp.

2.0 HISTORY AND REFERENCE GUIDE

The technique of airborne laser hydrography is based on a foundation of nearly two decades of extensive field experiments, cost-benefit studies, and simulations and theoretical analyses by the world-wide user community.

The concept of making bathymetric measurements with an airborne, pulsed laser system was born in the early 60's as an offshoot of a major effort to locate submarines. Initial hydrographic requirements were based on the need for a system which could supply tactical survey data from hostile territories. An extensive array of theoretical studies and system modeling efforts (e.g., Ott 1965, Sorenson et al. 1966, and Prettyman and Cermak 1969) were conducted in the late 60's in support of the anti-submarine program sponsored by the Naval Air Development Center (NADC). These basic efforts, coupled with the on-going field experiments at Scripps (Duntley 1971), supplied a great deal of the initial information needed for predictions of airborne laser bathymeter performance.

Hardware then appeared on the scene, and positive results were obtained in field tests of elementary bathymetric systems by Syracuse University Research Center's Hickman and Hogg (1969) and by the U. S. Naval Oceanographic Office's Pulsed Light Airborne Depth Sounder (PLADS) system (Cunningham 1972). Notable successes were also enjoyed in Canada by Carswell and Sizgoric (1974) and at NADC by Ott et al. (1971) who reported detecting bottom returns from a surprising 70-m depth in the very clear waters off Key West, Florida.

Continuing studies of light transport mechanisms (based on a laser firing into a large laboratory tank at Sparcom, Inc.) and development of design criteria for an airborne bathymetric system were co-sponsored by the Office of Naval Research (ONR), NOAA, and the U.S. Geological Survey (Hickman et al. 1972, Ghovanlou et al. 1973, Hickman and Ghovanlou 1973, and Hickman et al. 1974). Strong interest in the use of airborne pulsed lasers for bathymetric and fluorosensing applications was fostered in 1973 by the NASA symposium on the use of the lasers for hydrographic studies (Kim and Ryan 1974) which included representation from NASA, NOAA, ONR, NAVOCEANO, NADC, EPA, and the Canada Centre for Remote Sensing (CCRS).

In the next few years, further design, construction, and field testing of airborne laser systems was conducted by NASA (Kim et al. 1975), the Australian Department of Supply (Abbot and Penny 1975), NADC (Ferguson 1975, Shannon 1975, and Witt et al. 1976), and CCRS. Results were promising, and a second generation system, the Airborne Oceanographic Lidar (AOL), was designed for NASA by Avco Everett Research Laboratory, Inc. (Avco 1975).

Active NOAA participation in AOL bathymetry experiments was initiated with a proposal by Goodman (1974). Several symposia, co-sponsored by NASA and NOAA, were convened to establish design goals and user requirements for the AOL in areas of hydrography (Goodman 1975, Goodman 1976a) and fluorosensing. While the AOL was being built, a NOAA Laser Hydrography Development Project was established (Goodman 1976b), and a detailed test plan (Guenther 1977) was developed for field tests to be co-sponsored by NOAA and the newly formed Naval Ocean R&D Activity (NORDA).

Cost comparison and cost-benefit studies were conducted (Young et al. 1977, Enabnit et al. 1978, Shaughnessy and Young 1979) which quantified significant expected reduction in cost and manpower needs for shallow water hydrography with this technique compared to existing sonar procedures. The importance of this result should not be underestimated, because cost savings is one of the primary reasons for the construction of a civilian system. A "limited system design" study for a next generation hardware concept (Avco 1978) demonstrated how such a system could be configured.

The goals of the NOAA/NORDA/NASA AOL experiment were to assess the potential of the basic technique of airborne laser bathymetry in terms of accuracy and maximum penetration depth and to determine the effects of the numerous system and environmental parameters. The AOL has a very sensitive, quantum-limited receiver, and evaluation of the precision of the basic technique required knowledge of the limiting statistical precision of the AOL digital electronics. A Monte Carlo computer simulation of pulse location estimation procedures emulating AOL hardware produced the necessary results (Thomas 1977). The output of the AOL bathymetry test flights would ultimately

consist of roughly six million soundings. In order to extract the maximum information from this valuable data, a sophisticated data processing computer program was developed (Borman 1978, Guenther and Borman 1981) which included a special-purpose calibration procedure, various filters, assorted automated depth algorithms, regression analysis and statistical packages, a wave correction process, editing procedures, and plotting capability.

In 1977, shakedown and test flights of the AOL took place over Chesapeake Bay and the Atlantic Ocean near Wallops Island, Virginia, at sites selected on the basis of appropriate depths, weather, etc. (Swift 1977). Because the equipment was of novel and complex design and had not previously undergone shakedown flights, a number of difficulties were encountered; but most were overcome, and a successful test program was concluded (Goodman 1978). Preliminary results were presented in several forums (Guenther 1978, Guenther and Goodman 1978, Guenther et al. 1978), and an international symposium drawing 50 participants was convened to exchange progress reports and technical details with other on-going programs (Guenther and Goodman 1979). Final results of the NOAA test program of the AOL are reported in section 5 of this report; NASA participation has been described by Hoge et al. (1980).

In the same time frame, the on-going Australian program was described by Clegg and Penny (1978), and promising test results from the first Australian system were reported by Abbot et al. (1978). Canadian tests were described by O'Neil et al. (1978). Continuing efforts at NADC in surface interaction field tests and laser design were reported by Petri (1977) and Rankin and Ferguson (1978), respectively.

At this point, NORDA, under DMA sponsorship, wrote a purchase description and initiated a "Request for Proposal" for a dedicated, helicopter-mounted bathymetric system to be called the Hydrographic Airborne Laser Sounder (HALS). The contract was won in 1979 by Avco Everett Research Laboratory, Inc. of Everett, Mass. -- the builder of the AOL. The NORDA operational scenario has been described by Byrnes (1979).

NOAA program efforts codified the value of an airborne laser bathymeter in terms of benefits, performance, applicability, operations, and impacts

(Enabnit 1979a, Enabnit 1979b, Enabnit 1980a, Enabnit and Nield 1980). The effects of propagation-induced pulse stretching on accuracy and penetration were identified as the significant area of remaining technical risk, and analyses to remove the uncertainties were begun.

Scattering phenomena in the water cause significant spatial and temporal spreading of the returning energy (Duntley 1971), and the extent of this "pulse stretching" is required to determine the loss of peak return power for a given return energy for penetration calculations. Because pulse stretching affects only the bottom return pulse shape and not the surface return, the depth determining algorithm is severely impacted, and significant depth measurement biases can be incurred. From the outset of the AOL experiment, it was understood that the low laser power and design limited electronics of the AOL would preclude deep water tests where pulse stretching becomes significant, and that maximum penetration extrapolations based on theoretical models would be required as an adjunct to AOL field data. For these reasons, the modeling of pulse stretching for a wide range of environmental conditions became a top priority NOAA task.

A formal, analytical approximation to the scattering problem using diffusion theory indicated that the expected magnitudes of the propagation-induced pulse stretching biases could be larger than the allowed system error budget (Thomas and Guenther 1979). A more detailed solution was thus required, but analytical techniques were considered unsuitable due to the complexity of the multiple scattering events. A Monte Carlo simulation approach adapted from an existing atmospheric scattering program was therefore adopted, and a solution for the impulse response functions of the medium was produced, as seen in section 6. Depth measurement biases calculated from these waveforms by applying linear fractional thresholds (valid only for very short incident pulses or very deep water) were reported at various levels of detail in several forums (Guenther and Thomas 1980, Guenther and Thomas 1981a, and Guenther and Thomas 1981b).

An additional simulation was performed to investigate the effect of inhomogeneous optical properties on bias predictions. The result (Guenther and Thomas 1981c) is that the effect is acceptably small for expected water

clarity distributions. This is very important, because if it were not the case, the biases would not be correctable, and the overall technique would be in jeopardy.

Realistic return waveforms are calculated by convolving the impulse response functions (IRFs) with the laser source pulse of interest to produce what are called "environmental response functions" (ERFs). Signal processing and pulse location algorithms applied to the ERFs result in depth estimates which, when compared to the simulated depths, yield bias estimates which can, in turn, be tabulated and used as bias correctors if all the necessary input parameters are known. Specific bias sets have been calculated for two cases: linear fractional thresholds and the proposed HALS electronics involving a logarithmic amplifier, a delayed difference, and "constant fraction discriminator" detector (Guenther 1982). Preliminary results were described briefly in a primer on basic bias correction procedures (Guenther and Thomas 1981d). Detailed results can be found in Guenther and Thomas (1984a and 1984b), and a summary is included in this report as section 9.2.1.

Effects of pulse stretching on depth measurement precision were investigated by exercising in greater generality the Monte Carlo pulse location estimation simulator originally developed for the AOL hardware (Guenther and Thomas 1981e). Various depth determination algorithms were exercised while pulse width, pulse shape, digitization increments, additive noise levels, and amplifier gains were varied. Details are reported in section 9.3.1.

Horizontal positioning requirements and potential hardware solutions have been investigated by Rulon (1980), Faulkner and Gale (1981), and Casey (1982). Water transparency, remote optical parameter estimation, and laser surveyability studies have been conducted by Van Norden and Litts (1979), Murdock (1980), Enabnit et al. (1981), Phillips and Abbot (1981), Gordon (1982), Moniteq (1983a and 1983b), and Phillips and Koerber (1984). Weather constraints were investigated by Scott (1982). Detailed computer requirements are derived and described in Childs and Enabnit (1982). The complex interrelationships between system design and performance factors are described in Guenther and Thomas (1983) and are recounted here in section 10.

Detailed NOAA program rationale and goals are described in an "Issue Paper" (Enabnit 1982) which includes objectives, strategy, alternatives, and a full-scale implementation program encompassing system development, software development, integration, testing, logistics, and transition. The goals of the first phase of the NOAA Laser Hydrography Development Project have been met: the technique is judged viable, and the plans and specifications are prepared and well documented. A Technical Specification (Vitro 1980a) and Statement of Work (Vitro 1980b) were written for the Position and Attitude Measurement Subsystem and similar documents were produced for the Airborne Laser Bathymeter Subsystem (Vitro 1981a and 1981b) which consists of laser, optics, receiver electronics, and control computer. The program has been terminated due to lack of funding for the implementation phase. The current NOAA philosophy is to let other groups take the lead in development of airborne laser hydrographic systems. No further substantive efforts are within sight.

Progress in HALS system planning was described by Van Norden (1980) and Houck (1981). The HALS contract with hardware delivery scheduled for 1982 was terminated due to managerial and technical problems. The laser and certain other salvaged components are currently being flight tested by NASA at Wallops Flight Center with assistance from NADC. Plans are being made to restart a program with a new contractor. In a separate airborne hydrography program at the U.S. Naval Coastal Systems Center, a low-rate laser was used to calibrate depths from a multispectral scanner (Cooper 1979 and 1981). In the future, the multispectral scanner may be mated with the high-rate laser.

The Australians have successfully completed flight testing of their second generation (WRELADS II) scanning system as discussed by Abbot (1981) and Phillips (1981). Plans for an operational Laser Airborne Depth Sounder (LADS) program are discussed by Penny (1982). With strong support from the Royal Australian Navy Hydrographic Office (Calder 1981), the new system has been conceptually designed; applications software is being tested; and a hardware contract for LADS hardware is imminent.

The Canadian program originated at CCRS, as related by Ryan and O'Neil (1980) and O'Neil and Ryan (1981), has successfully concluded tests of their second generation profiling system. The program enjoys strong support and guidance from the Canadian Hydrographic Service (Monahan et al. 1982 and O'Neil 1983) and has moved into design, construction, and software support of an operational scanning system, as reported by Anderson et al. (1983), Malone et al. (1983), Gluch et al. (1983), and Moniteq (1983a and 1983b). Tests of the scanning system began in October 1984, and tests under operational conditions are scheduled this summer.

References

- Abbot, R.H. and Penny, M.F., 1975: Air Trials of an Experimental Laser Bathymeter. WRE-TN-1509, Weapons Research Establishment, Department of Defence (Australia), Salisbury, South Australia, 28 pp.
- Abbot, R.H., Watts, G.J., and Penny, M.F., 1978: WRELADS I Trials Report. ERL-0026-TR, Defence Research Centre Salisbury, South Australia.
- Abbot, R.H., 1981: WRELADS II Trials. Proceedings Laser Hydrography Symposium, 30 Sept. - 3 Oct. 1980, Australian Defence Research Centre, Salisbury, South Australia, Australia Department of Defence, 188-215.
- Anderson, N., Bellemare, P., Casey, M., Malone, K., MacDougall, R., Monahan, D., O'Neil, R., and Till, S., 1983: Beginning the Second Hundred Years -- The Laser Sounder. Proceedings of Centennial Canadian Hydrographic Service Conference, April 1983, Special Pub. 67 of Fisheries and Aquatic Services, Ottawa, Ontario, Canada, 7 pp.
- Avco Everett Research Laboratory, Inc., 1975: Airborne Oceanographic Lidar System Final Report. NASA Contract No. NAS6-2653, NASA Contractor Report CR-141407, Everett, Mass., 139 pp.
- Avco Everett Research Laboratory, Inc., 1978: Airborne Hydrography System Limited Design Report. NOAA Technical Memorandum NOS 27, National Oceanic and Atmospheric Administration, U.S. Department of Commerce, Washington, D.C., 55 pp.

Borman, K., 1978: Airborne Oceanographic Lidar Postflight Bathymetry Processor, Program Documentation Version 4.0. Planetary Sciences Dept. Report No. 004-78, EG&G/Washington Analytical Services Center, Inc., Riverdale, Md., 191 pp.

Byrnes, H.J., 1979: Operating Scenario for a Hydrographic Airborne Laser Sounder (HALS). NORDA Technical Note 34, Naval Ocean R&D Activity, NSTL Station, Mississippi, 30 pp.

Calder, M., 1981: WRELADS -- The Australian Depth Sounding System. Hydrographic Review LVII, 1, 26 pp.

Carswell, A.I. and Sizgoric, S., 1974: Underwater Probing with Laser Radar. Proceedings of The Uses of Lasers for Hydrographic Studies, Sept.12, 1973, Wallops Station, National Aeronautics and Space Administration, Wallops Island, Va., 123-140.

Casey, M.J., 1982: A Navigation System for the Scanning Lidar Bathymeter. The Canadian Hydrographic Service Technical Report, Department of Fisheries and Oceans, Burlington, Ontario, Canada, November, 51 pp.

Childs, J.D. and Enabnit, D.B., 1982: User Requirements and a High Level Design of the Hydrographic Software / Data Processing Subsystem of an Airborne Laser Hydrography System. NOAA Technical Report OTES 11, National Oceanic and Atmospheric Administration, U.S. Department of Commerce, Washington, D.C., 192 pp.

Clegg, J.E. and Penny, M.F., 1978: Depth Sounding from the Air by Laser Beam. Journal of Navigation, 31, 1, 52-61.

Cooper, M.T., 1979: Airborne Hydrographic Survey During READEX 1A-79. NCSC Technical Note TN498, Naval Coastal Systems Center, Panama City, Fla., 42 pp.

Cooper, M.T., 1981: An Active/Passive Multi-spectral Scanner for Airborne Hydrography. Proceedings Laser Hydrography Symposium, 30 Sept. - 3 Oct. 1980, Australian Defence Research Centre, Salisbury, South Australia, Australia Department of Defence, 305-335.

Cunningham, L.L., 1972: Test Report on Pulsed Light Airborne Depth Sounder (PLADS). Naval Oceanographic Office Technical Note 6620-102-72, U.S. Navy, 53 pp.

Duntley, S.Q., 1971: Underwater Lighting by Submerged Lasers and Incandescent Sources. SIO Ref. 71-1, Office of Naval Research Contract No. 00014-69-A-0200-6013 Final Report, Scripps Institution of Oceanography, San Diego, Calif., 261 pp.

Enabnit, D.B., Goodman, L.R., Young, G.K., and Shaughnessy, W.J., 1978: The Cost Effectiveness of Airborne Laser Hydrography. NOAA Technical Memorandum NOS 26, National Oceanic and Atmospheric Administration, U.S. Department of Commerce, Washington, D.C., 56 pp.

Enabnit, D.B., 1979a: Status of Airborne Laser Hydrography. Proc. National Ocean Survey Hydrographic Survey Conference, January 8-12, 1979, Seattle, Washington, National Oceanic and Atmospheric Administration, Washington, D.C., 34-1 - 34-13.

Enabnit, D.B., (Engineering Development Laboratory, National Oceanic and Atmospheric Administration, U.S. Department of Commerce, Riverdale, Md.) 1979b: Airborne Laser Hydrography: A Briefing Prepared for the Director of the National Ocean Survey. 32 pp. (unpublished manuscript).

Enabnit, D.B., 1980a: Airborne Laser Hydrography. Proc. National Ocean Survey Hydrographic Survey Conference, January 7-11, 1980, Gaithersburg, Md., National Oceanic and Atmospheric Administration, Washington, D.C., 261-282.

Enabnit, D.B., and Nield, V.K., 1980: Airborne Laser Hydrography. International Hydrographic Review (Monaco), LVII (2), 93-99.

Enabnit, D.B., 1981: An Evaluation of Laser Hydrography; The U.S. National Ocean Survey's Airborne Laser Hydrography Development Project; and The Hydrographic Software/Data Processing Subsystem of the NOS Airborne Laser Hydrography System. Proceedings Laser Hydrography Symposium, 30 Sept. - 3 Oct. 1980, Australian Defence Research Centre, Salisbury, South Australia, Australia, Department of Defence, 85-95, 96-107, 467-476.

Enabnit, D.B., Guenther, G.C., Williams, J., and Skove, F.A., 1981: An Estimate of the Area Surveyable with an Airborne Laser Hydrography System at Ten U.S. Sites. NOAA Technical Report OTES 05, National Oceanic and Atmospheric Administration, U.S. Department of Commerce, Washington, D.C., 46 pp.

Enabnit, D.B., 1982: FY 1983 Issue Paper -- Airborne Laser Hydrography. NOAA Technical Memorandum OTES 4, National Oceanic and Atmospheric Administration, U.S. Department of Commerce, Washington, D.C., 86 pp.

Faulkner, D., and Gale, M., 1981: WRELADS Position Fixing and Navigation. Proceedings Laser Hydrography Symposium, 30 Sept. - 3 Oct. 1980, Australian Defence Research Centre, Salisbury, South Australia, Australia, Department of Defence, 288-304.

Ferguson, G.D., 1975: Blue-Green Lasers for Underwater Applications. Proceedings SPIE Conference on Ocean Optics, Vol. 64, Aug. 19-20, 1975, San Diego, Calif., 150-156.

Ghovanlou, A.H., Hickman, G.D., and Hogg, J.E., 1972: Laser Transmission Studies of East Coast Waters. Technical Report No. 2, ONR/NOAA/USGS Contract No. N000-14-71C-0202, Sparcom, Inc., Alexandria, Va., 34 pp.

Gluch, T., Piwowar, J., Till, S.J., and O'Neil, R.A., 1983: The Bathymetric Estimator Search Technique for Processing Airborne Lidar Data. Proceedings of 8th Canadian Symposium on Remote Sensing, May 3-6, 1983, Montreal, Quebec, Canada, 7 pp.

Goodman, L.R., (Engineering Development Laboratory, National Oceanic and Atmospheric Administration, U.S. Department of Commerce, Riverdale, Md.) 1974: A Plan for Development of an Operational Laser Hydrography System. 48 pp. (unpublished manuscript).

Goodman, L.R., (ed.), 1975: Laser Hydrography User Requirements Workshop Minutes, January 22-23, 1975, National Oceanic and Atmospheric Administration, Rockville, Md., National Aeronautics and Space Administration, Wallops Flight Center, Wallops Island, Va., 143 pp.

Goodman, L.R., (ed.), 1976a: Laser Hydrography Technical Review Workshop Minutes, August 25-26, 1976a, NOAA/National Ocean Survey, Rockville, Md., National Oceanic and Atmospheric Administration, Rockville, Md., 127 pp.

Goodman, L.R., (Engineering Development Laboratory, National Oceanic and Atmospheric Administration, U.S. Department of Commerce, Riverdale, Md.) 1976b: Laser Hydrography Development Project Plan. 64 pp. (unpublished manuscript).

Goodman, L.R., 1978: Laser Hydrography. Proceedings Coastal Mapping Symposium, August 14-16, 1978, Rockville, Md., American Society of Photogrammetry, 105-110.

Gordon, H.R., 1982: Interpretation of Airborne Oceanic Lidar: Effects of Multiple Scattering. Appl. Opt., 21, 2996-3001.

Guenther, G.C., (Engineering Development Laboratory, National Oceanic and Atmospheric Administration, U.S. Department of Commerce, Riverdale, Md.) 1977: AOL Flight Test and Data Analysis Plan, 210 pp. (unpublished manuscript).

Guenther, G.C., 1978: Bathymetry Intercomparison: Laser vs. Acoustic. Proceedings Coastal Mapping Symposium, August 14-16, 1978, Rockville, Md., American Society of Photogrammetry, 111-124.

Guenther, G.C. and Goodman, L.R., 1978: Laser Applications for Near-Shore Nautical Charting. Proceedings of SPIE Ocean Optics V, Vol. 160, August 30-31, 1978, San Diego, Calif., 174-183.

Guenther, G.C., Goodman, L.R., Enabnit, D.B., Swift, R.N., and Thomas, R.W.L., 1978: Laser bathymetry for near-shore charting application (preliminary field test results). Proceedings of Oceans '78, September 6-8, 1978, Washington, D.C., MTS/IEEE, 390-396.

Guenther, G.C., and Goodman, L.R., (ed.), 1979: Proceedings Airborne Laser Hydrography Symposium III, October 5-6, 1977, NOAA/National Ocean Survey, Rockville, Md., National Oceanic and Atmospheric Administration, Rockville, Md., 248 pp.

Guenther, G.C. and Thomas, R.W.L., 1980: The Effect of Multiple Scattering in Water on Airborne Lidar Bathymetry Accuracy. Proceedings 10th International Laser Radar Conference, October 6-9, 1980, Silver Spring, Md., American Meteorological Society, 55-56.

Guenther, G.C. and Borman, K., 1981: Depth Estimation in the Airborne Oceanographic Lidar Postflight Bathymetry Processor. NOAA Technical Memorandum OTES 02, National Oceanic and Atmospheric Administration, U.S. Department of Commerce, Washington, D.C., 19 pp.

Guenther, G.C. and Thomas, R.W.L., 1981a: Depth Measurement Biases for an Airborne Laser Bathymeter. Proc. Laser Hydrography Symposium, 30 Sept. - 3 Oct. 1980, Australian Defence Research Centre, Salisbury, South Australia, Australia Department of Defence, 428-452.

Guenther, G.C. and Thomas, R.W.L., 1981b: Monte Carlo Simulations of the Effects of Underwater Propagation on the Penetration and Depth Measurement Bias of an Airborne Laser Bathymeter. NOAA Technical Memorandum OTES 01, National Oceanic and Atmospheric Administration, U.S. Department of Commerce, Washington, D.C., 144 pp.

Guenther, G.C. and Thomas, R.W.L., 1981c: Simulations of the Impact of Inhomogeneous Water Columns on the Temporal Stretching of Laser Bathymeter Pulses. NOAA Technical Report OTES 02, National Oceanic and Atmospheric Administration, U.S. Department of Commerce, Washington, D.C., 39 pp.

Guenther, G.C. and Thomas, R.W.L., 1981d: Bias Correction Procedures for Airborne Laser Hydrography. NOAA Technical Report OTES 03, National Oceanic and Atmospheric Administration, U.S. Department of Commerce, Washington, D.C., 104 pp.

Guenther, G.C. and Thomas, R.W.L., 1981e: Error Analysis of Pulse Location Estimates for Simulated Bathymetric Lidar Returns. NOAA Technical Report OTES 01, National Oceanic and Atmospheric Administration, U.S. Department of Commerce, Washington, D.C., 51 pp.

Guenther, G.C., 1982: Effects of Detection Algorithm on Accuracy Degradation from Logarithmic and Difference Processing for Airborne Laser Bathymetry Returns. NOAA Technical Report OTES 6, National Oceanic and Atmospheric Administration, U.S. Department of Commerce, Washington, D.C., 38 pp.

Guenther, G.C. and Thomas, R.W.L., 1983: System Design and Performance Factors for Airborne Laser Hydrography. Proceedings of Oceans '83, Aug. 29 - Sept. 1, 1983, San Francisco, Calif., IEEE/MTS, 425-430.

Guenther, G.C. and Thomas, R.W.L., 1984a: Effects of Propagation-Induced Pulse Stretching in Airborne Laser Hydrography. Proceedings SPIE Ocean Optics VII, Vol. 489, June 25-27, 1984, Monterey, Calif., 287-296.

Guenther, G.C. and Thomas, R.W.L., 1984b: Prediction and Correction of Propagation-Induced Depth Measurement Biases plus Signal Attenuation and Beam Spreading for Airborne Laser Hydrography. NOAA Technical Report NOS 106 CGS 2, National Oceanic and Atmospheric Administration, U.S. Department of Commerce, Washington, D.C., 112 pp.

Hickman, G.D. and Hogg, J.E., 1969: Application of an Airborne Pulsed Laser for Near-Shore Bathymetric Measurements. Remote Sens. of Env., 1, 47-58.

Hickman, G.D., Hogg, J.E., and Ghovanlou, A.H., 1972: Pulsed Neon Laser Bathymetric Studies Using Simulated Delaware Bay Waters. Technical Report No. 1, ONR/NOAA/USGS Contract No. N000-14-71C-0202, Sparcom, Inc., Alexandria, Va., 40 pp.

Hickman, G.D. and Ghovanlou, A.H., 1973: Preliminary Design Criteria, Performance and Limitations of an Airborne Laser Bathymetric System. Technical Report No. 3, ONR/NOAA/USGS Contract No. N000-14-71C-0202, Sparcom, Inc., Alexandria, Va., 49 pp.

Hickman, G.D., Gault, C.S., Ghovanlou, A.H., Friedman, E.J., and Hogg, J.E., 1974: Airborne Laser Shallow Water Bathymetric System. Final Report, ONR/NOAA/USGS Contract No. N000-14-71-C-0202, Sparcom, Inc., Alexandria, Va., 41 pp.

Hoge, F.E., Swift, R.N., and Frederick, E.G., 1980: Water Depth Measurement using an Airborne Pulsed Neon Laser System. Appl. Opt., 19, 6, 871-883.

Houck, M.W., 1981: The Hydrographic Airborne Laser Sounder (HALS) Development Program. Proceedings Laser Hydrography Symposium, 30 Sept. - 3 Oct. 1980, Australian Defence Research Centre, Salisbury, South Australia, Australia Department of Defence, 35-55.

Kim, H.H., Cervenka, P., and Lankford, C., 1975: Development of an Airborne Laser Bathymeter. NASA Technical Note TND-8079, National Aeronautics and Space Administration, Washington, D.C., 39 pp.

Kim, H.H. and Ryan, P.T., (ed), 1974: Proceedings of "The Use of Lasers for Hydrographic Studies", September 12, 1973, NASA Wallops Station, National Aeronautics and Space Administration, Wallops Island, Va., 207 pp.

Malone, A.K., Casey, M.J., and Monahan, D., 1983: Scanning Lidar Bathymeter: (1) Deployment Strategies and (2) Data Processing. Lighthouse, Journal of the Canadian Hydrographers Assn., 27, 2-12.

Monahan, D., Casey, M.J., and MacDougall, R.J., 1982: Comparisons Between Acoustic and Active and Passive Optical Depth Measuring Systems. Lighthouse, Journal of the Canadian Hydrographers Assn., 26, 30-34.

Moniteq Ltd., 1983a: Determination of Parameters of Significance for Accuracy Optimization of a Scanning Lidar Bathymeter. Final Report, Canadian Hydrographic Service Contract, Concord, Ontario, Canada, 129 pp.

Moniteq Ltd., 1983b: Development of Correction Algorithms for Accurate Interpretation of Lidar Bathymetry Data. Contract Report, Canadian Hydrographic Service Contract No. 31SS.FP802-1-2168, Concord, Ontario, Canada, 2 volumes.

Murdock, J.H., (Naval Postgraduate School, Monterey, California) 1980: The Transparency of Southeast Asian and Indonesian Waters. Master's Thesis, 160 pp.

O'Neil, R.A., Thomson, V., deVilliers, J.N., Gibson, J.R., 1978: The Aerial Hydrography Program at CCRS. Proceedings Coastal Mapping Symposium, August 14-16, 1978, Rockville, Md., American Society of Photogrammetry, 125-132.

O'Neil, R.A. and Ryan, J.S., 1981: Field Trials of a Lidar Bathymeter in the Magdalen Islands. Proceedings Laser Hydrography Symposium, 30 Sept. - 3 Oct. 1980, Australian Defence Research Centre, Salisbury, South Australia, Australia Department of Defence, 56-84.

O'Neil, R.A., 1983: Coastal Hydrography Using the CCRS Lidar Bathymeter. Proceedings of Offshore Göteborg '83, March 1-4, 1983, The Swedish Trade Fair Foundation, 10 pp.

Ott, L.M., 1965: Underwater Ranging Measurements Using Blue-Green Laser. NAVAIRDEVCEN Report No. NADC-AE-6519, Naval Air Development Center, Warminster, Pa., (CONFIDENTIAL).

Ott, L.M., Krumboltz, H., and Witt, A.K., 1971: Detection of Submerged Submarine by an Optical Ranging and Detection System and Detection of Pulses by a Submarine. Proc. 8th U.S. Navy Symp. of Military Oceanography (Vol. II), 18-20 May 1971, Naval Postgraduate School, Monterey, Calif. (CONFIDENTIAL).

Penny, M.F., 1982: Laser Hydrography in Australia. Proceedings of International Conference on Lasers '81, December 14-18, 1981, 1029-1042.

Petri, K.J., 1977: Laser Radar Reflectance of Chesapeake Bay Waters as a Function of Wind Speed. IEEE Trans. Geoscience Electron., GE-15, 2, 87-96.

Phillips, D.M., 1981: Effect of Water Turbidity on Laser Depth Sounding Performance. Proceedings Laser Hydrography Symposium, 30 Sept. - 3 Oct. 1980, Australian Defence Research Centre, Salisbury, South Australia, Australia Department of Defence, 336-346.

Phillips, D.M. and Abbot, R.H., 1981: An Aerial Survey of Water Turbidity and Laser Depth Sounding Performance Along the Queensland Coast. Australian Department of Defence Technical Report ERL-0192-TR, Defence Research Centre Salisbury, South Australia, 19 pp.

Phillips, D.M. and Koerber, B.W., 1984: A Theoretical Study of an Airborne Laser Technique for Determining Sea Water Turbidity. Australian J. Phys., 37, 75-90.

Prettyman, C.E., and Cermak, M.D., 1969: Time Variation of the Rough Ocean Surface and its Effect on an Incident Laser Beam. IEEE Trans. GE-7, 235-243.

Rankin, M.B. and Ferguson, G.D., 1978: A Short Pulse-Width Laser for Underwater Applications. Proceedings of SPIE Conf. on Ocean Optics V, Vol. 160, August 30-31, 1978, San Diego, Calif., 67-73.

Rulon, T., (Engineering Development Laboratory, National Oceanic and Atmospheric Administration, U.S. Department of Commerce, Riverdale Md.) 1980: Horizontal Location of Laser Measured Depths. 29 pp. (unpublished manuscript).

Ryan, J.S. and O'Neil, R.A., 1980: Field Trials of an Airborne Lidar Bathymeter. Proceedings of the 19th Annual Canadian Hydrographic Conference, March 20, 1980, Halifax, Nova Scotia, J. Canadian Hydrographers Assn.

Scott, R., 1982: Weather Constraints on Airborne Laser Hydrography Operations. NOAA Technical Memorandum OTES 3, National Oceanic and Atmospheric Administration, U.S. Department of Commerce, Washington, D.C., 14 pp.

Shannon, J.G., 1975: Correlation of Beam and Diffuse Attenuation Coefficients Measured in Selected Ocean Waters. Proceedings of SPIE Conf. on Ocean Optics, Vol. 64, Aug. 19-20, 1975, San Diego, Calif., 3-11.

Shaughnessy, W.J. and Young, G.K., 1979: Cost Comparison and Effectiveness Study of Airborne Optical Bathymetry Systems. Final Report, Defense Mapping Agency Contract MO-A01-78-4211, GKY & Associates, Inc., Alexandria, Va., 47 pp.

Sorenson, G.P., Honey, R.C., and Payne, J.R., 1966: Analysis of the Use of Airborne Laser Radar for Submarine Detection and Ranging. SRI Report No. 5583, Stanford Research Institute, (CONFIDENTIAL).

Swift, R.N., (Marine Science Consortium, Wallops Island Marine Science Center, Wallops Island, Virginia) 1977: Preliminary Report on Preflight Seatruthing for the Airborne Oceanographic Lidar Project. 102 pp. (unpublished manuscript).

Thomas, R.W.L., 1977: A Quantitative Analysis of Errors in the Interpretation of the AOL Charge Digitizer Output. WOLF Reference No. 4820-10, EG&G/Washington Analytical Services Center, Inc., Riverdale, Md., 38 pp.

Thomas, R.W.L. and Guenther, G.C., 1979: Theoretical Characterization of Bottom Returns for Bathymetric Lidar. Proceedings of the International Conference on Lasers '78, December 11-15, 1978, Orlando, Fla., Society for Optical and Quantum Electronics, McLean, Va., 48-59.

Van Norden, M.F., and Litts, S.E. (Naval Postgraduate School, Monterey, California) 1979: The Transparency of Selected U.S. Coastal Waters with Applications to Laser Hydrography. Master's Thesis, 162 pp.

Van Norden, M.F., 1980: The Hydrographic Airborne Laser Sounder: A Planning and Operational Scenario. Proc. 19th Canadian Hydrographic Conference, March 18-20, 1980, Halifax, Nova Scotia, J. Canadian Hydrographers Assn., 71-79.

Vitro Laboratories Division, 1980a: Technical Specifications for Procurement of a Position and Attitude Measuring Subsystem for an Airborne Laser Hydrography System. NOAA Contract No. NA-80-SAC-00706, Automation Industries, Inc., Silver Spring, Md., 105 pp.

Vitro Laboratories Division, 1980b: Contractor Statement of Work for Procurement of a Position and Attitude Measuring Subsystem for an Airborne Laser Hydrography System. NOAA Contract No. NA-80-SAC-00706, Automation Industries, Inc., Silver Spring, Md., 92 pp.

Vitro Laboratories Division, 1981a: Technical Specifications for Procurement of an Airborne Laser Bathymeter Subsystem for an Airborne Laser Hydrography System. NOAA Contract No. NA-80-SAC-00706, Automation Industries, Inc., Silver Spring, Md., 100 pp.

Vitro Laboratories Division, 1981b: Contractor Statement of Work for Procurement of an Airborne Laser Bathymeter Subsystem for an Airborne Laser Hydrography System. NOAA Contract No. NA-80-SAC-00706, Automation Industries, Inc., Silver Spring, Md., 92 pp.

Witt, A.K., Shannon, J.G., Rankin, M.B., and Fuchs, L.A., 1976: Air/Underwater Laser Radar Test Results, Analysis, and Performance Predictions. Report No. NADC-76005-20. Naval Air Development Center, Warminster, Pa., 293 pp. (CONFIDENTIAL).

Young, G.K., Lott, J., and Phillippe, J.T., 1977: Laser Hydrography Analysis (A Cost Comparison Study). Final Report, NOAA/NOS Contract, GKY & Associates, Inc., Alexandria, Va., 56 pp.

3.0 OPTICAL PROPERTIES OF THE WATER

A brief, phenomenological description of the key optical properties and parameters of water is presented here because these concepts and terms will be widely used in following sections. More rigorous and detailed descriptions can be found in references such as Duntley (1971), Gordon et al. (1975), and Gordon et al. (1979).

3.1 Secchi Depth

From everyday experience, we know that as objects are lowered into the water, they become less distinct, less visible, and eventually can no longer be seen. This effect forms the basis of the first device used for measuring water clarity: the Secchi disk. The depth at which a black and white disk (roughly 18 inches in diameter) disappears from view is called the "Secchi depth". "Clean" waters will have larger Secchi depths than "dirty" or more turbid waters. The disk disappears because the light traversing the water column is subject to absorption and scattering processes which reduce the magnitude of the reflected radiation and increase the volume backscatter noise background. The technique is only semi-quantitative since the results depend on a number of factors such as the angle and distribution of ambient illumination, surface wave structure, the type of particulates in the water, and the visual acuity of the observer, to name only a few (Pilgrim 1984). The Secchi depth is consequently an "apparent" water property, i.e., one which is not invariant with respect to changes in the incident radiance distribution.

3.2 Diffuse Attenuation Coefficient

A somewhat analogous measurement utilizing modern-day electronics involves the lowering of an appropriately filtered flat plate optical detector (photometer) through the water column to measure as a function of depth the attenuation of incident solar irradiance, $H_0(\lambda)$, at wavelength λ . Irradiance is defined as the direction-cosine weighted integral of the radiance distribution over a hemispheric solid angle. The downwelling irradiance, $H(\lambda, D)$, at a depth, D , decreases exponentially as

$$H(\lambda, D) = H_0(\lambda) e^{-K(\lambda)D}, \quad (3-1)$$

where $K(\lambda)$ is consequently defined as the "spectral diffuse attenuation coefficient". The term "diffuse" is used because light arrives at the detector from all directions in the upper hemisphere and is given cosine weighting by the diffuse surface of the flat collector. Averaged values of $K(\lambda)$ are typically obtained by measuring the slope of a linear regression of the log irradiance versus depth data over some range of depths.

For monochromatic radiation, $K(\lambda)$ exhibits a strong wavelength dependence which depends on the nature of suspended materials as seen in Fig. 3-1. The attenuation minimum for this "window" in the sea varies from about 480 nm (blue) for very clear, deep, ocean water to about 570 nm (yellow-green) for highly turbid coastal water. For the moderately clear coastal waters of interest for airborne laser hydrography, the minimum which dictates the required laser wavelength is around 535 nm (green). This is, coincidentally, very close to the wavelength of a frequency-doubled Nd:YAG laser.

Like Secchi depth, K is not strictly an "inherent" water parameter, i.e., one which is invariant to the incident radiance distribution. The value obtained will differ, for example, depending on whether the day is cloudy (diffuse incident radiation) or clear (a large collimated radiation component). Under clear conditions, a small functionality exists with the solar zenith angle (Baker and Smith 1979), and even in homogeneous water the value will vary somewhat with depth in shallow waters as the angular distribution of the light field is altered by scattering from collimated to diffuse. Because the magnitudes of these effects tend to be relatively small, K is often considered to be a "quasi-inherent" optical parameter. In order to bypass the depth effect in shallow water, the values of K typically reported are "asymptotic" values, i.e., the constant value to which measurements converge as the depth is increased (for homogeneous water). K is a very important parameter for airborne laser hydrography because, as will be seen in sections 4 and 8, it determines the bottom reflected signal energy and power at the airborne receiver and hence the maximum depth (penetration) from which useful soundings may be obtained.

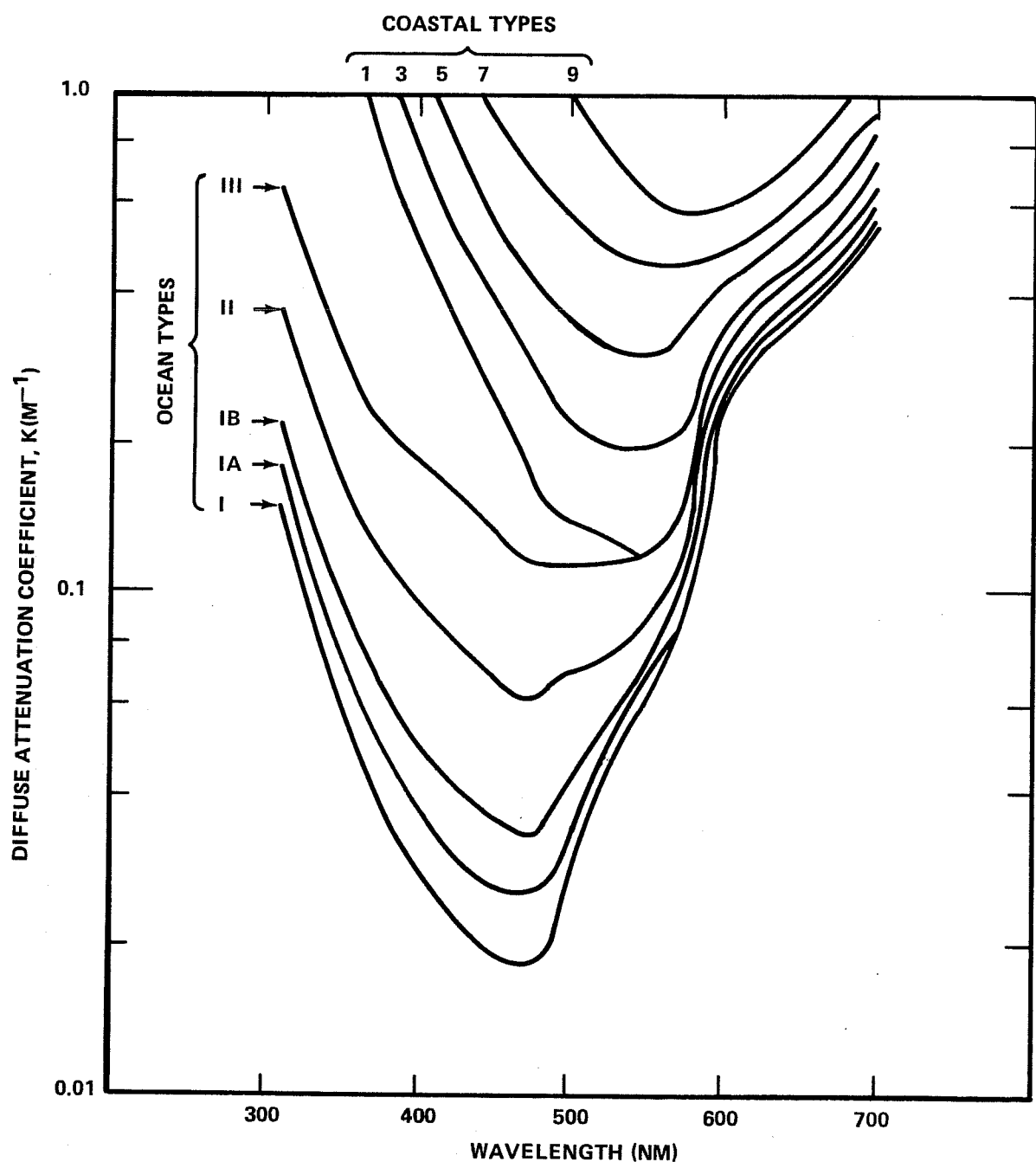


FIGURE 3-1. SPECTRAL DIFFUSE ATTENUATION COEFFICIENT
FOR OCEAN WATERS (REF: JERLOV, 1976)

3.3 Beam Attenuation Coefficient

To investigate "inherent" optical properties one must look directly at the scattering and absorption processes. Consider a narrow beam of collimated, monochromatic light in water with a source radiant flux, N_0 , and a detector behind a pinhole at a distance, d , as in Fig. 3-2. Absorption events reduce the flux (i.e., terminate photons), and scattering events deflect photons away from the pinhole so that they do not strike the detector. Both absorption and scattering losses behave as decreasing exponentials with increasing distance, and the radiant flux striking the detector is

$$N(\lambda) = N_0 e^{-a(\lambda)d} e^{-s(\lambda)d} = N_0 e^{-(a(\lambda) + s(\lambda))d} \equiv N_0 e^{-\alpha(\lambda)d}, \quad (3-2)$$

where $a(\lambda)$ is the "absorption coefficient", $s(\lambda)$ is the "scattering coefficient", and their sum, $\alpha(\lambda)$, is the "beam attenuation coefficient". Note that a , s , and α are inherent properties of the water, are spectral in character, i.e., depend on the wavelength, λ , and are expressed in units of inverse distance (i.e., m^{-1}). Henceforth, it will be understood that the optical properties are measured at the wavelength of interest, and the " (λ) " notation will be dropped.

Equation (3-2) can be understood in the following manner. If one draws a series of scattering events, such as in Fig. 3-3, it is clear that this geometry is viable regardless of the actual physical size of the diagram. Since the mean of an exponential occurs when the argument is unity, the mean free path (the average distance between scattering and absorption events), L , is related to α as $\alpha L = 1$. The average total number of absorption and scattering events remains constant as long as the ratio of linear distance traversed to mean free path (d/L) remains constant. Since $L = 1/\alpha$, the average number of scattering and absorption events experienced in traversing a depth, d , is equal to the dimensionless product, αd , which is termed the "optical depth". This means a constant αd product results in similar absorption and scattering events and similar losses regardless of whether α is large and d small or vice versa. The optical depth is thus the driving parameter for propagation-induced losses as seen in Eq.(3-2).

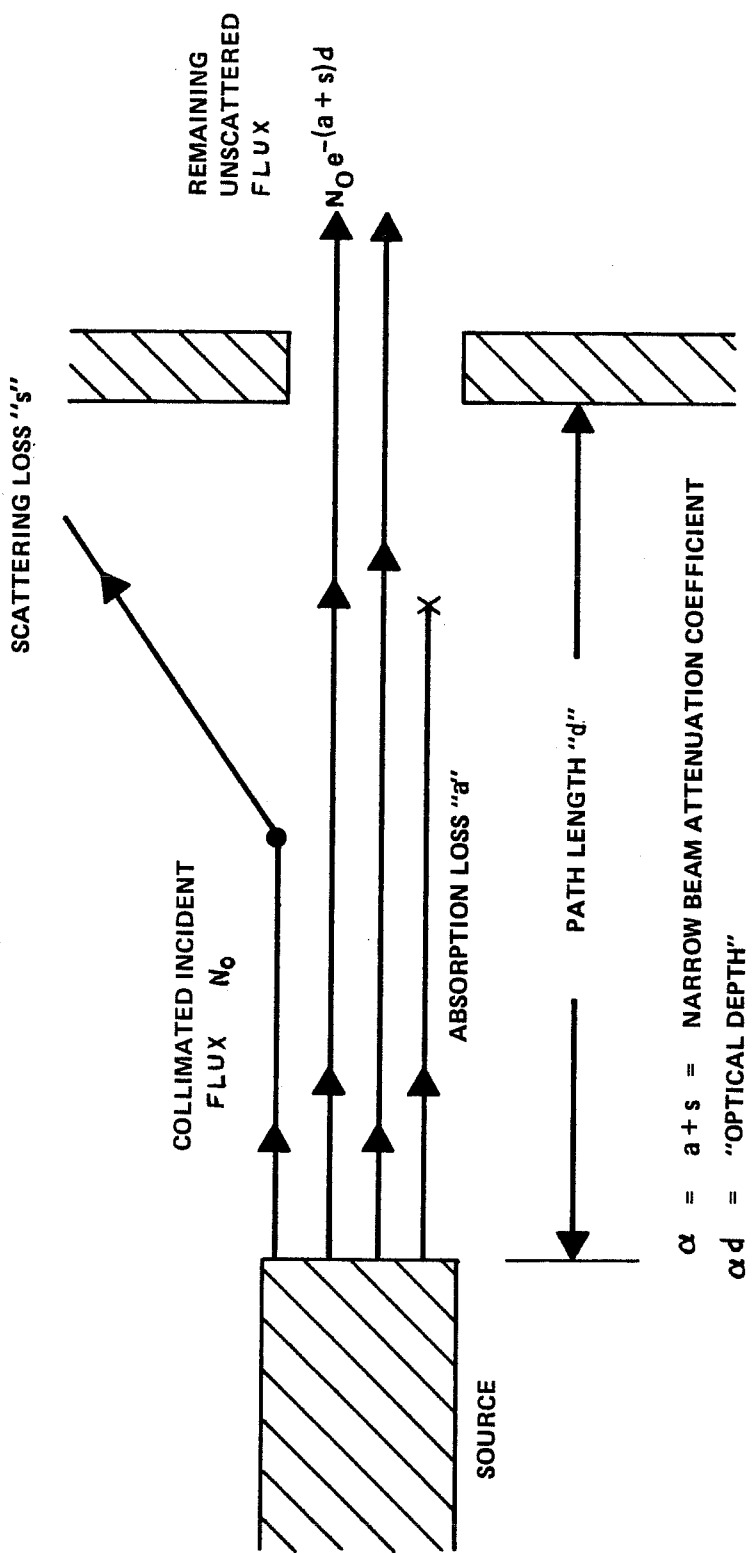


FIGURE 3-2. DEFINITION OF NARROW BEAM ATTENUATION COEFFICIENT

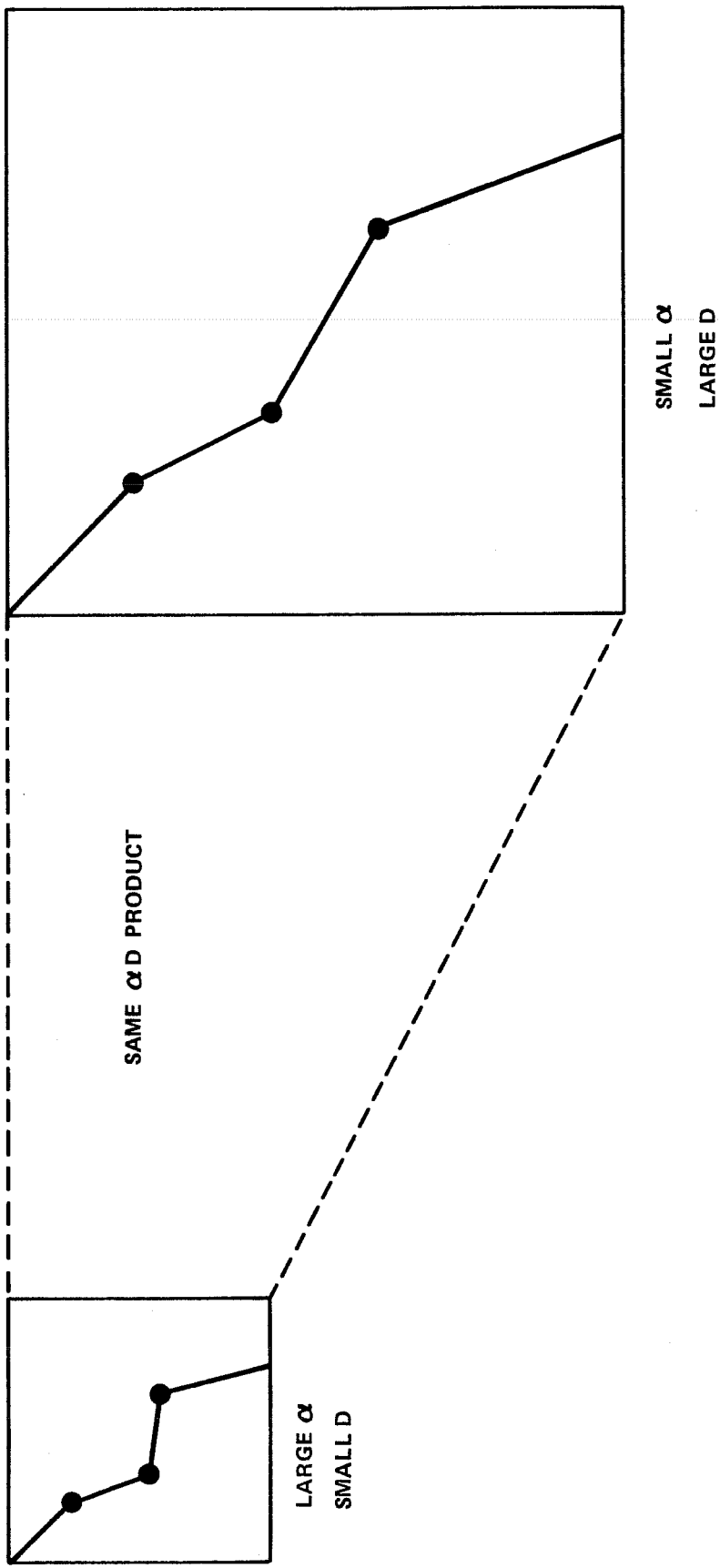


FIGURE 3-3. ILLUSTRATION OF SCALING RULE FOR DIFFERENT DEPTHS

The beam attenuation coefficient, α , is measured with an instrument called a "transmissometer" which is designed along the principles of Fig. 3-2. A very narrow beam of light is aimed at a detector over a fixed distance, d , and the fraction of the light reaching the detector, N/N_0 , is converted to a measure of α using Eq.(3-2) in the form $\alpha = -d^{-1} \ln(N/N_0)$. Values of α are always larger than K because scattered photons which are considered "lost" in the context of α may nevertheless provide illumination in a diffuse sense and thus not be excluded in a K measurement.

3.4 Scattering Phase Function

Instruments have also been developed to measure other inherent properties such as the absorption coefficient and the angular "volume scattering function" (VSF). The VSF, $\sigma(\psi)$, is defined as the ratio of radiant intensity scattered from a sample volume at an angle, ψ , from the incident direction to the irradiance received by the volume, divided by the volume. The scattering coefficient, s , is the integral of the VSF over a sphere:

$$s = 2\pi \int_0^\pi \sigma(\psi) \sin\psi d\psi. \quad (3-3)$$

Similarly, the "backscatter coefficient", s_B , is that portion of the total scattering which occurs into the backward hemisphere; i.e.,

$$s_B = 2\pi \int_{\pi/2}^{\pi} \sigma(\psi) \sin\psi d\psi, \quad (3-4)$$

where B is the "backscatter fraction". It will be seen in section 3.6 that the value of B affects the numeric value of a relationship between α and Secchi depth. The VSF can be renormalized into a probability density distribution, the so-called "phase function" (the probability of scattering into a unit solid angle in a given direction normalized to unity over all angles) by dividing the VSF by "s".

The scattering angle distribution, i.e., the phase function, for a given body of water depends strongly on the sizes, shapes, and indices of refraction of the entrained particles. The phase functions for typical natural waters are extremely peaked in the forward direction, as seen from the VSFs in

Fig. 3-4. Cumulative distribution functions derived from phase functions for relatively clean and relatively dirty coastal waters (Petzold 1972) are presented in Fig. 3-5 where it can be seen that between 25 % and 38 % of the scattering takes place within one degree of the incident direction and roughly 75 % within ten degrees. These phase functions are used to define the scattering angle distributions for the Monte Carlo simulations described in section 6.

3.5 Single-Scattering Albedo

The dimensionless ratio of total scattering to total attenuation, s/α , is defined as the "single-scattering albedo" and designated ω_0 . Since $\alpha = a + s$, it can be seen that $0 < \omega_0 < 1$, where zero indicates pure absorption, and unity implies pure scattering. For coastal waters, ω_0 ranges roughly between 0.55 and 0.93, with 0.8 to 0.9 being typical values. It is related to the absorption-to-scattering ratio, a/s , by the expression $\omega_0 = 1/(1 + a/s)$. The greatest physical influence on ω_0 is the domination of the water column by either organic or inorganic particulates. It will be shown shortly that there exists a relationship between K and α which depends almost solely on ω_0 .

3.6 Interrelationships of Parameters

Due to the similarity of the two measurements, one might expect some sort of quantitative relationship between K (measured with some stated optical bandpass) and the Secchi depth, Z_S . Various empirical expressions of the form $KZ_S = n_K$ have been reported where $1.1 < n_K < 1.7$, as seen in Fig. 3-6, but it has been shown by Gordon and Wouters (1978) that n_K is not fixed but rather depends in a complex way on the scattering and absorption properties of the water and the entrained particulates, and that values of n_K outside the above range are theoretically possible. Values for K can thus not be reliably inferred from Secchi disk data.

A fairly general empirical relationship has been found (Gordon and Wouters 1978) between α and the Secchi depth, Z_S , of the form $\alpha Z_S \sim n_\alpha$, where $6 < n_\alpha < 8$ (depending primarily on the backscatter fraction). This is somewhat surprising considering that α is an inherent parameter and Z_S is not,

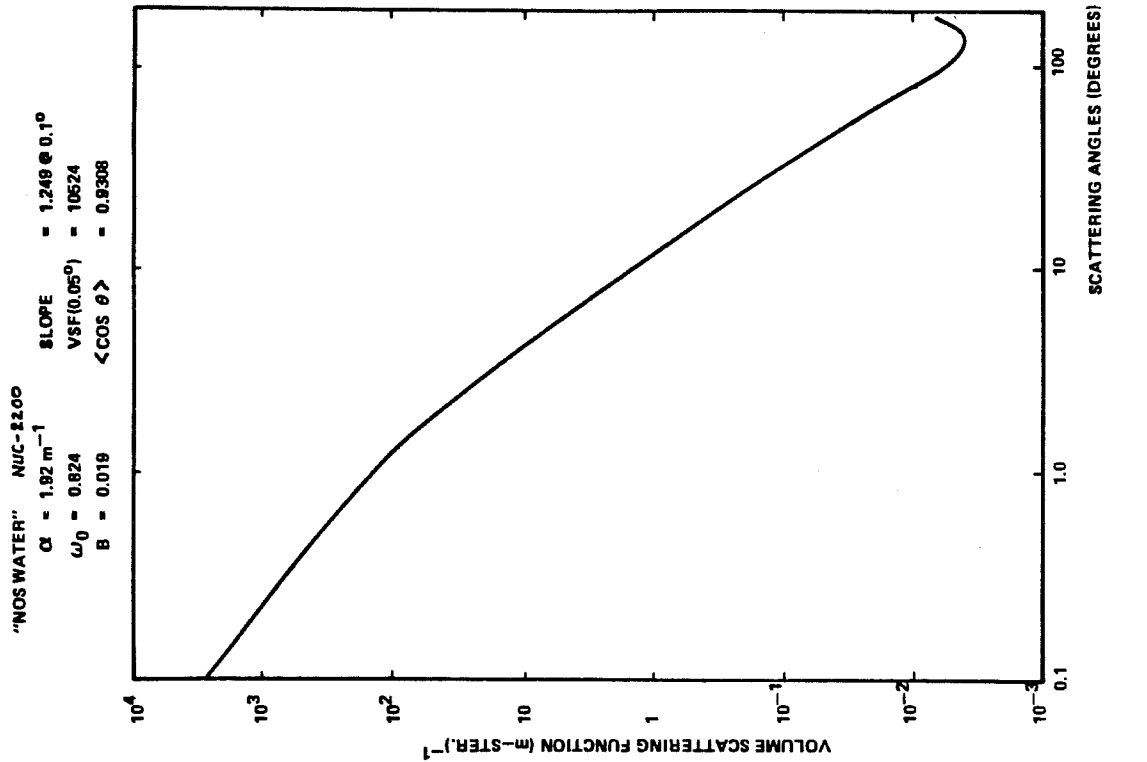
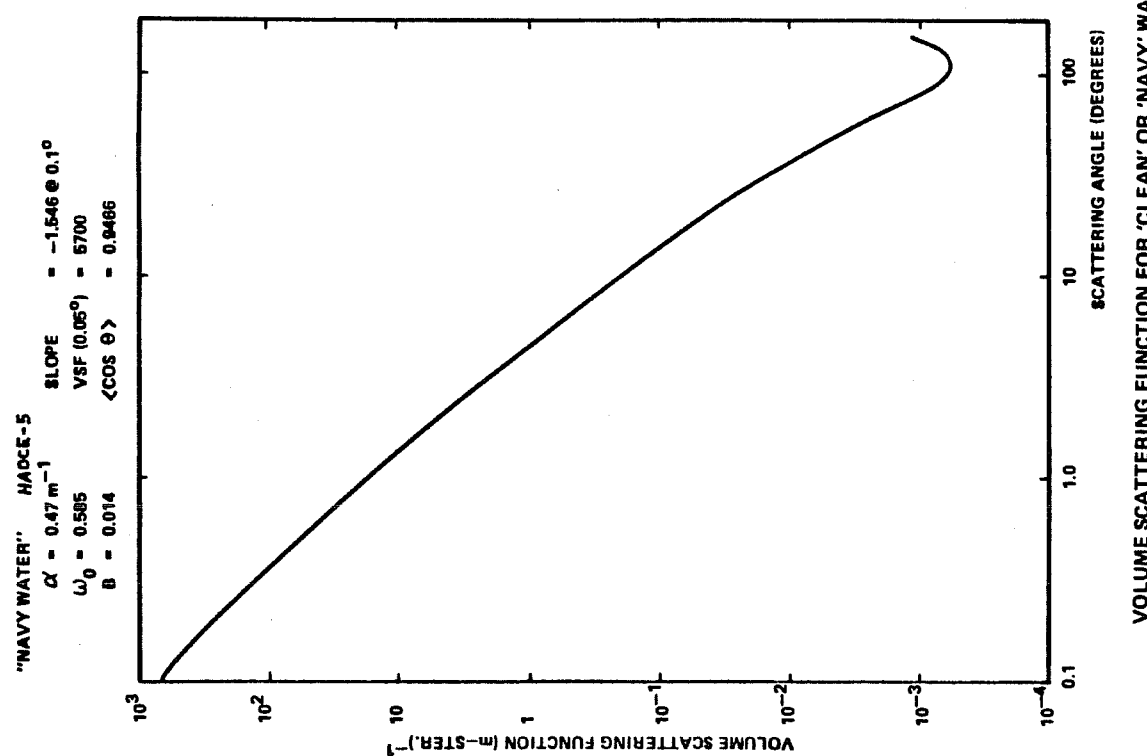


FIGURE 3-4.TYPICAL VOLUME SCATTERING FUNCTIONS (PETZOLD 1972)

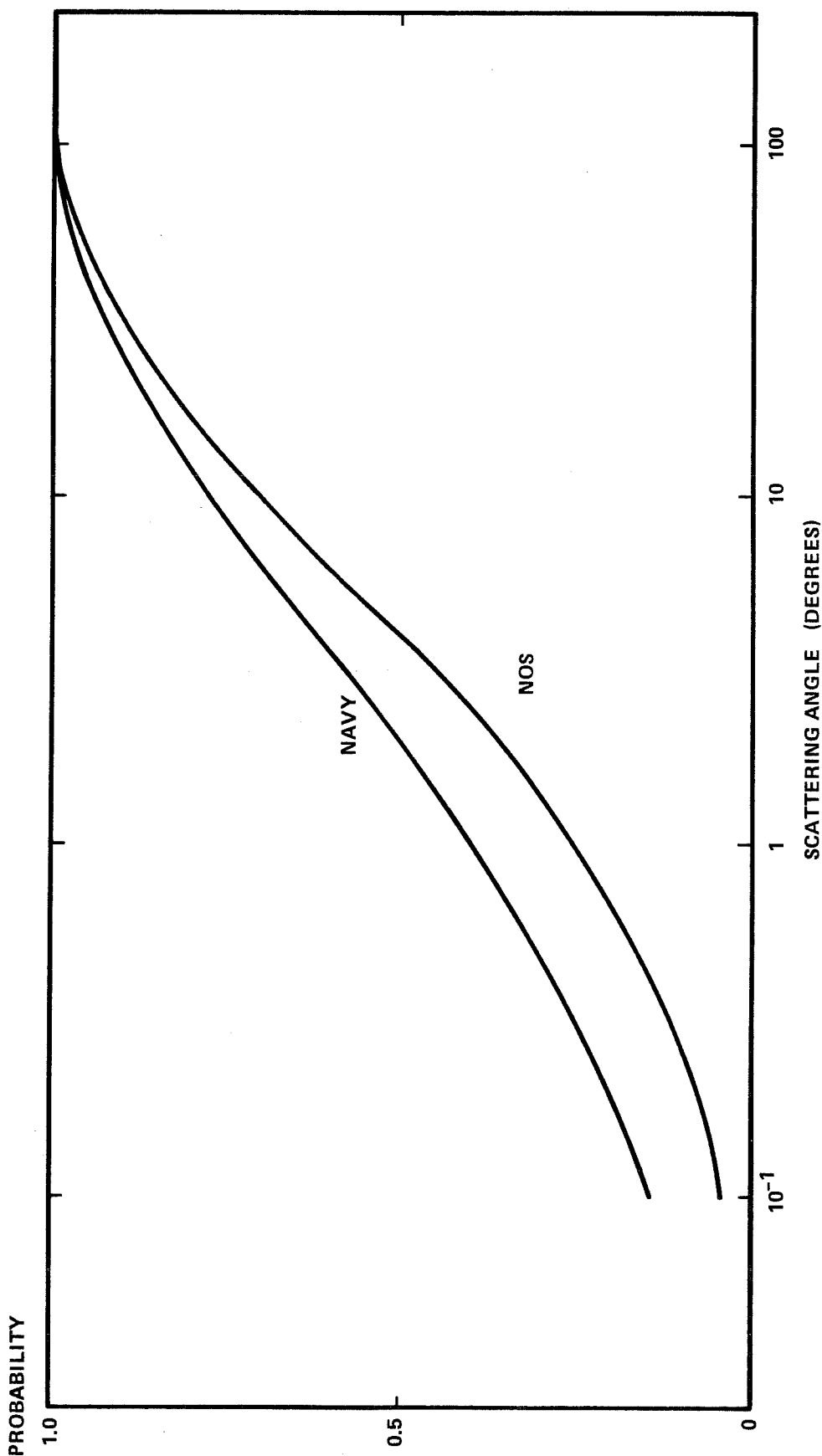


FIGURE 3-5. PROBABILITY OF SCATTERING THROUGH LESS THAN GIVEN ANGLE

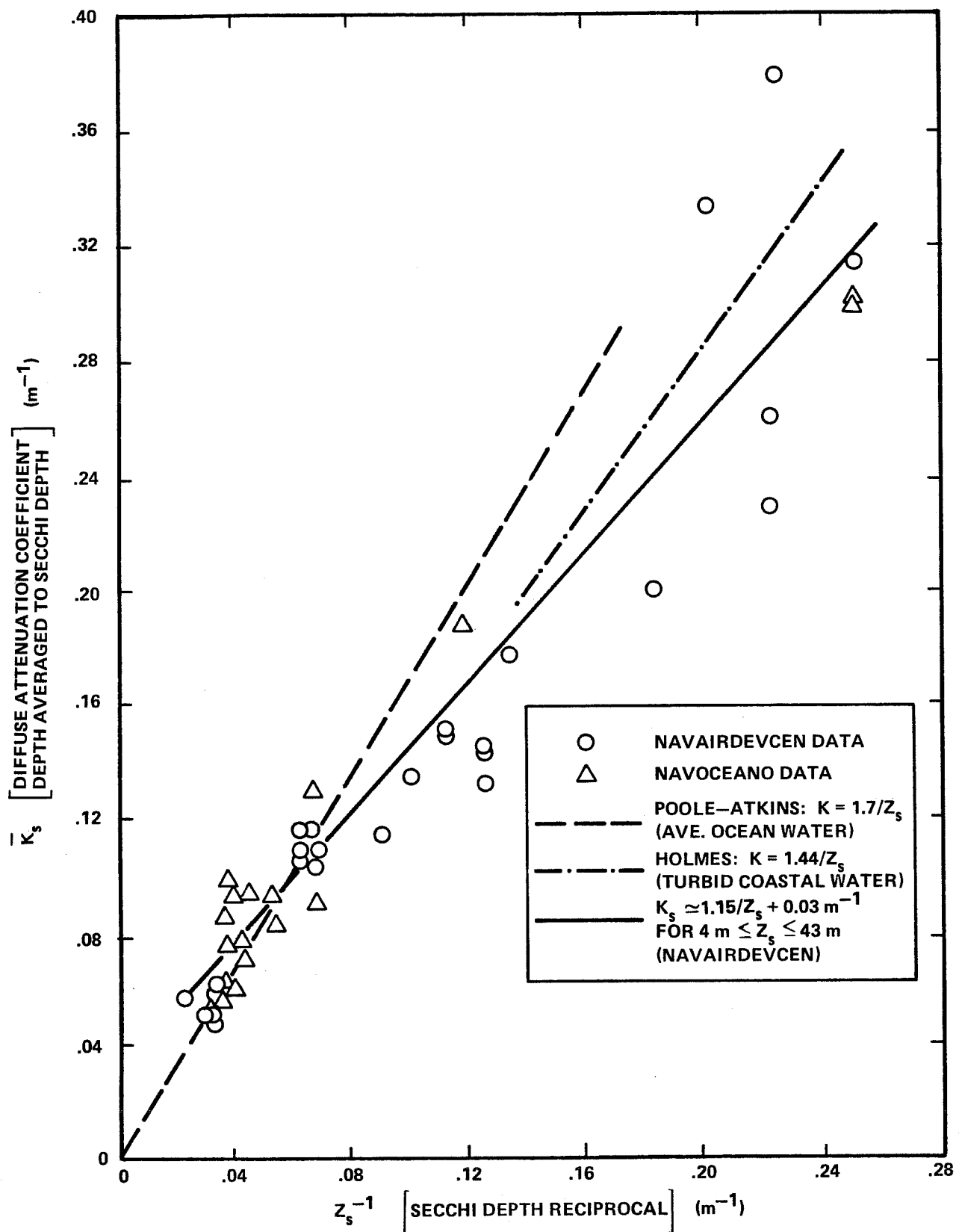


FIGURE 3-6. PLOT OF COMBINED NAVAIRDEVcen AND NAVOCEANO SECCHI AND DIFFUSE ATTENUATION COEFFICIENT DATA

and that K does not always correlate well with Z_s which shares a similar geometry. A clear, linear relationship between α and $1/Z_s$ was obtained during AOL seatruthing efforts. A value of $n_\alpha \sim 7.0$ was obtained, as seen in Fig. 5-10. Secchi depths may thus be used to estimate rough values of the beam attenuation coefficient.

It has been shown by experiment (Timofeyeva and Gorobets 1967), analytic scattering approximation (Prieur and Morel 1971), and Monte Carlo simulation results (Gordon et al. 1975, Guenther and Thomas 1981) that α and K are related by a well-defined functionality with ω_0 , as seen in Fig. 3-7. The ratio is not absolute but depends to a small degree on phase function (and also optical depth if the asymptotic value of K has not been achieved). For an average phase function the ratio can be expressed as

$$K/\alpha \approx [0.19 (1 - \omega_0)]^{\omega_0/2}, \quad (3-5)$$

where the functionality is from Timofeyeva, and the constant factor is a best fit to the Monte Carlo simulation results (the Timofeyeva factor was 0.23 for "milky" media). For a typical $\omega_0 = 0.8$, for example, it can be seen that $\alpha \approx 4K$. Estimates of ω_0 in the environment can be made from Fig. 3-7 or Eq.(3-5) by measuring both K and α . Also illustrated in Fig. 3-7 are bounding curves illustrating pure absorption and pure Rayleigh (molecular) scattering. It can be seen that, in typical waters, the diffuse attenuation coefficient is dominated by absorption. For $\omega_0=0.8$, K is composed of roughly one-fourth scattering and three-fourths absorption. The absorption fraction increases for smaller ω_0 .

Much of the U.S. Navy data (Shannon 1975, Witt et al. 1976) tends to fall in the limited range, $0.75 < \omega_0 < 0.9$. Because of this fairly small range, the K/α ratio appeared to be nearly constant, and the data were regressed with the relationship $K = 0.2\alpha + 0.04$. A similar relationship with different coefficients is reported in Phillips et al. (1984). It is imperative to understand that these are not general results, but merely the manifestation of a limited range in the ratio of organic to inorganic scatterers in the test regions. The relationships are different because they represent different dominant values of ω_0 . These curves would vary greatly if a different

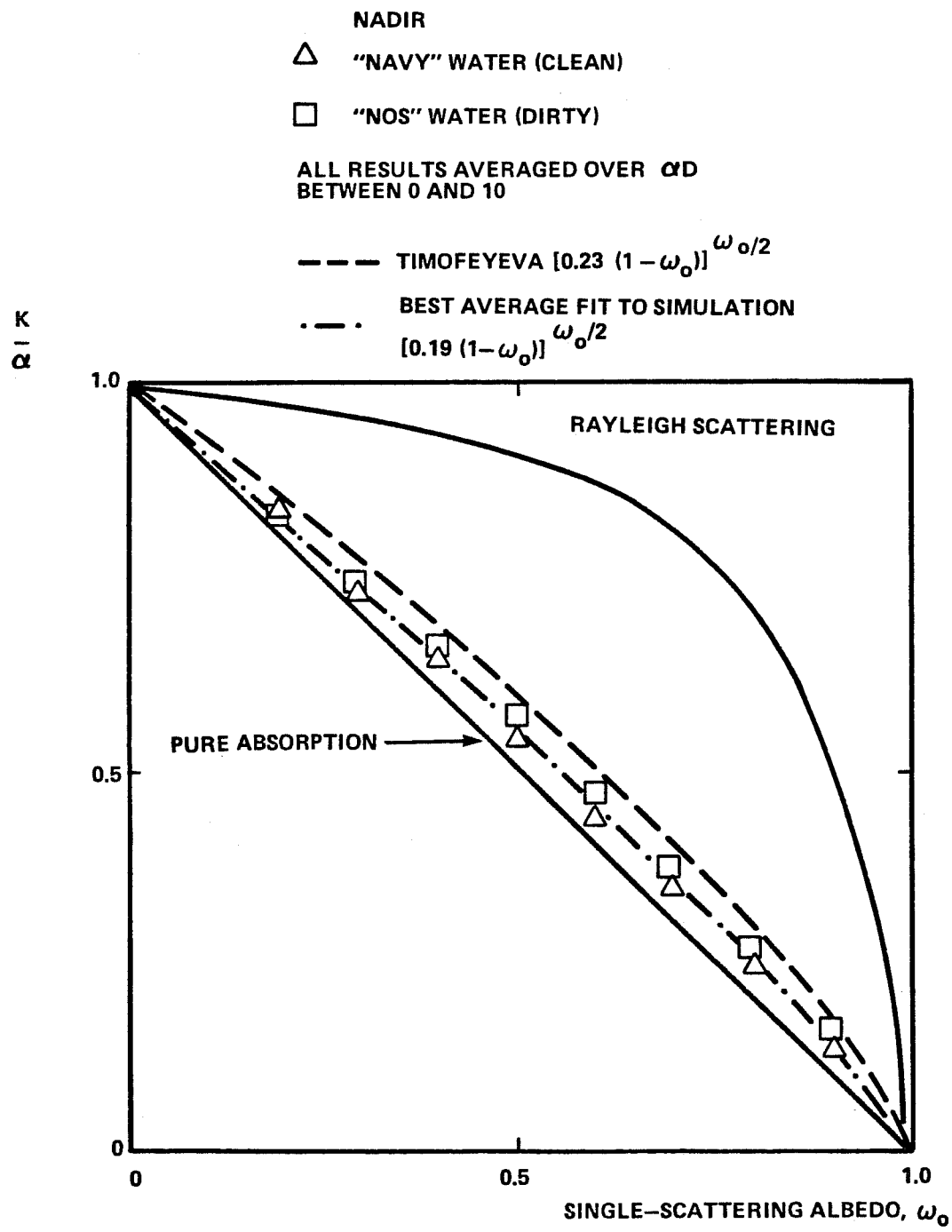


FIGURE 3-7. NORMALIZED ATTENUATION COEFFICIENTS AS FUNCTION OF SINGLE-SCATTERING ALBEDO

proportion of scattering types were introduced by, for example, storms or seasonal changes in biologically active areas. The K/α ratio, in fact, depends almost entirely on ω_0 , as seen in Fig. 3-7 and Eq.(3-5).

The single scattering albedo, ω_0 , is theoretically independent of α since it depends only on the a/s ratio, but in natural waters with "typical" scatterers and absorbers, there seems to be a propensity for certain ω_0 ranges to be associated with certain α values. This is illustrated in Fig. 3-8 which is a compilation of data from a large number of diverse reference sources. It can be seen that although there is a great deal of variability for $\alpha \leq 0.6$, for $\alpha \geq 0.6$ the values of ω_0 in nature tend to be in the range $0.6 < \omega_0 < 0.9$. For $\alpha > 1$, the average value of ω_0 is about 0.85.

It is of interest to note that the spread in ω_0 tends to be much smaller for some individual experimenters or groups than for the composite. Since many of the individual data sets come from wide ranges of differing geographical locations and seasons, the implication is that a significant fraction of the total variability evidenced may be due to systematic experimental error in the water clarity measurement apparatus or techniques. Considering the difficulty of the measurements and the great variability in equipment design and data reduction procedures, this is not too surprising.

The amount of energy backscattered by the water column depends linearly on $\sigma(\pi)$, the value of the volume scattering function at 180 degrees to the beam entry angle (see section 7). The values of $\sigma(\pi)$ measured by Petzold (1972) are seen in Fig. 3-9 to increase monotonically with "s", the scattering coefficient. Through this relationship, it may be possible to estimate values of "s" from airborne laser backscatter data, as noted in section 9.2.1. Although backscatter energy may sometimes appear to be linear with α (since α increases with increasing "s"), it is clear that this is not a general relationship because increasing the absorption, "a", will also increase α but not $\sigma(\pi)$.

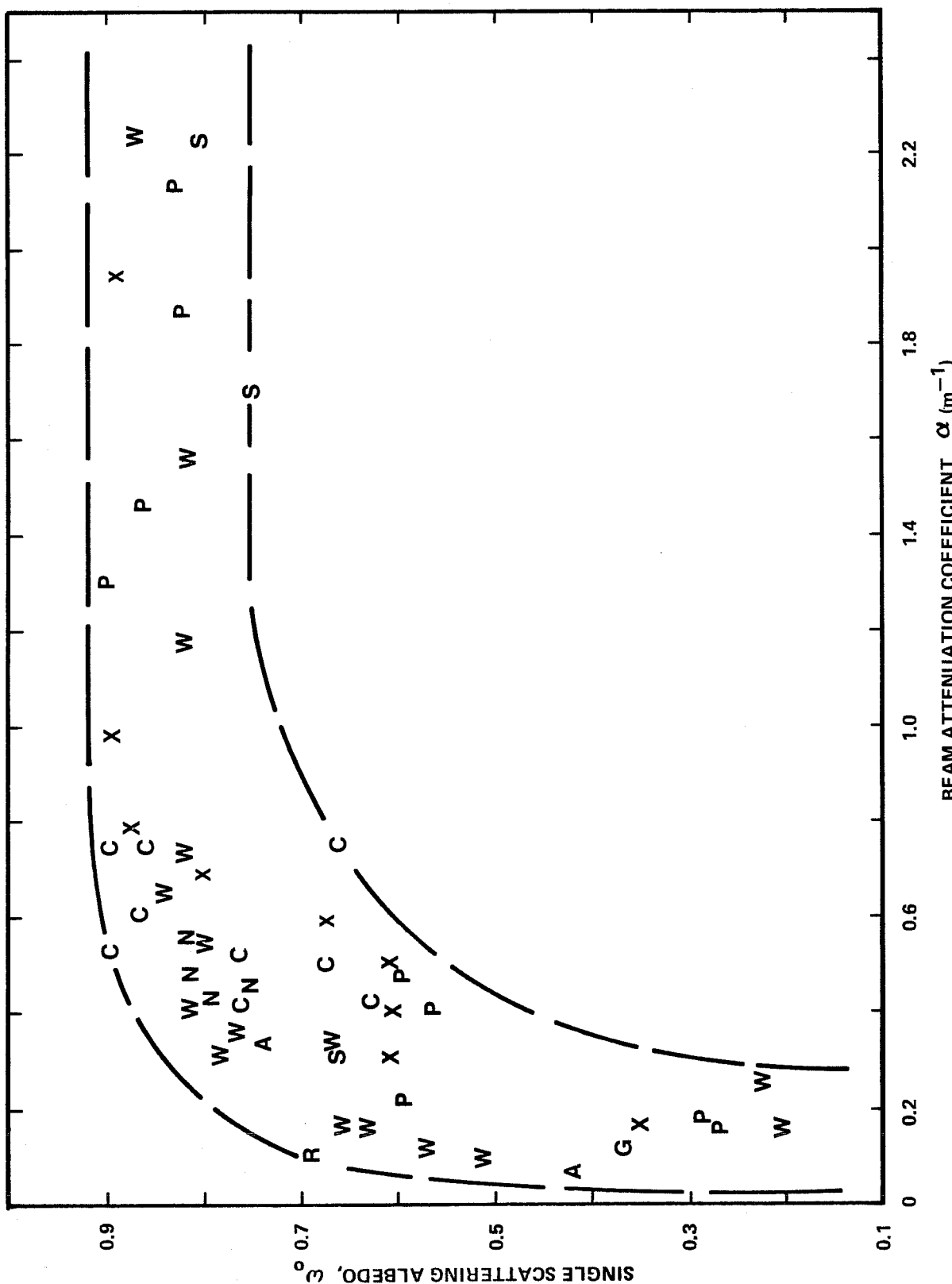


FIGURE 3-8. NATURALLY OCCURRING VALUES OF ω_0 VS. α

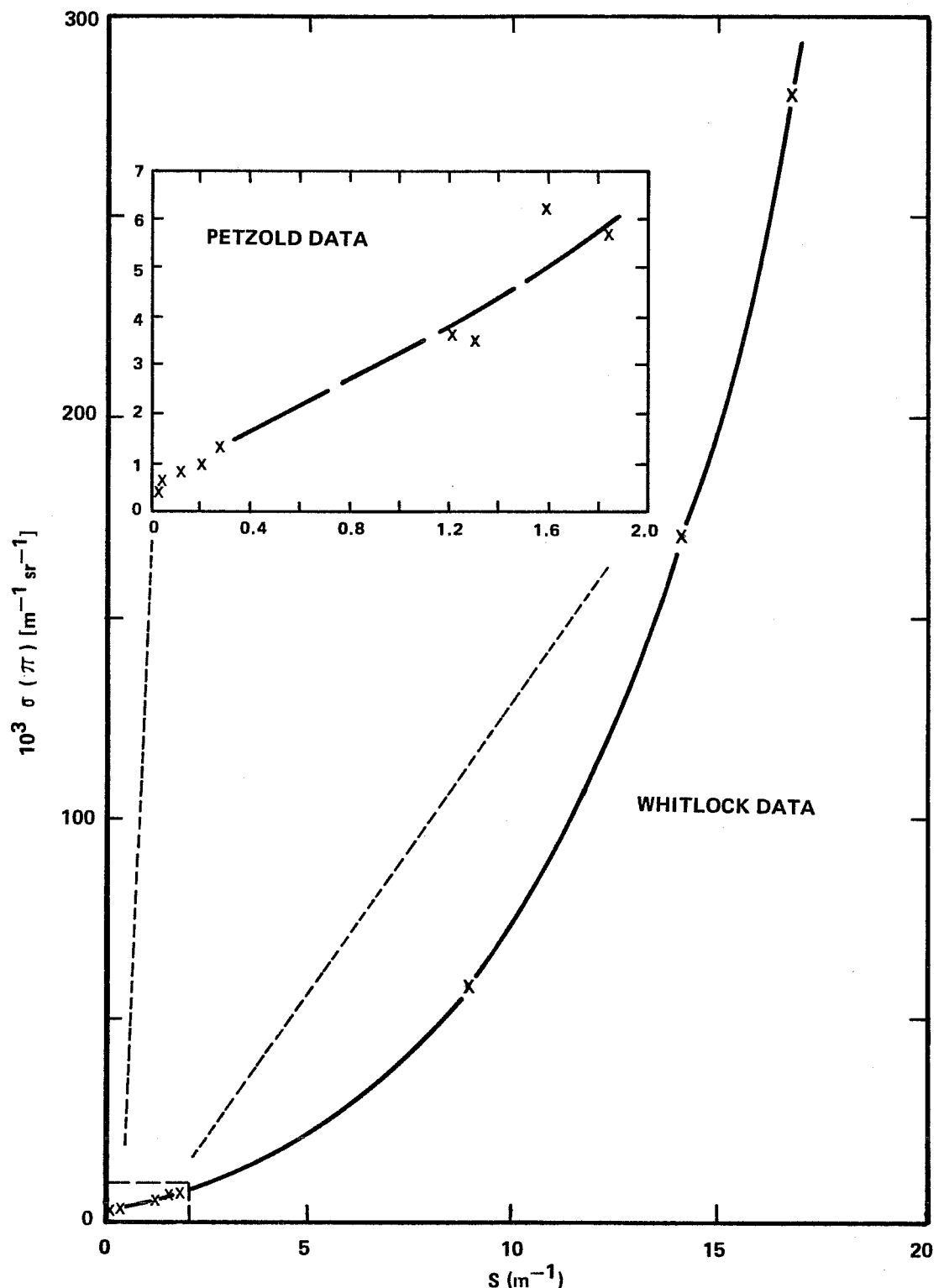


FIGURE 3-9. VOLUME SCATTERING FUNCTION AT 180° VERSUS SCATTERING COEFFICIENT

3.7 References

- Baker, K.S. and Smith, R.C., 1979: Quasi-Inherent Characteristics of the Diffuse Attenuation Coefficient for Irradiance. Proceedings of SPIE Ocean Optics VI, Vol. 208, Oct. 23-25, 1979, Monterey, Calif., 60-63.
- Duntley, S.Q., 1971: Underwater Lighting by Submerged Lasers and Incandescent Sources. SIO Ref. 71-1, Scripps Institution of Oceanography Visibility Laboratory, Univ. of Calif. San Diego, San Diego, Calif., 290 pp.
- Gordon, H.R., Brown, O.B., and Jacobs, M.M., 1975: Computed Relationships Between the Inherent and Apparent Optical Properties of a Flat Homogeneous Ocean. Appl. Opt., 14, 2, 417-427.
- Gordon, H.R. and Wouters, A.W., 1978: Some Relationships Between Secchi Depth and Inherent Optical Properties of Natural Waters. Appl. Opt., 17, 21, 3341-3343.
- Gordon, H.R., Smith, R.C., and Zaneveld, J.R.V., 1979: Introduction to Ocean Optics. Proceedings of SPIE Ocean Optics VI, Vol. 208, Oct. 23-25, 1979, Monterey, Calif., 15-55.
- Guenther, G.C. and Thomas, R.W.L., 1981: Monte Carlo Simulations of the Effects of Underwater Propagation on the Penetration and Depth Measurement Bias of an Airborne Laser Bathymeter. NOAA Technical Memorandum OTES 01, National Oceanic and Atmospheric Administration, U.S. Dept. of Commerce, Washington, D.C., 142 pp.
- Jerlov, N.G., 1976: Marine Optics. Elsevier Scientific Pub. Co., Amsterdam.
- Petzold, T.J., 1972: Volume Scattering Functions for Selected Ocean Waters. SIO Ref. 72-78, Scripps Institution of Oceanography, Visibility Laboratory, San Diego, Calif., 79 pp.

Phillips, D.M., Abbot, R.H., and Penny, M.F., 1984: Remote Sensing of Sea Water Turbidity with an Airborne Laser System. J. Phys. D: Appl. Phys. (Great Britain), 17, 8, 1749-1758.

Pilgrim, D.A., 1984: The Secchi Disk in Principle and in Use. The Hydrographic Journal, 33, July, 25-30.

Shannon, J.G., 1975: Correlation of Beam and Diffuse Attenuation Coefficients Measured in Selected Ocean Waters. SPIE Ocean Optics, Vol. 64, 3-11.

Timofeyeva, V.A. and Gorobets, F.I., 1967: On the Relationship Between the Attenuation Coefficients of Collimated and Diffuse Light Fluxes. Isv., Atmospheric and Oceanic Physics (Acad. of Sci. USSR), 3, 291-296 (166-169 in trans.).

Witt, A.K., Shannon, J.G., Rankin, M.B., and Fuchs, L.A., 1976: Air/Underwater Laser Radar Test Results, Analysis, and Performance Predictions. Report No. NADC-76005-20. Naval Air Development Center, Warminster, Pa., 293 pp. (CONFIDENTIAL).

4.0 BASIC CONCEPTS AND SYSTEM DESIGN

A typical airborne system consists of a pulsed blue-green laser transmitter, a scanning mirror, a receiver telescope, a narrow-band optical filter to suppress daylight background, a photomultiplier tube (PMT) detector, signal conditioning electronics, a waveform digitizer or real-time signal processor for depth determination, and a master control computer. The survey area consists of a wide swath under the aircraft sampled at discrete points as the pulsed beam is scanned according to some fixed pattern.

Depth measurements are based on the differential arrival times of the reflections of the laser beam from the air/water interface or "surface" and the sea floor or "bottom". The idealized geometry for timing is that a small portion of the beam is reflected from the surface while the remainder is refracted through the surface, traverses the water column along a slanted path, is diffusely reflected by the bottom, again traverses the water column (along the same slant path), and refracts back through the surface toward the receiver. The depth is calculated by halving the round-trip time in the water and correcting for the off-nadir geometry of the scanner.

The actual geometries, however, are far more complex due to physical interactions both at the surface and in the water column.

4.1 Basic Physical Concepts

4.1.1 Propagation Geometry

The propagation geometry associated with airborne laser hydrography is illustrated in Fig. 4-1. When a laser pulse is incident on the surface of a body of water, a fraction (less than 2 percent) is reflected back into the air and may be sensed by the receiver as the "surface return". The magnitude of the peak interface return power is a strong function of off-nadir beam entry angle and the wind speed as seen in Fig. 4-2 (Petri 1977). These effects are discussed in detail in section 7.2. Interface reflection at off-nadir angles to a receiver colocated with the transmitter requires the presence of wind-generated capillary waves which present tiny "facets" perpendicular to the

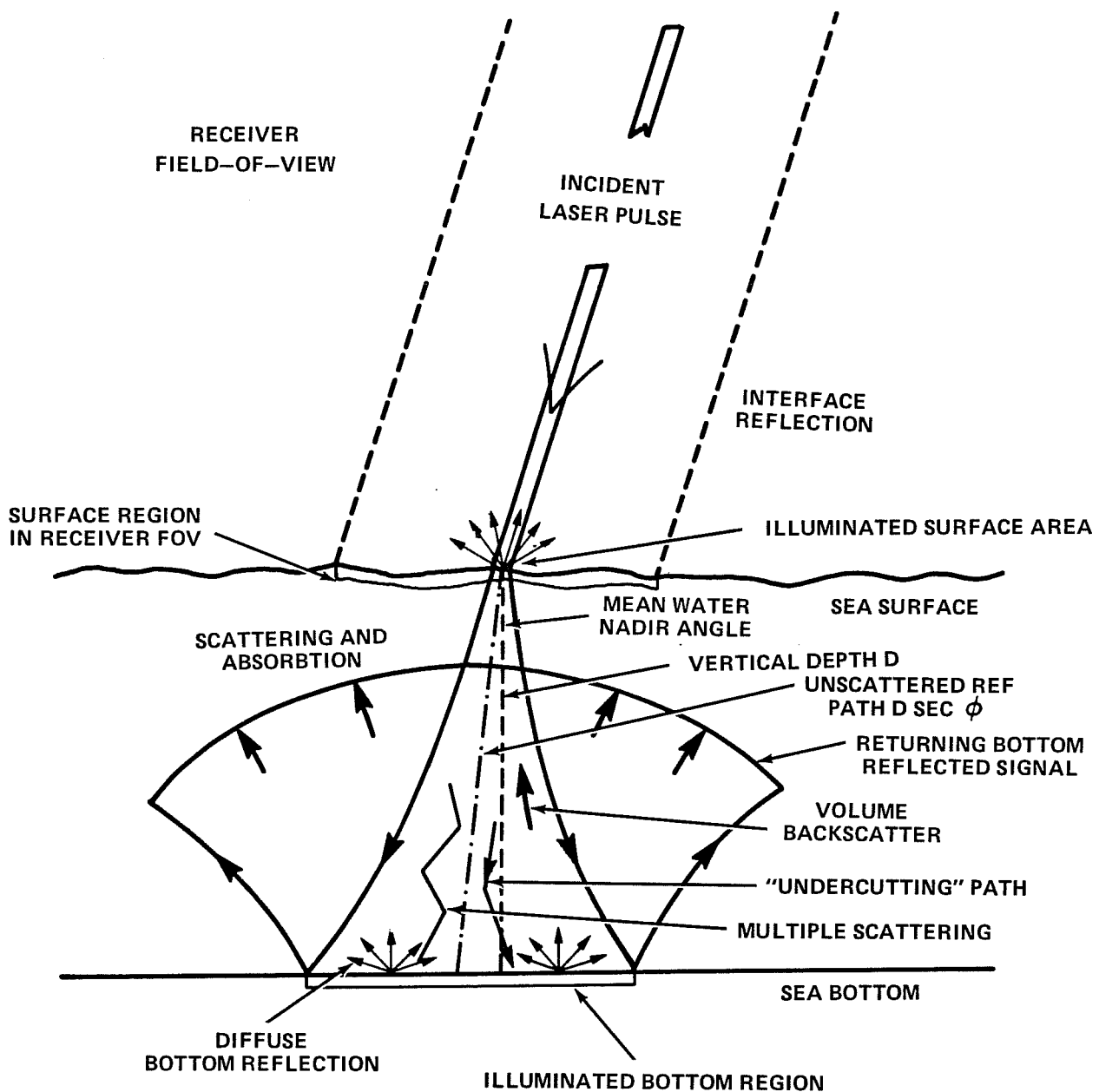


FIGURE 4-1. MEASUREMENT GEOMETRY

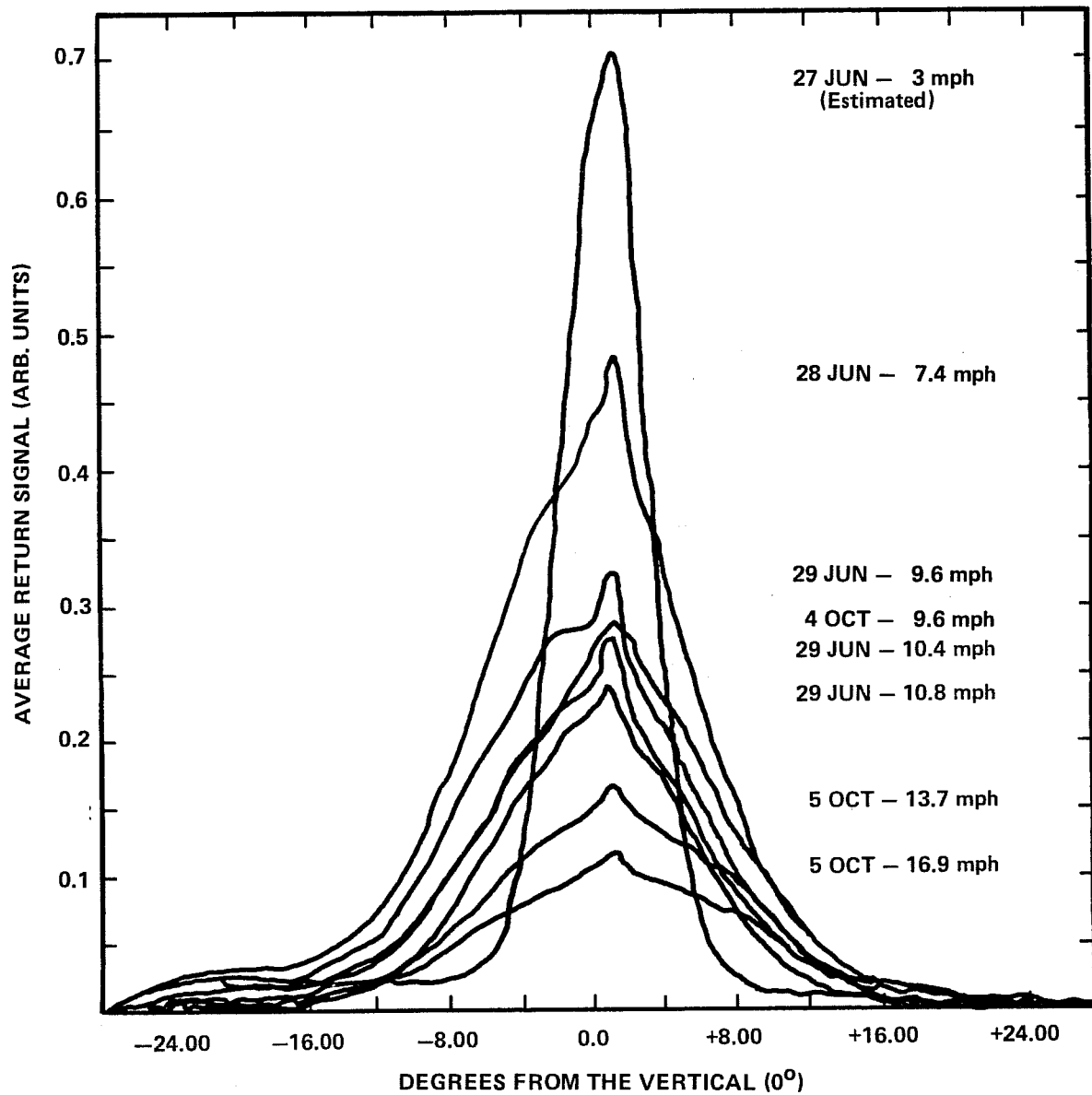


FIGURE 4-2 . NORMALIZED AVERAGE RETURN SIGNAL VS. SCAN ANGLE
(PETRI, 1977)

incident beam. If the necessary facets are absent due to insufficient wind speed for the selected scan angle, the interface return will not be received.

Instead, the first return will come from volume backscatter in the water column (section 7.4). For a green beam this can result in a serious depth measurement bias if the origin of the return is misidentified (section 9.2.2). A potential solution to this problem for Nd:YAG lasers is the transmission of the undoubled infrared (IR) beam colinearly with the frequency-doubled green beam. The IR return from the interface can be detected by a separate receiver channel. Because penetration in the IR is much less than in the green, the depth measurement bias due to a volume return, if it is strong enough to detect, would be small enough to ignore within the error budget. The magnitude of the IR volume return will be less than the green, but may still be detectable. If not, operation would have to be curtailed when the wind is calm and insufficient capillary waves are excited.

In order for the system to meet accuracy requirements, depth variations caused by surface waves must be reduced. Gravity waves at the surface introduce depth measurement errors both directly by their presence and by their modulation of the direction of the refracted beam to the bottom. The former wave height effects can be significantly reduced through the use of the laser altimetry data, while the latter "beam steering" errors, which are larger for larger scanner angles and are probably uncorrectable, will be seen to fit within the error budget (section 9.2.3). Wave correction can be accomplished by measuring the slant altitude to the local surface for each pulse and differencing this from the expected slant altitude (which is calculated from scan pattern, aircraft roll and pitch, and a mean sea level model constructed from previous pulses). Each altitude difference, corrected for aircraft motion and nadir angle, is assumed to be caused by waves and is applied as a corrector to the measured depth of the water column to yield an estimate of the mean water depth. Wave correction is discussed in more detail in sections 5.7.2 and 9.2.5.

Winds in excess of 15-20 knots (depending on fetch and duration) will cause a halt to operations due to many undesirable effects such as poor water clarity from resuspension of bottom sediments, whitecaps and foam on the

surface, loss of precision in the wave correction procedure, and larger beam steering errors. Typical wind speed distributions for various East Coast and Gulf Coast sites are shown in Fig. 4-3 (Scott 1982). The probabilities of daily operations calculated for these sites (based on wind, fog, and precipitation) are acceptably high, as seen in Fig. 4-4.

The remaining portion of the green laser pulse is refracted into the water column where scattering and absorption from entrained microscopic particulates cause it to spread out into a cone of continuously increasing angle, as seen in Fig. 4-5. Incident laser beam divergence is expected to be selected at a value less than ± 0.5 degrees. It can be shown geometrically that at the surface, the angular deviation of a ray in the water due to a wave slope is equal to one quarter of the wave slope angle. Average wave slopes for 10-20 knot winds are typically $\pm 10-15$ degrees (Cox and Munk 1954); this results in angular deviations of the refracted beam at the surface on the order of $\pm 3-4$ degrees. Measurements of beam spreading in water due to scattering (Duntley 1971) indicate significant net transport over much larger angles. The relative contributions to the total beam spreading angle are thus as depicted in Fig. 4-6 where it is clear that scattering in the water column is the dominant effect (see also Bobb et al. 1978).

A small fraction of the transmitted energy, whose magnitude decreases exponentially with optical depth, becomes incident upon the bottom with a lateral extent which depends on optical depth and single-scattering albedo, as seen on the left-hand axis in Fig. 4-7. Bottom distribution diameters have been calculated for 50% (d_{50}) and 90% (d_{90}) of the total energy. For optical depths of interest to coastal hydrography, the energy spreads out to diameters which are significant fractions of the water depth. For typical operating circumstances, the 3-dB diameter (d_{50}) at the bottom is equal to roughly half the water depth, and the effective beam width is thus on the order of 28 degrees. Although this is broader than the beams from many current sonar systems, it is not expected to pose a problem in the relatively shallow water of interest. Features very small compared to the depth may not be fully resolved, but most items of such size are now missed altogether because they fall between the sonar lines. Slightly greater resolution could be gained by operating with a sub-optimum receiver field of view, but only with a

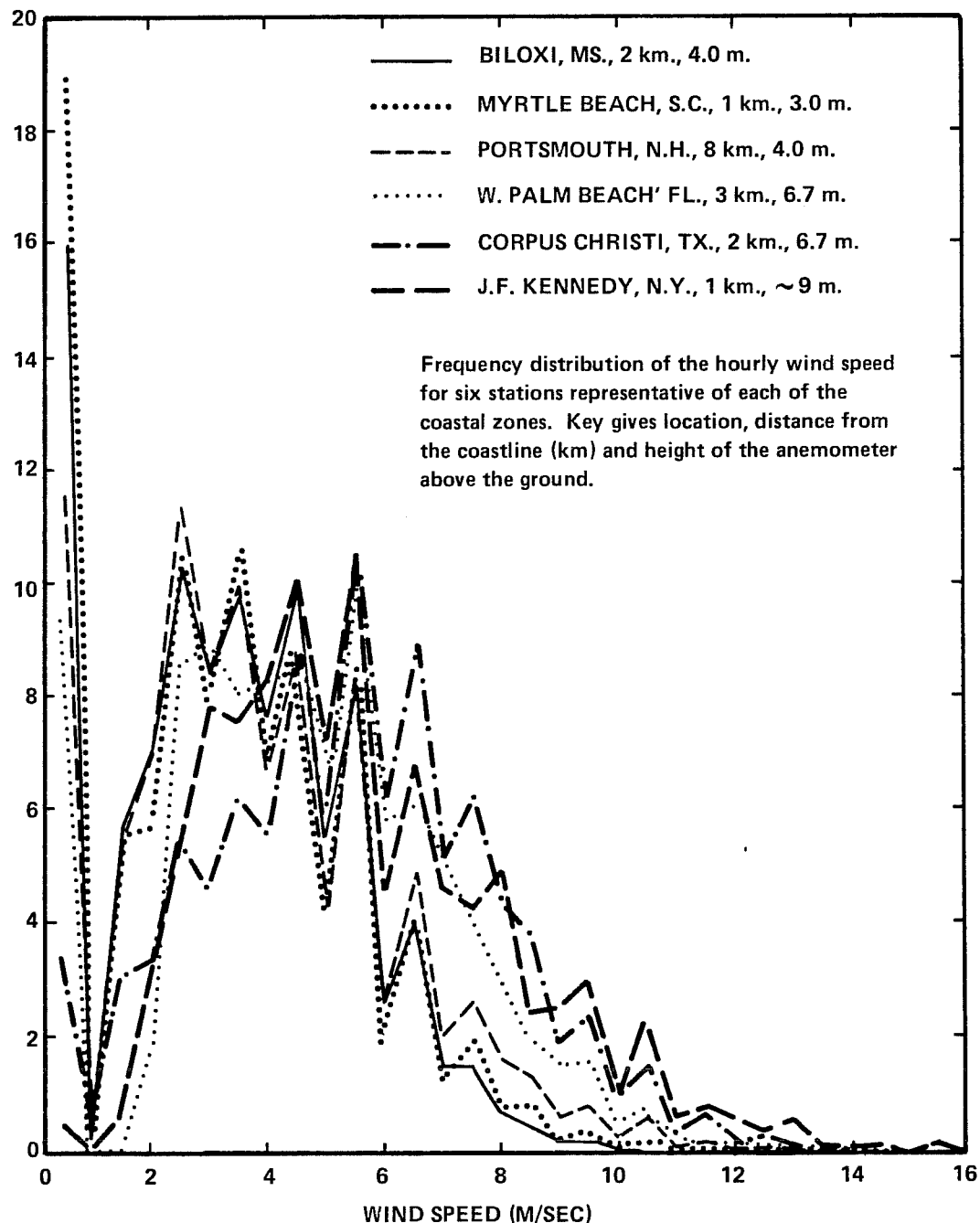


FIGURE 4-3 . WIND SPEED FREQUENCY

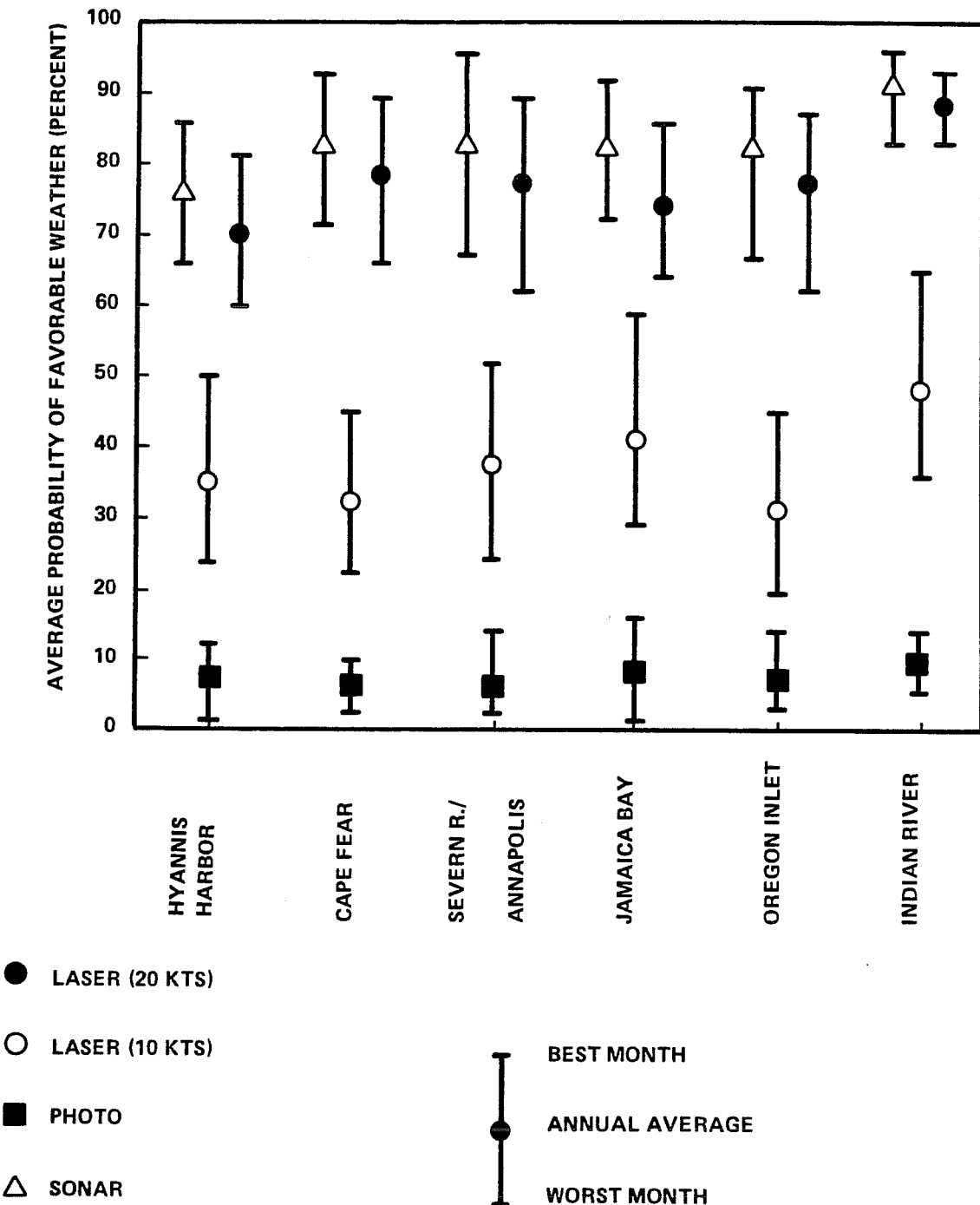


FIGURE 4-4. OCCURRENCE OF FAVORABLE WEATHER

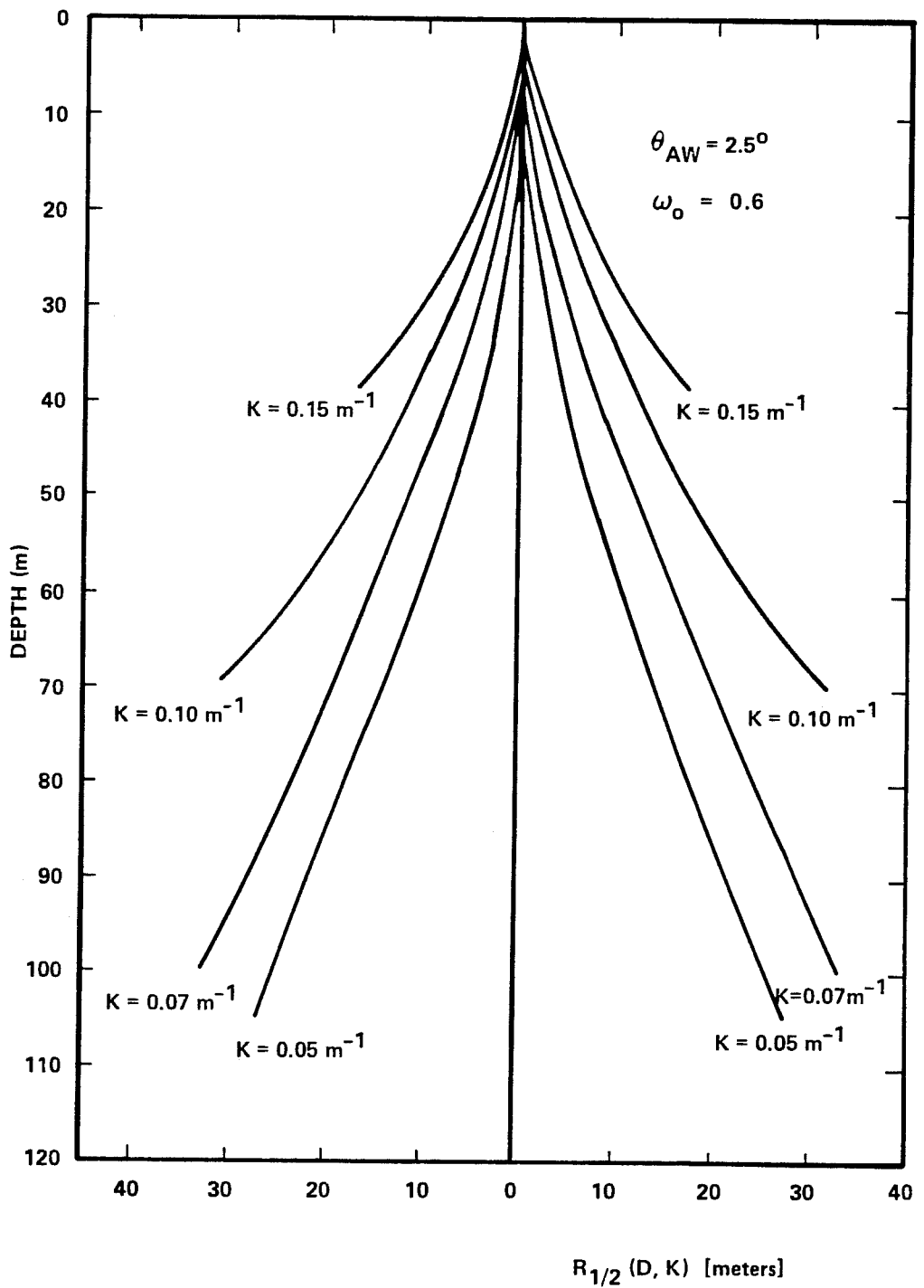


FIGURE 4-5. BEAM HALF-ENERGY RADIUS VS. DEPTH FOR "CLEAR" OCEAN WATERS (NADC)

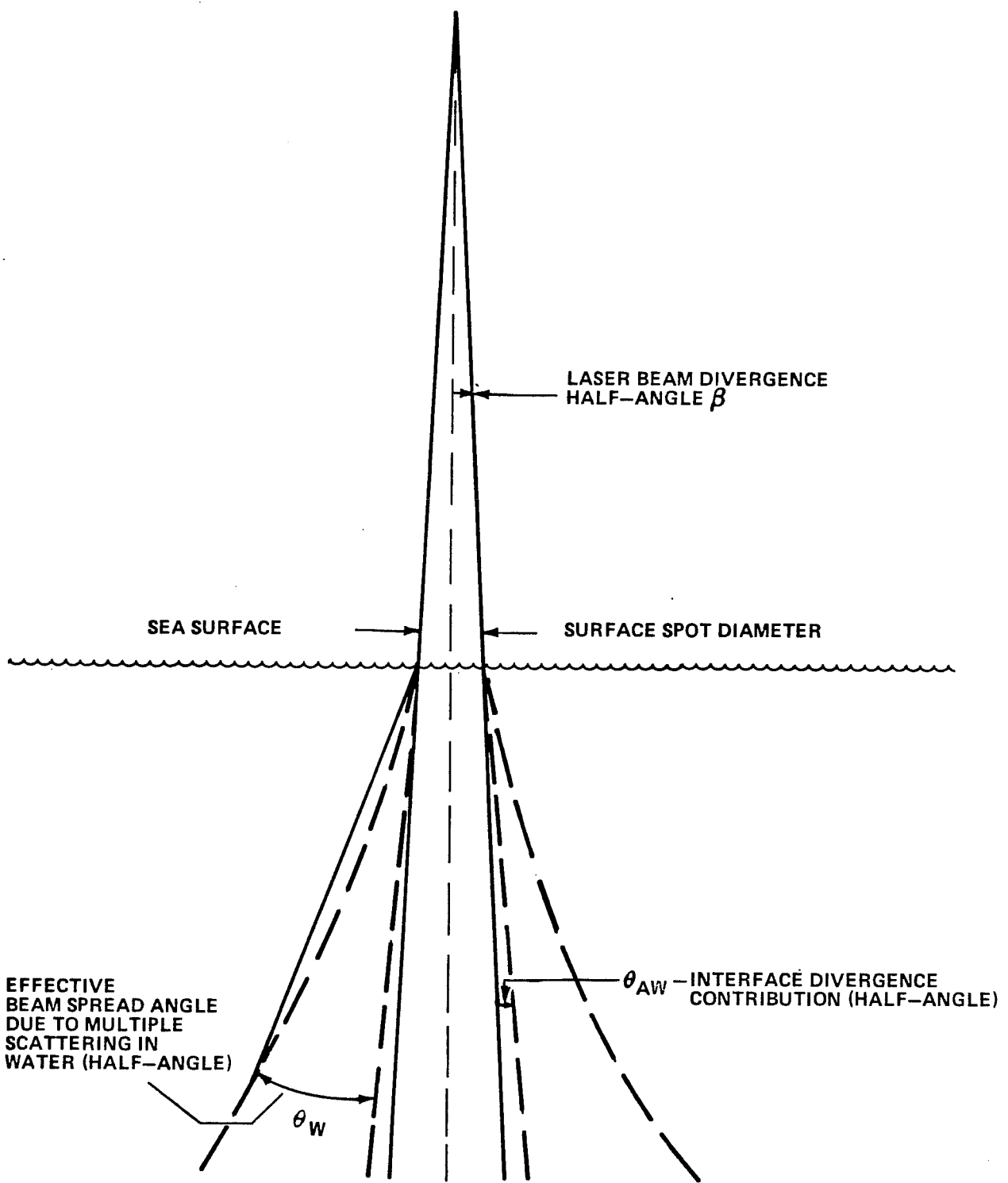


FIGURE 4-6. CONTRIBUTIONS TO BEAM SPREADING

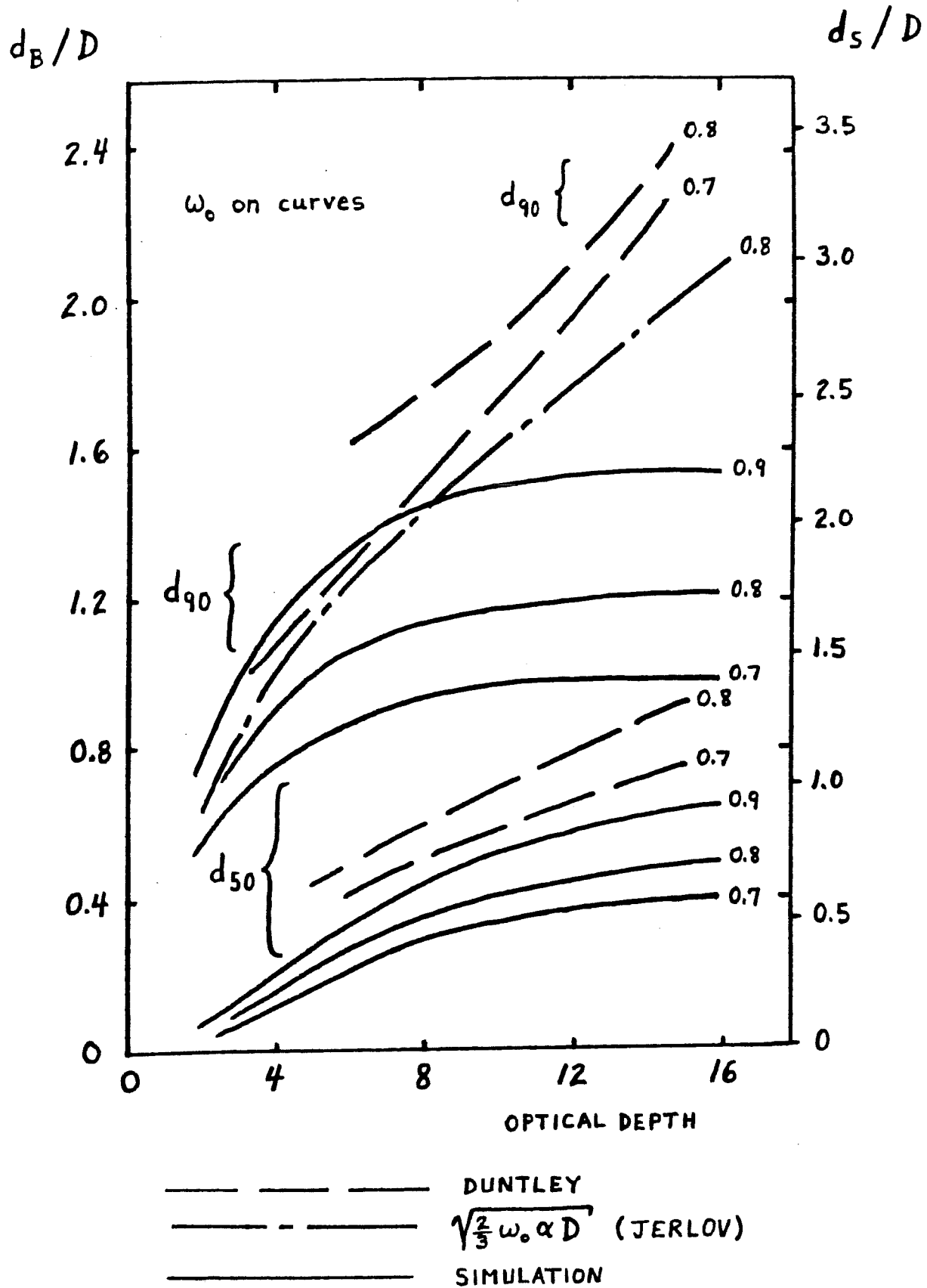


FIGURE 4-7. BOTTOM AND SURFACE DISTRIBUTION DIAMETERS
FOR SELECTED ENERGY FRACTIONS

corresponding loss in signal strength and penetration potential. By integrating cartesian strips perpendicular to the down-beam direction, it can be seen (Fig. 4-8) that the peak of the energy distribution for off-nadir entry is skewed slightly toward the aircraft due to the shorter (and hence less attenuated) paths of the photons undercutting the unscattered ray, as noted in Fig. 4-1.

A portion of the energy incident on the bottom (typically 4-15 percent depending on the bottom composition) is reflected in a more or less diffuse manner (Lambertian distribution) from the bottom back into the water column. Scattering and absorption processes again attenuate and stretch the pulse as it passes back to the surface where much of the remainder is refracted into the air. The airborne optical receiver can then intercept a small fraction of this returning, bottom reflected energy (whose magnitude depends on aircraft altitude, water depth and clarity, receiver aperture, and receiver field of view) and interpret it as the "bottom return".

Reciprocity (Chandrasekhar 1960) is a statement of symmetry or reversibility which, when applied to airborne lidar geometry, requires that the ensemble of viable scattering paths in the water be identical for downwelling and upwelling radiation, because the exiting photons must leave the medium in the opposite direction from which they entered in order to reach the receiver colocated with the laser source. In other words, reciprocity requires that the statistical ensemble of upwelling paths in the direction of a distant receiver for photons reflected at the bottom be identical to that for downwelling paths from a colocated transmitter. This is not a declaration that the downwelling and upwelling paths are physically identical, but rather that a single set of photon tracks can be regarded as representative for both cases. The subset of the downwelling paths utilized by upwelling radiation is determined by the weighting function of the bottom reflection. For Lambertian reflection, the difference is negligible because the arrival distribution is very similar. For this reason, the effective attenuation coefficient of the signal energy reaching a distant, airborne receiver is the same for both upwelling and downwelling directions, contrary to statements about separate downwelling and upwelling coefficients in Levis et al. (1974) and Measures (1984).

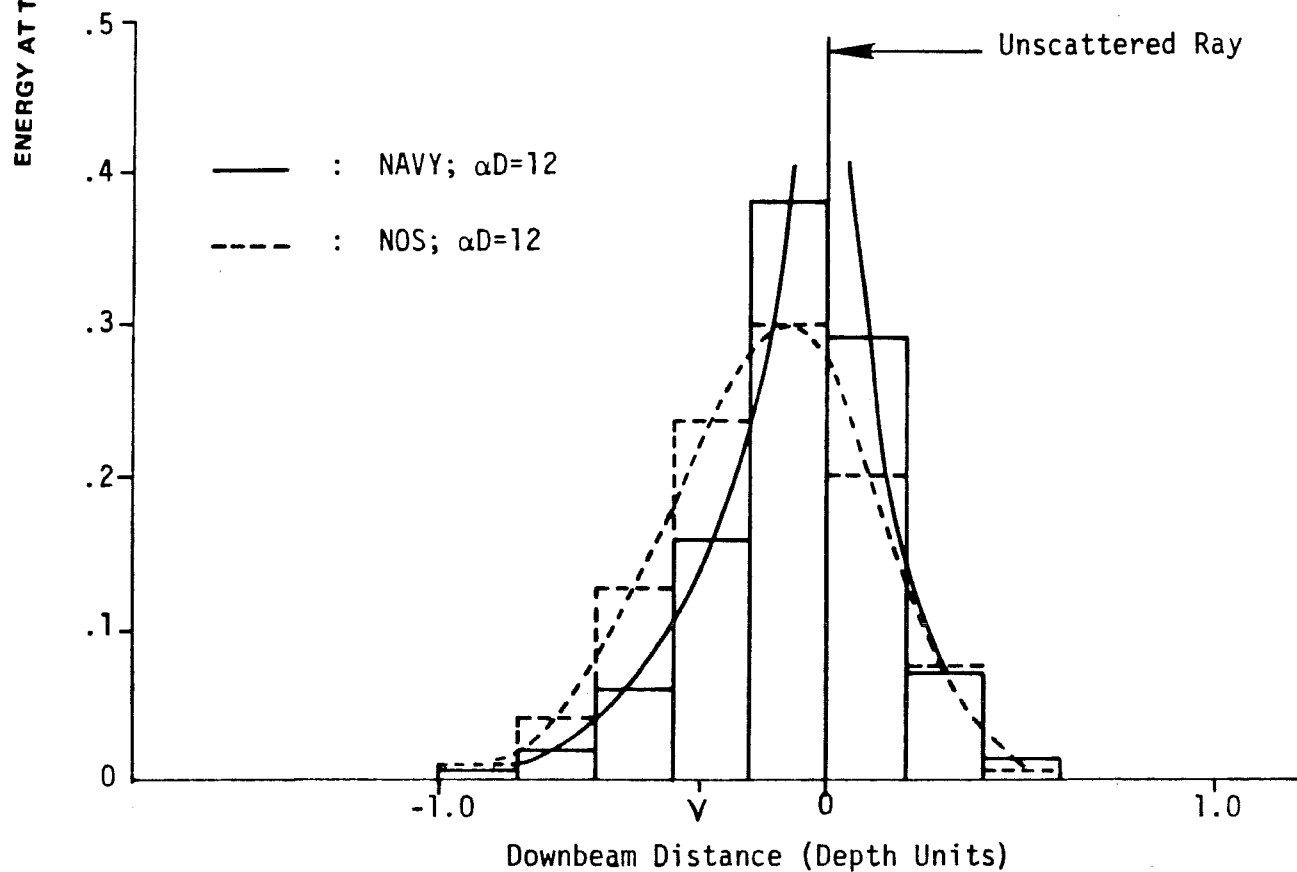
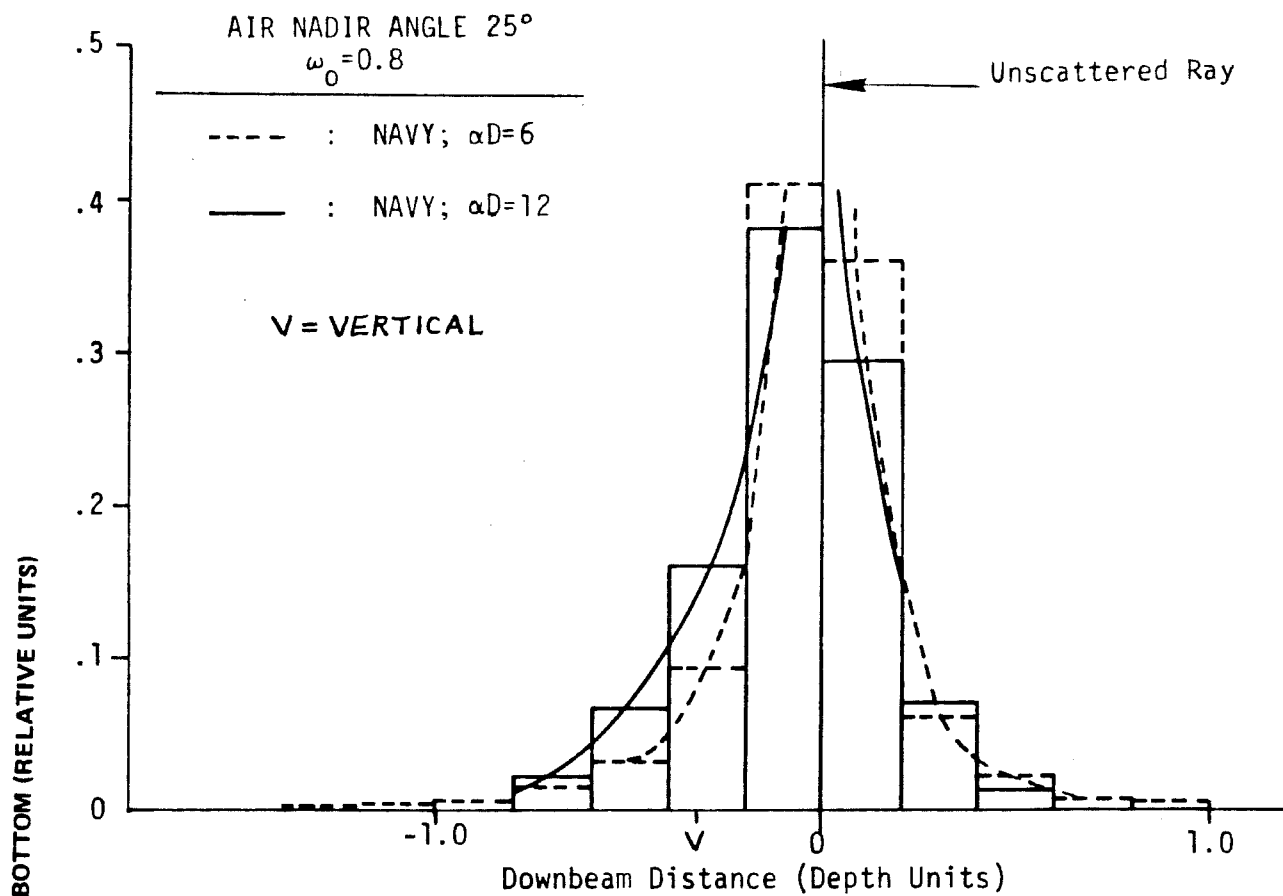


FIGURE 4-8. SPATIAL DISTRIBUTION OF PULSE ENERGY AT THE BOTTOM

Geometric dispersion and multiple scattering lead to temporal stretching of the received pulses. Because the returning energy comes from a fairly broad spatial distribution, the received pulse may be considerably longer than that transmitted. Its shape will be characterized by a power-law leading edge and a long tail, as seen in Fig. 4-9. This results in a drop in the peak power (for a given pulse energy) and depth measurement biases whose magnitudes depend strongly on the scanner nadir angle, the depth, water optical properties, and the pulse location algorithm. Leading edge pulse locators are required in order to minimize the resulting tendency for a depth measurement bias toward deeper depths. The energy returning late (in the tail) thus serves no useful purpose. This fact has strong bearing on the receiver field-of-view requirement and on the perception of what portion of the bottom energy distribution is "effective" in terms of a hydrographic sounding, i.e., the spatial resolution. Biases due to propagation-induced pulse stretching have been predicted by Monte Carlo computer simulation (Guenther and Thomas 1981 and 1984) and are discussed at length in section 9.2.1. These bias predictions can be used with field data as bias correctors if the driving input variables are known or can be estimated or if operation of the system is limited to certain parameter ranges for which the bias variation with unknown water optical properties is acceptably small.

From Fig. 4-1, one can see that bottom reflected upwelling energy spreads out widely in all directions in the water and is refracted into the entire upper hemisphere of air. In order to be detected, however, a fraction of that energy must be refracted in the direction of the airborne receiver. An airborne optical receiver will sense the bottom reflected energy returning through the water/air interface as an apparent energy source of a certain "diameter" at the water's surface. By invoking reciprocity, it can be seen that the effective surface diameter of bottom returning energy is the diameter of the autoconvolution of the bottom distribution. This will be larger than the diameter of the distribution at the bottom by roughly $\sqrt{2}$, as seen on the right-hand axis in Fig. 4-7. As noted in Guenther and Thomas (1984) and in section 8.2.5, the half energy diameter (d_{50}) is the minimum size of the surface area which should be encompassed by the receiver field of view for optimum penetration.

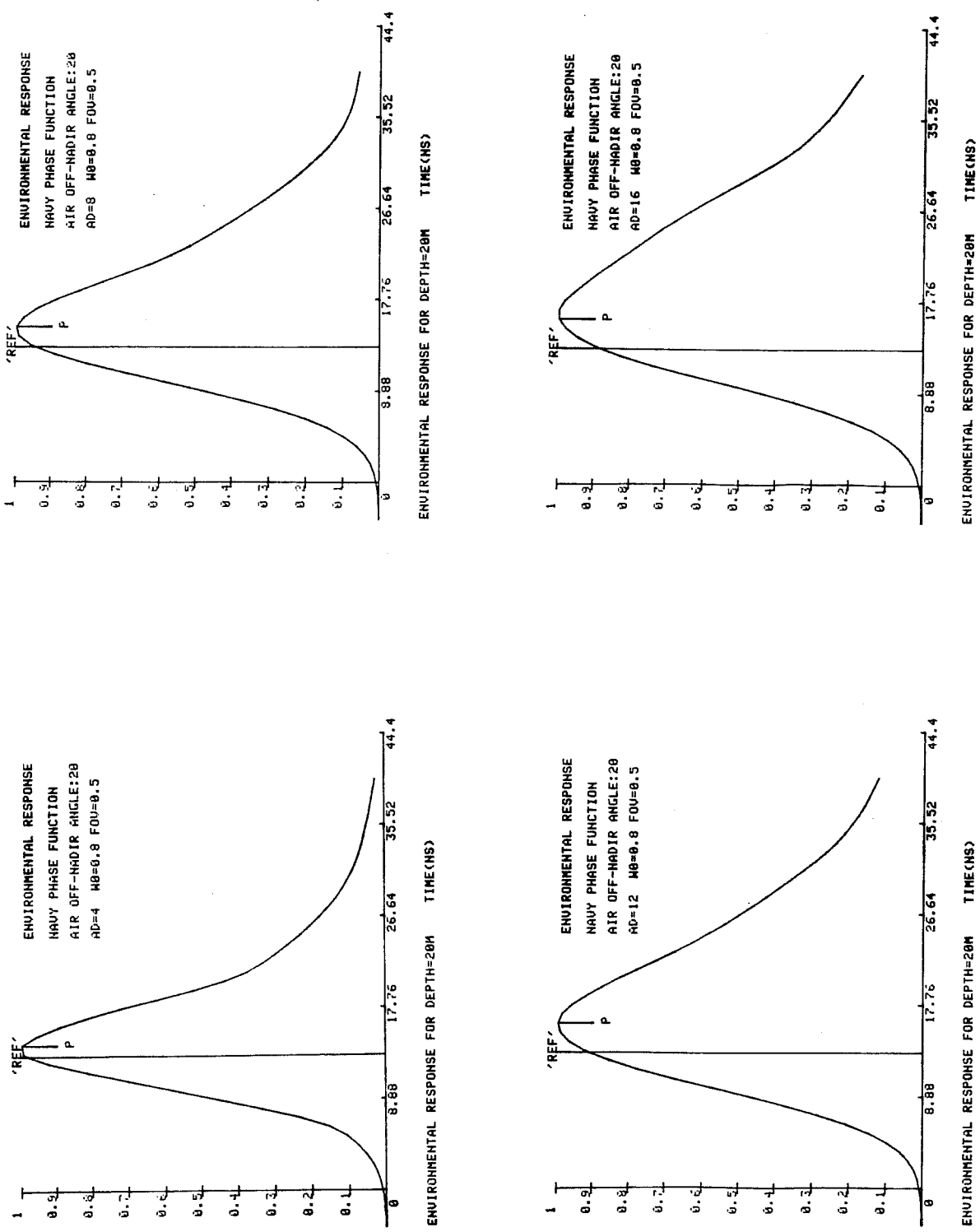


FIGURE 4-9. ENVIRONMENTAL RESPONSE FUNCTIONS
FOR VARYING OPTICAL DEPTHS

It is noteworthy that an airborne laser system can be used to detect schools of fish. It is quite possible that when large schools are irradiated, anomalously shallow, "false" returns could be received which would require editing. Bottom vegetation will also present an interesting signal processing challenge.

4.1.2 Return Waveform

A typical waveform of the returning pulse energy is shown in Fig. 4-10. Four signals are of major importance: the surface return, the volume backscatter return, the bottom return, and the background noise level. For an arrival time difference, Δt , between the detected surface and bottom returns, the estimated vertical water column depth (to first order) is $\frac{1}{2} c \Delta t \cos\phi$, where c is the speed of light in water (0.225 m/ns), and ϕ is the nadir angle in the water of the refracted pulse (of the unscattered ray at the surface neglecting wave effects).

The magnitude of the true surface (interface) return, which depends strongly on nadir angle and wind speed as noted in Fig. 4-2 and section 7.2, can be as much as seven decades stronger than a weak bottom return. This extreme amplitude dynamic range variation occurs within a time period of only tens or hundreds of nanoseconds. This causes the returning waveform to be very difficult to process and leads to undesirable side-effects such as spurious responses in the PMT and electronics. The shape and duration of the interface return are similar to the transmitted laser pulse -- except for a bit of stretching from waves. It is of the utmost importance that the trailing edge decay of the transmitted pulse be more rapid than the volume backscatter decay rate for the dirtiest water of interest. If this is not true, the tail of the interface return will be the dominant noise source and will cause greatly decreased penetration capability. In order to insure a clean and short trailing edge, the laser must be Q-switched, and an additional Pockels cell timed to decisively terminate the pulse may be desirable. For two-color systems, the green surface return should be heavily attenuated, preferably before the PMT, in order to reduce the amplitude dynamic range in the green receiver.

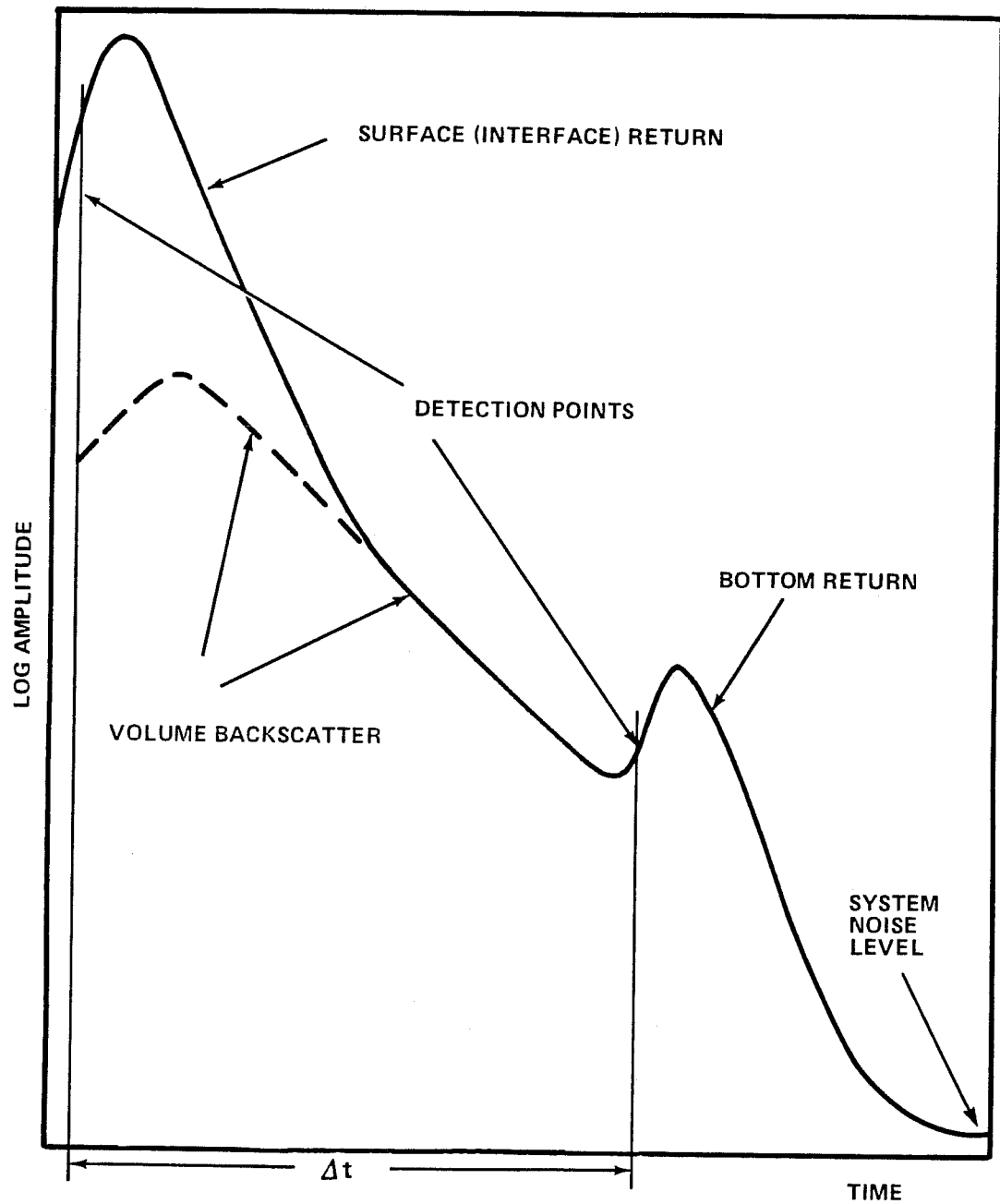


FIGURE 4–10. IDEALIZED BATHYMETRIC WAVEFORM

The peak of the volume backscatter occurs at a time between one and two times the interface return peak time (measured from the time of leading edge incidence), depending on water clarity, as seen in section 7.3. The peak magnitude is linearly proportional to the value of the volume scattering function at 180° and thus proportional to the scattering coefficient, as seen in section 3.6. The decay of the volume backscatter signal is basically exponential in time. It has been believed that the exponential decay rate for sufficient receiver field of view is equal to cK , where K is the diffuse optical attenuation coefficient (Witt et al. 1976, Gordon 1982). Based on Monte Carlo results, Phillips and Koerber (1984) propose a slightly smaller limiting value, a_c , where "a" is the absorption coefficient. Receiver field-of-view effects cause the actual slope to be somewhat larger; hence a practical value remains close to cK . In the absence of an interface return (low wind and/or high nadir angle), the peak of the volume backscatter may be detected as the "surface" return but, as noted, it does not occur at the same time as the interface return and will yield a biased depth result whose magnitude depends on the pulse width and wavelength (color). This problem must be recognized and properly handled (see section 9.2.2) in order to maintain required accuracy.

In shallow water, the surface and bottom returns merge. In order to measure the shallowest possible depths (under 2 m), some sort of merged pulse-width dependent depth algorithm would have to be developed. The need for extremely shallow water performance should be established by the user community before complicated and expensive procedures are invoked.

The magnitude of the propagation-stretched bottom return, for a typical source pulse and sufficient receiver field of view, as derived in section 8.2.2, depends exponentially on the KD product and decays exponentially in the time domain with a rate nCK , where n is a factor which depends to a limited extent on water optical properties but is roughly equal to 1.25 for practical applications. KD is a unitless parameter similar in character to the optical depth, αD , and may be considered as the "diffuse optical depth". The bottom return magnitude also exhibits inverse-square law behavior with slant altitude and linear behavior with other factors such as receiver aperture, bottom

reflectivity, etc. The primary loss factors are scattering and absorption in the water column.

For an airborne laser system, the maximum water depth from which useable bottom returns can be received is dictated by the transmitter pulse energy, the losses in the system and environment, and the dominant noise level. Extinction, i.e., loss of a useable signal, occurs as the bottom return sinks into the noise level. During the daytime, the solar radiation backscattered from the water column is prohibitively strong, and a very narrow-bandwidth "interference" filter centered on the laser wavelength is required to attenuate solar energy at all other wavelengths. Specular reflection of sunlight from the surface, i.e., the sun glint pattern, is far too strong even with a narrow bandwidth filter, and must be carefully avoided by flying at appropriate times of day if the latitude is low enough to cause the problem. The daytime limiting noise background, which is the volume reflected solar radiation inside the interference filter bandwidth, is typically several decades greater than the dark current in the PMT.

Nighttime operation is preferred (but by no means required) due to the lower background noise level and consequently increased penetration potential. The nighttime background level for a properly designed system will be the sum of the dark current of the PMT and thermal "Johnson" noise. For optimal nighttime operation, moon glint would best be avoided, particularly if the interference filter is removed, and the receiver electronics should be designed to be as close as possible to being shot-noise limited. From the above expressions it can be seen that the bottom return peak power is believed to decay exponentially at a rate slightly greater than that of the volume backscatter. This means that volume backscatter can be a limiting noise source for nighttime operation.

Because of the large attenuation and spreading of the light beam in water, airborne laser hydrography is limited to shallow water. Maximum penetration for given water conditions and aircraft altitude is dictated by the amount of pulse energy available at a high repetition rate from state-of-the-art lasers (up to eye-safety limitations which depend on altitude and transmitter divergence per sections 8.2.4 and 10.3). Penetration in murky

harbor or bay waters may be less than 10 m. Only in moderately clean waters will daytime depths beyond 30 m be regularly accessable, and 40-50 m (depending on the bandwidth of the interference filter) is probably a practical upper limit even for extremely clean water (section 8.5). Penetration at night could be as much as 60-70 m in extremely clean water, but this would be rare. There is a great deal of required survey area within these depth bounds where waterborne techniques are very slow and expensive. The prime benefits of airborne laser hydrography are the speed and economy with which these accessible shallow areas can be surveyed.

4.2 System Design and Parameterization

In order to cover a large area with soundings, the pulsed laser beam must be scanned away from the nadir to cover a swath below the aircraft. The scanner "pattern" on the surface is, of itself, not particularly important as long as the spatial density of the pulses is moderately uniform; but the range of beam entry nadir angles selected is of major importance to overall system performance, and the selection must not be made arbitrarily. One pattern which fulfills many requirements is the walking oval pattern from the nutating mirror used in the AOL and in the proposed HALS (see drawing in section 5.3). The major drawback, particularly when aircraft roll and pitch are considered, is that the range of nadir angles around a scan is larger than desirable for minimizing propagation-induced depth measurement biase errors when a "passive" bias correction scheme is used (Guenther and Thomas 1984 and section 9.2.1). An ideal scanning concept is a mirror gimballed in two axes by computer controlled servos which can utilize fed-back aircraft attitude information to automatically remove roll and pitch from the beam and produce a truly constant scan angle. A practical problem is that such a scanner can produce a great deal of vibration. The effects of the beam nadir angle on penetration and accuracy will be described in detail in following sections. Design criteria for the scanner nadir angle are compiled in section 10.2.

The pulse repetition rate, $r = 2\rho Hv \tan\theta$, is dictated by the desired sounding density, $\rho(\text{soundings}/\text{m}^2)$, and the swath area covered per unit time, $2Hv \tan\theta$, where H is the aircraft altitude, v is the aircraft speed, and θ is the wing-to-wing nadir angle. Because the cost-benefit for the overall technique is proportional to coverage rate (Enabnit et al. 1978), a reasonably

wide swath (on the order of 200 m) is desirable. Due to practical limitations on maximum off-nadir angle of roughly 15-25 degrees (depending on signal processing and pulse location algorithms) as detailed in sections 9.2 and 10.2, the 200-m swath width requires a minimum altitude of about 300 m. This is twice the value of 150 m at which pilots can safely fly during the daytime but about the minimum safe altitude preferred for night flights.

The average analog inverse sounding density for the NOAA Hydroplot sonar survey system is roughly $50 \text{ m}^2/\text{pulse}$ in detailed surveys, but only a small fraction of the soundings are digitized. Because the sonar soundings are very dense along sounding lines but much less dense from line to line, this does not provide an "equivalent" set of hydrographic information as a more-or-less uniformly sampled grid with the same average density. An inverse density of $50 \text{ m}^2/\text{sounding}$, for example, would require a 300/sec pulse repetition rate for a 200-m swath width at an aircraft speed of 150 kts. This is currently near state-of-the-art for frequency-doubled Nd:YAG lasers whose output energies are at least 2-3 mJ in 7-ns wide (FWHM) pulses. Flashlamp life also becomes an important factor in this regime because lamp changes are frequent and expensive. At this density, the pulses would be so closely spaced that four surrounding pulses would overlap the same bottom area (due to beam spreading as seen in section 8.2.5.3). It may be that the average density required of the laser system can be substantially lower (particularly for smaller scale surveys). This would lead to lower repetition rate requirements and higher potential pulse energy. At $250\text{m}^2/\text{sounding}$, which is between the analog and digitized sonar densities, a 60/sec rate would be sufficient. This is much less taxing on laser technology and would significantly reduce the data processing load. The ultimate decision on data density must be made in collaboration with the hydrographers for whom the data is intended.

Typical performance and design requirements for the hardware are listed in Table 4-1. A conceptual block diagram for an all-green system appears in Fig. 4-11. All major components such as clocks, position and attitude measurement (PAMS) data, displays, I/O, etc., are tied directly to the control computer. A sample timing diagram is shown in Fig. 4-12. The laser fires narrow pulses under computer control, through optics which determine the beam divergence, to a scanner which deflects and scans the beam in the desired

PARAMETER	PERFORMANCE REQUIREMENTS
LASER WAVELENGTH	One wavelength in the range 510-570 nm
LASER BANDWIDTH	\leq 1.0 nanometer
MAXIMUM LASER PULSE RATE	Min. Acceptable - 400 per sec. Goal - 600 per sec.
LASER PULSE RATE SELECTABILITY	Adjustable from 5 per sec to max
LASER PULSE WIDTH (FWHM)	\leq 6 ns
LASER PULSE RISE TIME	\leq 5 ns (10% to 90%)
LASER PULSE DECAY TIME	Natural exponential of time constant \leq 8 ns
REQUIRED MIN. DETECTABLE SIGNAL	100 Photons/ns 3.7×10^{-8} watts at 540 nm transmitted wavelength
REQUIRED MAX. DETECTABLE SIGNAL	3×10^{-7} multiplied by transmitted laser power, or as determined to preclude system saturation
OFF-NADIR SCAN ANGLE OF LASER BEAM	0° to 30° off-nadir, accurate to 1°; adjustable in 5° increments; may vary by no more than +0%-50% during 1 scan revolution
ACCURACY OF KNOWING SCAN ANGLE OF LASER BEAM	Consistent with ALBS determined positioning error budget
TRANSMITTED BEAM DIVERGENCE (FULL ANGLE)	Adjustable in 3 mr increments from 3 mr to 21 mr
ACCURACY OF KNOWING BEAM DIVERGENCE	± 1 mr RMS
RECEIVER FIELD OF VIEW (FULL ANGLE)	Adjustable in 10 mr increments from 20 mr to 80 mr and centered on transmitted laser pulse
ACCURACY OF KNOWING FIELD OF VIEW	± 2 mr RMS
AZIMUTHAL SCAN ANGLE RANGE OF LASER BEAM	As determined by contractor-proposed scan pattern
ACCURACY OF KNOWING AZIMUTHAL SCAN ANGLE OF LASER BEAM	Consistent with contractor-developed error budget

Table 4-1a. ALBS PERFORMANCE DESIGN REQUIREMENTS

PARAMETER	PERFORMANCE REQUIREMENTS
AZIMUTHAL SCAN ANGLE RATE OF LASER	Adjustable from 0 to rate determined by contractor to meet sounding distribution.
LASER PULSE ENERGY	Minimum acceptable - 2 millijoules Goal - 80 millijoules
LASER PULSE ENERGY VARIABILITY	$\pm 20\%$ RMS
LASER PULSE ENERGY ADJUSTABILITY	Adjustable from 1 millijoule to max. in 1 millijoule increments
ITEM POWER	≤ 3.4 kW
ITEM WEIGHT	≤ 800 lbs.
ITEM SIZE	(TBD)
OBSCURATION DISK	Adjustable 0 to 100% obscuration of transmitted beam footprint on sea surface. Adjustable in 10% increments
RECEIVER TELESCOPE EFFECTIVE AREA	Minimum acceptable - 500 cm^2 Desired - 725 cm^2 Goal - as large as possible consistent with exit hole size of aircraft
RECEIVER OPTICAL FILTER BANDWIDTH	≤ 3 nm typical containing laser wavelength. Must be suitable for reducing ambient daylight sensed. Must be readily removable.
SOUNDING DISTRIBUTION	Uniform to within $\pm 25\%$ at nominal operating parameters (Figure 3-2).
VERTICAL ACCELEROMETER	Vertical displacement determinable to ± 10 cm RMS over 1 minute period or better
SYNCHRONIZATION TIME	Resolution to better than 150 μsec , suitable for uniquely identifying pulses over $6\frac{1}{2}$ hour mission.
REAL TIME OF DAY	24 hour clock. Time recorded to nearest 1 minute with accuracy of at least ± 1 minute RMS.
SCAN PATTERN	Conic or near Conic desired. Scanning through vertical not allowed. Otherwise, shall be consistent with operating parameters and required sounding distribution.

Table 4-1b

PARAMETERS	PERFORMANCE REQUIREMENTS
DATA ACQUISITION ELECTRONICS	Quantum limited i.e. self-noise of system \leq shot noise for signals > 100 photons per nanosecond
MAXIMUM DEPTH MEASURING CAPABILITY OF SYSTEM (EXCLUDING WATER CLARITY LIMITATIONS)	Required - 70 meters Goal - 100 meters
MISSION ENDURANCE	4 hours with 1 change of recording media. Goal - 6½ hours
SLANT ALTITUDE MEASUREMENT ACCURACY	Required - 10 cm RMS Goal - 5 cm RMS

Table 4-1c

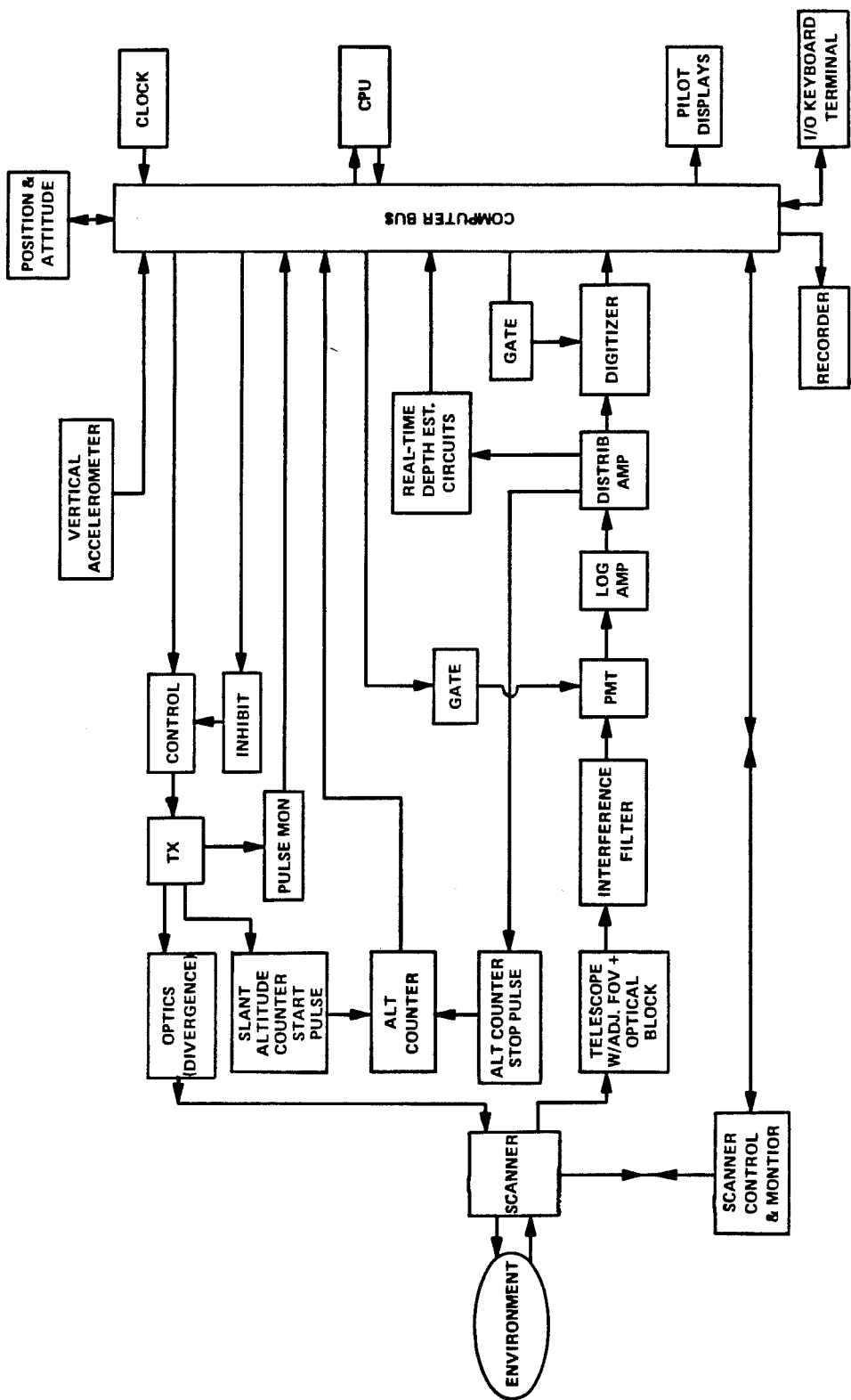


FIGURE 4-11. TYPICAL TRANSEIVER BLOCK DIAGRAM

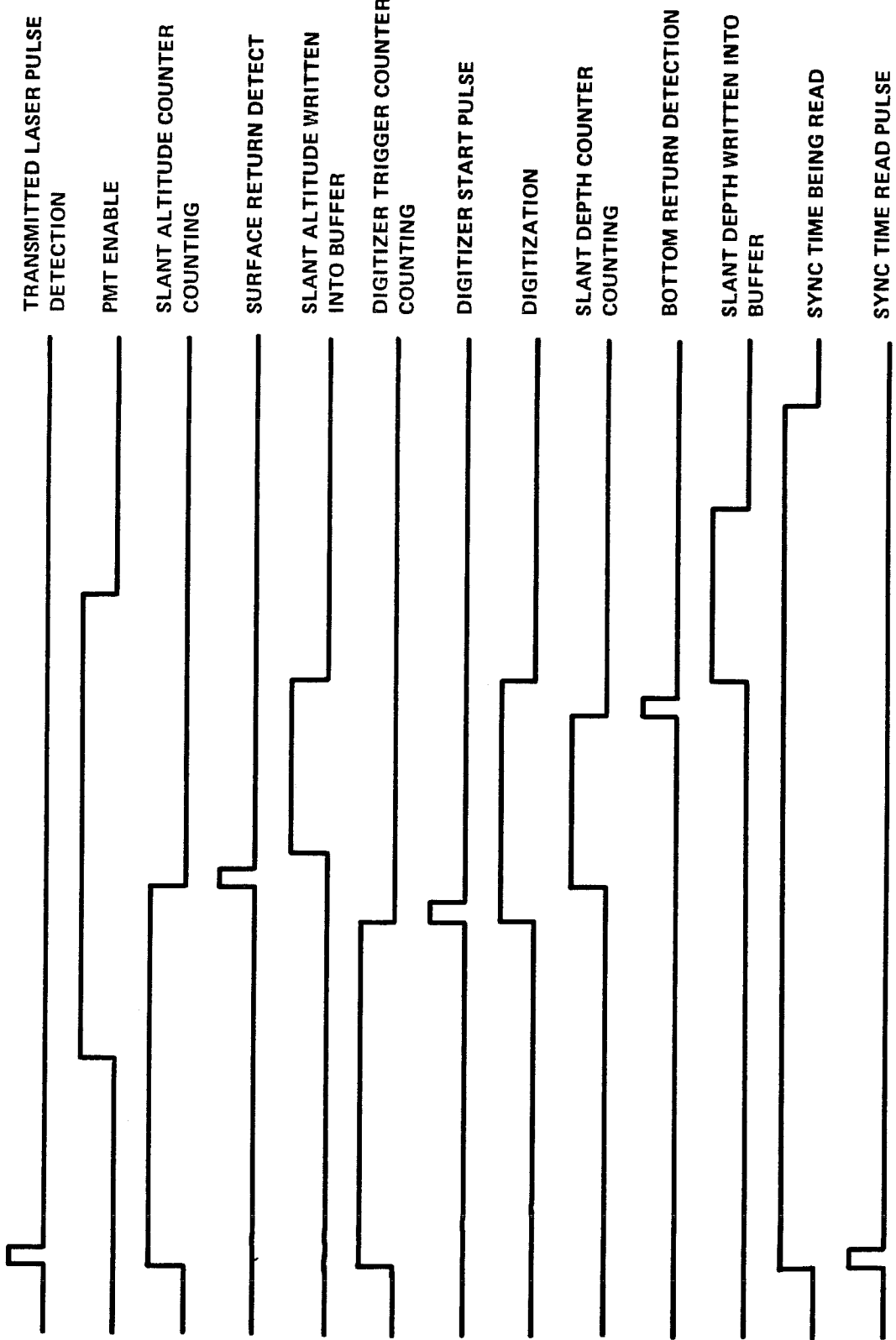


FIGURE 4-12. ALBS SUBSYSTEM TIMING DIAGRAM EXAMPLE

pattern on the water. A typical optical system concept is illustrated in Fig. 4-13. For two-beam systems, the beams must be colinear to avoid large depth errors due to pointing uncertainties. The use of polarization techniques depends on the desired penetration potential and the propagation-induced bias correction procedure. Polarizers are not beneficial for the bottom return because the added insertion loss cancels the potential benefits of improved contrast between the bottom return and the volume backscatter. Crossed polarizers can be used to reduce the magnitude of the sometimes very strong interface reflection. The reduction of the interface return is achieved at the cost of altering the backscatter information from which the scattering coefficient might be estimated. The "spot size" of energy arriving at the surface of the water is determined by the altitude of the aircraft and the divergence angle of the laser beam exiting the aircraft. The appropriate beam divergence will be chosen based on wave correction and eye-safety grounds, as will be seen in sections 8.2.4, 9.2.5, and 10.3.

The departing pulse starts a slant altitude counter used: 1) for enabling the PMT and signal processor / digitizer when the pulse nears the expected water surface, 2) for measuring the slant altitude of each pulse for wave correction procedures, and 3) for inhibiting further pulses should the altitude be low enough to cause eye-safety violations. The counter is stopped by the receipt of the surface return. Vertical aircraft accelerations are also measured to assist in the wave correction process because the aircraft motion spectrum and the spectrum of observed long-period swell can overlap. The characteristics of the outgoing pulse (peak power, width, etc.) are monitored to insure nominal operation.

The return waveform received from the environment is reflected by the scanner mirror into a telescope with adjustable field of view (FOV). The required receiver FOV, as noted in Fig. 4-7, will need to encompass a spot diameter equal to a significant fraction of the working depth. For a 40-m depth and a 300-m altitude, this means a full angle FOV of roughly 100 milliradians (mr). An example of the functionality between bottom return peak power and receiver FOV (from a low altitude Navy helicopter) is shown in Fig. 4-14. It can be seen that the power asymptotically approaches a maximum value as the FOV is increased toward the optimal value (which would have been

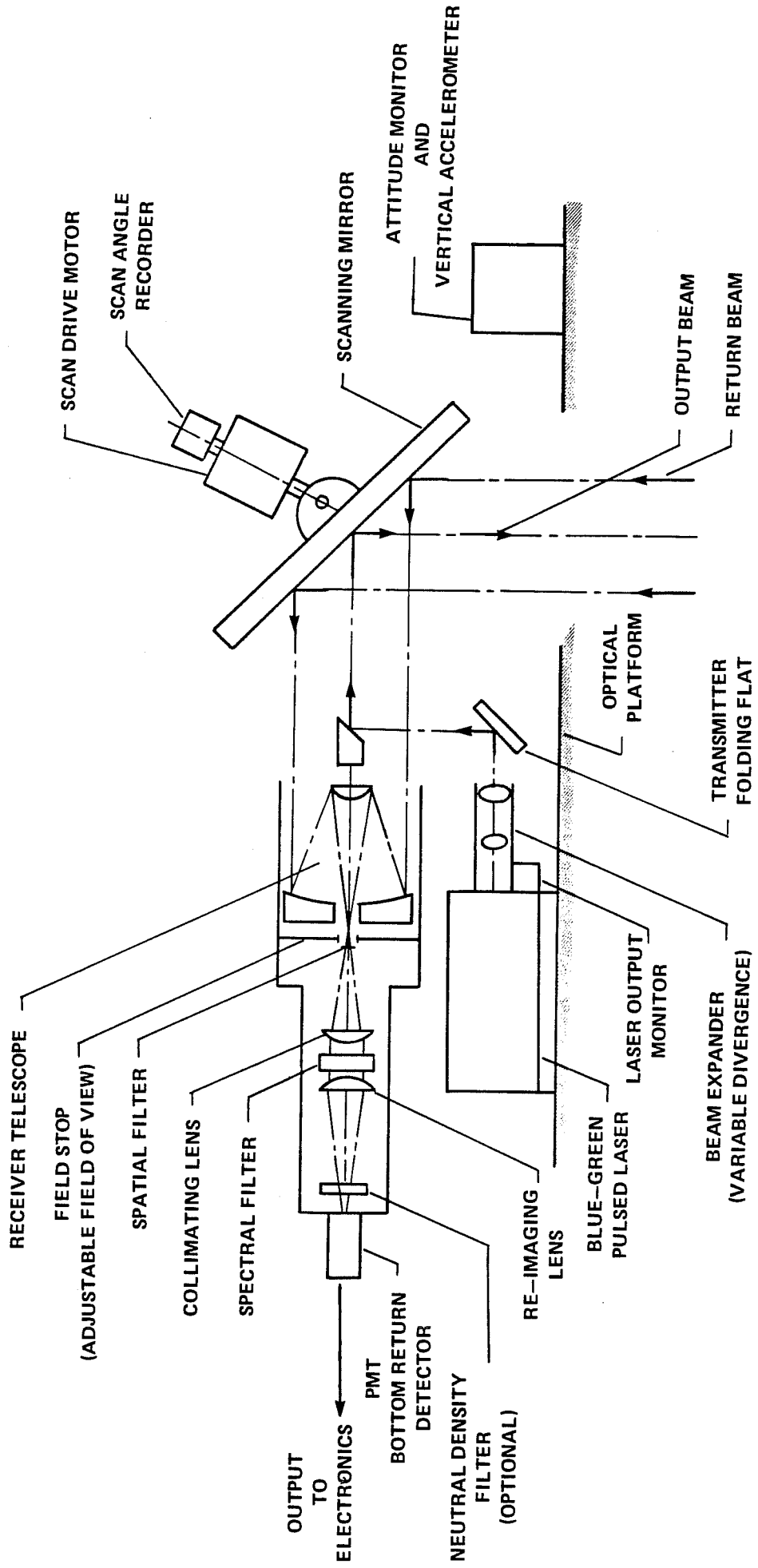


FIGURE 4-13. OPTICAL SYSTEM CONCEPT

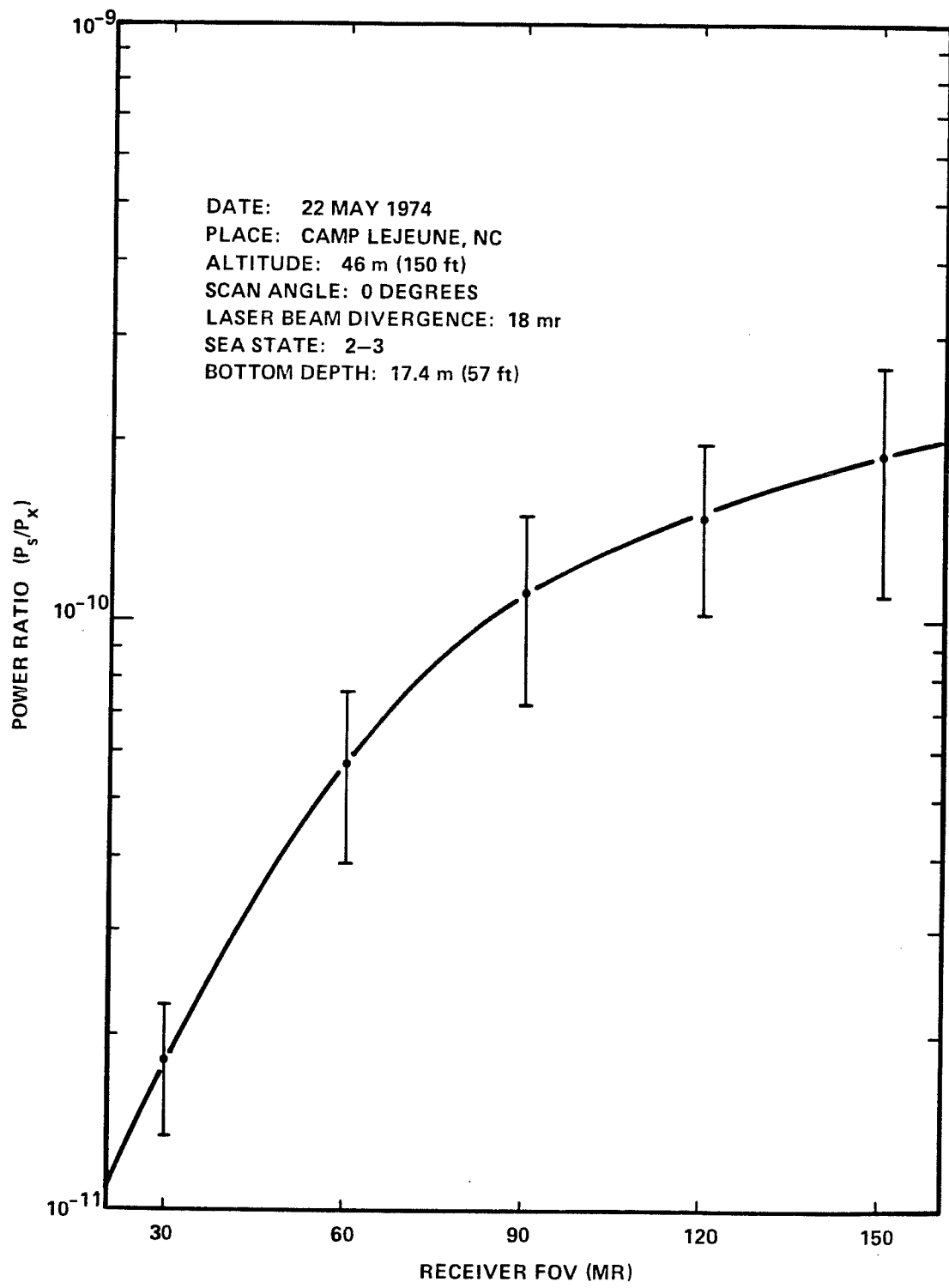


FIGURE 4-14. POWER RATIO AS A FUNCTION OF ORAD RECEIVER FOV (NADC)

roughly 250 mr for the illustrated case). An adjustable optical block in the center of the FOV might be included as a preferred alternative to polarizers to reduce the magnitude of the surface return. If used, however, the block distorts volume backscatter information, much as does polarization.

The telescope is followed by a spectral "interference" filter required for daytime operation. The bandwidth of the filter, which should be as narrow as possible within system constraints (such as FOV, size, and temperature stability), will probably be on the order of 0.5-2 nm centered on the laser wavelength. Because it has an inherent insertion loss, this filter should be bypassed or removed for nighttime operation when it is not needed. As seen in Fig. 4-15, there is a complicated relationship among FOV, filter bandwidth, and telescope focal length. In order to maintain high transmission factors, a large FOV requires a long focal length (to reduce incidence angle) or a wide filter bandwidth. The latter is very undesirable because it would limit daytime penetration; the former simply causes the system to be larger in size. A typical plot of estimated signal-to-noise ratio versus FOV is seen in Fig. 4-16. Small FOV's cause significant loss of SNR. From the last two figures, it is clear that the optical requirements for daytime operation are demanding and that one wants to insure a sufficient FOV.

The optical signal is converted to an electrical signal by the PMT which is a critical component that must be selected with care. A PMT is required for optical detection because solid-state detectors do not currently have the required combination of sensitivity, gain, and noise level. The device must be high speed (fast enough to not significantly degrade the incoming pulse rise time), have high quantum efficiency at the desired wavelength, and be free from anomalous high surface-signal-strength effects such as "ringing" or dynode "afterglow" which place stray signals into the waveform (both serious problems which demand attention (Miller 1981)). The PMT should be gated so that it can be turned "off" when unwanted energy is arriving (such as airglow from the departing pulse near the aircraft or the interface reflection) and, if desired, it can be gain-controlled as a function of time. The tube should be hand-selected to have the lowest possible dark current for optimal nighttime penetration. For a colinear, two-beam system, the infrared signal would be split off by the optical system and detected separately.

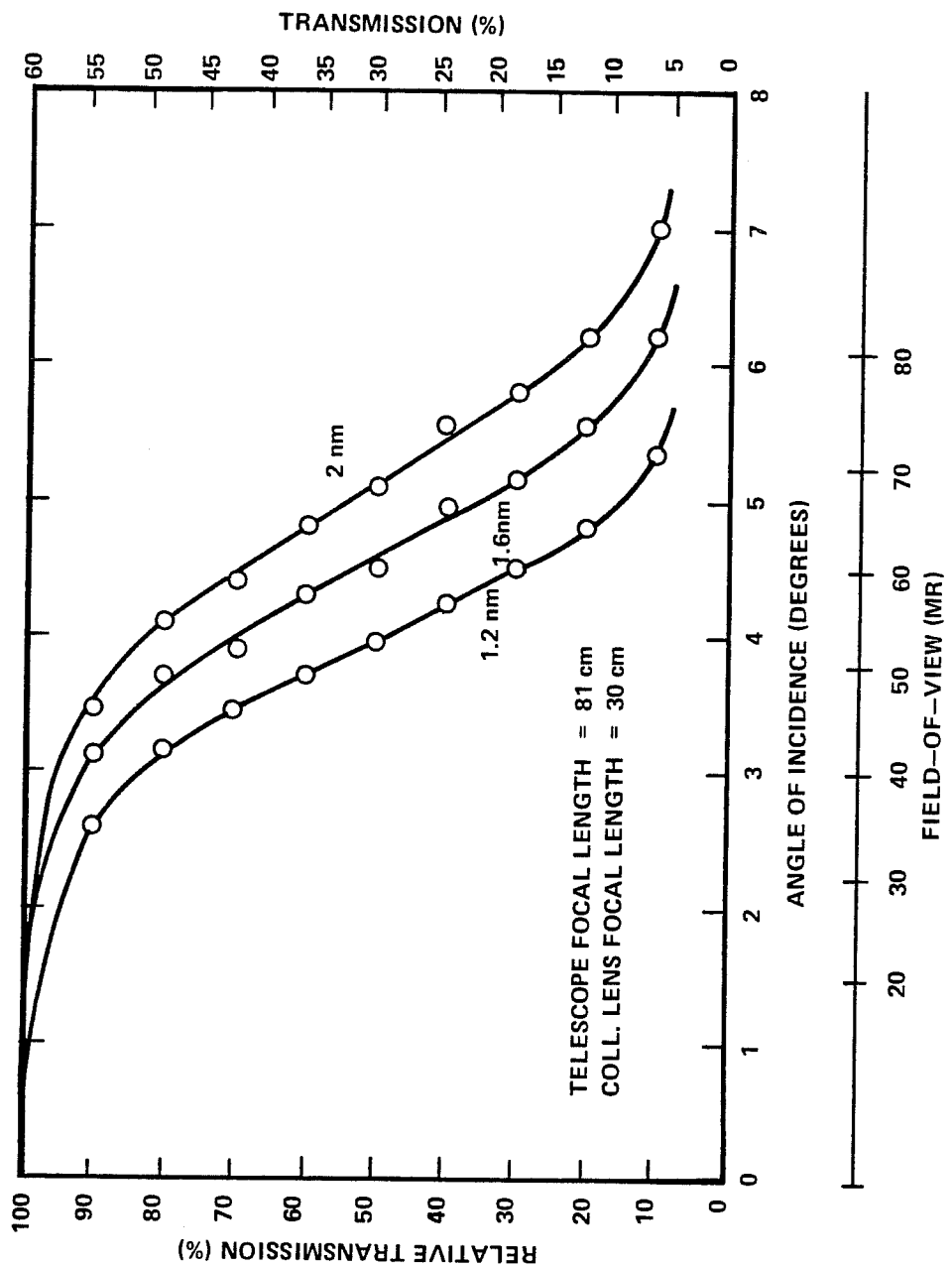


FIGURE 4-15. EFFECT OF INCIDENT ANGLE ON FILTER TRANSMISSION
(AVCO EVERETT)

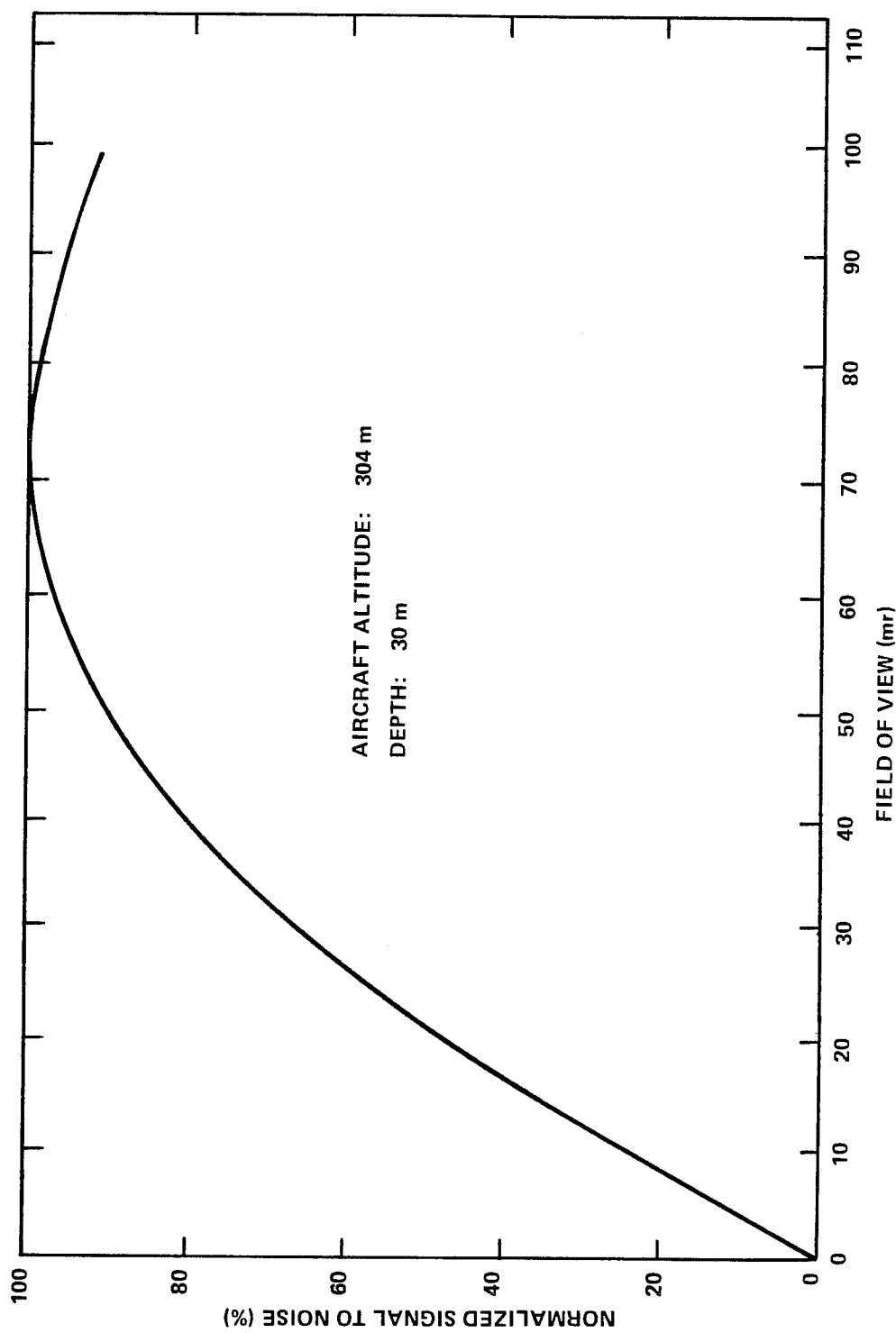


FIGURE 4-16. SIGNAL TO NOISE VS. RECEIVER FIELD OF VIEW
(AVCO EVERETT)

A logarithmic amplifier is a prime candidate for compressing the remaining large amplitude dynamic range which exists between relatively strong surface (or volume) returns and weak bottom returns, particularly at night when extra performance can be gained due to the much lower noise level. As noted in Guenther (1982), the resulting non-linear distortion of the waveform will cause a depth measurement bias (see section 9.3.2), but this is of moderate magnitude and can be compensated for. The only serious alternative to a log amp is a PMT with a time variable gain, or so-called "sensitivity-time control" (STC) (Krumboltz and Contarino 1978). With STC, the PMT gain would be kept low until after the receipt of the surface return and then either quickly raised to a higher fixed level or raised exponentially as a function of time to compensate for the exponential decay of the bottom return amplitude. This is beneficial because it can significantly reduce the after-pulse problem. The problem with the STC technique is that there may be a time during the transition for which a bottom return from a shallow depth could be distorted or lost. As with other proposed dynamic range reduction techniques, this would interfere with the determination of the scattering coefficient which is potentially useful for bias estimation purposes. Ultimately, some combination of STC and logarithmic amplifier may provide the best solution.

One of the most important decisions in system design philosophy is the selection of either on-board or post-flight depth calculation. For the former case, the airborne signal processing hardware and software are more complex and fallible, and depth decisions are irrevokable because the waveforms are discarded. For the latter, larger volumes of recording media will be generated. Due to the numerous physical effects and error sources engendered by this infant technology, the authors feel that the digitization, recording, and return of full waveforms for careful scrutiny during processing offers a significantly higher probability of accurate depth determination and successful operation. Rough depth estimates can nevertheless be calculated in real time to act as a data quality indicator. Whichever solution is selected, the waveform or depth information is appropriately tagged with ancillary information such as time, position, aircraft attitude, and system parameters and written onto magnetic media for further post-flight processing.

4.3 References

- Bobb, L.C., Ferguson, G., and Rankin, M., 1978: Laser Irradiance in the Sea: Theory and Experiment. Report No. NADC 78253-30, Naval Air Development Center, Warminster, Pa., 42 pp.
- Chandrasekhar, S., 1960: Radiative Transfer, Dover Publications, New York, N.Y., 385 pp.
- Cox, C. and Munk, W., 1954: Measurement of the Roughness of the Sea Surface from Photographs of the Sun's Glitter. JOSA 44, 11, 838-850.
- Duntley, S.Q., 1971: Underwater Lighting by Submerged Lasers and Incandescent Sources. SIO Ref. 71-1, Scripps Institution of Oceanography, Visibility Laboratory, San Diego, Calif., 275 pp.
- Enabnit, D.B., Goodman, L.R., Young, G.K., and Shaughnessy, W.J., 1978: The Cost Effectiveness of Airborne Laser Hydrography. NOAA Technical Memorandum NOS26, National Oceanic and Atmospheric Administration, U.S. Department of Commerce, Washington, D.C., 56 pp.
- Gordon, H.R., 1982: Interpretation of Airborne Oceanic Lidar: Effects of Multiple Scattering. Appl. Opt., 21, 2996-3001.
- Guenther, G.C. and Thomas, R.W.L., 1981: Monte Carlo Simulations of the Effects of Underwater Propagation on the Penetration and Depth Measurement Bias of an Airborne Laser Bathymeter. NOAA Technical Memorandum OTES 01, National Oceanic and Atmospheric Administration, U.S. Department of Commerce, Washington, D.C., 144 pp.
- Guenther, G.C., 1982: Effects of Detection Algorithm on Accuracy Degradation From Logarithmic and Difference Processing for Airborne Laser Bathymetry Returns. NOAA Technical Report OTES 06, National Oceanic and Atmospheric Administration, U.S. Department of Commerce, Washington, D.C., 37 pp.

Guenther, G.C. and Thomas, R.W.L., 1984: Prediction and Correction of Propagation-Induced Depth Measurement Biases plus Signal Attenuation and Beam Spreading for Airborne Laser Hydrography. NOAA Technical Report NOS 106 CGS 2, National Oceanic and Atmospheric Administration, U.S. Department of Commerce, Washington, D.C., 112 pp.

Krumboltz, H.D. and Contarino, V.M., 1978: An Optical Radar Receiver using Programmed Sensitivity Time Control. Proc. SPIE Optics V, Vol. 160, August 30-31, 1978, San Diego, Calif., 184-188.

Levis, C.A., Swarner, W.G., Prettyman, C., and Reinhardt, G.W., 1974: An Optical Radar for Airborne Use Over Natural Waters. Proc. Symposium on The Use of Lasers for Hydrographic Studies, Sept. 12, 1973, NASA/Wallops Flight Center, Wallops Island Va., National Aeronautics and Space Administration, Wallops Island, Va., 67-80.

Measures, R.M., 1984: Laser Remote Sensing. John Wiley & Sons, New York, N.Y., 510 pp.

Miller, M. (Avco Everett Research Laboratory, Inc., Everett, Mass.), 1981 (personal communication).

Petri, K.J., 1977: Laser Radar Reflectance of Chesapeake Bay Waters as a Function of Wind Speed. IEEE Trans. Geoscience Electronics GE-15, #2, 87-96.

Phillips, D.M. and Koerber, B.W., 1984: A Theoretical Study of an Airborne Laser Technique for Determining Sea Water Turbidity. Australian J. Phys., 37, 1, 75-90.

Scott, R., 1982: Weather Constraints on Airborne Laser Hydrography Operations. NOAA Technical Memorandum OTES 03, National Oceanic and Atmospheric Administration, U.S. Department of Commerce, Washington, D.C., 14 pp.

Witt, A.K., Shannon, J.G., Rankin, M.B., and Fuchs, L.A., 1976: Air / Underwater Laser Radar Test Results, Analysis, and Performance Predictions. Report No. NADC-76005-20. Naval Air Development Center, Warminster, Pa., 293 pp. (CONFIDENTIAL).

5.0 BATHYMETRIC FIELD TESTS OF THE "AIRBORNE OCEANOGRAPHIC LIDAR"

5.1 Introduction

An airborne lidar system has been extensively flight tested to study the operational feasibility of using a scanning, rapidly pulsed laser beam, projected into water from a fixed wing aircraft, for near-shore hydrographic charting applications. Field trials of the Airborne Oceanographic Lidar in the bathymetry mode were conducted by a NASA/NOAA team during the summer and fall of 1977 in the Atlantic Ocean and Chesapeake Bay. Five years were required from the inception of test planning in 1975 to the conclusion of data processing and analysis in 1980. The goal of determining the operational feasibility of the technique of airborne laser hydrography in terms of accuracy, penetration, and operational constraints was fully met with positive results. Field test results for vertical accuracy, penetration, environmental constraints, and effects of system parameters are discussed.

5.2 Background

During the past fifteen years, a number of increasingly sophisticated airborne laser ranging (lidar) devices have been tested to determine technical feasibility for hydrographic and other oceanographic applications (section 2). In 1974, a development program for a versatile airborne laser and data acquisition system, to be sponsored by the NASA Advanced Applications Flight Experiment (AAFE) program, was proposed jointly by NASA/Wallops Flight Center and Avco Everett Research Laboratory, Inc. Applications, requirements, specifications, and evaluation procedures for this "Airborne Oceanographic Lidar" (AOL) system were solicited and established through a series of meetings with interested parties (Goodman 1975 and 1976; Melfi 1975; and Avco 1976). The concept evolved with two major and separate modes of operation: bathymetric lidar, and fluorosensing. The system was designed and built by the Avco Everett Research Laboratory according to the specification listed in Table 5-1.

The objective of the Laser Hydrography Development Project within NOAA was to perform a broad-based evaluation of the general "technique" of airborne

TABLE 5-1a
AOL PERFORMANCE REQUIREMENTS
BATHYMETRY

Excitation Wavelength	5400 Å
Excitation Bandwidth	≤ 1 Å
Excitation PRF	≥ 400 pps
Excitation Pulse Width	≤ 4 nsec
Scanning Angle	± 15 deg from nadir and, fixed at nadir (non-scanning)
Scanning Rate	As required for one data point per 20 m ² (constant grid desirable)
Transmitter Beam Divergence	≤ 2 mr with variable beam expander
Receiver Spectral Resolution	5400 Å ± 2 Å (< ± 2 Å desirable)
Receiver FOV	5 mr to 20 mr, variable
Receiver Temporal Resolution	2.5 nsec
Receiver Dynamic Range	~10 ⁷
Polarization	Required for transmitter and receiver

TABLE 5-1b
AOL MEASUREMENT REQUIREMENTS SUMMARY
BATHYMETRY

Application	Coastal water charting; fish school detection and track
Area Coverage	One data point per 20 m^2 maximum, ± 5 deg from nadir; also capability to ± 15 deg from nadir
Maximum Measurement Depth	6 m with $a = 2 \text{ m}^{-1}$ required, $a = 3 \text{ m}^{-1}$ desired; 10 m with $a = 1 \text{ m}^{-1}$
Minimum Measurement Depth	0.6 m
Vertical Measurement Accuracy	± 0.3 m
Horizontal Measurement Accuracy	± 1.07 m⁽¹⁾
Sea State Conditions	Measurement required
Platform Characteristics	
Altitude	152 m to 609 m
Velocity	278 km/hr
Background Conditions	Day and night operation required
Ground Truth Data	Required via wide angle footprint camera and autotape
Attitude Stabilization	Not required

⁽¹⁾ AOL system contribution, at an aircraft altitude of 609 m, towards a stated 5 m RMS reading accuracy requirement. The aircraft positional and attitude readout RMS equivalency, at 609 m, is estimated to be ± 4.93 m.

TABLE 5-1c
AOL PERFORMANCE REQUIREMENTS
GENERAL

Operating Requirements

Mission time-line	One hour, typical
Operation with other installed systems	Required
Interface with other installed systems	Interface with LTN-51 INS and NASA 36 bit TCG required
System ground preparation time	One hour, maximum
Operator requirements	One man operation
System performance monitoring	Real time performance monitoring via scope(s), display(s), etc. required
In-flight bathymetry to fluoro-sensing interchangeability	Not required
Background monitor	Required for automatic go, no-go control
System operational altitude (unpressurized)	1,524 m (provide baro-switch to prevent operation above 1,524 m)
System non-operational altitude (unpressurized)	3,658 m
Operational relative humidity range-cabin	0 to 95%
Operational temperature range-cabin	32° to 100°F
Operational vibration profile	To be provided by NASA

laser hydrography. This was accomplished in a four part program by: 1) determining through field tests of the AOL bathymetric laser system, the capability of an optimized airborne laser system to meet or exceed NOS near-shore vertical accuracy requirements within a bounding set of system variables and environmental parameters; 2) assessing its cost effectiveness under "typical" operational conditions; 3) performing preliminary design work on a realizable, NOS operations-oriented system; and 4) investigating the impact of such a system on NOS operations such as fleet utilization, chart production, and survey requirements.

The AOL field tests were the foundation of this effort. The goals of the NOAA flight test program with the AOL system were to validate the overall feasibility of a bathymetric lidar system to provide high quality data under typical operational circumstances; to determine vertical error under a bounding range of system variables and environmental parameters and correlate error contributions with sources; to quantify system and environmental usage constraints to establish the operational "window"; and to model major contributions in a return signal strength equation to provide a sound basis for extrapolation of penetration results to the design specifications of an NOS bathymetric lidar system.

The AOL was designed in a compromise configuration which permits either lidar bathymetry or active fluorosensing to be conducted. Because of its unique dual nature, it was not possible to optimize performance in either mode separately. In view of the recognized inherent limitations of the AOL, the technical evaluation of the general "technique" of laser bathymetry for application to NOS requirements was broken into two parts: 1) evaluation of results from AOL field test data, and 2) extrapolation of these results, via analytic models and computer simulations, to the ultimate expected performance of the "technique".

Preliminary shakedown and experimentation with the AOL instrument in the bathymetric mode, installed in a NASA/Wallops Flight Center C-54 aircraft, was sponsored by NOAA/National Ocean Survey (NOS), the Defense Mapping Agency (DMA), and the Naval Ocean Research and Development Activity (NORDA), and conducted jointly by NASA and NOS.

5.3 System Description

The installation of the transceiver is diagrammed in Fig. 5-1. An open hatch in the C-54 aircraft was used to pass transmitted and received energy to and from a large scanning mirror which is mounted between the floor and exterior skin of the aircraft.

The AOL bathymetric configuration (Fig. 5-2) consists of three major subsystems: optics, electronics, and computer, as described in Avco (1975). The optical subsystem pictured in Fig. 5-3 includes: an Avco C-5000 gas (neon/nitrogen) laser with an unstable resonator (to improve beam divergence), an adjustable beam expander (for divergence control), and an optional polarizer; a 56-cm scanner mirror with drive motor and 14-bit angle encoder; a 30.5-cm diameter Cassegranian f/4 receiver telescope with adjustable field stop and baffles (0-20 milliradian (mr) field of view) and an optional polarizer; a 0.4 nm (4 Å) narrow-band interference filter to suppress ambient background; and a photomultiplier tube (PMT) detector (hand picked for its low dark current). The laser wavelength of 540.1 nm (green) is near the minimum of the Jerlov (1968) curves of diffuse attenuation coefficient for coastal water types. The laser peak output power is typically 2-4 kilowatts (kW), while approximately 0.5-1 kW exits the aircraft in the primary beam. Divergence is variable from 0-20 mr, and pulse repetition rate is variable up to a maximum of 400 Hz.

The scanner, as seen in Fig. 5-4, is a nutating design whose mirror axis is offset slightly from the axis of rotation. The resulting pattern on the earth's surface is a tightly interlocked series of pseudo-ellipses (actually slightly "egg"-shaped) which provides relatively uniform areal coverage (Fig. 5-5). The scanner can be operated either at a 5-Hz rotation rate or locked in a fixed position for non-scanning (fixed off-nadir angle) data acquisition. The nominal angle of the output beam with respect to the nadir is adjustable in five degree increments between zero and 15 degrees maximum deflection. The actual angle varies by a factor of $\sqrt{2}$ during each quarter of a scanner rotation.

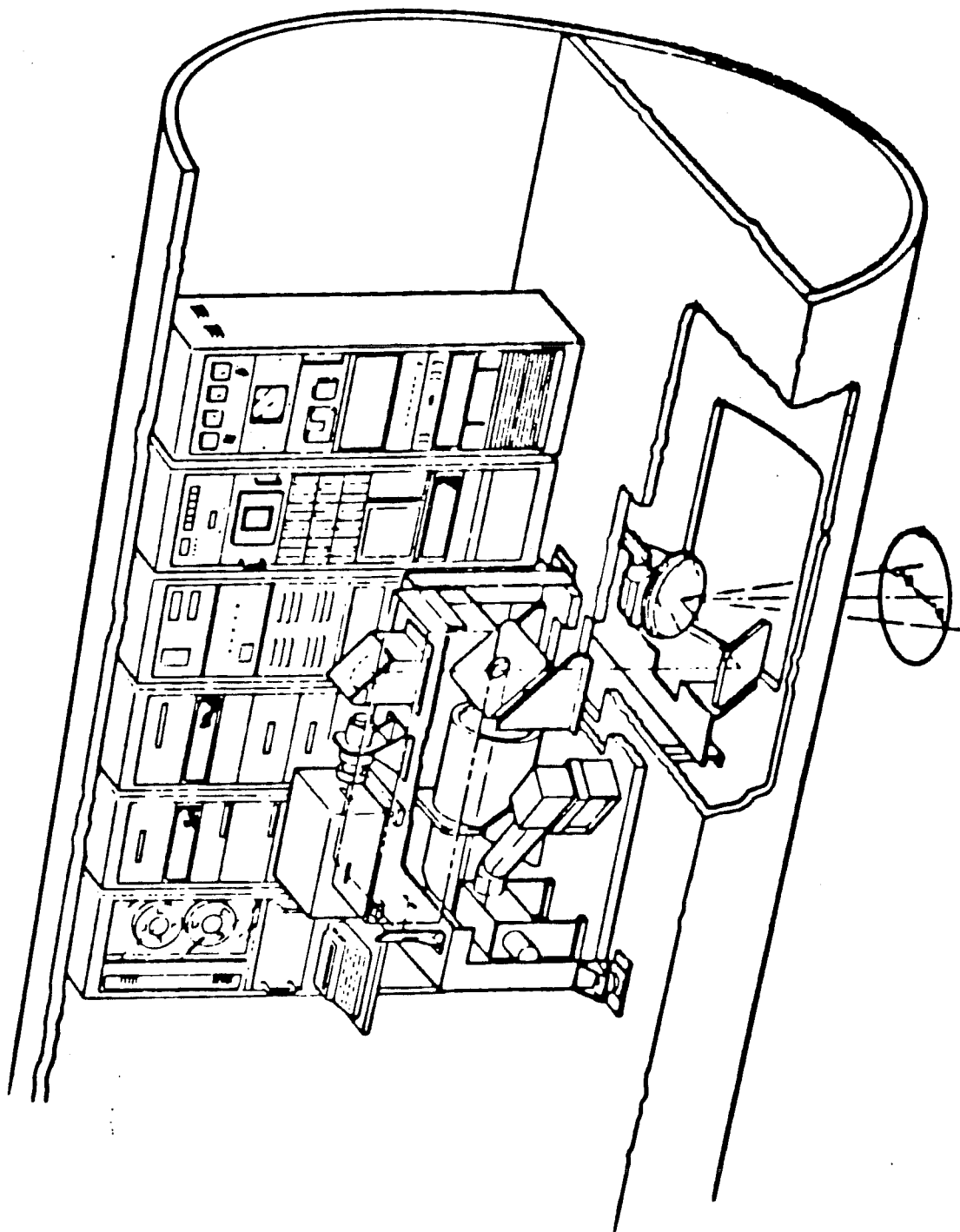


FIGURE 5-1. AIRBORNE OCEANOGRAPHIC LIDAR SYSTEM (AVCO)

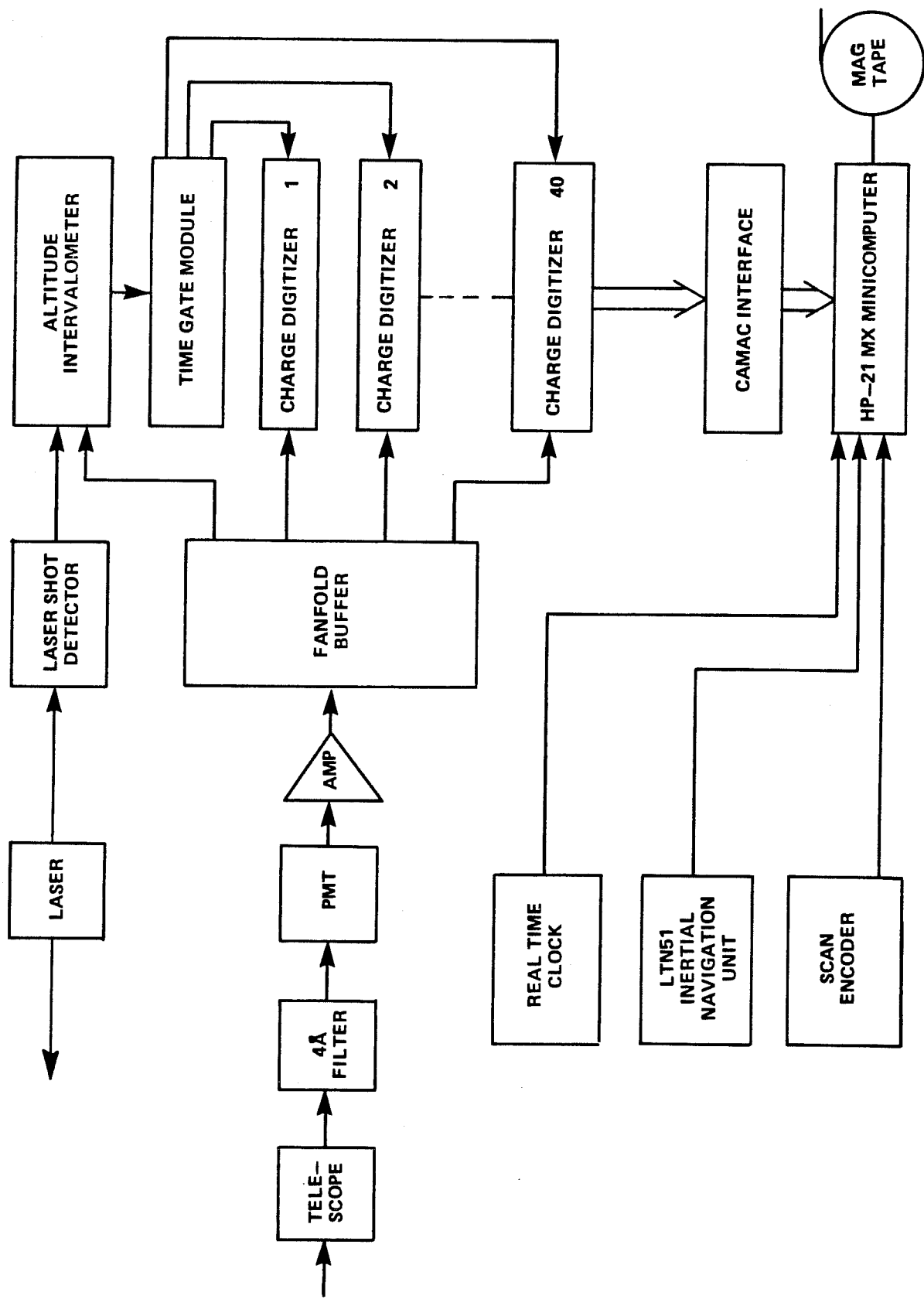


FIGURE 5-2. SCHEMATIC OF AOL HARDWARE CONFIGURATION

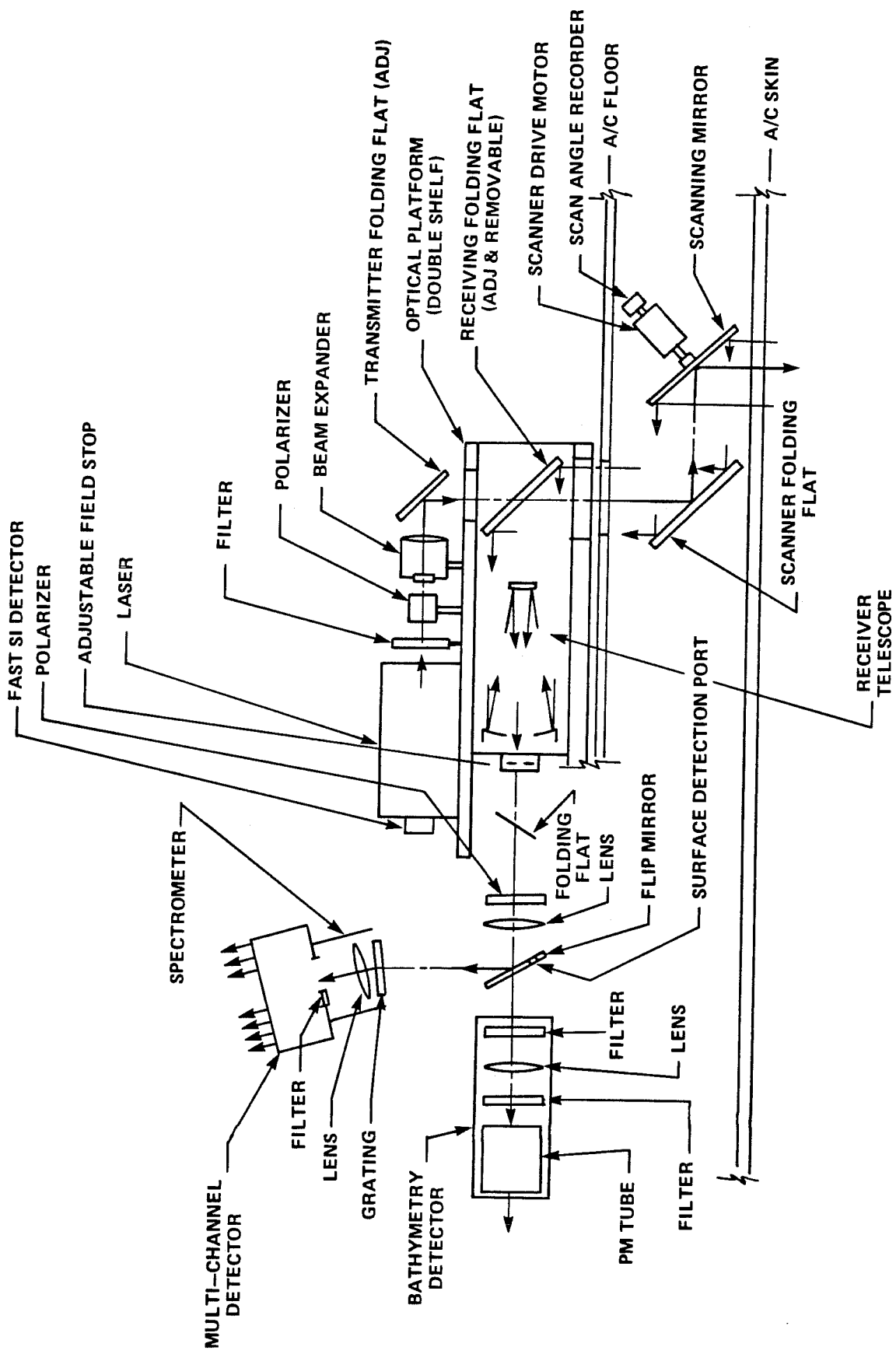


FIGURE 5-3. AOL OPTICAL SUBSYSTEM

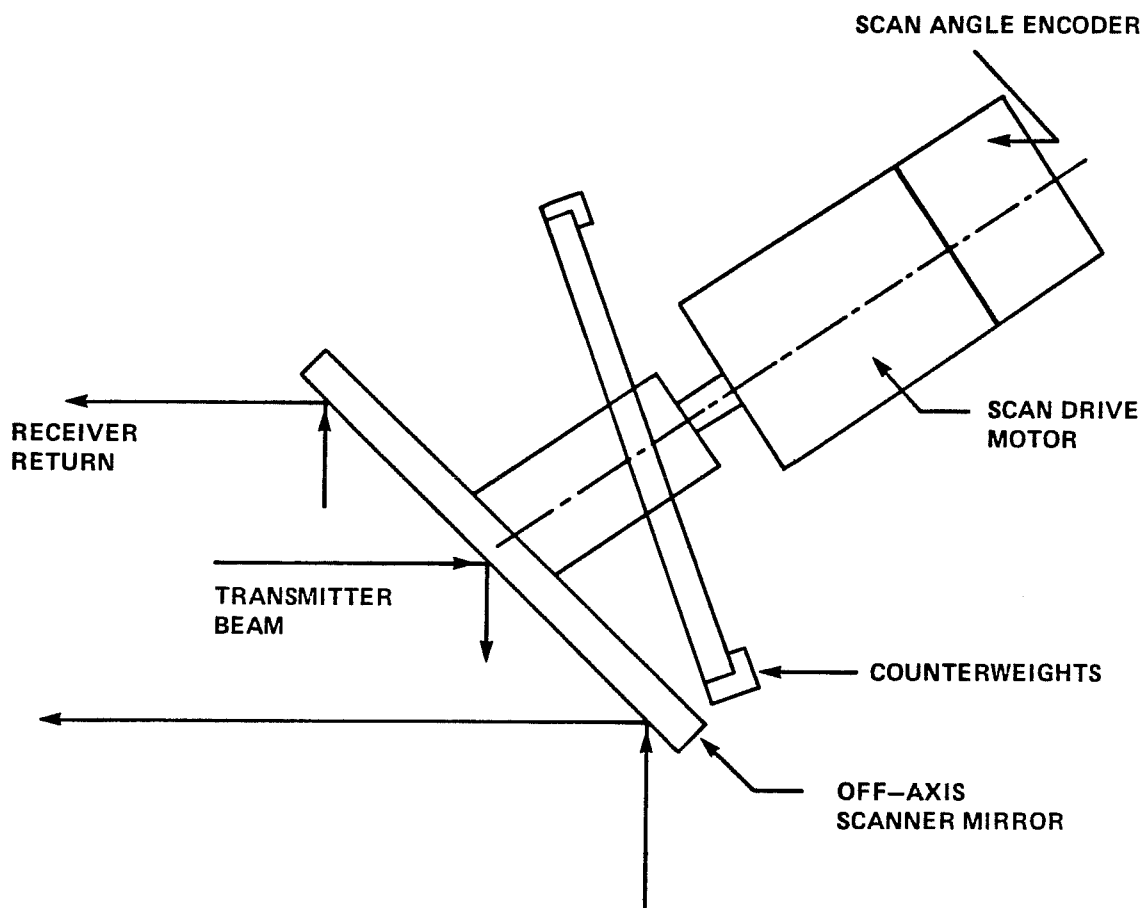
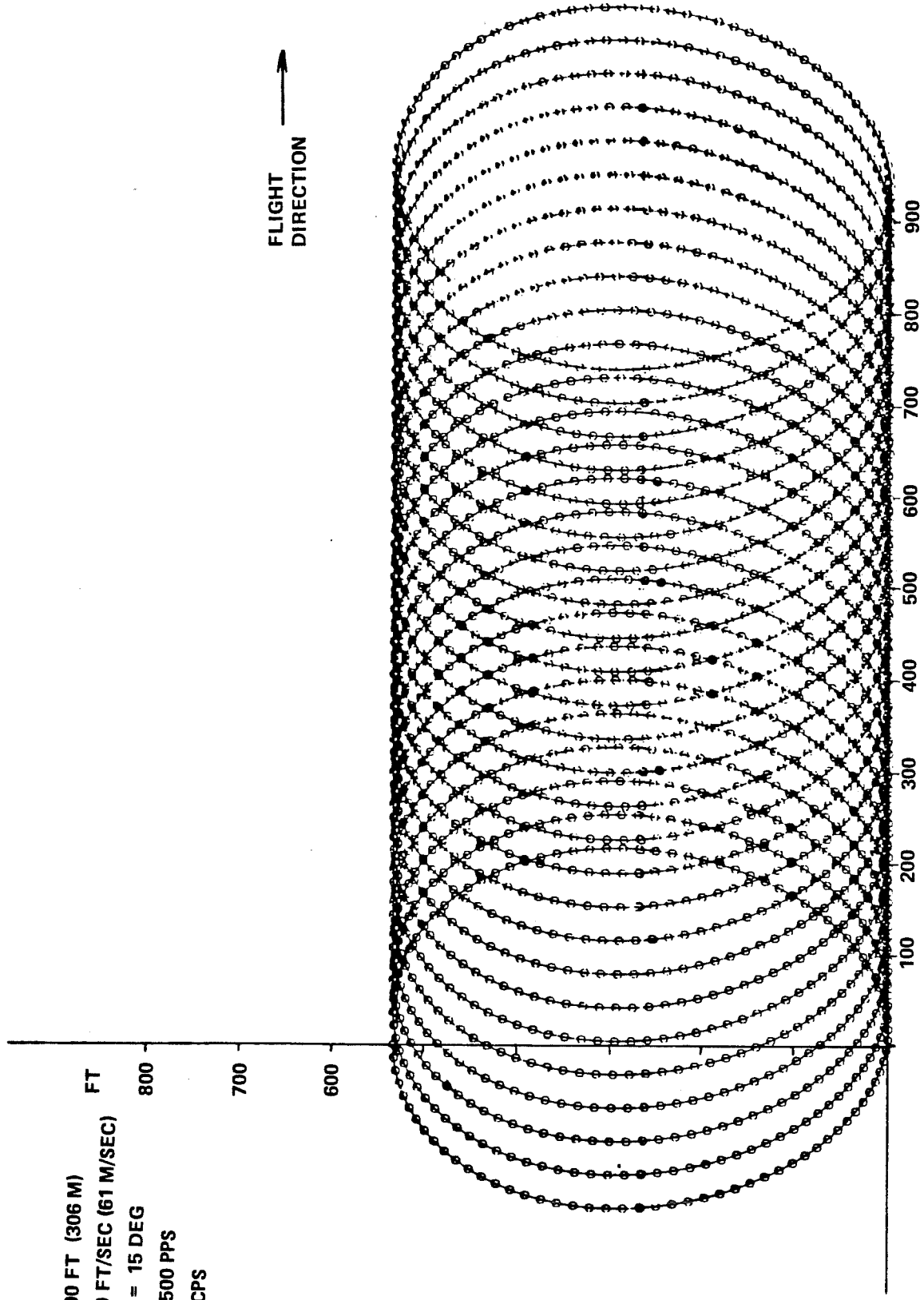


FIGURE 5-4. AOL NUTATING SCANNER



**FIGURE 5-5. ROTATING MIRROR SCAN PATTERN
PRODUCED BY AOL SYSTEM**

The electronics subsystem (Fig. 5-6) includes: amplification, discrimination, fanout, timing and gating functions; 40 charge digitizers (A/D converters); CAMAC interface; and appropriate power and control provisions. The 40 charge digitizers are gated sequentially at 2.5-ns intervals to provide 100 ns (or approximately 10 m) of useable depth range. The digitized signals are transmitted through the CAMAC interface to a Hewlett-Packard 21-MX minicomputer with disk and tape storage and CRT display capability. The computer controls data acquisition, elementary processing, display, and recording functions. An altitude intervalometer, operating in conjunction with a surface return detector, triggers the digitization process slightly prior to detection of the expected surface return. This permits digitization of the surface return and bottom return in the same data vector; this is very important, as it provides the surface return shape and location for subsequent off-line analysis. The altitude data can also be utilized to facilitate the removal of wave height variations from the depth calculations; this permits correction of the depths to the desired mean sea level.

Aircraft attitude and rough positional data are supplied to the computer from a Litton LTN-51 Inertial Navigation System (INS). A Universal Time Code Translator interfaced with the system provides precise "real time of day" for each laser pulse. The entire system (electronics, laser optics, and computer for both bathymetry and fluorosensing modes) weighs 2100 pounds and fitted comfortably in a small section of the C-54 cabin. (The AOL is now in a P-3.)

5.4 Field Test Program

5.4.1 Site Selection

Site selection for the AOL field tests was based on the following criteria: depths must range between one and ten meters; a combination of both flat and relatively high relief topography was preferred; radar tracking of the aircraft was imperative due to limitations of the LTN-51; the sites had to be logistically easy to reach by both aircraft and ground support vessels; the area must have suitable tide "control", typical water clarities must be appropriate to permit penetration to the bottom over sufficiently long portions of a flightline; and adequate meteorological support should be available 24 hours in advance for daily mission go/no-go decisions.

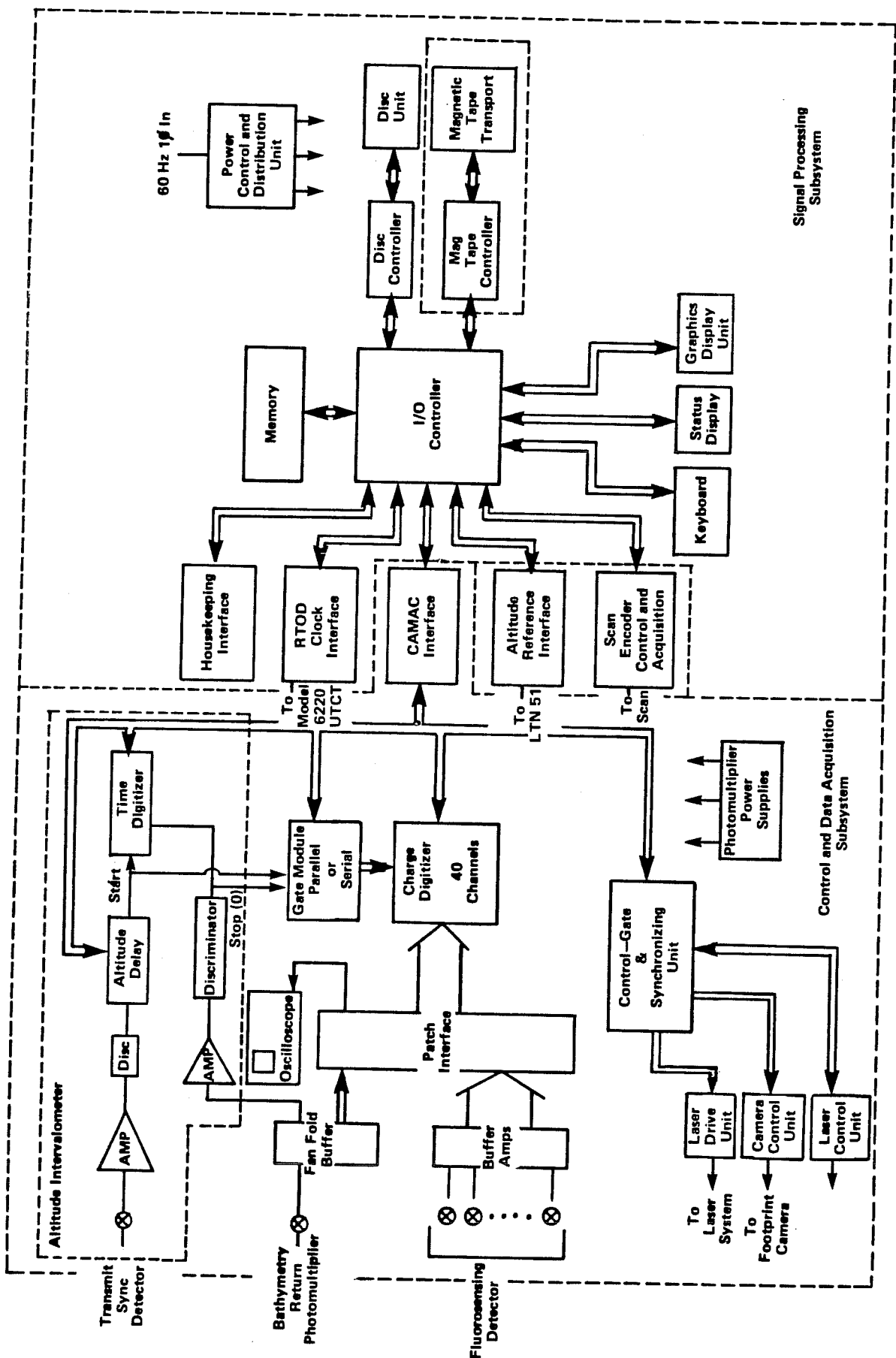


Figure 5–6. AOL Electronic System Block Diagram

Two test sites meeting these requirements were selected (Fig. 5-7) based on information obtained in a detailed sea-truthing study (Swift 1977): one in the Atlantic Ocean over Winter Quarter Shoal (several miles offshore from Assateague Island), and one in Chesapeake Bay -- Tangier Sound between Janes Island and Smith Island. Both sites were within a 25 nautical mile radius of the NASA Wallops Island radar tracking facility. These dissimilar areas provided the opportunity to investigate the effects of diversity in water clarity, depth, wind, and surface wave structure. The probability of successful missions in the Wallops Island vicinity based on precipitation, fog, and wind speed data from historical records were calculated and found to be acceptable (Fig. 5-8).

5.4.2 Support Data

A wide variety of ancillary supporting data was required for the flight tests in order to permit quantitative description of the system performance and the environmental restrictions on the operational window. The penetration of the AOL is limited primarily by the product of water depth and optical attenuation coefficient (as seen in sections 4 and 8). The latter is, for a given location and season, modulated temporally by wind, waveheight, precipitation, micro-organisms, and currents. Also affecting penetration are such things as bottom reflectivity and solar illumination. These parameters interact with system variables such as receiver field of view, altitude, scanner angle, and beam divergence to yield a highly complex set of relationships (see section 10) which must be unraveled to permit the quantization of specific effects. Adequate testing of the AOL thus depended on the quality and quantity of ground data specifically tailored to meet needs.

Primary support data acquired in conjunction with the flight tests include vertical control, horizontal control, water clarity, sea surface conditions, meteorology, and bottom reflectivity. The data were obtained as near the time of overflights as possible. A total of over one hundred vessel sorties or "cruises" were mounted in support of the program. Cruise data was coded directly into an 80-column format and punched onto computer cards for inclusion in a "sea-truth" data base.

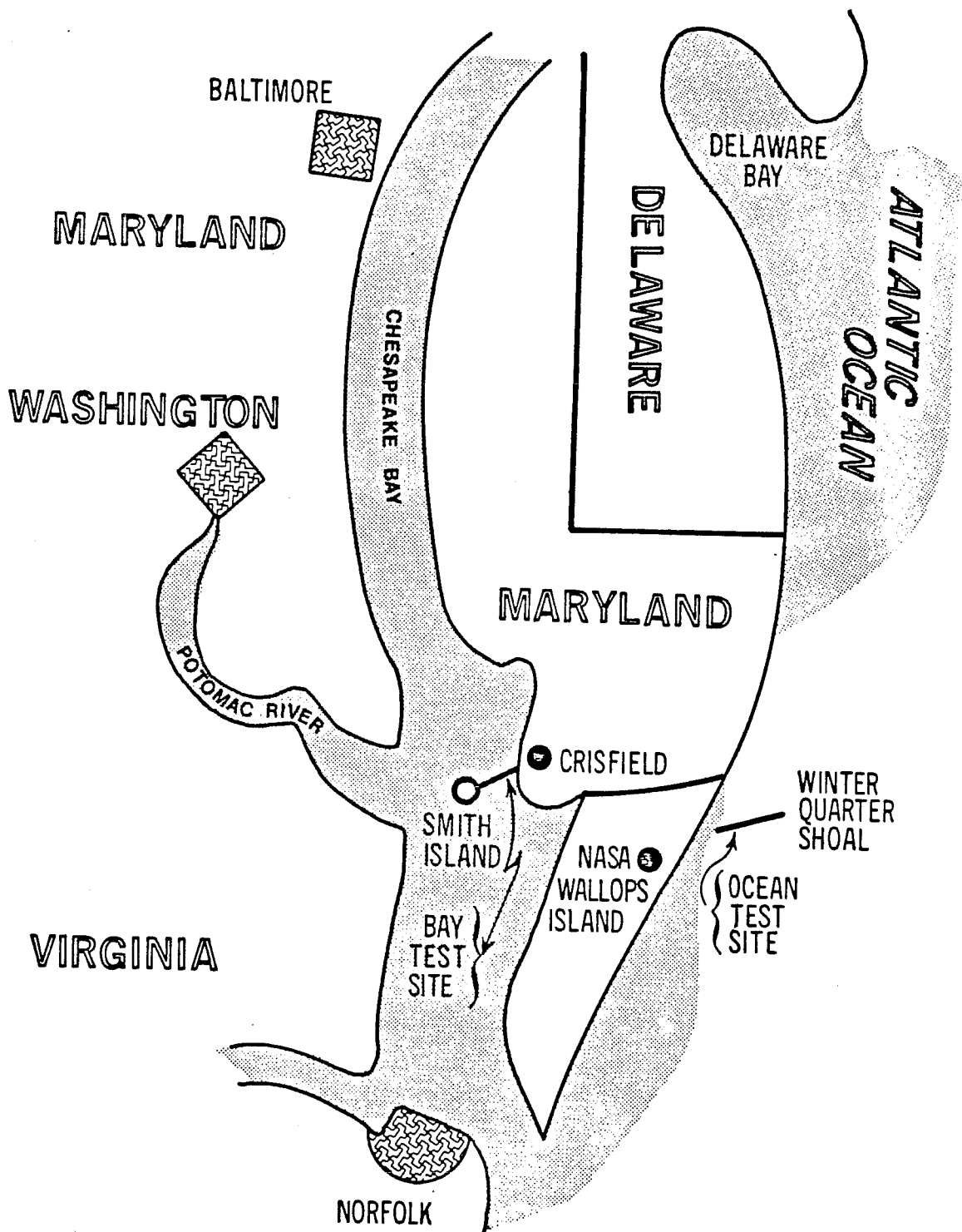


FIGURE 5-7. AOL TEST SITES

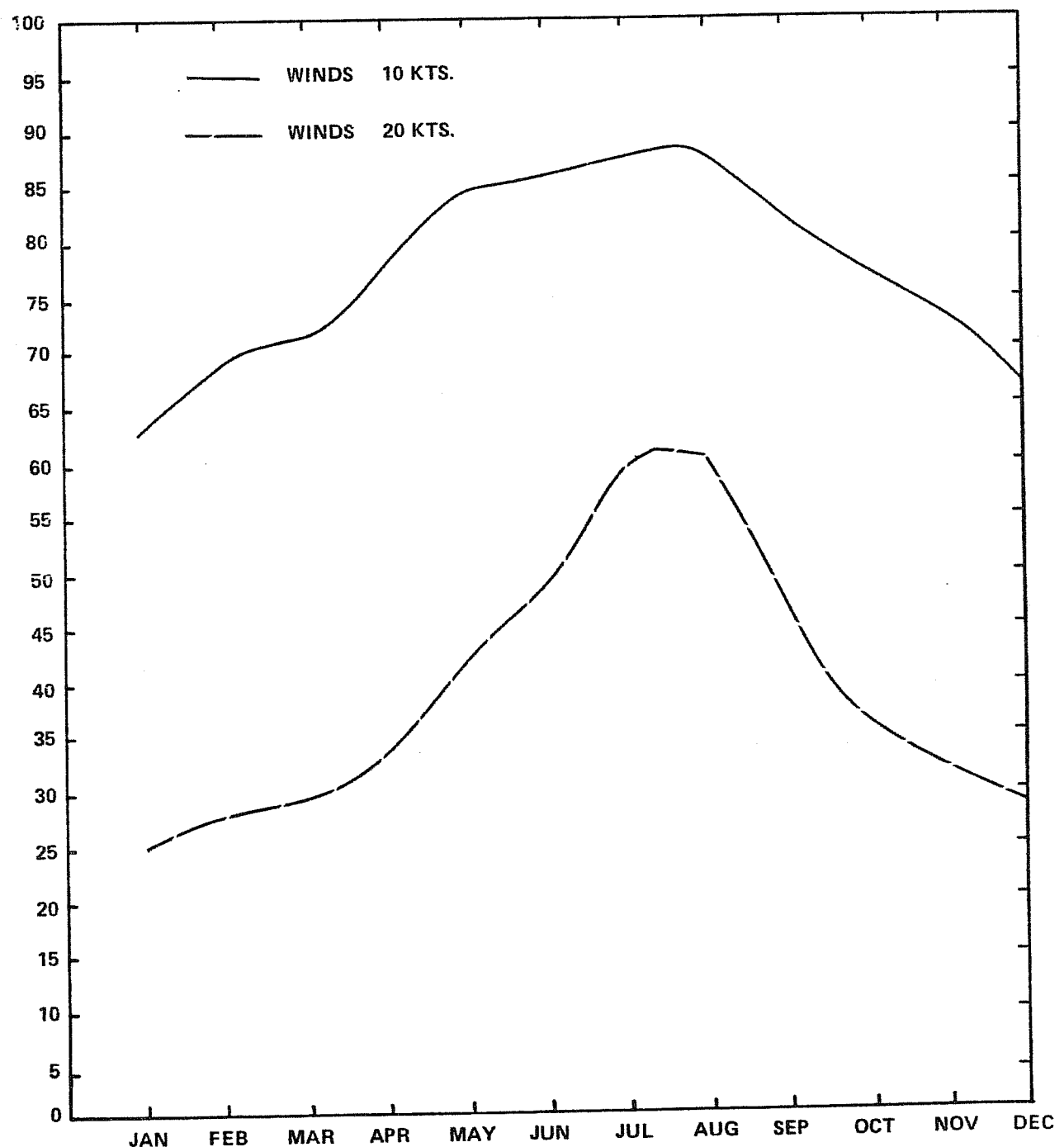


FIGURE 5-8. PROBABILITY OF DAILY LASER OPERATIONS FOR
WALLOPS ISLAND AREA

Vertical control consists of bathymetry and tide control. A bathymetric survey of the Tangier Sound flightline was conducted by an NOS vessel from the Atlantic Marine Center utilizing standard, automated, acoustic techniques. Horizontal control for this survey was a line-of-sight, high-frequency electronic positioning system with ground stations. Tide control was furnished by three continuously recording NOS tide gages at appropriate locations.

Navigation and positioning of the aircraft were accomplished with the tracking radar and plot-board capabilities available of NASA/Wallops Flight Center. Radar data are smoothed with a Kalman filter program to provide the highest possible accuracy. Radar data were merged with AOL data offline during processing to assign geographic coordinates to each laser sounding.

Water clarity measurements were made throughout the water column at numerous locations with a narrow beam transmissometer (Fig. 5-9) and were backed up with Secchi disk readings. A well correlated linear regression of beam attenuation coefficient (α) against inverse Secchi depth, Z_S , of the form $\bar{\alpha} = 7.0/Z_S - 0.16$ over the range $0.5 \leq \alpha \leq 6 \text{ m}^{-1}$ was noted, as seen in Fig. 5-10. This lends added credence to both sets of readings. Measurements were made in the vicinity of the flightline before, during, and after overflights. Attempts to measure diffuse attenuation coefficients (K) were foiled, with few exceptions, by baulky equipment. This is most unfortunate, because K , not α , is the correct parameter to use in describing laser penetration. K values have been inferred using Fig. 3-7 from measurements of α and a rough estimate of ω_0 from Fig. 3-8.

Winds were measured at the Wallops Island National Weather Service facility at several altitudes. Wind, waves, and visibility were measured subjectively from vessels at the flightline.

Bottom reflectivities in green and blue wavelengths were measured with a laboratory reflectometer. Grab samples were transferred in sealed plastic bags. Various handling and sample-preparation techniques were investigated and yielded essentially identical readings. Results are listed in Table 5-2.

Table 5-2. Sediment Reflectivities

<u>Sample Number</u>	<u>Site</u>	<u>Reflection %</u>		<u>Remarks</u>
		<u>Green</u>	<u>Blue</u>	
03	H	8.48	5.68	Course sand and shell fragments
05	I	8.06	3.87	Slightly course sand
06	J	8.14	6.48	Fine sand, some small shell fragments
07	K	6.84	5.31	Slightly course sand with some shell fragments
08	L	4.01	3.30	Fine sand, partially anaerobic (black)
09	L	12.80	8.23	Course sand and shell fragments
10	M	7.95	5.49	Course sand with some small pebbles
28	M	5.71	4.49	Very fine sand, slightly anaerobic
28A	M	8.54	5.78	Fine sand
29	M	9.79	6.52	Fine sand
30	L	6.78	4.62	Fine sand with some large shells
30A	L	6.76	5.34	Fine sand with some shell fragments
31	L	8.82	4.86	Course sand and shell fragments
32	L	11.45	6.94	Slightly fine sand
33	L	7.52	5.37	Fine sand
34	L	5.02	4.79	Very fine, anaerobic sand
34A	L	9.25	5.64	Slightly fine sand
35	L	8.88	5.58	Slightly fine sand
36	L	6.07	4.93	Fine sand
36A	L	6.94	5.28	Fine sand and shell fragments
37	K	3.15	3.11	Very fine anaerobic sand
38	K	9.48	5.78	Slightly fine sand
39	K	9.52	5.98	Slightly fine sand
40	K	7.13	5.35	Slightly course sand and shell fragments
40A	K	6.22	4.90	Slightly course sand and shell fragments
41	K	6.91	4.94	Slightly fine sand and some shell fragments
42	K	8.72	5.34	Mostly shells (large) with small amount of very course sand
43	J	9.91	5.93	Very course sand with many large shells
43A	J	5.54	3.93	Slightly course sand, small pebbles with large and small shells
44	J	8.66	7.47	Very fine sand and mud
45	J	8.21	5.70	Slightly course sand and many shell fragments
46	J	10.48	6.17	Slightly course sand, some shell fragments
47	I	9.49	5.22	Slightly course sand
48	I	7.87	4.20	Course sand and some pebbles
49	I	9.39	4.49	Course sand and pebbles, some shells
50	I	10.19	5.17	Very course sand and pebbles

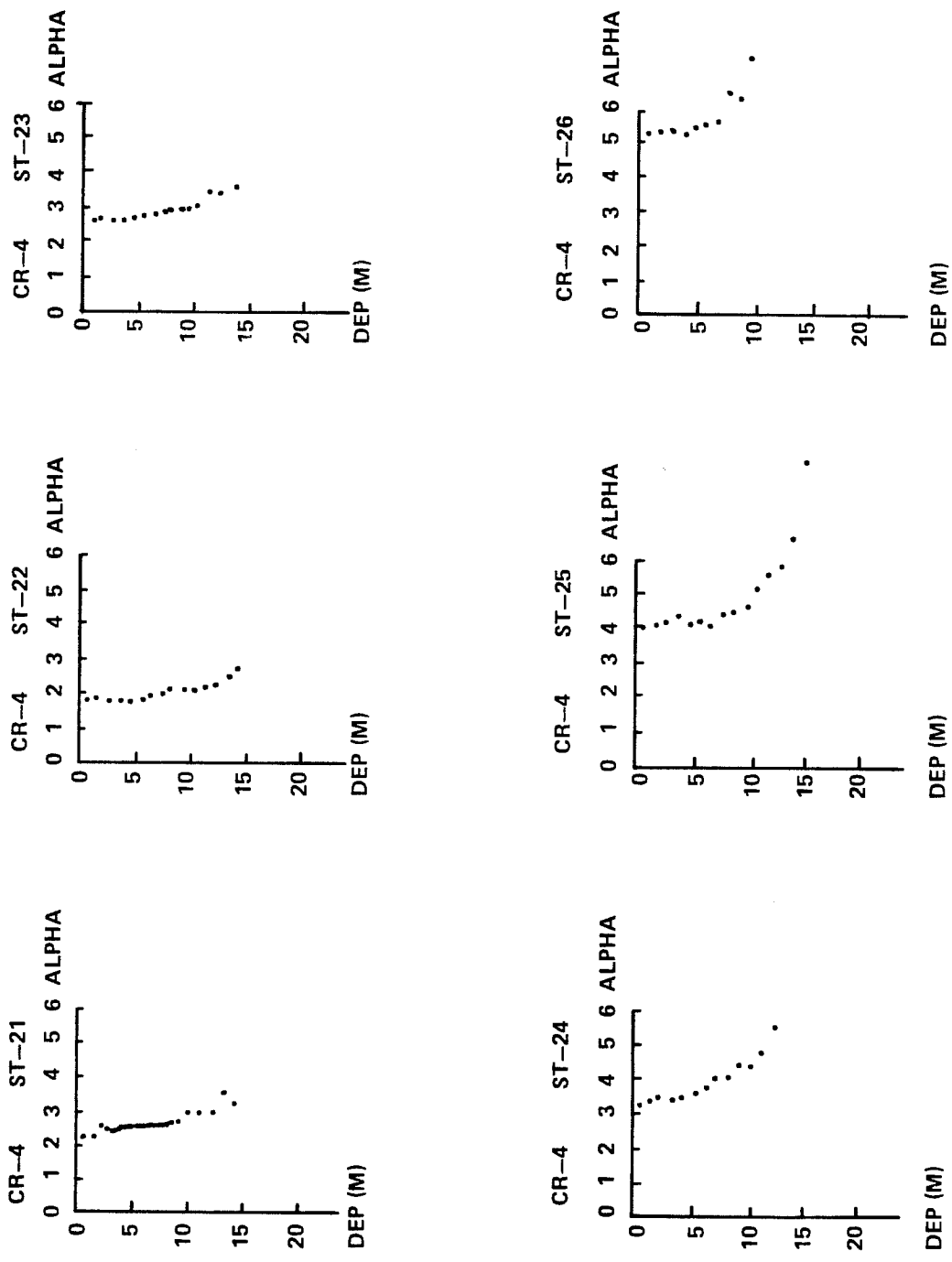


FIGURE 5-9. BEAM ATTENUATION COEFFICIENT PROFILES

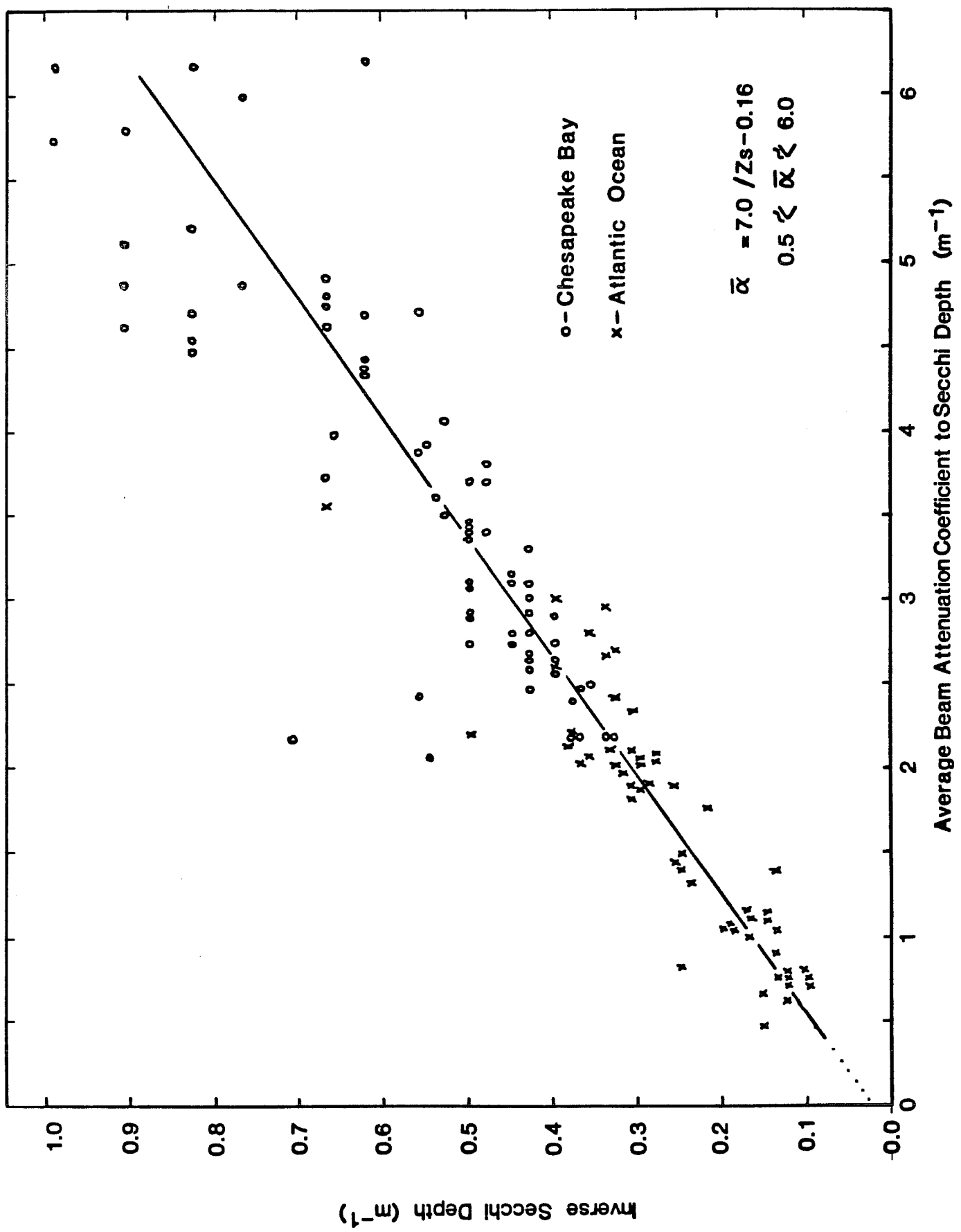


FIGURE 5-10. RELATIONSHIP BETWEEN BEAM ATTENUATION COEFFICIENT AND INVERSE SECCHI DEPTH

Table 5-3. AOL Test Priorities

<u>Variables</u>	<u>Priority</u>
Aircraft Altitude (500 feet, 1000 feet, 2000 feet)	1
Receiver Field of View (2 mr, 10 mr, 20 mr)	1
Scanner Nadir Angle (0°, 5°, 10°, 15°)	1
Transmitter Beam Divergence (2 mr, 10 mr, 20 mr)	2
Receiver Polarization (0°, 90°)	3
<u>Parameters</u>	
Water Depth (0 < D < 10 m)	1
Water Clarity (0 < $\bar{\alpha}$ D < 15; 0 < $\bar{\alpha}$ < 3 m^{-1})	1
Wind Speed/Wave Height (0 < w < 20 knots) (0 < h < 3 feet)	1
Solar Illumination Level/Angle (day and night; several hours after dawn and before dusk; noon; clear and cloudy)	2
Bottom Character (dark, light; clean, weedy)	3

5.4.3 Test Plans

"Variables" are herein defined as those quantities which can be altered at will. "Parameters" are considered to be those quantities which vary naturally and must be accepted as they are at any given time and place. Varying parameters experimentally thus consists of carefully choosing a time and place, based on some kind of foreknowledge, where the values of the parameters are expected to be those desired.

In order to thoroughly address the science and engineering objectives, a complete set of "independent" and "dependent" variables and parameters was defined. "Independent" variables and parameters chosen for investigation during the test phase are: water depth, water clarity, wind speed/wave height, solar illumination, bottom character, aircraft altitude, scanner off-nadir angle, receiver field of view, transmitter beam divergence, and detection algorithms. "Dependent" parameters studied for effects of the above are accuracy (precision, profile correlation, bias, and repeatability), hit probabilities, extinction coefficients, system attenuation coefficients, minimum resolvable depths, surface return signal strengths, bottom return signal strengths, and noise levels. AOL variables and parameters, presented with their ranges of variation, were prioritized for exhaustive variation during flight tests, as listed in Table 5-3.

Experiments were planned to permit the individual contributions to system error and usage constraints to be separated. A more or less exhaustive variation of all top priority variables and parameters against each other was desired to insure that the system could be properly characterized and completely understood. Because resources were limited, parameters could not be chosen at will; a detailed plan (tempered by a great deal of adaptability to changing environmental conditions) along with good predictive capability was required. Each mission was driven by a rigorous Mission Plan which was written around some particular aspect or requirement of the overall flight experiment plan. Each mission plan contained, at a minimum, the following information:

General Description - Explanation of mission objectives and approach.

Constraints - List and explanation of the environmental constraints affecting mission go/no-go decisions; information on additional mission science requirements.

Sea Truth Operations - Description of boat operations, departure times, run times, equipment requirements, etc.

Flight Operations - Flightline descriptions, altitudes, airspeeds, etc., for flight crew briefing.

Range Support - Description of desired radar complement, data rates, calibration procedures, beacon characteristics, etc.

Instrument - AOL set-up sheet(s) for the mission; includes all operating parameters and mode options for the mission.

Schedule - Overall activity schedule coordinating boat, aircraft, and range activities including preflight and postflight activities.

Staff and Communications - List responsible individual in each area and overall mission operations officer; includes communications information.

A typical mission (flight) lasted one to two hours and consisted of ten to 15 passes over a predetermined flightline. After each mission, a debriefing session was held with all involved personnel. This session was followed up by a written debriefing summary prepared by the mission operations officer.

Because these experiments were begun upon delivery of the system and with no flight experience whatsoever, the test flights were divided into two series: first, the "Flight Acceptance" tests which were shakedown flights to work out hardware problems and demonstrate system readiness; and second, the "User Flight Experiment" tests designed to provide the desired science and engineering data.

The general test strategy for the Flight Acceptance tests was to begin with optimal conditions, i.e., low α , moderate depths (1-5 m), 150-m aircraft altitude, 5 degree scanner nadir angle, no receiver polarization, 3-10 knot wind speed, low sea state (but not calm), maximum receiver field of view (20 mr), moderately low transmitter divergence (5 mr), clean sandy bottom, and moderate background light level (after dawn or before dusk, or night). A number of "identical" passes were made to investigate basic system variability and noise levels. Other passes were made to evaluate the optimum electronics configuration: amplifier gain, PMT voltage, etc. When confidence was gained through successful operations, the variables considered to have potentially minimal effect on the overall results -- transmitter beam divergence and receiver polarization -- were given sufficient scrutiny to permit them to be adjusted to and temporarily fixed at appropriate values while the effects of varying the higher priority variables and parameters over appropriate ranges were extensively studied. When successful operation was not reliably obtained, a fallback position of determining the specific cause(s) and reason(s) was undertaken.

Because of dwindling resources, the switch from Flight Acceptance tests to User Flight Experiment tests was made long before the system was properly qualified, and several hardware problems (mentioned later) were never fully resolved. Nevertheless, a four phase test program, as described in Table 5-4, was successfully undertaken.

The data base for each mission included a mission plan, the AOL system output tape(s), a digitized flight log of equipment settings and notes, a digitized ground data log, filtered radar tracking tapes, ground calibration data, a list of tape and data file numbers, a debriefing report, measured tide correctors, and sometimes ancillary materials such as footprint camera films, scope photos, and video tape of the monitor. All this was archived for subsequent multivariate analysis.

In 1977, 18 missions were flown with a total of 161 separate passes. An estimated total distance of 1000 linear nautical miles and 400 minutes of recorded data, comprised of five million soundings, were recorded. Aircraft speed was maintained at approximately 150 knots with altitudes ranging from

TABLE 5-4. AOL FIELD TEST SUMMARY

- PHASE 0: HARDWARE SHAKEDOWN; SIGNAL STRENGTH AND NOISE ASSESSMENT; PRELIMINARY ENGINEERING PARAMETER, CONSTRAINTS, AND TEST SITE EVALUATION.
- PHASE 1: INVESTIGATION OF ALTITUDE, RECEIVER FIELD OF VIEW, AND TRANSMITTER DIVERGENCE EFFECTS AT 5° OFF NADIR; DAY AND NIGHT, SCANNING AND FIXED.
- PHASE 2: INVESTIGATION OF OFF-NADIR ANGLE EFFECTS FROM 0° TO 12.6°.
- PHASE 3: SCANNING AND FIXED BATHYMETRIC FLIGHTS ON WELL SURVEYED BUOY LINE, NIGHT AND DAY; FLIGHT AROUND CHESAPEAKE BAY UTILIZING TARGETS OF OPPORTUNITY IN RIVERS, BAYS, INLETS, HARBORS, ETC.

150 - 600 m. Missions were flown in river, bay, and ocean waters; in summer and winter; clear and cloudy; night and day; for winds from 0 to 15 knots; with and without capillary waves; in water clarities with narrow beam attenuation coefficients varying from less than 1 m^{-1} to greater than 4 m^{-1} ; and with water depths from zero to over 10 m.

5.4.4 Data Processing

The tremendous volume of data acquired on even a single pass caused computer analysis to be mandatory. A wide variety of programs on a number of computers were developed for data verification, reduction, display, analysis, and troubleshooting as seen in Fig. 5-11. The primary analytic tool for AOL data analysis was a multifunction program called the "Processor" (Borman 1978, Guenther and Borman 1981). This program is extremely versatile because it is based on a free-form "keyword" input procedure with liberal defaults. Desired functions or procedures are easily activated and quantified by the inclusion of a single card in the setup deck.

Briefly, the Processor unpacks and interpolates the asynchronous system data tape, applies various calibration and noise suppression procedures, identifies surface and bottom returns and quantifies their location and amplitude under control of a highly parameterized tracking algorithm, performs wave height correction, prints and plots altitudes, depths, waveforms, statistics, and other requested information, and supplies regressions and correlation values for all combinations of eleven specially selected parameters. Sample outputs are included as Figs. 5-12a, b, c. An additional program was developed to compare airborne lidar soundings with corresponding launch acoustic soundings and regress differences against a given parameter set.

5.5 Flight Acceptance Tests

5.5.1 Hardware Problems

As one would expect, numerous problems were encountered both in preflight ground tests and in the initial Flight Acceptance tests. Many could not be

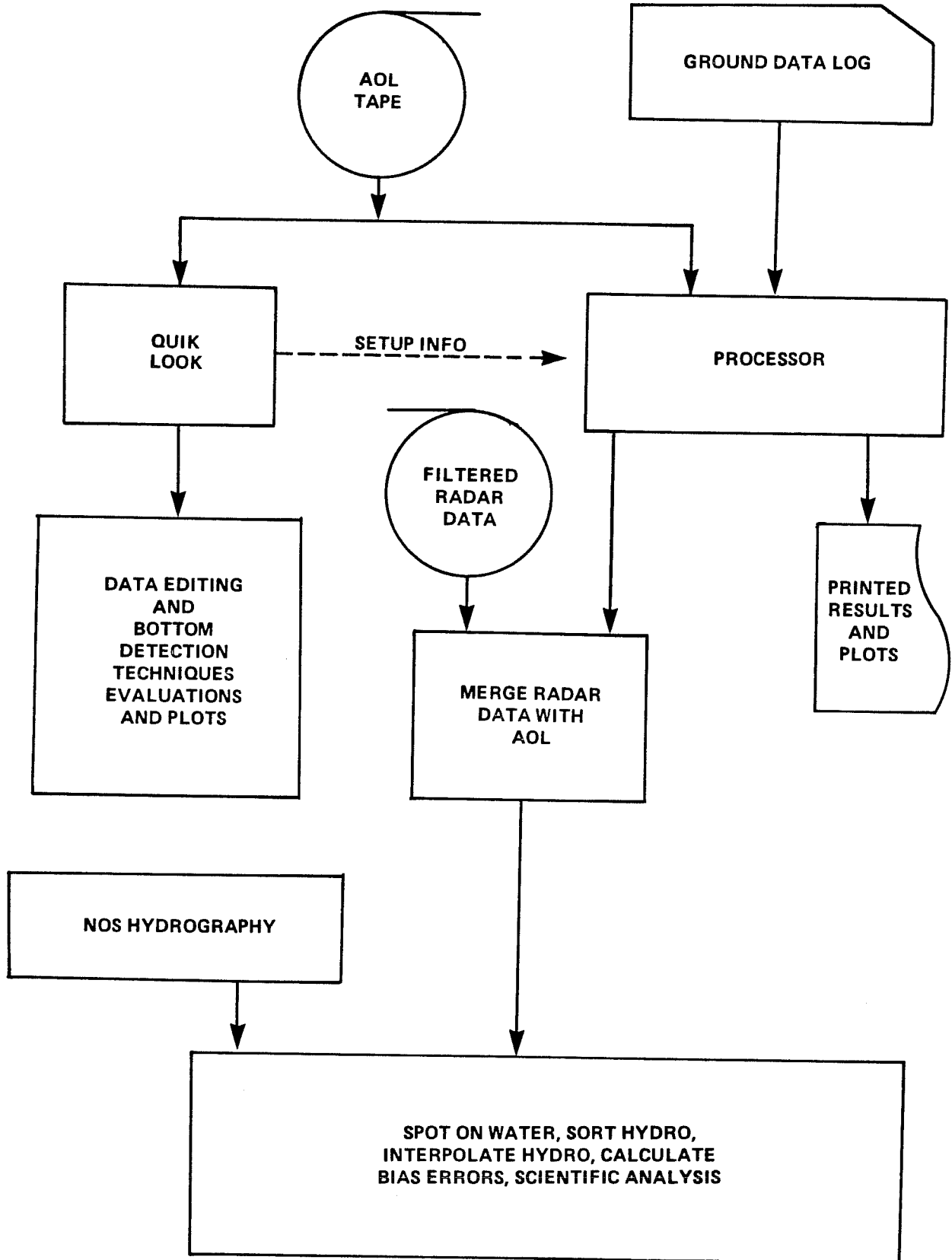


FIGURE 5-11. AOL DATA PROCESSING

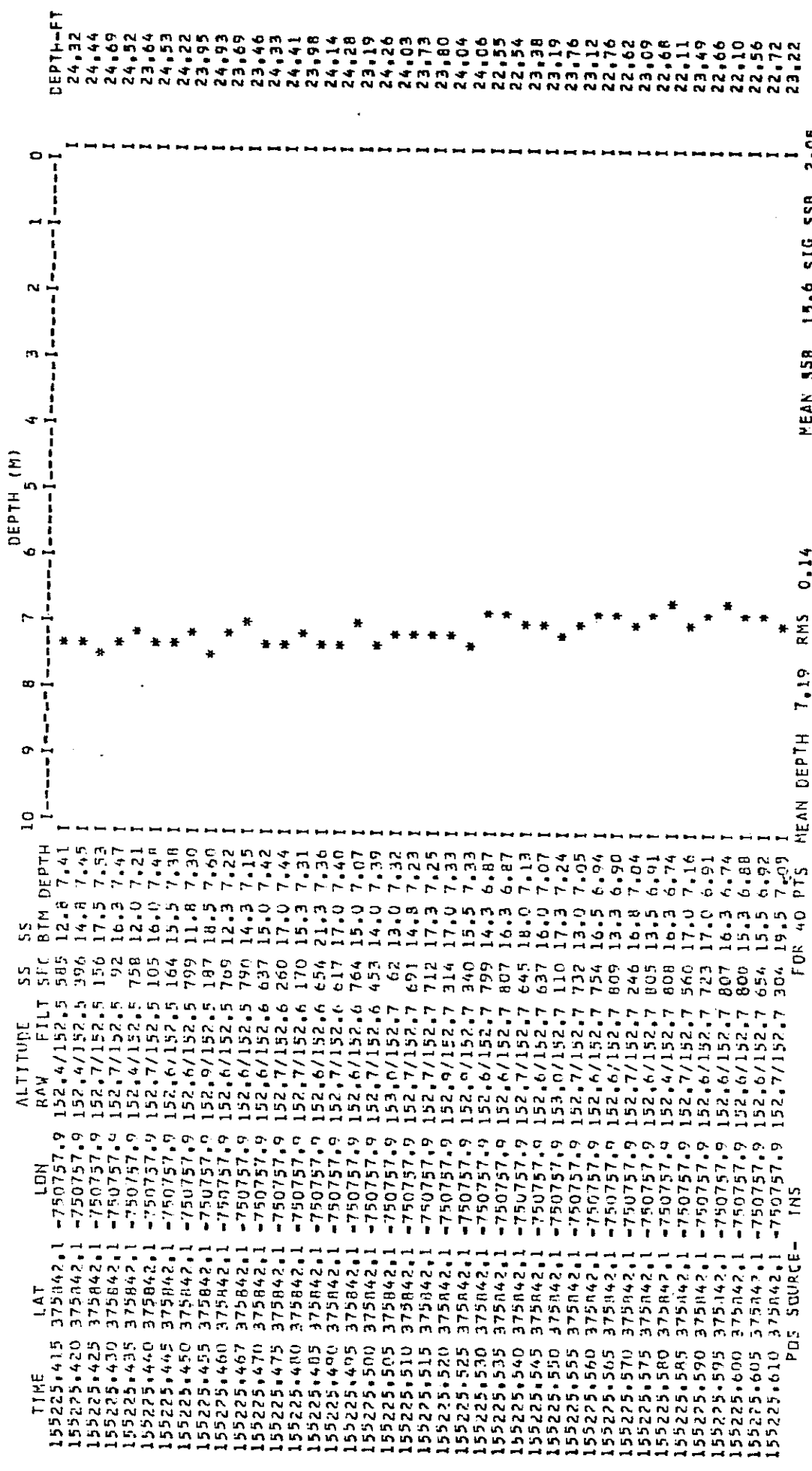


Figure 5-12a. AOL Processor Output: Depth Profile

1	RAW DEPTH	2 MNL DEPTH	3 KWL DELTA	4 FILT ALT	5 SFC SS	6 LASER POWER	7 BTM SS	8 BTM EGY	9 LN(EGY)	10 LN(SSB)	11 SHOT NO
CCRELATIONS											
1	1.0000										
2	0.4871	1.0000									
3	-0.4677	0.5641	1.0000								
4	2.0000	2.0000	2.0000	2.0000							
5	0.4712	0.0336	-0.4012	2.0000	1.0000						
6	2.0000	2.0000	2.0000	2.0000	2.0000	2.0000					
7	0.0617	-0.1072	-0.1552	2.0000	0.3363	2.0000	1.0000				
8	-0.5067	-0.3989	0.0972	2.0000	0.0784	2.0000	0.6541	1.0000			
9	-0.4904	-0.4256	0.0578	2.0000	0.0740	2.0000	0.6320	0.9404	1.0000		
10	-0.0033	-0.1616	-0.1457	2.0000	0.2852	2.0000	0.9795	0.6795	0.6800	1.0000	
11	-0.3611	0.3051	0.6154	2.0000	0.0426	2.0000	0.1110	0.3487	0.2496	0.0990	1.0000

Figure 5-12b. AOL Processor Output: Statistical Correlations

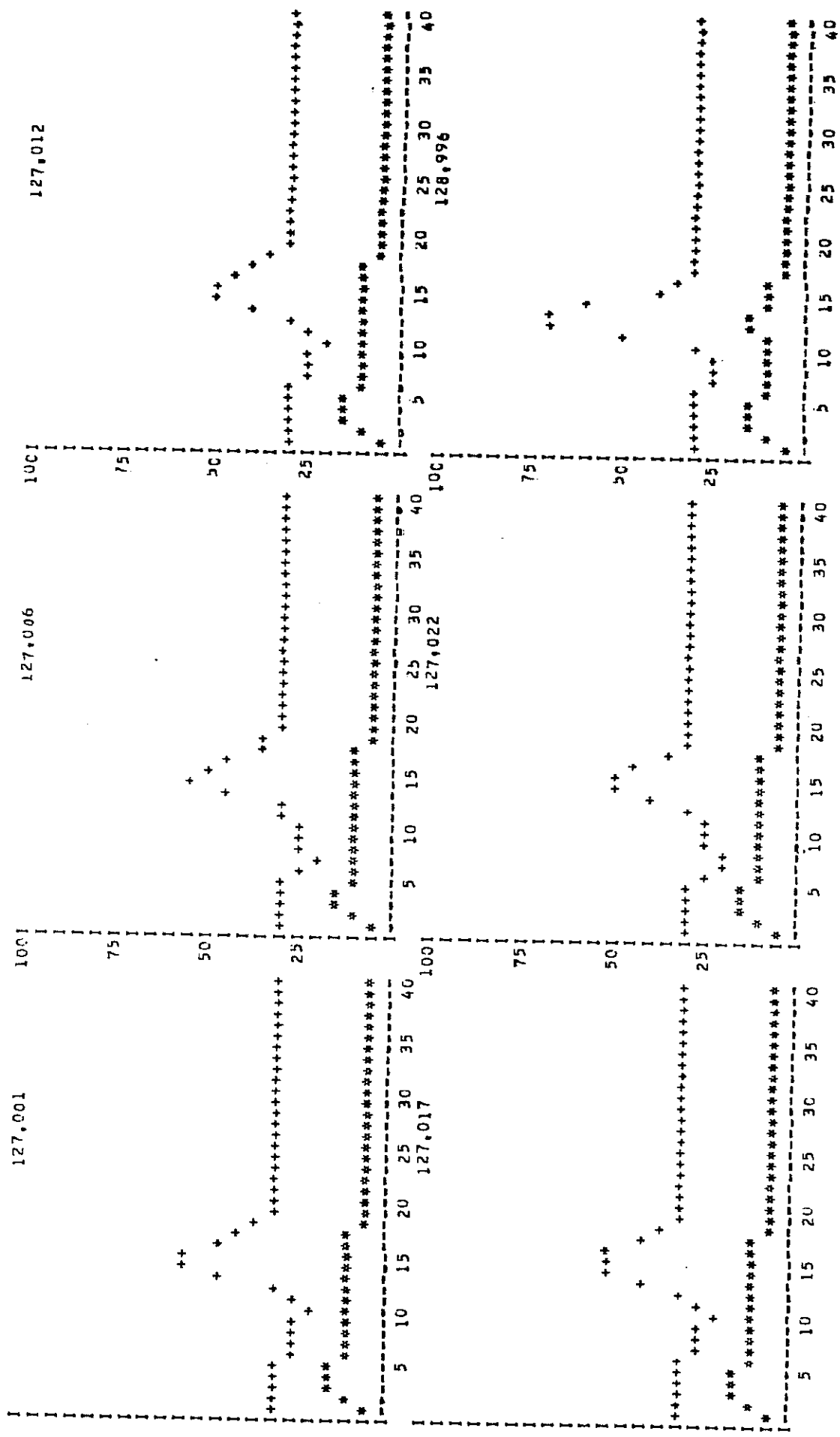


Figure 5-12c. AOL Processor Output: Bottom Returns

ameliorated with available resources and carried through into the user tests. Examples are:

- 1) The ambient temperature of the equipment racks was initially above the expected value; this aggravated temperature instability problems in the nominal 2.5-ns gate width of the charge digitizers. Using an extension of the analysis performed by Thomas (1977), it was determined that the gates could be widened to four nanoseconds without appreciable degradation of accuracy, provided the 2.5-ns start time interval was maintained. At this greater width, the temporal stability of the gate widths was significantly improved. Additional cooling fans were also added to the racks.
- 2) Experiments were conducted in which the original "161" unity-gain amplifier was replaced by either a "333" variable gain or a "612" fixed gain (10X) amplifier. The 612 was determined to provide superior performance and supplanted the 161 in the "standard" configuration.
- 3) The very narrow band (0.4 nm) optical "interference" filter was very temperative sensitive and should have been enclosed in a temperature controlled environment. Because it was not, the center frequency of the filter moved off the laser line and caused signficant loss of signal -- particularly in cold weather.
- 4) The system was not radiometrically calibrated during the program, and significant gain changes were discovered in the data after the test program. The PMT was periodically operated with excessive anode current during ground tests and underwent degradation in efficiency over a period of several months during the test program. This made it very difficult to compare later results with earlier flights.
- 5) The amplitude dynamic range of the system design was extremely limited and had a useful range of only 2-1/2 decades. In order to achieve the required sensitivity for weak bottom returns, the lower

end was set near the shot noise limit. Consequently, strong surface returns solidly saturated the electronics. Ringing was observed throughout the dynamic range, and weak bottom signals were swamped out. To resurrect the bottom returns, a special technique called "deep-water calibration" was developed as described in the next subsection.

- 6) Precise time/depth calibration of the digitizer gates was impractical due to bandwidth-limited test equipment and drifts with time, temperature, vibration, etc. Absolute depth calibration at any given time was probably no better than 0.5 ns (6 cm of depth). Occassional instabilities caused unexplained depth "wander" of as much as 20 cm, as evident in several ground tests using a fixed target reflector.
- 7) Laser power was considerably below the 30 kW originally advertised. Indeed, the total laser output in the green rarely exceeded 2.5 kW, and somewhat less than 1 kW exited the aircraft in the "primary" beam due to losses of power from the unstable resonator and transmitter optics. This significantly limited the maximum penetration potential of the system. The unstable resonator also caused the emission of an undesirable extra beam (much larger in divergence than the primary beam) which interfered with the determination of field-of-view effects.
- 8) The 20-mr maximum field of view is too small to receive the entire bottom return signal for a 150-m aircraft altitude.
- 9) The altitude intervalometer resolution was too coarse (15-cm steps) to permit the wave correction procedure to be optimized.
- 10) Numerous other problems were encountered with dropped data blocks, noisy scan encoder azimuth readouts, and anomalous signal populations to name just a few.

5.5.2 Deep-Water Calibration

The return signatures of the first data set were somewhat different from those anticipated. Typical returns are illustrated in Fig. 5-13. The surface returns are readily detectable, but the bottom returns, if there at all, are not evident and apparently buried in a combination of system and environmental noise. A crash effort was implemented to determine the extent and cause of the problem. If each individual return had randomly located maxima and minima, no procedure could extract weak bottom returns. It was quickly recognized, however, that the return signatures for all pulses appeared to be nearly identically congruent. This suggested that the first three listed noise sources -- those which were systematic in nature and independent of the bottom return -- provided the bulk of the problem.

The existence of several serious defects in the electronics subsystem, namely, 1) excessive ringing caused as a result of the relatively strong surface return pulses, and 2) significant long-term instabilities in the charge digitizer gate pulse widths created a situation in which the actual low amplitude bottom returns were completely masked by spurious but reproducible and predictable system noise. In order to significantly reduce the effect of these anomalies, a calibration technique was developed around the concept of measuring the system response in a region of deep water (from which no bottom return could be received) for each pass over the target area. The measured response was then subtracted from the experimental data sets to leave (hopefully) only the true bottom return energy as a signal for further analysis (Fig. 5-14).

Because the ringing amplitude in a data pulse is a strong function of the surface return amplitude, the calibration vector utilized had to be derived from pulses with similar surface return amplitudes. To this end, a set of calibration vectors was computed over subranges from the bounding range of surface return amplitude. Each data waveform was then corrected with a vector derived by interpolation (on the basis of surface return amplitude) between the nearest pair of available calibration vectors. This technique was not foolproof, but it was generally reliable. Excellent resolution of bottom

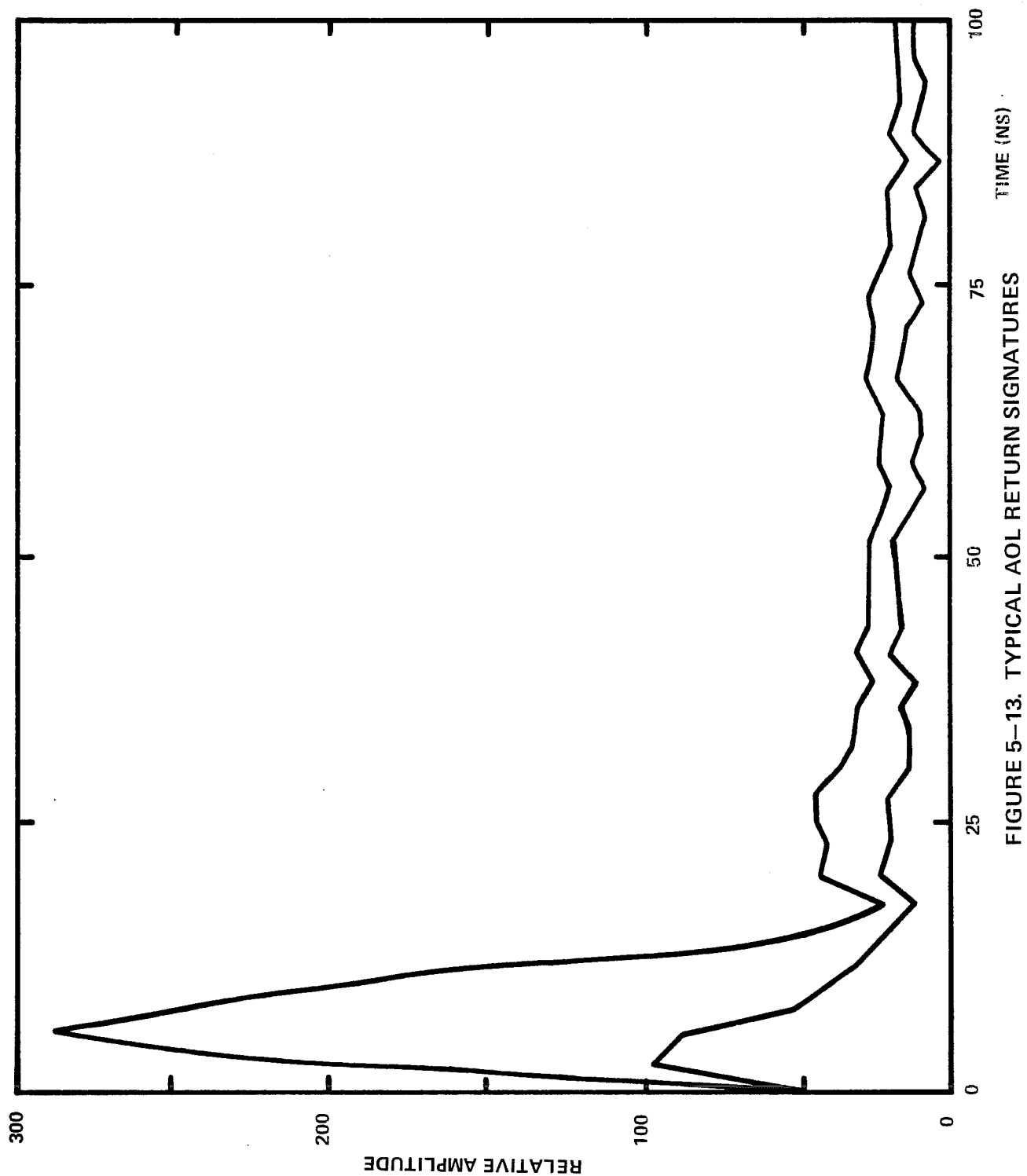


FIGURE 5-13. TYPICAL AOL RETURN SIGNATURES

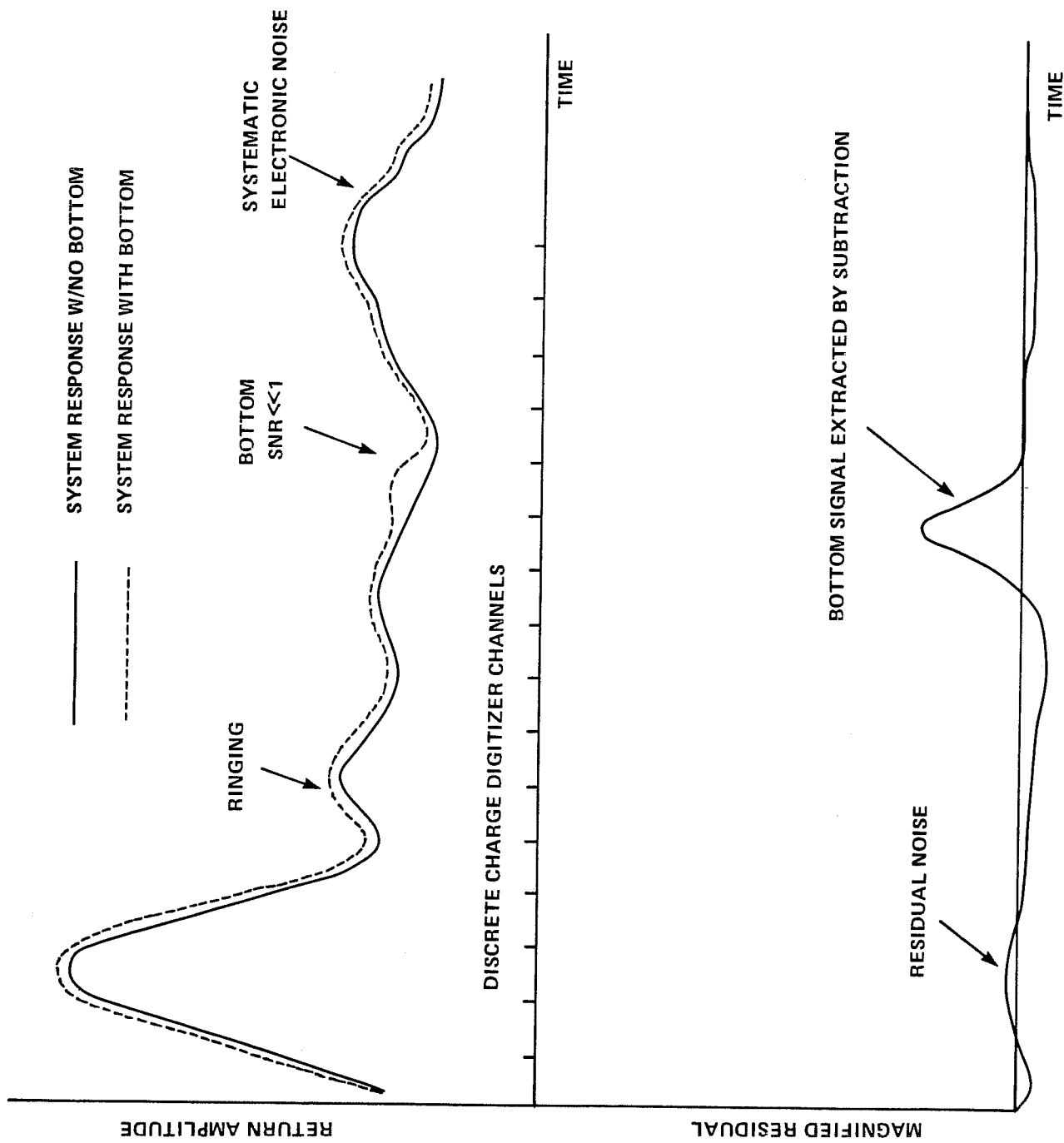


FIGURE 5-14. AOL DEEP WATER "CALIBRATION" PROCEDURE

returns was achieved even for very weak returns approaching the digitization limit of the system (approximately 50 nanowatts at the scanner).

A drawback was the fact that the calibrated or "residual" waveform could be bipolar and would exhibit negative values when elements of the deep-water vector was larger than their counterparts in the data sets. This resulted in many residuals consisting of a slightly negative (two or three discretes) pedestal upon which the bottom return was superimposed. Special processing algorithms were created to provide bias-free depth estimates from such pulses. Similarly, the residuals could exhibit positive plateaus if the calibration vectors were too small overall. Such plateau pulses were caused by another hardware defect: multiple pulsing of the charge digitizer gates by malfunctioning "one shots".

A side effect of the deep-water calibration was the suppression of the surface and volume returns. This was sometimes useful in very shallow water where the surface and bottom returns merged together. The residual bottom return could be detected without contamination from surface energy except for the difference between the actual surface return and the calibration vector. Due to minor variations in surface pulse width, this difference was evident in the residual as a frequent spike (usually negative) at the trailing edge of the surface return location.

5.6 Engineering Results from "User" Flight Tests

5.6.1 General

The effects on surface and bottom return signal strengths of water clarity, altitude, receiver field of view, nadir angle, transmitter divergence, wind, and night versus day were examined in the flight program. In order to maintain maximum experimental control and significantly simplify data processing, many test flights were conducted with the scanner fixed at a selected off-nadir angle but not rotating. In this way the off-nadir angle remained constant (as opposed to varying somewhat as it does through the scan pattern), a simplified wave corrector could be used, pulses were closely spaced so that a measure of pulse-to-pulse depth measurement precision could

be calculated, and depth comparisons against a sonar survey were greatly facilitated. The fact that the beam was not always scanning in no way affected the resulting measurements. Sufficient passes were flown in the scanning mode to permit its full evaluation.

The transmitter beam divergence, varied from two to ten milliradians, had virtually no effect on results. The only potential restriction was that the beam had to be large enough to provide high surface return probability. Resolution of features is not degraded with a larger divergence because the beam spreading in the water is much greater. Polarization effects were not studied in detail because it was discovered that the insertion loss of the polarizers negated the potential benefit of improved contrast between the bottom return and the volume scattering.

Bottom compositions typical in Chesapeake Bay caused no evident bottom detection difficulties. Reflectivities for sediments consisting of various grades of mud, sand, and shell fragments ranged between three percent and 13 percent with a median of approximately nine percent (Table 5-2). Significant bottom vegetation was present in neither test site. Future testing of systems will need to be planned for bottoms populated by various forms of broad and narrow leaf plants. It is expected that various types of vegetation could distort the bottom signal or cause a shallow bias in soundings.

5.6.2 Surface Return

As expected from previous NADC results (Petri 1977, as seen in Fig. 4-2), the interface return was a strong function of nadir angle, wind speed, and altitude (Fig. 5-15). Typical interface return strengths ranged from 1 to 25 microwatts of optical power into the scanner (ten to several hundred times larger than typical bottom returns). Behavior of the surface return with altitude was typically inverse square, but several effects -- namely charge digitizer saturation on the high signal strength end and the inclusion of the volume scattered energy on the low end -- sometimes caused the apparent power law exponent to be somewhat less than two. Sun glint proved to be no problem in AOL testing, because scanner nadir angles were not large

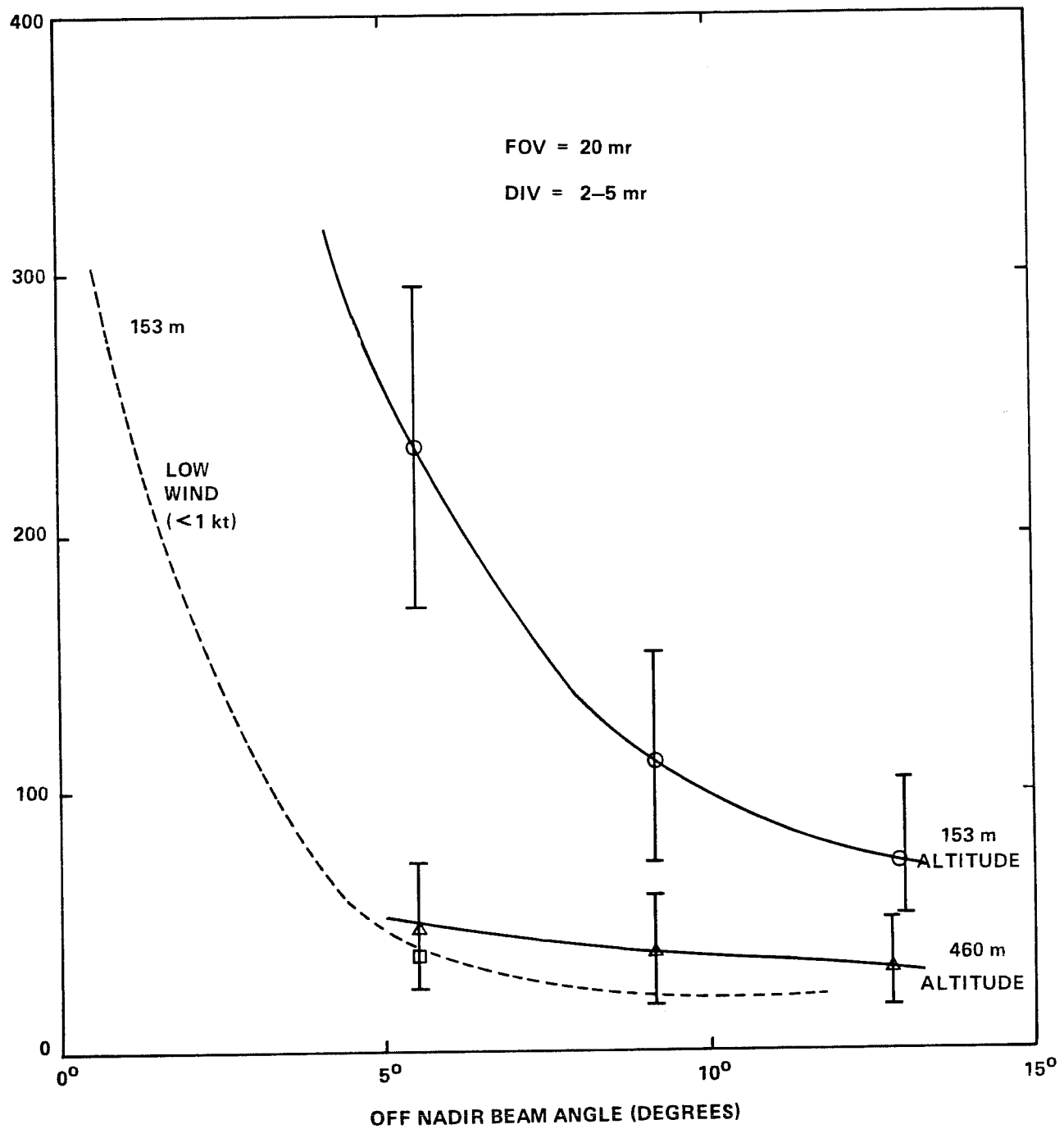


FIGURE 5-15. MEAN SURFACE RETURN AMPLITUDE VS.
OFF-NADIR BEAM ANGLE

enough to permit viewing of the glint pattern at the 38 degrees latitude of the test sites. (For low latitudes, noon-time summer operations might have to be curtailed).

Interface returns at nadir were very strong (and exceeded system capabilities) except for winds below about three knots where they became quite erratic (some very strong and some very weak depending on whether the slope of the smooth sea surface was perpendicular to the beam or not). The interface return strength drops off very quickly with increasing nadir angle due to a drop in the number of tiny capillary wave "facets" perpendicular to the beam. (For a complete mathematical description in terms of Cox-Munk wave slopes, see section 7.2). For larger nadir angles, higher winds are required to excite the required capillary wave slopes. For higher winds, the interface return strength drops more slowly with increasing nadir angles, and the overall dynamic range is less.

Because of the low laser power, low wind conditions sometimes resulted in loss of surface return as seen in Fig. 5-16. This was somewhat alleviated by lowering the surface return detection threshold level in the electronics. Surface returns at the PMT were stronger at night when the interference filter could be removed. Low surface return strength will not be a problem with a high power system, as seen below. Although the AOL was configured for a maximum nadir angle of 15 degrees, larger angles were deemed reasonable based on extrapolated test results. (For nadir angle limitations, see sections 9.2.2 and 10.2).

Volume backscatter was not generally evident in the raw waveforms due to the system ringing, the low laser power, and the relatively murky waters extant during testing (which caused a rapid decay rate). The "Deep Water Calibration" procedure removed the volume signal entirely from the "residual" waveform from which bottom returns were detected. For weak surface return strengths, however, it was noted that the shape of the surface return was distorted so that the peak occurred in the fourth charge digitizer "bin" instead of the customary third. It was determined that these were actually volume backscatter returns for the case where the interface return energy was too small to detect.

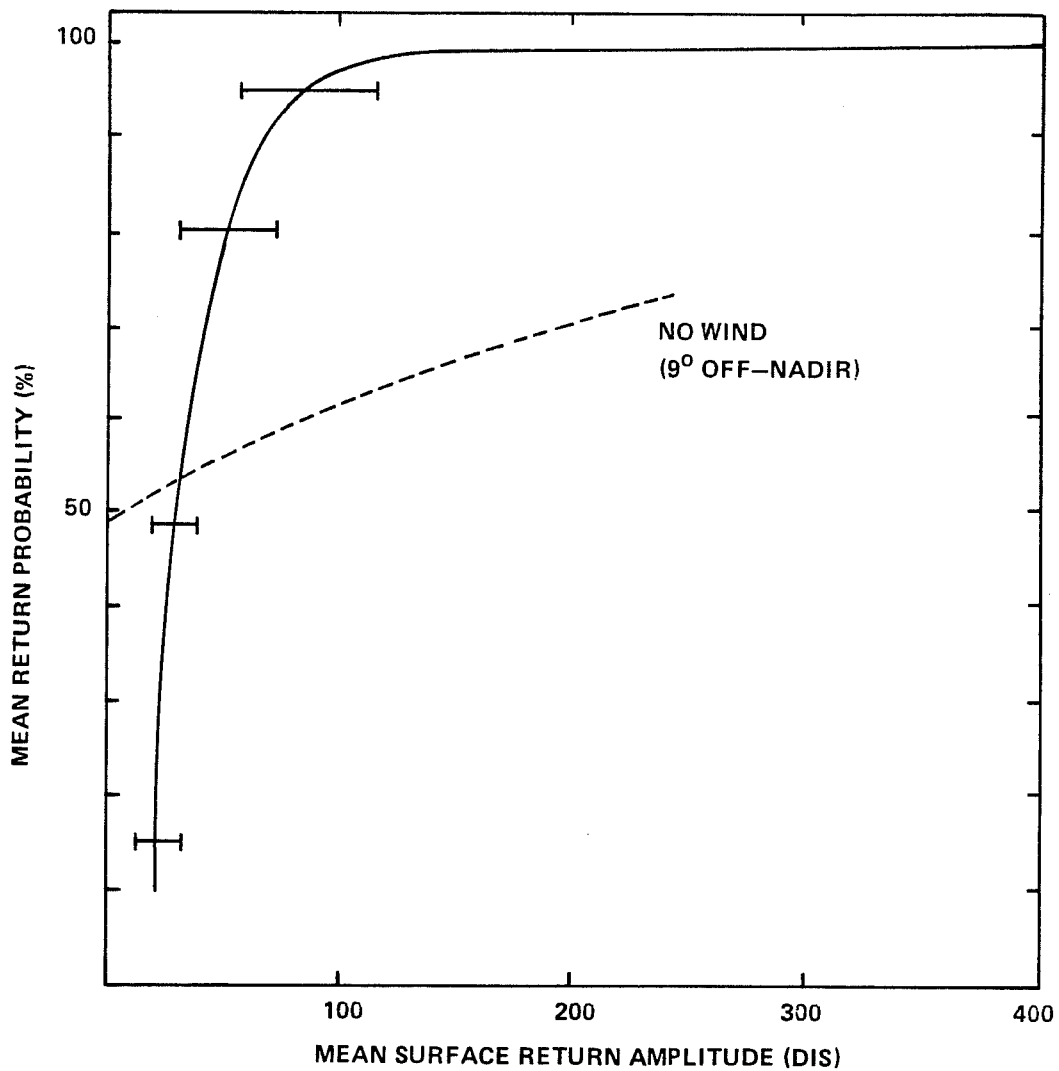


FIGURE 5-16. SURFACE RETURN PROBABILITY VS.
MEAN SURFACE RETURN AMPLITUDE

For a high power system, when the wind is too low to generate sufficient capillaries at the required angle, the interface return may disappear, but in this case, the volume return will be detected and interpreted as the "surface". This means that operations can be conducted even when no wind is blowing. It must be recognized, however, that this will lead to a shallow depth measurement bias (as discussed in sections 7.4 and 9.2.2) because the volume return occurs not from the interface but from a depth somewhere between the surface and one pulse width (FWHM) into the water (the exact amount depending on water clarity and pulse location technique). Volume backscatter "surface" returns resulted in shallow biases in several AOL tests as will be seen in section 5.8.3.

An unexpected relationship arose during AOL testing: the surface (interface) return strength was strongly correlated with the per-pulse measured depth (before wave correction). This was worrisome because it was difficult to determine cause and effect: i.e., was the measured depth a function of the surface return amplitude or visa versa? The former would be a very serious problem because of the implication on accuracy. Luckily, it was shown that the latter was true. Wind generated capillary waves tend to pile up near the wave crests; these in turn appear "bright". The wave troughs are more sheltered and have fewer and lower angle capillaries; they appear "dark". Because of this, the wave crests, where the water is truly deeper, had larger surface returns, and the wave troughs, where the water is shallower, exhibited smaller surface returns. The waves in the depth data were proven to be real -- not the effect of a surface return strength dependent depth algorithm -- because they correlated strongly with the same waves in the independent laser altimeter data.

5.6.3 Bottom Return

The PMT in the AOL was hand selected to have the lowest possible dark current -- about 0.2 nanoamps, according to the manufacturer. Because of this, bottom returns could be detected all the way down to a shot-noise limited level. Bottom returns estimated to be as low as 100 nanowatts were tracked successfully.

It was noted during the calculation of noise statistics that the PMT performance degraded significantly over a three month time period. The system was never radiometrically calibrated; if it had been, the problem would have been noted immediately. The loss of performance was traced to PMT damage from excessive anode currents sustained during ground tests. Because of this problem, it is not possible to directly compare absolute bottom (or surface) signal strength results from flight to flight.

The major factor determining bottom return signal strength is the KD product, as seen in section 8.2. For fixed KD, the altitude dependence is inverse square if the field of view is sufficient. For constant altitude, the bottom return strength is maximum at nadir and decreases -- albeit much more gradually than the interface return -- with increasing nadir angle. The contributors to this decrease are geometric: longer water paths and pulse stretching due to oblique incidence on the bottom.

The major system design feature affecting bottom signal strength is receiver field of view (FOV). This determines the size of the spot from which bottom reflected energy can be detected, as seen in sections 4 and 8.2.5. Typical AOL results are depicted in Fig. 5-17 for two altitudes. For given conditions, larger FOVs are required for lower altitudes. It is clear from Fig. 5-17 that even for the relatively shallow depth of 6 m, the AOL maximum FOV of 20 mr was insufficient to encompass all of the bottom return energy from a 150-m altitude. For deeper returns this problem would be even worse because the additional spreading incurred over the greater distance would lead to a wider bottom return energy distribution. It should be noted that in AOL results such as Fig. 5-17, the apparent FOV requirement is somewhat exaggerated due to the presence of stray energy outside the quoted beam divergence because of the undesirable properties of the unstable resonator. Higher altitudes decrease the FOV required but are not desirable (unless the swath width is insufficient) due to the added inverse-square loss. The AOL FOV should have been closer to 100 mr for operation to a 20-m depth from a 150-m altitude.

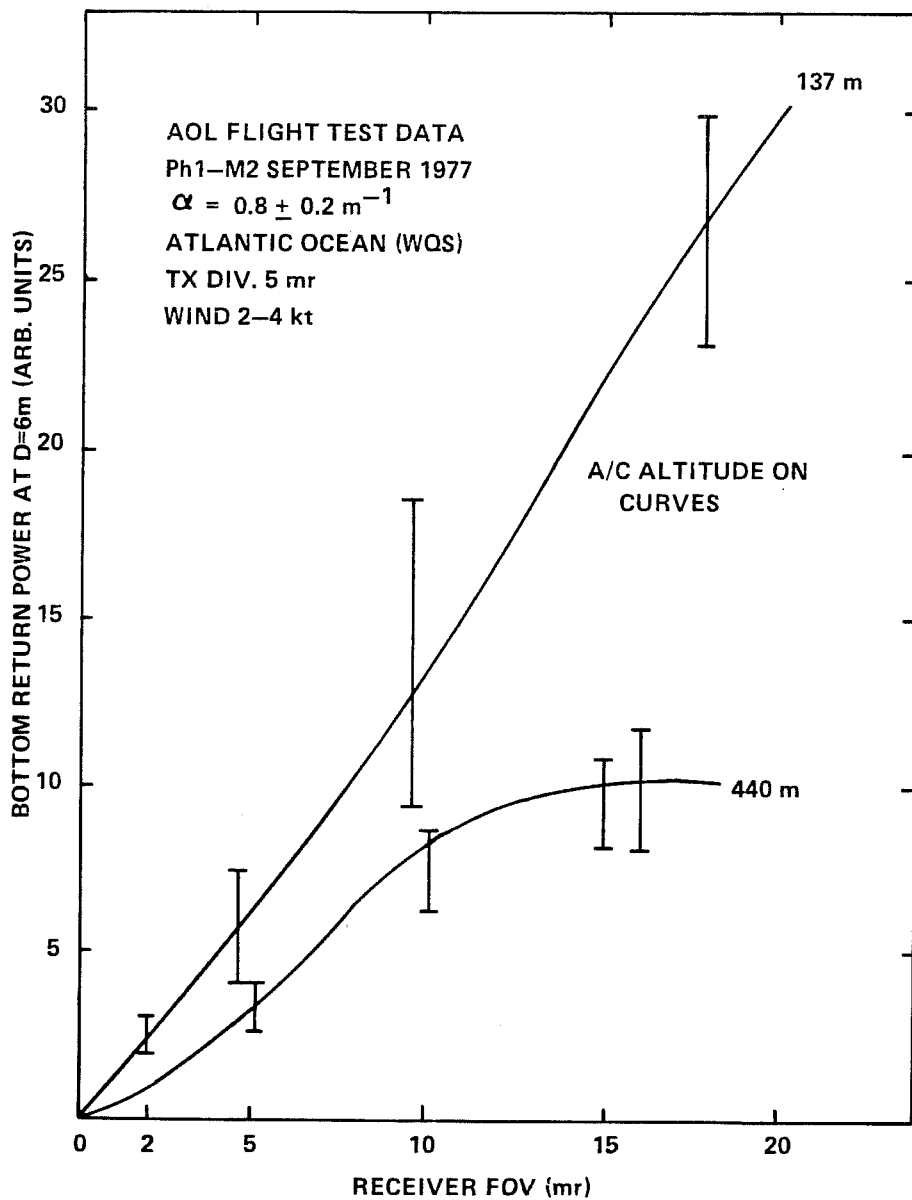


FIGURE 5-17. BOTTOM RETURN POWER AT D = 6 m
VS. RECEIVER FOV

The depth at which bottom returns become so weak that depth measurement precision becomes unacceptably degraded is defined as the "extinction" depth, D_m . In previous literature, the product, KD_m , has been identified as the "extinction coefficient". The implication is that, for a given system and altitude, this quantity is fixed and can be used to predict D_m if K is known. As seen in section 8.2.2, this is a pulse energy (rather than peak power) argument and does not include the effect of pulse stretching. In actuality, it has been shown for a 7-ns source pulse that the quantity $n(s, \omega_0)KD_m$ is constant, where $n(s, \omega_0)$ ranges between 1.0 and 1.3 for typical waters. It is absolutely incorrect to state extinctions in terms of αD_m because the penetration depends on K , not α , and the relationship between α and K depends strongly on the single-scattering albedo, ω_0 , as noted in section 3.6.

Extinction depths were determined for the AOL under water clarity conditions ranging from moderate to very turbid. Because of the low transmitter power, these depths were limited to less than about 8 m. Simultaneous measurements of K were desired, but the K -meter utilized failed repeatedly, and only α and Secchi readings were obtained. The α readings were converted to estimated K values using the equations and relationships presented in section 3. Measured values of $n(s, \omega_0)KD_m$, which varied considerably with altitude as expected, were obtained for both daytime and nighttime operation. For a 150-m altitude, typical values range from 2.3 during the day to a maximum of 3.3 at night (over twice the Secchi depth). This is surprisingly good considering the very low laser power. Extrapolation of these results to a higher powered system is reported in section 8.5.

Since the bottom return signal strength is exponential with increasing depth, an estimate of K can be obtained from the slope of a logarithm of bottom signal strength vs depth plot (assuming constant water clarity over the depth range). Typical plots of such AOL data are seen in Fig. 5-18. Values of K measured in this way were generally consistent with K estimates from in-situ α measurements and ω_0 assumptions.

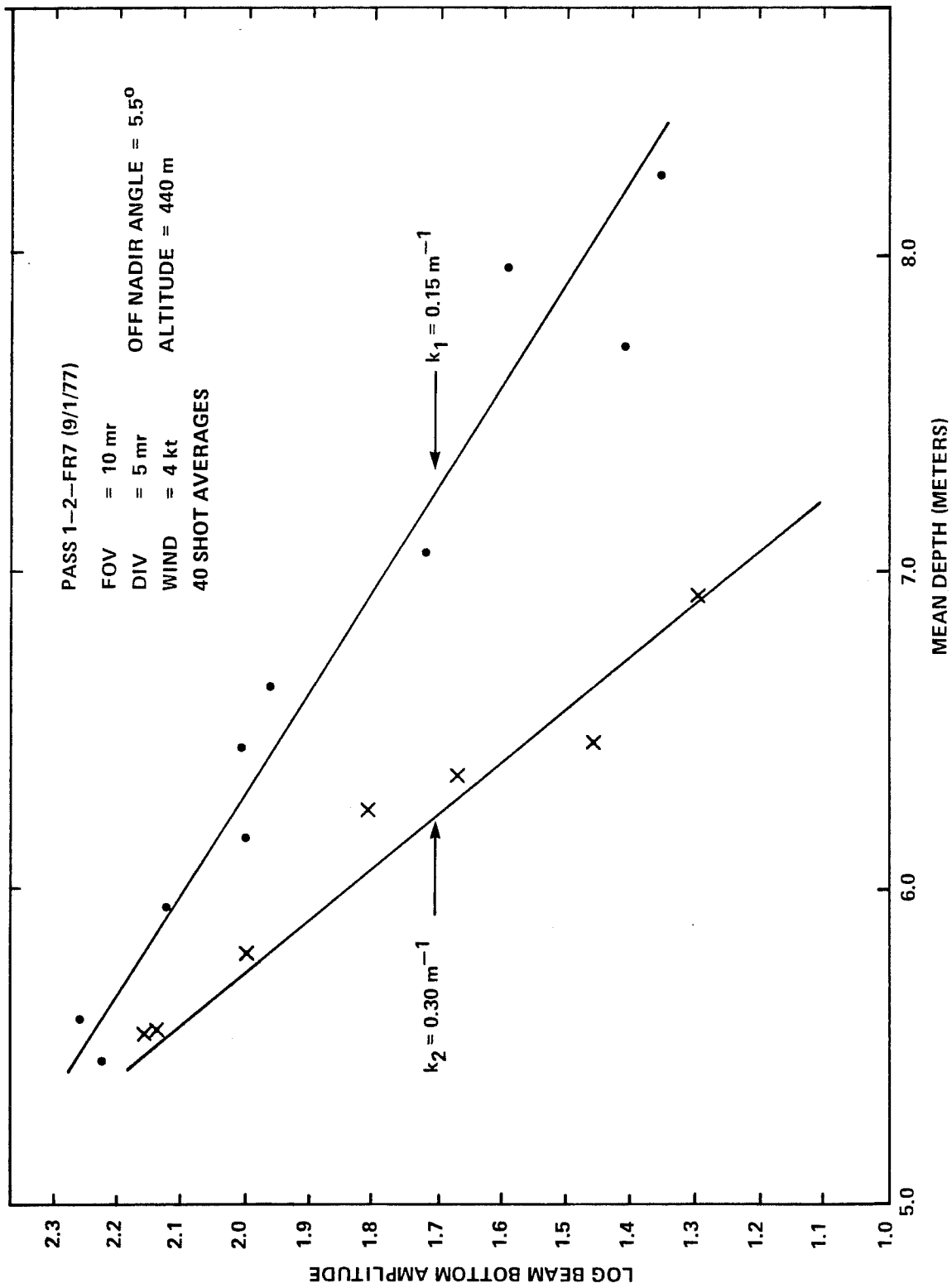


FIGURE 5-18. LOG MEAN BOTTOM SIGNAL STRENGTH VS. MEAN DEPTH

5.7 Bathymetric Performance

5.7.1 Controls

Vertical control for the AOL flight tests consisted of sonar bathymetry and tide control. A high density bathymetric survey of the Tangier Sound flightline was conducted by an NOS vessel from the Atlantic Marine Center utilizing standard, automated, acoustic techniques. Tide control for both acoustic and laser missions was furnished by three continuously recording NOS tide gages at appropriate locations. Horizontal control for this survey was a line-of-sight, high frequency electronic positioning system with ground stations. Positions have an expected uncertainty of 5 m.

Two flightlines in the Chesapeake Bay were surveyed. The first extended completely across Tangier Sound between Janes Island and Smith Island (a distance of approximately 12 km), and the second was centered on a line of buoys (off Janes Island) approximately 3 km long. The former was accomplished with 25-m line spacings, while a more concentrated effort on the latter led to roughly 10-m line spacings on the average. Depths were digitized every six seconds or approximately 25-m along the tracks, and a continuous, low depth-resolution analog record was also maintained to investigate major peak or valleys between digitizations.

Even with such close spacing of "truth" measurements, it is interesting to note that a small (and typical for the area) linear slope of two degrees produces a vertical deflection of 0.35 m (more than one foot) in ten meters. Practically, this means that a one foot high feature can reside between lines spaced 25 m apart, given only a scant two degree slope. Because of this, the acoustic data, while vital, is not the ultimate in "truth"; and differences between the two systems are not necessarily errors in the laser results.

Navigation and positioning of the aircraft were accomplished primarily with the tracking radar and plot-board capabilities available at NASA/Wallops Flight Center. The on-board LTN-51 Inertial Navigation System was prone to drift and was used only for a rough indication of general location (as well as roll and pitch data). The accuracy of real-time radar vectoring at the low

elevation angles required for the test site location was limited to about ± 100 m. Visual aids for the pilots such as buoys, lights, flags, etc., were only marginally successful. Consequently, attempts to fly particular, precisely located flight paths were not generally successful; each pass typically had an individual character and location within the stated bounds.

After the missions, radar data were smoothed with a Kalman filter program to provide the highest possible positioning accuracy. The post-flight aircraft position data have an expected uncertainty of at least 10 m. Combining this in quadrature with the 5-m uncertainty from the acoustic bathymetry leads to a combined uncertainty of about 11 m. Because a vertical error of 35 cm can accrue in this distance for a typical two degree slope, agreement between laser acoustic data sets to better than 30 cm must be considered a success. As it turned out, the depth profile correlations between laser and sonar were generally much better than that.

5.7.2 Precision and Wave Correction

Accuracy is divided into two basic concepts: precision and bias. Precision is a measure of self consistency and is related to random noise, while bias errors are determined by comparison with a separate standard and are "offset" or systematic errors. Some errors can be either systematic or random depending on the time or space scales involved.

The limiting precision of a system is dictated by the dominant noise background. For airborne laser hydrography this is solar background during the day and volume backscatter or PMT dark current at night. Other practical causes of imprecision arise from the environment. The largest such contributor is surface waves (both directly, and indirectly by beam steering, pulse stretching, and signal strength variations). Surface waves alter the local height of the water column and thus the measured depths. In order to evaluate the inherent precision of the instrument, this wave component must be reduced as much as possible by a correction procedure.

The precision of a set of non-scanning AOL depth measurements was defined as the standard deviation of measured depths about a linear (i.e., straight

line) fit to 40 consecutive data points (one page of computer output). At a 200-Hz pulse repetition rate and 75-m/sec aircraft speed, the 40 points represent 15 m of track length. This is a short enough distance that a linear fit is sufficient in all but the most extreme cases of topography. As seen in Fig. 5-19, this measure incidently includes in its magnitude actual bottom variations that diverge from linearity. It also includes any uncorrected wave noise. The lower bounds on these precision estimates are thus upper bounds on the actual system hardware random error.

A Monte Carlo computer simulation (Thomas 1977, Guenther and Thomas 1981e) was used to predict expected system precision as a function of bottom signal strength for various combinations of parameters such as laser pulse width and shape, charge digitizer gate width, pulse location algorithm, and system gain. Typical AOL precision results for nighttime operation with low wind are seen in Fig. 5-20. A comparison of field results with simulation results is shown in Fig. 5-21. It can be seen that the agreement is excellent, indicating that the system was performing properly and optimally. Precision curves for daytime operation are correspondingly higher as seen in Fig. 5-22.

When speaking of AOL depth precision, it must be recalled that the AOL was not conceived with high precision bathymetry in mind. This is evidenced by the following equivalences of distance (depth) measures related to AOL timing parameters: physical pulse length (7.5 ns) = 84 cm; gate length (4 ns) = 45 cm; gate separation (2.5 ns) = 28 cm. The 5-10 cm precisions quoted are the result of sophisticated processing software necessitated by the limitations of the hardware.

The basic concept of wave correction is depicted in Fig. 5-23. Two timing intervals are measured for each laser pulse: the time from the aircraft to a spot on the surface (the instantaneous aircraft slant range) and the time from the surface to the bottom (the instantaneous water slant depth). As seen in Fig. 5-24 for a typical data set, even for relatively low wind there is a strong correlation between the indicated raw depth measurement precision (standard deviation of the measured depths about the linear fit over a 40 pulse group) and the standard deviation of the instantaneous aircraft

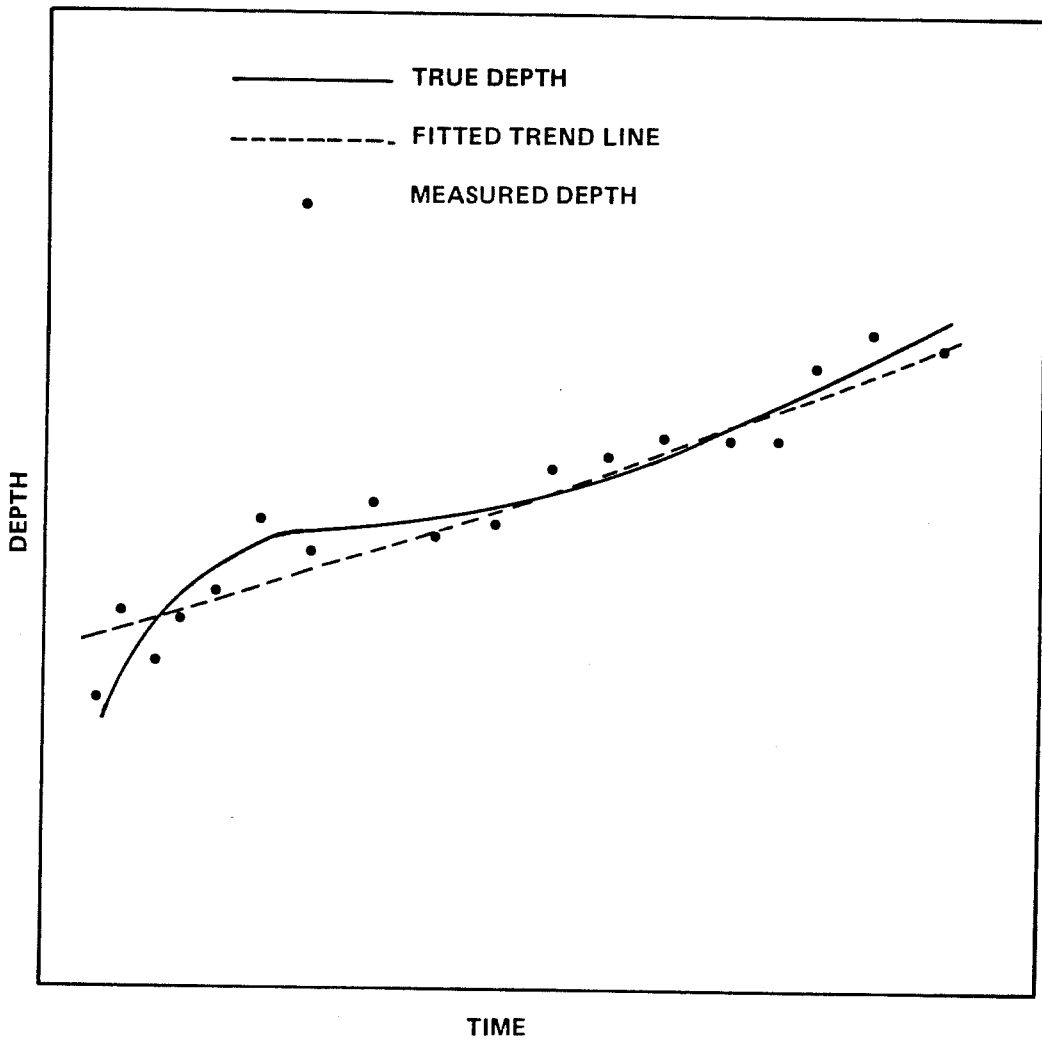


FIGURE 5-19. PROCEDURE FOR PRECISION EVALUATION

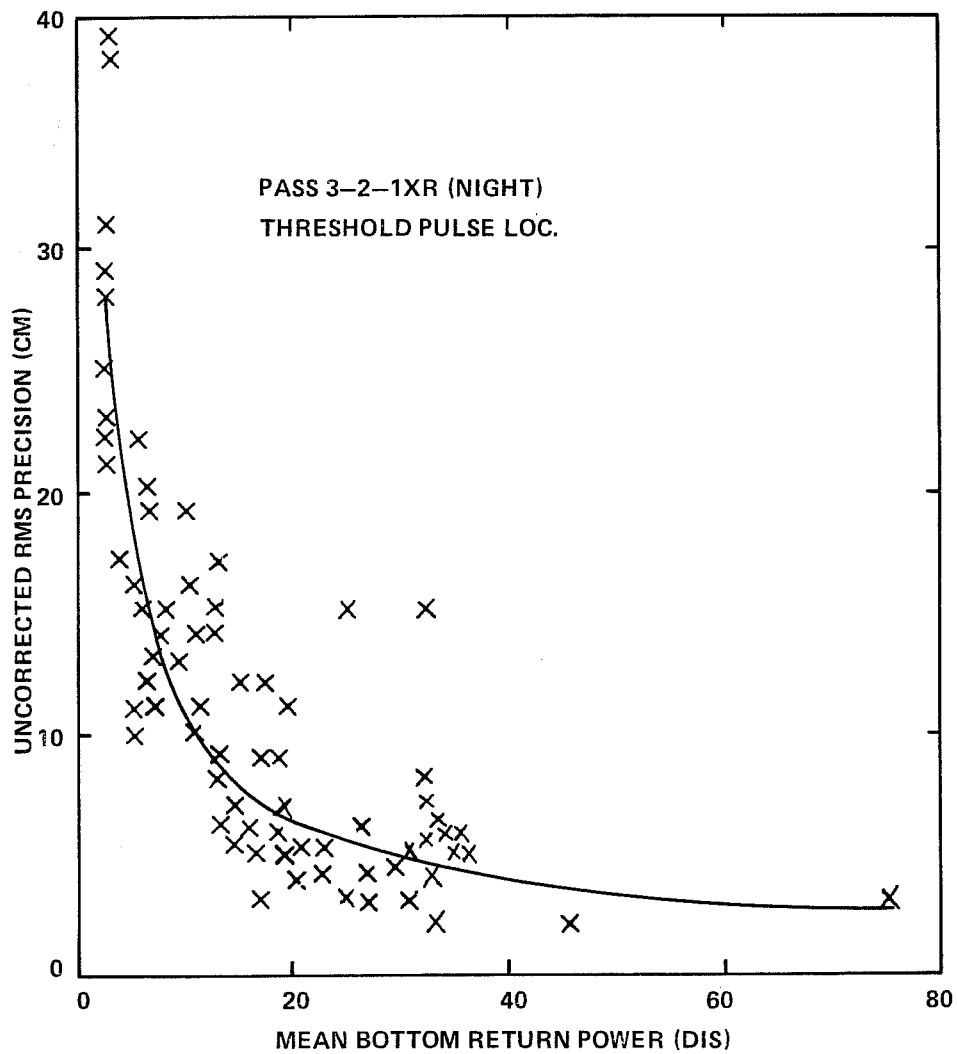


FIGURE 5-20. EXAMPLE OF DEPTH MEASUREMENT PRECISION
VERSUS MEAN BOTTOM RETURN POWER (NIGHT/BAY)

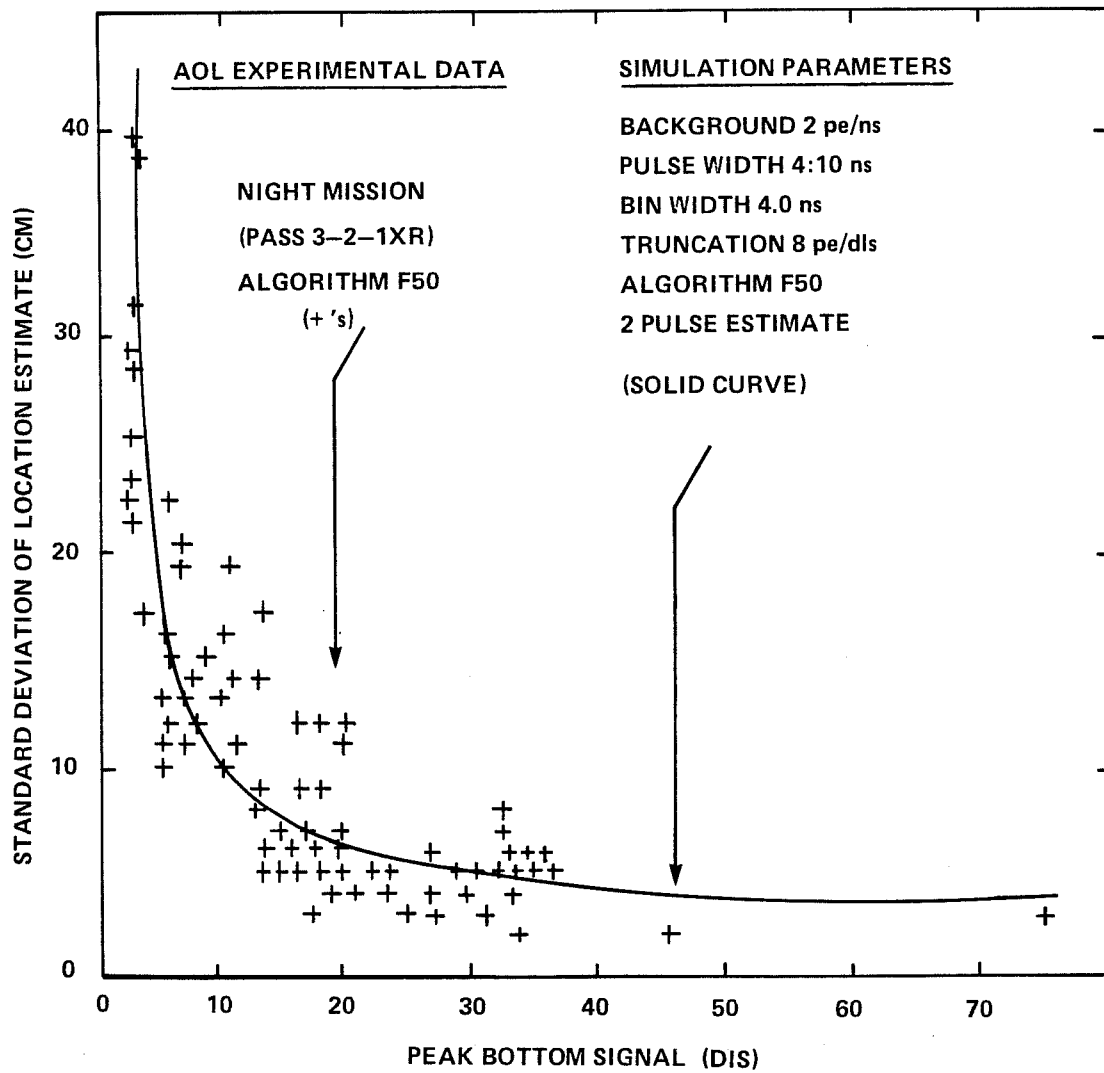


FIGURE 5-21. COMPARISON OF AOL PRECISION MEASUREMENTS WITH MONTE CARLO SIMULATION RESULTS

**WINTER QUARTER SHOAL
PASS 1-2-FR4 (9/1/77 - DAY
40 SHOT AVERAGES
EOF = 18 mr**

OFF NADIR ANGLE = 5.5°
ALTITUDE = 137 m
 $\alpha = 0.8 + 0.2 \text{ m}^{-1}$

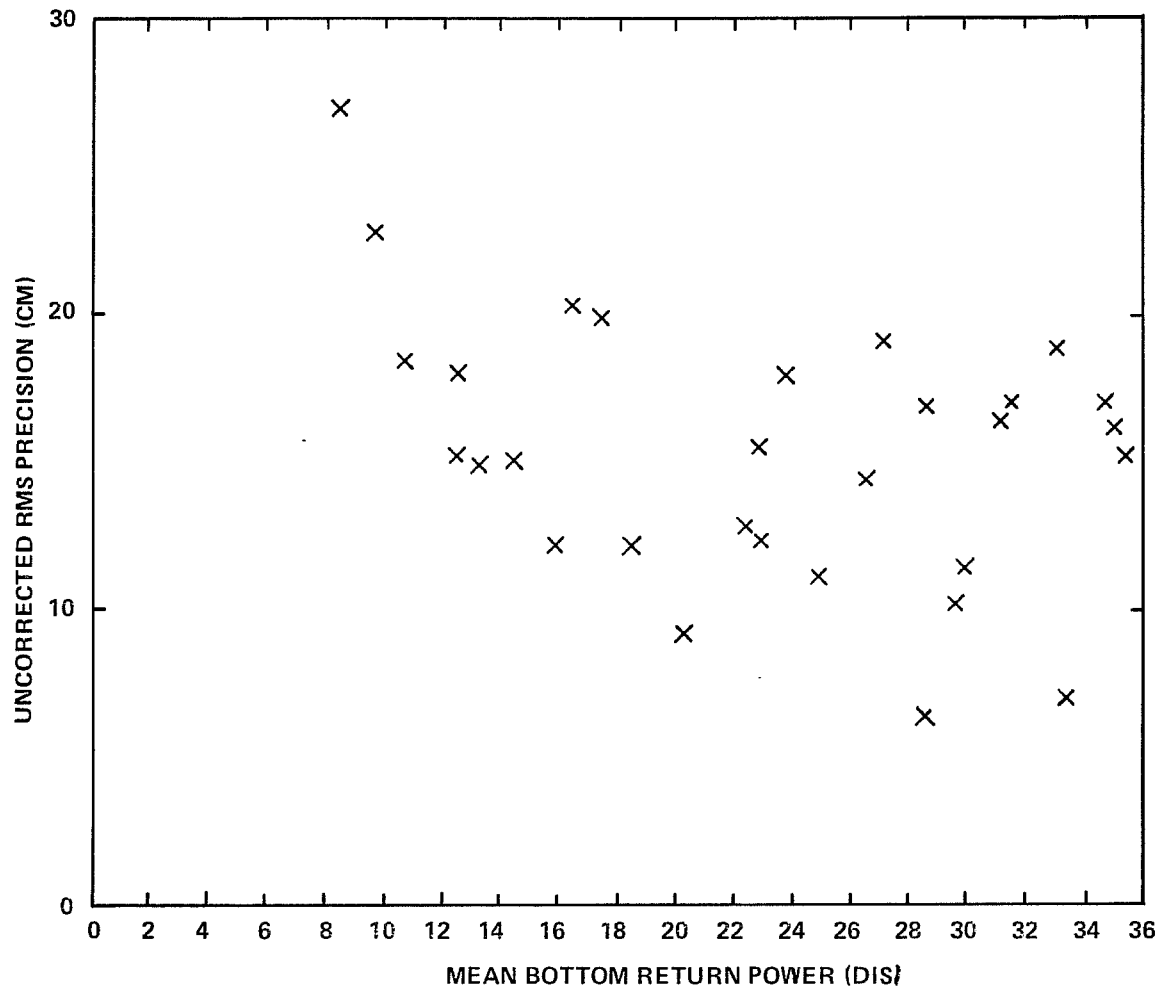


FIGURE 5–22. EXAMPLE OF DEPTH MEASUREMENT PRECISION VERSUS MEAN BOTTOM RETURN POWER (DAY/OCEAN)

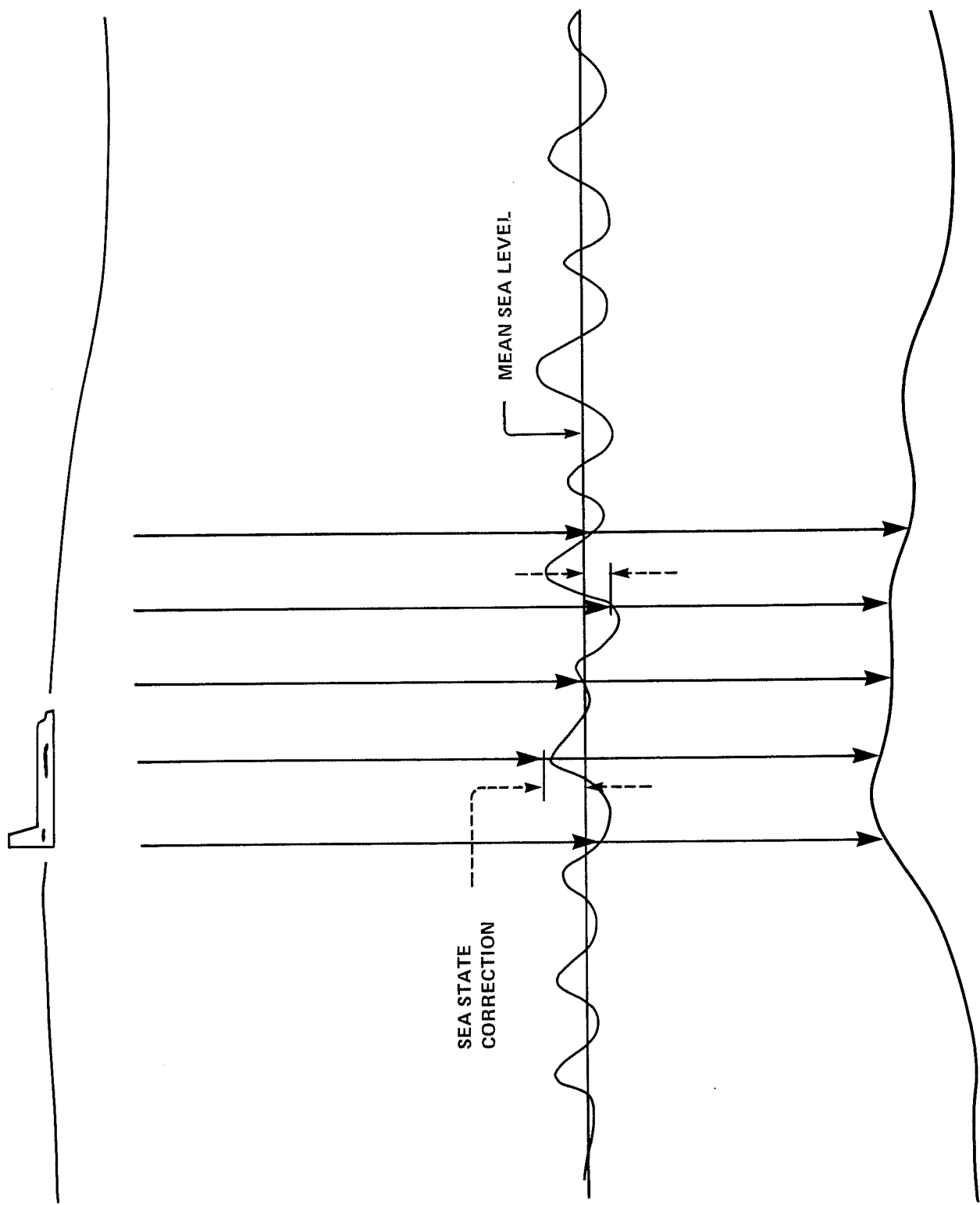


FIGURE 5-23. NON-SCANNING MODE WAVE CORRECTION GEOMETRY

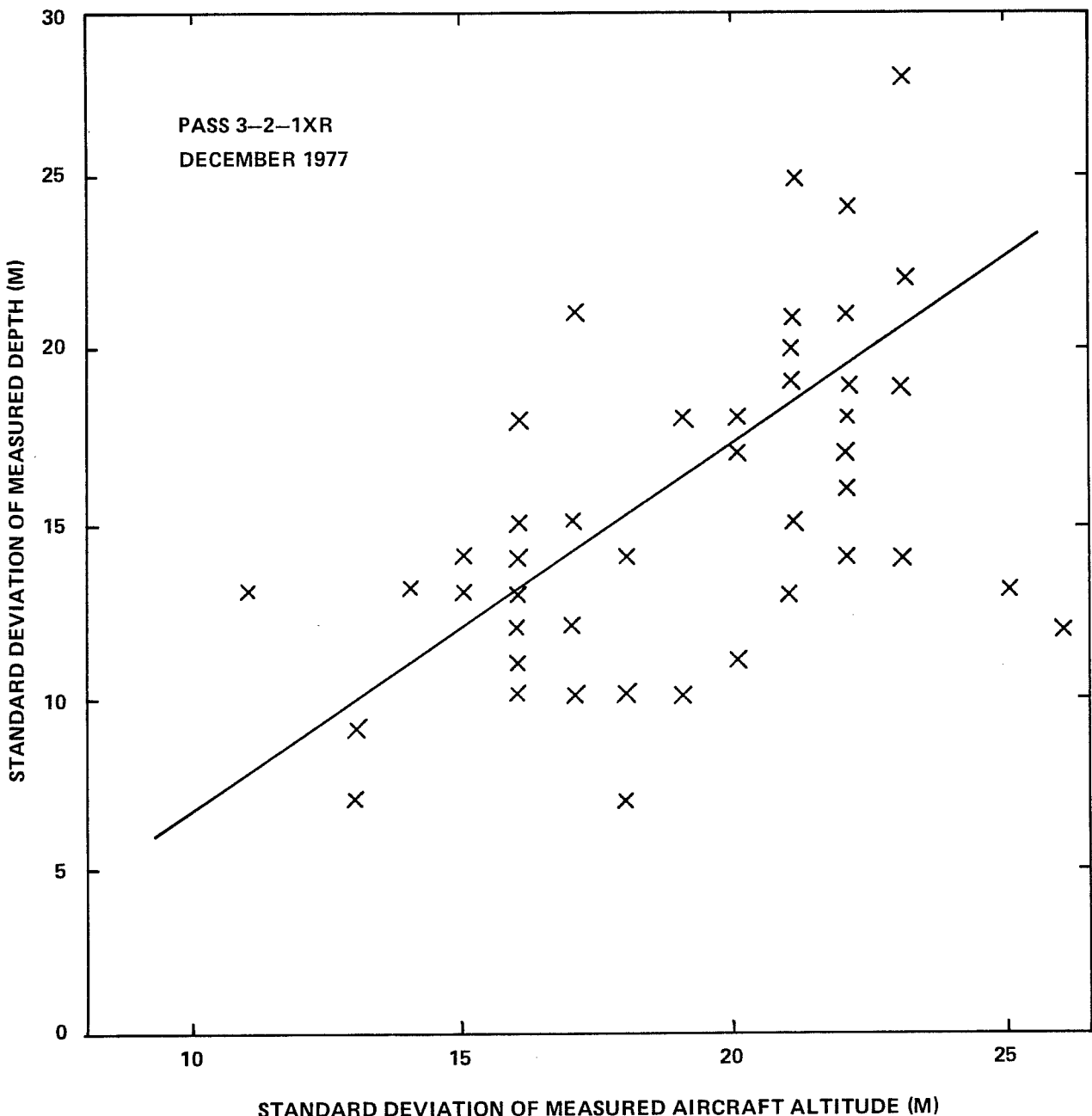


FIGURE 5-24. STANDARD DEVIATION OF MEASURED DEPTH
VS. STANDARD DEVIATION OF MEASURED
AIRCRAFT ALTITUDE

altitude about its mean. This implies that a significant fraction of the depth imprecision is due to surface waves.

Using a simplified argument, one can see from Fig. 5-23 that the aircraft flight path altitude and bottom contours change slowly with time while the waves vary rapidly. This implies that over short time periods, the distance from the aircraft to the bottom, i.e., the sum of the instantaneous altitude and the instantaneous depth for a non-scanning beam should be nearly constant -- irrespective of waves. This is clearly demonstrated to be the case with AOL results in Fig. 5-25 where instantaneous depth and altitude and their sum are plotted for 200 ns of non-scanning data. The standard deviation of the depth was 29 cm, that of the altitude 39 cm, but only 12 cm for their sum -- due to a correlation coefficient of -0.94. (Actually, other examples could have been selected for which the resultant standard deviation was even less; this data will be used shortly to explain yet another problem). An alternate description is seen in Fig. 5-26 which is a plot of measured altitude versus measured depth (for a different data set). In this case the standard deviations are nearly equal since the slope is -0.93.

It has been shown that more or less the same waves appear in both the altimeter data and the depth data. The waves, as determined from the altimeter data (about the mean instantaneous altitude), can thus be subtracted from the corresponding depth data to yield a water depth corrected to an estimate of the mean water level. Figure 5-27 presents a precision versus bottom signal strength plot contaminated by wave noise. Figure 5-28 presents the same data after application of the above wave-correction procedure. The effect is dramatic for all but the very weak signal strengths (whose imprecision comes from shot noise, not from waves). Another example is noted in Fig. 5-29 where it is seen that the precision of the wave-corrected data saturates at about 7.5 cm. This is caused by the coarse 15-cm discrete digitization levels in the AOL altimeter. Because of this limitation, high precision, wave free data was slightly degraded by the wave corrector. Again, however, wave noise in the middle signal strength range is significantly reduced. This is seen clearly in Fig. 5-30, a plot of corrected versus raw precision, which is divided into three regimes. Large standard deviations are basically unaffected because they are not due to wave noise; small standard

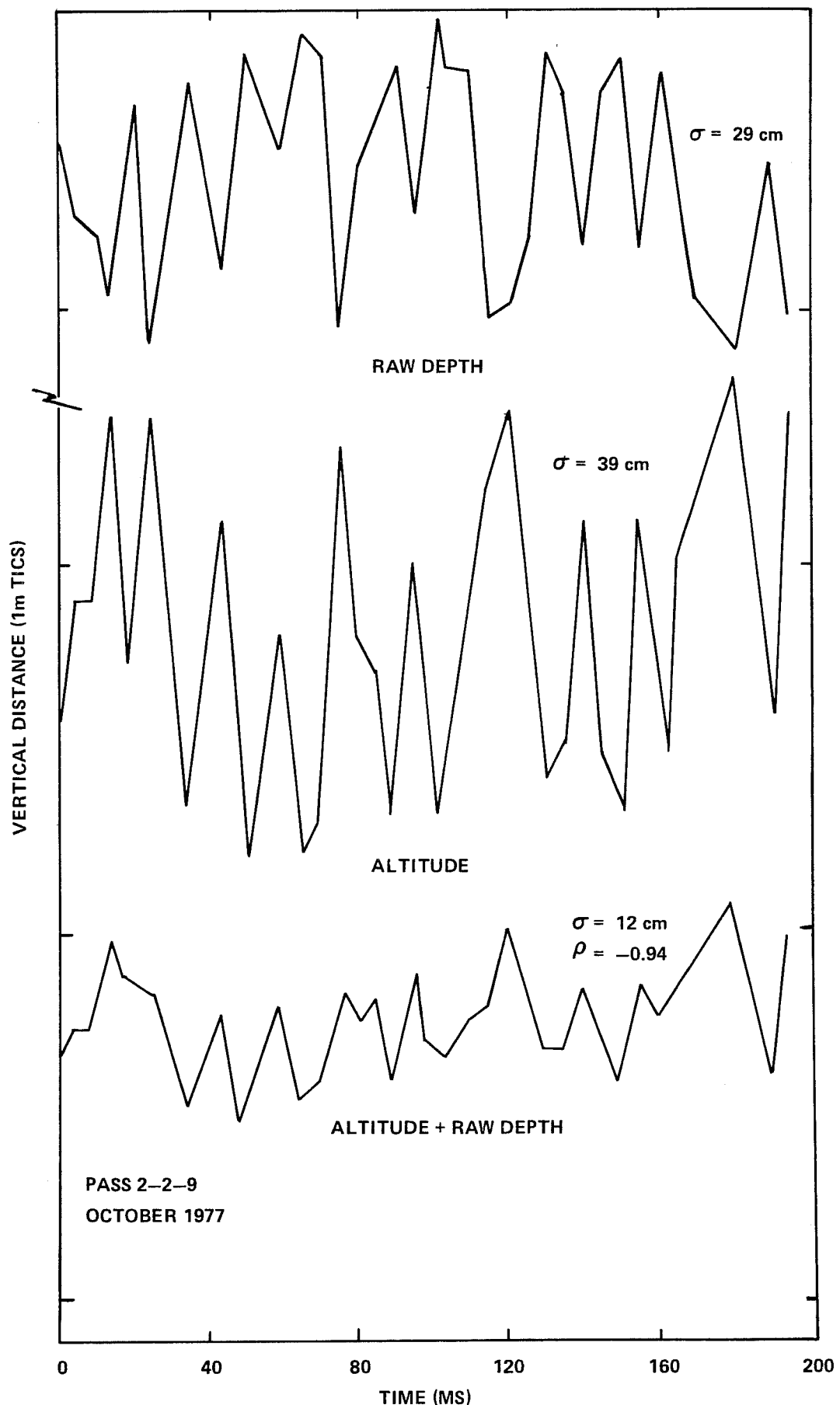


FIGURE 5-25. WAVE CORRECTION DEMONSTRATION

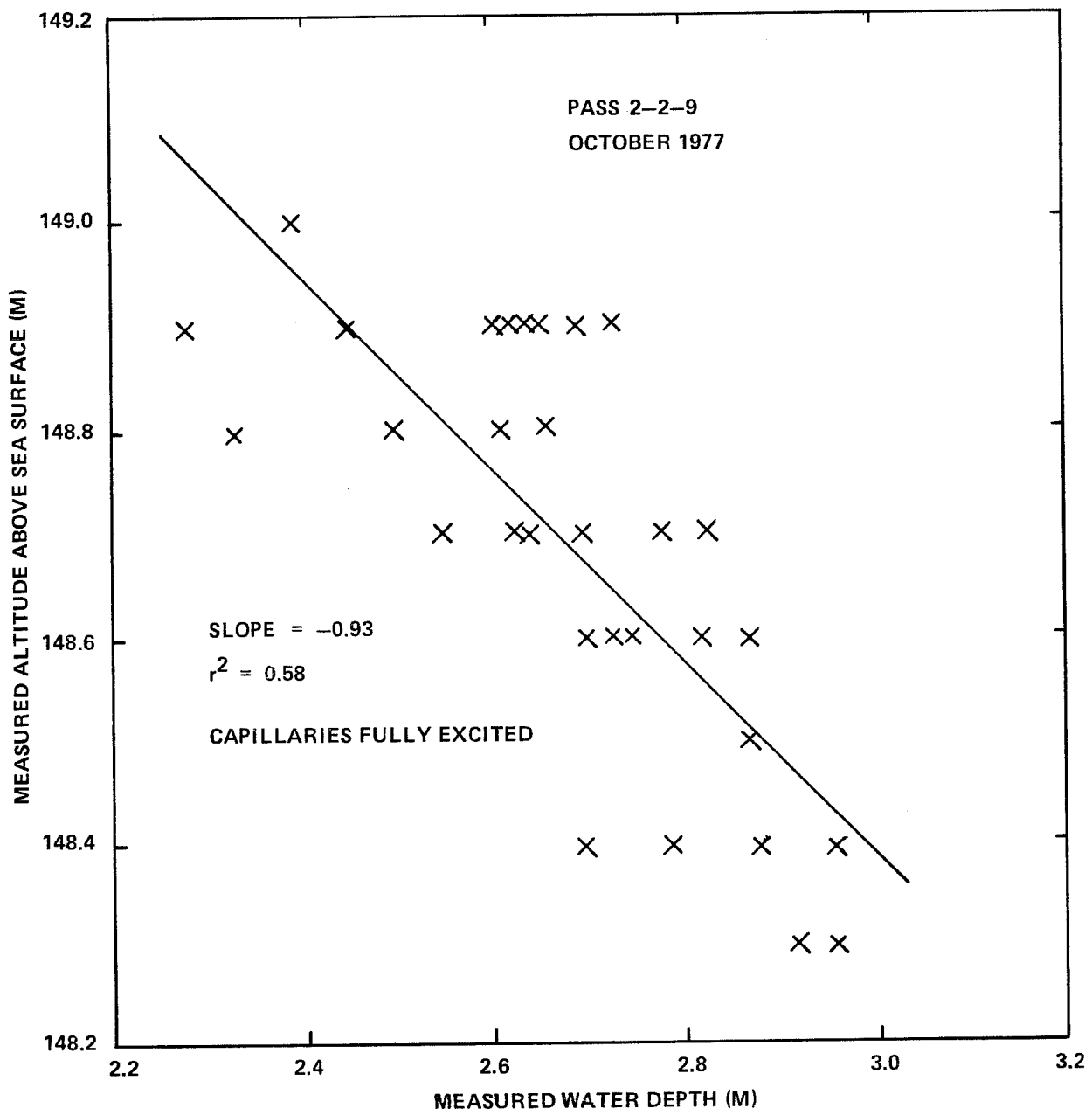


FIGURE 5-26. WAVE CORRELATION IN ALTITUDE AND DEPTH MEASUREMENT

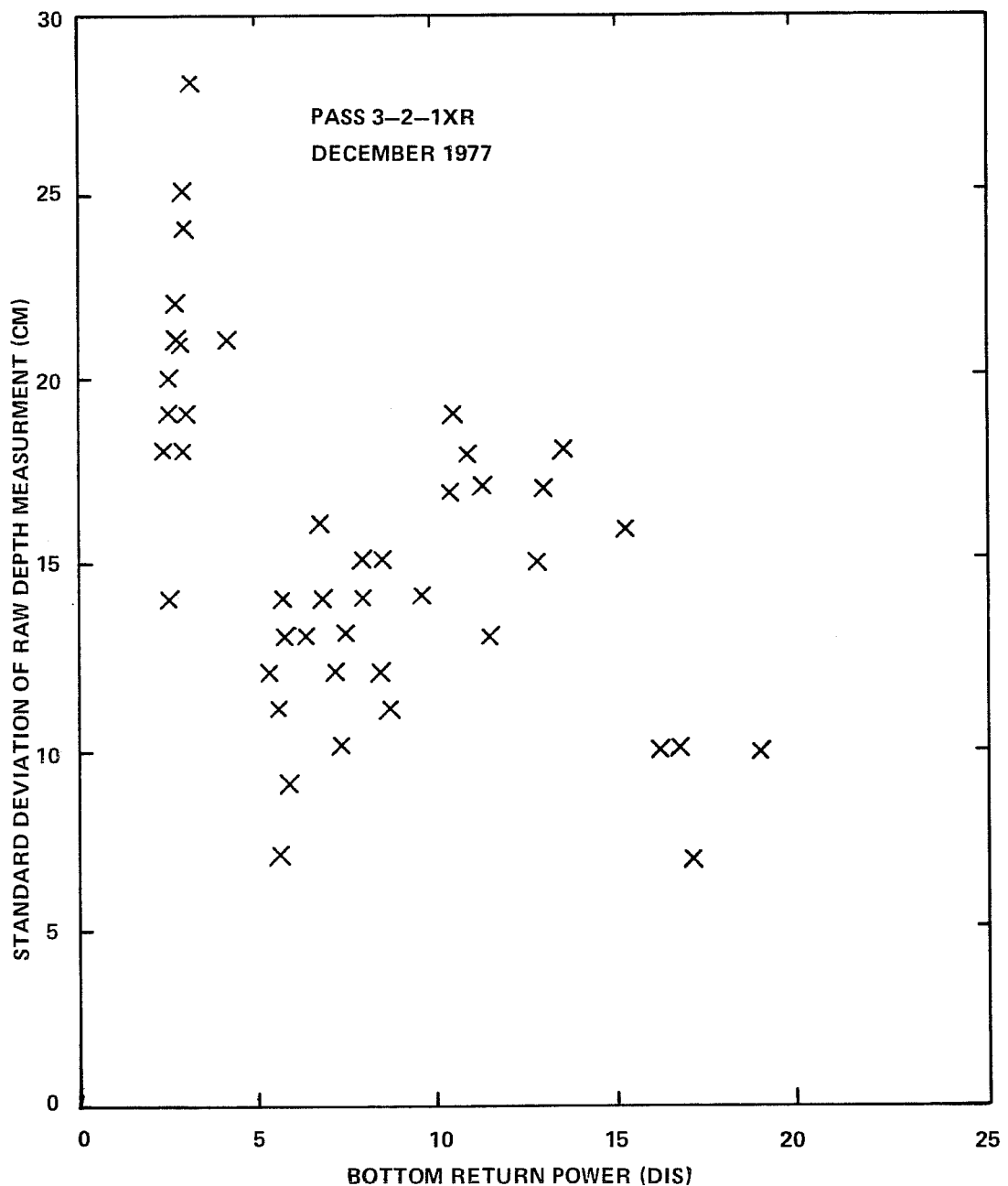


FIGURE 5-27. STANDARD DEVIATION OF RAW DEPTH MEASUREMENT
(CONTAMINATED WITH WAVE NOISE)
VS. BOTTOM RETURN POWER

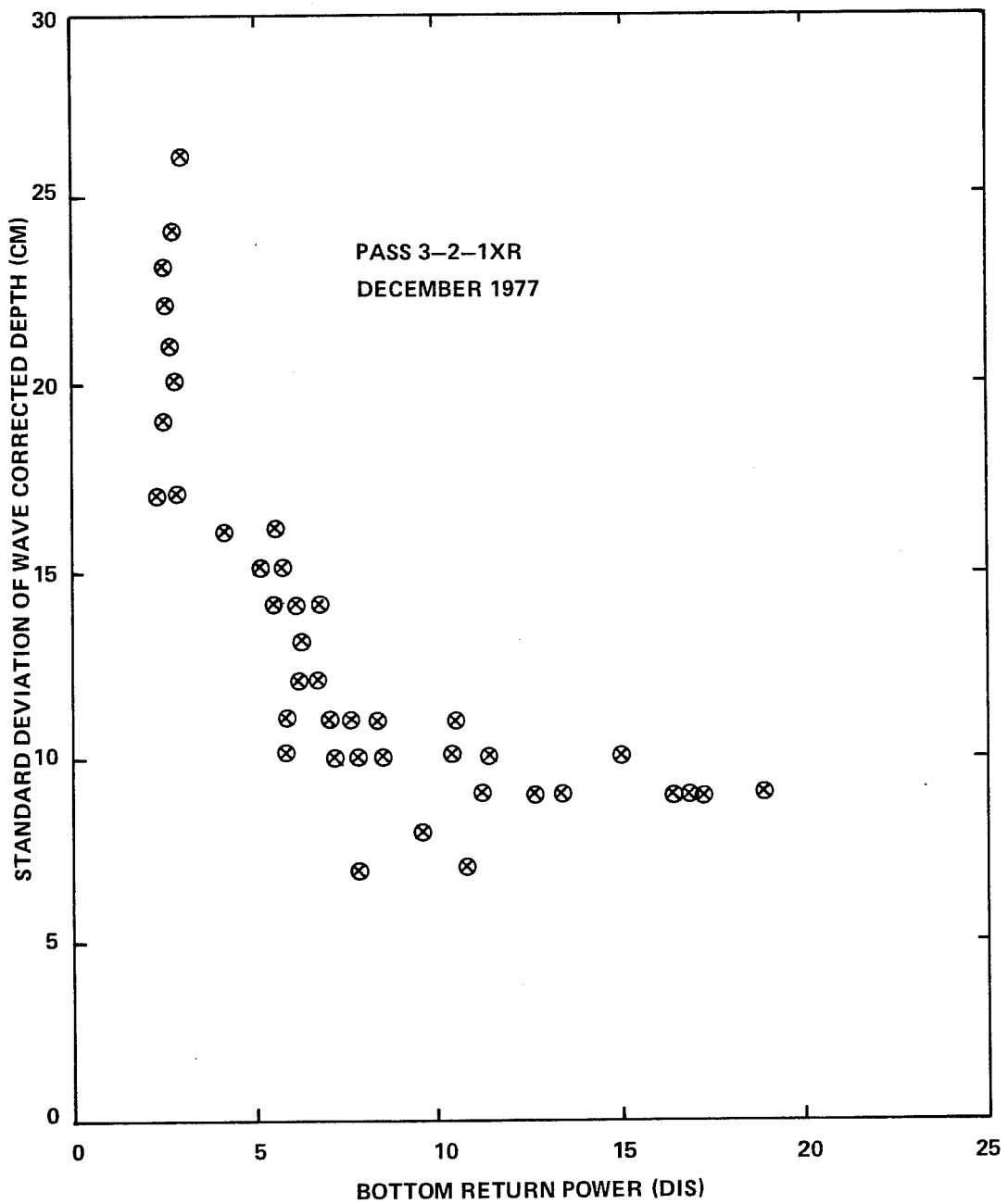


FIGURE 5-28. STANDARD DEVIATION OF WAVE-CORRECTED DEPTH VS. BOTTOM RETURN POWER

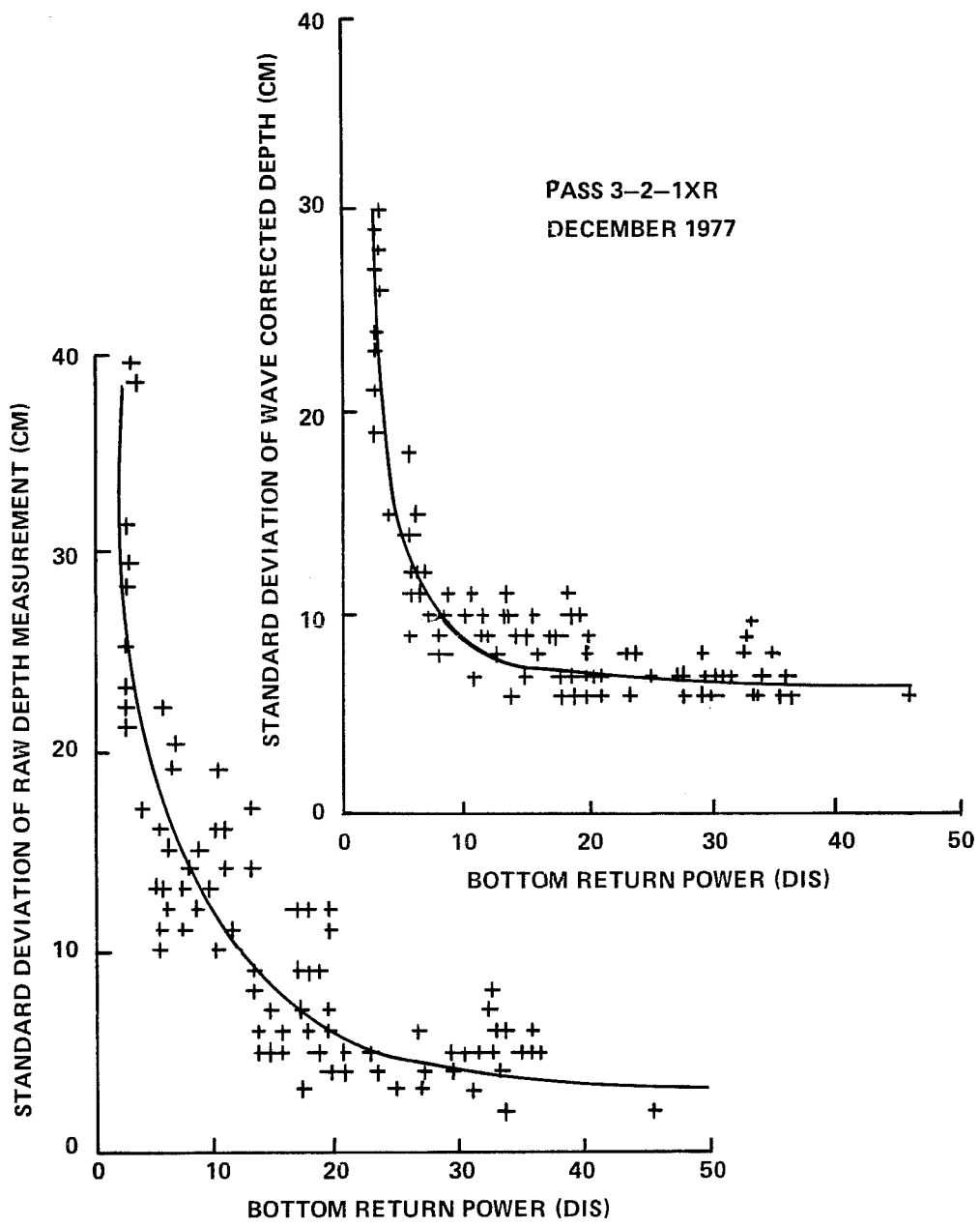


FIGURE 5-29. STANDARD DEVIATION OF DEPTH MEASUREMENT VS. BOTTOM RETURN POWER: EFFECT OF ALTITUDE DIGITIZER RESOLUTION

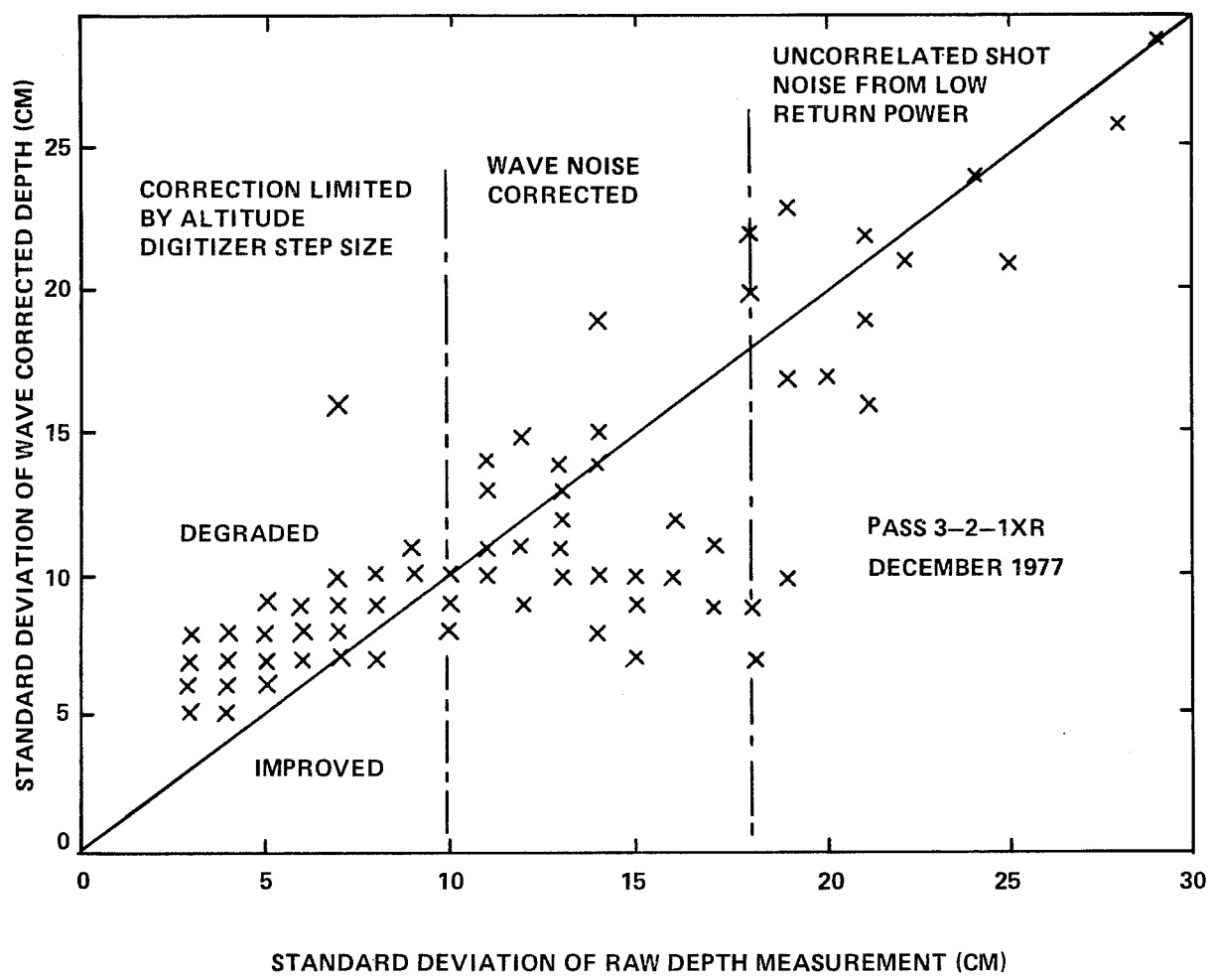


FIGURE 5-30. RESULTS OF WAVE-CORRECTION PROCEDURE

deviations are slightly degraded as noted above; while mid-range standard deviations are clearly improved by application of the wave corrector. In Fig. 5-31, a plot of the same data as in Fig. 5-24, it can be seen that the precision of the corrected depths no longer correlates with the precision of the slant altitudes; and in Fig. 5-32 it can be seen that the larger the correlation between slant altitude and depth, the smaller the standard deviation of the wave-corrected depths.

Figure 5-25 contained an example where there was excellent correlation between the locations of the waves, but the magnitudes differed -- thereby causing the sum to carry the character of the slant altitude. This same data is seen in Fig. 5-33; from the slope of -1.38 it is evident that the same waves sensed by the altimeter were somehow "magnified" compared to those measured in the water depths. (The reverse was also a possibility, but deemed not the case). The key to this enigma lies in the plot of surface return power versus instantaneous water depth (Fig. 5-34). The actual mean depth for this data is constant; the variations in measured instantaneous water depth between 1.8 m and 2.8 m are the result of surface waves. The behavior of the surface return power is unusual: for depths greater than about 2.3 m (the wave crests), the customary variance of surface return power is seen; but for depths less than 2.3 m (the wave troughs) the surface return power has decreased to a constant value. This data was obtained during low wind conditions. As noted previously, capillary waves tend to exist near wave crests. The stronger returns exhibiting customary variance are interface returns from the capillary waves on the crests. The low, constant power returns from the troughs (where the capillaries were not excited) are detections primarily of the weaker volume backscatter signal. A design flaw in the AOL is the cause of the "magnified" slant altitude waves. The altimeter surface return detector uses a fixed level threshold. For strong returns this triggers near the start of the pulse, but for weak returns, such as the volume backscatter returns, the threshold is reached just before the peak. The wave crests are thus detected earlier in the waveform and the wave troughs later; this exaggerates the peak to trough wave height. Since the leading edge of the AOL pulse is on the order of 7-ns wide, this could cause errors as large as ± 40 cm. In Fig. 5-33, the error measured is only about half this. This experience serves to point out the fact that fixed-level

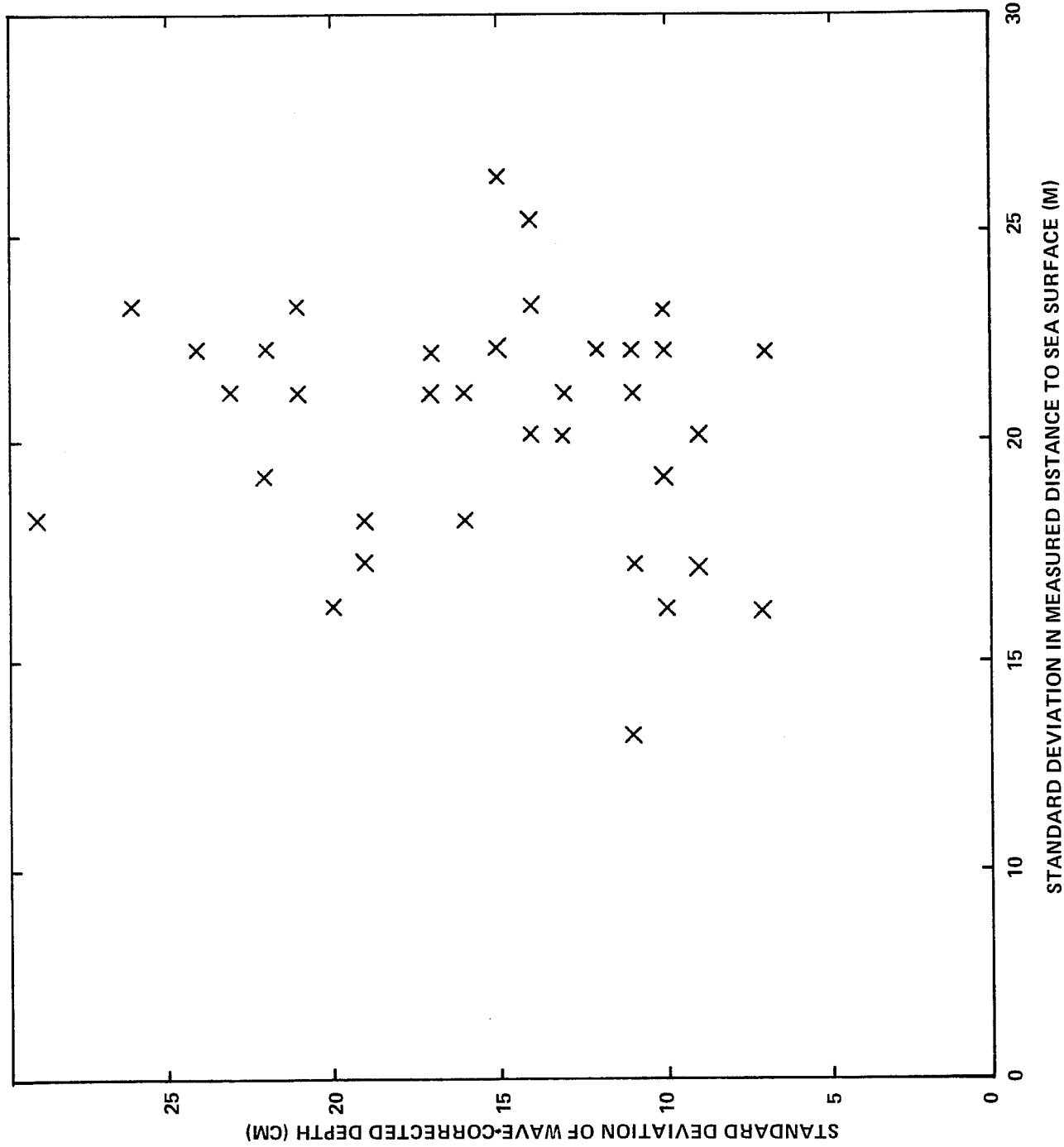


FIGURE 5–31. SCATTER PLOT OF WAVE-CORRECTED PRECISION VS. ALTIMETER DATA

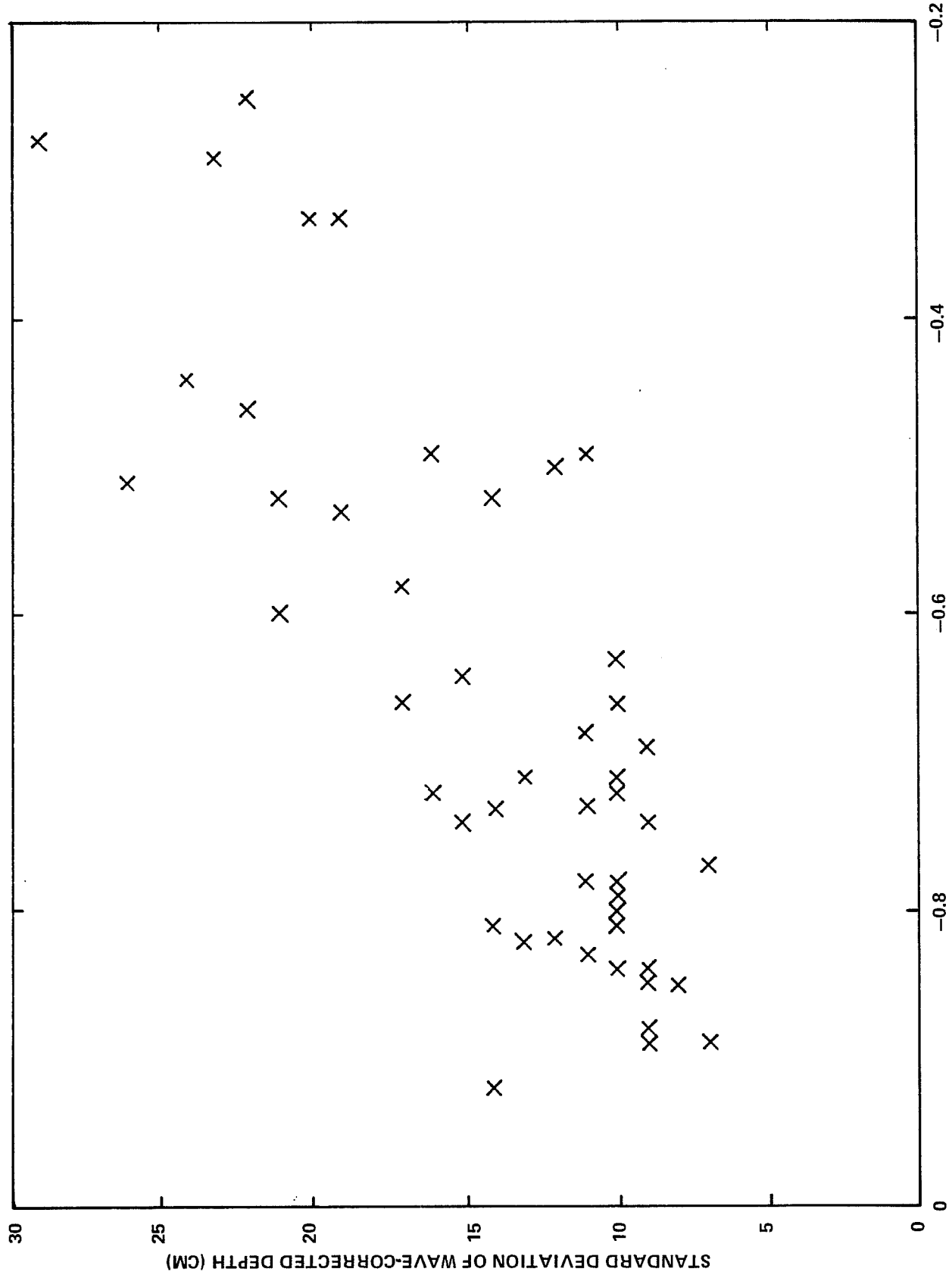


FIGURE 5-32. WAVE-CORRECTED PRECISION VERSUS CORRELATION COEFFICIENT

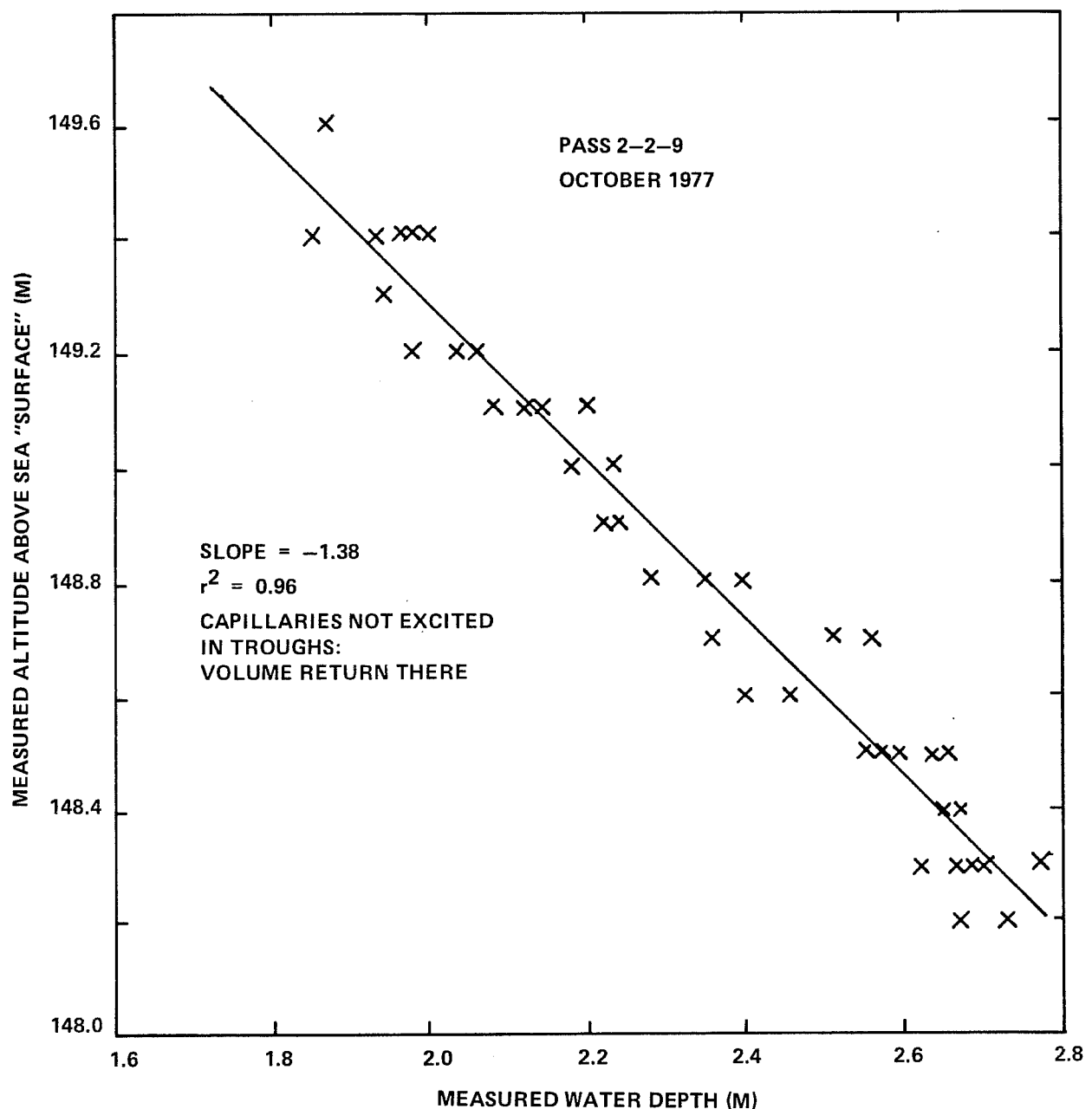


FIGURE 5-33. WAVE CORRELATION IN ALTITUDE AND DEPTH MEASUREMENT

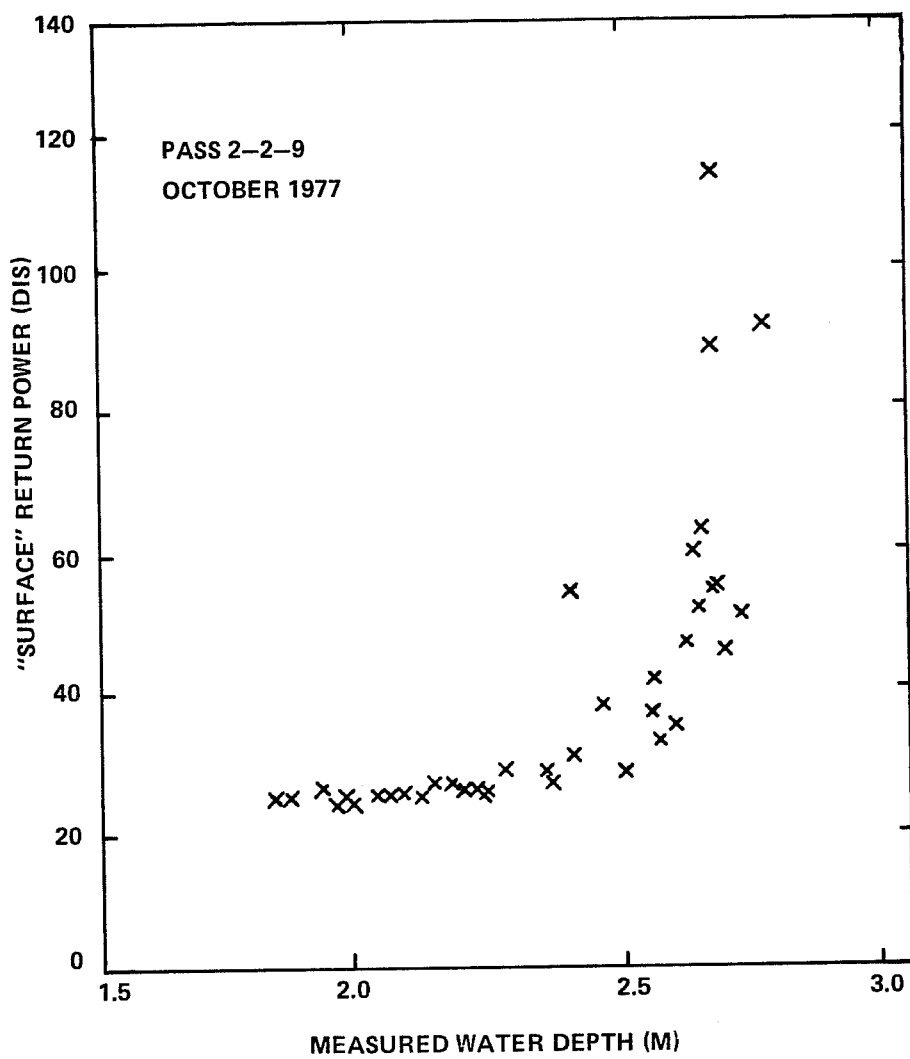


FIGURE 5-34. "'SURFACE' RETURN POWER VS.
MEASURED WATER DEPTH

threshold detectors, which are notorious for being signal strength dependent, must be avoided in future systems.

Wave correction for scanning data is slightly more complicated, but based on the same principles. For a single pulse, the instantaneous wave magnitude will be defined as the difference between a measured slant altitude and the predicted slant altitude (corrected for nadir angle). The key to this correction is thus the accurate prediction of the expected slant altitude to a flat surface at mean water level. For zero roll and pitch, the slant altitudes to a flat surface from the AOL nutating scanner would appear to be something like a biased sine wave at twice the scanner rate. The longer ranges in the scan pattern are in the wing-to-wing direction corresponding to the major axis of the ellipse. Slight non-zero roll and pitch angles, however, lead to distinct patterns such as seen in Fig. 5-35a simulation results and Fig. 5-35b flight data. The complex signal has two unequal maxima and two unequal minima per cycle which in general do not occur on the axes of the now distorted ellipse.

With knowledge of the scanner equations, these four minima and maxima can be used as input variables to determine both the altitude and attitude of the aircraft. Roll and pitch angles derived in this way from AOL data correlated convincingly with similar measurements from the on-board LTN-51 inertial navigator as seen in Fig. 5-36a, b. (The offset in the latter is due to the INS being zeroed for the standard two degree nose-up flight trim of the C-54. The results are actually identical.) It is expected that accuracies better than 0.1 degrees can be obtained in this way. The use of slant altitudes for this determination precludes the possibility of a roll or pitch bias from an external attitude measurement system which could cause severe problems in the wave correctors. Because the slant altitudes are measured not from a flat surface but from one contaminated with waves, individual ranges will be alternately long or short, and a least squares fit will be used to produce the desired attitude and altitude data. These can then be used to predict the expected slant altitude for each pulse, and the difference between this and the measured value (corrected for nadir angle) is the wave corrector for that pulse. This technique was used on a limited AOL data set and performed satisfactorily.

ALTITUDE = 476 M PITCH ANGLE = 2.0 DEG
A/C SPEED = 76 M/SEC ROLL ANGLE = -1.0 DEG
SCAN ANGLE = 10.0 DEG PRF = 400 PPS

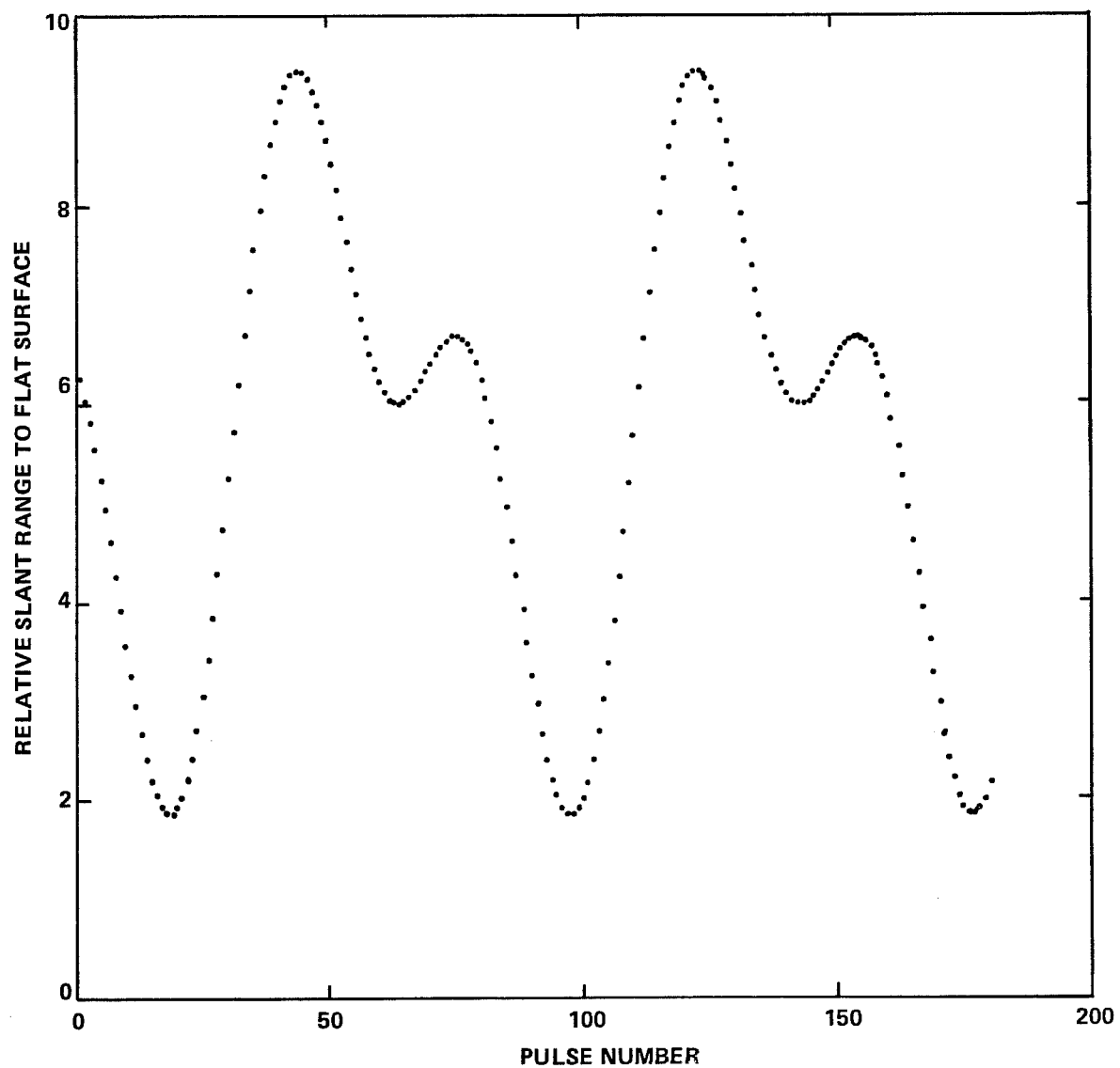


FIGURE 5-35a. AOL SCANNER SLANT ALTITUDE MODEL

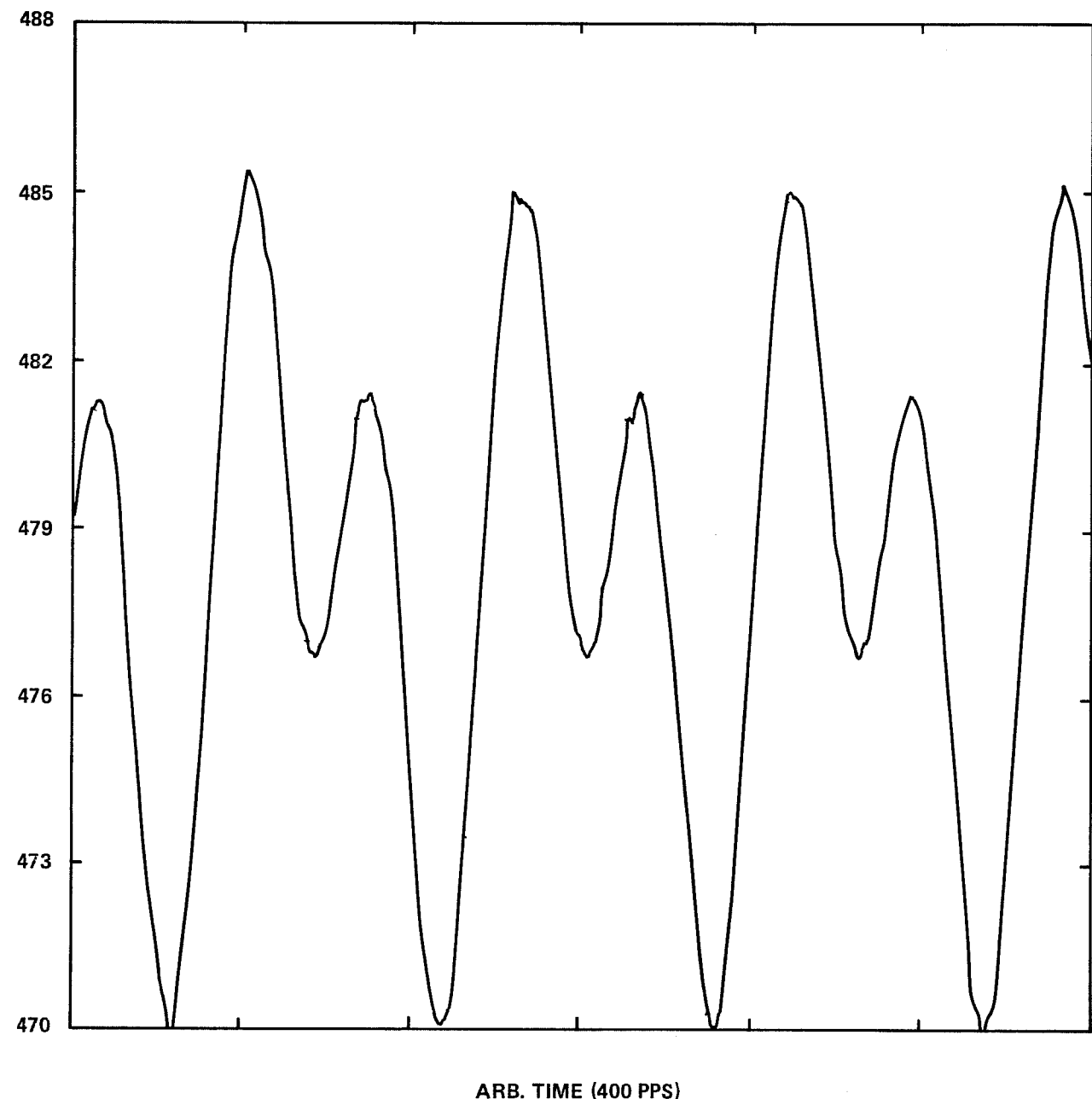


FIGURE 5-35b. AOL SLANT RANGE EXAMPLE

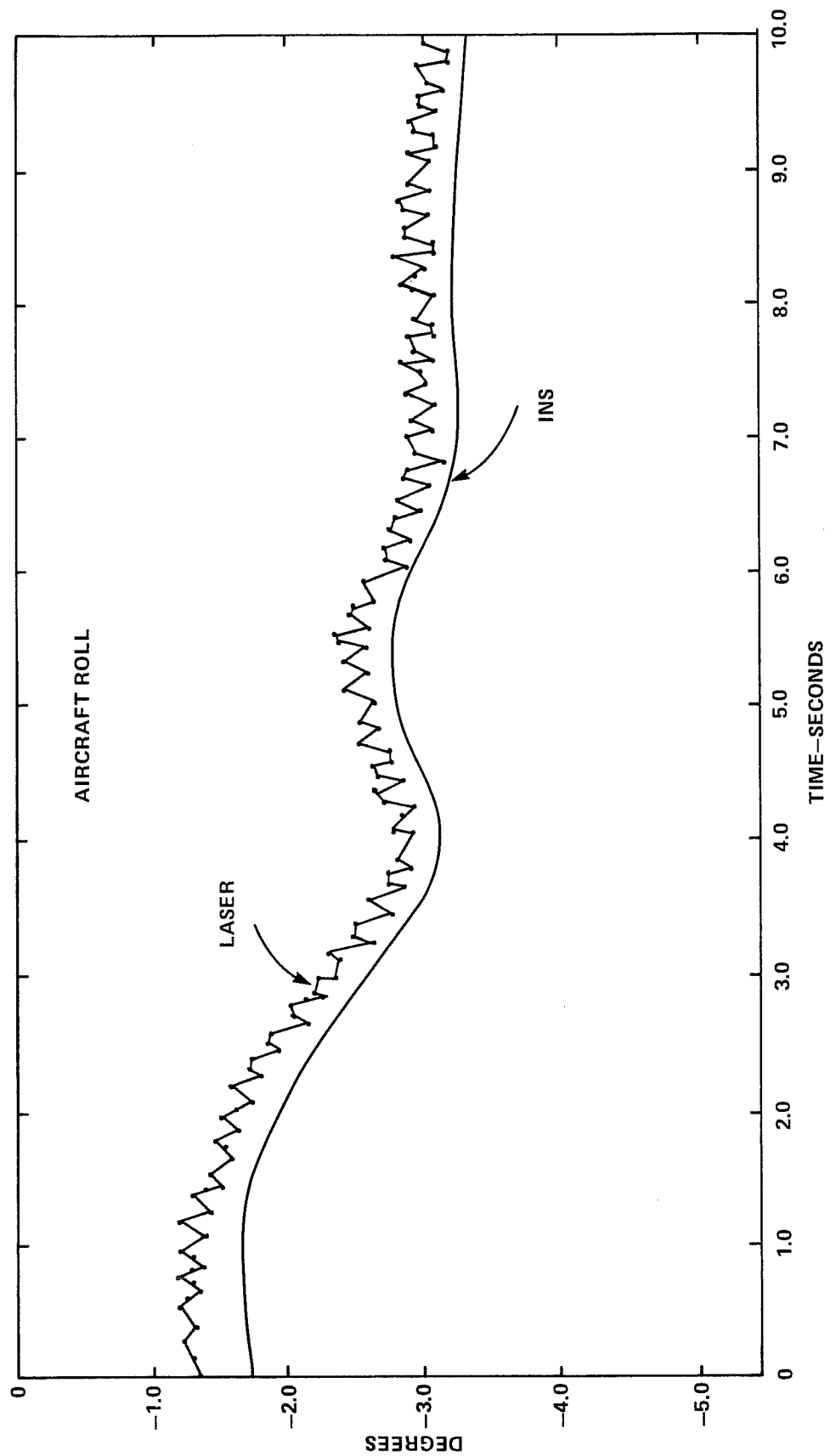


FIGURE 5-36a. AIRCRAFT ROLL DETERMINED FROM SLANT RANGES
COMPARED TO INERTIAL NAVIGATION SYSTEM

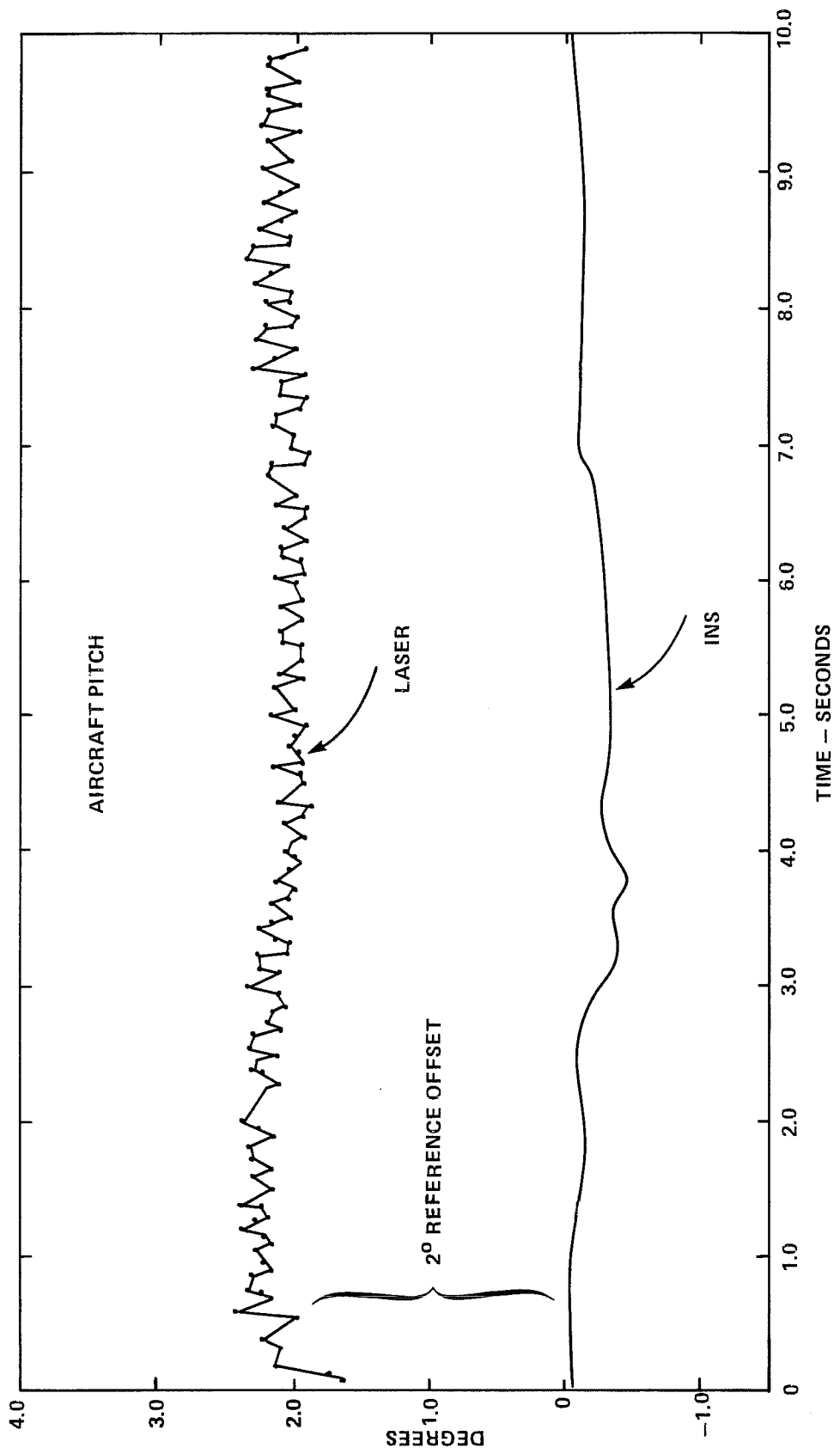


FIGURE 5-36b. AIRCRAFT PITCH DETERMINED FROM SLANT RANGES
COMPARED TO INERTIAL NAVIGATION SYSTEM

One other problem is noteworthy. The frequency spectrum of long period waves (swell) and rapid aircraft motions may overlap slightly. This would make it impossible to tell the difference between the two without additional information. This can be alleviated by the inclusion of a vertical motion sensor on the aircraft (such as the doubly-integrated vertical accelerometer later installed on the AOL). This measured aircraft motion can be corrected out so that the residual is due to long period swell of the water's surface.

5.7.3 Depth Measurement Accuracy

Although the term "accuracy" normally encompasses both precision and bias, precision has already been discussed. For the purposes of the ensuing presentation, the discussion of accuracy will deal solely with measures of comparison between two data sets. Three different measures will be discussed: repeatability, profile correlation, and bias.

During the flight acceptance tests over Winter Quarter Shoal in the Atlantic Ocean off Chincoteague, Virginia, laser measured depths were compared with chart data. As seen in Fig. 5-37, the results, although crude, were promising.

Repeatability was defined as the ability to fly over a track more than once and obtain nearly the same answer. It turned out to be difficult to fly over the same track, because the accuracy limit of the radar vectoring from the NASA/Wallops Flight Center plot board was about 100 m. As will be seen shortly, results were sometimes very good, but at other times significant differences were noted. It was decided that comparisons against the sonar survey would be preferable.

As noted earlier, a high density sonar survey of a 600-m wide swath between Janes Island and Smith Island in Chesapeake Bay was conducted by the National Ocean Survey in support of this project. Depth contours along flight lines were generated from this data base first by hand, and later on mylar sheets by a special feature of the NOS hydrographic plotting program. An example of the former is shown in Fig. 5-38 for which the agreement between

AOL BATHYMETRIC DATA (LINE)
CHART 5358 (U.S.C.G.S.), 1933 BATHYMETRIC DATA (CIRCLES)

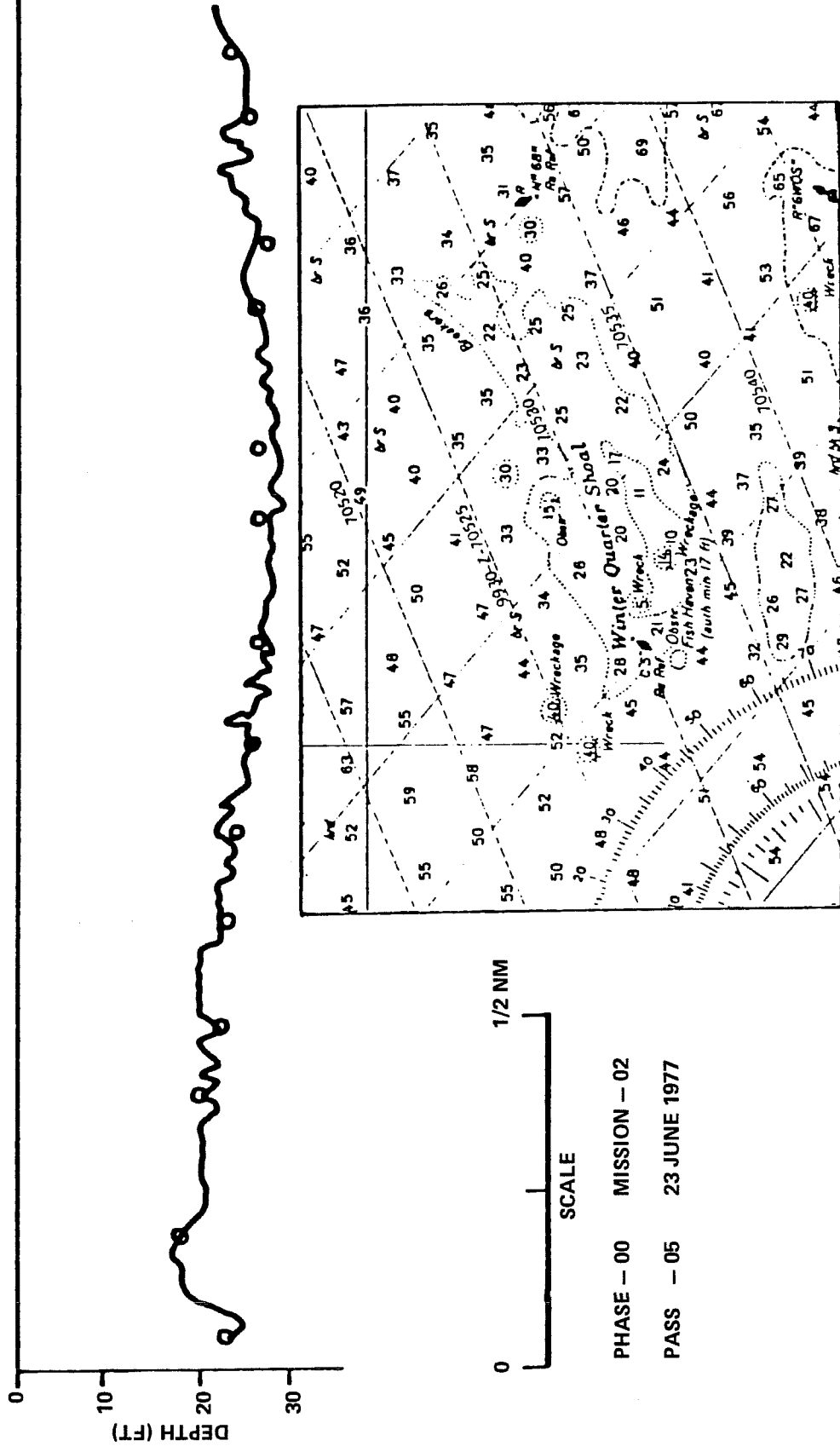


FIGURE 5-37. AOL DEPTH COMPARISON WITH CHART FROM FLIGHT ACCEPTANCE TESTS

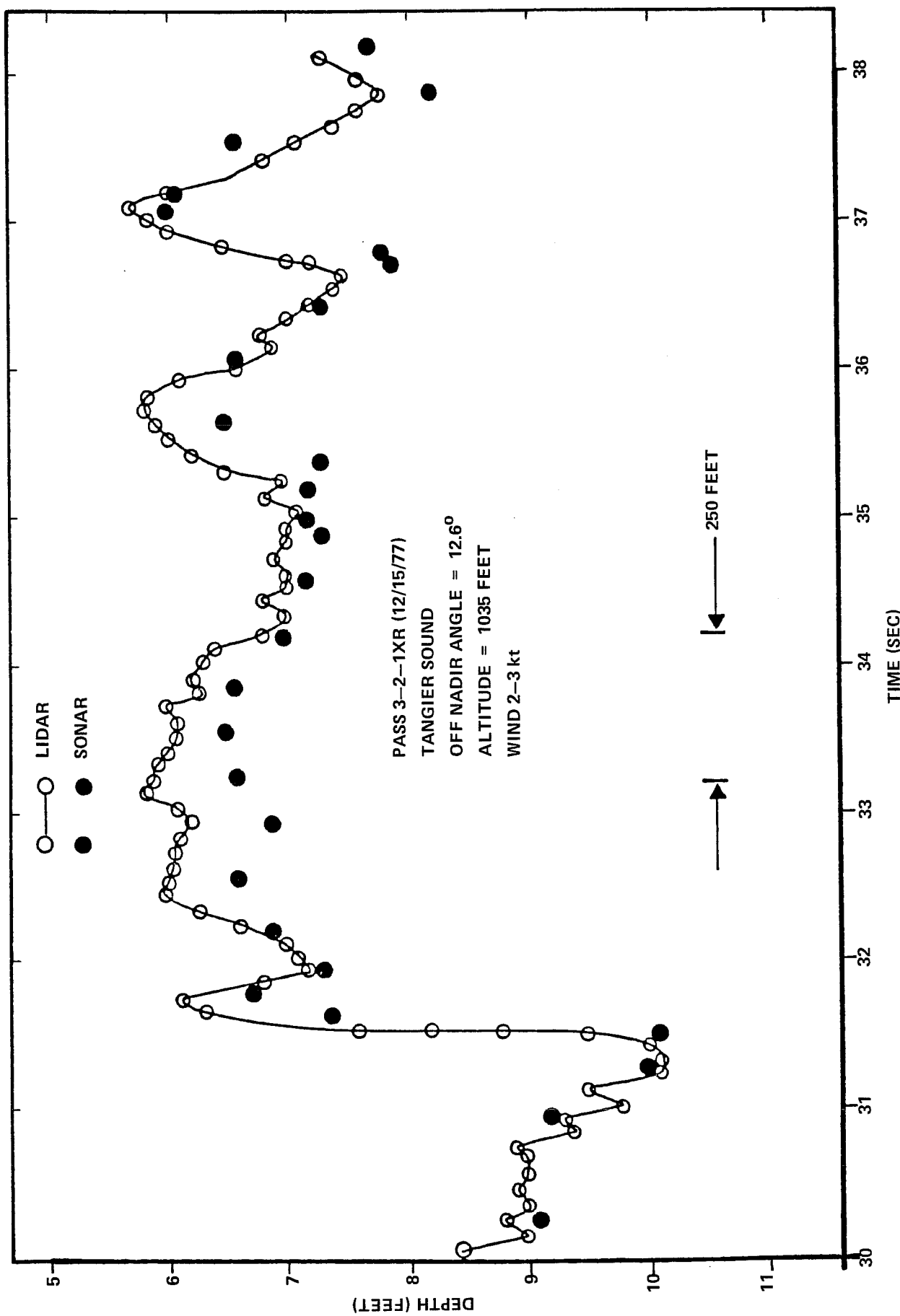


FIGURE 5-38. COMPARISON OF LASER AND ACOUSTIC DEPTH ESTIMATES

laser and sonar is excellent, with absolute differences of less than 20 cm and an RMS difference of roughly 10 cm.

More often than not, however, such agreement was not the case. A more typical example is depicted in Fig. 5-39 in which a significant deep bias of about 30 cm is noted. Even though the respective measurements disagree in absolute level it can be seen that, with the exception of a fixed bias, the curves are remarkably similar. This is clearly demonstrated in Fig. 5-40 in which the curves are moved to overlay one another. The two datum-free profiles (sonar and laser) correlate with each other to within a few centimeters! This was very significant because it was proof that both systems were, indeed, seeing the same bottom, and that the absolute differences were due to some sort of fixed (and hopefully correctable) bias.

The picture was further confused by the data in Fig. 5-41 for which a 30-cm shallow bias was noted. Again, as seen in Fig. 5-42, the profile correlation was amazingly good except for one small bump at the shallow end. This situation was particularly perplexing, because, as seen in Fig. 5-43, these two passes were flown over nearly the same flightline about 90 minutes apart. The repeatability was thus off by 60 cm between these two passes.

The deep bias could be explained, in principle, in terms of a concept which was just beginning to be investigated -- propagation-induced biases caused by pulse stretching from scattering in the water column (Thomas and Guenther 1979). Rough calculations indicated that 30-cm deep error under these conditions could be possible. The key to the remainder of the puzzle was the fact that the biases calculated for various flightlines correlated with only one parameter -- the surface return peak power. This surprising relationship is presented in Fig. 5-44. Shallow biases were only observed when the surface return power was very low due to lack of wind. It suddenly became clear that this meant that the "surface" returns detected were not from the interface at all, but rather from the volume backscatter. As seen in section 9.2.2 this difference is able to produce a shallow bias of about 60 cm which, when summed with the 30-cm deep bias from pulse stretching, yields a net 30-cm shallow bias as observed.

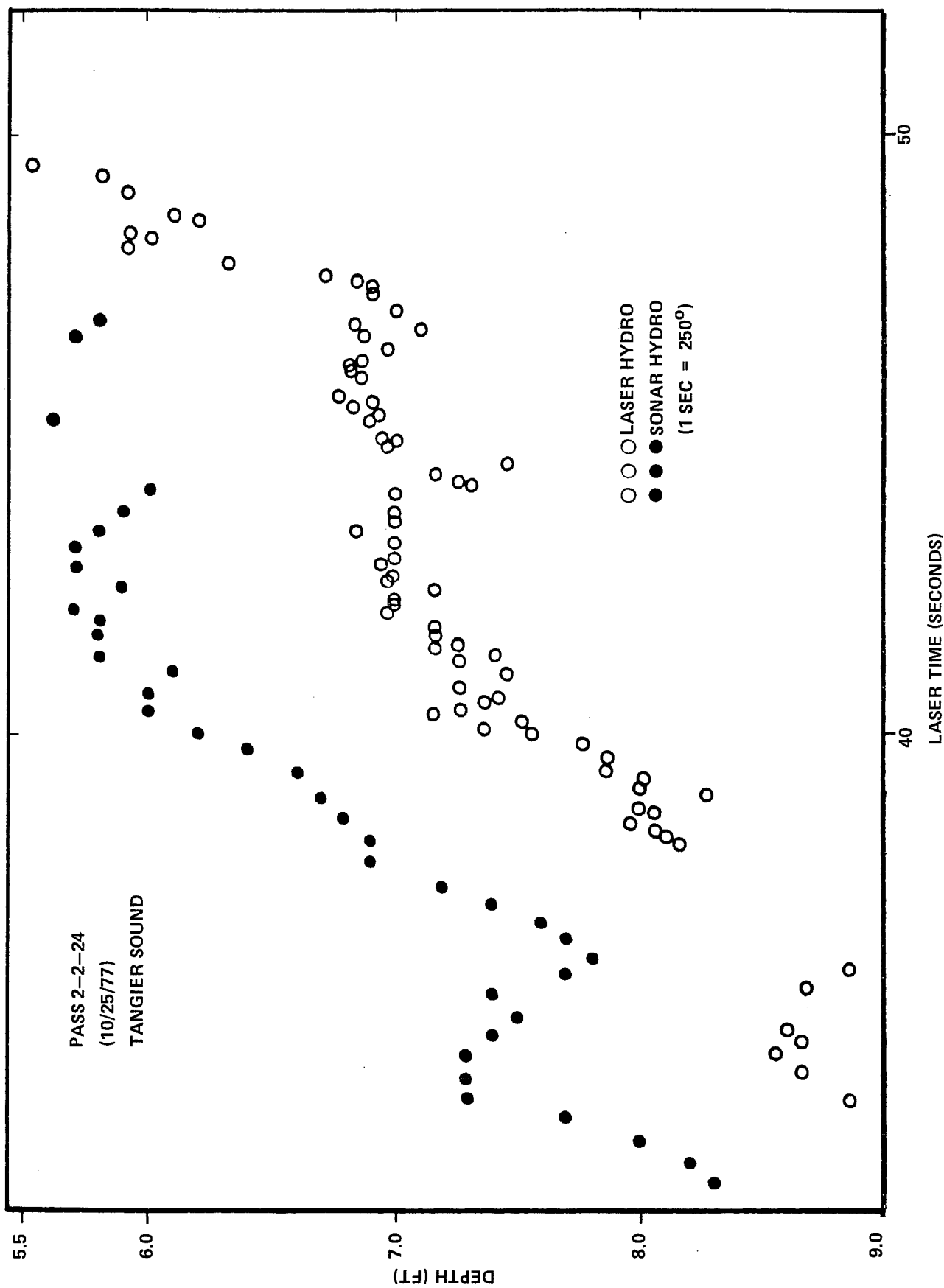


FIGURE 5-39. COMPARISON OF LASER AND ACOUSTIC DEPTH ESTIMATES INDICATING 1 FOOT DEEP BIAS

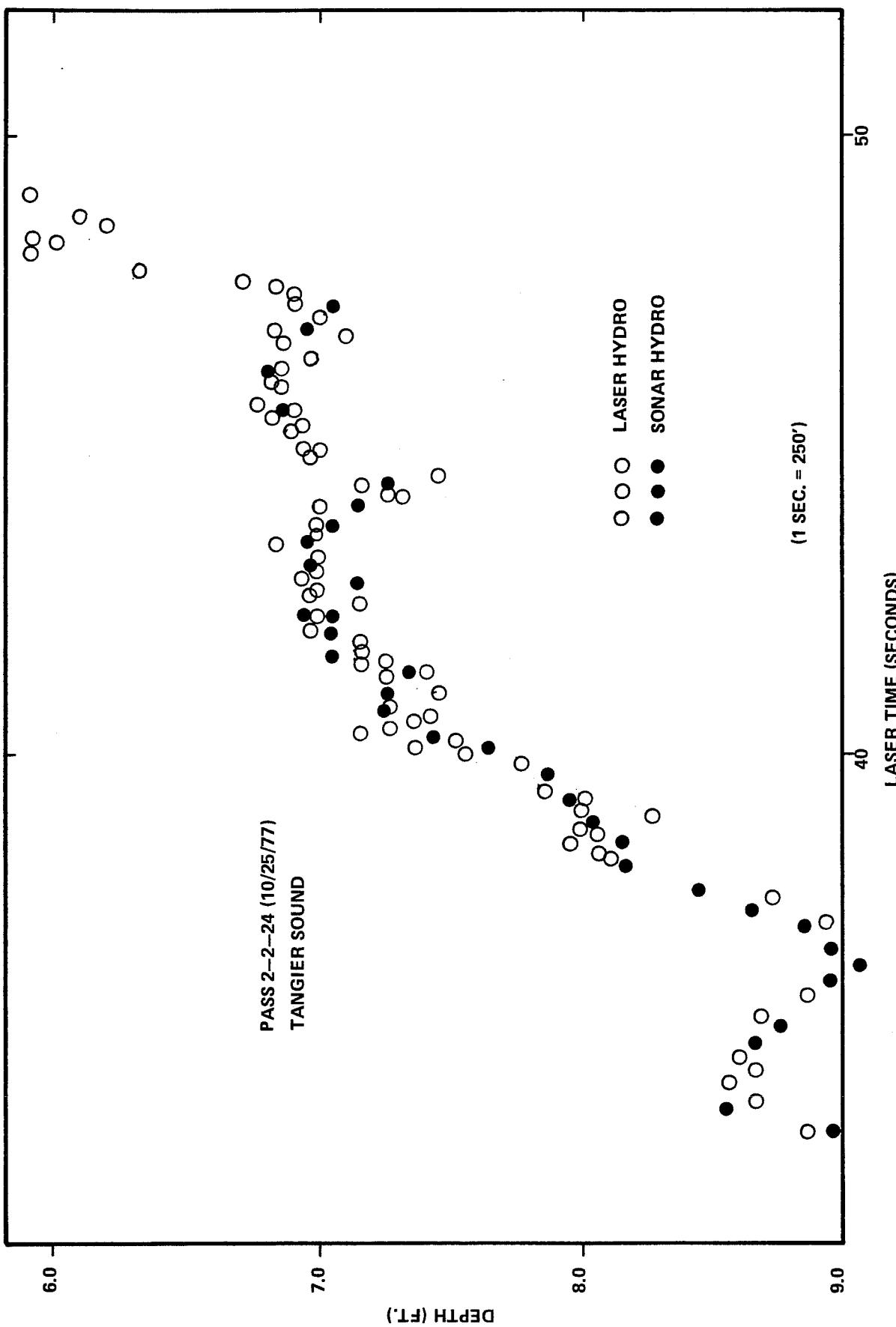


FIGURE 5-40. DATUM FREE PROFILE CORRELATION OF LASER AND ACOUSTIC DEPTH ESTIMATES

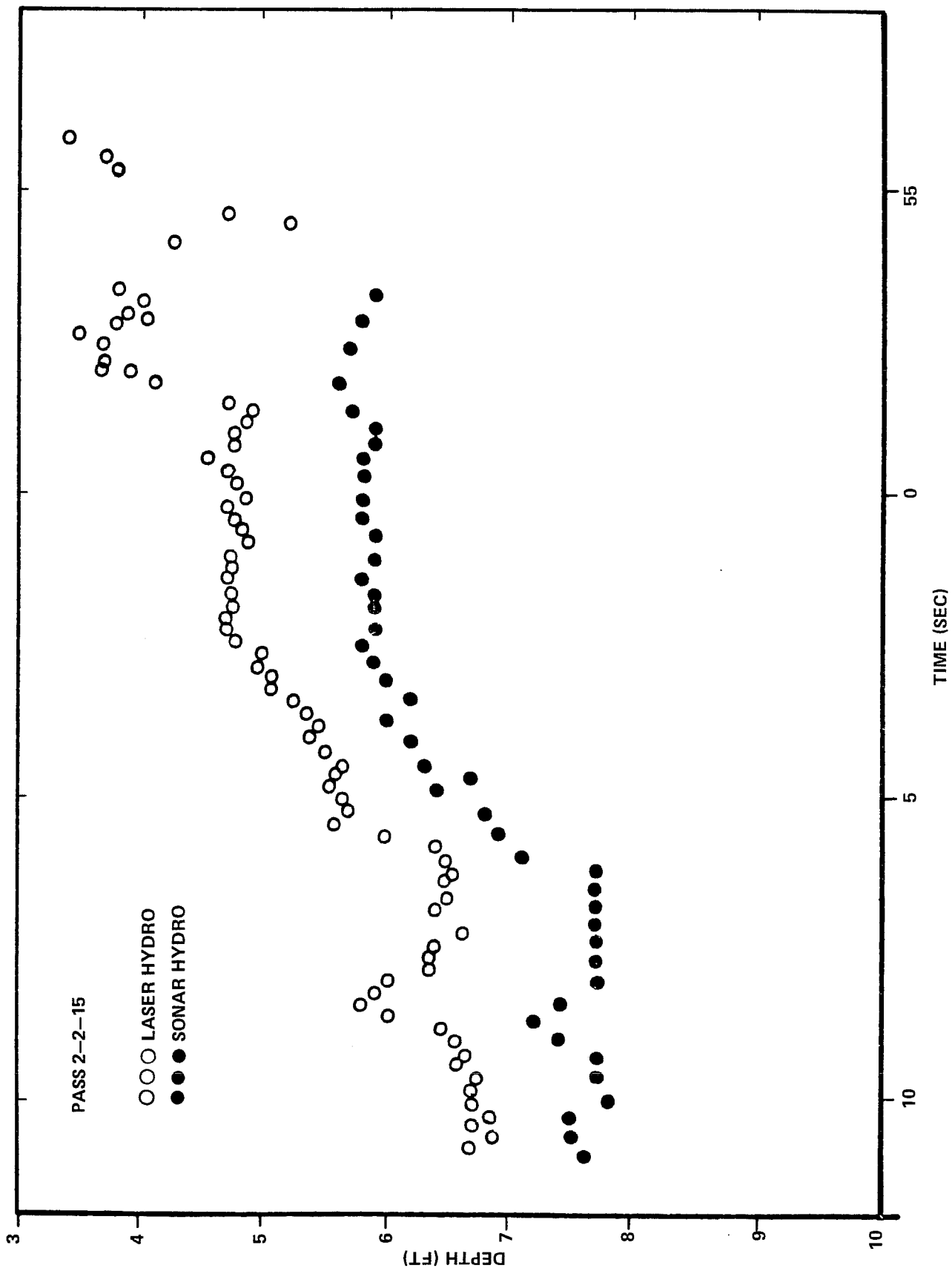


FIGURE 5-41. COMPARISON OF LASER AND ACOUSTIC DEPTH ESTIMATES INDICATING 1 FOOT SHALLOW BIAS

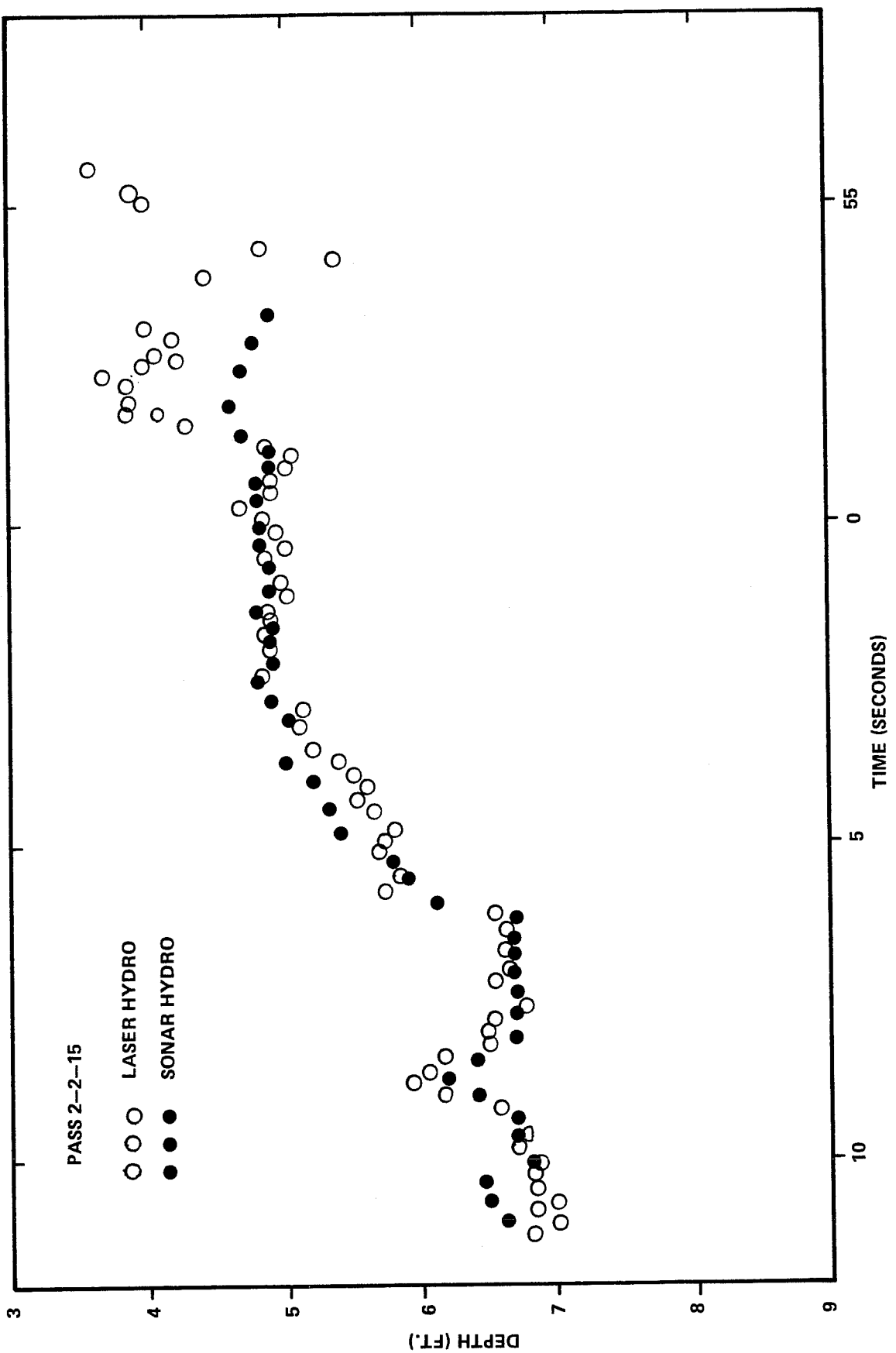


FIGURE 5-42. DATUM FREE PROFILE CORRELATION OF LASER AND
ACOUSTIC DEPTH ESTIMATES

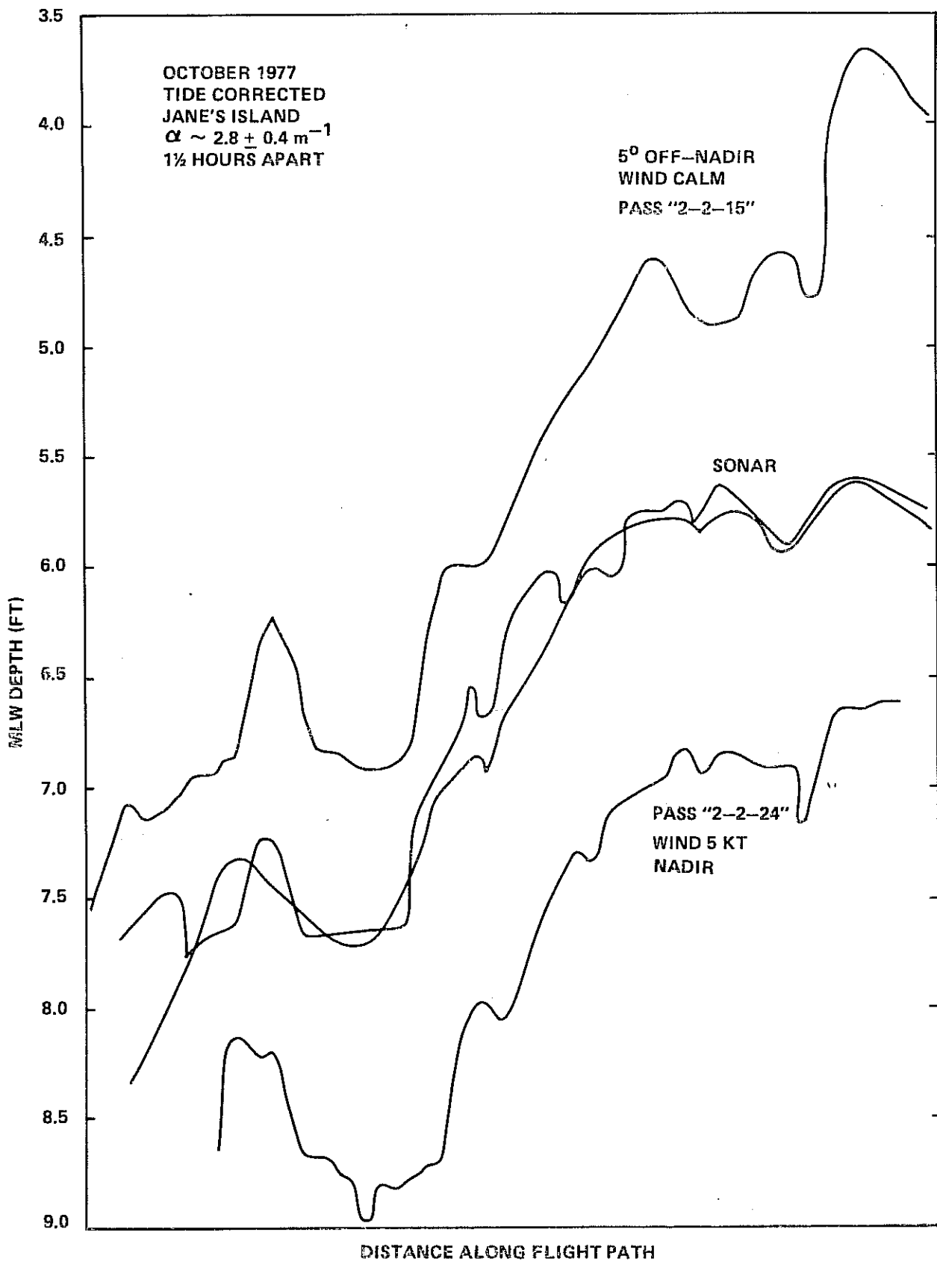


FIGURE 5-43. DEPTH PROFILES INDICATING DEEP AND SHALLOW BIASES FOR TWO WIND CONDITIONS

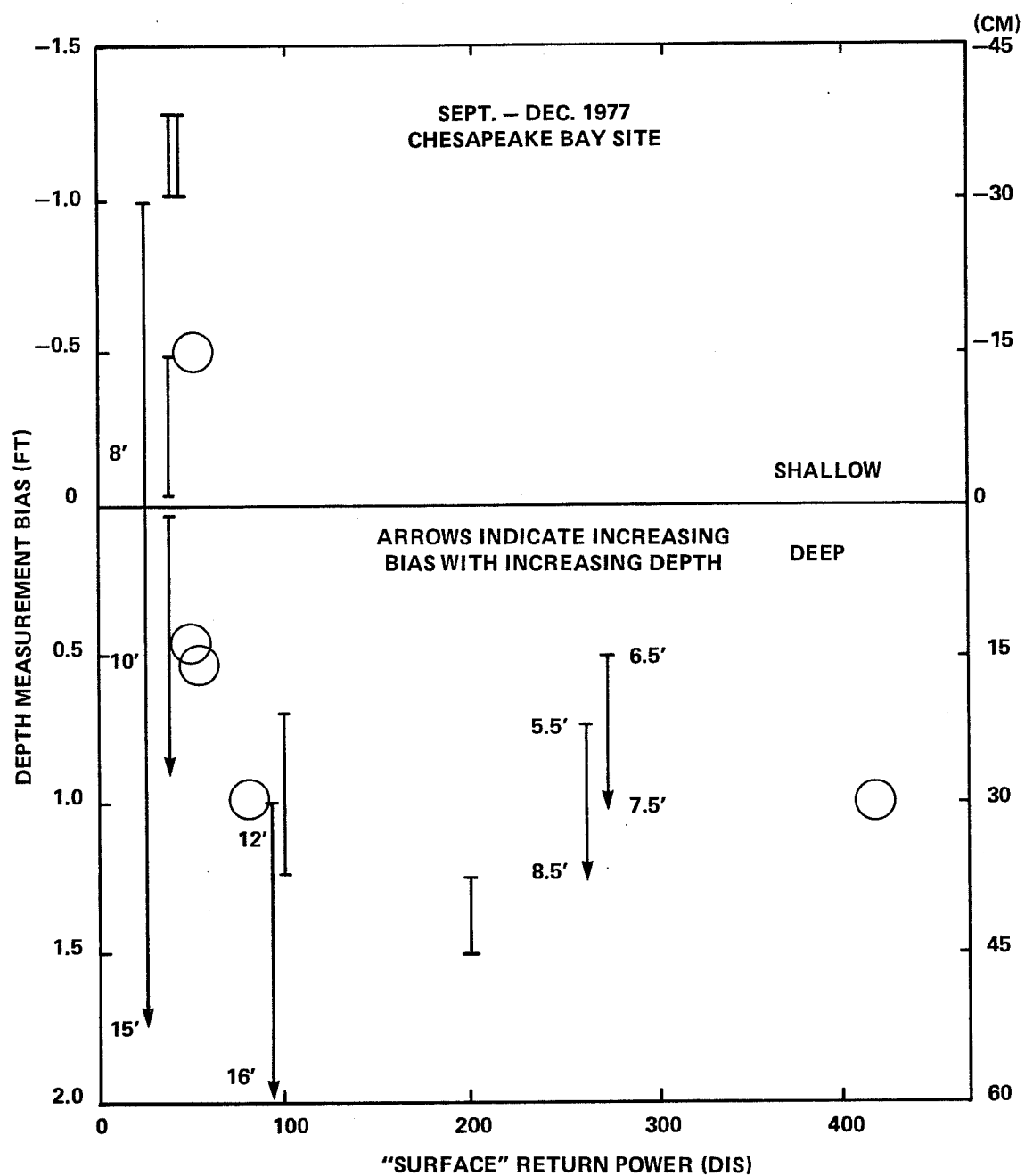
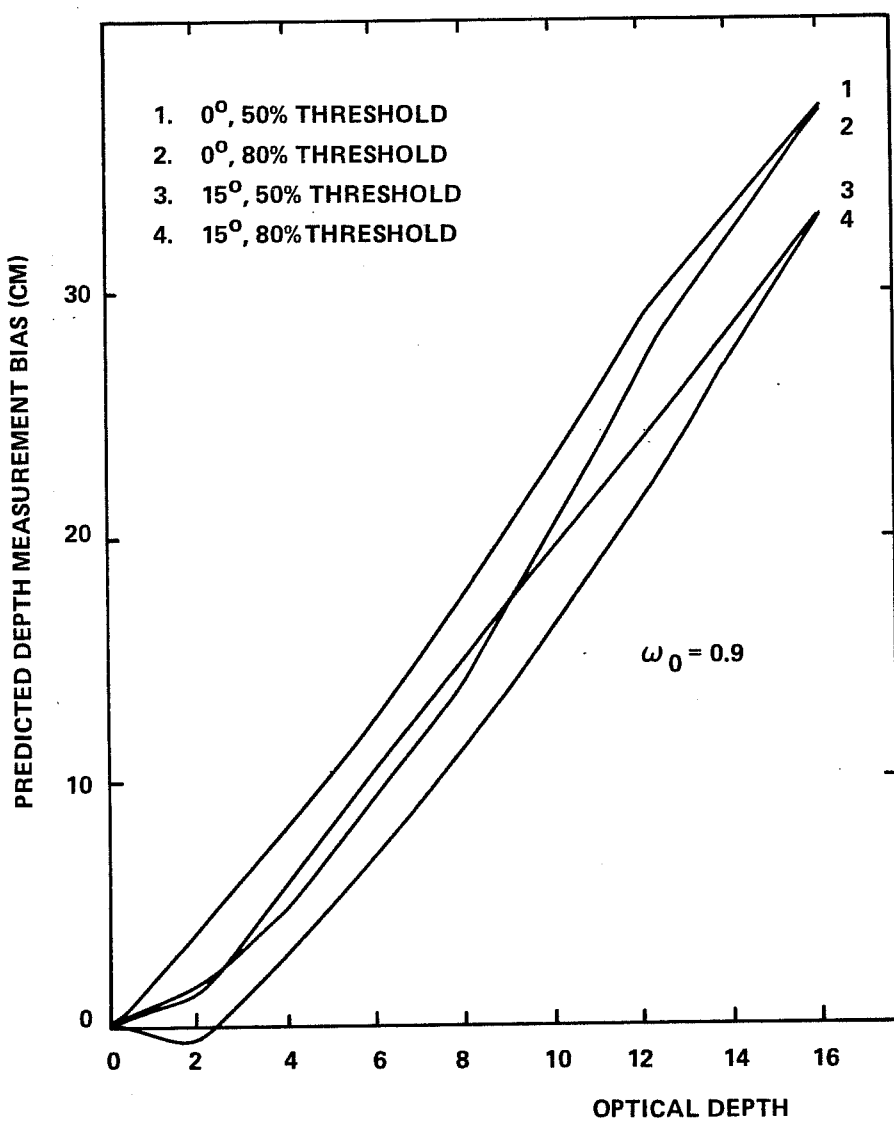


FIGURE 5-44. DEPTH MEASUREMENT BIAS VS. "SURFACE" RETURN POWER



**FIGURE 5–45. PREDICTED DEPTH MEASUREMENT BIAS
AT 5 M DEPTH VS. OPTICAL DEPTH**

Monte Carlo propagation simulations (Guenther and Thomas 1981a, b, c, d) have since been used to predict propagation-induced depth measurement biases (see sections 6 and 9.2.1). As seen in Fig. 5-45, these predictions for AOL parameters account for a major portion of the deep biases observed.

Future systems, in order to meet depth measurement accuracy standards, will have to be designed to reduce the error caused by the uncertain origins of the "surface" return between interface reflection and volume backscatter. Additionally, bias predictions will have to be applied to measured depths to remove the propagation-induced biases.

5.8 Conclusions

- 1) The feasibility of obtaining high precision (5-20 cm) bathymetric soundings in a typical operational environment with a scanning airborne lidar system was confirmed.
- 2) Excellent penetration ($nKD_m \approx 2.3$ day and ≈ 3.3 night) of typical coastal waters was achieved with a relatively low power laser (under 1-kW effective peak power).
- 3) Performance in the scanning mode at off-nadir angles up to the 15 degree system limit was satisfactory for conducting bathymetry.
- 4) The operational window for various system variables and environmental parameters was not unduly restrictive and should not lead to unreasonable mission constraints.
- 5) The mean precision of AOL soundings was excellent (typically less than 20 cm) and predictable with an existing model.
- 6) Profile correlation between NOS acoustic survey soundings and AOL lidar soundings was excellent, ranging from 2 to 15 cm RMS. This is much better than might have been expected.
- 7) Biases of up to 40 cm were noted; although these exceed NOS accuracy

standards, they were all explainable in terms of two processes: surface uncertainty and pulse stretching. Both can be removed in an operational system.

- 8) Wave correction using altitude intervalometer data was successfully demonstrated for scanning and non-scanning data.
- 9) Sophisticated pulse detection and location software was developed; it performed well both in low signal-to-noise ratio conditions and for depths as shallow as 45 cm (1.5 feet).
- 10) A large number of hardware design problems were noted. These must be corrected in future designs.
- 11) The surface interaction is extremely important to system performance. Future systems must be designed to operate within specifications regardless of whether the surface return comes from an interface reflection, from volume backscatter, or from a combination of both.

5.9 Acknowledgments

AOL bathymetry mode testing could not have been accomplished without the dedication of over forty individuals. Special recognition goes to Lowell Goodman who initiated and managed this complex interagency project and who acted as flight operations officer for the NOS field tests. The entire Airborne Laser Hydrography program in NOAA is the result of his farsighted leadership. I also wish to single out Bob Swift who was everywhere: making water measurements, flying the missions, and processing the data. The project could not have been a success without his drive, dedication, and boundless enthusiasm. I would like to specifically thank Frank Arbusto, Wayne Barbley, Chris Blue, Kurt Borman, Marion Butler, Bob Chase, Earl Frederick, Al Guzik, Tom Harmon, Frank Hoge, Bill Krabill, Doug Mason, Robert Navarro, Bob Scott, Bob Thomas, and Bill Townsend for their dedicated assistance, and the aircrew who flew long, tedious missions at perilously low altitude.

5.10 References

- Avco Everett Research Laboratory, Inc., 1975: Airborne Oceanographic Lidar System Final Report, NASA Contract No. NAS6-2653, NASA Contractor Report CR-141407, Everett, Mass., 139 pp.
- Avco Everett Research Laboratory, Inc., 1976: Presentation for Airborne Oceanographic Lidar System Applications Workshop Seminar. (unpublished manuscript).
- Borman, K., 1978: Airborne Oceanographic Lidar Postflight Bathymetry Processor, Program Documentation Version 4.0. Planetary Sciences Dept. Report No. 004-78, EG&G/Washington Analytical Services Center, Inc., Riverdale, Md., 191 pp.
- Goodman, L.R., (ed.), 1975: Laser Hydrography User Requirements Workshop Minutes, January 22-23, 1975, National Oceanic and Atmospheric Administration, Rockville, Md., National Aeronautics and Space Administration, Wallops Flight Center, Wallops Island, Virginia, 143 pp.
- Goodman, L.R., (ed.), 1976: Laser Hydrography Technical Review Workshop Minutes, August 25-26, 1976a, NOAA/National Ocean Survey, Rockville, Md., National Oceanic and Atmospheric Administration, Rockville, Md., 127 pp.
- Guenther, G.C. and Borman, K., 1981: Depth Estimation in the Airborne Oceanographic Lidar Postflight Bathymetry Processor. NOAA Technical Memorandum OTES 02, National Oceanic and Atmospheric Administration, U.S. Department of Commerce, Washington, D.C., 19 pp.
- Guenther, G.C. and Thomas, R.W.L., 1981a: Depth Measurement Biases for an Airborne Laser Bathymeter. Proc. Laser Hydrography Symposium, 30 Sept. - 3 Oct. 1980, Australian Defence Research Centre, Salisbury, South Australia, Australia Department of Defence, 428-452.

Guenther, G.C. and Thomas, R.W.L., 1981b: Monte Carlo Simulations of the Effects of Underwater Propagation on the Penetration and Depth Measurement Bias of an Airborne Laser Bathymeter. NOAA Technical Memorandum OTES 01, National Oceanic and Atmospheric Administration, U.S. Department of Commerce, Washington, D.C., 144 pp.

Guenther, G.C. and Thomas, R.W.L., 1981c: Simulations of the Impact of Inhomogeneous Water Columns on the Temporal Stretching of Laser Bathymeter Pulses. NOAA Technical Report OTES 02, National Oceanic and Atmospheric Administration, U.S. Department of Commerce, Washington, D.C., 39 pp.

Guenther, G.C. and Thomas, R.W.L., 1981d: Bias Correction Procedures for Airborne Laser Hydrography. NOAA Technical Report OTES 03, National Oceanic and Atmospheric Administration, U.S. Department of Commerce, Washington, D.C., 104 pp.

Guenther, G.C. and Thomas, R.W.L., 1981e: Error Analysis of Pulse Location Estimates for Simulated Bathymetric Lidar Returns. NOAA Technical Report OTES 01, National Oceanic and Atmospheric Administration, U.S. Department of Commerce, Washington, D.C., 51 pp.

Jerlov, N.G., 1968: Optical Oceanography. Elsevier Scientific Pub. Co., Amsterdam.

Melfi, S.R., 1975: Minutes of the Laser Fluorosensor Workshop. February 1975, Environmental Protection Agency, NERC/Las Vegas, Las Vegas, Nevada.

Petri, K.J., 1977: Laser Radar Reflectance of Chesapeake Bay Waters as a Function of Wind Speed. IEEE Trans. Geoscience Electronics GE-15, #2, 87-96.

Scott, R., 1982: Weather Constraints on Aircraft Laser Hydrography Operations. NOAA Technical Memorandum OTES 03, National Oceanic and Atmospheric Administration, U.S. Department of Commerce, Washington, D.C., 14 pp.

Swift, R.N., (Marine Science Consortium, Wallops Island Marine Science Center, Wallops Island, Virginia) 1977: Preliminary Report on Preflight Seatruthing for the Airborne Oceanographic Lidar Project. 102 pp. (unpublished manuscript).

Thomas, R.W.L., 1977: A Quantitative Analysis of Errors in the Interpretation of the AOL Charge Digitizer Output. WOLF Reference No. 4820-10, EG&G/Washington Analytical Services Center, Inc., Riverdale, Md., 38 pp.

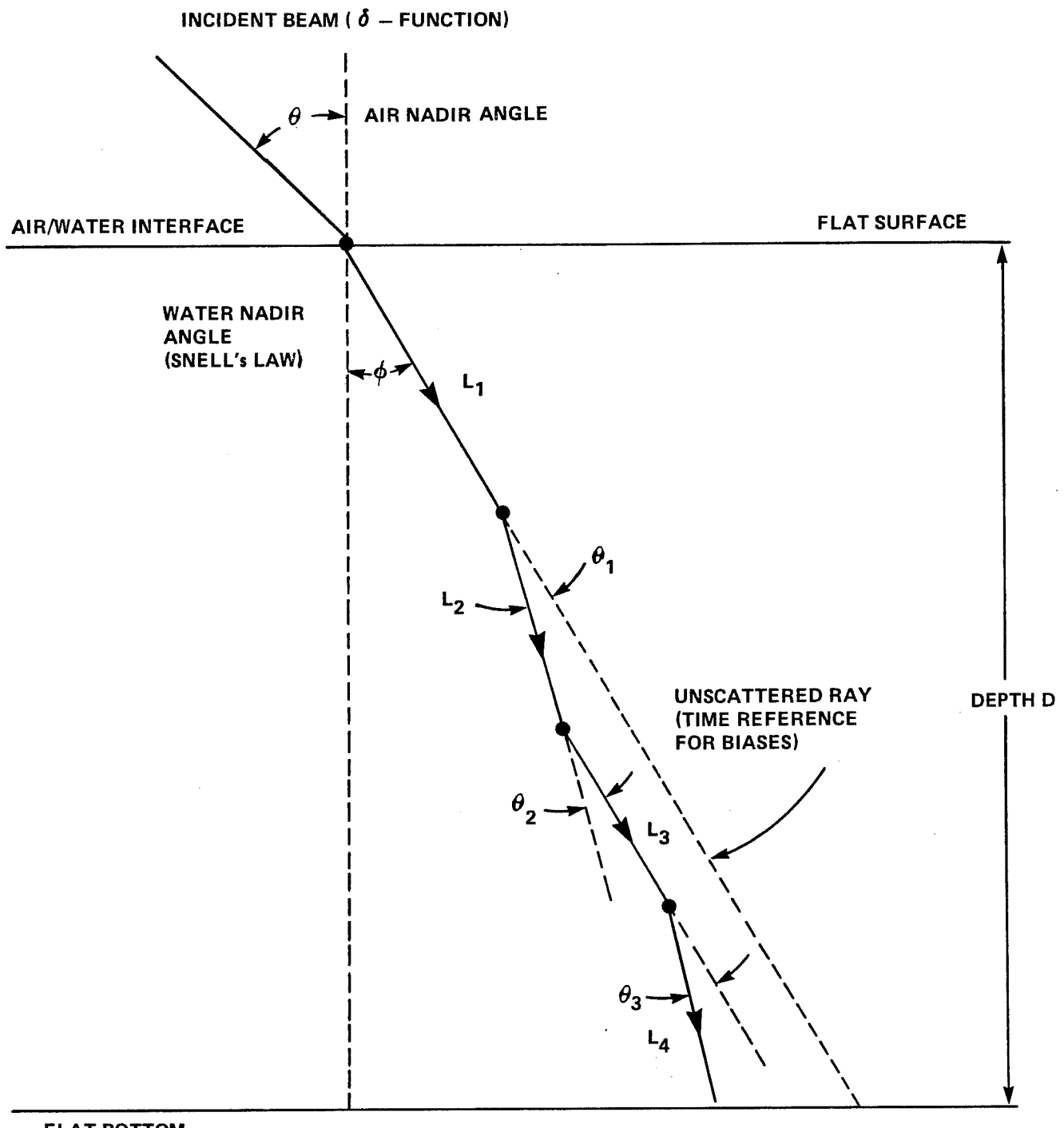
Thomas, R.W.L. and Guenther, G.C., 1979: Theoretical Characterization of Bottom Returns for Bathymetric Lidar. Proceedings of the International Conference on Lasers '78, December 11-15, 1978, Orlando, Fla., Society for Optical and Quantum Electronics, McLean, Va., 48-59.

6.0 MONTE CARLO PROPAGATION SIMULATION

6.1 Background

Analytical computations by Thomas and Guenther (1979) indicated the possibility of a significant depth measurement bias toward greater depths for operations of an airborne laser hydrography system at nadir. The bias arises from the lengthening of the total integrated path length due to the multiple-scattering transport mechanism by which the laser radiation spreads as it traverses the water column. This is the so-called "pulse stretching" effect. For off-nadir beam entry angles, the assumed or "reference" path is the unscattered ray in the medium (see Fig. 6-1) generated by Snell's Law refraction at a flat surface. There is a propensity for the core of the downwelling energy distribution to be skewed away from this path toward the vertical into the so-called "undercutting" region, due to the fact that the average path length is shorter, and hence the attenuation is less. The energy returning from this region tends to arrive at the airborne receiver earlier than that from the reference path for the same reason. This causes a depth measurement bias toward the shallow side. These two opposing biases superpose to yield depth estimates which, although they depend on water optical properties, are generally biased deep for small beam nadir angles and shallow for large nadir angles. The net biases can greatly exceed international hydrographic accuracy standards.

The key to the quantification of the effects of scattering is the generation of a set of response functions for the propagation geometry which characterize the temporal history of radiation reaching the receiver for an impulse input. Although various analytic approximations can be achieved via simplifying assumptions, the actual formal problem is effectively intractable due to the complexity of multiple scattering. Monte Carlo simulation is a practical method of generating these impulse response functions (IRFs). A powerful Monte Carlo simulation program has been developed and exercised to model the effect of underwater radiative transfer processes on airborne lidar signals for impulse laser inputs to homogenous and inhomogeneous water columns. The water parameters and systems constraints are appropriate to airborne laser hydrography systems presently under consideration for use in



RADIAL DISTRIBUTION

FIGURE 6-1. PROPAGATION SIMULATION GEOMETRY

coastal waters. Simulation results include full sets of spatial and temporal distributions. Horizontal resolution at the bottom and receiver field-of-view requirements are derived from the spatial results.

The impulse responses have been convolved with a realistic source pulse to yield expected bottom return signal characteristics, the so-called environmental response functions (ERFs), at a distant, airborne receiver. Appropriate volume backscatter decay has been added to the leading edge of each ERF. Depth measurement biases have been estimated by applying realistic signal processing and pulse location algorithms to the augmented ERFs. Resulting outputs are pulse shapes, peak power, and most importantly, depth measurement bias predictions. Bias sensitivities to input parameters are examined in detail.

It is important that the propagation-induced depth measurement biases be accurately calculated, because if the predicted biases exceed an acceptable magnitude, they can, at least conceptually, be applied to field data as bias correctors in post-flight data processing to maintain system performance within the error budget. Only a capsule of the basic techniques and outputs will be reported here because the simulations have been documented in great detail in Guenther and Thomas (1981a, b, c, and 1984). Major results of this work are reported in conjunction with the topics to which they pertain in following sections 8 and 9. These include spatial beam spreading and field-of-view requirements, peak pulse power for stretched pulses, and depth measurement bias predictions and proposed correction procedures.

6.2 Simulation Mechanics

In the Monte Carlo approach, the transport of photons to the bottom is modeled as a series of individual, random scattering and absorption events in the water column. Spatial and temporal distributions of photons arriving at the bottom are accumulated over a large number of representative paths. These distributions are then manipulated analytically to produce the estimated response at a distant airborne receiver.

6.2.1 Definitions

Traditionally, the mean free path for radiation transport through water has been described through a parameter called the "narrow-beam attenuation coefficient", α , which is compromised of two components: scattering and absorption. If "s" is the scattering coefficient and "a" is the absorption coefficient, then $\alpha = a + s$. Parameter values are wavelength dependent. For coastal waters, the minimum attenuation occurs in the green. Airborne bathymetric lidar systems operate in the green in order to maximize depth penetration potential. Numeric values reported here are appropriate for green wavelengths. If a monochromatic beam of radiance, N_0 , is incident on a column of water, then the amount that remains neither scattered nor absorbed after travelling a distance, d , is $N_0 \exp(-\alpha d)$. Since the mean of the exponential occurs at $\alpha d=1$, the mean free path, q , is equal to α^{-1} . The vertical "optical depth" of the medium, defined as the number of mean free path lengths required to vertically traverse the medium to the bottom for a depth, D , is D/q which is thus equal to αD .

In the simulation, the distance between scattering events is assumed to be exponentially distributed with a "mean free path", q . Individual path lengths, L , are generated from the expression $L = -q \ln \rho$, where ρ is a rectangularly distributed random variable in the interval $(0,1)$.

The "albedo for single scattering", ω_0 , as defined in section 3.5, is the average fraction of the incident energy at each scattering event that is not absorbed: i.e., $\omega_0 = (\alpha - a)/\alpha = s/\alpha$. For typical coastal waters, ω_0 ranges from about 0.55 to 0.93 at green wavelengths. In the simulations, photons are not actually eliminated by absorption as they might be in the real world. Following the method of Plass and Kattawar (1971), their behavior is represented by retaining photon weights (initially unity) which are multiplied by a vector of ω_0 values at each scattering event. In this way, the photons are not removed from the simulation, and results can be conveniently accumulated for many values of ω_0 at the same time.

Photons change direction at all scattering events. The scattering angle ψ from the incident direction is generated according to the "phase function",

$P(\psi)$, which defines the probability that the photon will scatter into a unit solid angle at ψ . Since the solid angle between ψ and $\psi + d\psi$ is $2\pi \sin\psi d\psi$, the probability of occurrence of ψ in that range is $p'(\psi) d\psi = 2\pi \sin\psi P(\psi) d\psi$. The phase function is the "volume scattering function" normalized to exclude specific water clarity conditions by dividing by the scattering coefficient. The random value of each simulated scattering angle, ψ_k , is generated by calculating and tabulating the cumulative probability for a given phase function as a function of ψ and sampling the interpolated results with values of ρ , where ρ is another rectangularly distributed random number between 0 and 1.

Typical phase functions for water at green wavelengths (Petzold 1972) exhibit very strong forward scattering. For the lidar simulations, two bounding phase functions for coastal waters designated "NAVY" or "clean" (Petzold HAOCE-5) and "NOS" or "dirty" (Petzold NUC-2200) were utilized. As seen in Fig. 3-4, these phase functions increase by a factor of more than 1,000 as the scattering angle diminishes from 10 to 0.1 degrees. The cumulative distribution functions in Fig. 3-5 demonstrate that roughly a quarter of the scattering occurs at angles of less than one degree and that three-fourths occurs under ten degrees. Scattering results both from opaque inorganic particles and translucent organics. Size distributions vary widely with location. The large forward scattering observed indicates that the dominant scatterers are inorganics of over micron size as well as organics of various sizes (Gordon 1974).

The "inherent" parameters α , ω_0 , and $P(\psi)$ are the independent descriptors of the transport medium characteristics required as inputs by the simulation and are thus also the optical properties upon which the biases are ultimately parameterized. The relationships between these parameters and the parameters governing the "apparent" properties of the medium have been discussed by Gordon et al. (1975). The most important apparent parameter is K , the so-called "diffuse attenuation coefficient", which is defined as the fractional rate of decay of the downwelling flux with depth. For small depths, K depends on both the depth itself and the angle of incidence of the radiation at the surface; but for larger depths these dependences become very small, and K approaches an asymptotic value. The ratio, K/α , as seen in Fig. 3-7 for

typical natural waters, is a monotonically decreasing function of ω_0 which has a value of unity when ω_0 is zero and which decreases towards zero as ω_0 tends to unity. There are small dependences on the phase function and optical depth, but these are unimportant for applications in coastal waters.

The energy loss of the downwelling beam as a function of depth, and hence the maximum useable "penetration" depth for a laser system, is most easily described in terms of K. In a similar fashion, K dictates the intensity and rate of decay of the volume backscatter signal preceding the bottom return. The biases, however, are not functionally dependent on K or KD, but rather on αD or sD . Combinations of α and ω_0 which produce the same value of K do not yield the same biases.

6.2.2 Downwelling Distributions

Spatial, temporal, and angular distributions of downwelling photons are accumulated at each of a series of optical depths between 2 and 16 as photons pass through these various levels. In this way, results for a complete set of bottom optical depths are generated in a single run. The lengths of the photon paths for photons reaching the bottom are summed to allow an evaluation of the associated time delay. The minimum time of transit to the bottom is $t_w = D/c$, where c is the velocity of light in water. The "time delay" for paths of length L_i is then computed as $t_D = \Sigma L_i/c - t_w$. By performing this computation for a large number of downwelling photons, the downwelling impulse response function $d(t_D)$ is accumulated as a histogram representing the probability distribution of arrival times of incident photons on the bottom. For simulations intended to produce peak power and depth measurement bias results, which need not conserve total energy, photons accruing delays of greater than a quarter or a half of the depth transit time (depending on the nadir angle) were terminated to save computer time because they would contribute only to the extended tail of the temporal distribution.

An important gain in the information content of the results arises from the realization that, for given values of αD and ω_0 , all temporal results scale linearly with the depth. This is illustrated in Fig. 3-3 where representative photon paths are shown for two cases with the same αD but with

different values of D. The photon paths for the two cases are geometrically "similar" so that the fractional time delays, t_D/t_w , are identical. The absolute time delays thus scale linearly with D, and one set of normalized response functions can be used to determine absolute results for all depths.

6.2.3 Impulse Response at a Distant Receiver

Several techniques were considered for completing the simulation to a distant airborne receiver. The direct geometric approach of tracking photon paths to a distant receiver after a return path through the water was considered impractical because the very low probability of such events would lead to excessive computer usage. The sometimes useful approach of "virtual" photons, termed the "method of statistical estimation" by Spanier and Gelbard (1969), involves the calculation and summing at each scattering event of weighted probabilities in the direction of the distant receiver. This approach was attempted, but lead to noisy, irreproducible behavior for as many as 10^5 incident photons due to the highly peaked nature of the Petzold coastal phase functions. The method was moderately successful with broader phase functions such as the "KB" function favored by Gordon et al. (1975) for clear ocean water.

The round-trip impulse response function (IRF) in the water can be computed from the downwelling distributions using the principle of "reciprocity" (Chandrasekhar 1960). Reciprocity is a statement of symmetry or reversibility which, when applied to airborne lidar, implies that the ensemble of viable scattering paths in the water is identical for downwelling and upwelling radiation, because the exiting photons must leave the medium in the opposite direction from which they entered in order to reach the distant receiver colocated with the laser source. In other words, reciprocity requires that the statistical ensemble of the unmodelled upwelling paths in the direction of a distant receiver for photons reflected at the bottom be identical to that for the simulated downwelling paths from a colocated transmitter. This is not a declaration that the downwelling and upwelling paths are physically identical, but rather that the set of simulated downwelling photon tracks can be regarded as representative for both cases. The subset of the downwelling paths utilized by upwelling radiation is determined by the weighting function for the bottom reflection.

To obtain a round trip impulse response function in the water, the computed impulse response $d(t_D)$ for downwelling transport can be convolved digitally over the upwelling distribution, $u(t_D)$. For an assumed Lambertian bottom reflection distribution, the upwelling distribution is computed by multiplying the weights of downwelling photons reaching the bottom by the cosine of their arrival nadir angles. The convolution result is the round-trip IRF at the water/air interface for an unlimited receiver FOV. This result, however, does not include the subsequent variation in the air-path length to the distant receiver across the upwelling surface distribution. This is an important effect which significantly alters the shape of the IRF, except perhaps at nadir where the air-path variation is not as great, and it cannot be neglected. For off-nadir angles, the shortest total round-trip path, as seen in Fig. 6-2, is no longer the one including a vertical path to the bottom, but rather, due to the shorter air path, one in which the photons arrive at the bottom closer to the aircraft. Thus, highly scattered energy which would have returned in the trailing edge of the IRF actually defines the leading edge. With the convolution approach, the temporal response varies in an unknown manner across the upwelling distribution, and the distant receiver IRF cannot be calculated.

In order to calculate the IRF at a distant, off-nadir receiver, one must know the time history of each returning photon and its location in the upwelling surface distribution. This can be accomplished by using the concept of reciprocity in a slightly different, more discrete way. As before, the simulated downwelling paths are judged to be representative of the upwelling paths for photons which will exit the water in the direction of the receiver, and specific upwelling paths are selected by Lambertian (cosine) weighting of the downwelling paths. Rather than implicitly computing the effect of all possible path pairings of the downwelling photons by convolution, one can form each possible path pair directly as seen in Fig. 6-3 for two sample paths. Propagation decay times of paired paths are combined with their appropriate geometric air-path delays from the surface exit location to the receiver. For selected fields of view, histograms of these total transit delay times are formed to produce the receiver IRFs.

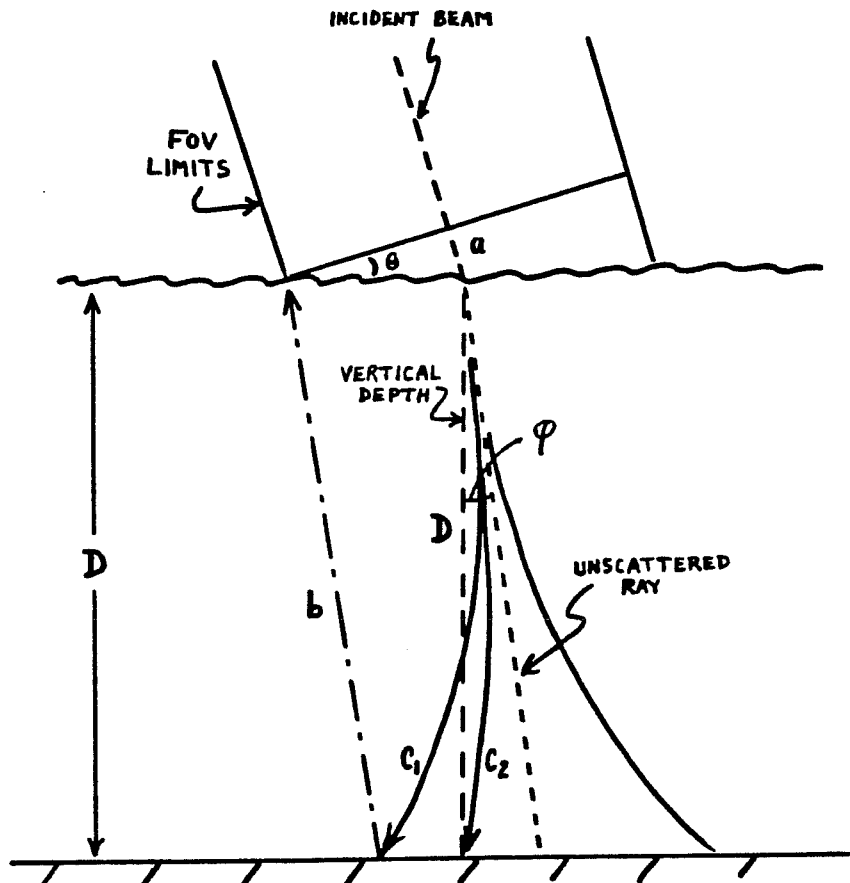


FIGURE 6-2. AIR PATH GEOMETRY

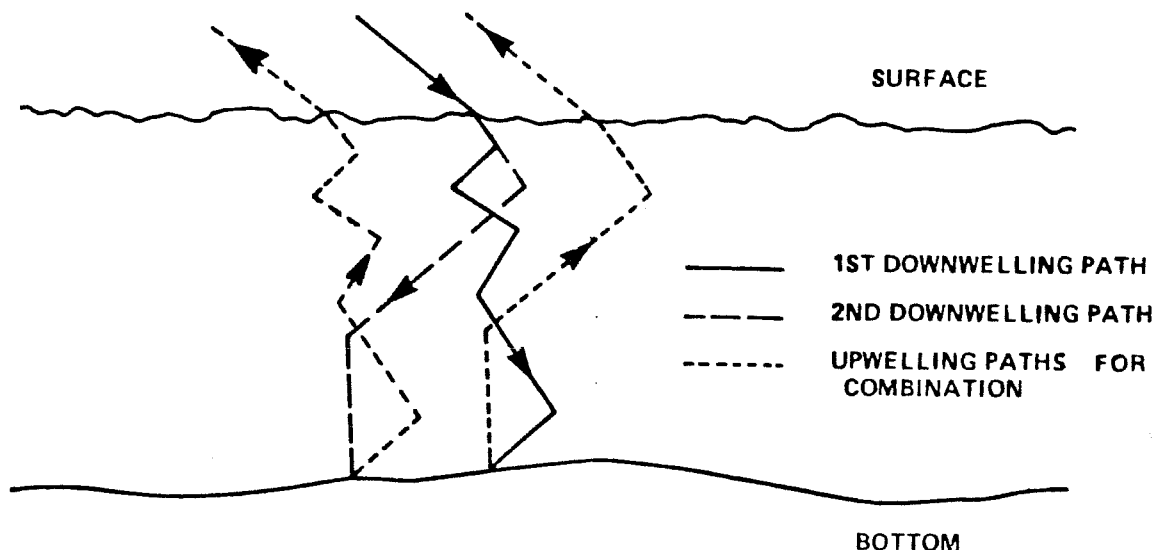


FIGURE 6-3. PATH PAIRING EXAMPLE

Since the set of all possible path pairs is not statistically independent, a smaller subset of these pairs can be used (to save computer time) with very little loss in information. Several variations of photon number and pairing combinations were examined in order to find the most cost-effective approach. Reported results are based on 1000 downwelling photon paths paired with a block of 25 randomly selected upwelling paths for a total of 25,000 round-trip paths. This is a minimum acceptable number, as the resulting IRFs are somewhat noisy for cases of high attenuation, i.e., concurrent low ω_0 and high αD . A larger number of photons and/or pairings would be beneficial, but a much larger set would be required to significantly improve performance.

6.2.4 Inhomogeneous Media

The simulations were primarily performed for homogeneous water in which the density and nature of the scattering particles are independent of depth. It is well known, however, that significant departures from homogeneity occur frequently in coastal waters. It was important, therefore, to assess the error magnitudes caused by using homogeneous case biases when significant departures from homogeneity occur. The existing Monte Carlo simulation program was modified (Guenther and Thomas 1981b) to permit simultaneous estimation of impulse response functions for several exaggerated vertical distributions of scatterers and absorbers, as seen in Fig. 6-4. The resulting IRFs were digitally convolved with a 7-ns triangular source pulse to produce the "environmental response functions" (ERFs). Linear fractional threshold pulse locators were applied to the ERFs to determine the biases and the differences in bias errors between the homogeneous case and the various inhomogeneous models. The biases, even for these extreme inhomogeneities, were found to differ from those of the homogeneous case by less than 10 cm. The simulation results for homogeneous waters are thus considered to be sufficiently representative for typical natural coastal waters.

6.3 Outputs

For each of the two phase functions, six simulation runs (with nadir angles in air of 0, 10, 15, 20, 25, and 30 degrees) were performed, for a

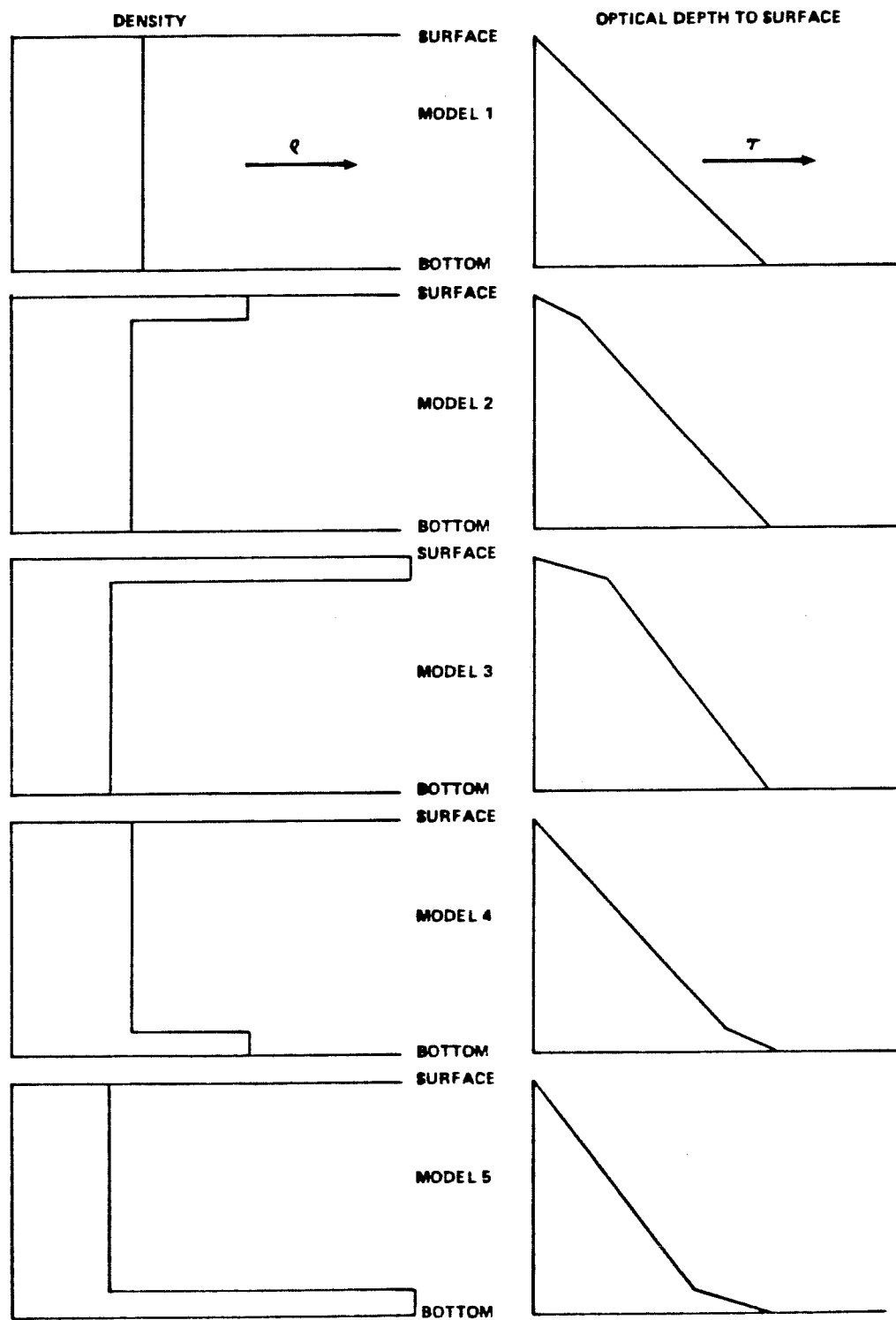
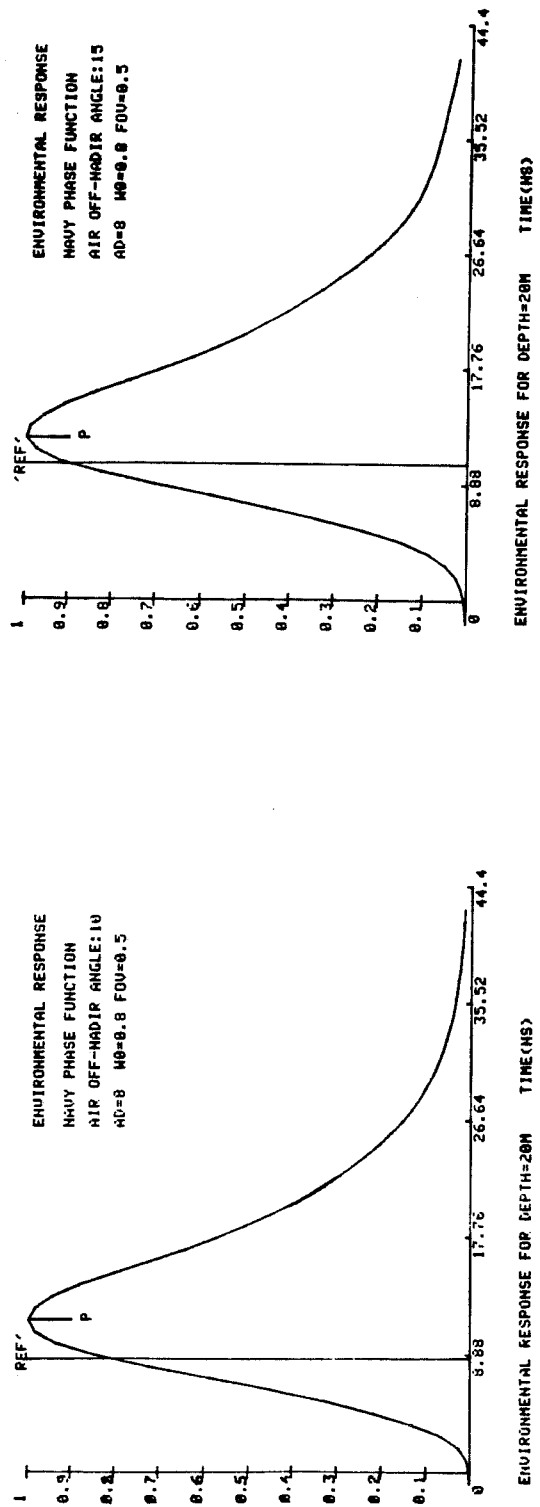
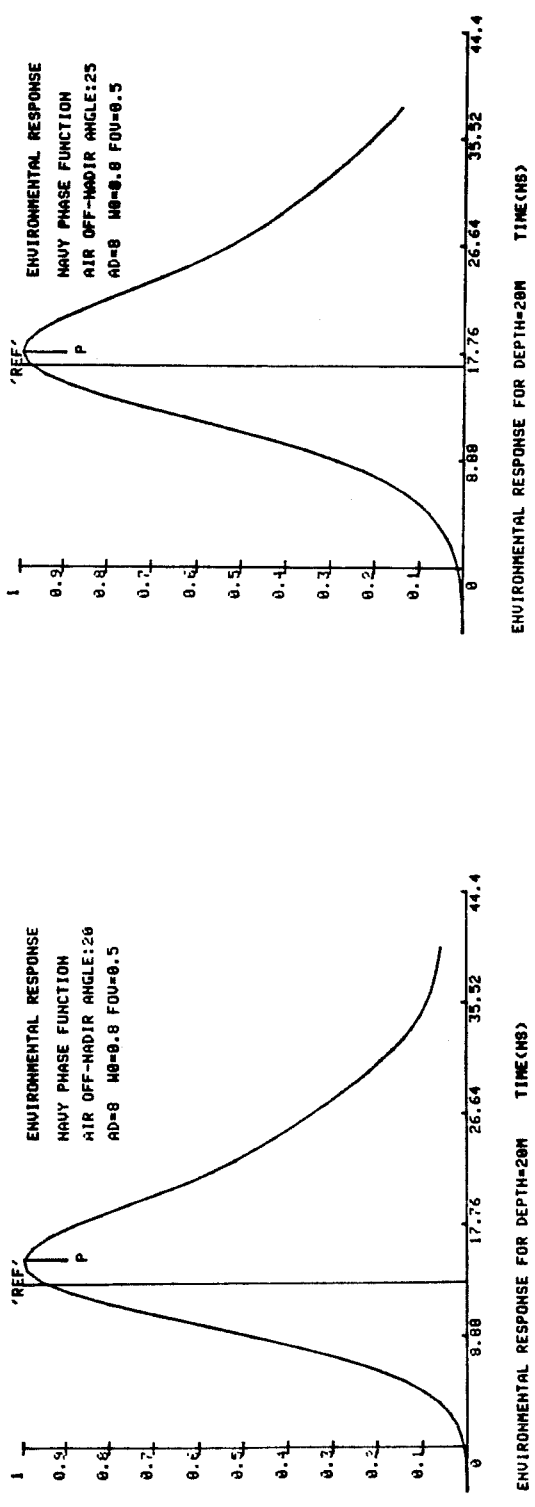


FIGURE 6-4,SCATTERING PARTICLE DENSITY AND OPTICAL DEPTH TO THE SURFACE



ENVIRONMENTAL RESPONSE FOR DEPTH=20M TIME(ns)



ENVIRONMENTAL RESPONSE FOR DEPTH=20M TIME(ns)

FIGURE 6-5. ENVIRONMENTAL RESPONSE FUNCTIONS FOR VARYING ANGLES

total of twelve runs. To insure comprehensive results sets, simulations over full ranges of αD (2 - 16), ω_0 (0.6 - 0.9), and FOV were run for each case. Five values of optical depth, three values of single-scattering albedo, and five values of FOV were employed in each simulation run so that 45 sets of results were generated in each run. Spatial and temporal bottom distributions were printed for each case. A data base containing 540 impulse response functions, each resolved into 50 time bins, has thus been created.

For finite source pulses, the temporal response functions are calculated by convolving a selected source function with the appropriate impulse response functions. Realistic lidar receiver inputs or "environmental response functions" (ERFs) have been computed by digitally convolving these IRFs, scaled to desired depths, with a 7-ns (FWHM) triangular source pulse which is representative of laser pulses from a state-of-the-art, high repetition rate, frequency-doubled Nd:YAG laser. Depth measurement biases for twelve different combinations of signal processing and pulse location algorithms have been calculated for these ERFs. Peak power and bias results are reported in sections 8.2.2 and 9.2.1, respectively. The ERFs and their associated peak powers and biases are archived on magnetic media for future use. Sample ERFs are seen in Fig. 6-5.

6.4 Acknowledgments

The conception, design, coding, modifications, and operation of the Monte Carlo simulation were carried out by Bob Thomas at EG&G/WASC. Without this pace-setting effort, we would still be dealing with only qualitative estimates. We thank Hyo Sang Lee for his insight and valuable critique. Partial funding for this work was provided by the Defense Mapping Agency, the Office of Naval Research, and the Naval Ocean Research and Development Activity.

6.5 References

Chandrasekhar, S., 1960: Radiative Transfer. Dover Publications, New York, N.Y., 385 pp.

Gordon, H.R., 1974: Mie Theory Models of Light Scattering by Ocean Particulates. Suspended Solids in Water. Plenum Press, Ed. Ronald J. Gibbs, 73-86.

Gordon, H.R., Brown, O.B., Jacobs, M.M., 1975: Computed Relationships Between the Inherent and Apparent Optical Properties of a Flat Homogenous Ocean, Appl. Opt., 14, 417-427.

Guenther, G.C. and Thomas, R.W.L., 1981a: Monte Carlo Simulation of the Effects of Underwater Propagation on the Penetration and Depth Measurement Bias of an Airborne Laser Bathymeter. NOAA Technical Memorandum OTES 01, National Oceanic and Atmospheric Administration, U.S. Department of Commerce, Washington, D.C., 144 pp.

Guenther, G.C. and Thomas, R.W.L., 1981b: Simulations of the Impact of Inhomogeneous Water Columns on the Temporal Stretching of Laser Bathymeter Pulses. NOAA Technical Report OTES 02, National Oceanic and Atmospheric Administration, U.S. Department of Commerce, Washington, D.C., 39 pp.

Guenther, G.C. and Thomas, R.W.L., 1981c: Bias Correction Procedures for Airborne Laser Hydrography. NOAA Technical Report OTES 03, National Oceanic and Atmospheric Administration, U.S. Department of Commerce, Washington, D.C., 104 pp.

Guenther, G.C. and Thomas, R.W.L., 1984: Prediction and Correction of Propagation-Induced Depth Measurement Biases plus Signal Attenuation and Beam Spreading for Airborne Laser Hydrography. NOAA Technical Report NOS 106 CGS 2, National Oceanic and Atmospheric Administration, U.S. Department of Commerce, Washington, D.C., 112 pp.

Petzold, T.J., 1972: Volume Scattering Functions for Selected Ocean Waters. SIO Ref. 72-78, Scripps Institution of Oceanography, Visibility Laboratory, San Diego, Calif., 79 pp.

Plass, G.N. and Kattawar, G.W., 1971: J. Atmos. Sci., 28, 1187.

Spanier, J. and Gelbard, E.M., 1969: Monte Carlo Principles and Neutron Transport Problems. Addison-Wesley Publishing Co., Reading, Mass.

Thomas, R.W.L. and Guenther, G.C., 1979: Theoretical Calculations of Bottom Returns for Bathymetric Lidar. Proceedings of the International Conference on Lasers '78, December 1978, Orlando, Fla., 48-59.

7.0 INTERFACE REFLECTION AND VOLUME BACKSCATTER CHARACTERISTICS

7.1 Background

The reflection of energy from the air/sea interface and by the volume backscattering immediately below involves a number of complex phenomena which have critical effects on system design and performance. Both of these reflections will be considered as "surface" return, because when the interface return is weaker than the volume return, the latter will be detected, although at a somewhat biased location, as will be seen. In one way, this is fortuitous because it potentially removes a serious operational constraint -- the need for sufficient wind to excite capillary waves with slope equal to or greater than the beam nadir angle. Indeed, wind is a negative factor because it generates waves for which corrections must be made, and it adds energy to the water column which resuspends bottom sediments in shallow waters thereby reducing the bottom return signal-to-noise ratio.

The depth measurement accuracy can be unacceptably compromised in four separate ways related to the surface: 1) by "beam steering" of the incident energy away from the direction expected for a flat sea due to refraction through wave slopes (as described in section 9.2.3); 2) by uncompensated water column depth variations due to waves (section 9.2.5); 3) by unrecognized or uncompensated variation of the surface return between interface reflection and volume scattering, depending on the wind, surface structure, and beam nadir angle (section 9.2.2); and 4) by surface return stretching (section 9.2.4). The surface interaction also has numerous potential indirect effects on penetration and on propagation-induced bias correction due to hardware-related problems such as limited receiver dynamic range, PMT "ringing" and "afterglow", and non-linear signal processing biases. It is imperative that the various effects of these surface return signals on all aspects of system performance be identified and quantized.

7.2 Interface Return

Throughout much of the evolution of airborne laser hydrography, it has been assumed that the surface return would come from an interface reflection,

and that the lack of same would preclude operation. Since only a scanning system is cost effective, off-nadir operation is an absolute requirement. If the sea surface were perfectly flat and mirror-like, no interface return at all would reach the transceiver because of the reflection geometry. In order to reflect energy back along the incoming path, the surface must contain tiny facets perpendicular to the beam. These facets are capillary waves, the tiny wavelets raised by the wind at speeds above two or three knots. The higher the wind speed, the higher the mean capillary wave slope angle, and the higher the beam nadir angle from which an interface return can be directed back into the direction of the airborne receiver.

The effects of wind generated waves on laser beam interface reflection were reported by Petri (1977) for work done from the Chesapeake Bay Bridge. Sample results, repeated in Fig. 7-1, demonstrate the effects of wind speed and beam nadir angle on received power. For low winds and nadir angles, the mean return is large, but the statistical variance (dynamic range) is also very large; i.e., some returns are very strong and some are very weak or nonexistent. For greater winds and nadir angles the mean returns are lower, but the variances are also lower; i.e., the returns are somewhat weaker on the average, but more reliable.

Petri reported measurements of the so-called mean effective "Lambertian reflectivity" of the interface at nadir, ρ_s^* , as seen in Fig. 7-2. This data set was fitted with the equation

$$\rho_s^*(w) = 214 \left(1 - \frac{w - 4.8}{12.2}\right)^{2.06} + 37 \quad (7-1a)$$

for wind speeds, w (knots), between 3 and 17 knots. This equation is unwieldy and exhibits undesirable behavior for $w > 17$ knots. The same data can be fitted with the expression

$$\rho_s^*(w) = 4.26 e^{-0.14 w} \quad (7-1b)$$

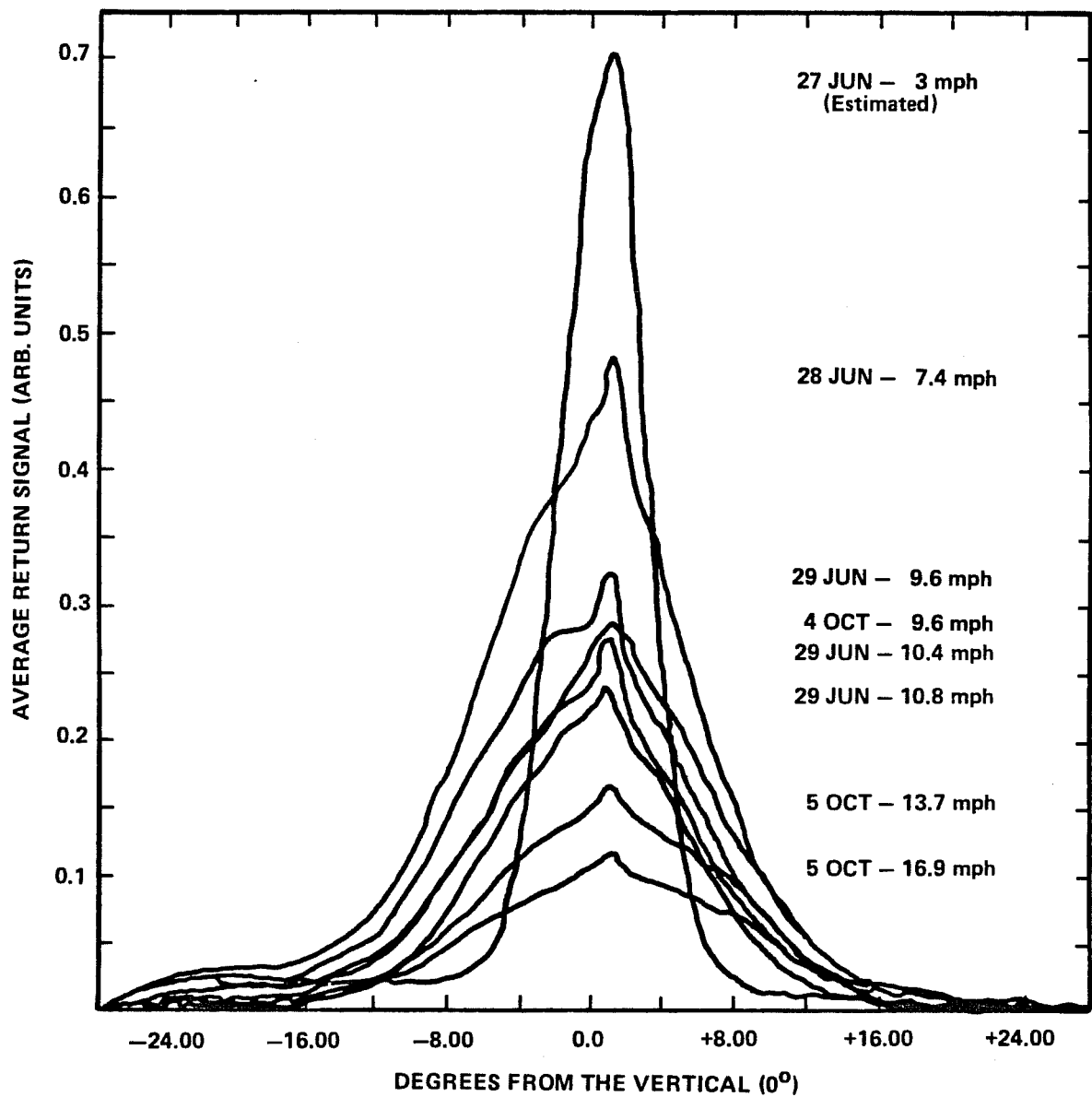


FIGURE 7-1 NORMALIZED AVERAGE RETURN SIGNAL VS. SCAN ANGLE
(PETRI, 1977)

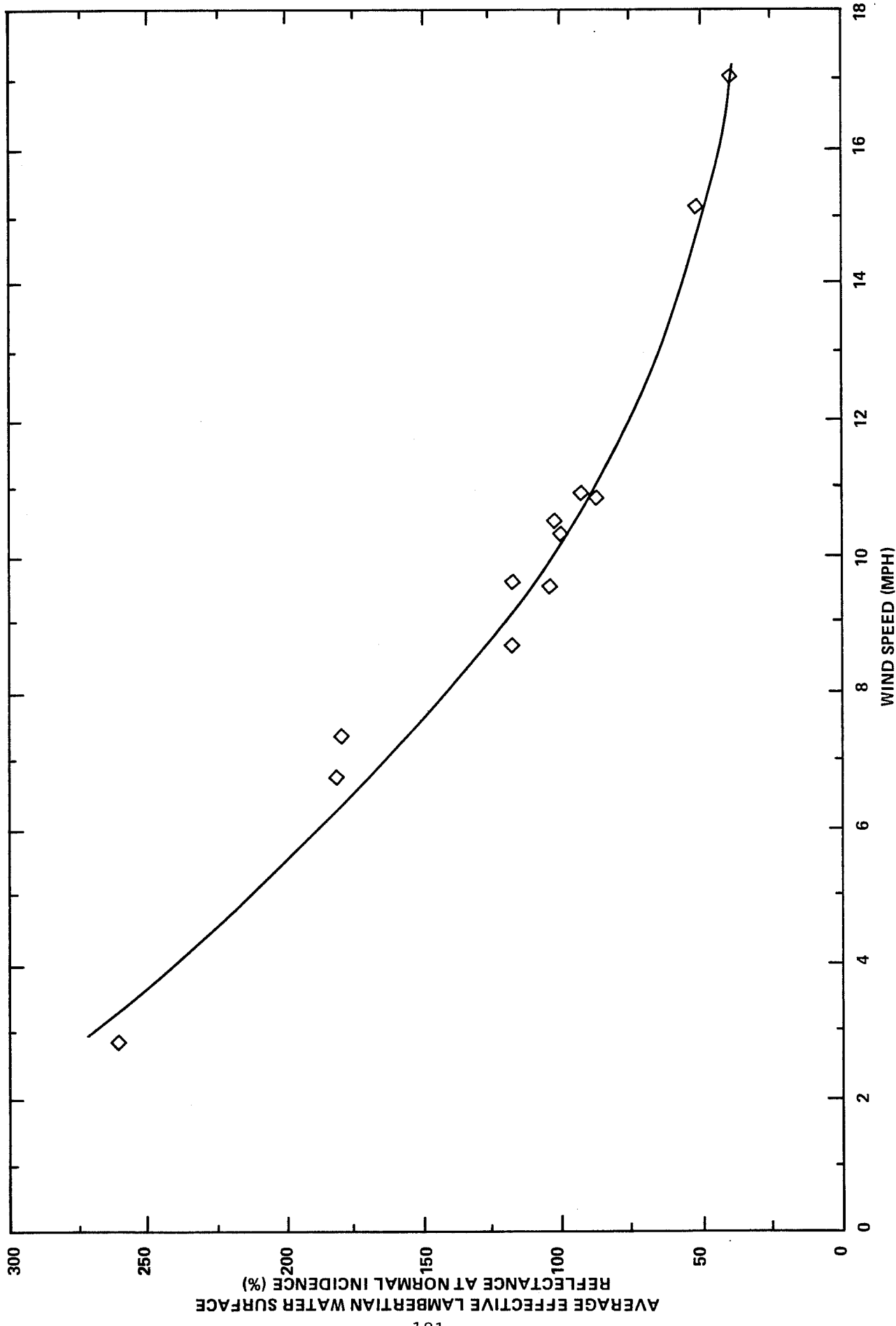


FIGURE 7-2. AVERAGE EFFECTIVE LAMBERTIAN REFLECTANCE VS WIND SPEED (PETRI 1977)

with a regression coefficient of $r^2 = 0.97$. This relationship behaves reasonably for $w > 17$ knots and will be used, arbitrarily, up to 25 knots.

A general expression for the mean peak interface return power, P_s , is

$$P_s = A \frac{\rho_s^*(w)}{\pi} \cos^2 \theta N(\theta, w), \quad (7-2)$$

where θ is the beam nadir angle in air, $N(\theta, w)$ is the normalized Cox-Munk wave slope distribution (Cox and Munk 1954), and, here and in following relationships, the system factors will be of the specific form

$$A \equiv n P_T A_R / H^2, \quad (7-3)$$

where n is the total system optical efficiency (receiver and transmitter), P_T is the transmitted peak laser power, A_R is the aperture area of the receiver telescope, and H is the aircraft altitude.

The quantity $\rho_s^*(w)/\pi$ is the effective surface reflectivity per unit solid angle which might be denoted simply $\rho_s(w)$, for example.

The basic Cox-Munk expression for the wind dependence of the mean surface reflectivity for a direction, d , with respect to the wind is

$$N_d(\theta, w) = e^{-\theta^2/2\sigma_d^2(w)}, \quad (7-4)$$

where d may be denoted as "u" for up/down wind or "c" for crosswind. The complete Cox-Munk expression also contains a complicated polynomial. Its effect has been evaluated and found to be small for cases of interest; it has thus been neglected for simplicity. The up/down wind RMS slope is

$$\sigma_u^2 = 0.00158 w(\text{kt}), \quad (7-5a)$$

and the RMS crosswind slope is

$$\sigma_c^2 = 0.003 + 0.00096 w(\text{kt}). \quad (7-5b)$$

A number of more recent determinations of σ_u and σ_c from various tank and environmental tests have been evaluated (i.e., Bobb 1979, Hughes et al. 1977), but the Cox-Munk values, measured from an aircraft, are believed to remain the most appropriate for this application. Tank tests tend to give higher slopes for a given wind speed due to a problem with scaling factors; the height or altitude of the wind measurement can also lead to reference problems.

A comparison of the Petri results with Eq.(7-4) (averaged over up/down and crosswind cases) is seen in Fig. 7-3, where the vertical scales between the two were normalized to equality for the three knot, nadir case. The agreement is quite good except for the three knot case where the Cox-Munk result exhibits slightly higher slopes. The reason for this discrepancy is the fact that the Cox-Munk data was acquired over the open ocean where residual waves exist regardless of the local wind, while the Petri data was taken in a narrow, relatively shallow bay which can become quite glassy during periods of low winds. Equations (7-4) and (7-5a,b) are thus verified experimentally and will be used in following analyses.

The effects of wind and nadir angle on the mean interface return power noted in Eq. (7-2) may be considered alone as a sort of "loss" factor of the form

$$L_s(\theta, w) \equiv \rho^* s(w) \cos^2 \theta N(\theta, w). \quad (7-6a)$$

Then Eq. (7-2) becomes

$$P_s = A L_s(\theta, w) / \pi. \quad (7-6b)$$

Equation (7-6a) has been inverted numerically for a series of fixed values of L_s between 10^{-1} and 10^{-7} to demonstrate graphically the effects of θ and w on P_s . The results are plotted in the form of constraint equations in a nadir angle - wind speed space in Figs. 7-4a, b, c. The up/down and crosswind components are presented in 7-4a and 7-4b respectively, and both are overlayed in 7-4c. It can be seen that for small nadir angles, the effect of varying wind speed is moderately small, but as the nadir angle increases, a small

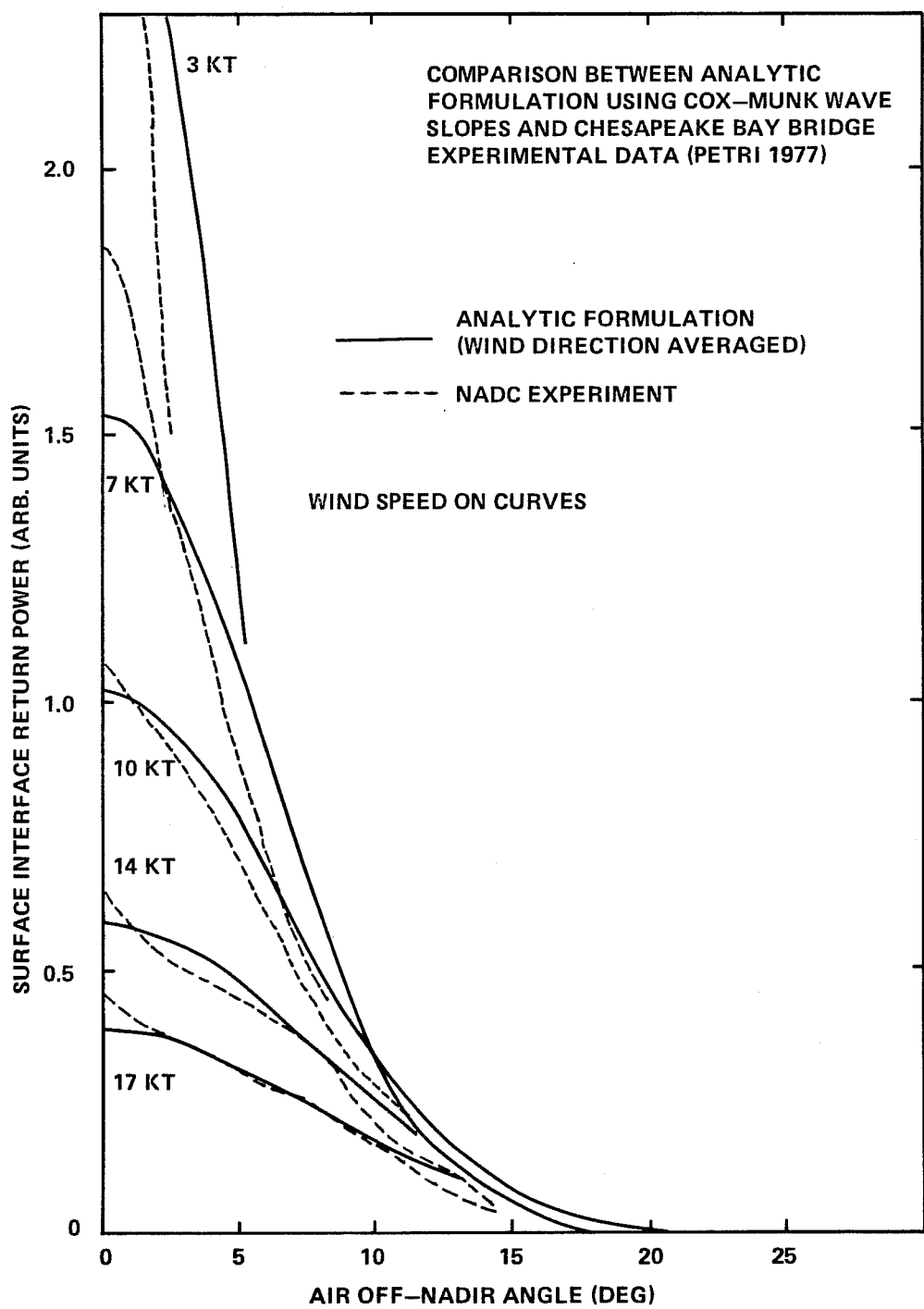


FIGURE 7-3. SURFACE INTERFACE RETURN POWER VS. AIR OFF-NADIR ANGLE AT VARIOUS WIND SPEEDS

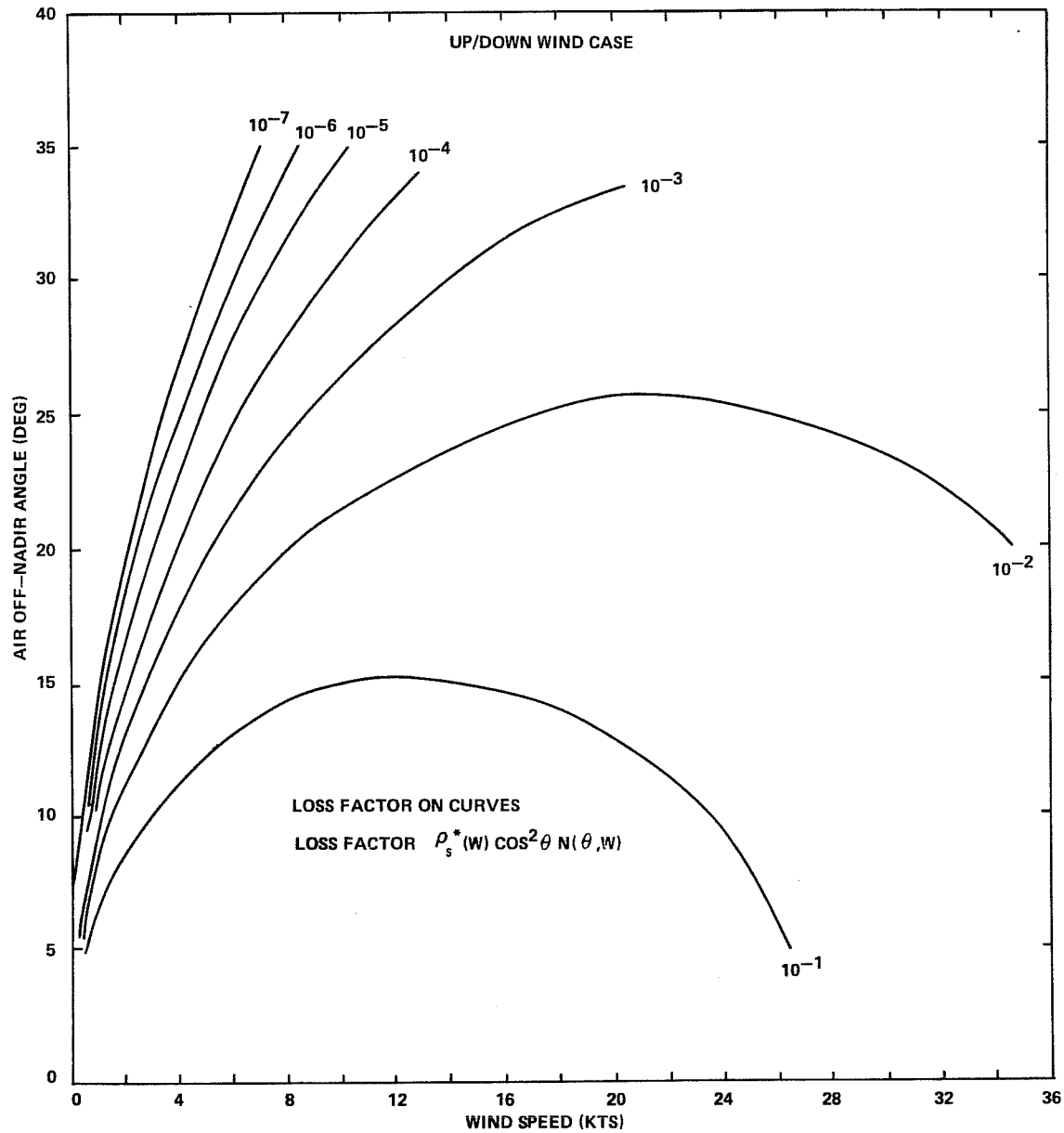


FIGURE 7-4a. SURFACE INTERFACE LOSS FACTOR CONSTRAINT EQUATIONS IN AIR OFF-NADIR ANGLE AND WIND SPEED

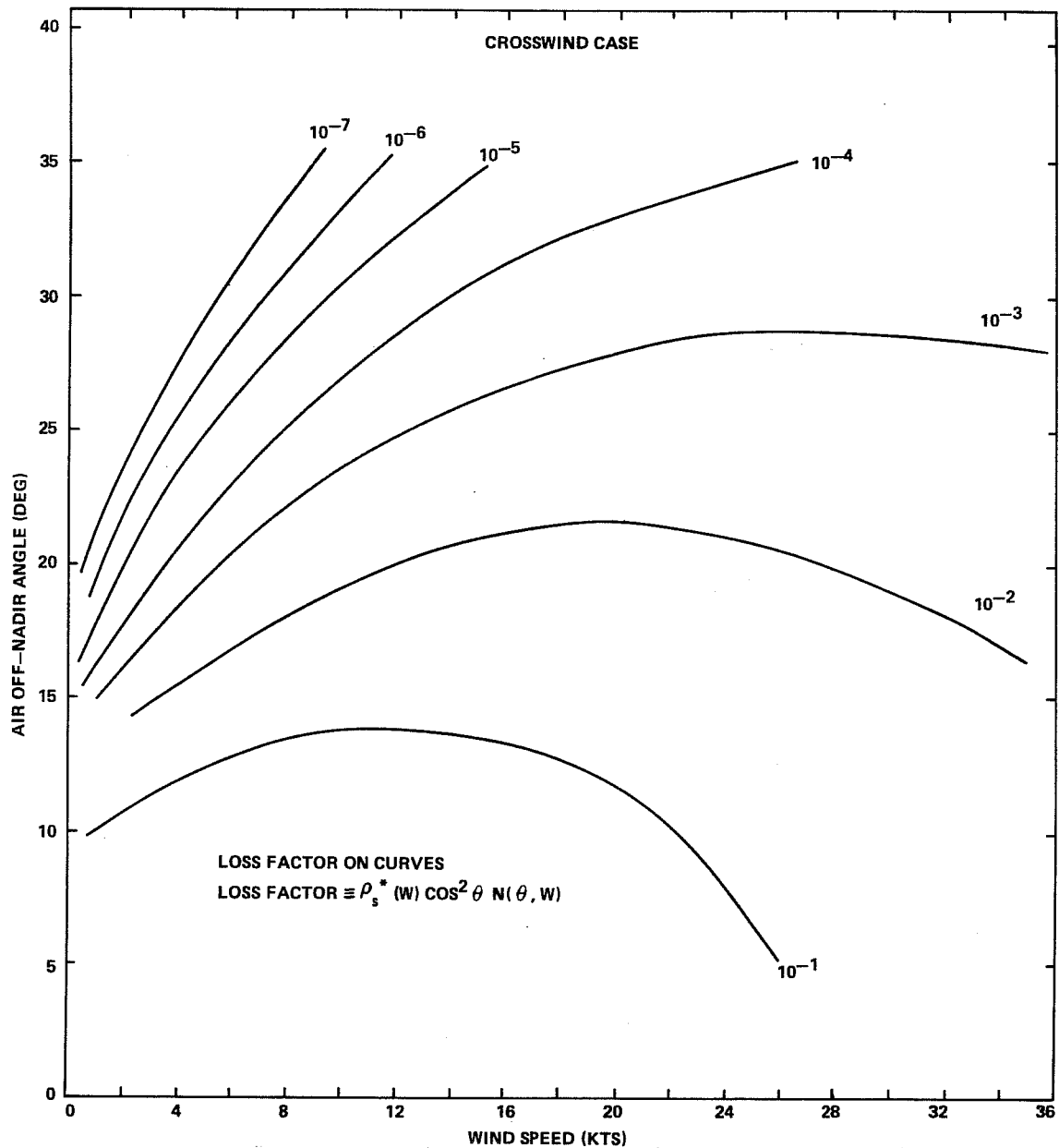


FIGURE 7-4b. SURFACE INTERFACE RETURN LOSS FACTOR CONSTRAINT EQUATIONS IN AIR OFF-NADIR ANGLE AND WIND SPEED

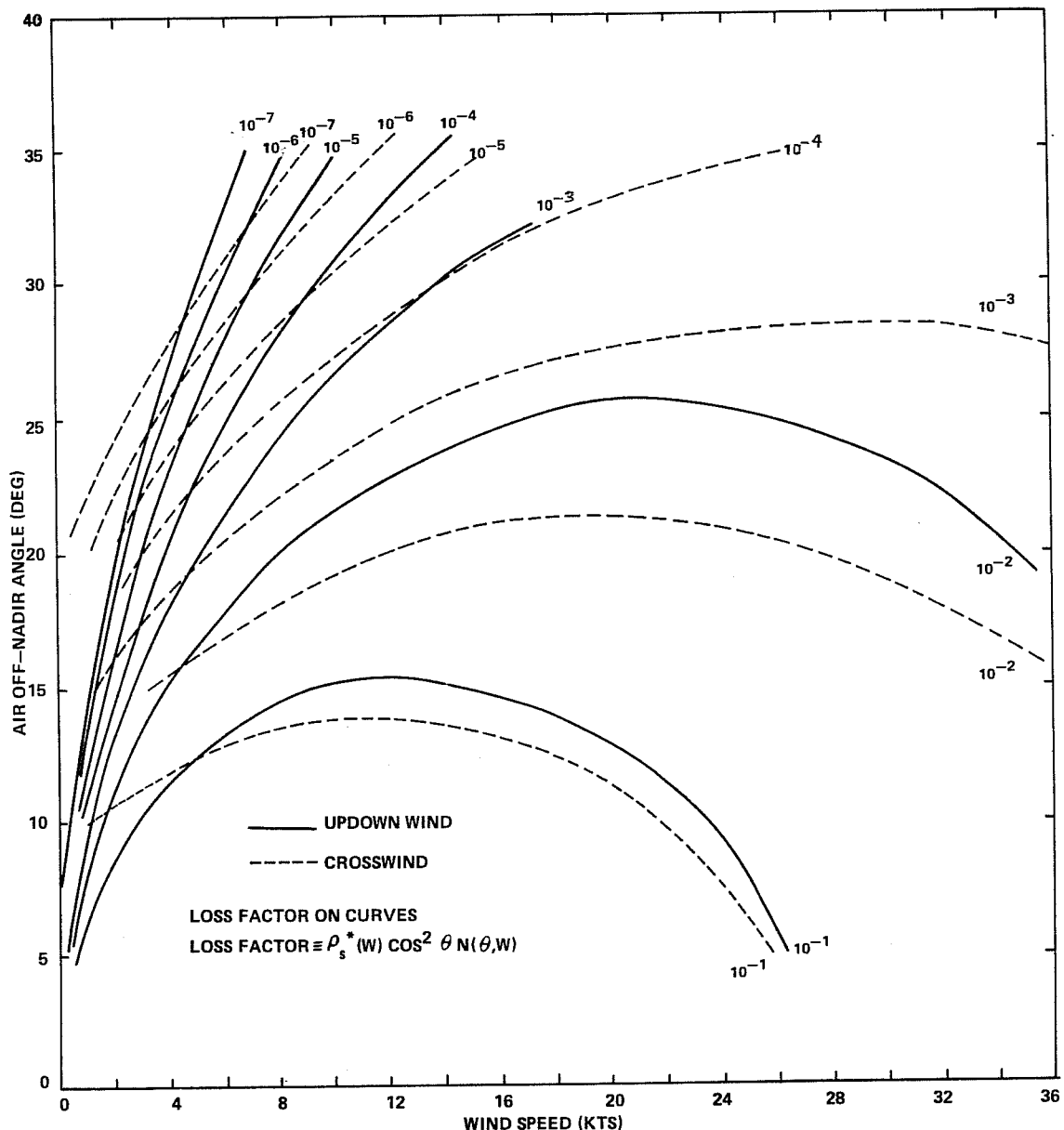


FIGURE 7-4c. SURFACE INTERFACE RETURN LOSS FACTOR CONSTRAINT EQUATIONS IN AIR OFF-NADIR ANGLE AND WIND SPEED

change in wind speed can have a dramatic effect in the interface return power, particularly in the up/down wind direction. It can also be seen that as much as an order of magnitude difference is observed between up/down and crosswind directions. This could lead to undesirable results in a scanning system if the potential effects of large (and cyclic) variations in P_s are not minimized by careful hardware and software design.

In practice, when the interface return magnitude is reduced below the level of the volume backscatter signal, the latter dominates. The net observed surface return magnitude will decrease no further, because the volume return, which does not depend on wind, establishes a minimum return signal level. The loss factor levels at which this occurs depend on water clarity and are derived in the next subsection.

It is of interest to look at the effects of the width of the sounding swath scanned under the aircraft on the interface return power results. Economics dictates that the swath should be as wide as possible to maximize the coverage rate. The swath width can be increased either by going to a higher altitude or by increasing the scanner nadir angle. Both of these increments have associated drawbacks: higher altitude increases inverse-square bottom return power losses which limit penetration, and higher nadir angles may cause accuracy problems, as will be demonstrated in section 9.2. Once a given swath width is selected, it may be achieved with, say, high altitude and low nadir angle, the reverse, or anything in-between. The effects of this choice on the interface return power will be shown here, and similar effects on the bottom return power will be viewed in section 8.2.6.

Since the swath width, B , is $B = 2H \tan \theta$, one can rewrite Eq. (7-2) in the form

$$P_s = \frac{4AH^2}{\pi B^2} \rho^* s(w) N(\theta, w) \sin^2 \theta. \quad (7-7)$$

Examples of this family of curves are plotted in Fig. 7-5 for three swath widths and a crosswind speed of $w = 10$ knots. The curves are characterized by a well defined peak at a nadir angle of roughly nine degrees and steeply sloping sides. It can be seen that P_s is low for small nadir angles because

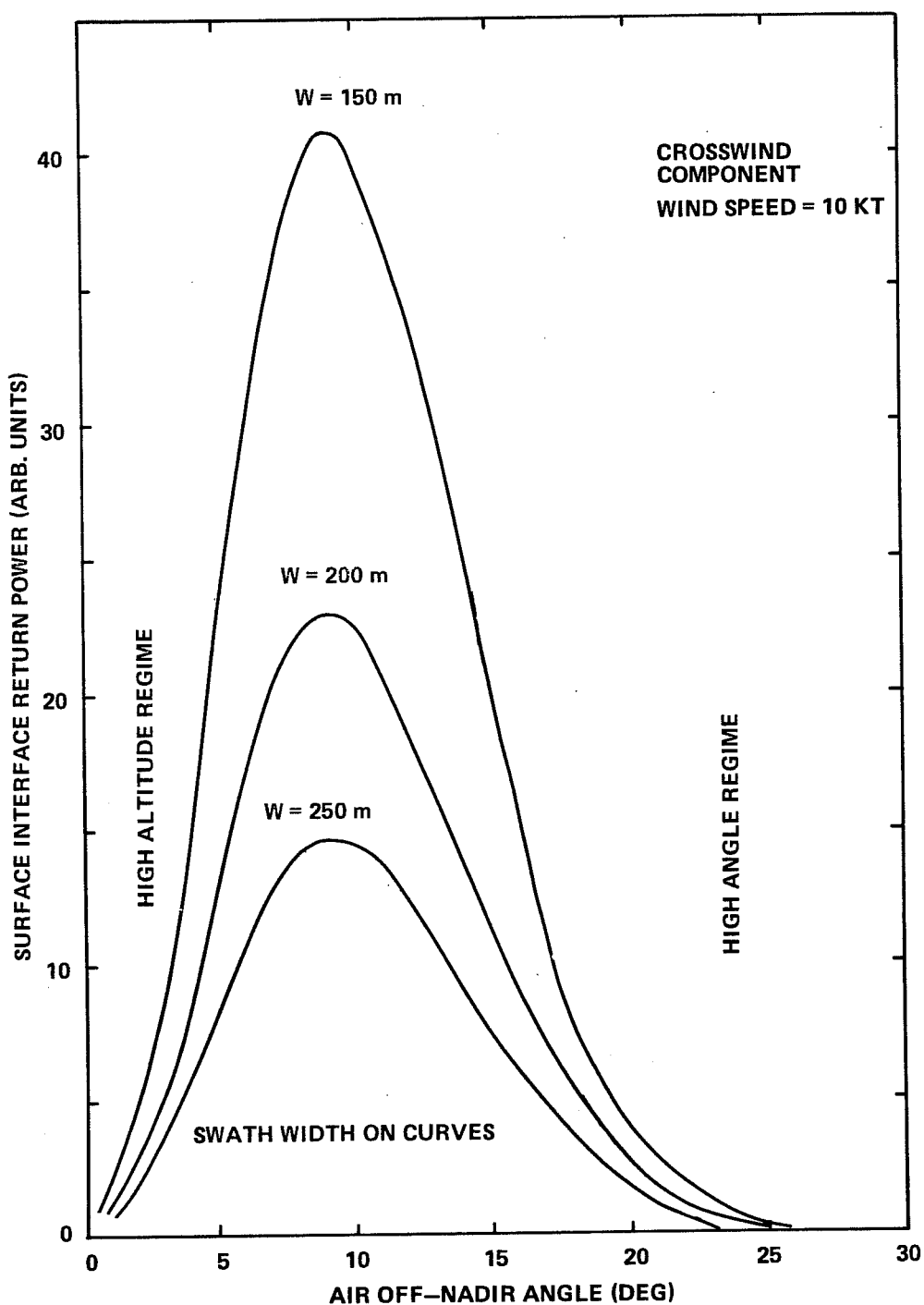


**FIGURE 7-5. SURFACE INTERFACE RETURN POWER
 VS. AIR OFF-NADIR ANGLE --
 CONSTANT SWATH WIDTH CURVES**

this implies a high altitude (for the fixed swath width); and similarly, P_s is low for large nadir angles because of the lack of sufficient capillary wave slopes. The locations of the peaks vary as a function of wind speed as seen in Fig. 7-6. The up/down wind component (not shown) leads to an almost identical curve. The Petri data for low wind regimes in wind dominated areas is included for comparison.

The result is that for winds in the 3 to 17-knot range, the maximum interface return power for a fixed swath width occurs at nadir angles between 6 and 11 degrees. One would prefer to operate at larger nadir angles to minimize the receiver amplitude dynamic range problem and the ringing caused by strong interface returns. The tails of excessively large interface returns can also mask the early portion of the volume return to the extent that they might not be useful as a measure of water clarity (as described in the next subsection).

It is important to note here that the results which have been presented are means averaged over a wave field. As was seen in section 5.8.2, more complex, detailed effects may be observed in the field for a narrow-beam wave profiling situation. Examples of such effects are the evidence of stronger returns from wave crests and weaker returns from wave troughs; and the false indication obtained during low wind conditions of larger than actual peak-to-peak wave heights (in both the altimeter and instantaneous depth measurement) due to the transition from interface returns from crests to volume returns from wave troughs with insufficiently excited capillaries. These are very real and serious effects which must be taken into consideration during system hardware and software design and also during field tests and operations.

The expressions for P_s developed in this subsection will be combined in the final subsection with an expression for the volume return peak power, P_v , developed in the next subsection to yield a set of constraint curves which will illustrate the ratio, P_v/P_s , as a function of nadir angle and wind speed.

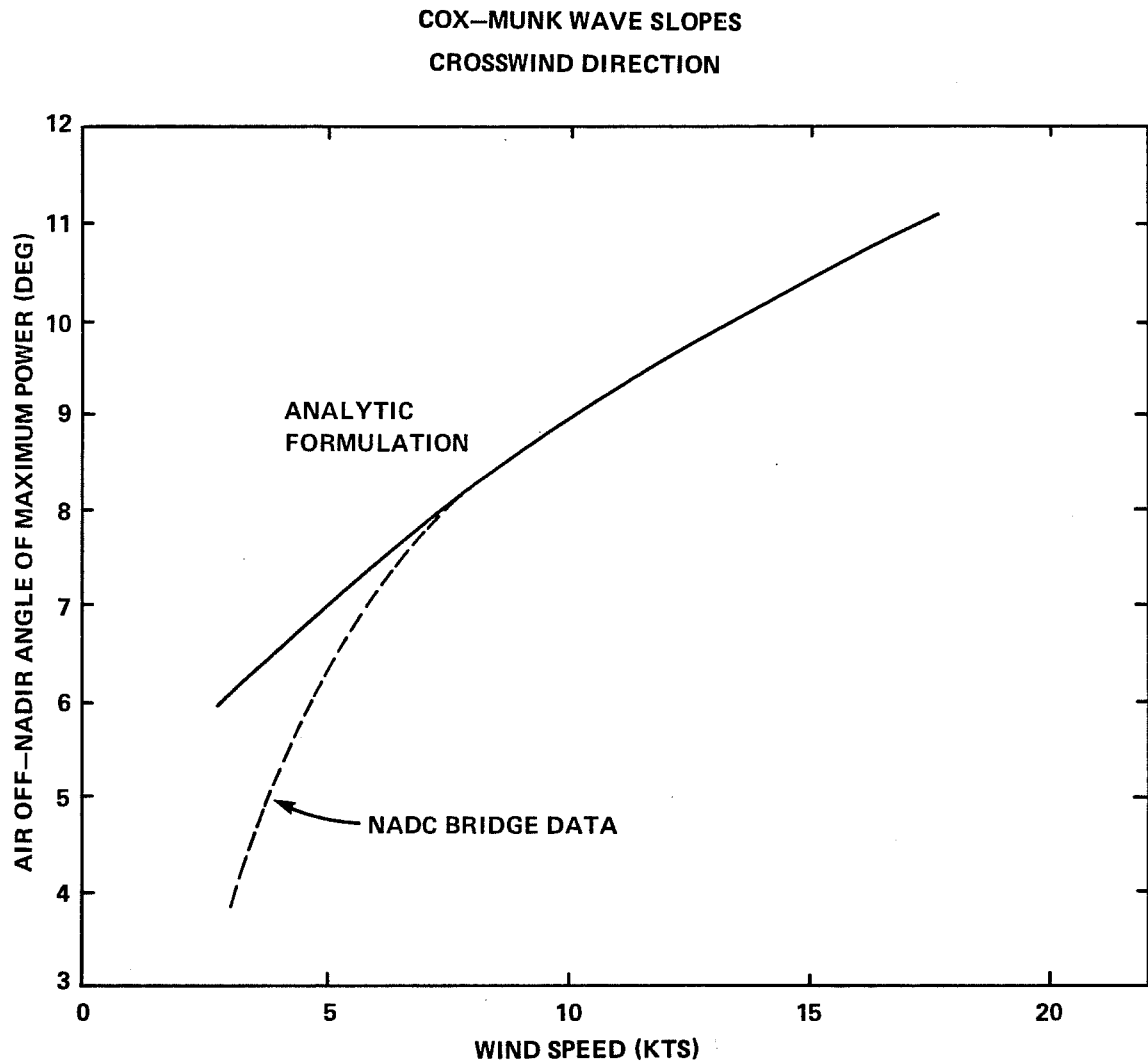


FIGURE 7-6. AIR OFF-NADIR ANGLE OF MAXIMUM SURFACE INTERFACE RETURN POWER FOR CONSTANT SWATH WIDTHS VS. WIND SPEED

7.3 Volume Backscatter Return

The magnitude of the volume backscatter power can be written in the form

$$P_V = \frac{A}{n_w^2} \rho_V(\sigma, k, t) \cos^2 \theta, \quad (7-8)$$

where A is defined in Eq.(7-3), n_w is the index of refraction of water, σ is the volume scattering function, k is an "attenuation" coefficient related to water clarity and receiver field of view (FOV), t is time, and $\rho_V(\sigma, k, t)$ is the backscatter reflectivity per unit solid angle (analogous to $\rho_S(w) \equiv \rho^*_S(w)/\pi$ for the interface). The n_w^2 term appears because the effective solid angle is increased upon refraction through the interface into the air. It can be shown that surface waves have no significant effect on this expression.

The functionality of ρ_V depends on water clarity and on the shape, duration, and wavelength of the incident laser pulse, as well as the receiver FOV. A simplified model has been solved analytically (Miller 1980, Thomas 1980) for a triangular pulse of temporal width " t_0 " (FWHM or half base width). The model assumes multiple forward downward scattering, high-angle backscatter events, and multiple forward scattering back to the surface. The results are defined in the following terms. Let time, t , be measured from a reference which is zero when the peak of the incident pulse is at the air/sea interface. Define variables $X \equiv kct$, $X_0 \equiv kct_0$, and $X_p \equiv kct_p$, where "c" is the speed of light in water, and t_p is the time of the peak of the volume power return. For $0 \leq X \leq X_0$, (the time range between the peak of the pulse striking the interface and the trailing tip of the pulse entering the interface), the temporal form of the volume backscatter reflectivity is

$$\rho_V(\sigma, k, X) = \frac{\sigma(\pi)}{2k} \left[1 + \frac{1}{X_0} (1 - X - 2e^{-X} + e^{-(X+X_0)}) \right], \quad (7-9)$$

where $\sigma(\pi)$ is the value of the volume scattering function at 180 degrees at the wavelength of interest. This waveform peaks at a time

$$X_p = \ln(2 - e^{-X_0}) \quad (7-10)$$

with a value equal to

$$\rho_{v,m}(\sigma,k) = \frac{\sigma(\pi)}{2k} (1 - X_p/X_0). \quad (7-11)$$

Note that $0 \leq X_p \leq X_0$; that $X_p \rightarrow X_0$ for very clean water; and that $X_p \rightarrow 0$ for very dirty water. This means that if the volume return is used as the surface return, a depth measurement bias will be incurred. For a green laser pulse of typical 7-ns duration, the magnitude of this bias can exceed the permissible system error limitation. This is discussed at length in section 9.2.2.

Eq. (7-8) can be written for the peak backscatter power in terms of a "loss" factor (as Eq. (7-6)) in the form

$$P_v = A L_v(\sigma,k,\theta)/\pi, \quad (7-12a)$$

where

$$L_v(\sigma,k,\theta) \equiv \frac{\pi}{n_w^2} \rho_{v,m}(\sigma,k) \cos^2 \theta. \quad (7-12b)$$

Typical values of L_v for quite clean and fairly dirty waters have been plotted over the Fig. 7-4b crosswind data in Fig. 7-7. As seen below, an excellent approximation for k for reasonably large receiver FOV is the diffuse attenuation coefficient, K . Quantitative values of $\sigma(\pi)$ were obtained from Petzold (1972), and associated K values were calculated from the corresponding α and ω_0 values using the modified Timofeyeva relationship of Eq.(3-5). It can be seen that for typical 10 to 20 knot winds, the crosswind interface return peak power drops below the volume return peak power for nadir angles between 20 and 25 degrees for "dirty" water and between 25 and 30 degrees for "clean" water. Again it must be emphasized that the L_s curves are mean results, and that the variance of the peak interface return power is generally quite large. These curves are means, not absolute bounds.

For $X > X_0$, i.e., the entire pulse in the water, the backscatter decay power curve is described as

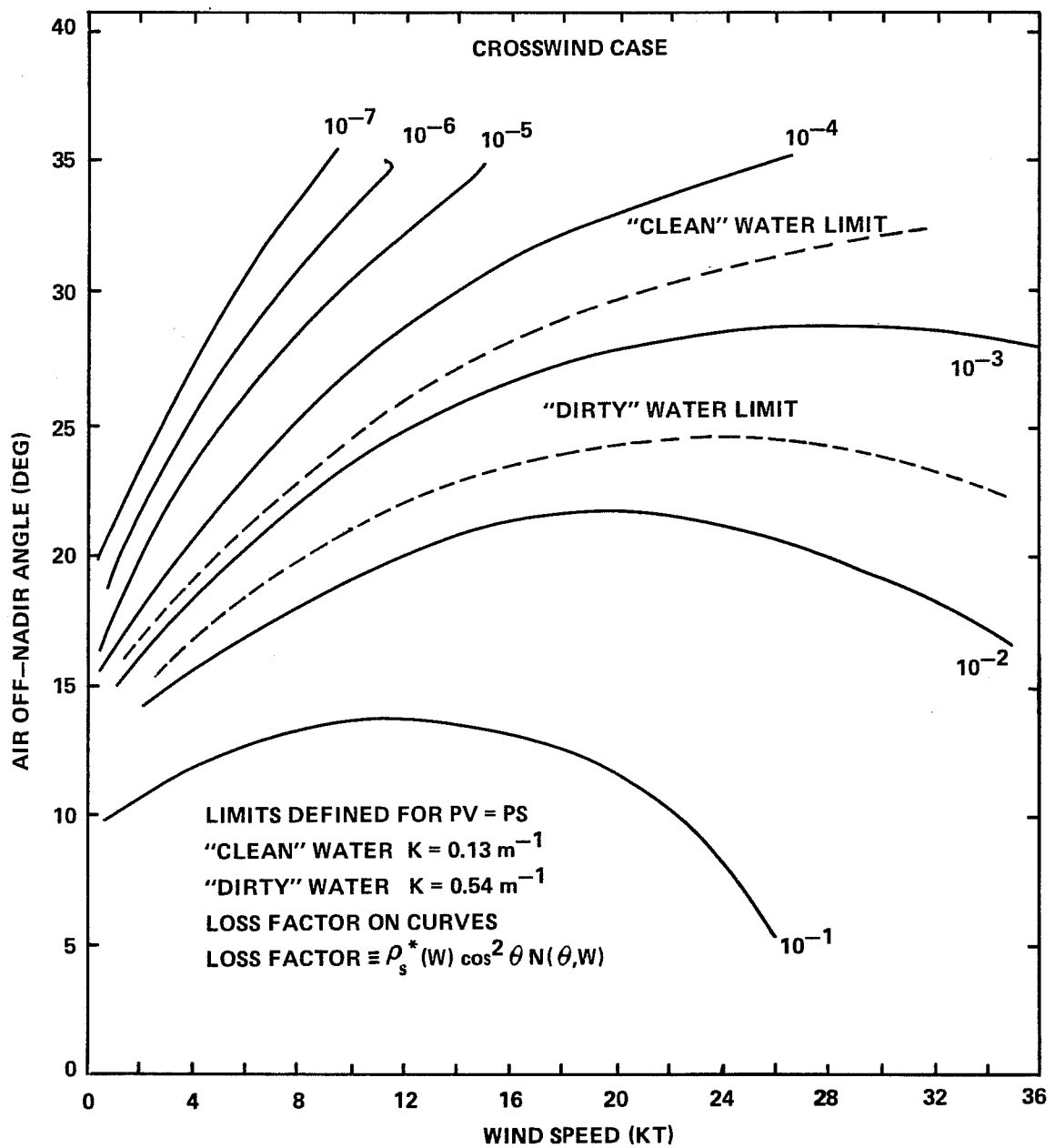


FIGURE 7-7. LIMITING VALUES OF SURFACE RETURN
LOSS FACTOR (FOR $PV=PS$) FOR TYPICAL
BOUNDING WATER CLARITY CONDITIONS

$$\rho_V(\sigma, k, X) = \frac{\sigma(\pi)}{2kX_0} (e^{X_0} + e^{-X_0} - 2) e^{-X}. \quad (7-13)$$

Note that this is a simple temporal exponential with a slope equal to $-ck$. In general, the value of k lies between absolute bounding values of " a ", the absorption coefficient, and α , the beam attenuation coefficient, depending on the receiver FOV (Phillips and Koerber 1984). For practical FOVs, the value will be somewhat greater than " a " and quite close to K , the diffuse attenuation coefficient. A measurement of the log-backscatter slope from typical field data thus provides an indirect measure of something on the order of K or " a ", depending on the receiver FOV.

The magnitude of the log-backscatter decay slope extrapolated back to a time $t = 0$ (peak at interface) is

$$\rho'_V(\sigma, k, 0) = \frac{\sigma(\pi)}{2kX_0} (e^{X_0} + e^{-X_0} - 2). \quad (7-14a)$$

This can be rewritten as

$$\rho'_V(\sigma, k, 0) = \frac{\sigma(\pi)X_0}{2k} \left[\frac{1}{X_0^2} (e^{X_0} + e^{-X_0} - 2) \right], \quad (7-14b)$$

which is instructive because the term in brackets, for $0 \leq K \leq 0.5 \text{ m}^{-1}$, is equal to 1.05 ± 0.025 . One can thus write

$$\rho'_V(\sigma, k, 0) \approx \frac{\sigma(\pi)X_0}{2k} = \frac{\sigma(\pi)ct_0}{2} \equiv \rho'_V(\sigma, 0). \quad (7-15)$$

Since c and t_0 are constants, the magnitude of the extrapolated backscatter slope at the surface, $\rho'_V(\sigma, 0)$, is proportional to $\sigma(\pi)$, the volume scattering function at 180 degrees.

The relationship between $\sigma(\pi)$ and the total scattering coefficient, s , for a wide variety of natural waters (Petzold 1972 and Whitlock et al. 1981) was seen in Fig. 3-9. This calibration curve permits values of $\sigma(\pi)$ estimated in the above manner from airborne field data to be translated to values of s . This is of great interest because values of s thus derived could be used in estimating propagation-induced biases which are parameterized on sD , the scattering optical depth, as noted in Guenther and Thomas (1984) and seen in

section 9.2.1. Any value which derives solely from an amplitude (return power) measurement, however, is prone to errors. The system must remain in absolute radiometric calibration, and results will also depend on altitude, noise sources, and other factors such as interface return power (a masking effect).

7.4 Volume to Interface Peak Power Ratio

As noted earlier, when the interface return becomes significantly smaller than the volume return, the latter dominates. The peak location of the volume backscatter, as seen in Eq. (7-10), can be as much as a pulse width deeper in the water than the interface return. If the interface return is absent, this will cause a shallow bias in the depth measurement, whose magnitude depends on the water clarity, laser wavelength, pulse width, and pulse location algorithm. This bias, which was evident in AOL field test data as noted in section 5.8.3, is described in more detail in section 9.2.2. For a 7-ns source pulse, the bias magnitude for typical pulse location algorithms will be roughly 30 cm. It cannot be removed by the wave correction process but must be made sufficiently small by some technique. This is a major problem which needs resolution for every system because the surface return will "flip flop" back and forth between interface reflection and volume backscatter depending on environmental parameters and beam nadir angle, as seen in the following analysis.

The dominance of the interface or volume returns as a function of wind speed and direction, water clarity, and nadir angle can be determined by looking at the ratio of P_V from Eq. (7-12) with P_S from Eq. (7-6) as follows:

$$\frac{P_V}{P_S} = \frac{L_V(\sigma, k, \theta)}{L_S(\theta, w)} = \frac{\pi \rho_{V,m}(\sigma, k)}{n_w^2 \rho_S^*(w) N(\theta, w)} . \quad (7-16)$$

This equation has been inverted and solved for the combinations of wind speed and direction, nadir angle, and water clarity (diffuse attenuation coefficient) which define constraint equations for values of $P_V/P_S = 0.1, 1.0$, and 10. These results are summarized in Figs. 7-8a, b, c; the first two

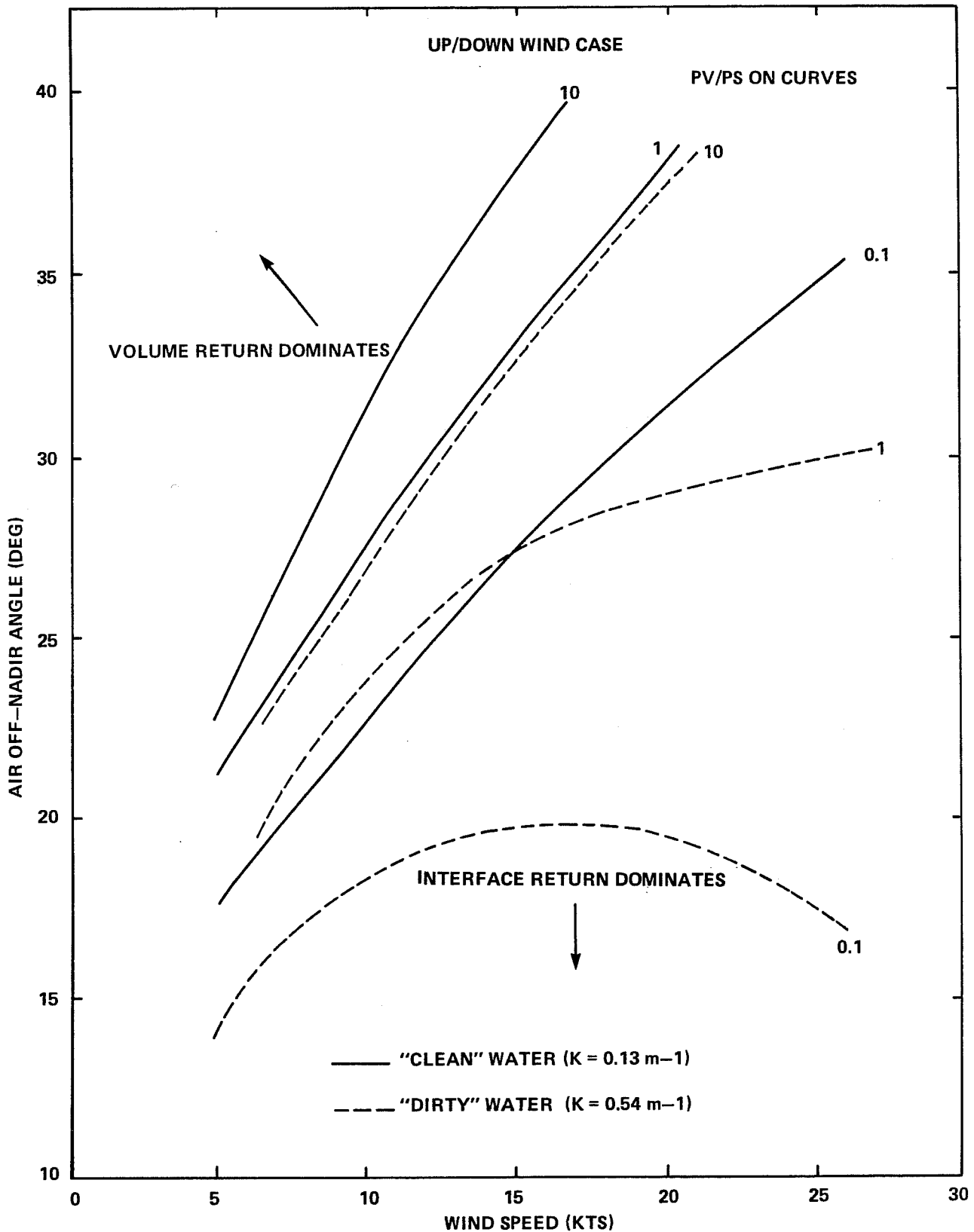


FIGURE 7-8a. VOLUME TO INTERFACE RETURN RATIO CONSTRAINT EQUATIONS: WIND AND OFF-NADIR ANGLE EFFECTS

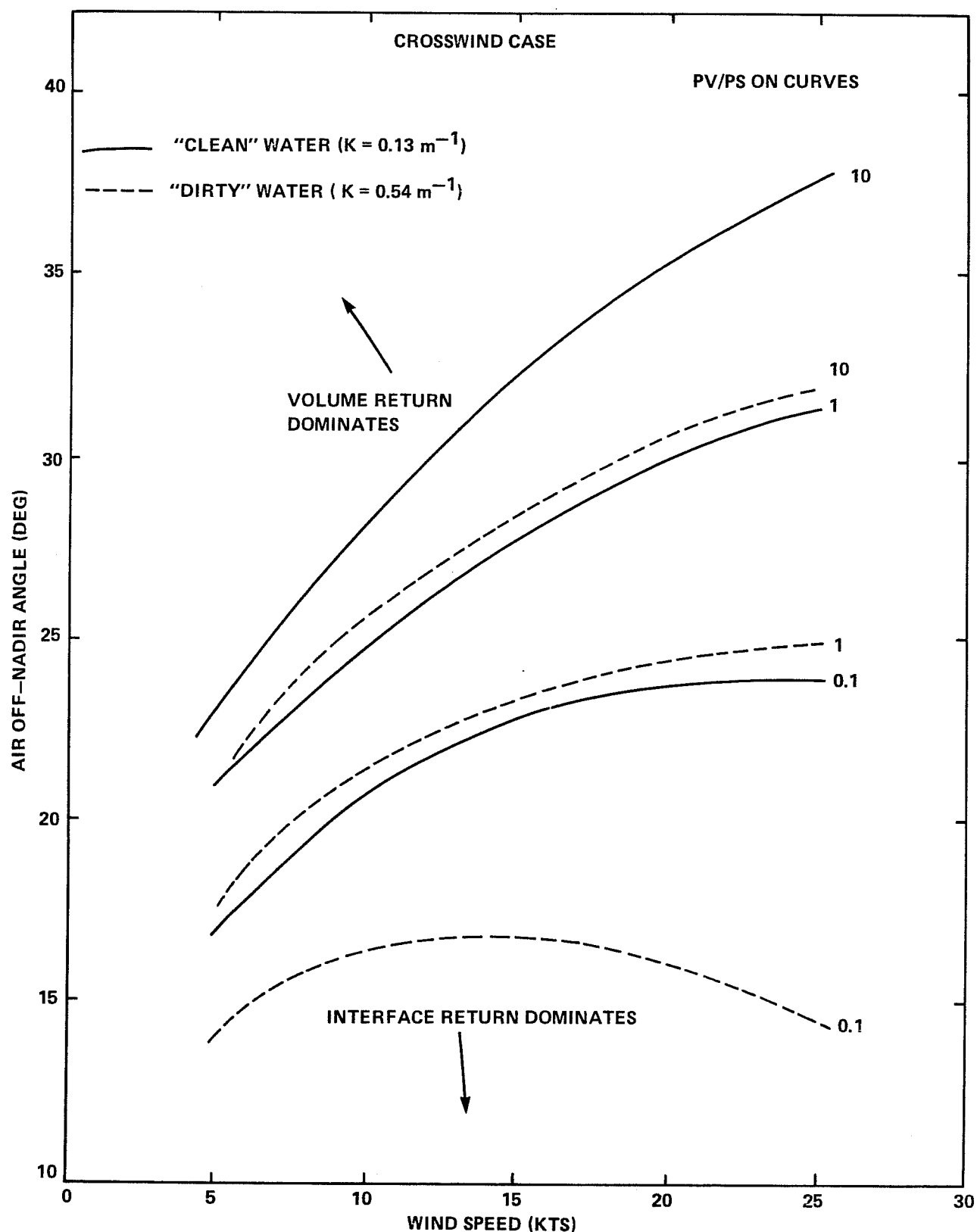


FIGURE 7-8b. VOLUME TO INTERFACE RETURN RATIO CONSTRAINT EQUATION: WIND AND OFF-NADIR ANGLE EFFECTS

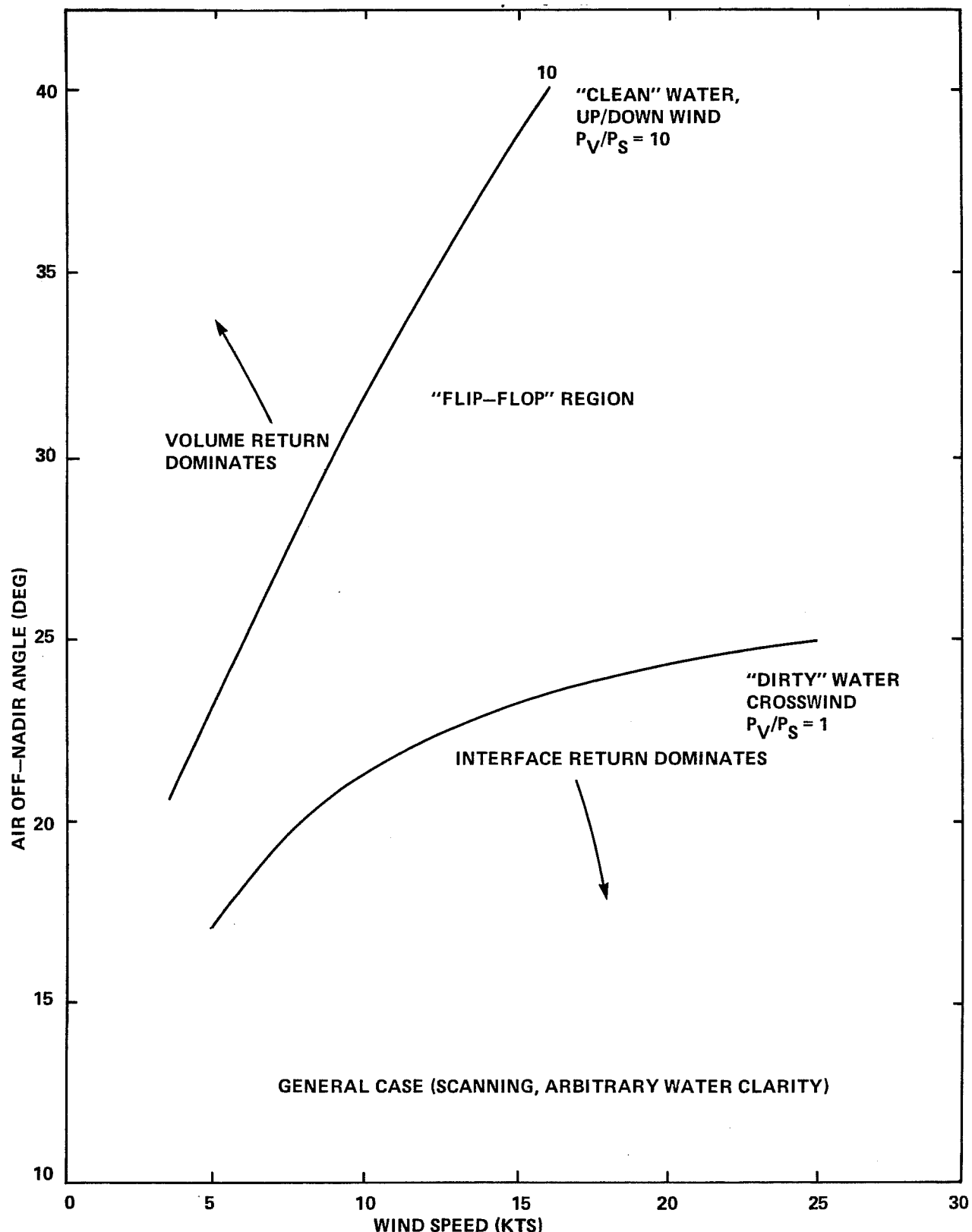


FIGURE 7-8c. VOLUME TO INTERFACE RETURN RATIO CONSTRAINT EQUATION:
WIND AND OFF-NADIR ANGLE EFFECTS

are for up/down and crosswind results, respectively, and the third is a distilled summary. These constraint curves, like those in Figs. 7-4a, b, c, should be thought of as defining regions in the nadir angle - wind speed space. For example, the zone above a curve denoting $P_v/P_s = m$ is the region where $P_v/P_s > m$.

If $P_v/P_s < 1$, the interface return, which rises more quickly than the volume return, will generally dominate in a pulse location procedure. This rough bound then, will mark the regime below which the mean surface return will occur from the interface. For the same reason, one would expect that for the volume return to dominate, P_v/P_s would probably need to be greater than, say, 10; this region lies above the $P_v/P_s = 10$ curve. In the region between these rough bounds, the surface returns will be a combination of the two, and the apparent surface location will "flip flop" or alternate randomly back and forth somewhere between the interface return and the volume return, depending on the whims of wave statistics. Because the scanner samples all angles with respect to the wind, the overall bounding constraints of the uncertainty or "flip-flop" region, as seen in Fig. 7-8c, must be based on the "worst case" conditions: these are "clean" water in the up/down direction for volume domination and "dirty" water in the crosswind direction for interface domination.

It can be seen that for winds in excess of ten knots, interface returns will predominate for nadir angles below 20 to 25 degrees, but the intended operating window for a typical airborne lidar system may lie within the "flip-flop" region -- particularly in the crosswind direction. It will be seen in section 9 that nadir angles greater than 15-25 degrees (the value depending on signal processing) are unacceptable due to a number of growing error sources. It is thus clear that volume-only operation is not possible for any reasonable nadir angle. If aircraft roll is compensated, it may be possible for a 15-degree off-nadir system to depend on interface returns alone, except for situations with winds under 5 knots where operations might have to be curtailed unless something is done to reduce the magnitude of the flip-flop error. At 5-degrees roll, however, at least 8 knots would be required. Systems operating in the 20 - 25 degree regime will definitely experience flip-flop problems. For such cases, it is imperative that the depth

measurement hardware and software be designed in such a manner that the error due to this uncertainty is kept well within the error budget. Details of this problem are treated in section 9.2.2. The magnitude of the flip-flop error can be reduced, for example, by reducing the source pulse width (the error would be acceptably low at 2-ns FWHM) or increasing the effective attenuation coefficient of the water column by using a colinear infrared beam to detect the surface. The use of a Raman scattered "surface" return might also be investigated further.

7.5 Acknowledgments

I would like to thank Merlin Miller, Bob Thomas, Bill Pearce, and Lloyd Bobb who made contributions to these calculations.

7.6 References

- Bobb, L.C., Ferguson, G., and Rankin, M., 1979: Capillary Wave Measurements. Appl. Opt., 18, 8, 1167-1171.
- Cox, G. and Munk, W., 1954: Measurement of the Roughness of the Sea Surface from Photographs of the Sun's Glitter. JOSA, 44, 11, 838-850.
- Guenther, G.C. and Thomas, R.W.L., 1984: Prediction and Correction of Propagation-Induced Depth Measurement Biases plus Signal Attenuation and Beam Spreading for Airborne Laser Hydrography. NOAA Technical Report NOS 106 CGS 2, National Oceanic and Atmospheric Administration, U.S. Department of Commerce, Washington, D.C., 112 pp.
- Hughes, B.A., Grant, H.L., and Chappell, R.W., 1977: A Fast Response Surface Wave Slope Meter and Measured Wind-Wave Moments. Deep Sea Research, 24, 1211-1223.
- Miller, M. (Avco Everett Research Laboratory, Inc., Everett, Mass.), 1980 (personal communication).

Petri, K.J., 1977: Laser Radar Reflectance of Chesapeake Bay Waters as a Function of Wind Speed. IEEE Trans. Geoscience Electronics GE-15, #2, 87-96.

Petzold, T.J., 1972: Volume Scattering Functions for Selected Ocean Waters. SIO Ref. 72-78, Scripps Institution of Oceanography, Visibility Laboratory, San Diego, Calif., 79 pp.

Phillips, D.M. and Koerber, B.W., 1984: A Theoretical Study of an Airborne Laser Technique for Determining Sea Water Turbidity. Australian J. Phys., 37, 75-90.

Thomas, R.W.L. (EG&G/Washington Analytical Services Center, Riverdale, Md.) 1980 (personal communication).

Whitlock, C.J., Poole, L.R., Usry, J.W., Houghton, W.M., Witte, W.G., Morris, W.D., and Gurganus, E.A., 1981: Comparison of Reflectance with Backscatter and Absorption Parameters for Turbid Waters. Appl. Opt., 20, 3, 517-522.

8.0 BOTTOM RETURN SIGNAL AND PENETRATION

8.1 Introduction

The economic viability of an airborne laser hydrography system depends on the existence of large areas of relatively shallow water from which satisfactory bottom returns can be detected. In the fairly flat east and Gulf coast offshore regions, a few extra meters of penetration capability can add a great deal of additional surveyable area. It is vital, therefore, that every possible effort be made during system design to maximize the penetration capability wherever practical.

This is a complex task because a great many parameters affect penetration in indirect ways, and design tradeoffs must be made against other requirements. A number of such tradeoffs are discussed in this section. It will be seen that the ultimate constraints derive from matters of accuracy, swath width, sounding density, allowable size/weight, and state-of-the-art laser design.

The shape, duration, and magnitude of laser hydrography bottom returns depend in a complex way on the source pulse, the beam nadir angle, the depth of the water, the optical properties of the water, and the bottom topography. Impulse response functions parameterized on these variables for a flat bottom have been derived by Monte Carlo simulation (Guenther and Thomas 1981a, b), as reviewed in section 6. Actual bottom returns have been determined by convolving the impulse response functions with an appropriate source pulse. The resulting pulse shapes and attendant depth measurement biases (Guenther and Thomas 1984) are seen in section 9.2.1. The maximum penetration capability of an airborne laser hydrography system, which depends on the peak power of the bottom return pulses (even though the detection should not be made at the peak due to noise considerations), is the subject of this section. Results are based primarily on the peak power of convolutions of the impulse response functions with a 7-ns (FWHM) triangular source pulse. Results for other pulse widths of that general magnitude will be similar.

8.2 Signal Equation

The basis for determining the performance of any communications system is the received signal equation. The level at which this signal becomes unacceptably noise contaminated determines the maximum range. In the case of airborne lidar bathymetry, a pulsed laser transmitter is communicating with a colocated receiver via a complicated channel which consists of two passes through the atmosphere, two passes through the undulating air/water interface, two passes through a highly scattering and absorbing water column of variable clarity, and a bounce off a poorly reflecting bottom. Over the years, the return power equation has appeared in a variety of forms because the propagation in the water has not been well understood. Indeed, some effects can only be estimated through Monte Carlo propagation simulations. There is no ultimate or "correct" form; refinements and improvements can be made as new simulation or experimental data become available. The version described here is considered to be the most comprehensive available at this time.

8.2.1 Bottom Return Pulse Energy

In its basic form, the so-called "radar" equation for airborne laser hydrography bottom return pulse energy can be written

$$E_R = E_T^n L R \frac{\Omega_R}{\Omega_B} F e^{-2kP}, \quad (8-1)$$

where E_R is the received pulse energy,
 E_T is the transmitted pulse energy,
 n is the combined optical loss factor for the transmitter and receiver optics,
 R is the bottom reflectivity,
 Ω_R is the solid angle subtended by the receiver,
 Ω_B is the effective solid angle of the bottom-reflected energy above the air/water interface,
 F is a loss factor to account for less than sufficient receiver field of view (FOV),
 k is an attenuation coefficient which depends on water clarity,
 P is the effective slant path length in the water to the bottom, and

L is a factor recognizing small, negligible environmental losses such as atmospheric absorption and scattering and air/water interface reflections.

Losses for the former are small (ten to twenty percent) for altitudes of interest in clear air and can generally be omitted for the sake of simplicity. The two percent reflection losses through the air/water interface are insignificant. The individual factors in Eq.(8-1) will now be discussed in detail.

It has been demonstrated through the Monte Carlo propagation simulations (section 6) that k is virtually identical with K , the diffuse attenuation coefficient of the water for the clear sky case. This seemingly simple result is not as obvious as it appears. A tight beam enters the water on the downwelling path, but the bottom reflection initiating the upwelling path is diffuse. This has led some (i.e., Levis et al. 1975) to write an expression in the form $E_R \propto \exp[-(k_1 + k_2)P]$, where $k_1 \sim \alpha$ for the downwelling path, and $k_2 \sim K$ for the upwelling path. The requirement that such an apparently logical expression ignores is the fact that the upwelling energy must be refracted in the direction of the distant airborne receiver to be detected. The crucial concept, which was used with the Monte Carlo propagation simulations, is termed "reciprocity". Reciprocity is a statement of symmetry which, in this context, says that because the exiting photons must leave the medium in the exact opposite direction from which they entered in order to reach the distant receiver, the ensemble of allowed scattering paths in the water is identical for upwelling and downwelling radiation. Indeed, the upwelling distribution is nothing more than the downwelling distribution weighted by the cosine of the arrival angle at the bottom to account for the (assumed) Lambertian reflection. It turns out that this weighting has little practical effect because the arrival distribution has characteristics similar to a Lambertian, and the upwelling and downwelling distributions are nearly identical. It follows that the energy attenuation coefficients are virtually equal in both directions, and these are, by definition, equal to K for collimated incident radiation. Thus $E_R \propto \exp(-2KP)$.

If the beam nadir angle in air is θ , the refracted nadir angle in water of the unscattered ray from a flat surface is $\phi = \sin^{-1}(0.75 \sin\theta)$, and the unscattered path length to the bottom for a depth D is $P = D \sec\phi$. This simple ray model does not explicitly include any corrections for beam spreading due to scattering. The bottom "spot" is asymmetric in the up/down-beam direction with respect to the unscattered ray, due to the oblique incidence. As seen in Fig. 4-8, for off-nadir beam entry angles the peak of the energy density distribution is slightly nearer the aircraft than the unscattered ray due to the path length being shorter and hence favored. Multiple scattering, on the other hand, increases the integrated path length to the bottom. The net result of these effects is a complex functionality on beam nadir angle which can only be resolved by computer simulation. Details will not be examined here because the important parameter for penetration is not the integrated pulse energy but rather the peak return pulse power. The effects of scattering and off-nadir beam angles (which are inextricably entwined) on peak return power are described later in this section.

Scattering spreads the beam out spatially to a great extent and dictates a not insubstantial receiver field-of-view requirement which can pose significant hardware difficulties as noted in sections 8.2.5.3 and 10.4. An insufficient FOV which spatially excludes a portion of the returning signal reduces the F factor below unity in a highly complex way which depends on the FOV, water parameters, depth, altitude, and the duration of the incident source pulse. This problem is examined in section 8.2.5.

The solid angle subtended by the airborne receiver from an altitude H is $\Omega'_R = A_R \cos^2\theta / H^2$. For an assumed Lambertian bottom reflection, the effective solid angle of the bottom reflection in the water is $\Omega_W = \pi$. Upon refraction through the air/water interface this angle increases by a factor n_w^2 , where n_w is the index of refraction of water, so that $\Omega'_B = n_w^2 \Omega_W = n_w^2 \pi$. In the limiting case of high altitude and shallow water depth, the solid angle ratio would then be $\Omega'_R/\Omega'_B = A_R \cos^2\theta / \pi n_w^2 H^2$. For the general case where the water depth is not necessarily considerably smaller than the altitude, it has been shown (Levis et al. 1974) that the exact expression is $\Omega_R/\Omega_B = A_R / \pi(n_w H \sec\theta + D \sec\phi)^2$. This can be approximated by the simpler expression

$$\Omega_R/\Omega_B \approx A_R \cos^2\theta / \pi (n_w H + D)^2, \quad (8-2)$$

which gives virtually the same results for practical parameter values. Eq. (8-1) thus takes the form

$$E_R \approx \frac{E_T n R F A_R \cos^2\theta}{\pi (n_w H + D)^2} e^{-2KD \sec \phi}. \quad (8-3)$$

8.2.2 Bottom Return Peak Power

Since pulse detections are based on the instantaneous pulse power, not the integrated pulse energy, Eq. (8-3) must be converted to one which describes the peak pulse power. Propagation-induced pulse stretching strongly affects the relationship between pulse energy and peak power; i.e., the greater the stretching, the lower the peak power for a given amount of energy. Peak power relationships and functionalities are presented in detail in Guenther and Thomas (1984), and the following results are extracts.

For a finite source pulse, the pulse returning to the receiver is the convolution of the source pulse with the impulse response function (IRF) of the propagation medium. The energy curves represent the bounding case of no pulse stretching. The opposite bounding case is that of the IRFs for which a functionally different equation can be developed. These curves decay more rapidly with increasing optical depth due to the effects of pulse stretching. For a practical system with a 5 - 10 ns source pulse, the peak power curves will lie between these two extremes, as depicted schematically in Fig. 8-1. For low optical depths, where the IRFs are of short duration compared with the source pulse, the ERFs will approximate the source pulses, and the peak power values will approximate the energy case. For high optical and physical depths, where the IRF can become significantly longer than the source pulse, the ERFs are similar to the IRFs, and the peak power curves will converge to the IRF case. The rate of transition between these extremes depends on the incident pulse width. Pulse stretching and the associated loss of power compared to energy will not be evident until the duration of the IRF becomes significant compared to the width of the source pulse.

Specific peak power results have been generated for ERFs obtained by convolving the Monte Carlo-derived IRFs with a 7-ns (FWHM) triangular source pulse. For optical depths up to 16 and for depths of at least 40 m, the peak power results can be represented by exponentials with an effective increase in the system attenuation coefficient. This can be described by the form $P_R \propto \exp(-2nKD \sec\phi)$, where, in general, $n = n(s, \omega_0, \theta)$, and ϕ is the nadir angle of the unscattered ray in the water. This is an understandable result based on the schematic representation in Fig. 8-1. The values of $n(s, \omega_0, \theta)$ are derived from semi-log plots of peak power versus optical depth for various fixed values of θ , ω_0 , and α , as seen in Fig. 8-2. The slopes of these lines are quite constant except at very low αD , and the nadir angle effect is quite small as noted by the dashed curves for 0 and 25 degrees at $\alpha = 0.8 \text{ m}^{-1}$. The slopes are modeled as $-2nK\alpha^{-1} \sec\phi$; by measuring the slope and knowing K/α from ω_0 via Fig. 3-7, one can determine the values of n . In this way, the uncertainty in ϕ due to undercutting is automatically included in the calculated values of n .

The calculated values of n are plotted in Fig. 8-3a for nadir incidence as a function of α and parameterized on ω_0 . The dependence on the scattering phase function is small except at $\omega_0 = 0.9$, as separately noted on the figure. The residual nadir angle effect is quite small, as seen by the dotted line for 25 degrees at $\omega_0 = 0.8$. A plot such as Fig. 8-3a can be slightly misleading, because it represents exhaustive combinations of all possible parameter values, many of which are highly unlikely in natural waters. The ranges of ω_0 values typically associated with given α 's in the environment were presented in Fig. 3-8. These practical bounds are denoted in Fig. 8-3b as heavy lines. This changes the behavior of n considerably, from one which decreases from large values for increasing α to one which rises gradually from small values with increasing α .

Various levels of approximation may be used for describing n depending on the estimation accuracy desired. A decent first-order approximation is simply to say $n \approx 1.25$ for all cases. A slightly better fit, good to ± 0.1 , is provided by the expression $n \approx 1 + 0.27 \alpha^{0.24}$, valid for all θ and ω_0 but limited to $\alpha \leq 2 \text{ m}^{-1}$. A more detailed fit can be obtained, if desired, in the forms $n = A \alpha^{-B}$ or $n = A s^{-B}$. The latter is more rigorous phenomenologically.

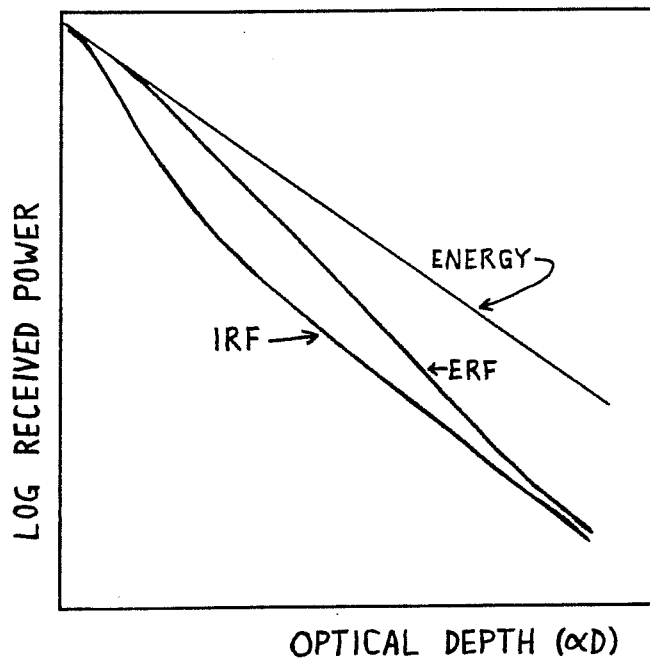


FIGURE 8-1. SCHEMATIC REPRESENTATION OF ERF PEAK POWER FUNCTIONALITY

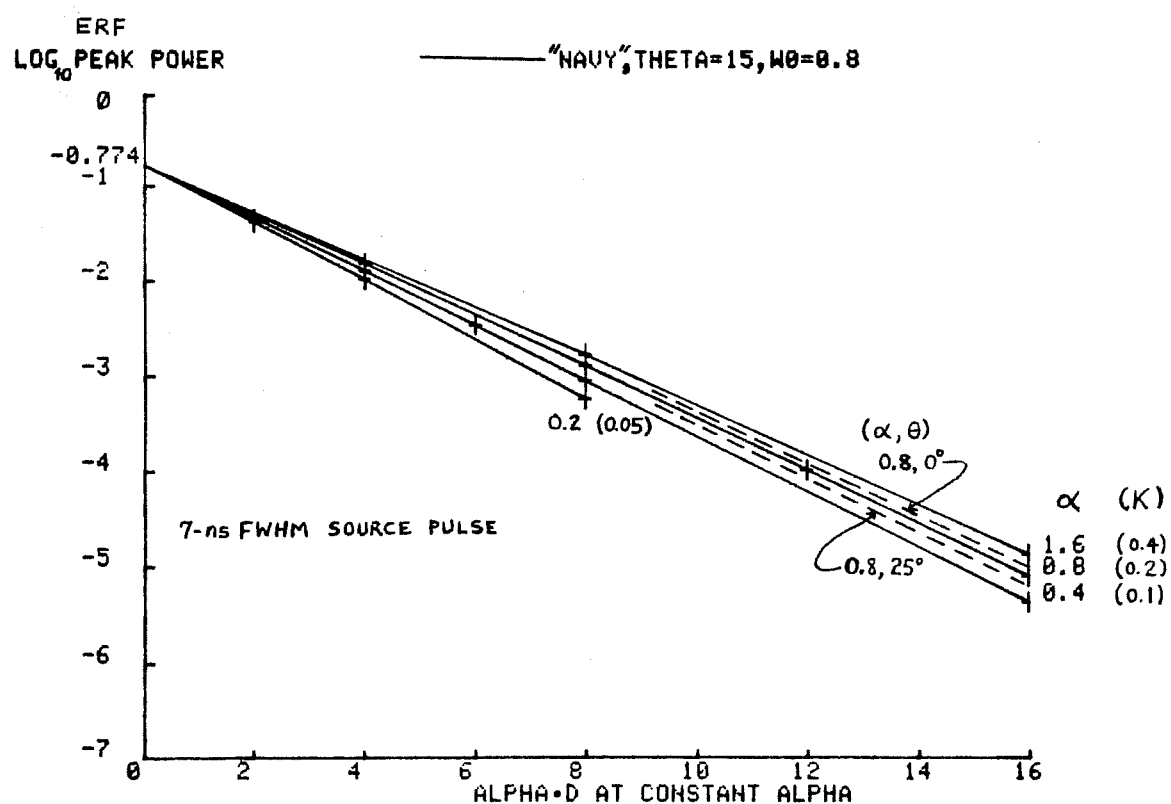


FIGURE 8-2. ERF PEAK POWER DECAY

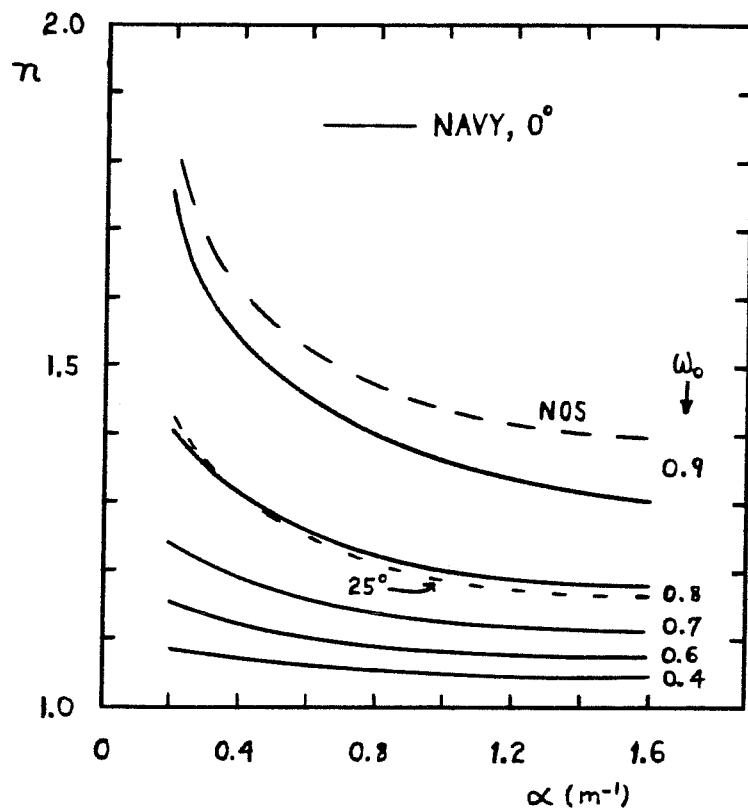


FIGURE 8-3a. FULL EXPONENTIAL POWER DECAY FACTOR FUNCTIONALITY

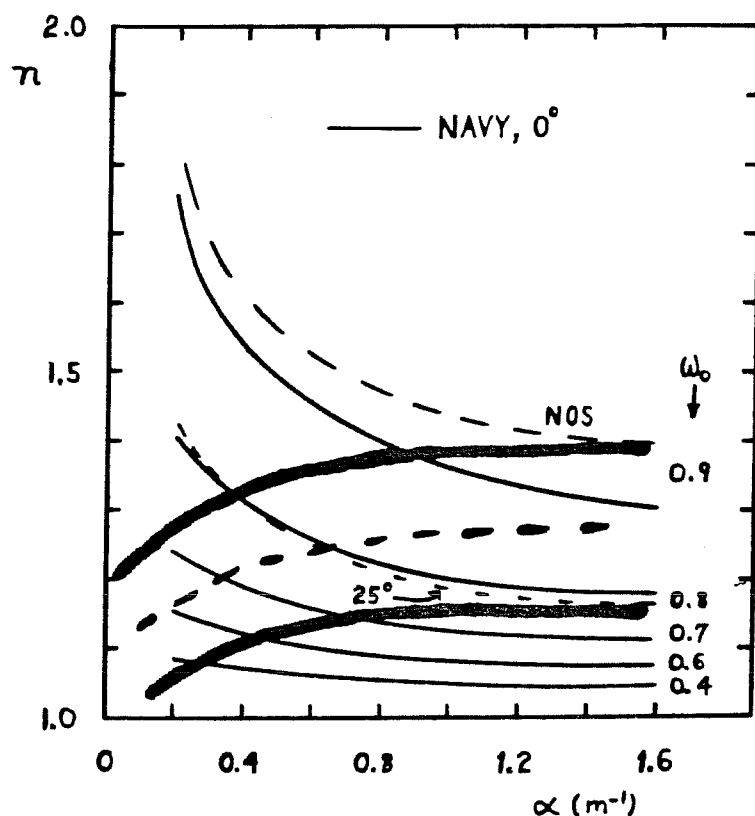


FIGURE 8-3b. PRACTICAL EXPONENTIAL POWER DECAY FACTOR

and was adopted. The most straightforward fits are obtained with the A's and B's expressed not directly in terms of ω_0 , but rather in s/a which is equal to $\omega_0/(\omega_0 - 1)$. The selected model is thus

$$n(s, \omega_0, \theta) = A(s/a, \theta) s^{-B(s/a, \theta)}, \quad (8-4)$$

The coefficients A and B can be expressed in the forms $A = c_1 + c_2(s/a)$ and $B = c_3(s/a)^{c_4}$. The fits for various ranges of beam entry nadir angle are found in Table 8-1.

Table 1. Regression coefficients for exponential power decay factor.

θ	c_1	c_2	c_3	c_4
$0^\circ - 15^\circ$	1.02	0.032	0.032	0.79
$15^\circ - 25^\circ$	1.03	0.035	0.042	0.69
25°	1.05	0.036	0.050	0.60
35°	1.11	0.024	0.072	0.54

One minor added refinement is possible. The curves of P_R vs. αD for fixed α are slightly flatter at small αD 's where they approximate the energy case. The extrapolated slopes from higher αD thus intersect the P_R axis ($\alpha D = 0$) slightly above the actual value of P_T . An equation of the form $P_R \propto P_T \exp(-2nKD \sec\phi)$ consequently underestimates P_R slightly. To correct for this effect, the ratios of the extrapolated slope intercepts, P_T' , to P_T have been calculated and denoted as "m" such that $P_R \propto m P_T \exp(-2nKD \sec\phi)$. A plot of m vs. α for a range of nadir angles and $\omega_0 = 0.8$ is seen in Fig. 8-4. The m values are not as well-behaved as the n's, but they need not be, since they are linear rather than exponential factors. To a first order, one might simply select $m \approx 1.25$. For typical operational circumstances of $0.7 < \omega_0 < 0.9$, $0.2 < \alpha < 2 \text{ m}^{-1}$, and $15^\circ < \theta < 25^\circ$, an estimate good to about ± 0.1 for either phase function is $m \approx 1.1 + 0.19 \alpha$. In reality, the magnitude of this effect compensates for ignoring the air path losses and a little practical system detuning. It can consequently be ignored, as well, except for special cases where high accuracy is required, such as the estimation of water parameters.

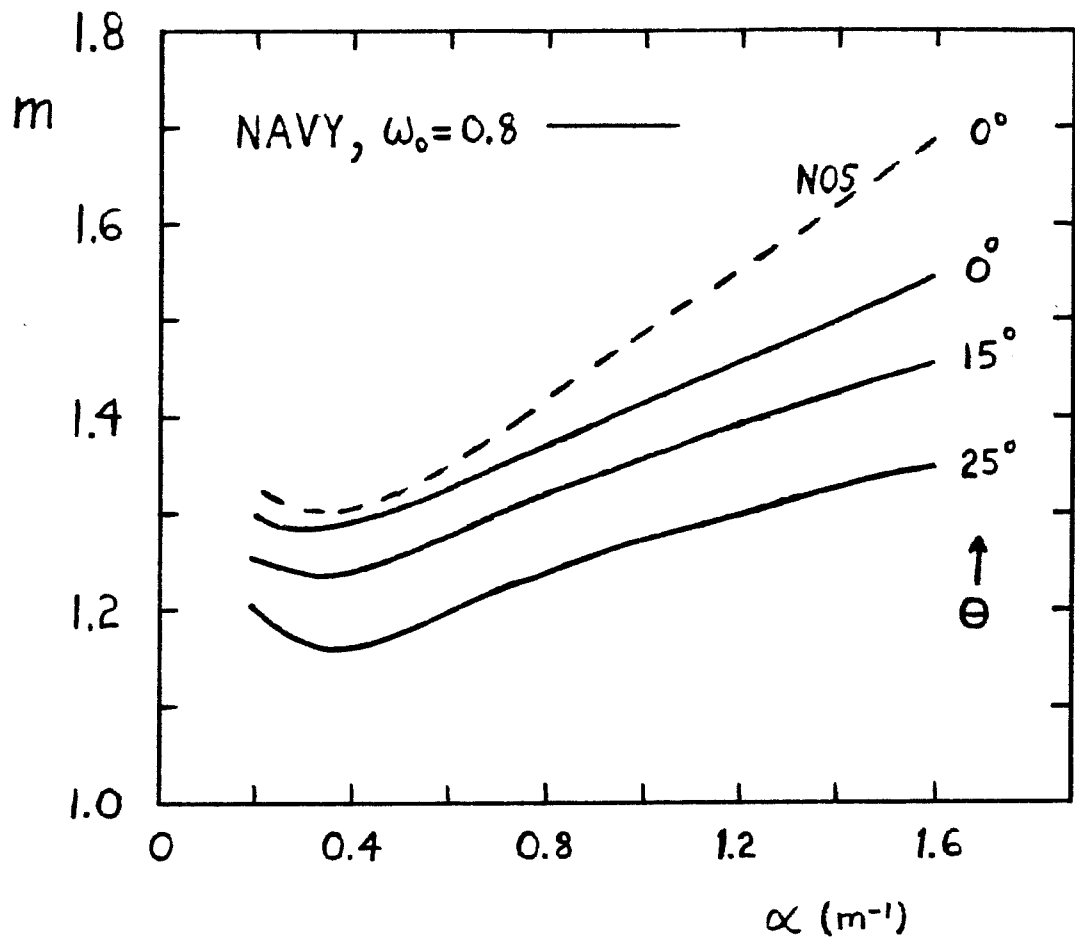


FIGURE 8-4. LINEAR POWER FACTOR

For a practical case with a 7-ns source pulse, the peak power received from the bottom return, obtained by converting Eq. (8-3), may thus be described effectively as

$$P_R = \frac{(m) P_T n R F_p A_R \cos^2 \theta}{\pi (n_w H + D)^2} e^{-2 n(s, \omega_0, \theta) K D \sec \phi}, \quad (8-5)$$

where the n's are as reported previously.

This signal rides atop the volume backscatter signal (see section 7.3) which decays roughly as $\exp(-2KD)$ with increasing depth. From the above form, it can be seen that a so-called "extinction coefficient", ξ_m , expected to be fairly constant for all water conditions (for a given system with specified altitude, nadir angle, etc.) can be defined in the form $\xi_m = nKD$. Examples of this are seen in section 8.5. Since pulse stretching causes the peak bottom return power to decay at a rate which is slightly faster with increasing depth than the volume backscatter signal, the latter appears to be a limiting noise source for nighttime operation.

The field-of-view factor, F_p , is different than that for the energy equation because, as seen in section 8.2.5, a loss of energy does not necessarily lead to a significant loss in peak power. An insufficient FOV which spatially excludes a portion of the returning signal reduces the F_p factor below unity in a highly complex way which depends on the FOV, water parameters, depth, altitude, and the duration of the incident source pulse. No detailed relationships have been derived for F_p other than to note the FOV required to maintain a value near unity.

It is important to reiterate here (because of confusion and expediencies in the past) that neither the bottom return energy nor the peak power depend unambiguously on the optical depth, αD . The optical depth alone cannot be used to predict maximum penetration depths because these are seen to depend explicitly on KD , and the relationship between K and α is a very strong function of ω_0 . Furthermore, pulse stretching adds additional losses which have been characterized as an increased exponential loss factor.

8.2.3 Incremental Power Sensitivity

It can be seen from Eq. (8-5) that a relatively small change in D can result in a large change in P_R because of the exponential form. This also means that a large power increment is necessary to obtain a marginal depth increase. It is clear that doubling, for example, the transmitted power does not double the maximum penetration depth. Indeed, the depth increment depends not just on the power increment, but on the initial power as well. This can be seen more clearly if Eq. (8-5) is written in the abbreviated form $P_{B,m}/P_T = A \exp(-aKD_m)$, where a and A are constants, and $P_{B,m}$ is the minimum useful bottom return power defining the maximum penetration depth, D_m . This can easily be manipulated into the form

$$D_m = \frac{1}{aK} \ln \left(\frac{A P_T}{P_{B,m}} \right), \quad (8-6)$$

from which it can be seen that

$$\frac{dD_m}{dP_T} = \frac{1}{aKP_T}. \quad (8-7)$$

This demonstrates that for large P_T , the incremental increase in maximum penetration depth with increasing laser power is very small. Indeed, we see that, for example, if $a = 2.6$, $K = 0.15 \text{ m}^{-1}$, and $P_T = 10^5 \text{ watts}$, then $dD_m/dP_T = 2.6 \times 10^{-5} \text{ m/watt} = 2.6 \text{ m}/10^5 \text{ watts}$. Under these circumstances, D_m will be about 20m (as seen in section 8.5). Hence, at this power level and water clarity, increasing the transmitted power by 100 percent adds only about ten percent to the maximum depth capability (considering the average slope between the two power levels). Because of the K in the denominator of Eq. (8-7), the return ratio is even smaller for more turbid water.

8.2.4 Implications of Eye-Safety Requirement and Wave Correction Techniques

These seemingly dissimilar concepts are related because they are the key factors which dictate the selection of the transmitter beam divergence. An ANSI eye-safety standard specifies the maximum energy density permissible at the surface of the water from which people may be viewing the aircraft. For a dark-adapted pupil, the energy density at the location of the nearest possible

observer must be no greater than $\epsilon_{\max} = 5 \times 10^{-3}$ Joules/m² for the scanning mode where only a single pulse can impinge the eye. For a full beam divergence angle, ψ , and transmitted pulse energy, E, out of the aircraft, geometry dictates

$$\left. \frac{\psi^2}{E} \right|_{\min} = \frac{4}{\pi H^2 \epsilon_{\max}} . \quad (8-8)$$

This expression can be used to calculate either the minimum divergence for a given pulse energy or the maximum pulse energy for a given divergence.

It is important to make the distinction that although eye safety is based on energy density, penetration is dictated by the peak power associated with the integrated pulse energy as seen in Eqs. (8-3) and (8-5). This means that penetration can be increased by increasing both the pulse energy and the beam divergence, so as not to exceed ϵ_{\max} . The limiting factor will then be either a beam divergence restriction (such as wave correction or spatial resolution) or the maximum pulse energy which can be generated by the laser at the required repetition rate.

Because the pulse energy in the water spreads out considerably due to scattering, degradation of spatial resolution due to a moderate incident beam divergence is not a problem. It is not outrageous to consider a surface spot diameter as large as, say, 4.5 m, which would be obtained from a 300-m altitude with a 15-mr divergence. For beam nadir angles larger than 20 or 30 degrees, however, the use of large beam divergences would cause a depth measurement bias (as seen in section 9.2.4) which would need to be corrected. The primary selection criterion for beam divergence thus revolves around the problem of wave correction. This problem is discussed more fully in section 9.2.5 where a variety of techniques from very narrow to very broad beams are discussed. The results demonstrate a preference for a broad beam of 10-15 mr divergence. This is a very important decision, because it makes the difference between being limited by the eye-safety constraint or by state-of-the-art laser technology. This can be seen by exercising Eq.(8-8), as follows.

As of this writing, the typical output energy for a high repetition rate (400/sec), narrow pulse-width (7 ns FWHM) Nd:YAG laser is about 2-3 mJ. If

wave correction techniques dictated a narrow beam of, say, 3.3 mr for a 50-cm surface spot diameter from a 150-m altitude, then the maximum transmitted pulse energy permitted would be limited to $E_{\max} = \psi^2 \pi H^2 \epsilon_{\max}/4 = 1 \text{ mJ}$. For a 15-mr divergence, however, $E_{\max} = 20 \text{ mJ}$. In this case, eye safety would not be an important limitation, and such large beam divergence operation could benefit from more advanced, high-energy lasers in the future. Since E_{\max} varies as the square of the altitude, the results for a 300-m altitude are even more striking: 35 mJ for a 10-mr divergence, and 80 mJ at 15 mr. As noted in the previous section, however, even large increases in power yield only marginally increased penetration depths. The tradeoff then becomes one of marginally increased penetration versus such factors as laser lifetime and reliability, external power source requirements on the aircraft system, size/weight, and added biases.

8.2.5 Receiver Field-of-View Effects

8.2.5.1 Spatial Distributions

As was noted in section 4.1, scattering in the water column causes the beam to spread out spatially into an expanding cone. The extent of the spreading depends in a complex manner on the geometry, the optical depth, the phase function, and the single-scattering albedo of the water. For off-nadir angles, the energy density distribution is significantly skewed toward the vertical due to reduced attenuation, as seen in Fig. 4-8. The skewness is more pronounced for higher optical depths, higher off-nadir angles, and more highly scattering phase functions such as "NOS". This early-arriving energy has a large effect on the shape of the impulse response function (IRF).

Quantitative relationships for the spatial extent of the beam have previously been developed by analytic approximation and physical measurements. Concise energy distributions for a variety of water types were measured in a laboratory tank by Duntley (1971). Unfortunately for our purposes, these results were based on a detector whose shape was a spherical "cap", all of which was at a constant distance from the laser source. The geometry of interest for laser hydrography is a tilted plane. A simple analytic expression based on small-angle forward scattering approximations reported by Jerlov

(1976) has the same drawback in that it does not treat the increased optical depths for off-axis paths. Not surprisingly, therefore, his radial energy distribution predictions are in fair accordance with the Duntley measurements, although somewhat larger due to the simplistic assumptions.

Distribution diameters for various energy fractiles for a planar detector (consistent with airborne laser hydrography geometry) have been estimated as an ancillary output of the Monte Carlo propagation simulation (Guenther and Thomas 1981a) developed for calculating depth measurement bias correctors and peak bottom return power. Plots of 50-percent energy and 90-percent energy distribution diameters, d_B , normalized to vertical water depth, D , are shown in Fig. 8-5 (left axis) for nadir entry and several values of ω_0 . The curves, which are averaged between NAVY and NOS phase functions, are labeled d_n for the n^{th} percentile energy fraction contained within. Curves for RMS diameters fall between the two values shown. The Duntley curves for 50 and 90-percent energy fractions are included for comparison. A curve derived from the Jerlov relationship, which yields an RMS diameter, is also included for $\omega_0 = 0.8$.

A fundamental and important functional difference is noted between the Duntley results to a spherical cap and the simulation results to a plane. The Duntley and Jerlov fractional diameters continue to rise with increasing optical depth, while the simulation results saturate. This behavioral difference is attributed to the disparate geometries. In the Duntley experiment, the off-axis radiation traversed the same path length as the on-axis radiation. For a planar target, the added attenuation length for non-axial paths causes a significant reduction in the signal magnitude received at larger angles. This results in a reduction of the effective "spot" diameter -- particularly at large optical depths. This differential path length effect is much more pronounced for d_{90} than for d_{50} due to the larger net angles, and the Duntley d_{90} results consequently differ from the simulation by more than the d_{50} results. It can be seen that for large optical depths the simulation results indicate that the diameter of the 50-percent energy fraction at the bottom is roughly half the water depth, and the diameter of the 90-percent energy fraction is slightly greater than the water depth. Mean and RMS diameters fall between these bounds.

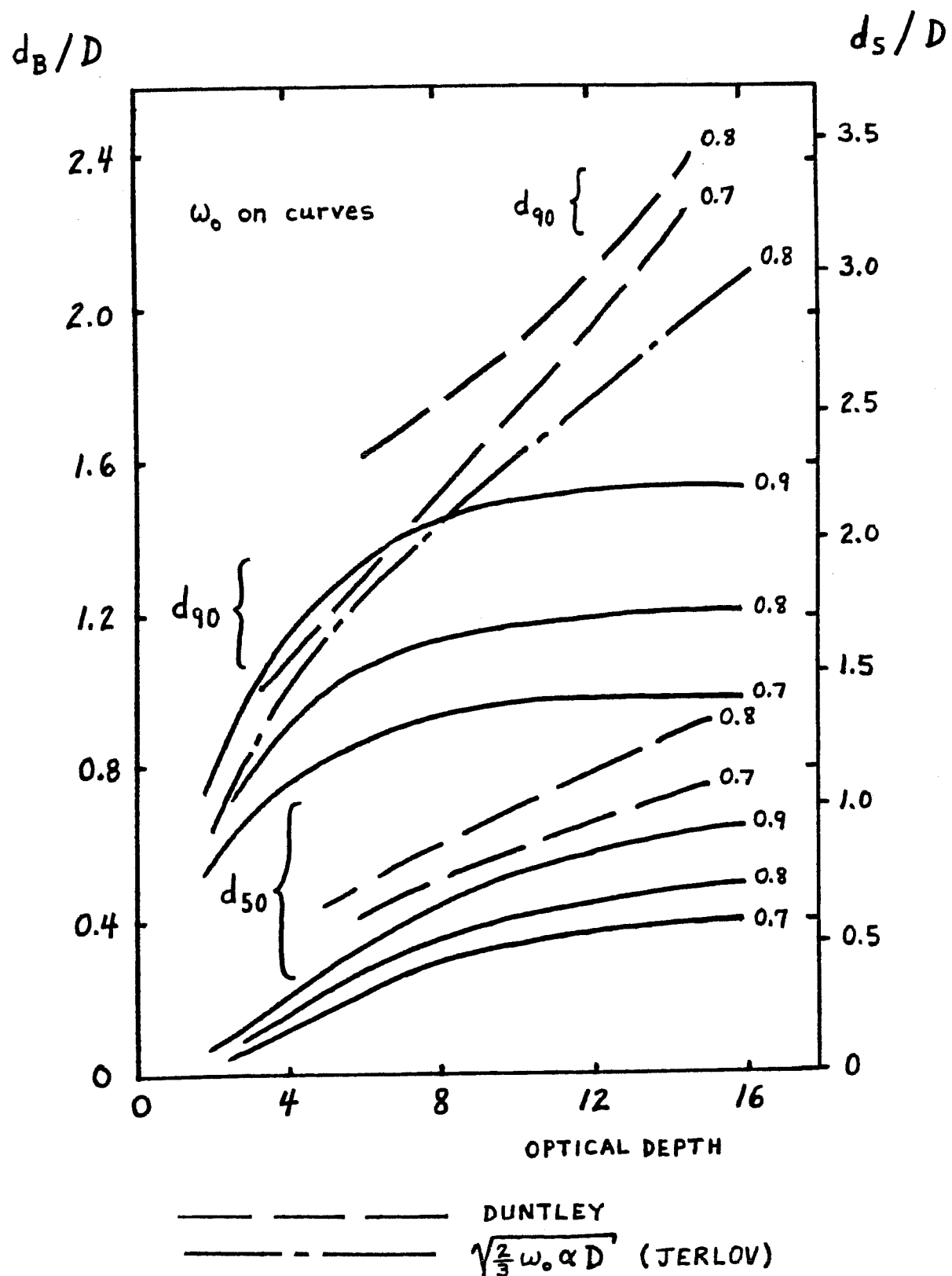


Figure 8-5. Bottom and Surface Distribution Diameters for Selected Energy Fractions

Although one thinks of a laser beam as being a highly collimated probe, it can be seen that such is not the case in water. The beam is scattered by entrained particulates into an expanding cone whose size increases as the scattering optical depth of the medium increases. Based on the above results, the effective angular beam width at the bottom for a 50-percent energy fraction is about $2 \tan^{-1}(0.25) = 28$ degrees. (Half the pulse energy is a suitable criterion for purposes of selecting the receiver field of view (FOV) to sustain penetration potential, as will be seen shortly.) This means that an airborne lidar cannot provide detailed profilimetry with horizontal resolution on the order of several meters at typical operating depths in the 20 m - 40 m range. The soundings, rather, are center-weighted averages over an area with a diameter of roughly half the water depth. This fact is somewhat misleading, however, in that small but not insubstantial shoal objects such as coral heads or large rocks will nevertheless reduce the measured depth because leading-edge pulse location algorithms are sensitive to the early-arriving energy. If somewhat higher resolution were required for some special task, a narrower effective beam width could be obtained by limiting the receiver FOV. The tradeoff is concomitant loss of peak power and, hence, penetration capability. In optically shallow water, this loss might be an acceptable compromise.

As noted in section 6.2, the principle of reciprocity dictates that the upwelling, bottom reflected energy traverses a set of paths statistically similar to the downwelling paths. This means that the diameter of the surface distribution of reflected bottom energy can be derived from a convolution of the bottom energy density distribution with itself. The resulting surface diameter of upwelling bottom return energy will be somewhere between one and two times the equivalent bottom diameter, depending on the exact shape of the distribution. For a Gaussian distribution the factor is $\sqrt{2}$. Surface diameters for this approximation are indicated on the right-hand axis in Fig. 8-5. For an estimated surface diameter, d_s , of the selected bottom-reflected energy fraction for nadir entry, the 50-percent energy criterion is $d_s(50) \approx 0.7 D$, and for a 90-percent criterion, $d_s(90)$ is over twice that. The FOV requirement thus depends strongly on what measured "spot" size is pertinent.

The primary effect of FOV is the determination of the bottom return signal-to-noise ratio (SNR) and, hence, the maximum useable depth or "penetration" capability. If the FOV is too small, the peak bottom return power and associated maximum penetration depth will be reduced. For nighttime operation, a larger than necessary FOV is benign, but in daylight, an excessive FOV will increase the solar noise level and, again, reduce penetration. The FOV "requirement" is thus the FOV which maximizes the SNR or, more simply, that which is just large enough not to significantly reduce the peak bottom return power (not the energy). The relationships between power, energy, and source pulse width will now be examined.

8.2.5.2 Temporal Effects

Leading edge pulse location algorithms are sensitive to signal power, and the FOV requirement must, therefore, be determined for peak power, not for pulse energy. The relationship between these two is dictated by pulse stretching. If the environmental response function (ERF) is similar to the source pulse (the case if no significant stretching), then any reduction in pulse energy due to lack of sufficient FOV is achieved with a corresponding drop in peak power (because the duration of the ERF cannot decrease below the duration of the source pulse). If the ERF, on the other hand, is significantly stretched and appears more like the impulse response function (IRF), then a loss of energy due to modest truncation of the periphery of the spatial distribution can and will be accomplished by a temporal shortening of the tails of the IRF and ERF with little or no loss of peak power. This is a beneficial feature because, in deep water where the FOV requirement is greatest, the pulse stretching is also greatest. A modest fraction of the pulse energy from the trailing edge can be discarded without a significant drop in the peak pulse power -- thus reducing the necessary energy fraction and the actual FOV requirement. For a given pulse width, the peak power of the ERF begins to drop quickly as the IRF width is decreased through the source width. The FOV requirement based on power detectors is thus a much more complex function of depth than when energy alone is considered.

It is apparent that the duration of the source pulse (in comparison to the duration of the depth-scaled IRFs) can play a role in the FOV requirement.

This somewhat unexpected result will be demonstrated via a semi-quantitative argument as follows. Consider a typical curve of peak power versus receiver FOV such as seen in Fig. 8-6 from a system with a 15-ns wide source pulse. The peak power nears its maximum value (for this particular case) at about 100 mr. If the FOV is reduced below this value, the peak power is reduced, indicating (from the above argument) that the duration of the IRF for this FOV is on the order of the source pulse width (even though it might be longer if the FOV were greater). If the pulse width were suddenly reduced to, say, 5 ns, the IRF width would be considerably longer than the new source, and could be reduced (by reducing the FOV, for example) to about 5 ns without significantly decreasing the peak power of the ERF. This means that the FOV requirement for a fixed geometry has been reduced by shortening the time duration of the incident laser pulse.

This is a very important result. It means that the FOV requirement for a short pulse system is smaller than that for a long pulse system. It can be demonstrated by geometric arguments that the temporal width of the FOV-limited IRF will be roughly proportional to the square of the FOV. For the given example, then, the FOV required for the 5-ns source pulse should drop to about 58 mr compared to the 100 mr for the 15-ns source pulse, for the same water depth, optical properties, and altitude.

This effect is limited between certain bounds, however. There will be no further increase in FOV requirements as the source pulse width becomes greater than the infinite FOV IRF, because the IRF cannot be made any wider to increase the peak power of the ERF. Similarly, the FOV requirement cannot be further reduced by decreasing the source pulse width to a value less than the width of the zero FOV IRF because the IRF cannot be made any narrower.

The concept that the IRF has a certain minimum width for zero FOV stems from the fact that photons emerging from the medium at the point of entry may have undergone substantial multiple scattering and consequential pulse stretching on their round trip to the bottom and back. Reciprocity in this case requires that the photons must effectively retrace their downward paths to exit the medium at their entry points in the exact opposite direction. In this special case, the convolution of the downwelling distribution with a

cosine-modified version of itself degenerates into a simple product with the times doubled for the round trip. This concept has been used to calculate the zero FOV IRFs from the downwelling temporal distributions. An example is seen in Fig. 8-6 plotted along with the infinite FOV IRF. Because the IRFs scale with depth, the range of source pulse widths over which the FOV requirement will be affected varies with depth.

Figure 8-6, with $\alpha D = 12$, $\theta = 25^\circ$, and $\omega_0 = 0.8$, will be used for illustration. Suppose the depth of interest is 20 m. The relationship between "vertical transit time" units, τ , and actual time, t , is $\tau = c t/D = 0.225(\text{m/ns}) \times t(\text{ns})/\text{D(m)}$. Thus $t(\text{ns}) = 4.44 \tau \text{ D(m)}$. The width (FWHM) of the infinite FOV IRF is roughly $\tau_\infty = 0.193$, and the width of the zero FOV IRF is about $\tau_0 = 0.068$. Then $t_\infty = 17 \text{ ns}$, and $t_0 = 6 \text{ ns}$. For these circumstances the FOV requirement will vary with source pulse width for source widths between 6 and 17 ns. If the depth were reduced to 10 m, the range of effect would be 3 to 8.5 ns.

The major points to be understood from this demonstration are 1) the fact that field measurements of the FOV dependence of the bottom return peak power cannot be generalized for systems with widely differing source pulse temporal widths, and 2) that the use of the smallest practical pulse width will be a benefit as far as minimizing the FOV requirement is concerned.

8.2.5.3 System Design

It is important to know the maximum FOV requirement before system design, because a FOV that is too small will reduce penetration potential. On the other hand, it is not desirable to build an unnecessarily large FOV because this increases the physical length and diameter of the optical train. The bandwidth of the narrow-band interference filters used to reduce the solar background noise is the primary factor in determining the daytime background noise level and hence the daytime penetration capability. The wider the bandwidth, the less the maximum penetration depth. These filters are limited in their ability to process off-axis radiation. The narrower the filter bandwidth, the smaller the permitted off-axis entry angle. Large FOVs have large associated off-axis angles unless the separation distances are made

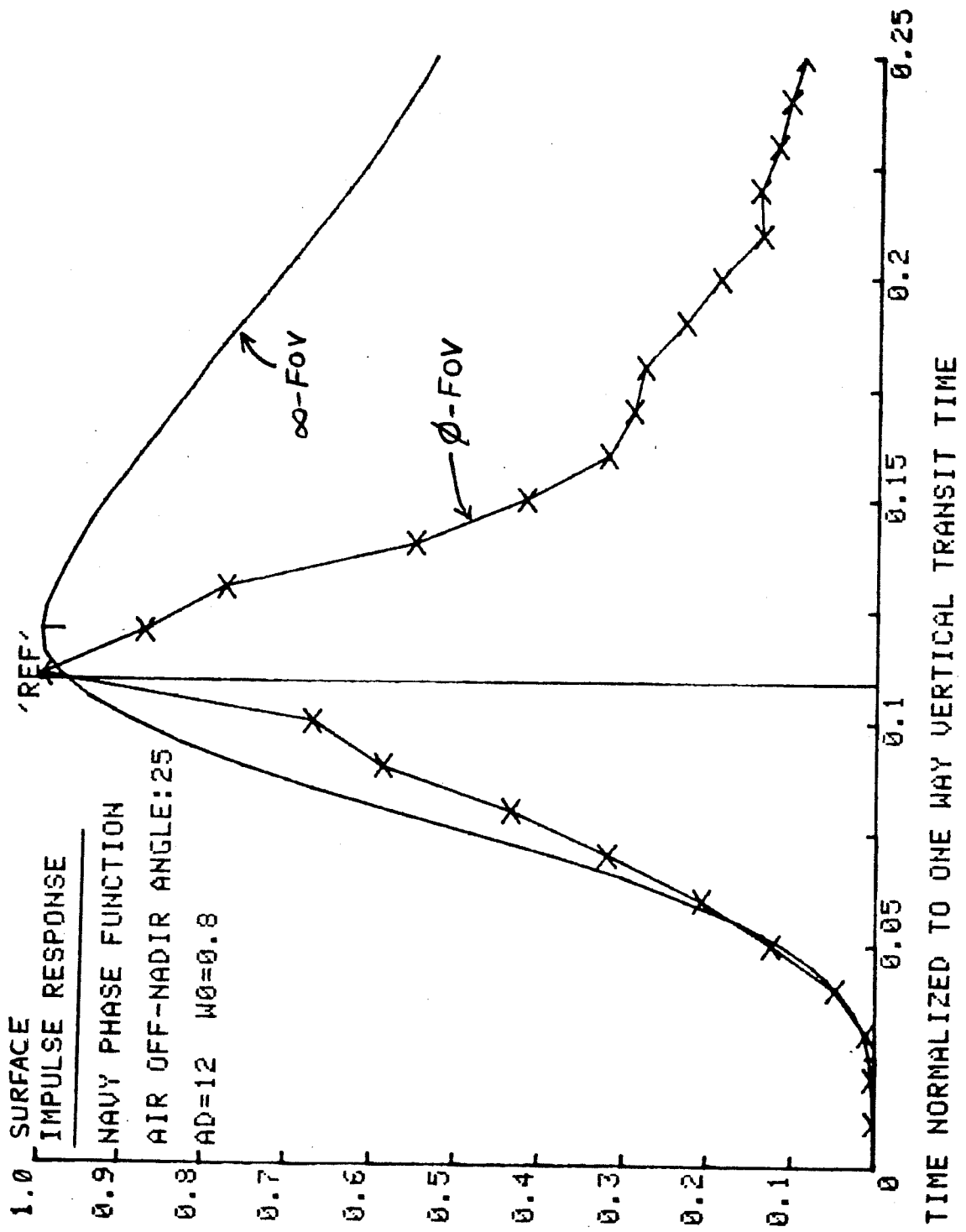


FIGURE 8-6. ZERO FIELD-OF-VIEW RESPONSE FUNCTION

large. One cannot gain penetration, therefore, by using a larger FOV if that FOV requires an increase in filter bandwidth due to limited separation distance dictated by the system size/weight requirements or limited available filter dimensions. In order to have both large FOV and small bandwidth, the optical train must therefore be of large dimensions. Nighttime operation avoids this problem by permitting the filter to be removed except for conditions of bright moonlight.

Armed with the above spatial and temporal signal information, how does one estimate the FOV requirement for a practical system? At best, the question can only be answered semi-quantitatively for limited parameter ranges. In the temporal example, it was seen that, for the typical operating conditions selected, a 7-ns source pulse was sufficiently short to result in the smallest possible FOV requirement for depths in excess of 20 m. Under these circumstances, the result will be dictated by the scattering geometry, and the receiver FOV requirement can be estimated by observing the behavior of the Monte Carlo spatial distributions.

The Monte Carlo results of Fig. 8-5 are repeated with an added highlight in Fig. 8-7. For small physical and optical depths, say two to four, the IRF is short, and the ERF approximates the source pulse. Any loss of energy results directly in a loss of peak power because the ERF cannot become narrower than the source pulse. For this case, therefore, the d_s/D required would derive roughly from the d_{90} curve. For large physical and optical depths, the ERF takes the character of the IRF and is significantly wider than the source pulse. Moderately restricting the FOV will reduce the pulse energy, but not the peak power, by truncating the tail of the IRF, as seen in Fig. 8-8. By examining the effect of reduced FOV on IRF shapes, it has been noted that the peak height is not significantly reduced until d_s/D becomes less than about 0.7, which, from Fig. 8-7 corresponds roughly to a 50-percent energy fraction.

The heavy band drawn across Fig. 8-7 is an estimate of the overall d_s/D requirement according to these arguments. The function rises only slightly toward small optical depths because, even though the required energy fraction is larger, the relative expansion of the beam due to scattering is less. For a practical system, the receiver FOV can be safely set to the high αD value

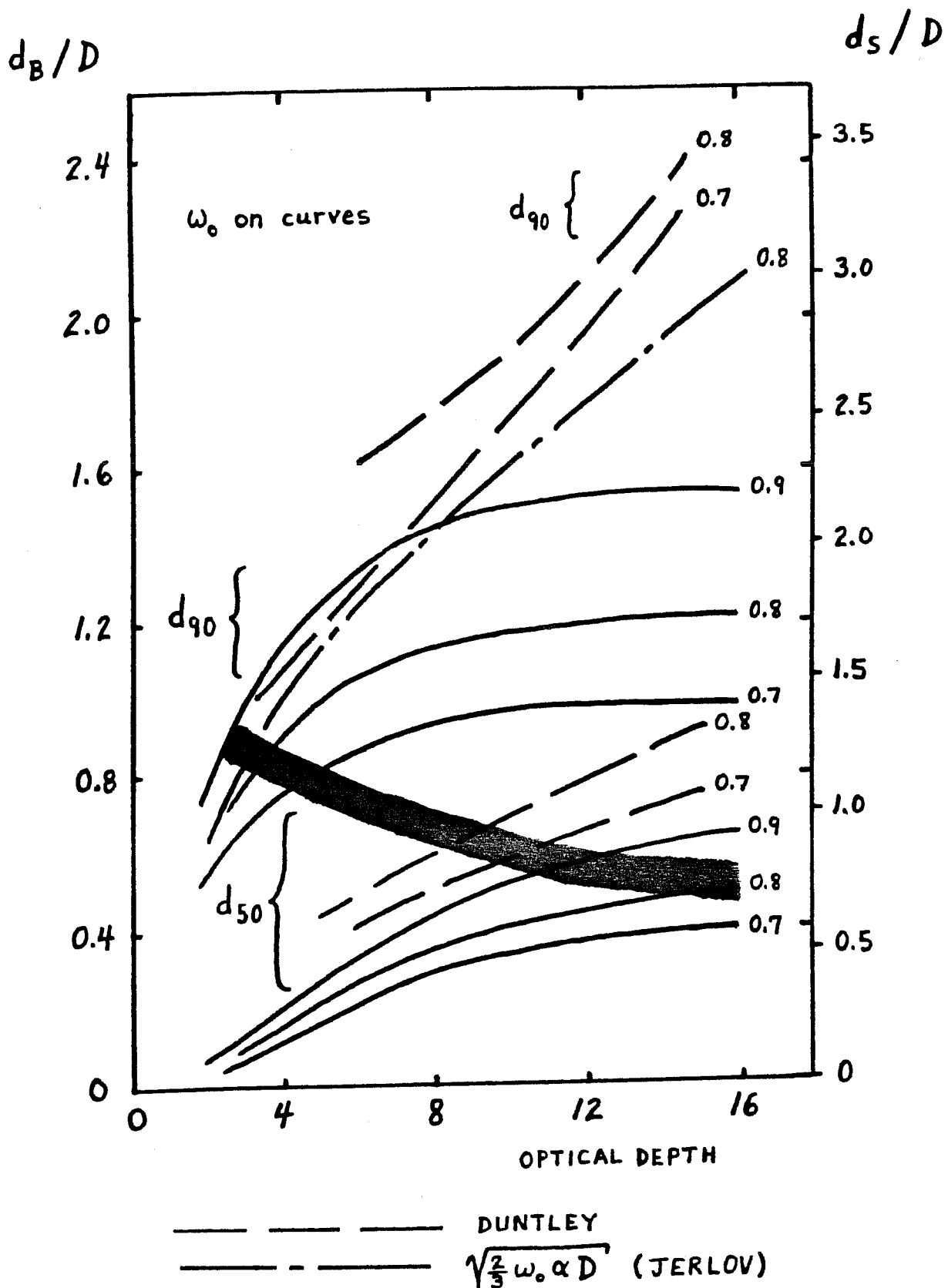


Figure 8-7. Receiver Field-of-View Requirement

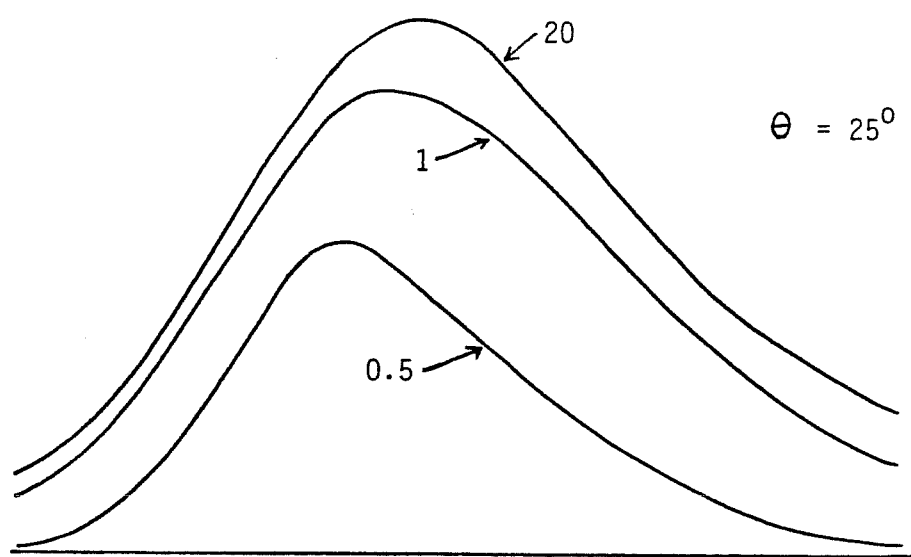
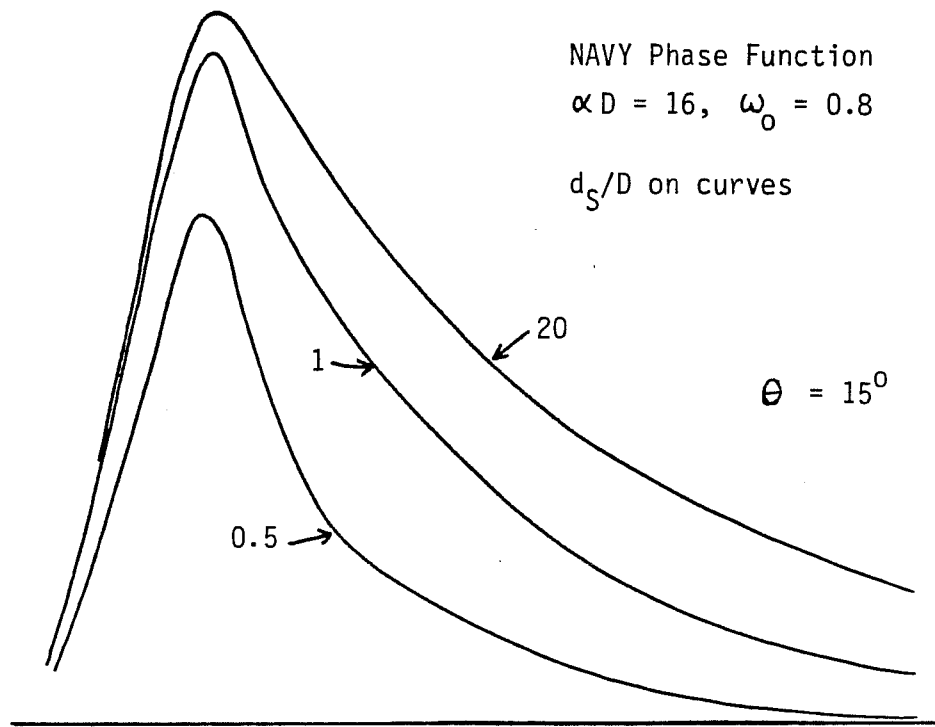


Figure 8-8. Field of View Effect on High Optical Depth IRFs

where d_s/D is smallest, since at smaller optical depths a slight loss of power will not significantly affect performance. The best estimate for a practical FOV requirement is thus a surface spot diameter for the receiver of roughly 0.7 D which corresponds roughly to a 50-percent energy criterion at large optical depths. For an aircraft altitude, H, the necessary full angle FOV would be $\psi_{FOV} \approx d_s/H \approx 0.7D/H$. The FOV desired for a typical aircraft altitude of 300 m and a depth of 35 m would thus be about 80 mr. A FOV of this size is fairly large for a compact optical system, but nevertheless achievable.

This result is relatively independent of nadir angle. For off-nadir angles, the irradiated bottom dimension is larger roughly by $\sec\phi$ due to the additional slant distance to the bottom, but the FOV needed to encompass the resulting surface spot is smaller by $\cos\theta$. For the relatively small angles of interest, these functions effectively cancel, thus leaving the FOV requirement virtually the same as for the nadir calculation.

8.2.6 Nadir Angle Effect for Constant Swath Width

The sounding swath width under the aircraft depends on the altitude and beam nadir angle. Various combinations of altitude and nadir angle can be invoked to yield a given swath width, but these combinations will result in different values of bottom return power. This is the same idea as related in section 7.2 for the interface return power. If Eq. (8-5) is reduced to the simplified notation

$$P_R = A f(\theta) \cos^2\theta / H^2, \quad (8-9)$$

then for a swath width $B = 2 H \tan\theta$, one can alternately write

$$P_R = 4 A f(\theta) \sin^2\theta / B^2. \quad (8-10)$$

The forms of $f(\theta)$ for various values of beam entry nadir angle, depth, and water optical properties, have been derived numerically from the peak powers of the ERFs obtained from the Monte Carlo propagation simulation. Plots of P_R vs. θ from Eq. (8-10) exhibit peaks at angles ranging between 30 degrees for a 40-m depth to 45 degrees for a 5-m depth. The nadir angles, θ_m , at which these functions peak represent the angles at which the bottom return peak

power is maximized for the given sounding swath width under the aircraft. Physical depth is the driving independent variable, as variations with the other parameters are much smaller. The data can be fitted with a linear regression of the form θ_m (deg) $\approx 44 - 0.29 D(m)$ to within better than ± 2 degrees over the depth range $5 < D < 40$ m. The peak power is lower at lower angles because these imply higher altitudes with larger resulting inverse-square losses, and also lower at higher angles due to the increasing drop in $f(\theta)$ at large angles. Experimental return power results obtained by the Naval Air Development Center (Witt et al. 1976) for a 17-m depth indicated corroborating values for θ_m in the range between 36 degrees and 45 degrees.

The meaning of these results is that for a given selected swath width, the bottom return peak power will be optimized if the swath width is achieved with as low an altitude and as large an off-nadir scanner angle as possible. The chief limitation on nadir angle is depth measurement accuracy. As noted in section 9.2, nadir angles in excess of roughly 15 to 25 degrees (depending on the signal processing) could lead to unacceptably large errors (in the context of a ± 30 -cm total error budget) due to propagation-induced biases and beam steering at the surface. Since the maximum possible beam nadir angle (up to depth measurement accuracy limits) is desirable for maximum return power, the remaining tradeoff is swath width versus altitude. Greater swath widths can be covered from a higher altitude, but at the price of reduced bottom return peak power (penetration) due to the inverse-square power loss. Thus large shallow areas can be more economically surveyed from a higher altitude, as long as the penetration and data density (at the given laser repetition rate) are sufficient.

8.3 Noise Sources

8.3.1 Daytime

For daytime operation the limiting noise source is associated with the solar background radiation passed through the narrow-band interference filter. The noise power from this source takes the form

$$P_{N,D} = I_S A_S \Delta B A_R \eta_R \cos^2 \theta / H^2, \quad (8-11)$$

where I_S is the solar irradiance reflected from the water column (not including the sun-glint reflected from the interface) -- a typical value is $0.02 \text{ watts/m}^2\text{-nm-ster}$,
 A_S is the area within the receiver field of view on the surface ($\approx \pi H^2 \sec^2\theta \tan^2(\psi/2)$), where ψ is the full FOV angle),
 ΔB is the bandwidth of the interference filter,
 A_R is the effective aperture area of the receiver telescope,
 η_R is the optical efficiency of the receiving optics,
 θ is the beam nadir angle in air, and
 H is the aircraft altitude.

For ac-coupled electronics, the square root of $P_{N,D}$, not the value of the level itself, is the statistical "shot noise" associated with this daylight background level, and hence the pertinent value for "noise".

The FOV requirement, as discussed in the preceding subsection, is that the surface spot area, A_S , defined by the receiver FOV be sufficient to encompass a significant portion of the returning, bottom reflected radiation. Note that for $H \gg D$, Eq. (8-11) has the same dependence on A_R and H as the bottom return signal equation (Eq. (8-5)). This means that for background-limited daytime operation, the signal-to-noise ratio (SNR) varies as $\sqrt{A_R}/H$. A larger receiver telescope aperture or a lower altitude (even for fixed A_S maintained by increasing the FOV) will only marginally increase the SNR and penetration potential. At night, both of these factors are fully beneficial, and the SNR varies as A_R/H^2 .

The only controllable factor in Eq. (8-11) which can be reduced without also reducing the bottom return signal is the filter bandwidth. Daytime penetration depths are thus strongly dependent on this one factor (for given transmitted power and water clarity). The smaller the filter bandwidth, the less the solar noise level, and the greater the maximum penetration potential.

Very narrow-band filters have several associated problems. First, they must be temperature compensated in an oven to remain at the correct center frequency, and second, they are very limited in their ability to pass off-axis

radiation. Since large fields of view have off-axis energy at correspondingly larger angles for a given focal length, it is difficult to have both a narrow bandwidth and a wide FOV. The only way this can be accomplished is by increasing both the diameter of the filter and the focal length of the optical train. The filters generally are only produced up to a certain size, however, and long optical trains impact the system size/weight constraints. The bandwidth should be selected to be as small as possible within the limitations of the required receiver FOV and physical size. One does not want to sacrifice FOV to implement a very narrow-bandwidth filter (thereby reducing both signal and noise) because that would limit nighttime performance for which the filter can be removed.

8.3.2 Nighttime

The noise sources for nighttime operation are 1) volume backscatter, 2) the sum of thermal "Johnson" noise and photomultiplier (PMT) dark current, 3) moon glint and volume-reflected moonlight, 4) spurious signals, and 5) statistical shot noise associated with the total signal plus noise level. For a well-designed system, all of these sources are significantly smaller than the solar background for practical filter bandwidths, and maximum penetration depths at night will thus be correspondingly greater than for daytime operation. The system must be designed to minimize spurious responses and thermal noise. PMT dark current can be minimized by specification of the proper tube type and hand selection of a specific tube with the lowest possible dark current. The effects of moon glint and volume-reflected moonlight have not been modeled, but it is expected that operating with moon glint in the receiver FOV is undesirable. As with sun glint, occurrence depends on latitude and scanner nadir angle, and avoidance can be achieved by appropriate selection of flight times. The effects of volume scattered moonlight with and without the interference filter are best determined in the field. The limiting noise sources for nighttime operation are expected to be volume backscatter of the laser beam, moonlight, or, if the system electronic noise is very low, perhaps shot noise.

8.3.3 Electronics

It has been observed (Contarino 1981, Miller 1981, Houck 1982) that certain and probably all PMTs produce small but problematic spurious signals after the receipt of a strong signal (such as the surface return). These stray signals can be detected as false bottom returns or can add energy to a true bottom and cause a depth measurement error. It is thus desirable to limit the magnitude of the green interface return by avoiding operation near nadir where the reflections are strongest.

The surface returns (interface and volume both) can be significantly reduced by polarization techniques, but this results in loss of penetration due to polarizer insertion losses and potentially in a loss of accuracy due to distortion of the volume backscatter signal from which the scattering coefficient might be estimated to use in propagation-induced bias correction procedures. Another dynamic range reducing option, the use of an optical block in the center of the FOV to reduce the surface return, would lose less penetration, but would have the same deleterious effect on estimation of the scattering coefficient. The use of "sensitivity-time control" (STC) (section 4.2) would preserve penetration but could lose or distort some bottom returns during the turn-on transient. The backscatter signal could be restored, if desired, if the gain function were well known. The subject of surface return and dynamic range reduction is a very serious problem which must be carefully considered in the design of each system.

8.4 Waveform Model

Equations for interface return (Eq. (7-2)), volume return (Eq. (7-8)), bottom return (Eq. (8-5)), and day (Eq. (8-11)) and night noise sources have been incorporated into a BASIC program (on a Tektronix 4051) which calculates the total radiometric waveform for given input system variables and environmental parameters and plots the results for six different depths up to a selected maximum. Maximum penetration can be determined by inspection for any desired signal-to-background ratio criterion. An example output is presented in Fig. 8-9.

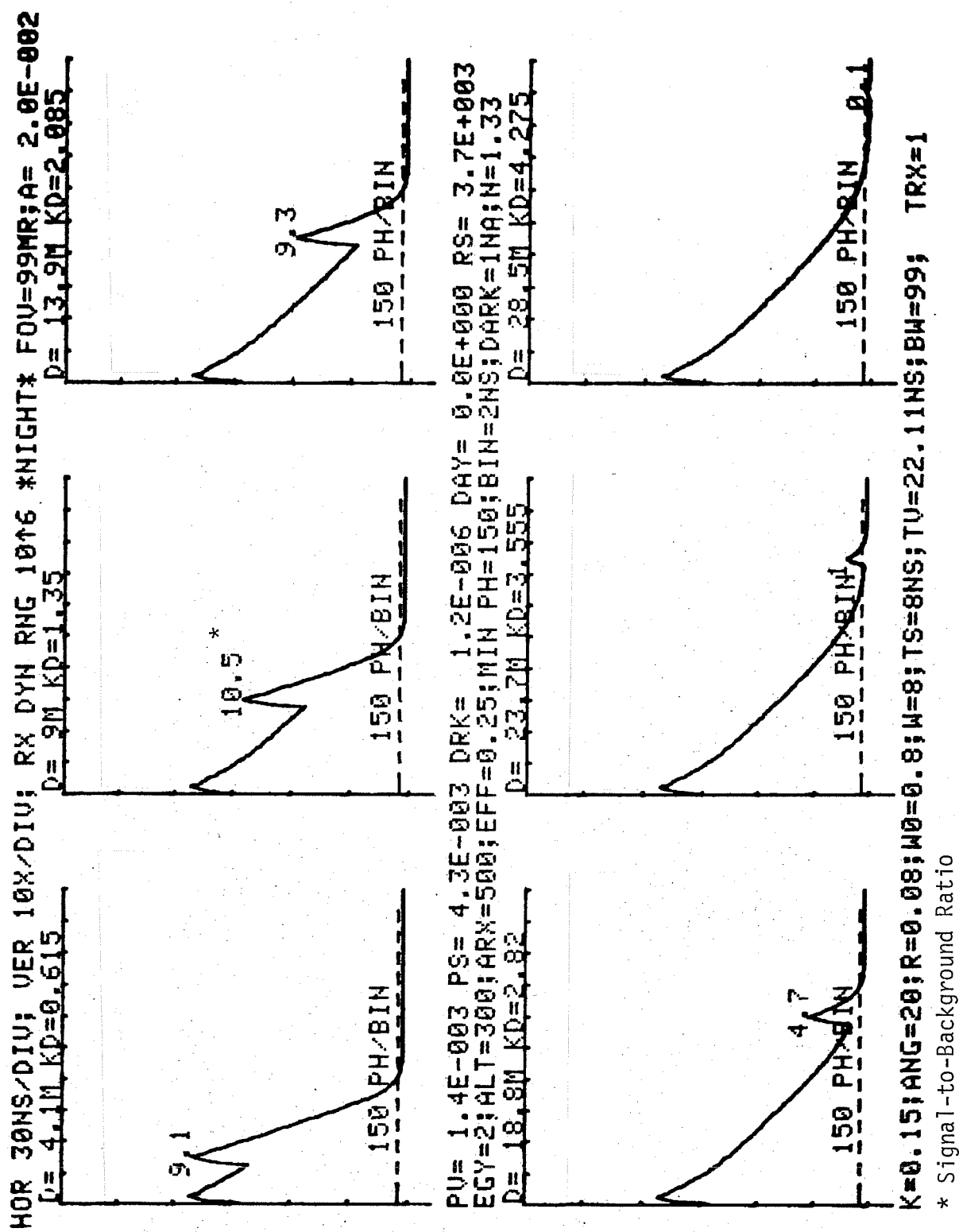


Figure 8-9. Sample Waveform Simulator Output

The program has been verified by comparing outputs with results from experimental systems including the AOL, an AVCO airborne mapper system, and the Australian WRELADS II. An example of the excellent agreement with the latter is seen in Fig. 8-10, where the results are plotted over an Australian figure (Phillips and Abbot 1981) representing the maximum penetration depths obtained experimentally as a function of α . As can be seen, the comparison is remarkably good. (Note: the maximum penetration does not, in general, depend on α but rather on K . This result would be somewhat different for different values of ω_0 because of the relationship between K and α developed in section 3.)

Maximum penetration and return waveforms for any system and set of conditions can be determined by exercising the program over the appropriate input parameters. This is a powerful tool for performance prediction. Example results are presented in section 8.5.3.

8.5 Penetration Predictions

8.5.1 AOL Flight Test Extrapolation

The NASA Airborne Oceanographic Lidar (AOL) System, as used for bathymetric field tests in 1977 (section 5), was limited to very low laser power and small receiver FOV. Measurable penetration depths were correspondingly small. The receiver was, however, very sensitive and shot-noise limited. Equation (8-5) can be used to relate extinction depths between various systems as follows. For a given system with measured K and D_{max} one can write

$$P_{min} = A P_T e^{-2(nKD)_{max}} \sec\phi , \quad (8-12)$$

where P_{min} is the minimum useable power for accurate depth measurement for that system, A is the product of unlisted parameters, and P_T , n , K , D , and ϕ are as defined earlier. For a second system with $P_{min,2} = q P_{min,1}$, one can then write

$$q A_1 P_{T1} e^{-2(nKD)_{max,1}} \sec\phi_1 = A_2 P_{T2} e^{-2(nKD)_{max,2}} \sec\phi_2 . \quad (8-13)$$

TRIAL 249T 9 AUGUST 1980
NORTH QUEENSLAND

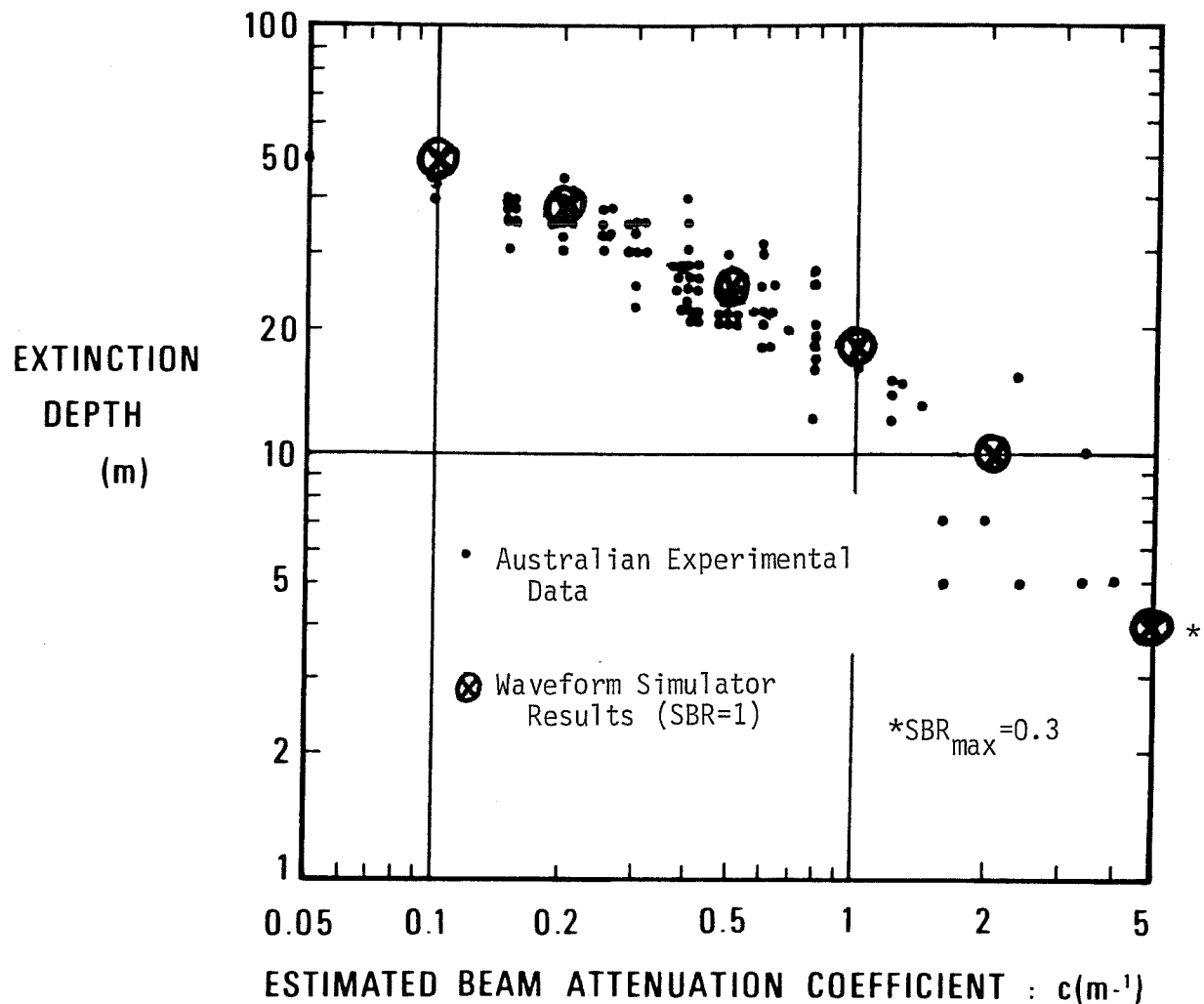


Figure 8-10. Comparison of Extinction Depths for Australian Experimental Data and Waveform Simulator Results

This equation can be solved for $(nKD)_{\max,2}$, for desired values of A_2 , P_{T2} , and ϕ_2 , given knowledge of the parameters and performance of the first system.

For purposes of illustration, the AOL results will be extrapolated to a prospective system. For simplicity, assume $q = 1$, $A_1 = A_2$, and $\phi_1 = \phi_2$. Equation (8-13) then becomes

$$P_{T1} e^{-2(nKD)_{\max,1} \sec\phi} = P_{T2} e^{-2(nKD)_{\max,2} \sec\phi},$$

and thus

$$nKD_{\max,2} = \frac{\ln \left(\frac{P_{T2}}{P_{T1}} \right) + 2(nKD)_{\max,1} \sec\phi}{2 \sec\phi}. \quad (8-14)$$

The peak output power of the AOL was roughly 1 kW (P_{T1}), and the performance to be extrapolated was a nighttime result of $D_{\max} = 5.5$ m achieved from a 150-m altitude for $\phi = 11^\circ$, $\alpha = 2.75 \text{ m}^{-1}$, $K \approx 0.5 \text{ m}^{-1}$, $\omega_0 \sim 0.9$, and $n_1 \approx 1.3$. The predicted "extinction coefficient" for our proposed alternate system is then

$$(nKD)_{\max} = \frac{\ln P_T (\text{kW}) + 7.30}{2.04}. \quad (8-15)$$

If we are interested, for example, in predicting penetration with 280-kW peak pulse power, the result would be

$$(nKD)_{\max} = \frac{\ln (280) + 7.30}{2.04} = 6.3. \quad (8-16)$$

For water with $K = 0.15 \text{ m}^{-1}$ ($n \approx 1.19$), for example, this would be achieved at a depth of $D_{\max} = 35$ m. It is understood, of course, that a larger receiver field of view is required to maintain $F = 1$ for these deeper depths.

The specific AOL performance cited as an input to this calculation can be used in a more general case with Eq. (8-13) to predict penetration for any shot-noise limited system under similar nighttime conditions given the additional information that for the AOL, $A_R = 730 \text{ cm}^2$, and the transceiver nighttime optical efficiency is $n = 0.25$.

8.5.2 Australian Results

The D_{\max} vs. α data (Fig. 8-10) and relationship from Phillips and Abbot (1981) can be converted into an appropriate extinction coefficient for the WRELADS II system as seen with the aid of Table 8-1. It must be remembered, however, that strictly speaking, D_m is a function of K , not α , and that these results are predicted using Fig. 3-8 for assumed, unmeasured values of ω_0 for the given α 's.

Table 8-1. Extinction Descriptions for Daytime, Nadir Operation

A	B	C	D	E	F	G	H
α	αD_m	assumed ω_0	K/α	KD_m	K	$n(s, \omega_0)$	nKD_m
0.1	4.2	0.30	0.74	3.1	0.074	1.05	3.26
0.2	7.0	0.50	0.55	3.9	0.110	1.11	4.33
0.5	11.6	0.75	0.29	3.4	0.145	1.23	4.18
1	14.9	0.82	0.24	3.6	0.24	1.23	4.43
2	17.4	0.85	0.21	3.7	0.42	1.25	4.63
5	19.3	0.87	0.19	3.7	0.95	1.30	4.81

From the Phillips and Abbot relationship $D_m = (0.019 + 0.048\alpha)^{-1}$, the α values in column A can be converted to the αD values in column B. Using the data in Fig. 3-8 which represent a sampling of the propensity for certain values of ω_0 to be associated with certain values of α in natural waters, probable values of ω_0 have been inferred as listed in column C. The K/α versus ω_0 data from Fig. 3-7 were then invoked to provide estimates of K/α for column D. These were multiplied by αD_m (column B) to get KD_m as reported in column E.

It can be seen from column E that KD_m is nearly independent of α while αD_m is a very strong function of α . Values of $n(s, \omega_0)$ for the tabulated α and ω_0 values are seen in column G, and finally, the extinction coefficient, nKD_m , is in column H. The average value of nKD_m is 4.27, the standard deviation is

0.54, and the coefficient of variation is 0.13. Considering the many uncertainties and approximations involved, particularly the selection of ω_0 , this is a reasonable expression of constancy coming from a 50X range of α and an almost 5X range of αD . This daytime result was achieved at nadir from a 150-m altitude with a 5-mJ pulse of 5-ns width (roughly 1 MW peak power), a 250-cm² aperture, a 40-mr FOV, and a 0.2-nm filter bandwidth. These results, also, could be used with Eq. (8-13) as a reference from which to extrapolate to another system.

8.5.3 Waveform Model Predictions

Various sets of simulated system variables have been exercised over a range of environmental parameters. For example, let $H = 300$ m, $A_R = 500$ cm², $R = 0.08$, $n = 0.25$, $\theta = 20^\circ$, $E = 2$ mJ ($P = 280$ kW), $\Delta\lambda = 2$ nm for daytime operation, PMT dark current = 1.0 na for nighttime, and set the source pulse trailing-edge decay time constant to 8 ns. Sample results are seen in Fig. 8-9. The selection of a minimum useable bottom signal or signal-to-noise ratio for a real system depends on false alarm and detection probabilities, the signal processing and pulse location algorithm, and desired measurement precision. For the sake of illustration, a minimum value of signal-to-background ratio (SBR) equal to 0.5 has been selected; this provides what appears from the waveforms to be an easily useable signal. It is important to note that the SBR is not the same thing as the SNR which would typically be much larger. (When using this simple procedure, one must take care to also note the absolute signal level in case shot noise becomes a dominant factor.) Extinction coefficients (nKD_m) for this case are plotted in Fig. 8-11 for both day and night conditions.

It can be seen that the extinction coefficients for this case, $nKD_m \approx 3.0$ for day and 5.1 for night, are fairly constant across a wide range of K . (The extinction coefficients from Table 8-1 adapted from Australian daytime results are somewhat larger due to higher power, lower altitude, etc.) The rolloff at large K occurs because the slope of the volume backscatter becomes steeper than the natural decay of the trailing edge of the surface return (which mirrors the incident laser pulse). The tail of the interface return then becomes the dominant noise source and causes extinction at shallower depths

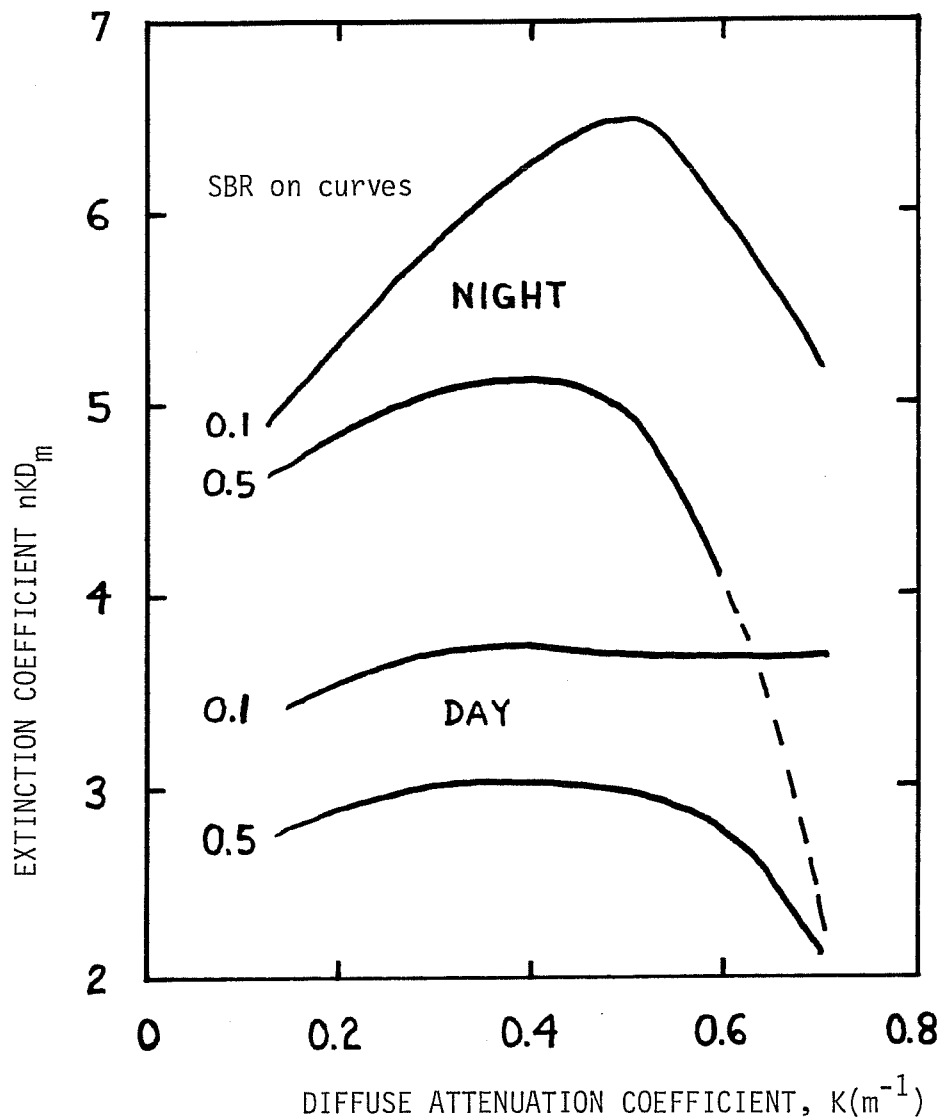


Figure 8-11. Extinction Coefficients for Typical System Parameters
(2 mJ pulse energy, 300-m altitude, 20° off nadir)

than could have been achieved for the given daylight background or dark current. This demonstrates the importance of quenching the laser pulse tail at the most rapid possible rate. This can be accomplished, as in the HALS design for example, with a separate Pockels cell timed to chop off the otherwise much longer natural signal decay from the laser cavity.

It is important to note that although the selected parameters include a fairly substantial 2-mJ pulse (a peak pulse power of 280 kW), the daytime extinction depth for $K = 0.3 \text{ m}^{-1}$ is only 8 m. This is not a very impressive performance. The extinction coefficient is, however, a very strong function of the useable signal-to-background ratio (SBR). If the pulses can be accurately detected and located at $\text{SNR} = 10$, for example, the equivalent SBR for a typical background level of 10^4 photons would be 0.1. For this case the extinction coefficients would be increased to those indicated in Fig. 8-11. Here the daytime result is about 3.8 and the nighttime about 5.8. It is very important from the standpoint of penetration that the signal processing, detection, and location procedures be optimized to the greatest possible extent. This is an area of great potential gains.

If other parameters are fixed, reducing the bandwidth to 10 Å (1 nm) and raising the peak power to 10 MW (70 mJ pulse energy) leads to daytime extinction coefficients around 5. The maximum depth would then be about 14 m for $K = 0.3 \text{ m}^{-1}$. For the 70 mJ pulse, the extinction coefficient at night would be between 6.6 and 6.8 (depending on the SBR) for 1 na dark current and between 7.3 and 7.8 for 0.1 na dark current. The latter equates to a maximum depth of 21.7 m for $K = 0.3 \text{ m}^{-1}$ and 43.4 m for $K = 0.15 \text{ m}^{-1}$. It is clear that nighttime operation provides distinctly superior performance.

The AOL extrapolation from (Eq. (8-16)) can be compared with model results as a validity check. For nighttime circumstances similar to the AOL test conditions but with a pulse energy of 2 mJ (peak power of 280 kW), the model predicts $nKD_m \approx 5.5$ for a SBR of three which is a best estimate of the AOL detection level. The latter is a bit less than the extrapolated value of 6.3 and is probably more accurate.

8.6 Conclusions

Because of the large attenuation and spreading of a light beam in water, airborne laser hydrography is limited to fairly shallow water. Only in relatively clear waters will daytime depths beyond 30 m be regularly accessible, and 40 - 45 m (depending on the bandwidth of the interference filter) is probably a practical upper limit even for extremely clean water. Penetration at night could be as much as 60 - 70 m in extremely clean water.

There is a great deal of required survey area within these depth bounds where conventional waterborne techniques are very slow and expensive. The prime benefits of airborne laser hydrography are the speed and economy with which these accessible shallow areas can be surveyed.

System penetration and accuracy performance and cost/benefit advantages are clearly superior at night. Cost/benefit calculations and preliminary operational procedure plans have been based on total flight times of only 12 hours per week. It is logical that these hours be flown at night. It is important that the system design be clearly optimized for nighttime operation. In order to maximize performance, daytime operations would best be limited to reconnaissance duties whenever possible.

8.7 Acknowledgments

I would like to recognize the invaluable contribution of Bob Thomas in developing the Monte Carlo propagation simulation upon which many of these results are based. I would also like to thank Scott Stickles who gave unselfishly of his time in assisting with the analytic description of the simulation outputs.

8.8 References

Contarino, V.M., (The Pennsylvania State University, Radnor Center for Graduate Studies) 1981: An Experimental Laser Radar Receiver for Airborne Ocean Bottom Profilimetry. Masters Term Paper, 55 pp.

Duntley, S.Q., 1971: Underwater Lighting by Submerged Lasers and Incandescent Sources. SIO Ref. 71-1, Office of Naval Research Contract No. 00014-69-A-0200-6013 Final Report, Scripps Institution of Oceanography, Visibility Laboratory, San Diego, Calif., 261 pp.

Guenther, G.C. and Thomas, R.W.L., 1981a: Monte Carlo Simulations of the Effects of Underwater Propagation on the Penetration and Depth Measurement Bias of an Airborne Laser Bathymeter. NOAA Technical Memorandum OTES 01, National Oceanic and Atmospheric Administration, U.S. Department of Commerce, Washington, D.C., 144 pp.

Guenther, G.C. and Thomas, R.W.L., 1981b: Simulations of the Impact of Inhomogeneous Water Columns on the Temporal Stretching of Laser Bathymeter Pulses. NOAA Technical Report OTES 02, National Oceanic and Atmospheric Administration, U.S. Department of Commerce, Washington, D.C., 39 pp.

Guenther, G.C., and Thomas, R.W.L., 1984: Prediction and Correction of Propagation-Induced Depth Measurement Biases plus Signal Attenuation and Beam Spreading for Airborne Laser Hydrography. NOAA Technical Report NOS 106 CGS 2, National Oceanic and Atmospheric Administration, U.S. Department of Commerce, Washington, D.C., 112 pp.

Houck, Max (Naval Ocean R&D Activity, Code 550, NSTL Station, Miss.) 1982 (personal communication).

Levis, C.A., Swarner, W.G., Prettyman, C., and Reinhardt, G.W., 1974: An Optical Radar for Airborne Use Over Natural Waters. Proc. of Symposium on the Use of Lasers for Hydrographic Studies, September 12, 1973, NASA/Wallops Flight Center, Wallops Island, Va., U.S. National Aeronautics and Space Administration, Wallops Island, Va., 67-80.

Miller, Merlin (AVCO Everett Research Laboratory, Inc., Everett, Mass.) 1981 (personal communication).

Phillips, D.M. and Abbot, R.H., 1981: An Aerial Survey of Water Turbidity and Laser Depth Sounding Performance Along the Queensland Coast. Electronics Research Laboratory Technical Report ERL-0192-TR, Defence Science and Technology Organization, Defence Research Centre Salisbury, South Australia, 19 pp.

Witt, A.K., Shannon, J.G., Rankin, M.B., and Fuchs, L.A., 1976: Air/Underwater Laser Radar Test Results, Analysis, and Performance Predictions. Report No. NADC-76005-20. Naval Air Development Center, Warminster, Pa., 293 pp. (CONFIDENTIAL).

9.0 DEPTH MEASUREMENT ACCURACY

9.1 Introduction

9.1.1 Background

Depth measurement accuracy and maximum penetration depth are two of the most important performance parameters of an airborne lidar hydrography system. They are interrelated in that the maximum penetration is defined as the depth at which the measurement errors become unacceptably large. Penetration implies not just the capability to detect but also to accurately locate a return signal. Useful penetration is limited, therefore, not by detection but by the accuracy requirement which is the primary concept upon which system design must be predicated.

The ultimate accuracy of such a system depends on parameters in three general areas: the environment, the hardware (including signal processing), and post-flight error corrections based on error prediction models. Each of these categories has a number of specific errors associated with it. The resultant error from all sources in all categories combined must fall within the hydrographic standards being met. International hydrographic standards currently require an accuracy no worse than ± 30 cm to a depth of 30 m and ± 1 m to a 100-m depth. Since no statistical interpretation accompanies these bounds, their application is unclear. For practical reasons, an RMS or 1σ value will be assumed.

One must also consider whether every laser sounding must individually achieve the standard or only specially processed and "selected" soundings at a density appropriate for the survey scale. This is an important consideration because of the reduction of random errors which can be achieved by various spatial averaging techniques. Since the density of soundings laid down can greatly exceed the number which can be handled by regional data centers or put on charts, the sounding-selection process is a very important area which must be addressed before a system is fielded.

The detailed design of an airborne lidar bathymetric system (consisting of a laser transmitter, scanner and receiver optics, data acquisition electronics, data recording, analysis, and control computer, and integrated attitude, navigation, and positioning electronics) is extremely complex and involves a number of difficult hardware tradeoffs at a state-of-the-art level. It is vital that no hardware configuration be selected before a careful analysis is performed to determine the impact of that design on the inherent accuracy potential of the instrument. In order to determine under what conditions (if any) a given system can meet the required accuracy specification, all potential error sources must be quantified for a wide variety of controllable and uncontrollable, measurable and unmeasurable parameters such as water optical properties, wind speed, surface waves, water depth, off-nadir scanner angle, non-linear processing techniques, and pulse location algorithm. A number of such error sources and their functionalities are reported in this section.

9.1.2 Error Handling Procedures

Measurement errors are customarily divided into two major categories: "random" variations about some mean value (imprecision) and "systematic" offsets (bias). In a complex system such as an airborne lidar bathymeter, this simplistic description is potentially misleading. In general, an error magnitude can depend on the value of a particular parameter. If, under certain circumstances, that parameter is fixed or remains nearly constant, the resultant error is a "bias". Under other circumstances, the parameter may vary in some random or at least uncontrolled manner; under such conditions the resulting error will appear as a loss of precision. To further complicate the picture, bias-type errors can be modeled over a parameter set and the predicted magnitude subtracted from the measurements in a post-processing step. The remaining error is then the difference between the actual error and the predicted error. This may look like a loss of precision against some parameters and a bias error against other parameters. If the bias model contains parameters for which values cannot be obtained, the estimation of these unknown values will lead to systematic errors which may appear to be precision or bias errors depending on the rate of change in the unknown parameter. The rate of change of these "variable biases" compared to some

time frame of interest is thus the primary factor which determines whether an error is handled as an imprecision or as a bias.

The time frame of interest for airborne laser hydrography is on the order of a few minutes -- the time it takes to fly a "line" of hydrography. Errors which vary in a random, bipolar manner within a line will be dealt with in terms of "precision"; errors which vary from line to line will be considered to be biases. This is an important distinction to make, because when dealing with several precision-type errors one can use an RMS value; when dealing with several known biases, the full range or peak-to-peak values of their sum must be maintained within the error budget. Because biases add algebraically, their functionalities should be modeled and the estimates used to correct the data sets wherever possible. If unmodeled, statistically independent peak biases are added in quadrature (which is perhaps the only practical way to report their net effect), it must be understood that a certain percentage of measurements, i.e., whole lines, could incur a net bias in excess of the quoted value (when driving parameters are such that they all happen to add in the same direction).

Random errors are typically described in terms of their root-mean-square (RMS) magnitude. Such errors add in quadrature, i.e., as the root sum of squares of the RMS values. If n random errors, each of RMS magnitude, M , are added, the resultant RMS magnitude is $M\sqrt{n}$. As will be seen, the number of potential depth measurement error sources associated with airborne lidar bathymeters is large; assuming $n \sim 9$ results in $\sqrt{n} = 3$. If the hydrographic accuracy requirement of ± 30 cm is considered to be an RMS (1σ) value, then the maximum RMS random error permitted from each individual source is less than $\pm 30/3 = \pm 10$ cm. This number will be used wherever possible to establish constraints in the bounds of the variables and parameters defining the operational window for subsequent error model analysis predictions.

Although certain hydrographers may balk at using a 1σ definition, for which 32 percent of the errors are larger than the stated bound, it is doubtful that the error potential of airborne laser hydrography is better than this, over a broad range of circumstances. Many feel that if operational sonar were subjected to the same level of analysis, the errors would be no

smaller. Individual prospective users must accept the tradeoff between extreme accuracy and added utility.

9.1.3 Outline

Section 9.2 covers environmentally induced errors. These basic errors will affect all systems (although the magnitudes of some such errors depend on the exact signal processing hardware and software). Section 9.3 reviews error sources related to signal acquisition and processing. The error magnitudes and behavior, which depend strongly on the particular system design and operational parameters, will be examined for two very different signal processing concepts.

9.2 Environment-Based Errors

9.2.1 Propagation-Induced Pulse Stretching and Geometry

9.2.1.1 Background

Of the many error sources associated with airborne laser hydrography, one of the potentially most serious is the effect of underwater light propagation, i.e., the scattering of the optical beam into a cone of continually increasing angle as seen in Fig. 4-1. The basic premise of airborne laser hydrography is that the water depth can be determined by measuring the round-trip transit time for a short-duration light pulse which travels to the bottom and back to the surface along a fixed path at a known angle from the vertical. This model does not take into consideration the spreading of the beam in the water caused by scattering from entrained organic and inorganic particulate materials.

Lidar bottom return pulses vary considerably in shape and arrival time depending on the water depth, the scanner angle, the incident laser pulse width, the optical properties of the water, the airborne system signal processing electronics, and the depth determining algorithm or procedure. These perturbations of the return signals will cause depth measurement biases which can be quite large. Depth measurement biases are calculated as differences from the expected round-trip time for the unscattered or

"reference" path. Analytical computations by Thomas and Guenther (1979) indicated the probability of a significant bias on the deep side for operations of the system at nadir. This bias arises from the multiple scattering mechanism by which the laser radiation is transported through the water. This is the so-called "pulse stretching" effect. For off-nadir beam entry angles, undercutting causes the peak in the energy density distribution at the bottom to be closer to the aircraft than the unscattered ray (Fig. 4-8), because the shorter paths are less attenuated. For off-nadir angles, two competing effects thus exist -- the path lengthening due to multiple scattering, and a path shortening due to energy returning early from the "undercutting" region. The net result is a bias in the measured slant range which can be either deep or shallow. The relative magnitudes of these effects depend strongly on the beam entry nadir angle and the optical properties of the water, but, in general, the magnitude of the net bias can greatly exceed international hydrographic accuracy standards.

The impact of these effects on the estimated depth is influenced both by the temporal profile of the incident laser pulse and the return pulse processing electronics, but the key to the quantification of the effect is the generation of a set of response functions for the medium which characterize the temporal history of the radiation reaching the receiver for an impulse input. In other words, the first step in the estimation of these bias errors is the determination of the impulse response functions (IRFs) of the medium for various permutations of the relevant optical parameters.

Although various approximations can be made, the formal analytical problem is virtually intractable due to the complexity of the multiple scattering. A Monte Carlo simulation is the only practical method of generating realistic impulse response functions. Indeed, if other theories existed for computing these functions, they would need to be subjected to simulation validation in order to be confident that the generated functions were appropriate to the specified inherent properties of the water column. As introduced in section 6, a Monte Carlo propagation simulation including scattering, absorption, and geometry effects has been exercised (Guenther and Thomas 1981a) to determine the bottom return IRFs at an airborne receiver as a function of nadir angle, depth, phase function, optical depth, and single-

scattering albedo. The water parameters and system constraints of the computations are appropriate to airborne laser hydrography systems presently under consideration for use in coastal waters. The basic integrity of the simulation has been successfully validated by comparing energy decay rates with previously documented relationships from the literature, such as the ratio of diffuse to beam attenuation coefficients versus single-scattering albedo (Gordon et al. 1975, Timofeyeva and Gorobets 1967). Detailed descriptions of physical processes, simulation mechanics, and validation criteria are discussed in Guenther and Thomas 1984b and reviewed in sections 4 and 6. Highlights and summary information are reported here to emphasize general procedures, trends, and results. Results pertaining to spatial distributions and penetration were reported in section 8.

An output data set consisting of 540 impulse response functions derived for various parameter sets has been generated. Example IRFs are seen in Fig. 9-1. It is important to note that although the signal attenuation is a function of KD, the IRF shape is a function of αD and not KD. This is illustrated in Fig. 9-2 where very different IRFs result from equal values of KD.

The actual bottom return pulses arriving at an airborne receiver from the environment (and hence termed the "environmental response functions" or ERFs) can be predicted by convolving depth-scaled IRFs with the incident source pulse from the laser transmitter. Typical bottom returns and peak power results have been calculated by digitally convolving the depth-scaled IRFs with an incident laser source pulse of triangular shape having a half width (FWHM) of 7 ns. This pulse shape is a reasonable representation of the bulk of the output pulse from a state-of-the-art, high repetition rate, Nd:YAG blue-green laser. Example ERFs are seen in Fig. 9-3.

Depth measurement biases have been calculated (Guenther and Thomas 1981b, 1984a,b) by applying several diverse signal processing and pulse location algorithms to these ERFs: a straightforward amplitude threshold proportional to the peak height applied to the linear input (the so-called linear fractional threshold or LFT) and the complex HALS protocol (for the U.S. Navy's Hydrographic Airborne Laser Sounder) which involves logarithmic amplification,

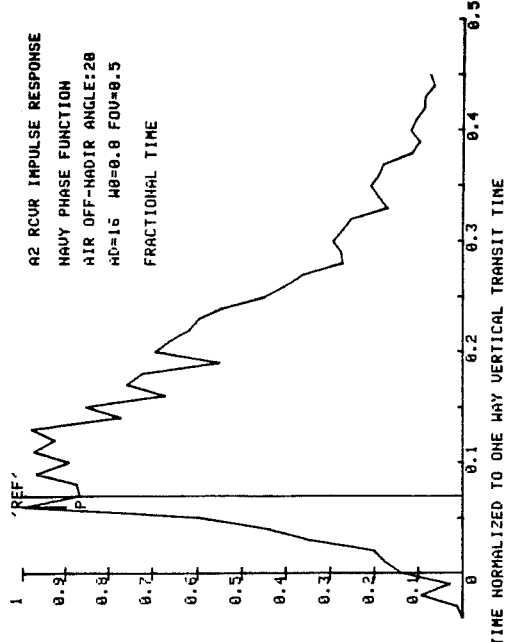
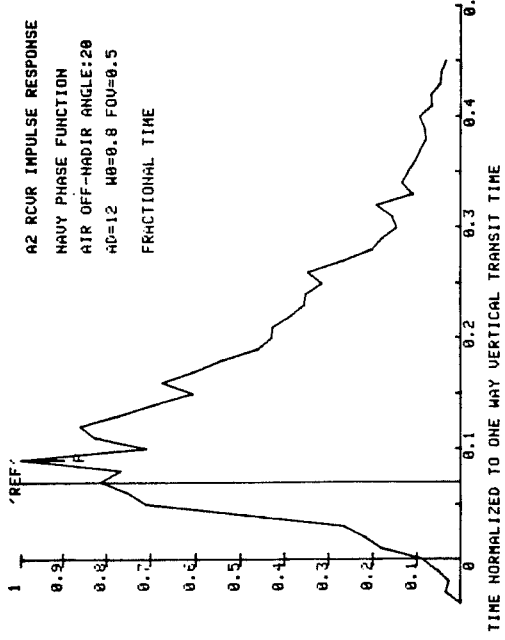
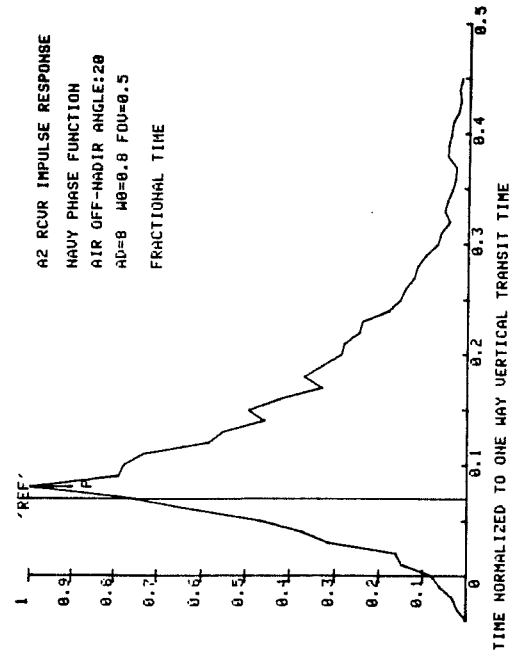
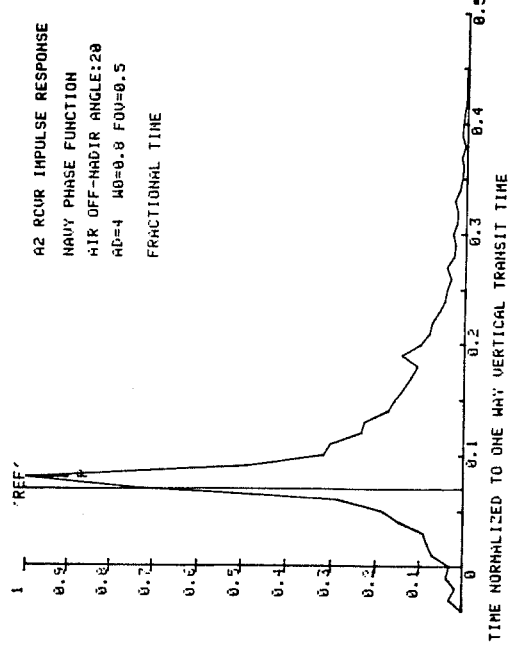


FIGURE 9-1. IMPULSE RESPONSE FUNCTIONS FOR VARYING OPTICAL DEPTHS

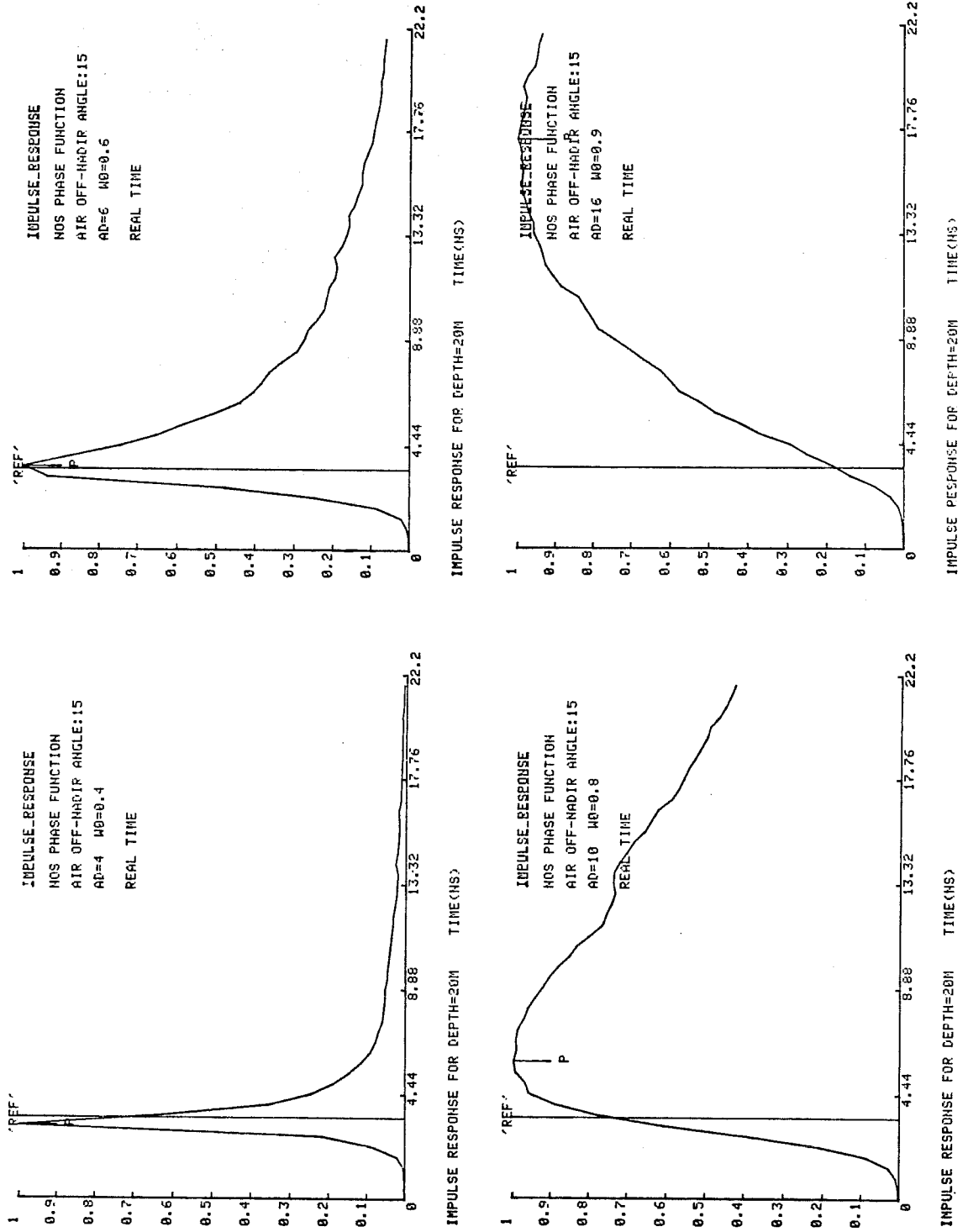
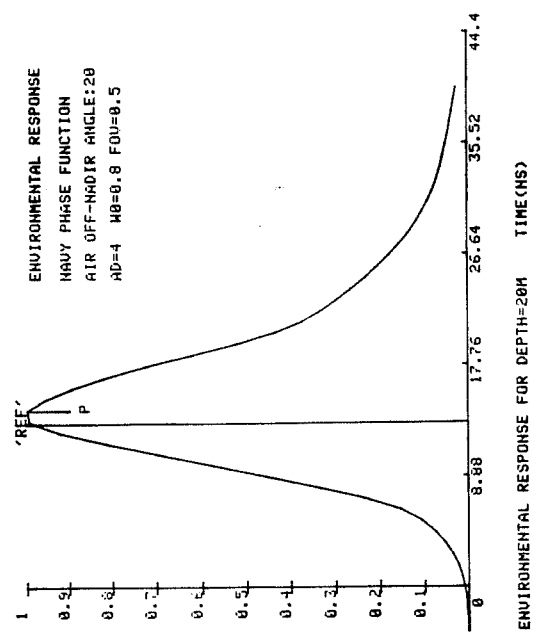
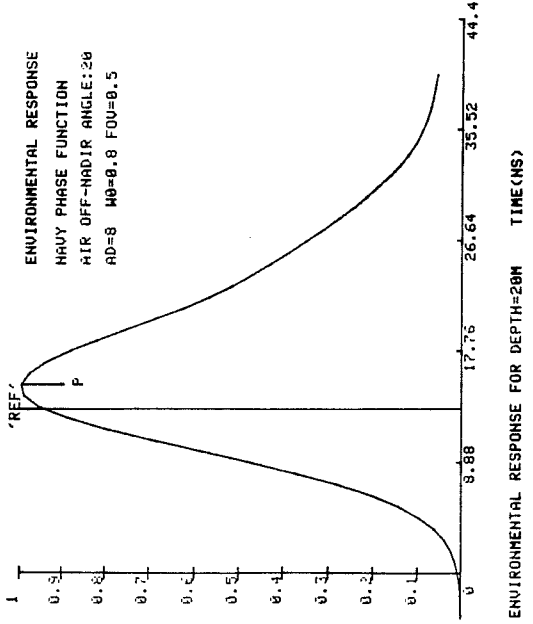


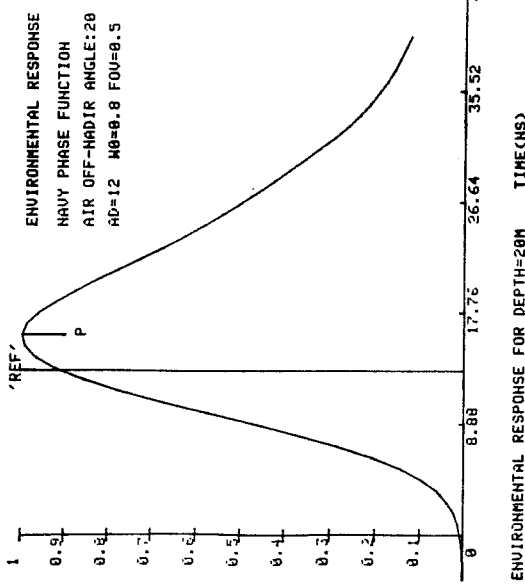
Figure 9-2. Impulse Response Functions with Constant K_D ($=3$)



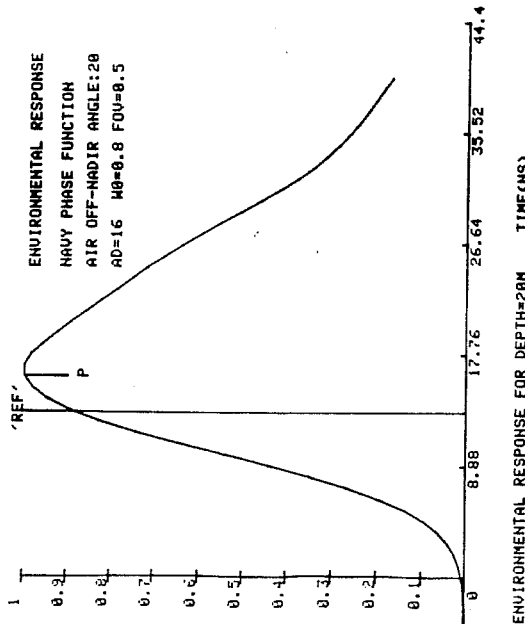
ENVIRONMENTAL RESPONSE FOR DEPTH=20M TIME(纳秒)



ENVIRONMENTAL RESPONSE FOR DEPTH=20M TIME(纳秒)



ENVIRONMENTAL RESPONSE FOR DEPTH=20M TIME(纳秒)



ENVIRONMENTAL RESPONSE FOR DEPTH=20M TIME(纳秒)

FIGURE 9-3. ENVIRONMENTAL RESPONSE FUNCTIONS

FOR VARYING OPTICAL DEPTHS

a time-delayed difference operation, and pulse location by a constant fraction discriminator (CFD) algorithm. Further details of the HALS processing can be found in Guenther (1982). It is very important that the propagation-induced biases be accurately calculated, because if the predicted biases exceed an acceptable magnitude, they can, at least conceptually, be applied to field data as bias correctors in a post-flight processing step to maintain system performance within the error budget.

The first simulations performed were for homogeneous scattering media only. In other words, it was assumed that the density and nature of the scattering particles in water were independent of depth. It is well known, however, that significant departures from homogeneity occur frequently in coastal waters. It was important, therefore, to assess the potential for error in using homogeneous case corrections when significant departures from homogeneity occur. The existing Monte Carlo radiative transfer simulation program was modified (Guenther and Thomas 1981c) to allow convenient simultaneous estimation of the IRFs for a number of different vertical distributions of scatterers and absorbers, as seen in Fig. 6-4. Outputs were obtained for vertical optical depths up to 16, six different values of single-scatter albedo, and input nadir angles of 0 and 25 degrees. The resulting IRF's were digitally convolved with a 7-ns triangular source pulse to produce the ERF's. Linear fractional threshold pulse locators were applied to the ERF's to determine the bias errors and the differences in bias errors between the homogeneous case and the various inhomogeneous models. The results for these exaggerated inhomogeneities indicate that the use of bias correctors derived for the homogeneous case should result in errors of less than 10 cm.

The magnitudes of the bias correctors depend not only on the water and flight parameters, but also on the basic design of the receiver elements. In practice, because of the extremely large dynamic range inherent in incoming pulse amplitudes (as much as seven decades), some form of amplitude compression will generally be required in the receiver hardware. Any form of non-linear signal processing has the potential to alter the biases significantly from those for linearly processed signals. The most commonly used compression technique, logarithmic amplification, causes an extreme alteration in the shape of the leading edge of the pulse and a correspondingly

large change in depth measurement biases resulting from locators applied to these distorted pulses.

Depth measurement bias predictions are necessarily parameterized on their driving inherent water properties (such as beam attenuation coefficient and single-scattering albedo) and system variables such as beam nadir angle. If all these parameters are known or can be estimated, the bias predictions obtained from the appropriate ERFs can be applied to field data as bias correctors to greatly reduce the magnitude of the raw biases in post-processing. As will be seen in the next subsections, the biases are large enough for most circumstances that some type of bias correction procedure is considered mandatory if international hydrographic accuracy standards are to be met. It will thus be necessary either to provide continuous estimates of key water optical properties based solely on specially processed, ancillary flight data, or to restrict operational parameters in such a way that the resulting variation in biases with unknown water parameters falls within the error budget. Estimation of the relevant inherent water parameters from ancillary airborne lidar data poses a significant problem which could strongly impact system hardware design and data processing requirements. Potential estimation techniques are discussed after the bias functionalities are reported.

9.2.1.2 Bias Computation

For a given set of depth-specific bottom return pulses (ERFs) parameterized on beam nadir angle and water optical properties, the first step in calculating depth measurement bias predictions is the modeling of the various signal processing and pulse location estimation procedures. After the appropriate transfer functions have operated on the input signals, the apparent depth is calculated from the time interval between the detection locations of the surface return and bottom return pulses. For the reported biases, the source pulse was used directly as the surface return pulse (a mirror-like reflection from a flat surface), and a common pulse location algorithm was applied to each. It is conceivable that separate optimization of the surface and bottom return detection algorithms might be desirable. If so, locating the two pulses at different thresholds, for example, would cause

an additional bias which depends only on the shape of the interface return and which could be removed with a pre-calculated corrector.

Linear fractional threshold detections are obtained directly from the ERFs. Because the HALS processing involves two time-delayed differences, however, the resulting pulse detection time depends not only on the shape of the ERF, but also on the log slope of the volume backscatter signal which precedes it. The effect can be quite significant in "dirty" waters where the backscatter slope is steep. In order to provide accurate bias predictors for the case of HALS processing, the specific volume backscatter signal associated with each ERF has been appended to the start of that ERF.

For a given ERF, the parameters αD , D , and ω_0 are specified. The value of α is thus known, and given ω_0 , the K/α ratio can be derived from the "best fit" relationship shown in Fig. 3-7. K is thus uniquely defined for each ERF. The decay of the volume backscatter power is exponential in time with a log slope roughly equal to $-cK$, where c is the speed of light in water. For HALS processing, the volume backscatter signal for each ERF is constructed in log space by extrapolating a line of appropriate slope backward from the first point of the logged ERF. This composite signal is then further processed, as follows.

Three waveforms associated with the log/difference/CFD process are seen in Fig. 9-4. At the top is the logged ERF input with associated volume backscatter tail; in the middle is the output of the delayed difference operation; and at the bottom is an internal CFD signal for which the positive-going zero crossing is the detection point. The delayed difference operation applied to the decaying volume backscatter signal produces a constant negative level into the CFD which violates one of the assumptions associated with performance of the CFD circuit. The negative input level, whose magnitude increases with decreasing water clarity, causes delayed detections and leads to added positive biases which depend on the delay times, water clarity, signal-to-background ratio, etc. These perturbations of the propagation-induced biases by the processing protocol automatically become part of the final results, however, and need not be separately handled.

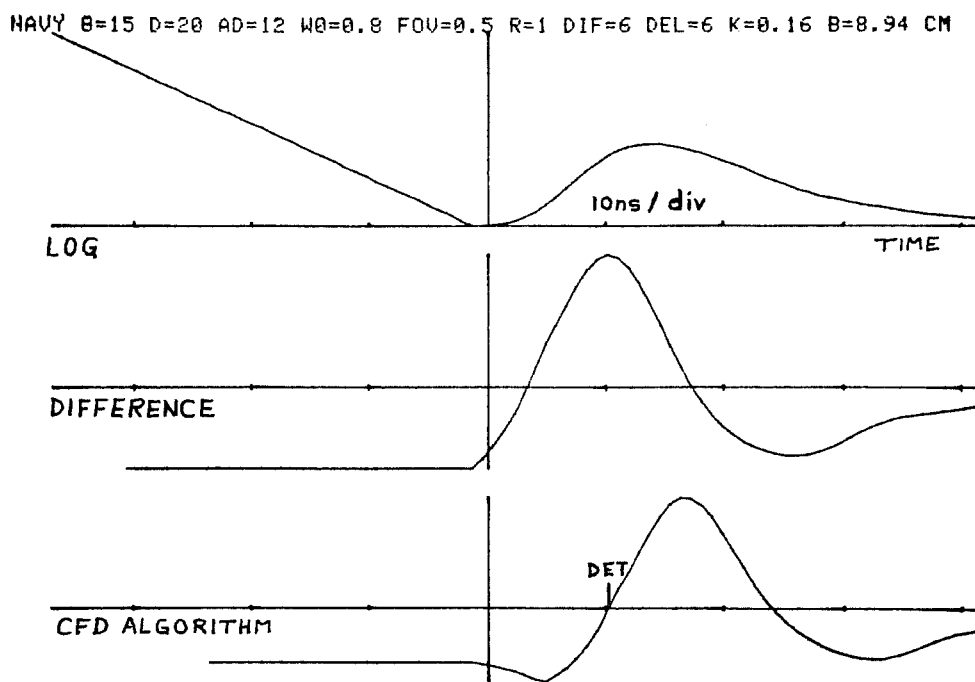


FIGURE 9-4. TYPICAL CFD WAVEFORMS

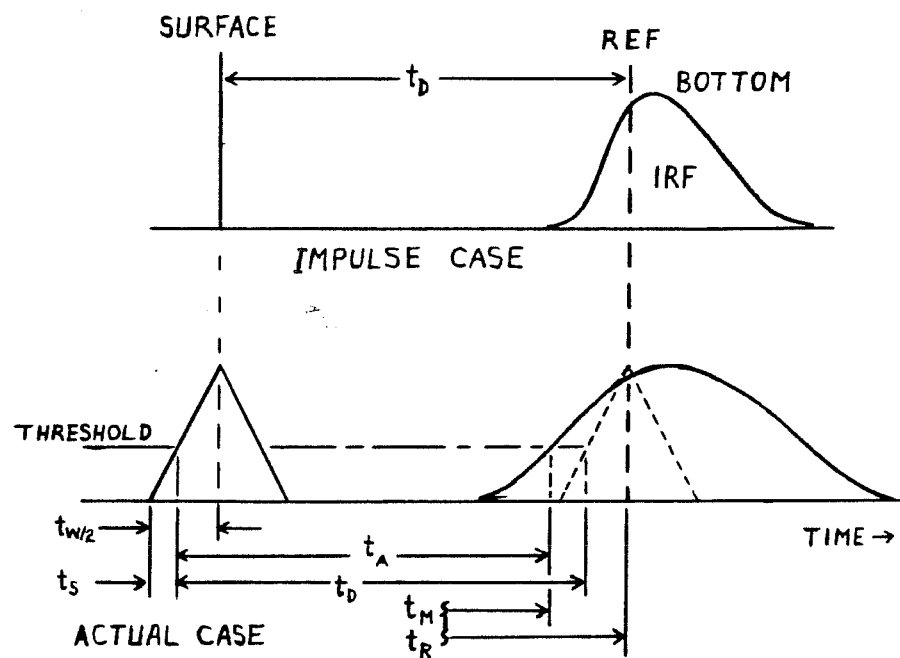


FIGURE 9-5. BIAS CALCULATION TIMING DIAGRAM

The bias calculation for any signal processing and pulse location algorithm is based on the timing diagram shown in Fig. 9-5, where t_D is the time associated with the "true" slant range, and t_A is the time associated with the "apparent" slant range measure at the detection point. The "measured" bottom pulse location time, t_M , for a given algorithm and the "reference" time, t_R , for the unscattered ray can be measured from any consistent starting time, as long as it is the same for both, because only their difference is important. The surface pulse half-width (half base width or FWHM) is $t_W/2$, and the surface pulse location time, t_S , is measured from the start of that pulse. It can be seen in Fig. 9-5 that t_D and t_A are related by the expression

$$t_D = t_S + t_A + t_R - t_M - t_W/2. \quad (9-1)$$

The slant range bias time, t_B , is then

$$t_B \equiv t_A - t_D = t_M - t_R - t_S + t_W/2, \quad (9-2)$$

and the associated depth measurement bias will be $B = (c t_B \cos\phi)/2$, where B is positive for "deep" biases and negative for shallow biases. To calculate the bias time, t_B , one obtains $t_M - t_R$ from the processed bottom return pulse and t_S from the processed surface return pulse. As was noted in Guenther (1982) for HALS processing, the detection time, t_S , on a high signal-to-background ratio (P_m/B) triangular pulse is equal to the CFD delay. The CFD delay has thus been used for t_S in calculating HALS biases. This relationship becomes less exact for $P_m/B \gtrsim 10$ and for significantly different pulse shapes. If extremely weak or highly distorted surface returns were encountered, a set of correctors (parameterized on P_m/B) would be necessary. HALS biases are small but non-zero at $\alpha D=0$ due to the P_m/B effect.

Biases were calculated for all combinations of physical depth, receiver parameters, pulse location algorithms, and relevant water optical properties (phase function, optical depth, and single-scattering albedo). The biases and their functionalities are discussed in the following subsections.

9.2.1.3 Bias Sensitivities

Because the depths are measured with leading edge pulse location algorithms, the biases are based primarily on the photons which traverse the shortest, and hence least attenuated paths. The shape of the leading edge is thus largely determined by the scattering, rather than the absorption characteristics of the water. It makes sense, therefore, to consider the scattering optical depth, $sD = \omega_0 \alpha D$, the mean number of scattering events to the bottom, as a likely candidate for the major functional bias dependence, regardless of separate values of ω_0 and αD . Wilson (1979) showed similar functionalities for the radiance and irradiance distributions.

This relationship is demonstrated for LFT at 25 degrees off nadir with the NAVY phase function in Fig. 9-6. The three curves in each family are for ω_0 values of 0.9, 0.8, and 0.6. The groupings, in general, are relatively tight regardless of nadir angle, depth, or processing protocol, although the groups exhibit less variation for LFT processing than for the more complex and non-linear CFD processing. Similar groupings occur for the NOS phase function but at somewhat different bias values. This is a useful result because it reduces the number of bias-driving parameters whose values are not known a priori from three (phase function, αD , and ω_0) to two (phase function and $\omega_0 \alpha D$).

Figures of bias functionalities supporting the text are plotted with either optical depth or scattering optical depth as the independent variable. Optical depth has been used at times for clarity or convenience, often where a single "average" value such as $\omega_0=0.8$ is plotted. In such cases the results may be easily generalized by multiplying the abscissa values by the appropriate ω_0 . Note for all bias plots: under ALG for "algorithm", the description block in the figures lists an "L" for LFT followed by the threshold fraction in parentheses or a "C" for CFD followed by values for P_m/B and the CFD delay in nanoseconds, respectively. All HALS examples shown are for a difference operation with a 6-ns delay.

The sD dependence is by no means "perfect" because of the effects of signal processing. For example, with HALS-type processing, the effect of the

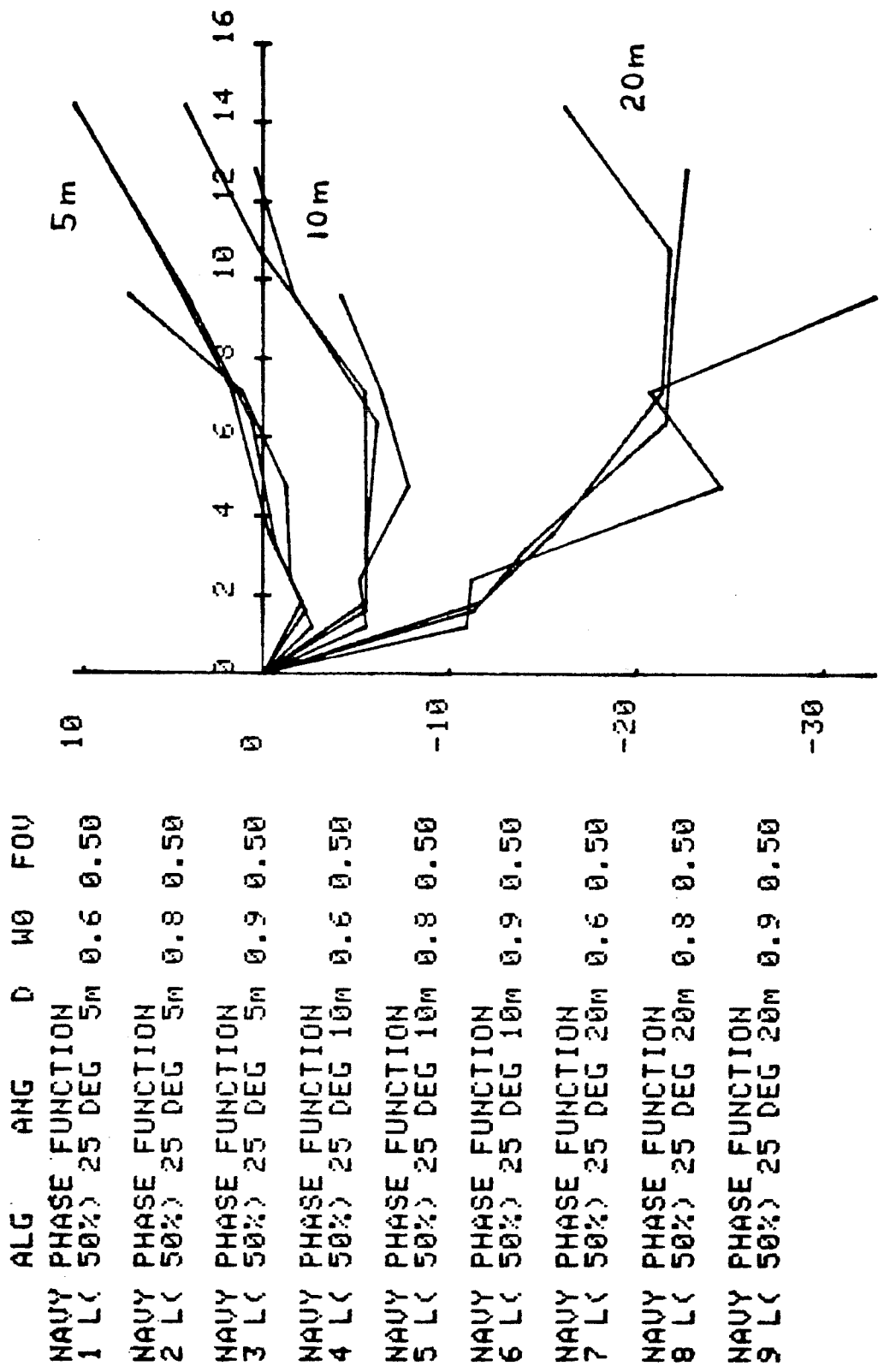


Figure 9-6. DEPTH MEASUREMENT BIAS (CM) VS SCATTERING OPTICAL DEPTH

volume backscatter signal competes with the ω_0 effect. By itself, small ω_0 leads to more negative biases due to higher absorption and an emphasis on the shortest path -- which is in the undercutting region. On the other hand, for a given α , lower ω_0 leads to higher values of K and larger negative input levels to the CFD from the backscatter signal. This, in turn, leads to delayed detections and subsequently more positive biases, particularly at shallow depths and low P_m/B . This is strikingly evident at 5-m depths. The net results of this competition are depth and ω_0 effects which are somewhat different for HALS processing than for LFT.

Two phase functions from Petzold (1972), one for relatively "clean" or "NAVY" water and one for relatively "dirty" or "NOS" water, have been selected as representative bounding cases for natural coastal waters of interest. The phase function effect is demonstrated in Figs. 9-7 and 9-8. For nadir angles of 10° or more, the differences are typically under 10 cm between the phase functions. These bias differences are considered to be small enough that an average value between the two can be used for bias prediction. For that reason, much of the following demonstration of bias sensitivities will highlight only one, the "NAVY" phase function.

The effects of the air nadir angle on bias for depths of 5 m, 10 m, 20 m, and 40 m are seen in Figs. 9-9 - 9-12 and 9-13 - 9-16 for LFT and HALS respectively. Note in each case the orderly progression toward more negative (shallow) biases as the nadir angle increases. This is due to the proportionately larger effect of "undercutting" at larger incident angles. It can be seen that there is tremendous variation in both the bias trends and magnitudes for the two different processing and pulse location protocols. The HALS log/difference/CFD biases are consistently more negative due mostly to later detection on the surface return but also partly to earlier detection on the leading edge of propagation-stretched bottom returns. Note also the tendency toward larger biases (both positive and negative) at larger physical depths due to the fact that the depth acts as a scaling factor for the normalized time delays. The effect of physical depth for constant nadir angles is illustrated directly in Figs. 9-17 and 9-18.

ALG ANG D W0 FOU
 NAVY PHASE FUNCTION
 1 L(50%) 10 DEG 10m 0.8 0.50
 NOS PHASE FUNCTION
 2 L(50%) 10 DEG 10m 0.8 0.50
 NAVY PHASE FUNCTION
 3 L(50%) 10 DEG 20m 0.8 0.50
 NOS PHASE FUNCTION
 4 L(50%) 10 DEG 20m 0.8 0.50
 NAVY PHASE FUNCTION
 5 L(50%) 20 DEG 10m 0.8 0.50
 NOS PHASE FUNCTION
 6 L(50%) 20 DEG 10m 0.8 0.50
 NAVY PHASE FUNCTION
 7 L(50%) 20 DEG 20m 0.8 0.50
 NOS PHASE FUNCTION
 8 L(50%) 20 DEG 20m 0.8 0.50

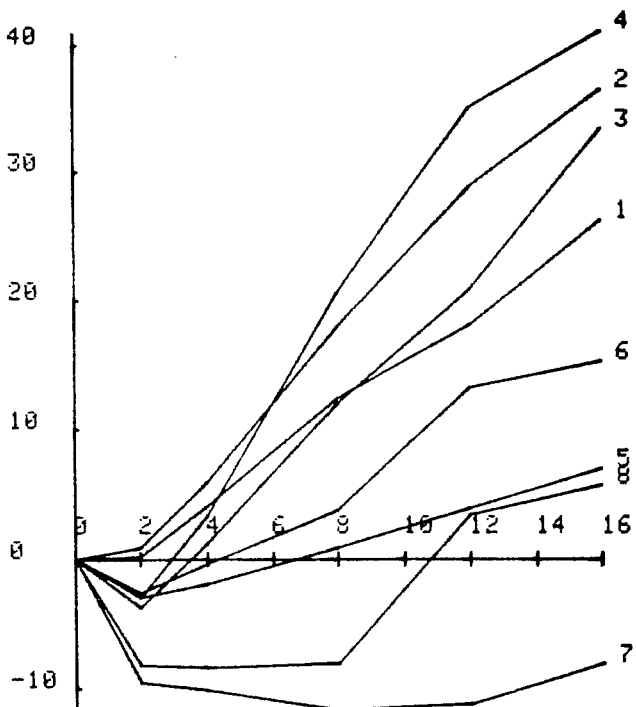


FIGURE 9-7. DEPTH MEASUREMENT BIAS (CM) VS OPTICAL DEPTH

ALG ANG D W0 FOU
 NAVY PHASE FUNCTION
 1 C(3, 6) 10 DEG 10m 0.8 0.50
 NOS PHASE FUNCTION
 2 C(3, 6) 10 DEG 10m 0.8 0.50
 NAVY PHASE FUNCTION
 3 C(3, 6) 10 DEG 20m 0.8 0.50
 NOS PHASE FUNCTION
 4 C(3, 6) 10 DEG 20m 0.8 0.50
 NAVY PHASE FUNCTION
 5 C(3, 6) 20 DEG 10m 0.8 0.50
 NOS PHASE FUNCTION
 6 C(3, 6) 20 DEG 10m 0.8 0.50
 NAVY PHASE FUNCTION
 7 C(3, 6) 20 DEG 20m 0.8 0.50
 NOS PHASE FUNCTION
 8 C(3, 6) 20 DEG 20m 0.8 0.50

$\Delta = 6 \text{ ns}$

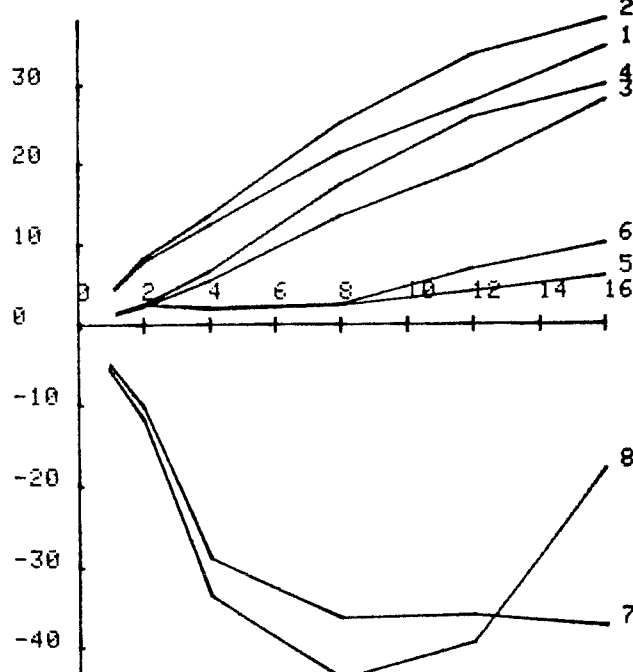


FIGURE 9-8. DEPTH MEASUREMENT BIAS (CM) VS OPTICAL DEPTH

ALG ANG D W0 FOU
 NAVY PHASE FUNCTION
 1 LC 50% 0 DEG 5m 0.8 0.50
 NAVY PHASE FUNCTION
 2 LC 50% 10 DEG 5m 0.8 0.50
 NAVY PHASE FUNCTION
 3 LC 50% 15 DEG 5m 0.8 0.50
 NAVY PHASE FUNCTION
 4 LC 50% 20 DEG 5m 0.8 0.50
 NAVY PHASE FUNCTION
 5 LC 50% 25 DEG 5m 0.8 0.50
 NAVY PHASE FUNCTION
 6 LC 50% 30 DEG 5m 0.8 0.50

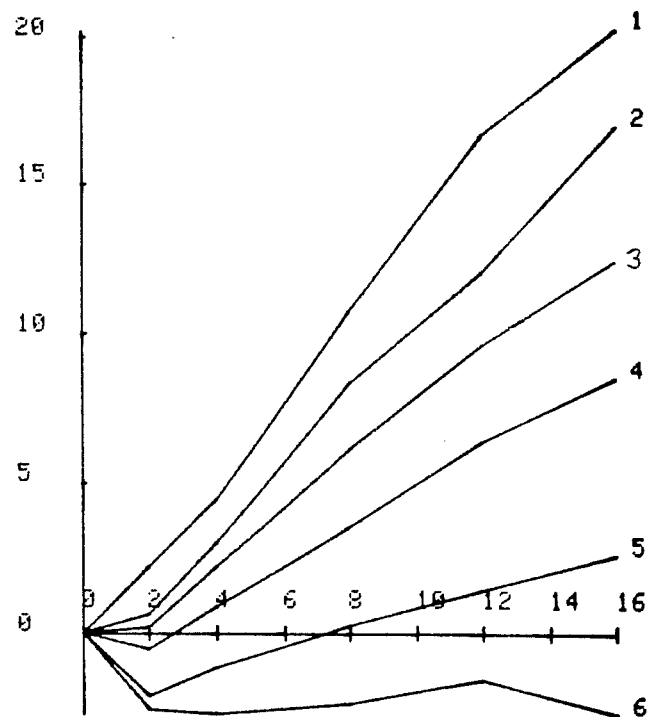


FIGURE 9-9. DEPTH MEASUREMENT BIAS (CM) VS OPTICAL DEPTH

ALG ANG D W0 FOU
 NAVY PHASE FUNCTION
 1 LC 50% 0 DEG 10m 0.8 0.50
 NAVY PHASE FUNCTION
 2 LC 50% 10 DEG 10m 0.8 0.50
 NAVY PHASE FUNCTION
 3 LC 50% 15 DEG 10m 0.8 0.50
 NAVY PHASE FUNCTION
 4 LC 50% 20 DEG 10m 0.8 0.50
 NAVY PHASE FUNCTION
 5 LC 50% 25 DEG 10m 0.8 0.50
 NAVY PHASE FUNCTION
 6 LC 50% 30 DEG 10m 0.8 0.50

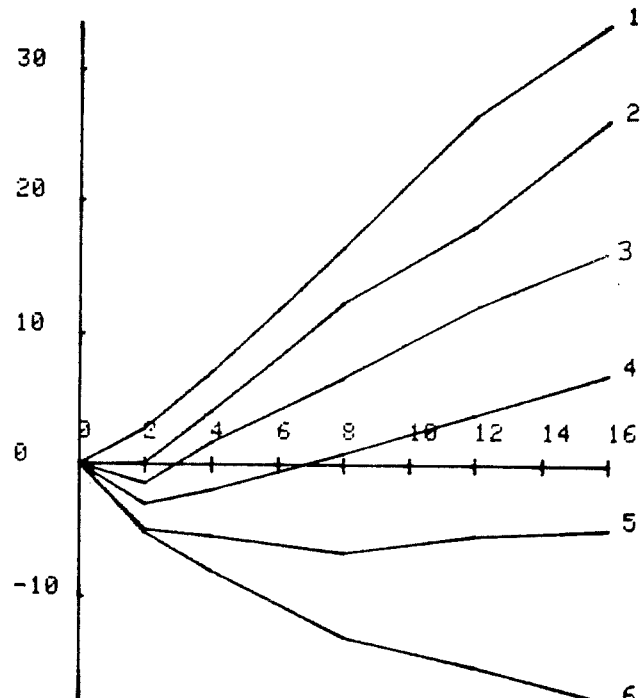


FIGURE 9-10. DEPTH MEASUREMENT BIAS (CM) VS OPTICAL DEPTH

ALG ANG D W0 FOU
 NAVY PHASE FUNCTION
 1 L(50%) 0 DEG 20m 0.8 0.50
 NAVY PHASE FUNCTION
 2 L(50%) 10 DEG 20m 0.8 0.50
 NAVY PHASE FUNCTION
 3 L(50%) 15 DEG 20m 0.8 0.50
 NAVY PHASE FUNCTION
 4 L(50%) 20 DEG 20m 0.8 0.50
 NAVY PHASE FUNCTION
 5 L(50%) 25 DEG 20m 0.8 0.50
 NAVY PHASE FUNCTION
 6 L(50%) 30 DEG 20m 0.8 0.50

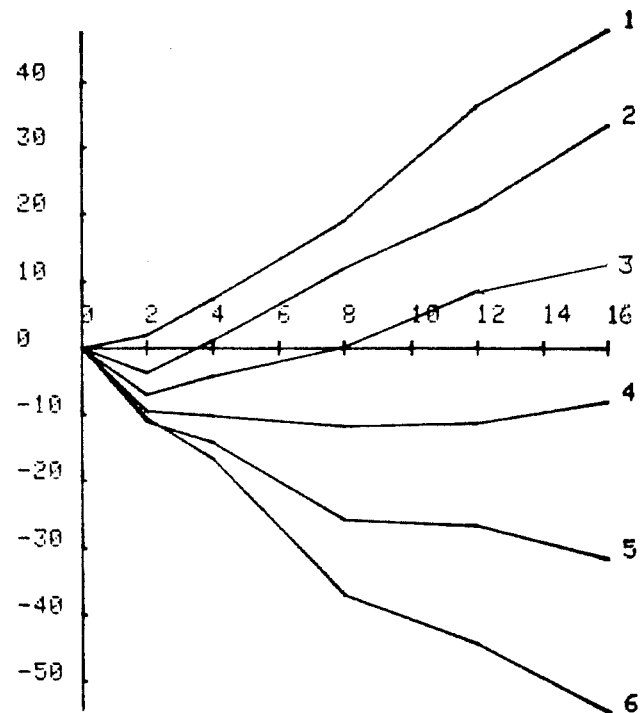


FIGURE 9-11. DEPTH MEASUREMENT BIAS (CM) VS OPTICAL DEPTH

ALG ANG D W0 FOU
 NAVY PHASE FUNCTION
 1 L(50%) 0 DEG 40m 0.8 0.50
 NAVY PHASE FUNCTION
 2 L(50%) 10 DEG 40m 0.8 0.50
 NAVY PHASE FUNCTION
 3 L(50%) 15 DEG 40m 0.8 0.50
 NAVY PHASE FUNCTION
 4 L(50%) 20 DEG 40m 0.8 0.50
 NAVY PHASE FUNCTION
 5 L(50%) 25 DEG 40m 0.8 0.50
 NAVY PHASE FUNCTION
 6 L(50%) 30 DEG 40m 0.8 0.50

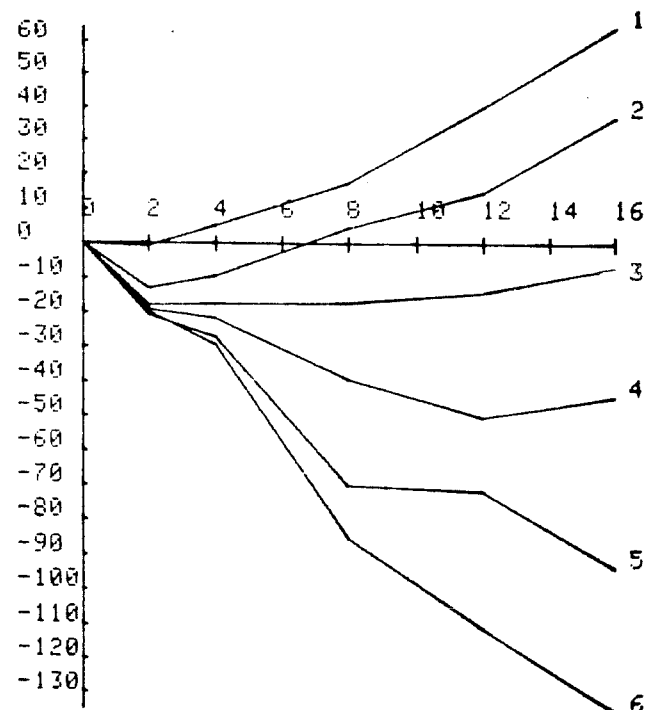


FIGURE 9-12. DEPTH MEASUREMENT BIAS (CM) VS OPTICAL DEPTH

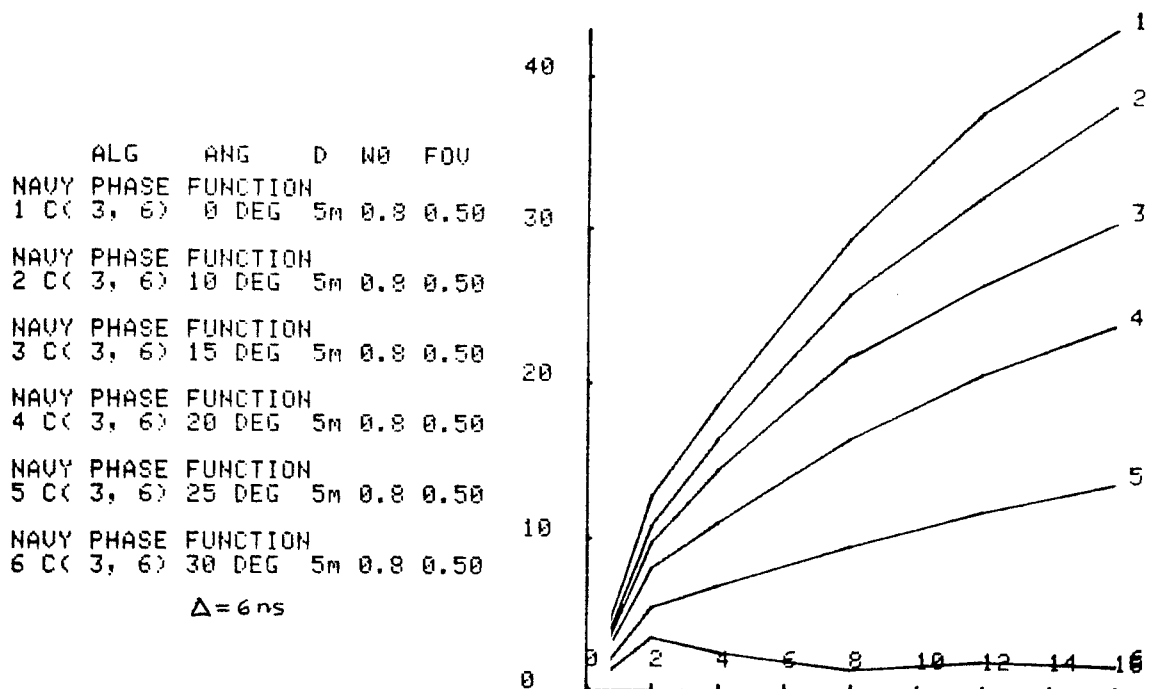


FIGURE 9-13. DEPTH MEASUREMENT BIAS (CM) VS OPTICAL DEPTH

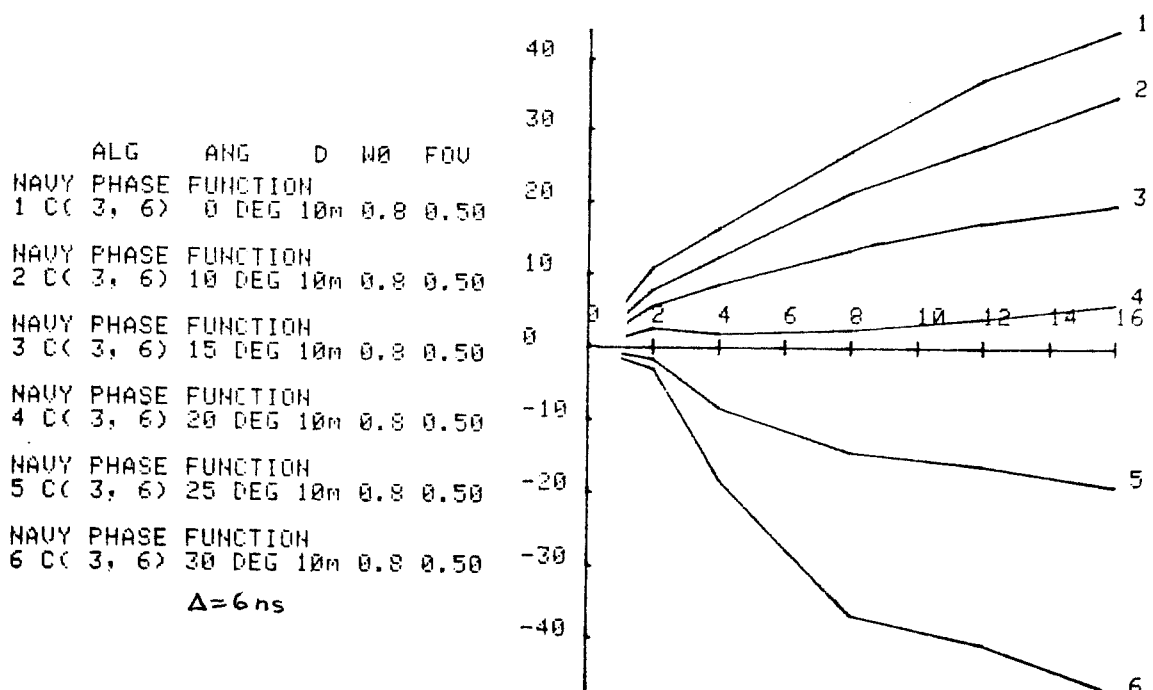


FIGURE 9-14. DEPTH MEASUREMENT BIAS (CM) VS OPTICAL DEPTH

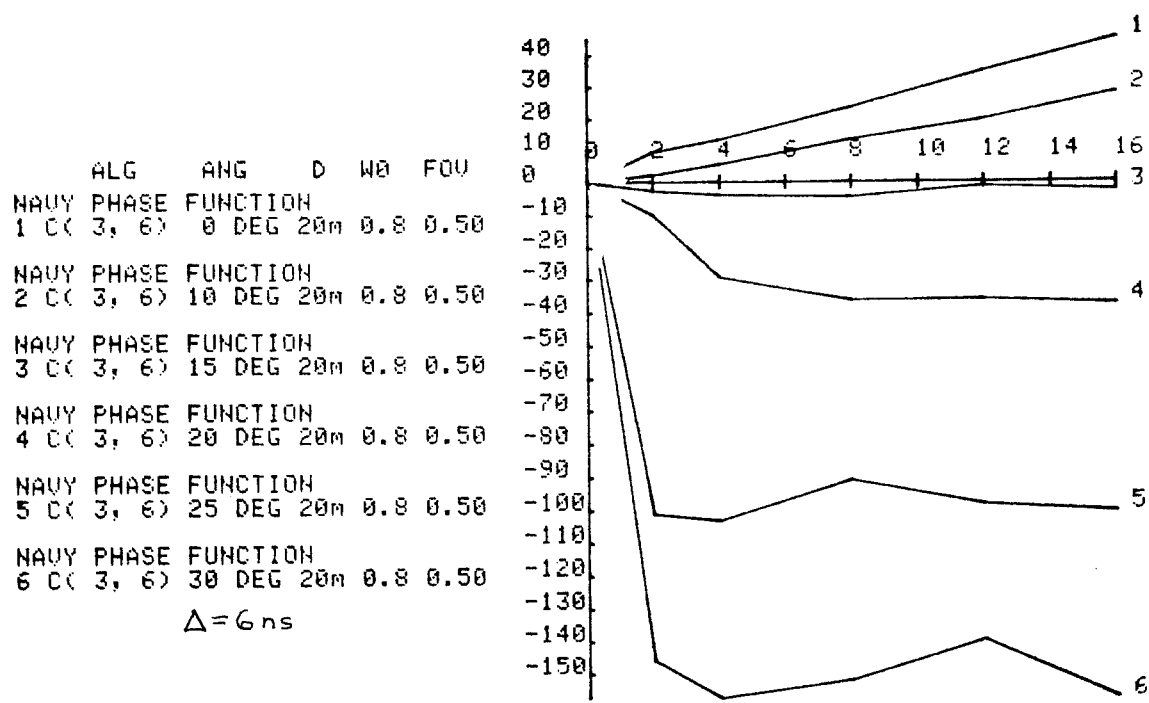


FIGURE 9-15. DEPTH MEASUREMENT BIAS (CM) VS OPTICAL DEPTH

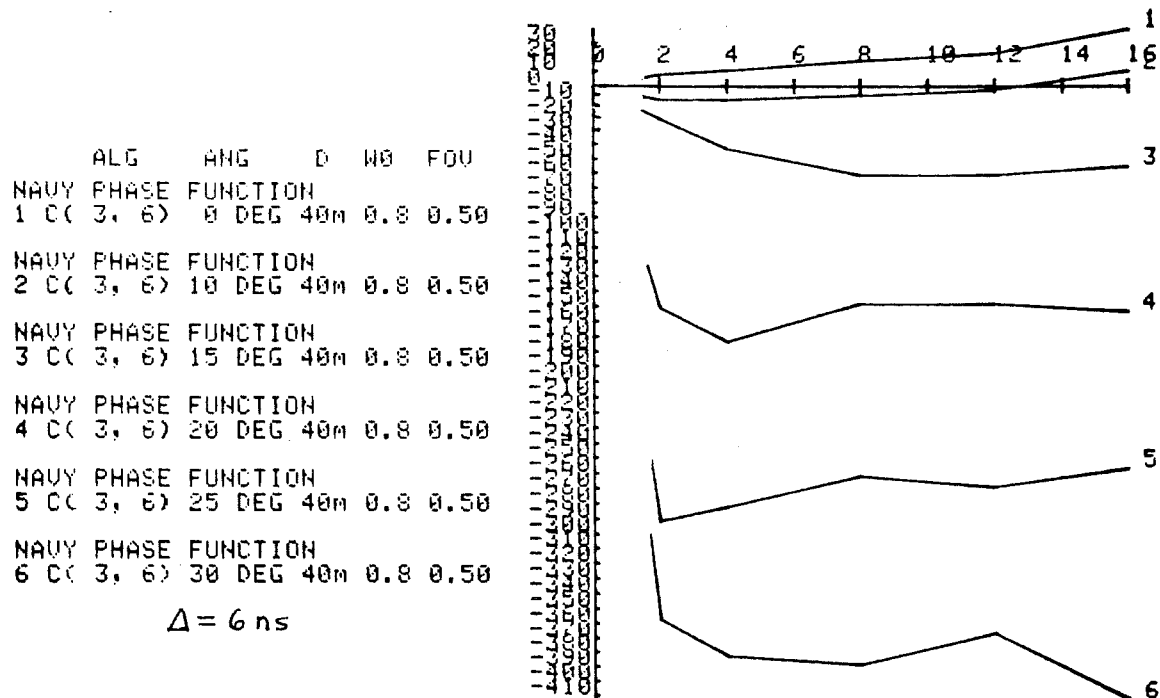


FIGURE 9-16. DEPTH MEASUREMENT BIAS (CM) VS OPTICAL DEPTH

	ALG	ANG	D	W0	FOV
1	NAVY PHASE FUNCTION	LC(50%)	20 DEG	5m	0.8 0.50
2	NAVY PHASE FUNCTION	LC(50%)	20 DEG	10m	0.8 0.50
3	NAVY PHASE FUNCTION	LC(50%)	20 DEG	20m	0.8 0.50
4	NAVY PHASE FUNCTION	LC(50%)	20 DEG	40m	0.8 0.50
5	NAVY PHASE FUNCTION	LC(50%)	25 DEG	5m	0.8 0.50
6	NAVY PHASE FUNCTION	LC(50%)	25 DEG	10m	0.8 0.50
7	NAVY PHASE FUNCTION	LC(50%)	25 DEG	20m	0.8 0.50
8	NAVY PHASE FUNCTION	LC(50%)	25 DEG	40m	0.8 0.50

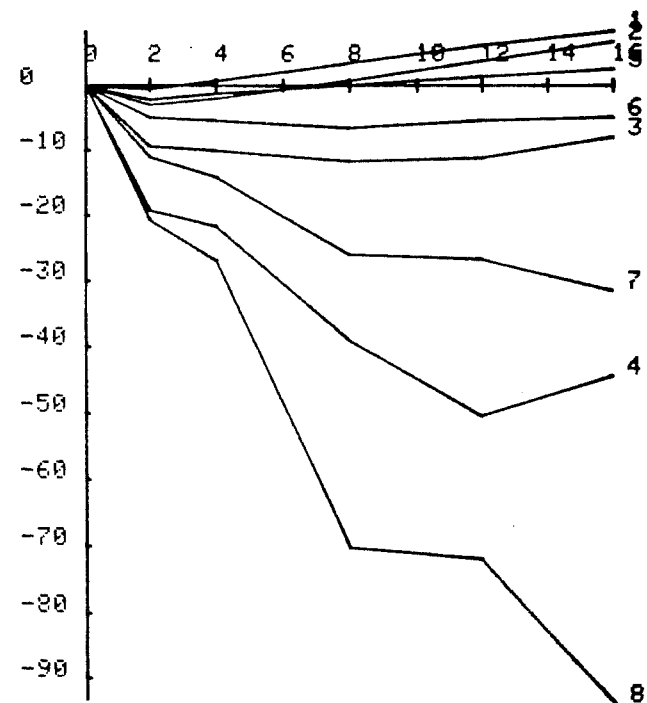


FIGURE 9-17. DEPTH MEASUREMENT BIAS (CM) VS OPTICAL DEPTH

	ALG	ANG	D	W0	FOV
1	NAVY PHASE FUNCTION	CC(3, 6)	15 DEG	5m	0.8 0.50
2	NAVY PHASE FUNCTION	CC(3, 6)	15 DEG	10m	0.8 0.50
3	NAVY PHASE FUNCTION	CC(3, 6)	15 DEG	20m	0.8 0.50
4	NAVY PHASE FUNCTION	CC(3, 6)	15 DEG	40m	0.8 0.50
5	NAVY PHASE FUNCTION	CC(3, 6)	20 DEG	5m	0.8 0.50
6	NAVY PHASE FUNCTION	CC(3, 6)	20 DEG	10m	0.8 0.50
7	NAVY PHASE FUNCTION	CC(3, 6)	20 DEG	20m	0.8 0.50
8	NAVY PHASE FUNCTION	CC(3, 6)	20 DEG	40m	0.8 0.50

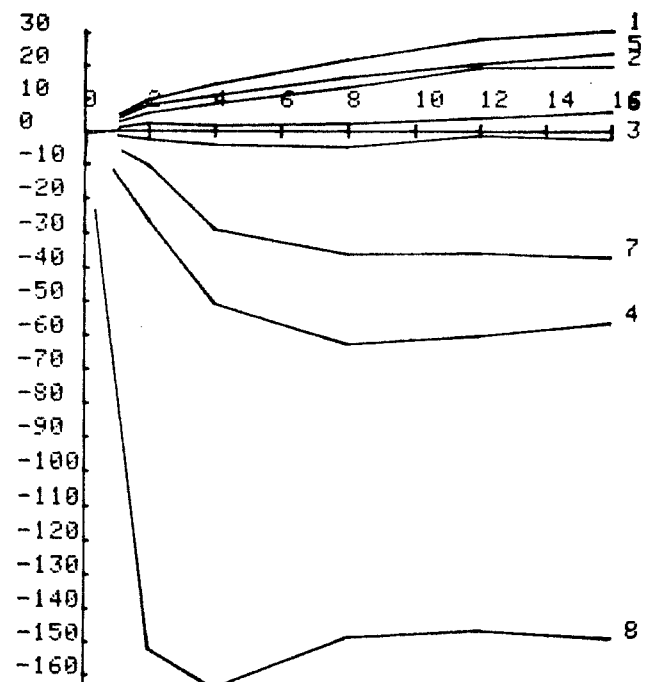


FIGURE 9-18. DEPTH MEASUREMENT BIAS (CM) VS OPTICAL DEPTH

It may be noted in Figs. 9-15, 9-16, and 9-18 that the HALS biases for large nadir angles and moderate-to-large depths become very large and negative for optical depths as small as 2. By analyzing the waveforms, it can be seen that these biases are real but an artifact of the processing. The algorithm detects prior to the desired time because of the existence in these cases of a plateau very close to the zero level in the internal CFD signal on which positive-going zero crossings are detected. This effect is undesirable because a small variation in return shape, receiver field of view, or a small amount of noise can cause a huge variation (and hence error) in the measured depths. This is a serious problem which would have to be dealt with if the HALS protocol were used operationally.

Since neither phase function, ω_0 , nor α can be practically measured from the air, operational variables such as nadir angle must be purposefully selected to minimize the resulting bias uncertainties. This fact is illustrated in Figs. 9-19 and 9-20 for the nadir case at a depth of 20 m. The biases are large and a strong function of $\omega_0\alpha D$. For LFTs, the uncertainty in phase function alone results in bias uncertainties of 20 cm at high optical depths. For these reasons, operation near nadir is undesirable.

The effect of receiver field of view (FOV) is seen in Figs. 9-21 and 9-22. The parameter used to define FOV in all bias plots is the radius of the spot viewed on the surface by the telescope scaled to the depth of the water (r_s/D). Previous plots have all been for $r_s/D=0.5$ ($d_s/D = 1$), which, as noted earlier, is a value that has been determined to be both appropriate and realizable. Reducing that by a factor of two is seen to have an effect on the biases of typically less than 10 cm. Larger FOVs have slightly larger biases.

The effect of the pulse location threshold fraction at a 20-m depth is demonstrated in Fig. 9-23. The 20% threshold yields more negative biases than the 50% threshold because detection occurs relatively earlier on the stretched bottom return pulse. The reverse is true for the 80% threshold. The variation in bias magnitude with nadir angle is larger for lower thresholds; the higher thresholds are thus preferred. They are also superior from the point of view of precision (section 9.3.1, Guenther and Thomas 1981d) because low thresholds are inherently noisier. Similar relationships apply for other depths.

ALG ANG D W0 FOU
 NAVY PHASE FUNCTION
 1 L(50%) 0 DEG 20m 0.8 0.50
 NAVY PHASE FUNCTION
 2 L(50%) 0 DEG 20m 0.6 0.50
 NOS PHASE FUNCTION
 3 L(50%) 0 DEG 20m 0.9 0.50
 NOS PHASE FUNCTION
 4 L(50%) 0 DEG 20m 0.8 0.50

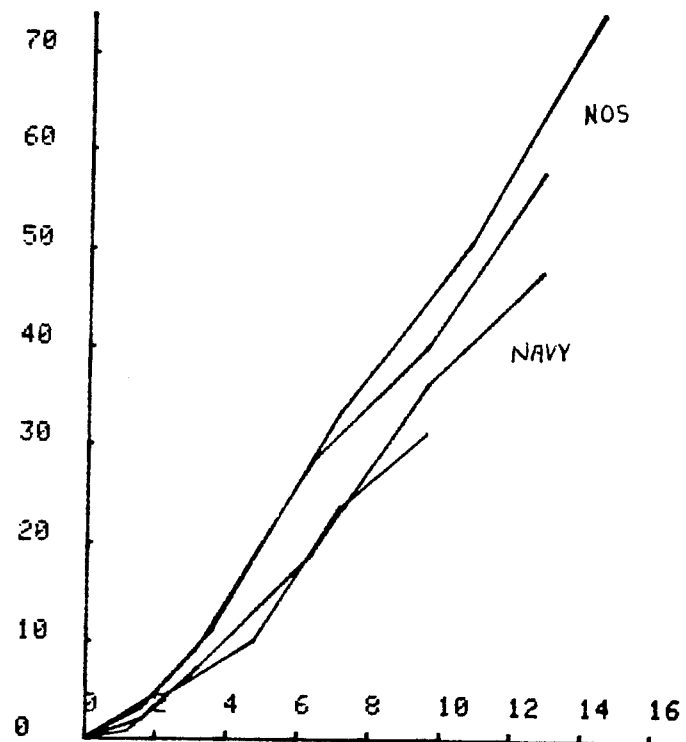


FIGURE 9-19. DEPTH MEASUREMENT BIAS (CM) VS SCATTERING OPTICAL DEPTH

ALG ANG D W0 FOU
 NAVY PHASE FUNCTION
 1 C(3, 6) 0 DEG 20m 0.8 0.50
 NAVY PHASE FUNCTION
 2 C(3, 6) 0 DEG 20m 0.6 0.50
 NOS PHASE FUNCTION
 3 C(3, 6) 0 DEG 20m 0.9 0.50
 NOS PHASE FUNCTION
 4 C(3, 6) 0 DEG 20m 0.8 0.50

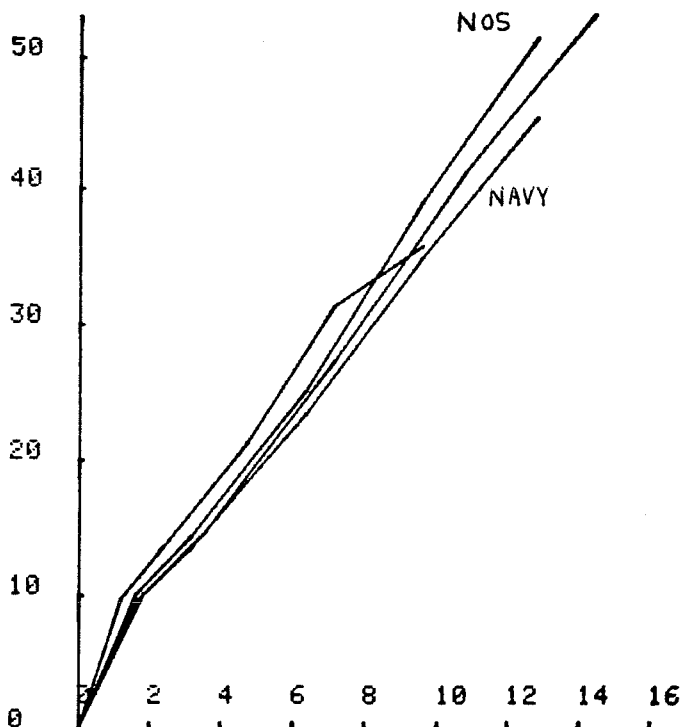


FIGURE 9-20. DEPTH MEASUREMENT BIAS (CM) VS SCATTERING OPTICAL DEPTH

ALG	ANG	D	W0	FOV
NAVY PHASE FUNCTION				
1 L(50%)	10 DEG	10m	0.8	0.25
NAVY PHASE FUNCTION				
2 L(50%)	10 DEG	10m	0.8	0.50
NAVY PHASE FUNCTION				
3 L(50%)	10 DEG	20m	0.8	0.25
NAVY PHASE FUNCTION				
4 L(50%)	10 DEG	20m	0.8	0.50
NAVY PHASE FUNCTION				
5 L(50%)	25 DEG	10m	0.8	0.25
NAVY PHASE FUNCTION				
6 L(50%)	25 DEG	10m	0.8	0.50
NAVY PHASE FUNCTION				
7 L(50%)	25 DEG	20m	0.8	0.25
NAVY PHASE FUNCTION				
8 L(50%)	25 DEG	20m	0.8	0.50

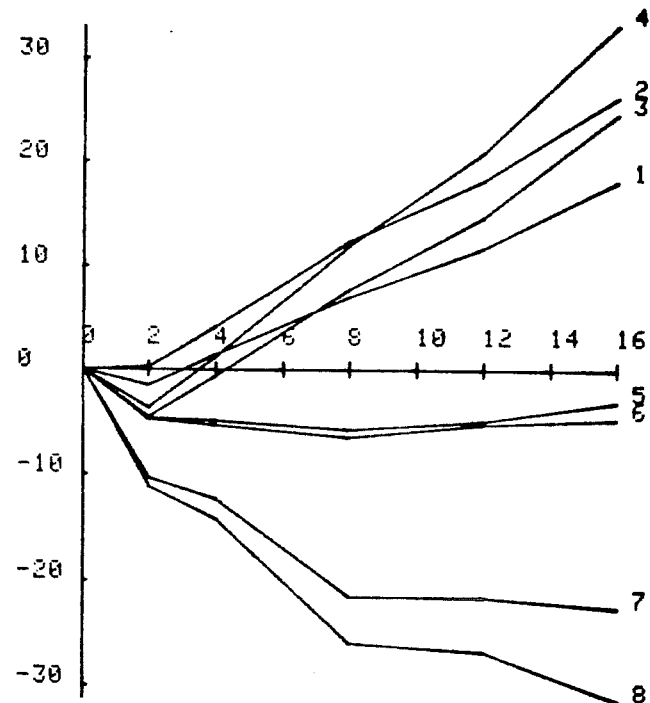


FIGURE 9-21. DEPTH MEASUREMENT BIAS (CM) VS OPTICAL DEPTH

ALG	ANG	D	W0	FOV
NAVY PHASE FUNCTION				
1 C(3, 6)	10 DEG	10m	0.8	0.25
NAVY PHASE FUNCTION				
2 C(3, 6)	10 DEG	10m	0.8	0.50
NAVY PHASE FUNCTION				
3 C(3, 6)	10 DEG	20m	0.8	0.25
NAVY PHASE FUNCTION				
4 C(3, 6)	10 DEG	20m	0.8	0.50
NAVY PHASE FUNCTION				
5 C(3, 6)	20 DEG	10m	0.8	0.25
NAVY PHASE FUNCTION				
6 C(3, 6)	20 DEG	10m	0.8	0.50
NAVY PHASE FUNCTION				
7 C(3, 6)	20 DEG	20m	0.8	0.25
NAVY PHASE FUNCTION				
8 C(3, 6)	20 DEG	20m	0.8	0.50

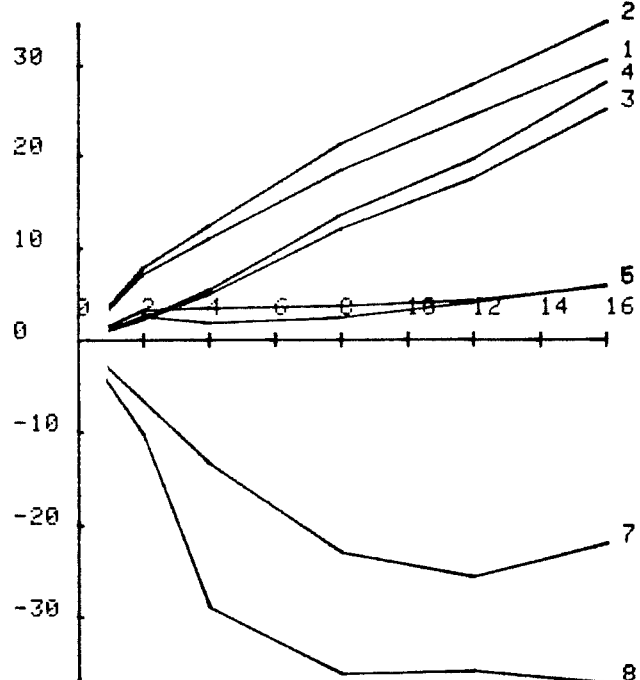


FIGURE 9-22. DEPTH MEASUREMENT BIAS (CM) VS OPTICAL DEPTH

ALG ANG D W0 FOV
 NAVY PHASE FUNCTION
 1 L(20%) 15 DEG 20m 0.8 0.50
 NAVY PHASE FUNCTION
 2 L(50%) 15 DEG 20m 0.8 0.50
 NAVY PHASE FUNCTION
 3 L(80%) 15 DEG 20m 0.8 0.50
 NAVY PHASE FUNCTION
 4 L(20%) 20 DEG 20m 0.8 0.50
 NAVY PHASE FUNCTION
 5 L(50%) 20 DEG 20m 0.8 0.50
 NAVY PHASE FUNCTION
 6 L(80%) 20 DEG 20m 0.8 0.50
 NAVY PHASE FUNCTION
 7 L(20%) 25 DEG 20m 0.8 0.50
 NAVY PHASE FUNCTION
 8 L(50%) 25 DEG 20m 0.8 0.50
 NAVY PHASE FUNCTION
 9 L(80%) 25 DEG 20m 0.8 0.50

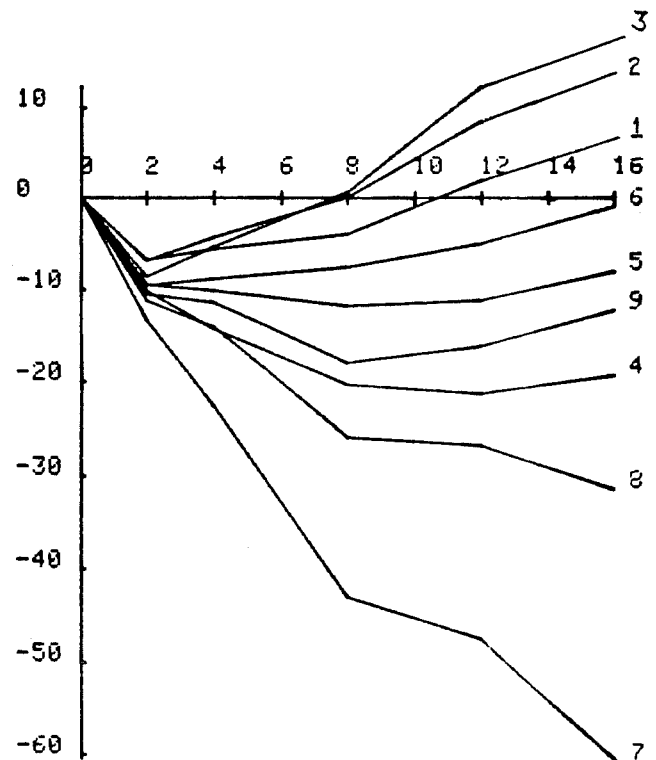


FIGURE 9-23. DEPTH MEASUREMENT BIAS (CM) VS OPTICAL DEPTH

ALG ANG D W0 FOV
 NAVY PHASE FUNCTION
 1 C(3, 3) 10 DEG 20m 0.8 0.50
 NAVY PHASE FUNCTION
 2 C(3, 6) 10 DEG 20m 0.8 0.50
 NAVY PHASE FUNCTION
 3 C(3,10) 10 DEG 20m 0.8 0.50
 NAVY PHASE FUNCTION
 4 C(3, 3) 15 DEG 20m 0.8 0.50
 NAVY PHASE FUNCTION
 5 C(3, 6) 15 DEG 20m 0.8 0.50
 NAVY PHASE FUNCTION
 6 C(3,10) 15 DEG 20m 0.8 0.50
 NAVY PHASE FUNCTION
 7 C(3, 3) 20 DEG 20m 0.8 0.50
 NAVY PHASE FUNCTION
 8 C(3, 6) 20 DEG 20m 0.8 0.50
 NAVY PHASE FUNCTION
 9 C(3,10) 20 DEG 20m 0.8 0.50

$\Delta = 6 \text{ ns}$

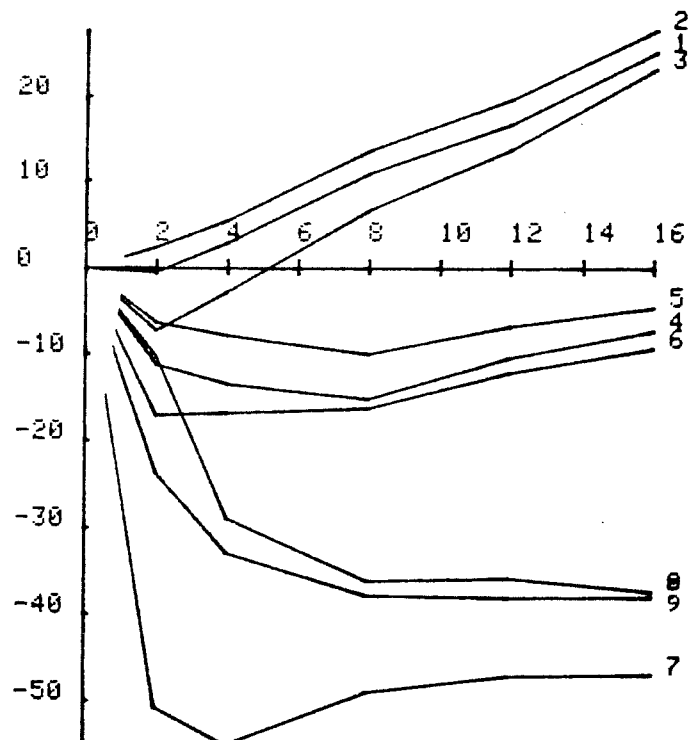


FIGURE 9-24. DEPTH MEASUREMENT BIAS (CM) VS OPTICAL DEPTH

For the HALS processing algorithm, the duration of the difference delay must be roughly equal to the risetime of the source pulse. Shorter values reduce the available signal amplitudes, and longer values lead to large, deep biases and large bias variation (see next subsection) at low depths or optical depths. This is due to distortion of the resulting waveform caused by the influence of the volume backscatter signal which precedes the bottom return. All results presented here are for a difference delay of $\Delta = 6$ ns which nicely matches the 7-ns source risetime used for generating the ERFs.

The analog of LFT fraction for CFDs is the CFD time delay. It has been shown (Guenther 1982) that the ratio of the delay to the pulse risetime for log/difference/CFD processing is roughly equivalent to the threshold fraction for an LFT. The detection points are determined mainly by the delay times, however, and are not as sensitive to pulse shape as those for fractional thresholds. As seen in Fig. 9-24 the effect of the CFD delay on the biases is small, because the detection points shift on the bottom returns by an amount nearly equal to those on the surface returns. The effect of the delay on biases could have been larger, however, were it not for competing effects associated with the volume backscatter slope and the difference operation.

Log/difference/CFD processing has a disadvantage in that there is an additional degree of freedom in the bias dependency -- the so-called P_m/B ratio which is a measure (in linear space) of the peak signal-to-background ratio. Figure 9-25 details the effect of P_m/B on biases for difference and CFD delays of 6 ns and typical P_m/B values of 1, 3, and 10. Note that if P_m/B is not specified in the bias correction procedure, an additional ± 10 cm uncertainty will result. This effect is generally larger than the effect of varying CFD delays. It will be seen shortly that this added error component is unacceptably large if the total bias uncertainty is to be limited to ± 15 cm, and that for this type of processing, P_m/B will need to be estimated for each return.

Bias curves for "typical" operating parameters for a 50% LFT are seen in Figs. 9-26 - 9-28. It can be seen in comparison with earlier figures that selection of the appropriate range of nadir angles (20° - 25° in this case)

ALG ANG D W0 FOU
 NAVY PHASE FUNCTION
 1 C(1, 6) 10 DEG 20m 0.8 0.50
 NAVY PHASE FUNCTION
 2 C(3, 6) 10 DEG 20m 0.8 0.50
 NAVY PHASE FUNCTION
 3 C(10, 6) 10 DEG 20m 0.8 0.50
 NAVY PHASE FUNCTION
 4 C(1, 6) 15 DEG 20m 0.8 0.50
 NAVY PHASE FUNCTION
 5 C(3, 6) 15 DEG 20m 0.8 0.50
 NAVY PHASE FUNCTION
 6 C(10, 6) 15 DEG 20m 0.8 0.50
 NAVY PHASE FUNCTION
 7 C(1, 6) 20 DEG 20m 0.8 0.50
 NAVY PHASE FUNCTION
 8 C(3, 6) 20 DEG 20m 0.8 0.50
 NAVY PHASE FUNCTION
 9 C(10, 6) 20 DEG 20m 0.8 0.50

$\Delta = 6 \text{ ns}$

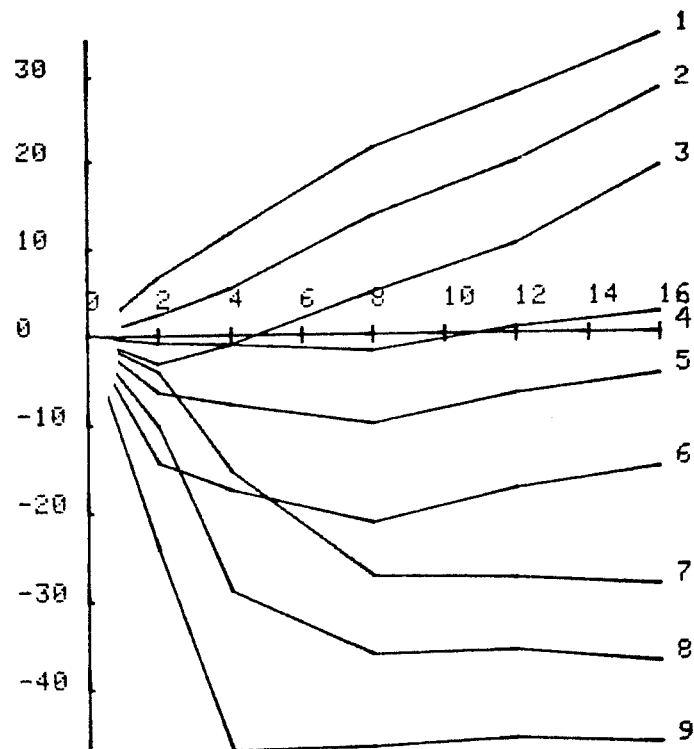


FIGURE 9-25. DEPTH MEASUREMENT BIAS (CM) VS OPTICAL DEPTH

ALG ANG D W0 FOU
 NAVY PHASE FUNCTION
 1 L(50%) 15 DEG 5m 0.6 0.50
 NOS PHASE FUNCTION
 2 L(50%) 15 DEG 5m 0.9 0.50
 NAVY PHASE FUNCTION
 3 L(50%) 15 DEG 10m 0.6 0.50
 NOS PHASE FUNCTION
 4 L(50%) 15 DEG 10m 0.9 0.50
 NAVY PHASE FUNCTION
 5 L(50%) 15 DEG 20m 0.6 0.50
 NOS PHASE FUNCTION
 6 L(50%) 15 DEG 20m 0.9 0.50
 NAVY PHASE FUNCTION
 7 L(50%) 15 DEG 40m 0.6 0.50
 NOS PHASE FUNCTION
 8 L(50%) 15 DEG 40m 0.9 0.50

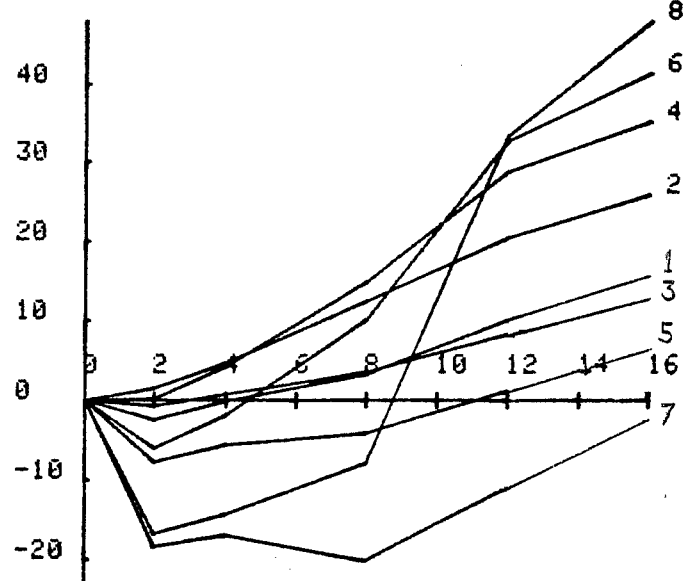


FIGURE 9-26. DEPTH MEASUREMENT BIAS (CM) VS OPTICAL DEPTH

	ALG	ANG	D	W0	FOV
NAVY PHASE FUNCTION	1	L(50%)	20 DEG	5m	0.6 0.50
NOS PHASE FUNCTION	2	L(50%)	20 DEG	5m	0.9 0.50
NAVY PHASE FUNCTION	3	L(50%)	20 DEG	10m	0.6 0.50
NOS PHASE FUNCTION	4	L(50%)	20 DEG	10m	0.9 0.50
NAVY PHASE FUNCTION	5	L(50%)	20 DEG	20m	0.6 0.50
NOS PHASE FUNCTION	6	L(50%)	20 DEG	20m	0.9 0.50
NAVY PHASE FUNCTION	7	L(50%)	20 DEG	40m	0.6 0.50
NOS PHASE FUNCTION	8	L(50%)	20 DEG	40m	0.9 0.50

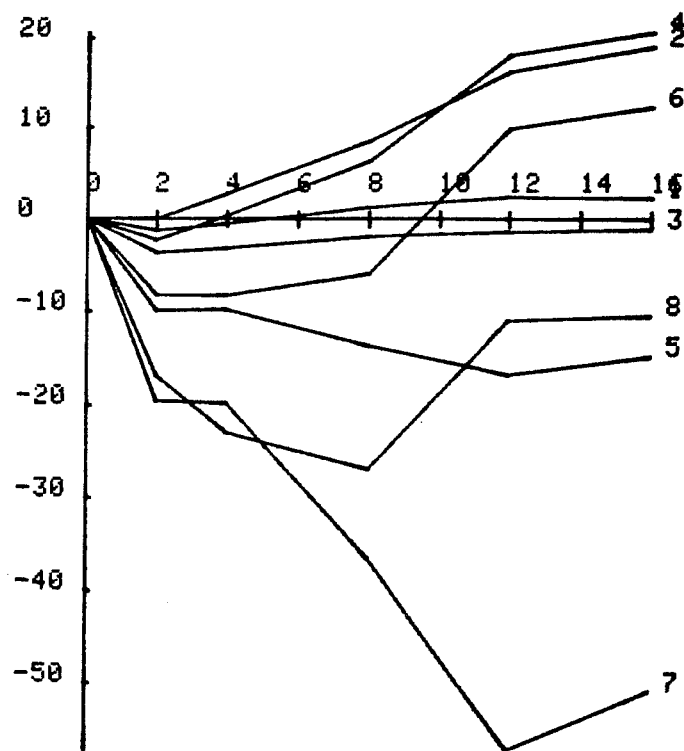


FIGURE 9-27. DEPTH MEASUREMENT BIAS (CM) VS OPTICAL DEPTH

	ALG	ANG	D	W0	FOV
NAVY PHASE FUNCTION	1	L(50%)	25 DEG	5m	0.6 0.50
NOS PHASE FUNCTION	2	L(50%)	25 DEG	5m	0.9 0.50
NAVY PHASE FUNCTION	3	L(50%)	25 DEG	10m	0.6 0.50
NOS PHASE FUNCTION	4	L(50%)	25 DEG	10m	0.9 0.50
NAVY PHASE FUNCTION	5	L(50%)	25 DEG	20m	0.6 0.50
NOS PHASE FUNCTION	6	L(50%)	25 DEG	20m	0.9 0.50
NAVY PHASE FUNCTION	7	L(50%)	25 DEG	40m	0.6 0.50
NOS PHASE FUNCTION	8	L(50%)	25 DEG	40m	0.9 0.50

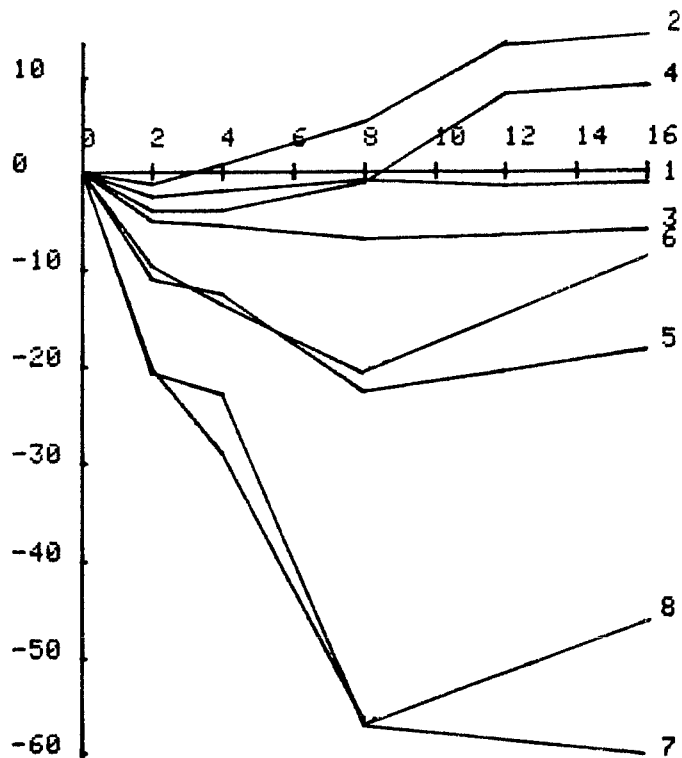


FIGURE 9-28. DEPTH MEASUREMENT BIAS (CM) VS OPTICAL DEPTH

can significantly reduce the bias variation with optical and physical depth. To depths of 20 m, the residual variations are primarily due to phase function and single-scattering albedo. In the 20° - 25° range, the 5 - 20-m biases are seen to be limited to ±20 cm. Biases for greater depths become increasingly shallow.

Biases for a range of "typical" operating conditions for HALS log/difference/CFD processing are seen in Figs. 9-29 and 9-30 for the two phase functions. The overall ranges of biases are larger than for a 50% LFT, and are larger even for single P_m/B values. The 15° nadir angle which balances the bias range about zero is significantly smaller than that for LFTs (20° - 25°).

9.2.1.4 Bias Variation

For bias correction purposes, predicted biases can be utilized only to the extent that the driving independent parameters are known. During flight operations, those parameters which are known or can be reasonably estimated are nadir angle, water depth, processing protocol, receiver field of view, and, if necessary, peak signal-to-background ratio. Water optical parameters which are unknown and difficult to estimate in real time from lidar returns are phase function and scattering optical depth. The critical question is to what accuracy the biases can be predicted without the latter information. As will now be seen, detailed knowledge of water optical properties is not necessary for satisfactory bias correction accuracy if the scanner nadir angle is appropriately limited to a value which produces minimum bias variation for unknown conditions.

For various combinations of known parameters, the bounding bias predictions, based on total uncertainty in phase function and scattering optical depth, have been extracted from the data base. For this procedure, ω_0 values of 0.6 and 0.8 were associated with the NAVY phase function, and 0.8 and 0.9 with the NOS. The optical depth was considered unknown over the range from 2 to 16. For fixed values of nadir angle and depth, the mean values of the bounding bias pairs and the variations from these means to the bounding values have been calculated.

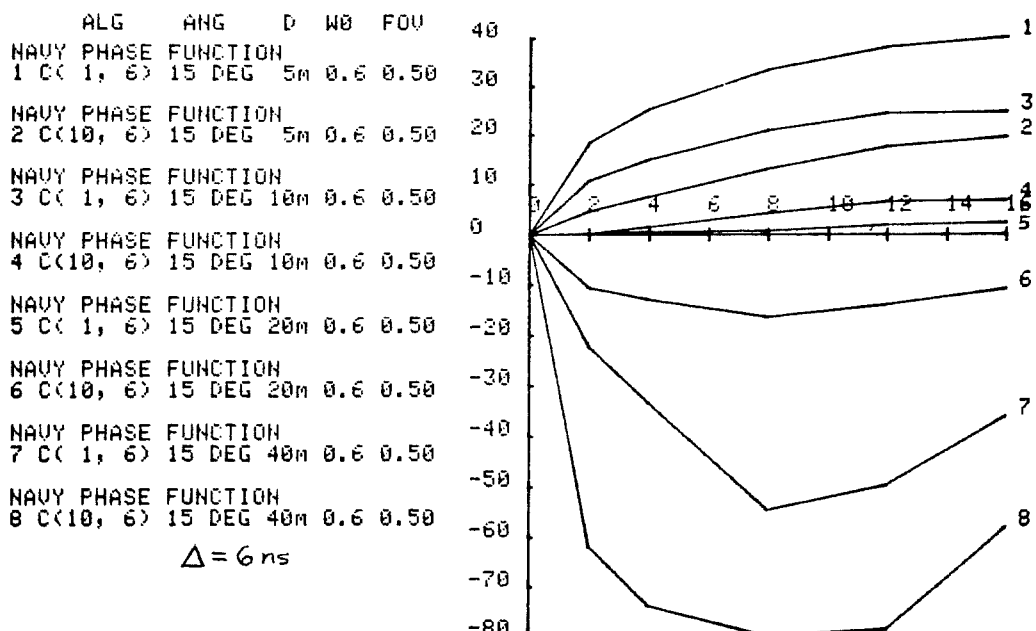


FIGURE 9-29. DEPTH MEASUREMENT BIAS (CM) VS OPTICAL DEPTH

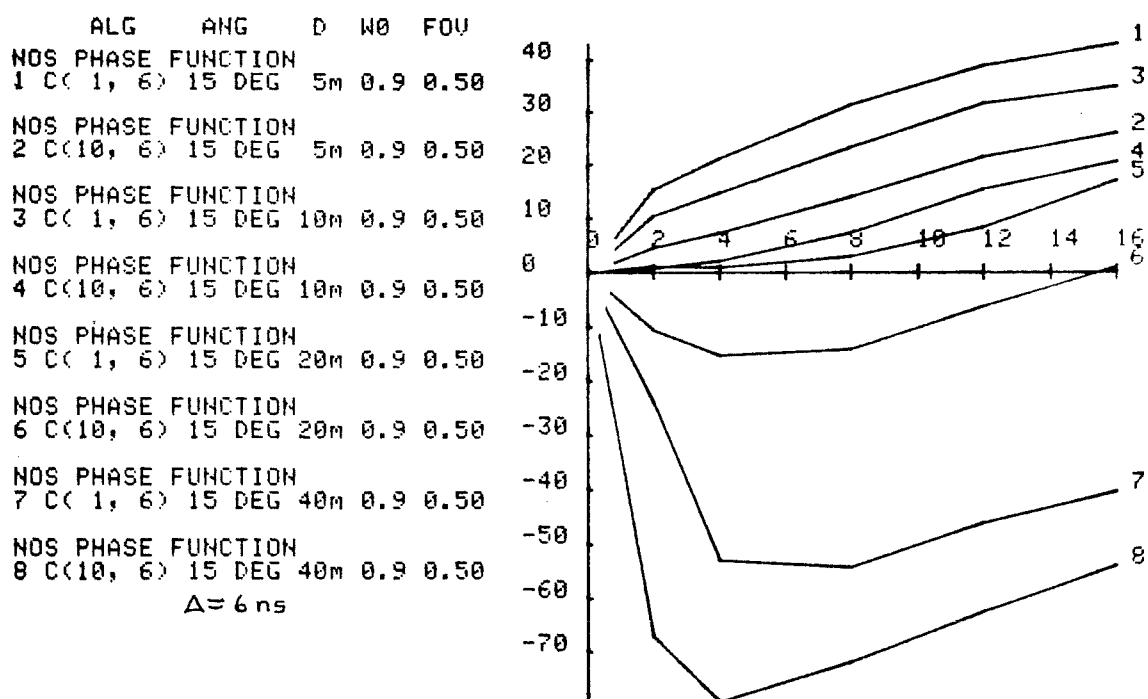


FIGURE 9-30. DEPTH MEASUREMENT BIAS (CM) VS OPTICAL DEPTH

The means of the bounding bias pairs or "mean extrema" biases are the optimum bias predictors from the point of view that they minimize the worst-case bias prediction errors over all unknown water clarity conditions. They are neither the average nor the most probable biases. The variations from the extrema means to the extrema, the so-called "half-ranges," are those worst-case errors. In other words, if the reported mean of the bounding biases for a given nadir angle and depth is used as a "passive" bias corrector, the error in the resulting depth estimate due to the effect of unknown water clarity parameters should never be larger than the reported variation or half-range. If these bias variations can be constrained to acceptable bounds by the selection of appropriate ranges of operating variables, then precalculated mean biases can be applied to measured depths as correctors, and water clarity parameters need not be estimated from field data. If the bias variations are too large, however, "active" bias correctors calculated from real-time, pulse-to-pulse estimates of water optical properties will be necessary. It would be beneficial to avoid this considerably more taxing procedure, if possible.

The magnitudes and functionalities of the bias extrema means and half-ranges about the means for various LFT and CFD cases are presented in Figs. 9-31 - 9-37. The bias variations or half-ranges for a 50% LFT are plotted as a function of nadir angle in Fig. 9-31 for depths from 5 to 40 m and for a FOV (R/D) of 0.5. The main feature of this data is the existence of minima in the bias variation curves. These minima occur as the bias trends switch from being lengthened by multiple scattering to being shortened by undercutting. The resulting mean biases for these bias variation minima are thus generally fairly small. At a 20-m depth the minimum for this case is at a nadir angle of 23°, while at 40 m the minimum is at 20°. For depths of 5 m and 10 m the minima are beyond 30°.

The critical issue is the magnitude of the bias variation with unknown water parameters. In a total error budget of ± 30 cm, no more than 15 cm can be allotted to this error source. This is noted on the figures by a dashed line. It can be seen in Fig. 9-31 that bias variations for the old 20-m depth requirement are less than 15 cm for nadir angles between 20° and 26°. For 5-m and 10-m depths, bias variations are under 15 cm beyond angles of 13° and 19°,

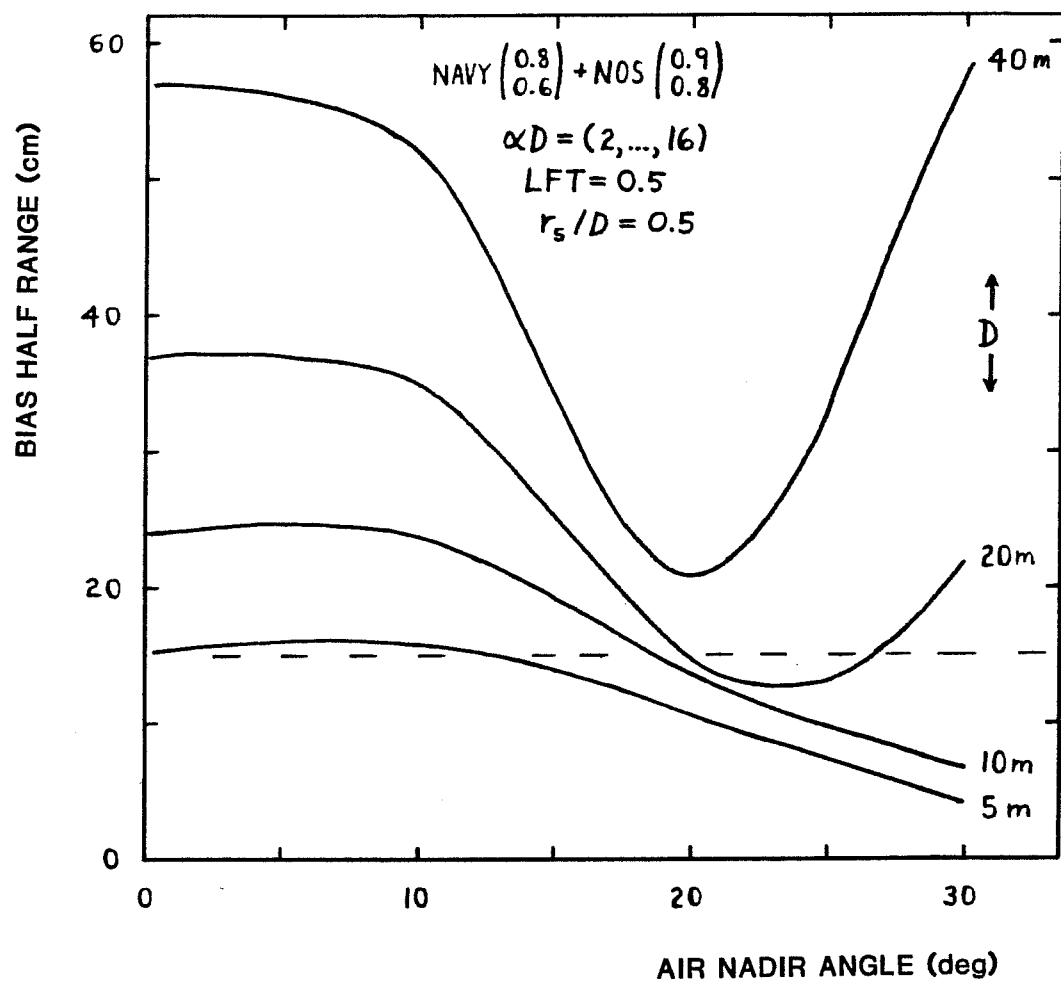


FIGURE 9-31. BIAS VARIATION FOR LFT 50%

respectively. At 40 m, the minimum variation is 21 cm, and, by interpolation, the 30-m minimum variation at 22° is about 17 cm, which slightly exceeds the desired (but somewhat arbitrarily selected) value. For this processing scheme, 22° is thus the desired operating angle. Uncontrolled aircraft roll and pitch will cause larger errors which would best be suppressed by using an attitude-stabilized scanning mirror. Operation at suboptimal angles will lead to errors in bias prediction which exceed international standards. At nadir, for example, the bias variation for a 50% LFT is seen to be ± 37 cm at a 20-m depth and ± 47 cm at 30 m. The mean extrema biases for the 50% LFT case are plotted versus depth and nadir angle, respectively, in Fig. 9-32.

Because the range of unknown optical depths from 2 to 16 is quite large, it was felt that even marginally increased knowledge of that parameter might reduce the bias variations. To that end, the same procedure was repeated for the case where αD is known (or assumed) to be either less than or greater than 8. The resulting minimum half-range for $2 < \alpha D < 8$ is quite a bit smaller, but the half-range for $8 < \alpha D < 16$ is virtually the same as for $2 < \alpha D < 16$. For the high αD case, the angular range for which the bias variation is less than 15 cm expands only slightly to 19° - 28°. This means that most of the total variation occurs at high αD s, and that much higher resolution in an αD estimate would be required to significantly reduce the bias variation.

The half-range curves for the case of a 20% LFT are similar to their 50% LFT counterparts except that the half-range minima have been shifted to slightly lower nadir angles. For a 20-m depth, the minimum is at 20°, and for a 15-cm bias uncertainty, the nadir angle range is 17° to 23°. The 40-m minimum is 20 cm at 17°. By interpolation, the 30-m minimum is about 16 cm at 19.5°. The reason for the shift of the minimum to lower angles is that these mean extrema biases are more negative for given depths and nadir angles than those for the higher threshold. The crossover point thus occurs at lower nadir angles. This case is less attractive than for the 50% LFT for an unrelated reason: the resulting random error component is much larger.

The character of the bias variations and mean extrema biases for HALS processing is less definitive than for the LFT case. First, the sensitivity to the lower end of the optical depth range is much greater. Because water

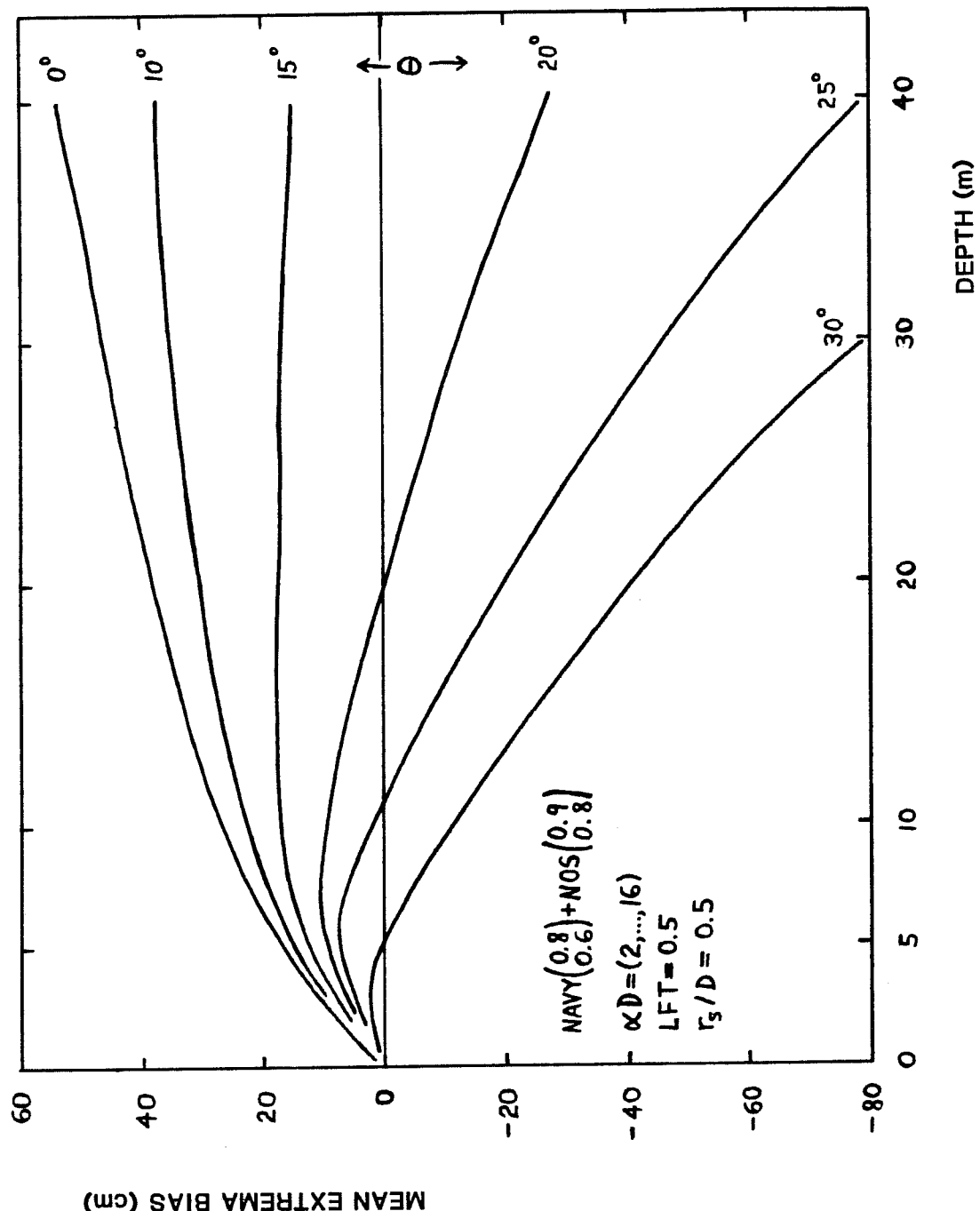


FIGURE 9-32. MEAN EXTREMA BIASES FOR LFT 50%

clarity tends to decrease as depth decreases, it is felt that a lower limit of 2 is appropriate for practical use. If that range were expanded to 0 - 16 instead of 2 - 16, however, significant differences would result due to the frequently large biases evidenced even for $\alpha D=2$. Secondly, because of the previously mentioned plateau in the CFD signal for cases with large nadir angles, low optical depths, and high physical depths (very clean water), the biases will depend heavily on the exact pulse location logic in a real, noisy system. The early detections reported here for the noise-free, idealized case lead to large but fairly constant negative biases across a wide range of optical depths. Slightly altered (more sophisticated) logic could result in much later detections and increased bias dependence on optical depth (and hence increased bias variations and decreased mean extrema biases). Even though the bias variations with optical depth for the idealized case may be relatively low for large biases, operation under such conditions would be undesirable due to sensitivity of the exact bias values to uncertainties in nadir angle, random errors in the simulation results, and random noise in the actual signals. Because of these problems, results for the offending cases, which luckily fall outside the operational region of interest, will not be presented.

Figure 9-33 shows the bias variation for HALS processing with a difference delay and a CFD delay of 6 ns for a range of (unknown) peak signal-to-background ratios (P_m/B) from 1 to 10. The minimum half-range at a 20-m depth for this case is 17 cm, and the combined minimum over the 5 - 30 m depth range is 20 cm at 14.5° . The reason for the increase in the minimum bias variation over the LFT cases is the added degree of freedom represented by P_m/B . Because the minimum value is unsatisfactorily large, specific information on P_m/B will be required. Bias half-ranges and mean extrema biases for P_m/B fixed at values of 1 and 10 are plotted in Figs. 9-34 - 9-35 and 9-36 - 9-37. Although the half-ranges are quite similar, the mean extrema biases differ by about 10 cm. The 20-m half-range minima are 9 cm and occur at angles of $14^\circ - 15^\circ$. At a 20-m depth, the 15-cm level is not exceeded for nadir angles in the range $14.5^\circ \pm 4^\circ$. These angles are smaller than those for the LFT cases. The mean extrema biases for the given conditions are more negative than for LFTs, and they change more rapidly with varying nadir angle.

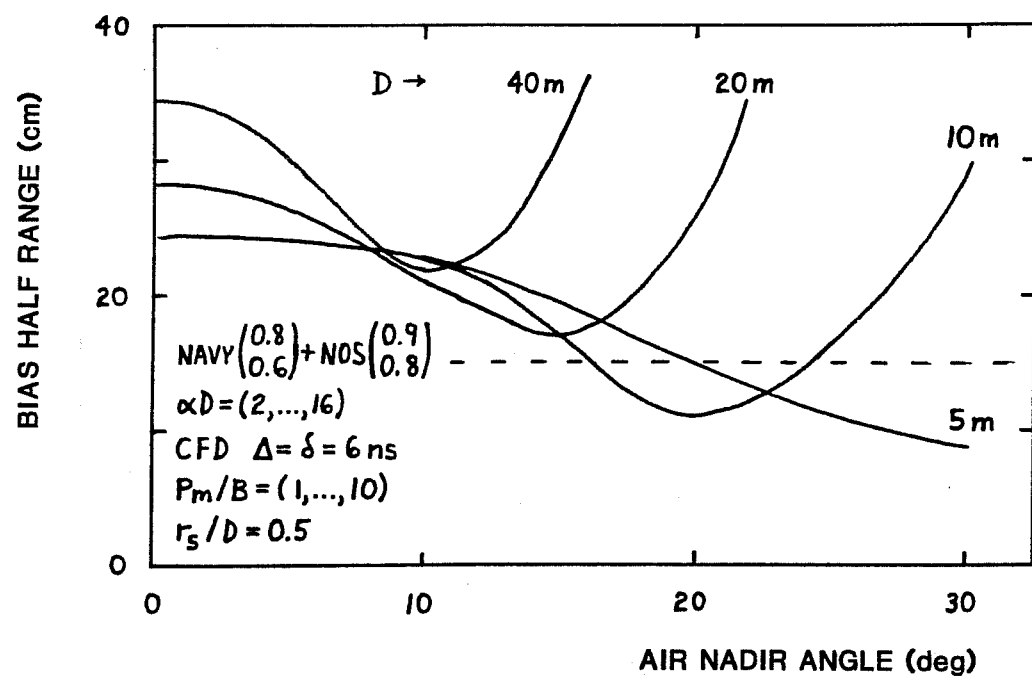


FIGURE 9-33. BIAS VARIATION FOR CFD (6, 10, 20)

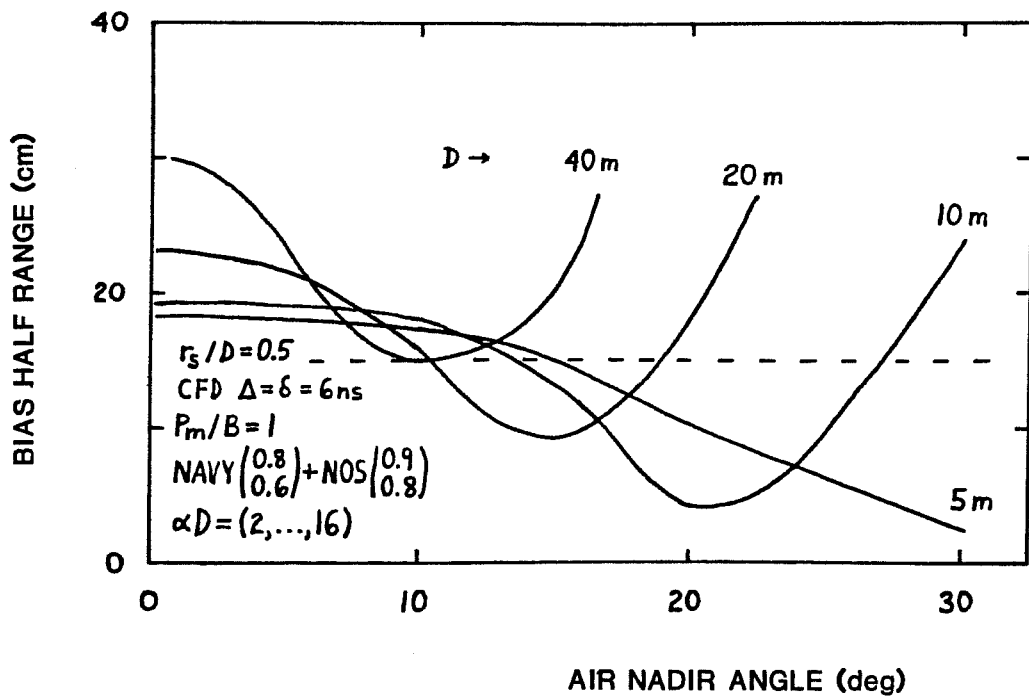


FIGURE 9-34. BIAS VARIATION FOR CFD (6, 6, 1)

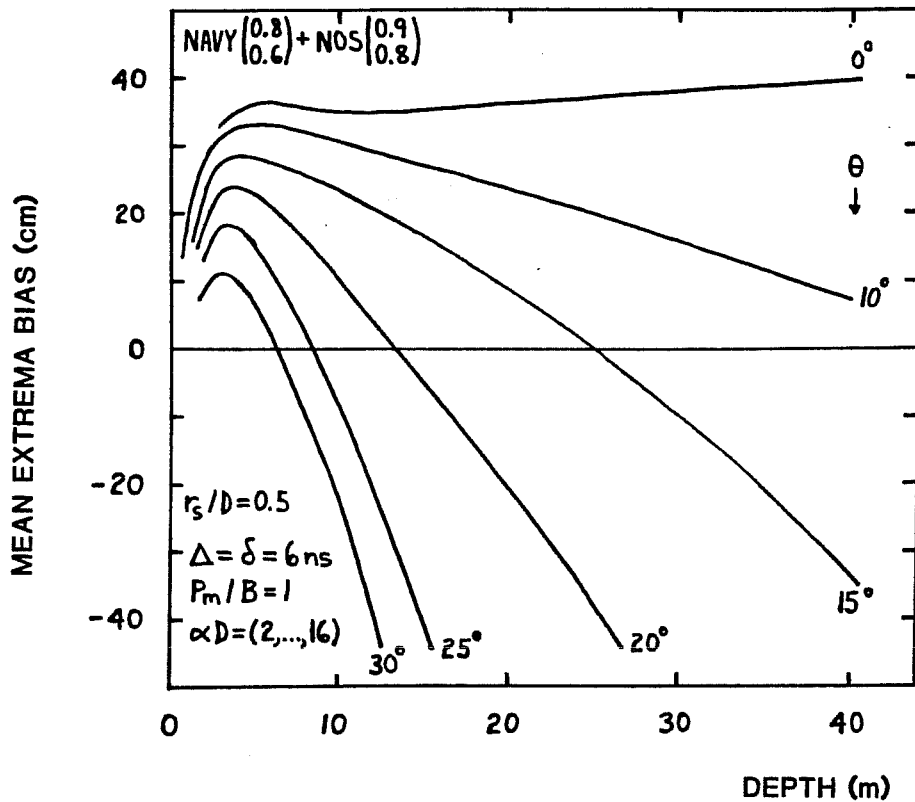


FIGURE 9-35. MEAN EXTREMA BIASES FOR CFD (6, 6, 1)

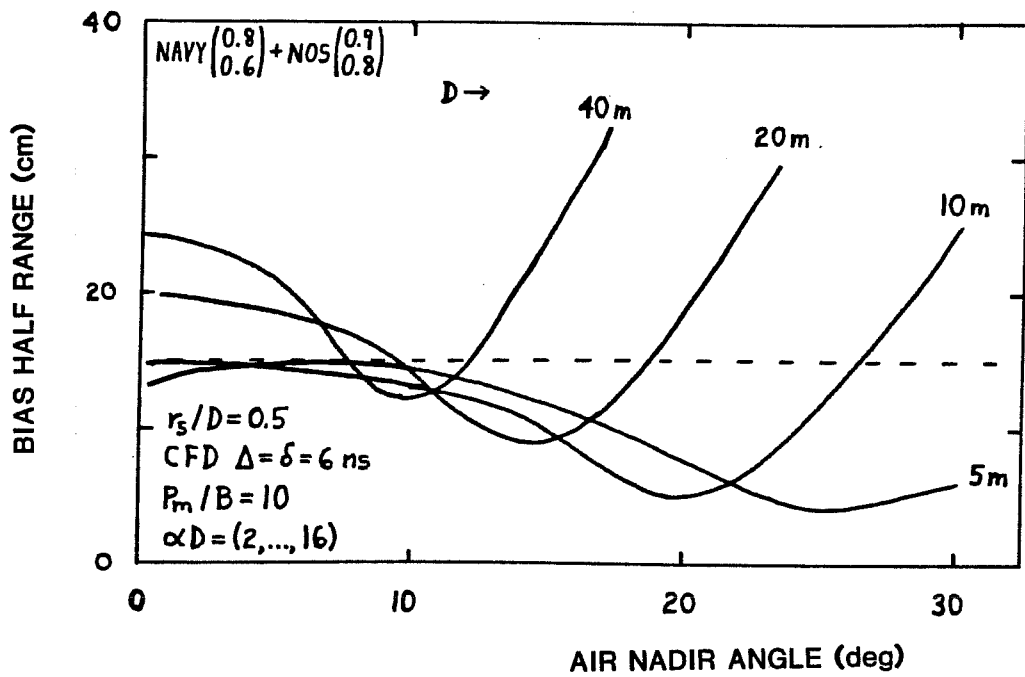


FIGURE 9-36. BIAS VARIATION FOR CFD (6, 6, 10)

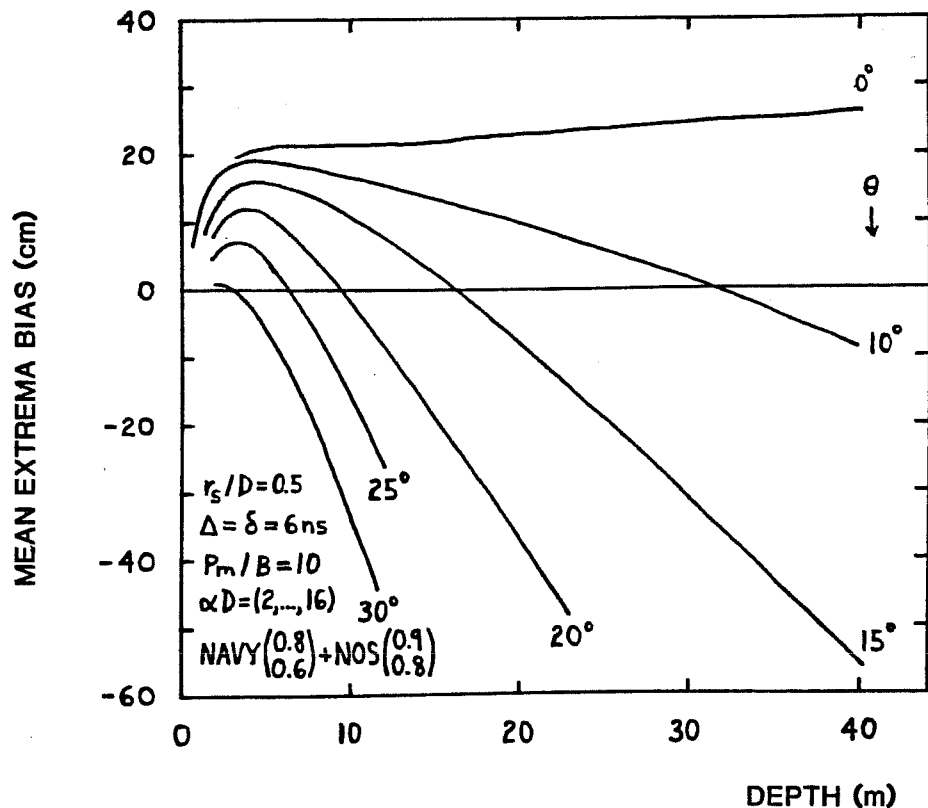


FIGURE 9-37. MEAN EXTREMA BIASES FOR CFD (6, 6, 10)

The most constraining circumstances for minimum and maximum nadir angle (for half-ranges not to exceed ± 15 cm) occur for 5-m and 30-m depths, respectively. For $P_m/B=1$, the 5-m half-ranges exceed 15 cm for angles less than 15° , while for $P_m/B=10$, the 30-m half-ranges exceed 15 cm for angles greater than 15.5° . The desired operating angle for the HALS processing scheme is thus 15° . An attitude-stabilized scanning mirror is again highly desirable. Curves for CFD delays of 3 and 10 ns are similar due to the previously noted relative insensitivity of the biases to that parameter. As with the LFT case, splitting biases into two optical depth ranges does not provide a means of significantly improving performance, even though the functionalities are somewhat different.

9.2.1.5 Bias Correction

9.2.1.5.1 Active Bias Correction

As seen in section 9.2.1.3 the propagation-induced depth measurement biases depend functionally on the scattering optical depth. Mean extrema biases calculated in the preceding subsection are tabulated in Appendix 9A. The direct or "active" application of these specific bias predictions as bias correctors to field data would require sufficiently accurate measurement or estimation of the driving water optical parameter, namely, the scattering coefficient. The operational scenario for airborne laser hydrography does not include sea-truth measurements. Sufficiently dense and synoptic in-situ measurements of the scattering coefficient cannot be economically collected over the large and diverse areas required, and its value cannot be obtained from ancillary, passive remote sensing devices. The only viable alternative is thus estimation of the scattering coefficient or the scattering optical depth from quantifiable features of the returning laser waveforms.

The most straightforward and reliable parameter available from the return waveform is the volume backscatter exponential decay coefficient, k_b . It has been proposed by Gordon (1982) that for sufficiently large receiver FOV, the value of k_b in shallow water appears to be roughly equal to the value of the diffuse attenuation coefficient, K , of the water. Also for the large field-of-view case, Phillips and Koerber (1984) argue that k_b is equal to the

absorption coefficient, a value slightly smaller than K. For limited fields of view, the backscatter decay coefficient is somewhat larger than for the large-FOV case. For a practical system FOV, this would increase the Phillips and Koerber coefficient to a value again very near K. In summation, the value of K, or something very near it, can be estimated from individual lidar returns.

The problem is that there is no sufficiently accurate way of obtaining an estimate of the required scattering coefficient, s, from K. From a plot of s versus K data for natural waters, as seen in Fig. 9-38 (accumulated from a variety of sources), it can be seen that the scatter in the functional propensity is too large. At $K=0.15 \text{ m}^{-1}$, for example, the values of s range

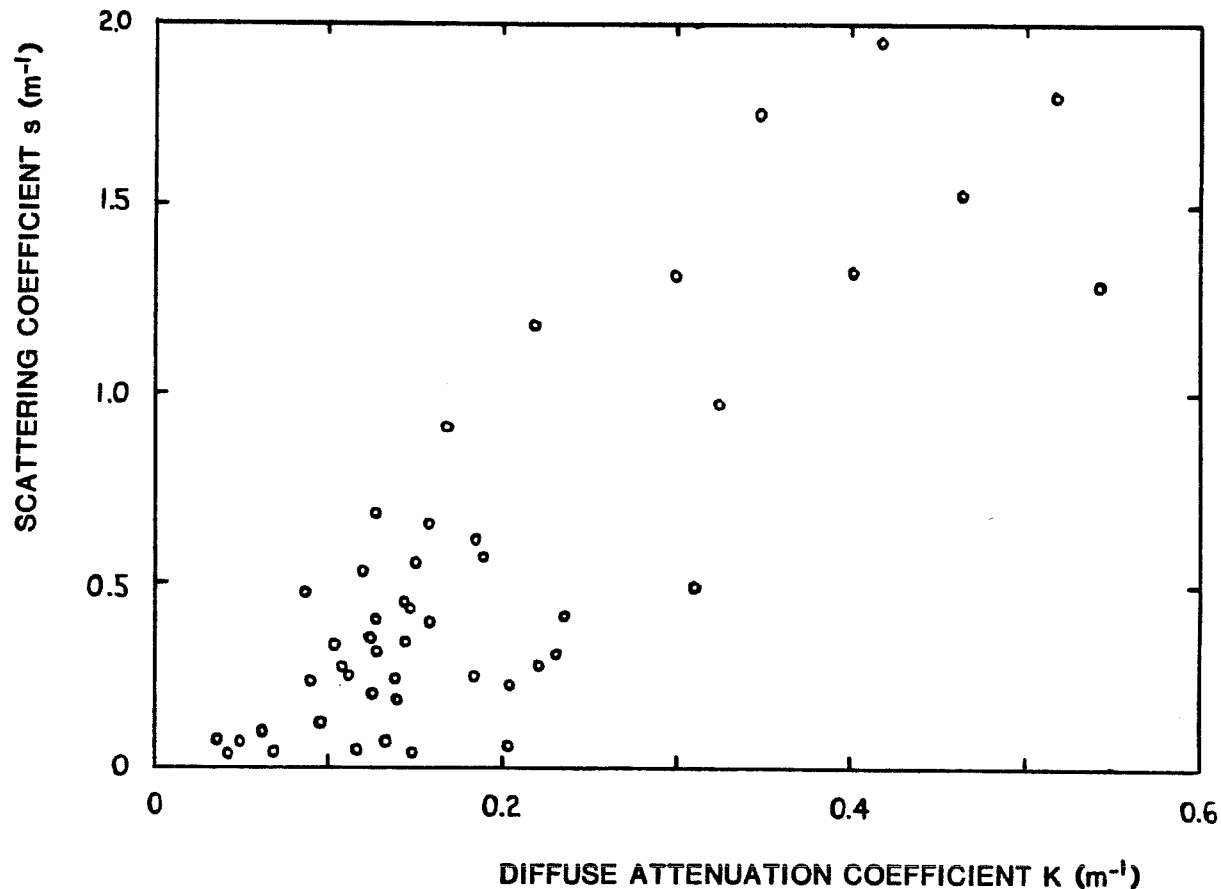


FIGURE 9-38. SCATTERING COEFFICIENT vs. DIFFUSE ATTENUATION COEFFICIENT
MEASURED IN NATURAL WATERS

over a factor of 9, which is far too large to be of use. Similarly, if one notes the propensity for $\omega_0 \approx 0.8$ in many coastal waters, one could make a rough estimate of α from the K/α relationship in section 4. One could then further estimate $s = \omega_0 \alpha \approx 0.8\alpha$. For actual cases where $0.6 < \omega_0 < 0.9$, the double errors arising from this approximation are again far too large for the resulting estimates to be of practical use.

Two procedures, involving the return waveforms, which offer some promise have been investigated in some detail. These are the use of extrapolated volume backscatter amplitude to estimate s , and the use of bottom return pulse width to estimate sD . Both procedures, which are discussed in detail in Guenther and Thomas 1984b, have attendant problems which cause them to be of questionable utility.

For the first case, the quantity of interest is based on an absolute magnitude, i.e., a system voltage level, not a relative quantity such as a slope. Errors in estimating key quantities in the return signal equation lead to errors in the estimate of s . This means that the lidar system must be constantly maintained in a state of absolute radiometric calibration. Errors would arise from varying amplifier gains and PMT voltages, temperature-dependent optical signal variations, dirty optics, laser power fluctuations, etc. In order for this technique to be of use, the waveforms must be recorded and returned for evaluation in post-flight data processing. The system must contain no nonlinear processes such as partial optical blocks or variable, real-time gain control which affect the shape of the backscatter tail. The laser source pulse must be sharply terminated so the tail of the surface return does not add significant energy into the backscatter signal. The technique will not work in relatively shallow water where the backscatter slope is too short to be accurately extrapolated and is contaminated by the surface and bottom return energies. Furthermore, the automated estimation of backscatter slopes from lidar waveforms would be difficult, time consuming, and the results frequently imprecise. Finally, the estimate of s depends on a calibration curve of s versus the value of the volume scattering function at 180 degrees. The existing Petzold data set of volume scattering functions would need to be further confirmed and expanded to ensure accuracy.

In the second case, it has been noted by H. S. Lee (Moniteq 1983) that the pulse widths (at half the peak height), like the depth measurement biases, depend strongly on the $\omega_0 \alpha D$ product, rather than on ω_0 and αD separately. This leads to the concept that measurement of the bottom return pulse widths might be able to provide estimates of sD of sufficient precision to be used as an input (independent variable) for "actively" selecting an appropriate depth measurement bias predictor/corrector for each individual sounding. In order for such a technique to be practical, however, a number of criteria must be met. The basic functionality must hold at all nadir angles of interest. The effect of varying phase function must be small, because it is uncontrollable and unknown. A procedure must be found to "deconvolve" the bottom return (i.e., the ERF) to yield an estimate of the IRF which is accurate enough to maintain the key depth scaling property. Pulse widths must be accurately determined from weak and noisy signals. In addition, the effect of environmental effects on the pulse widths must be small and the added computing burden reasonable. None of these requirements are fully met in practice.

9.2.1.5.2 Passive Bias Correction

For use as bias correctors, the mean extrema biases presented in section 9.2.1.4 for a 7-ns source pulse can be either tabulated or fitted analytically. Smoothed biases tabulated at 5 m, 10 m, 20 m, 30 m, and 40 m can be interpolated linearly over depth and nadir angle, with very small residual errors, for nadir angles up to and including 25°. Alternately, if algebraic representations are desired, the biases can be described in the form

$$B(cm) = aD^n - bD^m(1 - \cos\theta)^k, \quad (9-3)$$

where B is the bias in centimeters, D is the depth in meters, and θ is the air nadir angle. The coefficients a , b , n , m , and k can be adjusted to fit the bias curves for various cases of signal processing algorithms and parameters. Table 9-1 presents sets of coefficients for the mean extrema bias curves shown in Figs. 9-32, 9-35, and 9-37 along with their respective RMS of fit and maximum deviation of fit calculated for depths from 5 m - 20 m and nadir angles of 15° - 25° for LFT and 10° - 20° for CFD. The fits themselves are valid from 0° - 25° and for depths to 40 m, as well.

Table 9-1. Bias Fitting Coefficients for Eq. 9-3[#]

Case	Fig.#	a	b	n	m	k	RMS (cm)	max. dev. (cm)
LFT 50% ^A	9-32	6.5	27.0	0.58	1.25	1.26	2.5	4.7
LFT 20%	--	8.3	21.5	0.46	1.16	0.98	1.3	2.3
HALS [*] $\Delta=\delta=6$ ns, $P_m/B=1$	9-35	32.8	37.4	0.043	1.28	1.18	2.5	5.7
HALS $\Delta=\delta=6$ ns, $P_m/B=10$	9-37	15.9	21.8	0.13	1.59	1.30	2.6	6.8

* $\Delta \equiv$ difference delay, $\delta \equiv$ CFD delay

valid for 7-ns source pulse

^A best for $D \geq 7$ m

Linear interpolation of tabulated values provides a slightly more accurate, if more cumbersome, representation of the simulation outputs, but it is possible that the inherent smoothing action of the analytic fit over all parameters may provide slightly more consistent results. Regardless of whether CFD biases are derived from tables or a formal expression, they will have to be calculated by interpolation or extrapolation from the two given values of P_m/B . As seen in Guenther (1982), the estimation should be performed linearly on the $\log(P_m/B)$.

9.2.1.5.3 Bias Correction Conclusions

If the scattering optical depth can be adequately estimated on a pulse-to-pulse basis from the air, detailed bias predictions such as those tabulated in Appendix 9A -- for a 7-ns source pulse and LFT or HALS processing -- can be interpolated or regressed to produce bias correctors. The ability to accurately or efficiently perform this estimation, however, is questionable.

The extrapolated backscatter magnitude technique for estimation of the scattering coefficient, though theoretically feasible, appears to be relatively impractical in application due to severe hardware, software, and accuracy problems.

Although pulse widths appear to be a plausible parameter from which scattering optical depth and hence propagation-induced depth measurement biases could be estimated on a pulse-to-pulse basis, there are a number of error sources which, when summed, would significantly reduce the effectiveness of the estimation. The results, although not foolproof, could provide a limited measure of bias correction, particularly for non-optimal nadir angles, if the computing burden were acceptable. This may be the largest drawback. It is difficult to recommend a technique with such a low benefit/cost ratio.

It appears to be practical to restrict the nadir angle of operation to a range appropriate for minimizing the biases (for the pulse processing and location algorithms selected). One can then apply predicted mean extrema biases as simple, passive bias correctors. These were quantified in the preceding section (Eq.(9-3) and Table 9-1) for a 7-ns source pulse and LFT or HALS processing. For other signal and data processing protocols, a new set of biases and associated mean extrema and variances would have to be derived from the ERFs in accordance with the previously described procedures.

9.2.1.6 Conclusions

The impact of underwater light propagation mechanisms on the depth measurement accuracy of airborne laser hydrography has been investigated via a powerful Monte Carlo computer simulation procedure. The simulation program provides a set of paths for downwelling photons arriving at the bottom for given sets of optical parameters and system variables. The resulting temporal and spatial distributions are used to compute impulse and actual source or "environmental" response functions at a distant, off-nadir, airborne receiver.

Depth measurement biases caused by scattering and absorption of the beam in the water column are calculated from environmental response functions, based on the 7-ns source pulse, for several typical signal processing and pulse location algorithms. These biases have been developed for bounding ranges of optical parameters in coastal waters and for all combinations of typical operational system variables. The only external input is the "phase function" scattering distribution. The sensitivity of the biases to phase function is small, but reported biases could differ somewhat from field data

should the selected Petzold functions prove not to be representative at small angles.

Resultant biases may be either deep due to multiple scattering or shallow due to geometric undercutting, depending on nadir angle, water depth, and water optical properties. The strongest functionalities are with scattering optical depth, nadir angle, and signal processing and pulse location algorithms. It has been found that the net bias magnitudes can be large compared to international accuracy standards, and that the biases should therefore be corrected out of operational, raw depth data.

These bias predictions, in the form of look-up tables or regressions, can be used as "active" bias correctors for operational data on a pulse-to-pulse basis if the scattering optical depth can be estimated from the waveforms with sufficient accuracy. Because of the significant problems involved in estimating the scattering coefficient or scattering optical depth from the air, however, an alternate approach is presented. It has been shown that for certain limited ranges of scanner nadir angles, whose magnitudes depend on signal processing protocol, the bias variations due to unknown water optical parameters are less than ± 15 cm at a 20-m depth and ± 20 cm at a 30-m depth. These optimal nadir angles, in the $15^\circ - 23^\circ$ range, are appropriate for system operation in terms of desired swath width and aircraft altitude.

Constraining operations to preferred nadir angles via appropriate scanner design will permit "passive" bias correction using mean extrema biases which depend only on readily available information such as nadir angle, depth, and minor functionalities such as field of view and, for log/difference/CFD processing, signal-to-background ratio. For linear processing with a fractional threshold pulse location algorithm or for log/difference/CFD processing, the optimum nadir angles and mean extrema biases reported herein may be used for bias correction. For other signal processing and pulse location protocols, corresponding mean extrema bias functionalities must be calculated, and new matching nadir angles must be selected for minimum bias variation.

Systems operating without active bias correction or not within the optimal nadir angle range for passive bias correction will experience uncertainties in depth measurement biases, as functions of unknown water optical properties, which can be significantly larger than international hydrographic accuracy standards permit. Even with limited ground-truth measurements of optical properties, such errors are unavoidable due to the inherent patchiness of coastal waters.

9.2.1.7 Acknowledgments

The conception, design, coding, and operation of the Monte-Carlo simulation were carried out by Bob Thomas at EG&G/WASC. Propagation-induced biases could not have been calculated without this pace-setting effort. Gratitude is expressed to H. Sang Lee for his insightful ideas and critique. This work was supported in part by the Defense Mapping Agency, the Naval Ocean Research and Development Activity, and the Office of Naval Research.

9.2.2 Interface/Volume Backscatter Uncertainty

An airborne lidar bathymeter determines the water depth by measuring the time difference between the arrivals of the "surface" and bottom reflections. This simple scenario is complicated by the fact that, as seen in section 7, two different signals are generated in the near-surface region: the "true" specular relection from the air/sea interface, and a diffuse, backscattered return from particulates in the underlying water column. It is necessary to know whether the indiscriminate use of either interface or volume returns (depending on which dominates for given values of off-nadir angle, wind speed, and water clarity) will lead to an unacceptably large depth measurement error for typical pulse location algorithms.

Notation was developed in section 7 where $X \equiv kct$, $X \equiv kct_0$, and $X = 0$ when the peak of the source pulse strikes the air/water interface. The value of k for practical receiver fields of view was seen to be typically close to the value of K , the diffuse attenuation coefficient. The equations describing the leading edge of the volume backscatter return power for a triangular source pulse of width, t_0 , (FWHM) are

$$P_v \propto 1 + (e^{-(X + X_0)} + X - 1) / X_0 \quad (9-4)$$

for $-X_0 \leq X \leq 0$, and

$$P_v \propto 1 + (1 - X - 2e^{-X} + e^{-(X + X_0)}) / X_0 \quad (9-5)$$

for $0 \leq X \leq X_0$.

The peak of the volume backscatter return lies at

$$X_p = \ln(2 - e^{-X_0}), \quad (9-6)$$

which occurs somewhere between $X = 0$ and $X = X_0$ depending on the value of X_0 and hence on K .

A typical volume backscatter return, along with the corresponding source pulse, is plotted in Fig. 9-39. The depth measurement bias between the two is evident as a time difference between the two returns at any given threshold level. Biases calculated for a range of typical K values are plotted as a function of threshold fraction (of the peak) in Fig. 9-40 for a 7-ns FWHM source pulse. Results for other source pulse widths scale ^{nearly} linearly. It can be seen that for useful threshold fractions, the surface uncertainty biases for reasonably clean water are typically in excess of 30 cm and can be as large as 60 cm. This means that depth measures for which the surface returns come from the volume backscatter (due to lack of capillary wave slopes large enough to generate a colinear interface reflection) will be 30-60 cm shallower than the true depth. Such biases are unacceptably large and must somehow be reduced to under 10 cm.

As discussed in section 7.4 and seen in Fig. 7-8c, the parametric region in which the mean surface return strengths for the two returns are nearly equal lies well within the bounds of system operation for typical wind speeds and nadir angles larger than 15 degrees. Furthermore, as seen in section 5.8.2, wave crests and wave troughs can have greatly different reflection characteristics under given circumstances. It is unrealistic, therefore, to consider limiting system design to either interface-only or

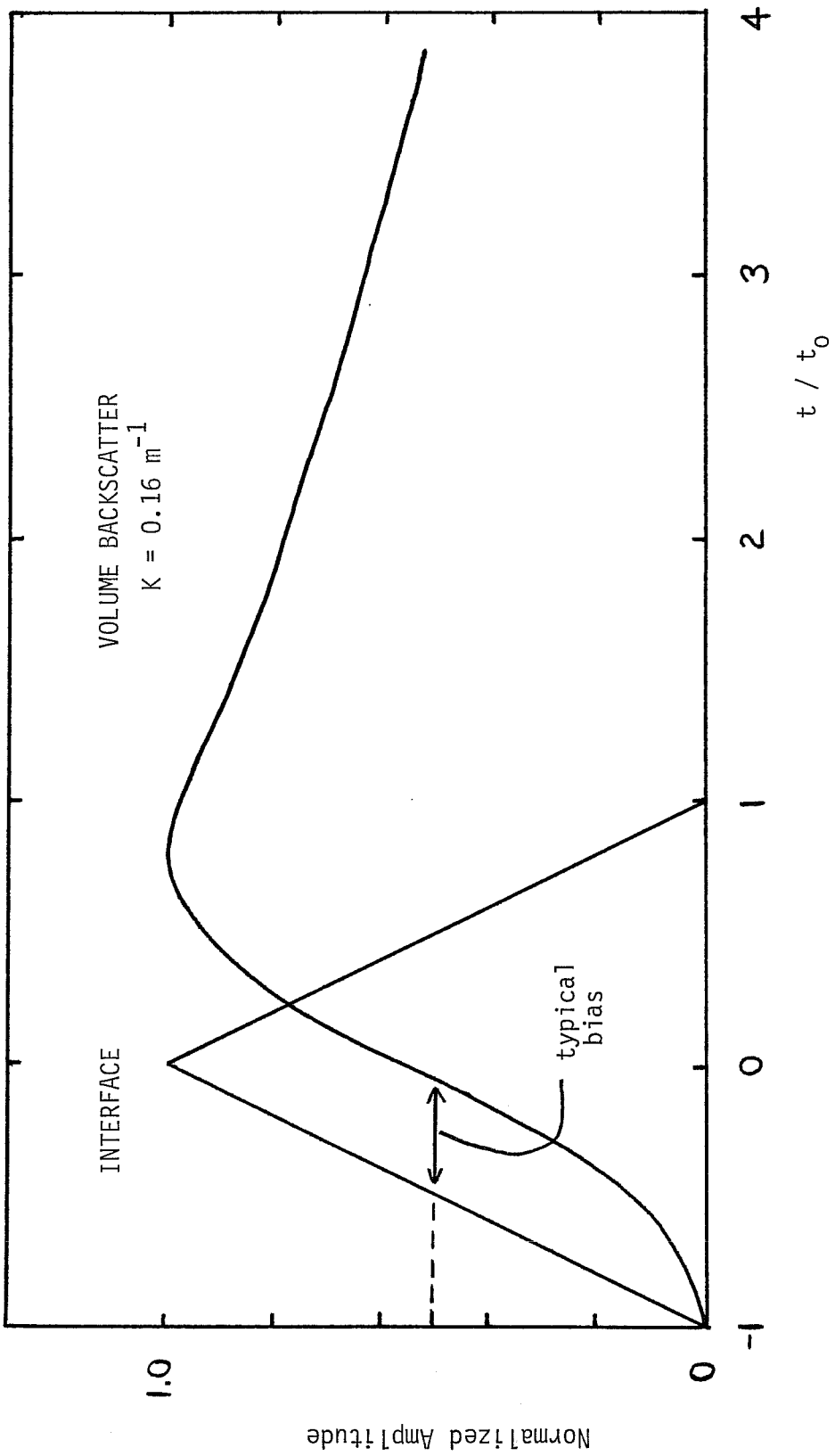


Figure 9-39. Comparison of Interface Reflection and Volume Backscatter Temporal Shapes (normalized to equal peak height)

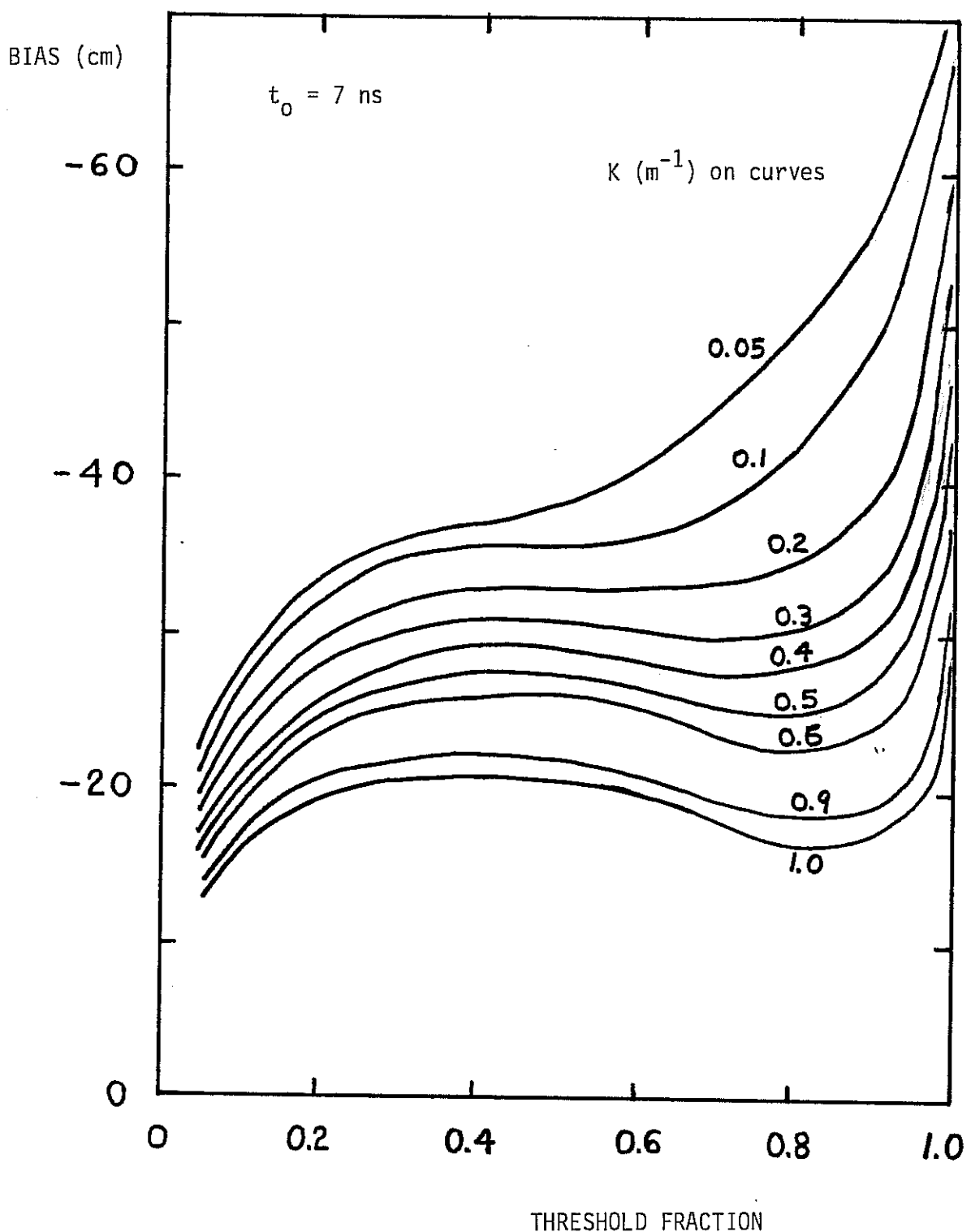


Figure 9-40. Shallow Depth Measurement Bias caused by detecting Volume Backscatter Return rather than Interface Return

volume-only conditions for nadir angles much in excess of 10 degrees. These returns are frequently of nearly equal magnitude, and on a pulse-to-pulse basis, one dominant return may originate at the interface, a second from the volume, and the next from anywhere between, depending on the relative signal strength components. To describe this uncertainty, I have coined the term "flip-flop".

The flip-flop bias must be either reduced in magnitude or recognized and corrected. The simplest way, conceptually, to reduce the magnitude is to shorten the source pulse. To limit the bias to 10 cm for moderate effective threshold fractions would require a pulse no wider than 2 ns FWHM. A laser with the required characteristics is presently not available, and this problem emphasizes that the development of a narrow-pulse laser would be valuable. An alternate means of reducing the magnitude of the error is the use of a colinear infrared beam to detect the surface. The bias error between interface and volume returns for this design is smaller due to reduced penetration of the water column at this wavelength. It is not known, however, whether the magnitude of the infrared volume return is sufficient for surface detection. If not, surface return probability would be reduced during low wind conditions. Another alternative which has not been studied in detail is the potential use of the Raman energy backscattered from the water for the surface return. The signal magnitude might be small, but the origin is unambiguous. There would be a small water clarity dependent error.

The alternative is recognizing the origin of the surface return and applying appropriate correctors where necessary. It may be possible to recognize a volume return by risetime, shape, or amplitude. Risetimes for the volume backscatter as a function of K are plotted in Fig. 9-41. Surface waves and off-nadir geometry, however, also cause stretching of the interface returns; this may make the discrimination difficult. Alternately, all returns with surface amplitudes below a certain threshold might be assumed to be volume returns and appropriately corrected, or they might be ignored in order to attempt to limit returns to interface only. In this mode, beam nadir angles would have to be restricted to values depending on the available wind, and operations during low wind conditions would have to be curtailed.

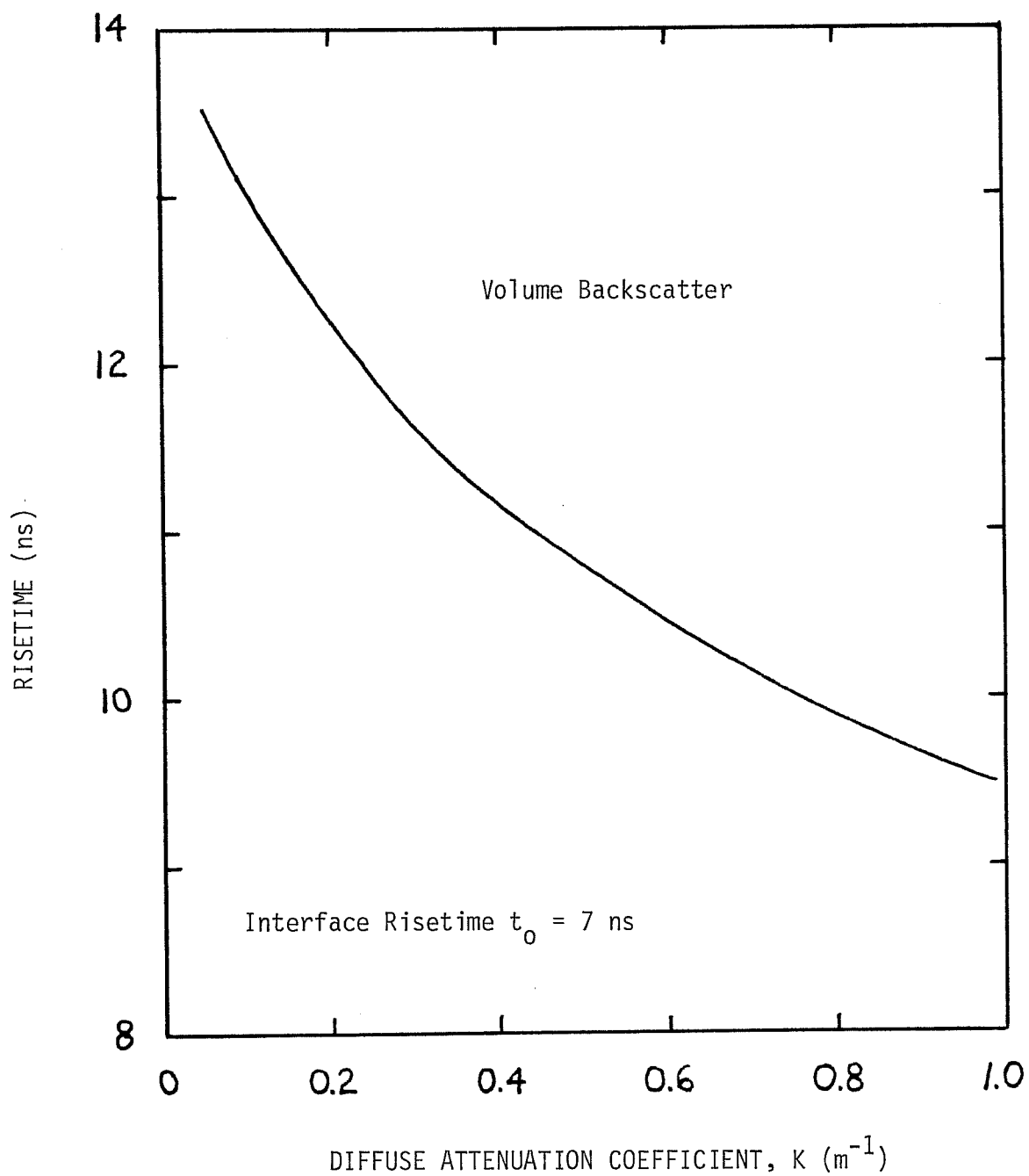


Figure 9-41. Volume Backscatter Risetime (0-100%) vs. K for 7-ns FWHM Triangle Input Pulse

Surface uncertainty is a problem which must be carefully addressed in each system design.

9.2.3 Beam Steering at the Air/Water Interface

When an off-nadir source pulse refracts through a flat horizontal interface, the unscattered ray in the water traverses the medium at an angle with respect to the nadir dictated by Snell's law. If an incident pulse enters the water through the sloping side of a wave, the unscattered refracted ray will traverse a slightly different path to a different location on the bottom. The positioning error is relatively small compared to the requirement and not a problem, but the path length in the water to the bottom is different. The path length difference from the flat surface case, modified by the cosine of the angle, is a depth measurement error. If the dominant wave slopes are individually and randomly sampled, this error source will be a random error and appear as a loss of depth measurement precision.

The effect of these slopes depends on how they are distributed as a function of water wavelength and on the size of the incident illuminated surface spot. The character and magnitude of the beam-steering error thus depends on the transmitter beam divergence and the aircraft altitude. In one limiting case, a highly-collimated spot profiles the sloping smooth face of a gravity wave. The refracted beam will be entirely deflected in one direction, and the measured depth will be biased to the full extent of the slope. This is the worst-case condition. In the other limiting case, an expanded spot illuminates a large number of capillary and gravity waves. The beam energy will be averaged over all slopes and spread equally on both sides of the Snell angle for a flat sea. The measured depth will be biased only a negligible amount because the undercutting paths are slightly shorter and hence "preferred" due to lower attenuation; this bias will be small compared to the undercutting induced by scattering in the water column, as seen in sections 6 and 9.2.1. In reality, the gravity waves have patches of capillary waves of significantly steeper RMS slopes. Illuminating a capillary-laden single gravity wave slope would lead to a mean beam steering bias associated with the gravity wave slope but with a larger beam spread about the mean due to the capillary slopes. Undercutting from this beam spread could increase or

decrease the net bias slightly, depending on the sign of the slope. The preferred situation is thus to illuminate as many wavelengths of the dominant wind generated gravity waves as possible. This will produce the smallest beam-steering errors.

The geometry for the calculation is seen in Fig. 9-42 where the beam nadir angle in air is denoted θ , the wave slope is denoted Ω , the water nadir angle of the unscattered ray for a horizontal surface is ϕ , and the water nadir angle for the given wave slope is ψ . Snell's law for the wave slope can be written

$$\sin(\theta - \Omega) = 1.33 \sin(\psi - \Omega), \quad (9-7)$$

from which

$$\psi = \Omega + \sin^{-1}[0.75 \sin(\theta - \Omega)]. \quad (9-8)$$

If Ω is the RMS wave slope, then the RMS fractional depth error for the unscattered ray due to this "beam steering" effect is

$$E_\Omega / D = 1 - \sec\phi \cos\psi. \quad (9-9)$$

This is actually an overestimate of the error because the effective water nadir angle to the bottom will be somewhat smaller due to the preferential undercutting of the Snell ray by energy scattered in the water column combined with the fact that preferred pulse location algorithms detect on the leading edge of the bottom return.

RMS gravity wave slopes as a function of wind speed were estimated by Cox and Munk (1954) from measurements where capillary waves were suppressed by an oil slick. For wind speeds, w^* , measured at a standard height of 12.5 m, the RMS slopes added in quadrature for up/down and crosswind cases were expressed as

$$\Omega^2 (\text{rad}^2) = 0.008 + 0.00156 w^* (\text{m/s}). \quad (9-10a)$$

The constant term represents the presence of residual waves under conditions of no wind stress, and is somewhat dependent on the actual weather conditions

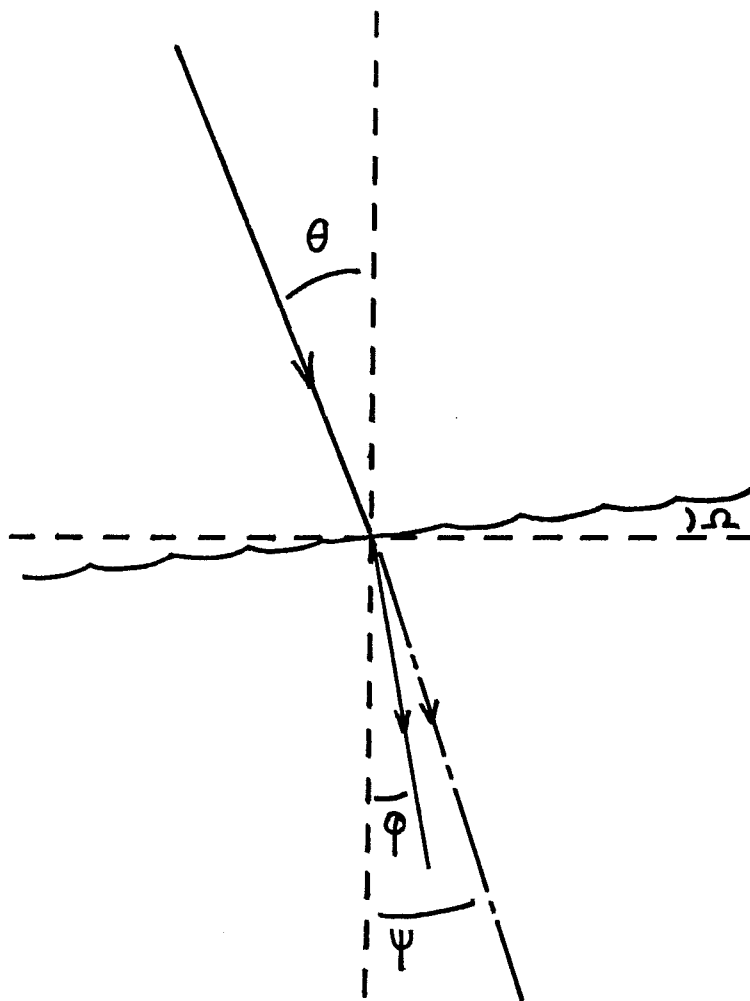


Figure 9-42. Surface Refraction Geometry

extant at the time. A theoretical relationship based on directional spectra is reported by Kinsman (1965), recounting the results of Neumann from 1953. The RMS result, for wind speed, w , measured "at anemometer height", for a general direction with respect to the wind, is

$$\Omega^2 (\text{rad}^2) = 0.00159 w (\text{m/s}). \quad (9-10b)$$

This functionality includes only the wind stress term which is amazingly, if perhaps somewhat serendipitously, similar to the independently obtained Cox-Munk value. The Cox-Munk expression, being more representative of physical reality, will be used for analysis of the worst case condition.

For wind speeds of 2.5, 5, and 7.5 m/s (roughly 5, 10, and 15 knots) the RMS slopes resulting from Eq. (9-10a) are 6.3, 7.2, and 8.0 degrees, respectively. It is assumed that winds in excess of 15 knots will generally preclude operations due to degradation of water clarity and the formation of whitecaps. The worst-case RMS beam-steering errors calculated with these slopes from Eq. (9-9) for the unscattered ray at a 20-m depth as a function of θ are seen in Fig. 9-43. The errors for negative values of Ω are nearly equal to those for positive Ω , and need not be reported separately. For the worst case of an unscattered beam, it can be seen that for a precision limitation of ± 10 cm RMS, the maximum permissible beam nadir angles in air occur at about 13, 11, and 10 degrees for 5, 10, and 15 knot winds, respectively. Such small angles would be unacceptably limiting from the standpoint of passive bias correction, as seen in section 9.2.1, as well as being less than desirable in terms of coverage swath width. It has been estimated from the Monte Carlo propagation simulation results that the use of the effective water nadir angle of the scattered energy, rather than the unscattered ray, will increase these maximum off-nadir angles in air over worst-case results by from 5 to 10 degrees in the 10 to 25 degree region. Exact values depend strongly on signal processing and the pulse location algorithm.

These larger angles, although a significant improvement, are not sufficiently large for all operational cases envisioned. It is thus considered mandatory to illuminate as many gravity wave wavelengths as possible. In order to restrain the beam-steering error to no greater than the

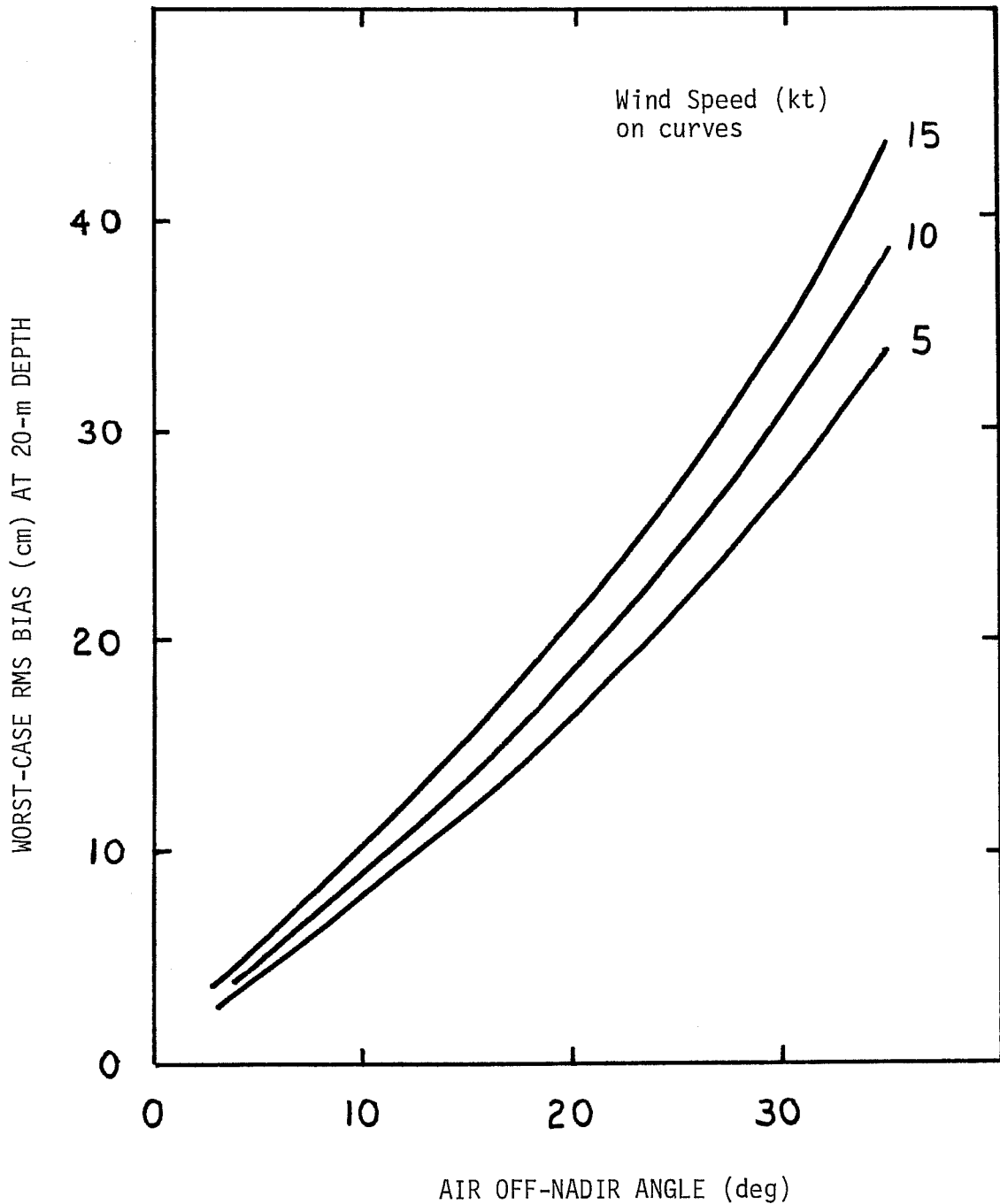


Figure 9-43. Worst-Case Depth Measurement Bias at 20-m Depth caused by Gravity Wave Beam Steering

± 10 cm level, the transmitter beam divergence should be made as large as possible without causing additional errors due to geometric effects such as those noted in the next subsection. Incident beam diameters as large as 3 - 4.5 m are both reasonable and desirable. Such large beam diameters provide the added benefit of lower energy density, so that eye-safety can be maintained even with very high-powered lasers.

9.2.4 Surface Return Geometric Pulse Stretching

When a very short laser pulse at a nadir angle, θ , with a full beam divergence angle, 2β , reflects from a flat surface perturbed by capillary waves, the round-trip time difference, Δt , between the longest and shortest paths is

$$\Delta t = 2H [\sec(\theta + \beta) - \sec(\theta - \beta)]/c, \quad (9-11)$$

where H is the altitude and c is the speed of light in air. Table 9-2 contains a compilation of Δt values for various, θ , 2β , and H .

The effect of the time delay on the surface return pulse shape depends on the temporal width of the surface pulse. Let the source pulse be triangular with a base width of $2t_0$ ($t_0 \equiv \text{FWHM}$). For large Δt (greater than $2t_0$) the resulting surface return will rise to its peak value just prior to $2t_0$ (the end of the pulse fraction arriving from the shortest path) and have a flat top until it decays in a manner symmetric with the leading edge. For $\Delta t < 2t_0$, the resulting surface return will be symmetric and rise a peak value between times t_0 and $2t_0$.

Because energy returns to the receiver first from the shorter paths "undercutting" the beam axis, the net result is an early surface detection and hence a deep bias for the depth measurement whose magnitude depends on t_0 , Δt , and the effective threshold fraction, f . The exact biases are difficult to calculate, and consequently several simplified models have been considered. The worst-case example is a spatially square pulse (rather than circular) with a flat density distribution (rather than Gaussian). For this geometry the bias time, τ , as a fraction of Δt can be represented roughly as in

Fig. 9-44. It can be seen there that for $0.1 < f < 0.9$, $\tau \sim \gamma \Delta t$ where $0.1 < \gamma < 0.35$, as long as $\Delta t < 2t_0$. For $\Delta t > 2t_0$, $\tau \sim t_0(0.5 \Delta t/t_0 - 0.4)$ for $0.2 < f < 0.9$, and $\tau (f = 1) = \Delta t/2 - t_0$. Note that the biases grow very rapidly for $\Delta t > 2t_0$. Biases based on Fig. 9-44 are reported in the last column of Table 9-2 for $t_0 = 7$ ns. It can be seen that the biases grow rapidly with increasing nadir angle, divergence, and altitude. A 30-degree nadir angle would cause serious errors for nearly all cases, while a 20-degree angle at 15 mr / 300 m also presents a potential problem.

Table 9-2. Time Differences (ns) and Worst-Case Biases (cm)
Due to Beam Divergence

2β (mr)	θ (deg)	H (m)	Δt (ns)	Maximum Bias (cm) ($t_0 = 7$ ns; $f = 0.5$)
5	10	150	1.1	2
5	20	150	2.5	5
5	30	150	4.3	11
5	10	300	2.3	4
5	20	300	5.0	11
5	30	300	18.7	75
10	20	300	10	28
15	10	150	3.6	9
15	20	150	7.8	19
15	30	150	13.3	44
15	10	300	7.2	18
15	20	300	15.5	52
15	30	300	26.7	118

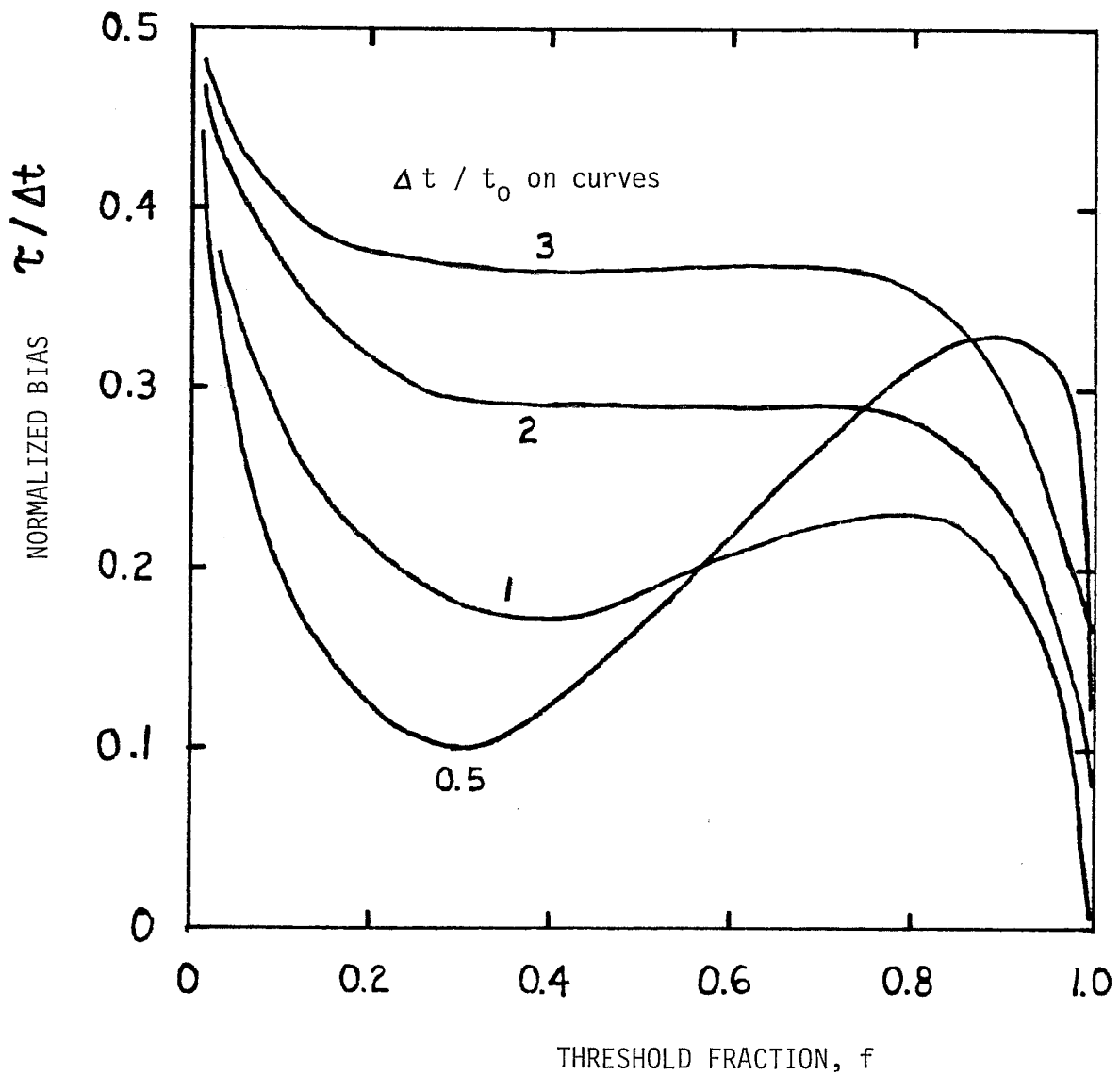


Figure 9-44. Normalized Worst-Case Surface Return Pulse Stretching Bias

For a realistic circular pulse cross section with Gaussian decay, the contribution from the very early arriving energy will be significantly less than for this worst-case estimate, and the actual biases will consequently be less than those reported in Table 9-2. This will reduce the biases to acceptable levels except for 30-degree nadir angles and the 20°/15mr/300m case which could still be a problem and should preferably be avoided unless an ad hoc bias corrector is applied. Surface return geometric stretching is thus not a problem except in extreme cases of high divergence, high nadir angle, and high altitude.

9.2.5 Wave Correction

The goal of hydrography is to measure the mean depth from the local water surface. The appropriate tide corrector is then applied to convert this depth to a desired datum, such as mean lower low water. A single airborne laser hydrography pulse measures the instantaneous depth of the water column, including superposed waves, in a small region whose size is dictated by the aircraft altitude and the laser beam divergence. This region may be much smaller or much larger than a typical dominant water wavelength depending on the wave correction technique selected and the sea state, but in general, the measured instantaneous depth will need to be corrected to the overall mean water level in order to meet international hydrographic accuracy standards. Wave correction techniques and results from the AOL experiment are described in detail in section 5.7.2.

For a given selected altitude, the key parameter in the wave correction procedure is the transmitter beam divergence. One can consider three regimes for divergence: 1) very small (1 - 2 mr) for profiling most gravity waves; 2) very large (100-200 mr) for averaging out most gravity waves; and 3) moderate (10 - 15 mr) for averaging out smaller waves and profiling larger ones. The first technique leads to immediate problems with unacceptably low maximum penetration depths for eye-safe laser pulse energies and large beam-steering errors; it must be rejected. The second method causes severe problems due to loss of spatial resolution and to stretched surface returns which lead to large depth measurement errors and interference with bottom returns in shallow water; it must be rejected. The third method provides a fortunate compromise with none of the above disabling problems.

The selection of beam divergences in the 10 to 15-mr range is one of the few straight-forward choices which can be made in the selection of airborne lidar system variables. This is an acceptable middle ground for eye safety, spatial resolution, and wave averaging requirements. It was seen in section 8.2.4 that the 10-15 mr range permits quite high eye-safe laser pulse energies in the range from 35-80 mJ for a 300-m aircraft altitude. The irradiated surface spot diameters for these cases are 3 m and 4.5 m. These will not cause a serious degradation in spatial resolution because, as seen in section 8.2.5.1, the scattering in the water causes even a very small surface source to spread to an effective diameter at the bottom of over half the depth. In 20-m of water, for example, this would lead to a zero-divergence diameter of approximately 14 m. The diameter of the convolution of this bottom distribution with a 4.5-m surface source will be approximately the quadrature sum of the two diameters, i.e., $(4.5^2 + 14^2)^{0.5} = 14.7$ m. As can be seen, the use of a fairly large beam divergence does not significantly affect the spatial resolution at typical working depths. The fact that the resulting fractional increase in the bottom diameter is larger for smaller depths is of no consequence because a 5-m bottom spot diameter in shallow water is quite acceptable. Surface spot diameters in the 3 - 4.5 m range will yield a weighted average water level for equal or smaller wavelengths (such as would be generated locally by moderate winds).

The maximum wave height regime in which the system is expected to be fully operational is "Sea State 3" with peak-to-trough wave heights of up to 1.5 m -- at which point white caps form. This condition is excited by winds of up to 15 knots (Beaufort 4). Typical resulting wavelengths for this operating range are expected to be on the order of 5 - 40 m for locally generated waves. For the East Coast, ocean swell generated by distant events has wavelengths roughly between 40 m and 140 m for water depths under 40 m.

It is necessary to reduce the effect of these waves and swell on the depth measurements to a residual of $\pm 10 - 15$ cm (1σ). There are three regimes of interest. Waves with wavelengths under 3 - 4.5 m, depending on the transmitter divergence (and altitude), will be averaged out within the surface spot. Wind-driven waves with larger wavelengths will be profiled and actively removed from the depth data in post-flight software. Long period swell with

substantial energy overlapping the aircraft motion spectrum can be distinguished and removed if the system has integrated vertical accelerometer data. It has been demonstrated by NASA with the Airborne Oceanographic Lidar system that doubly-integrated vertical accelerometer data can provide vertical displacement estimates accurate enough over time periods of sufficient length to remove aircraft motion which would otherwise contaminate the ocean swell spectrum.

It was noted earlier that for wavelengths smaller than the surface spot diameter, the calculated depth would be based on a weighted average water level. This is a sort of "passive" wave correction. There are errors associated with this procedure, but their magnitudes are very difficult to estimate. If the waves were uniformly reflective, the fraction of the surface return energy from the crests would arrive first, followed by the energy from the slopes, and finally from the troughs. It is clear that the success of the passive wave corrector depends to a certain extent on the signal processing and pulse location algorithm. Detection of the surface waveform at very low or very high thresholds would emphasize crest or trough locations, respectively. The 50 percent threshold determined in section 9.3.1 to be optimal from the point of view of low random noise and pulse location bias errors and insensitivity to varying pulse widths would also seem to be the best choice from the standpoint of optimally estimating the mean water level for passive wave correction.

The waves, however, are not uniformly reflective. The weighting factor in passive wave correction is related to the previously mentioned (section 5.8.2) propensity for capillary waves to build up near the gravity wave crests. This, in turn, causes them to reflect much more energy back to the receiver than the neighboring troughs in which the capillaries are weak. This causes a high probability of early surface detection which carries with it a depth measurement bias on the deep side. The magnitude of this bias is a complex function of wave height and length, wind speed, beam nadir angle, beam azimuth angle, laser pulse temporal width, altitude, beam divergence, processing electronics, and pulse location algorithm. In the 3 - 4.5 m surface spot diameter range, it is unlikely that the maximum surface height variation for encompassed wavelengths will exceed 1/14 of the largest

wavelength or 32 cm. For the 32 cm wave heights, the maximum error for a 7-ns source pulse width and a threshold at half the peak height is about 8 cm. This is an acceptable offset within the error budget. For smaller wave heights, the bias will be correspondingly lower. The largest absolute wave height difference which can occur in a 4.5 m diameter for a 14 percent surface slope (roughly the maximum before breaking occurs) is 64 cm. The resulting potential 16-cm bias is a bit large but could easily be recognized and halved on an ad hoc basis in the software by applying a waveheight-dependent offset of 8 cm or less.

For a scanning system, the active wave corrector for each pulse is determined as the difference between the predicted and measured slant altitudes. The predicted slant altitudes must be calculated from a least squares estimate of the mean water level derived from a number of preceding slant altitude measurements in the scan pattern, the measured roll, pitch, and yaw of the aircraft, and the scanner equations. The wave height estimate determined from the instantaneous slant altitude data is then applied as a corrector to the depth measurement data to move the datum from instantaneous water column height to mean water level. This is a very complex but very important piece of software. Small depth measurement errors will accrue from altimeter digitization intervals, from the residual errors in the surface fit, from uncertainties in aircraft attitude, and from other factors pertaining to the interface reflection such as the beam size, the wave lengths and slopes, and the capillary structure. Based on the AOL experience it is expected that, with properly designed hardware and software, these errors can be limited to the desired ± 10 cm RMS.

One further surface wave induced error can accrue due to the beam spreading in the water. The principle upon which active wave correction is based assumes that the pulse energy remains in the same medium (i.e., water) from the detected surface reference level (for that pulse) to the bottom and back to the surface reference level. This is not always true because, if the beam enters the water predominantly through a crest, beam spreading can cause a significant fraction of the returning energy to pass through the water/air interface in troughs before it reaches the reference level (which for that pulse was at a wave crest). The time spent travelling from the trough

interface to the crest reference level is in air where the speed of light is 33 percent faster than in water. This can easily be shown to lead to a shallow depth measurement error of 12.5 percent of the waveheight; i.e., if all of the energy incident through a crest returned through troughs, the depth error for a 100-cm waveheight, for example, would be 12.5 cm. For a 20-m depth and a 4.5-m incident surface spot size, the surface spot size of the effective returning bottom reflected energy will be about 15 m, and the maximum waveheight variation over that diameter for a maximum 14 percent slope would be about 100 cm. In actuality, a significant portion of the returning energy will exit through the crest near the point of incidence, and only a fraction will exit through troughs. The actual error incurred will be less than the worst-case 12.5 cm value and can consequently be ignored. A complementary deep error can happen in reverse for pulses entering troughs, but the magnitude would be even smaller because wave crests tend to occupy a much smaller fraction of the total surface area.

It has been seen that the wave-correction procedure is a complex but vital requirement for meeting the system depth measurement accuracy standard. The procedure selected sets limits in the selection of design variables such as transmitter beam divergence which, in turn, affect performance characteristics such as eye safety, penetration, and accuracy. A technique has been recommended whose parameters match well with other system requirements and for which residual errors seem to be within acceptable bounds.

9.3 System-Based Errors

9.3.1 Pulse Location Estimation

9.3.1.1. Introduction

The limiting precision with which depth estimates can be made depends on a number of hardware and software parameters such as laser pulse width and shape, signal digitization bin widths or charge integration times, and pulse detection and location algorithms and their parameters. The basic accuracy standard for hydrography in "shallow" water (less than 30 m) is ± 30 cm. This is the total permissible error accumulated from all sources including random

error, bias, tide control, positioning, waves, etc. It is estimated that a maximum of roughly half this error budget, ± 15 cm, should be allocated for "precision", i.e., lack of short-term (pulse to pulse) repeatability. This is equivalent to ± 1.3 ns of round-trip time in water. In this domain (near gigahertz frequency) it may be perceived that extremely stringent requirements are incumbent on the receiving electronics system and the processing algorithms -- particularly in view of the fact that a practical laser pulse is expected to be emitted with a "half width" (FWHM) of no less than about 5 ns and will be further stretched as it propagates through the water. It is thus vital to have a means of selecting and evaluating design parameters based on their inherent accuracy potential. The purpose of this study has been to provide results upon which such judgements can be based.

The simulations herein described have been conducted for linearly processed pulses with algorithms and parameter ranges consistent with state-of-the-art laser and electronics hardware in such a way that the effects on the accuracy of algorithm or parameter trade-offs can be explicitly resolved. In this way, development programs for unavailable components can be prioritized not only by their cost but by their cost-effectiveness. Furthermore, pulse location techniques, whether implemented in hardware or software, analog or digital, may be selected to provide the optimum balance between random and bias errors over a typical range of operating conditions. This will permit the selection of the best alternatives within the constraints of resources, technology, and operational restrictions.

The method selected for the solution of these problems is a Monte Carlo computer simulation employing a Poisson count generator. This program has been exercised to generate precision and offset results for the estimated temporal location of representative laser pulses. Pulse sizes, shapes, and charge integration times are varied over appropriate ranges. A number of location estimators including variations on peak, centroid, and threshold detectors are examined. Comparisons with experimental results are presented. Hardware and software design parameters for an airborne lidar hydrography system are discussed. The description reported here is condensed from Guenther and Thomas (1981d).

9.3.1.2 Description of the Simulation

9.3.1.2.1 Concept

The concept to be simulated consists of an input pulse waveform sampled by a series of discrete, temporally adjoined quantum accumulation intervals which, in effect, integrate charge from adjacent time slices across the superimposed pulse. In practice, this could be the results of sampling a pulsed lidar signal from the output of the photocathode of a photomultiplier tube with an a/d converter. (The simulation is performed at the output of the photocathode since this location represents the lowest signal level and thus dictates the limiting signal-to-noise-ratio for the system.) The resultant output is a series of cardinal numerals representing the time-sampled amplitudes of the input pulse. These integer values are subject to Poisson statistics; that is to say, for any fixed mean input signal or photoelectron arrival "rate" in a time slice, the distribution of output values from that time "bin", over a number of pulses, will be Poisson. The optional selection of Gaussian statistics instead of Poisson statistics in data set generation has been included in the code for its ability to save computer time when large mean rates are involved.

The simulation process consists first of generating a large number (typically 100 or more) of digitized pulse waveforms, or "data sets", with Poisson distribution about a specified mean signal. A given set of pulse location estimation "procedures" are then applied to each data set. For the laser bathymetry application, eight procedures have been applied; these consist of center of peak bin, centroid of a specified band of bins surrounding the peak, and frontwards- and backwards-looking proportional thresholds at the 20, 50, and 80 percent levels (illustrated in Fig. 9-45). The mean location, standard deviation, standard error in the mean, and success probability (fractional number of location determinations compared to the number of attempts) for the ensemble of data sets are calculated for each procedure. A bias may be obtained for each procedure by noting the difference between the calculated mean location and the "true" or expected location.

Forward **Backward**
Searching **Searching**
↔ ←

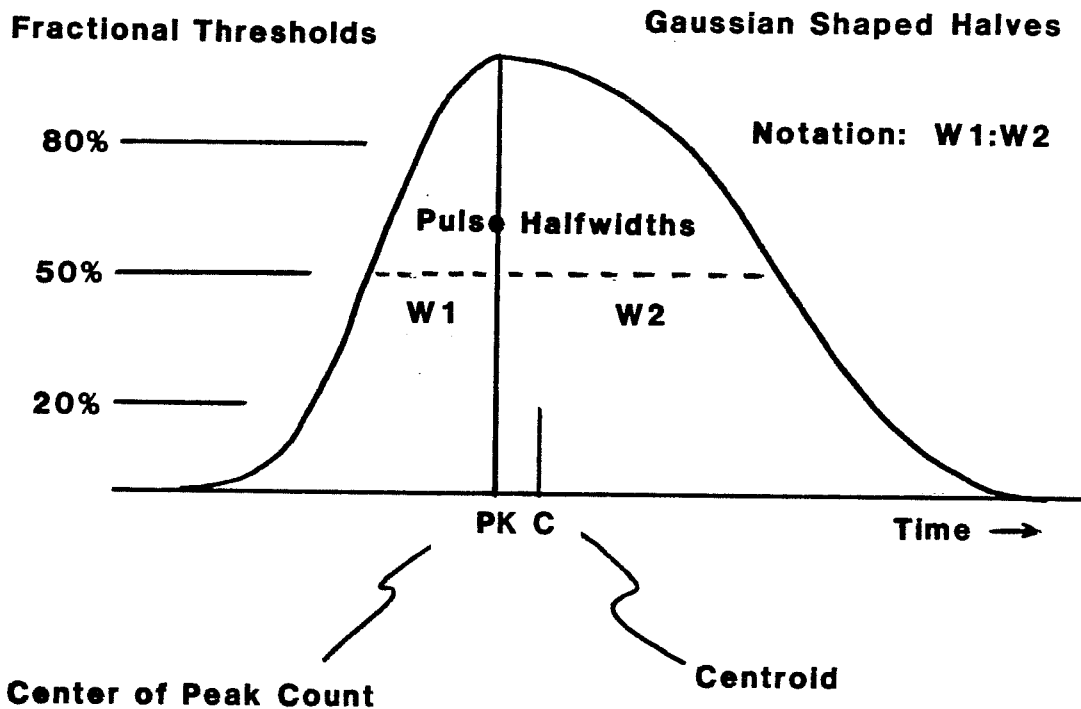


Figure 9-45 Input Pulse Shape and Pulse Location Algorithms

The simulation is performed over the ensemble of data sets to determine pulse location statistics for a single pulse, but a bathymetric measurement is based on two independent pulses: the surface return and the bottom return. The "precision" or standard deviation of a simulated bathymetric measurement is then the root sum of squares (RSS) of the standard deviations for two independent pulses, and biases are summed algebraically to obtain the bathymetric bias for the procedure. The probability of a successful depth measurement is the product of the individual success probabilities.

9.3.1.2.2 Data Synthesis

Consider a continuous waveform representing an analog pulse superimposed arbitrarily on a time axis which has been divided into a number of adjacent "increments" or time slices of equal width. In each increment, or "bin", the analog signal is integrated and normalized to yield a single value which is displayed as a constant output level for the duration of that bin. The shape of this digital representation will depend strongly on the location of the input peak with respect to the edges of the time bins as seen in Fig. 9-46.

It is clear that if random amplitude noise is added to the time bins, a peak location solidly in the center of a time bin will generally remain in that bin, but a peak location near the edge between two bins will cause the sampled peak to jump back and forth between the two. The standard deviation of the estimate of a pulse location procedure can rightfully be expected to be larger for the latter case -- by an amount which depends on the procedure, the pulse width, and the bin width.

In an operational situation, the actual pulse locations may generally be assumed to be uniformly and randomly distributed over the space from the bin edge to bin center. Simulations are performed in which mean rate input pulses are placed at a number of equally spaced locations across the width of a bin and the output standard deviation of the location estimate is averaged over all cases, as follows. If the mean pulse location (for a given algorithm) for the i^{th} peak location across the bin is M_i and the variance about that mean is V_i , the overall variance for peak locations uniformly distributed across the width of a bin is

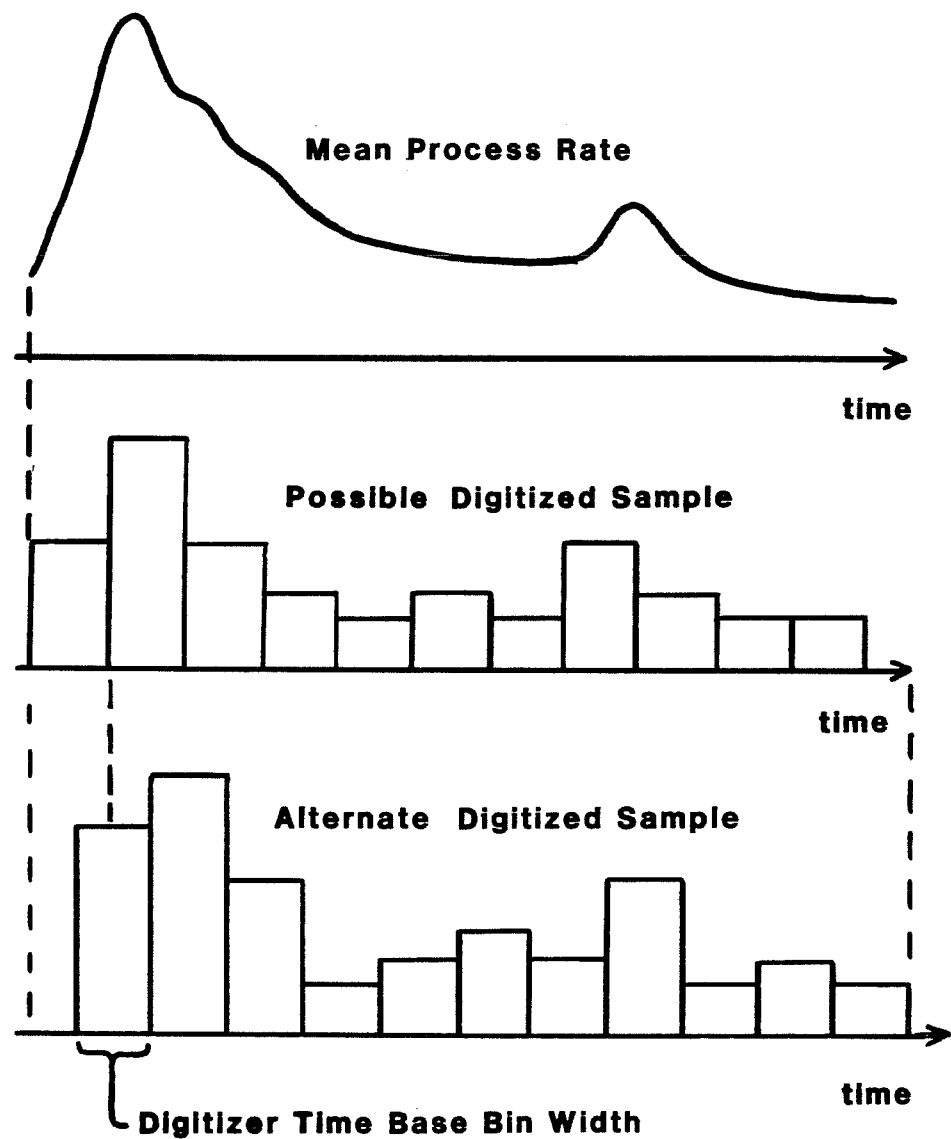


Figure 9-46. Illustration of Digitization Timing

$$V = \frac{1}{r} \sum_{i=1}^r (V_i + M_i^2) - \frac{1}{r^2} \left(\sum_{i=1}^r M_i \right)^2 , \quad (9-12)$$

where r is the number of positions sampled. Simulations have been performed for $r = 10$.

While the simulator possesses the capability to generate a broad range of pulse shapes, the specific mean rate distributions, $f(t)$, considered here are generally of Gaussian character (recall Fig. 9-45). (This temporal pulse shape is completely different from and should not be confused with the probability distribution involved.) The asymmetric shapes utilized to simulate arriving laser pulses consist of a Gaussian leading edge of a given width combined with a Gaussian trailing edge with a different (longer) width. Triangular shaped pulses have also been examined, and results are very similar. Pulse shape and width will henceforth be denoted by listing the one standard deviation (1σ) leading and trailing-edge widths (in nanoseconds) separated by a colon, i.e., 3:5 or 5:20.

All pulse location procedures to be tested are applied to the same ensemble of data sets; this insures that observed differences are due to the procedures and not statistical anomalies in data set generation. Random errors in the output statistics for pulse location procedures due to the particular random number sequences involved in data set generation can be constrained to any desired level by selection of a sufficiently large number of data sets per ensemble. A minimum value of 100 data sets per ensemble was used; this provides an expected standard error in the estimate of the standard deviation of pulse location (for a given procedure) of $1/\sqrt{2n} = 1/\sqrt{200} \sim 7$ percent.

Bathymetric lidar is intended for daytime use as well as night. Under daylight conditions, the lidar return pulses are superimposed on the additive background level of the volume reflected solar background. In the simulator, a selectable constant mean background rate is added to all bins in the mean rate input pulse data prior to generation of the probability tables and data sets. This mean rate, having exerted its influence on the distribution of

Poisson counts, is then subtracted from all data sets prior to pulse detection/location in order to simulate a realistic system in which this would be accomplished to remove any pulse location bias which could be caused by an uncorrected background level. Negative values generated by this subtraction are set to zero.

The gain of the system and the number of bits in the digitizer act to truncate certain ranges in the number of photoevents into a discrete "count." For example, if 10 photoevents are required to produce a single count, then both 21 and 29 photoevents will produce 2 counts, while 30 photoevents will produce 3 counts. This truncation effect can alter counting statistics, and hence the number of photoevents per count is included in the simulation as an input variable.

9.3.1.2.3 Pulse Location Estimators

The first step in pulse location is pulse detection. In the simulation, a pulse is "detected" at the site of the maximum integer in the data set or the first of equal maxima. The location and magnitude of the detected peak are stored for use in the pulse location procedures. Three basic types of pulse location procedures have been analyzed: these are center of peak bin, centroid of a region linked to the peak bin, and threshold.

If we were to base our pulse location estimation only on a selected count, i.e., the peak, we would have to assign the pulse location to an arbitrary point within the corresponding time bin. With no further information, we could do no better than choose the middle of the time bin to be the required location. In reality, pulse peaks will be distributed uniformly across the bin width. The minimum RMS error for a peak detector is thus the bin width divided by the square root of twelve (the standard deviation of a uniform distribution). A procedure which allows a location estimate anywhere within a bin would therefore be preferable. With little "a priori" knowledge of the return pulse shape, curve fitting estimators and correlators appear to be overambitious; we have thus considered centroid and threshold estimators.

Centroid based locators are defined by choices of the length of the centroid region, whether the length is fixed or variable (depending on the pulse width), and of the relative location of the peak within the region (i.e., a centroid of only the leading edge, one balanced symmetrically or asymmetrically on the peak, or one encompassing the entire pulse energy). Results are reported for slightly asymmetric centroids (matched to pulse shape) of various lengths keyed to the peak bin.

Threshold based locators can be categorized as fixed level or fractional (ratioed to peak height), and they can be forward searching or backward searching (in time). The performance of any of these variations depends strongly on the specific threshold level selected. In the simulation, the exact threshold location is selected by identifying the bin in which the specified level is passed and interpolating to a fractional location between that and the previous bin based on the peak signal amplitudes involved.

9.3.1.3 Results

9.3.1.3.1 Prediction of AOL Performance

This pulse location estimation (PLE) simulator was originally conceived for the purpose of predicting the limiting precision (random depth measurement error as a function of bottom return signal strength) imposed by the hardware in the NASA/AVCO Airborne Oceanographic Lidar (AOL) system which was being test flown for NOAA in the bathymetry mode (section 5). Without this information, there would have been no way of allocating the measured random errors between basic design constraints and unknown causes which would require further investigation. As seen in Fig. 5-21, the system precision (for calm sea conditions) and the simulation results are in excellent agreement. Not only did this give us confidence that the AOL was performing to its design limits, but it also, in turn, verified the performance of the simulation for further predictive purposes.

The simulation also produced a rather surprising result: fractional threshold algorithms (among others) applied to single asymmetric pulses yield offsets (compared to the "true" location) toward the tail of the pulse with

magnitudes as large as 30 cm for the cases studied. It is important to note that, in a two pulse measurement, these offsets will be self cancelling to the extent that the two pulses have the same shape and duration. For a "stretched" bottom return, however, a net depth measurement bias in the deep direction will result as the difference between the offsets for the two single pulse cases. The offsets (and hence resultant bias) are very small for small (20 percent) threshold fractions and can become large for high (80 percent) threshold fractions. For example, given a 2.5-ns bin width and a 20 photoelectrons per nanosecond (pe/ns) peak rate, a pulse stretching from 3:5 ns to 5:20 ns would exhibit a 5-cm bias with a 20 percent threshold, a 6-cm bias with a 50 percent threshold, and a 13-cm bias with an 80 percent threshold.

9.3.1.3.2 Sensitivity Studies

In a shot-noise limited system, the measurement accuracy depends not only on the ratio of return signal strength to ambient background, but on the absolute magnitudes of these two individual components. Simulations have been conducted for two diverse conditions: low absolute rates (consistent with AOL performance) and high absolute rates (consistent with the design parameters of the Hydrographic Airborne Laser Sounder (HALS) designed by AVCO for the U.S. Navy). The distinction arises not from different environmental conditions (such as night versus day), but rather from different transceiver configurations (output power, optics, etc.).

Low Signal Rates

When photon arrival rates are low, counting statistics and the resulting shot-noise level are very sensitive to factors which cause changes in the rates. Such factors as pulse width, integration time (bin width), and amplifier gain (truncation in digitization) are important because they will have larger effects here than in high rate systems. Simulations were performed for all combinations of the parameter sets listed in Table 9-3.

Table 9-3. Simulated Parameters and Procedures

Pulse width: 1:2 ns, 3:5 ns, 4:10 ns, 5:20 ns (as defined in Fig. 9-45)

Bin width: 1.5 ns, 2.5 ns, 5.0 ns

Algorithms: centroid (a 6-bin window with the peak in bin 3 denoted "6C3"), center of peak count (denoted "PK"), and forward- and backward-looking fractional thresholds at 20 percent, 50 percent, and 80 percent of the peak amplitude (denoted F20, F50, F80, B20, B50, and B80).

For the AOL case, the mean peak rate was varied from 2 photoelectrons per nanosecond (pe/ns) to 20 pe/ns in steps of 2 pe/ns. The solar background for daytime operation was estimated to be 8 pe/ns, while the dark current of the PMT was estimated to be 2 pe/ns for nighttime operation. Truncation levels of 1, 4, and 8 pe/"discrete" count were exercised. Sample results appear in Figs. 9-47 through 9-61.

The effect of the pulse location algorithm is examined for the case of a typical unstretched pulse at night in Figs. 9-47 and 9-48 which present mean pulse location and the standard deviation about that mean (as function of the peak signal strength) for various algorithms. Notation used in identifying the algorithms on the plots is listed in Table 9-3.

It can be seen in Fig. 9-47 that as the peak signal strength is reduced, the mean pulse location remains constant and stable for all algorithms except F20 until about 6 pe/ns (a peak signal to mean background ratio of S/B=3). The F20 result (i.e., for a forward-looking 20 percent threshold searching from the beginning of the data set) becomes unstable for peak signals of less than 12 pe/ns. This is indicated by the drop in the mean F20 pulse location below its (correct) high signal strength value. This drop is caused by shot-noise induced false early detections generated in the region between the start of the data set and the true 20 percent threshold location.

This results, as clearly evidenced in Fig. 9-48, in a very large standard deviation for the F20 algorithm below a peak signal strength of 10 pe/ns. The

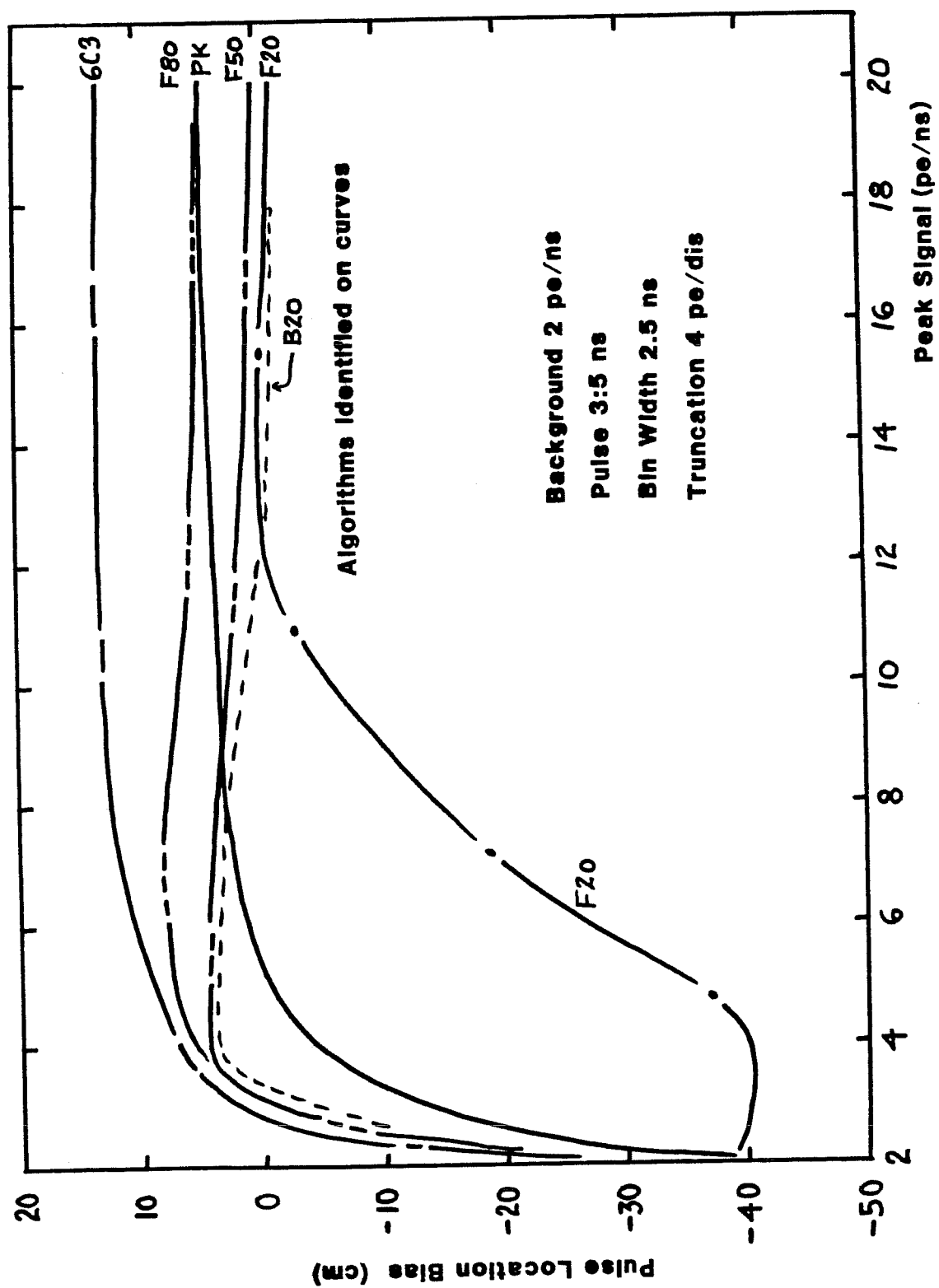


Figure 9-47. Biases for Nominal Pulse at Night

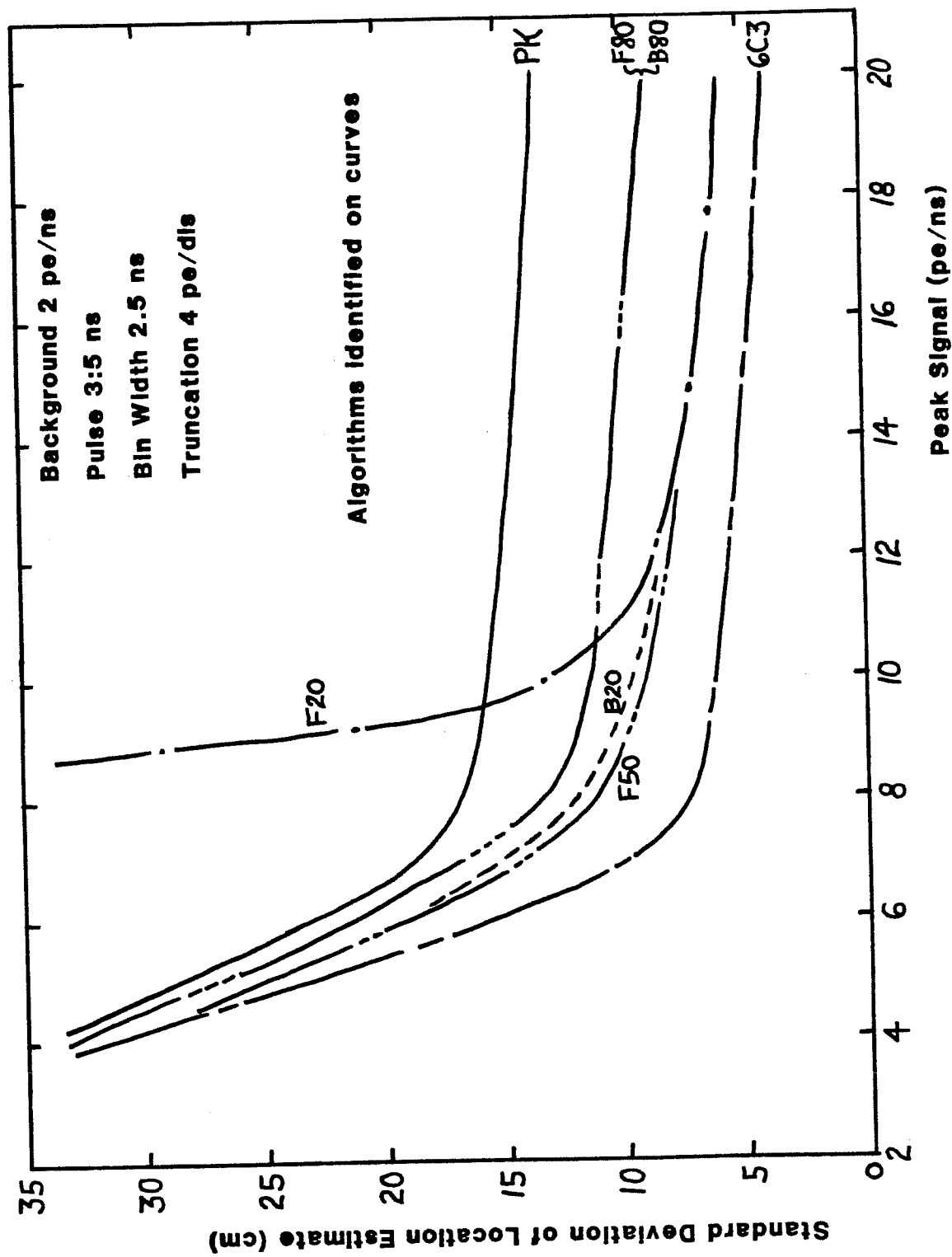


Figure 9-48, Precision for Nominal Pulse at Night

remaining algorithms produce pulse location precisions (with magnitudes related to the algorithm) which do not increase significantly until the peak signal rate drops below about 8 pe/ns ($S/B=4$). It can be seen that, for this parameter set, the best performance (lowest asymptotic standard deviation at high peak rates) from a threshold detector is about 6 cm at 20 pe/ns derived from B20, F50, and B50; while F80 and B80 are slightly noisier at 9 cm. Peak detection at 13 cm is much noisier and yields a standard deviation twice as large as that for the preferred algorithms. The 6-point asymmetric centroid is, in this case, well matched to the pulse and hence offers the lowest standard deviation of 4 cm. This will not always be the result, however, because the precision of a centroid-based pulse location estimate depends strongly on the "matching" of the size and location of the centroid window to the given pulse. The high standard deviation associated with the peak location is, however, as will be seen, a general result.

A similar set of results is presented in Figs. 9-49 and 9-50 for a stretched (e.g., by underwater propagation) return pulse. It is seen in Fig. 9-49 that the results for the means are similar to but subtly different from those for the previous "nominal" pulse. The peak location is biased above its actual location by the high probability of detecting a peak (caused by noise spikes) on the long, slowly-decaying trailing edge of the pulse. As the peak signal rate is reduced, several of the fractional threshold derived means rise slightly (rather than fall as in the previous example) for the same basic reason. The F20 algorithm again becomes unstable below 6 pe/ns due to early detections in the noise preceding the pulse.

Most precision results for this case, as seen in Fig. 9-50, are qualitatively similar to the former case, but quite different quantitatively. One major qualitative difference is the relative performance of the centroid detector whose standard deviation of 28 cm (at 29 pe/ns) falls far above that for the 20 percent and 50 percent thresholds and just below that of the peak detector at 33 cm. This occurs because the 6 bin window is no longer large enough to encompass the entire pulse, and the centroid result "jitters" with the movement of the peak detector to which it is tied. In addition, the B80 at 30 cm is not as good as the F80 at 21 cm due to the flatter shape of the top of the pulse. The F50 and B20 at 10 cm are again preferred; the F20 is

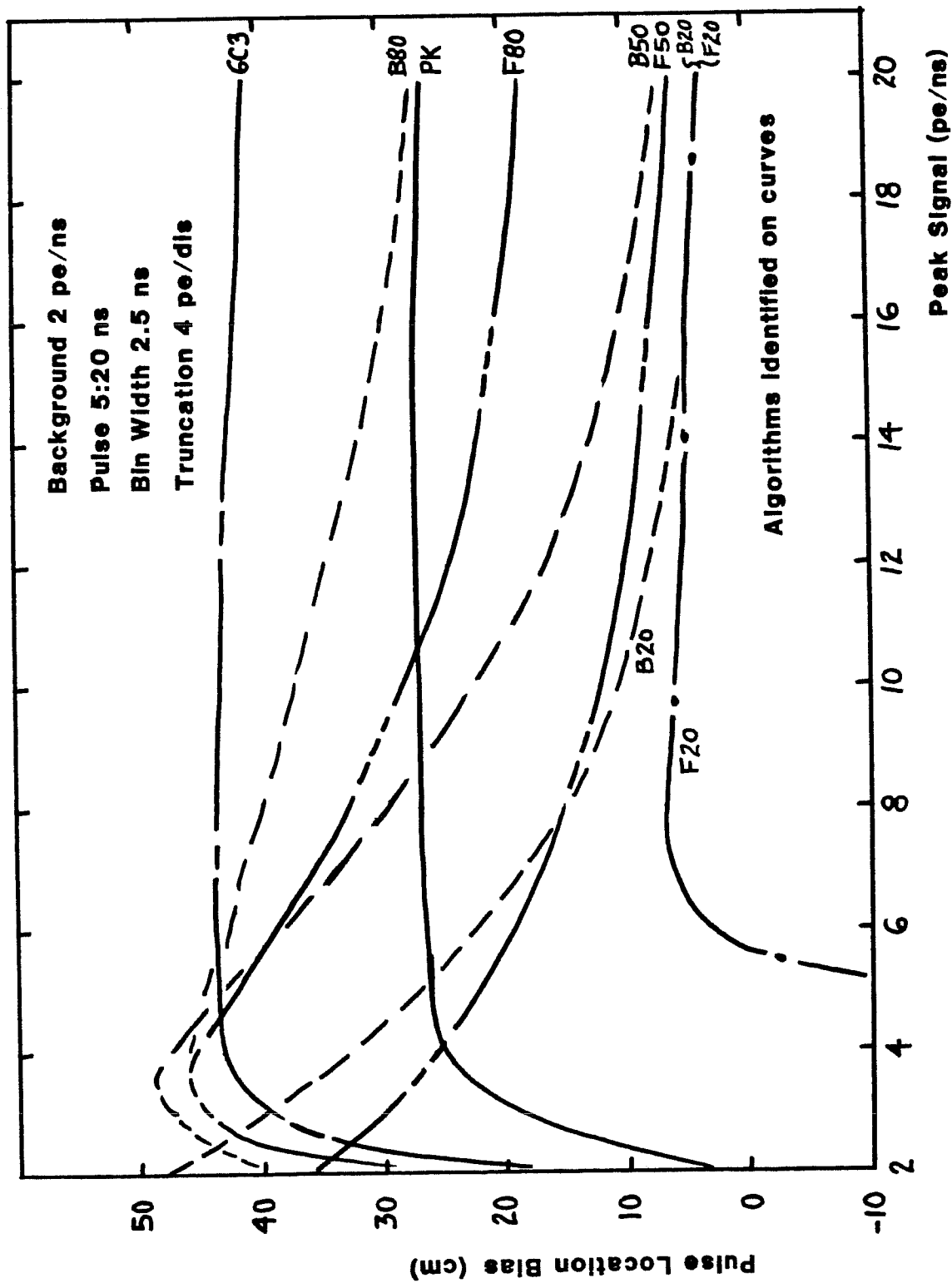


Figure 9-49: Blases for Stretched Pulse at Night

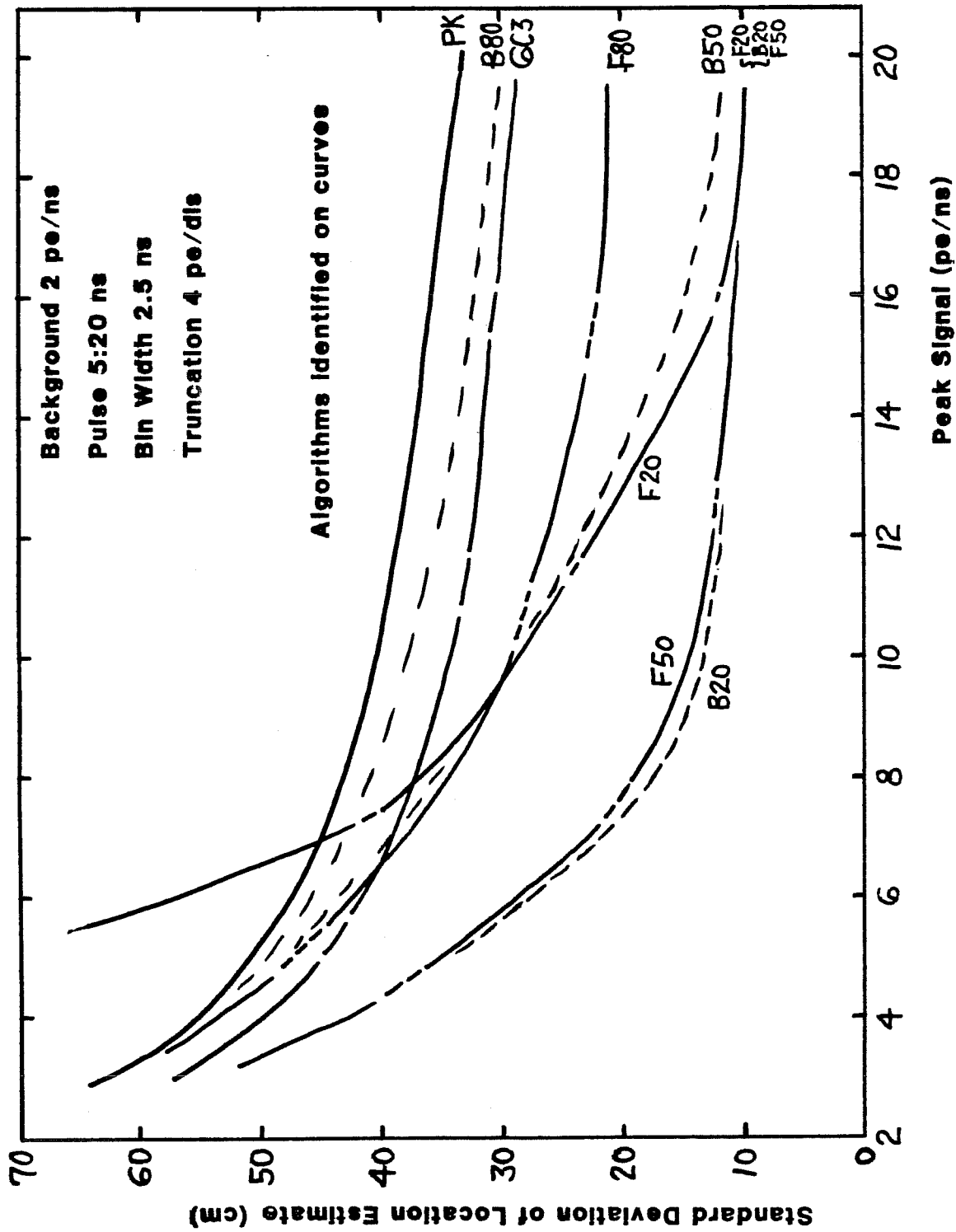


Figure 9-5a. Precision for Stretched Pulse at Night

lost in the noise at low signal levels, and the B50 is still feeling the effects of the elongated pulse shape as evidenced by unusually prolonged elevated values at middle-sized peak signal rates.

It is very important to note the effect of the increased pulse width on the limiting precision of the various algorithms. In the field, the bottom return pulse width will increase with increasing depth (as noted in section 9.2.1). It would not, therefore, be appropriate to select an algorithm whose basic precision limitation is strongly sensitive to pulse width. The aforementioned limiting precision results are compiled in Table 9-4.

Table 9-4. Effect of Pulse Width on Limiting Precision
(at 20 pe/ns) for Various Algorithms with 2.5 ns Bins

Algorithm*†	Limiting Precision (cm)		Increase (cm)
	Pulse width 3:5 ns	5:20 ns	
6C3 centroid	4	29	25
PK (peak)	14	33	19
B20 threshold	6	10	4
F50 threshold	6	10	4
F80 threshold	9	21	12
B80 threshold	9	30	21

It is clear that the B20 and F50 algorithms not only produce some of the lowest standard deviations for unstretched pulses but also are the least sensitive to pulse stretching. This is further illustrated in Fig. 9-51 which compares the performance of a peak detector against F50 for increasing pulse widths.

* for notation see Table 9-3

† F20 and B50 are excluded due to poor performance as described in the text

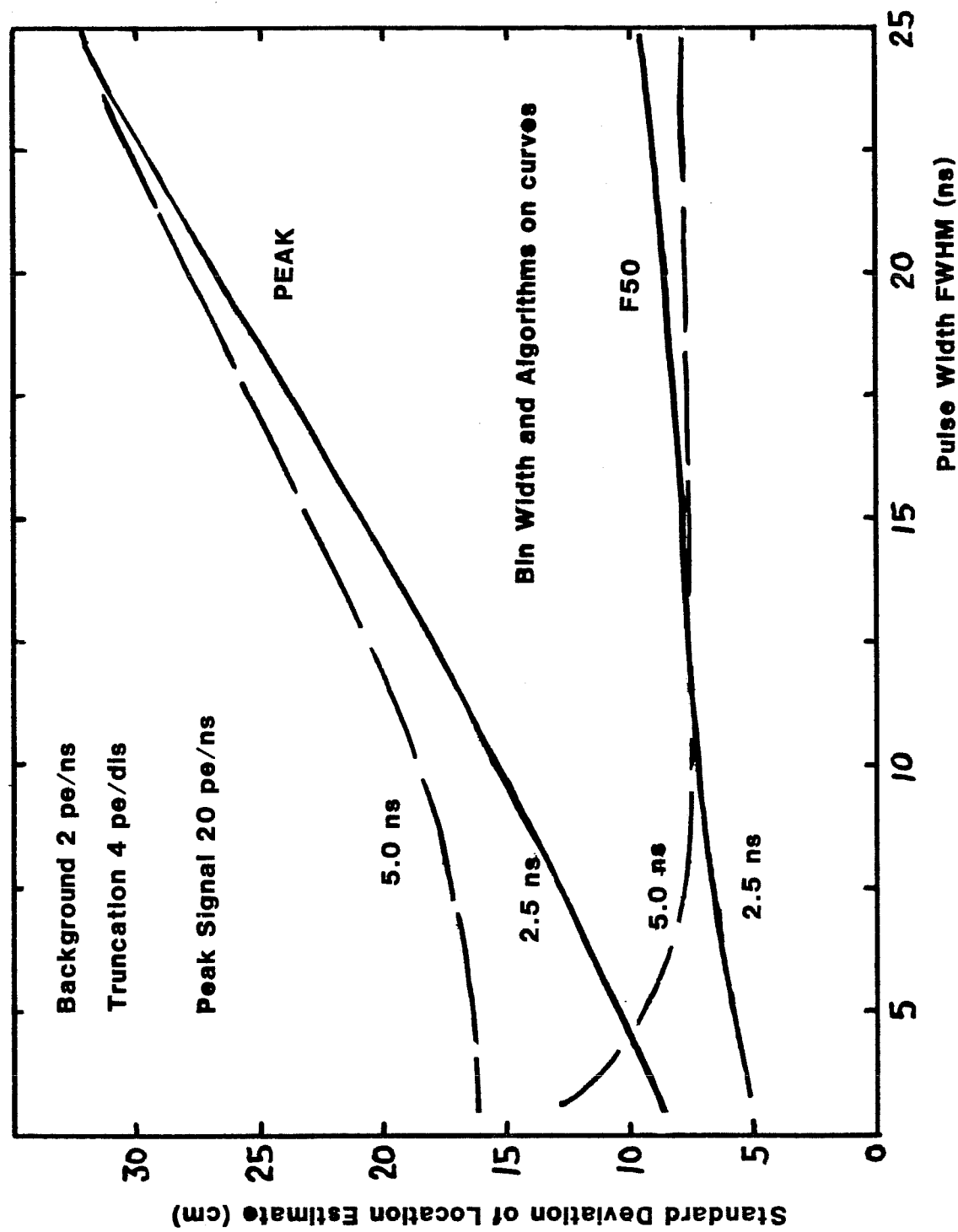


Figure 9-51. Effect of Pulse Stretching for Two Algorithms

The choice of the "optimum" threshold fraction (defined in terms of the lowest standard deviation) depends to a certain extent on both pulse width and bin width as seen in Fig. 9-52. Here we see the value of the mean peak signal strength required to reduce the standard deviation of the pulse location estimate to 10 cm or less as a function of the threshold fraction.

For narrow (1:2 ns) pulses fairly large threshold fractions are preferred. As the pulse width increases to 3:5 ns, a minimum forms at a threshold fraction of about 0.5. As the width increases to 5:20 ns, the required signal becomes larger and higher threshold fractions become increasingly undesirable, particularly for narrow bin widths. The increase in required signal is due to the decreasing slope at the detection point. The increasingly poor performance for narrow bins is a result of the classic struggle between resolution and accuracy. As the bin size is decreased, the resolution improves, but the encompassed signal in each bin decreases, and the counting statistics cause the overall accuracy to degrade. Over a range of pulse widths, it can be seen in Fig. 9-52 that the optimum threshold fraction lies in the range from 0.3 to 0.6. For the cases illustrated, the wider 5.0-ns bin results in slightly better performance for pulse widths of 3:5 ns and greater. This bin size effect will be illustrated again after a few other sensitivities are examined.

Figures 9-53 and 9-54 illustrate the effect of raising the background rate to 8 pe/ns to simulate the effect of daytime operation. A comparison of these curves with Figs. 9-48 and 9-50 indicates that results for most algorithms are remarkably similar in shape and limiting value (at high signals) and that the curves are basically shifted toward higher peak rates with the "knees" occurring at about 10 pe/ns ($P/B \sim 1.2$). An exception is F20 which can be seen (in Fig. 9-53 at the upper right corner and mid-group in Fig. 9-54) to have been made even worse than before (as might be expected). The effect of the increased (solar) background on the F50 algorithm is seen directly in Fig. 9-55 for nominal and stretched pulses. For peak signal strengths beyond about 12 pe/ns the differences are reasonably small compared to the desired error budget.

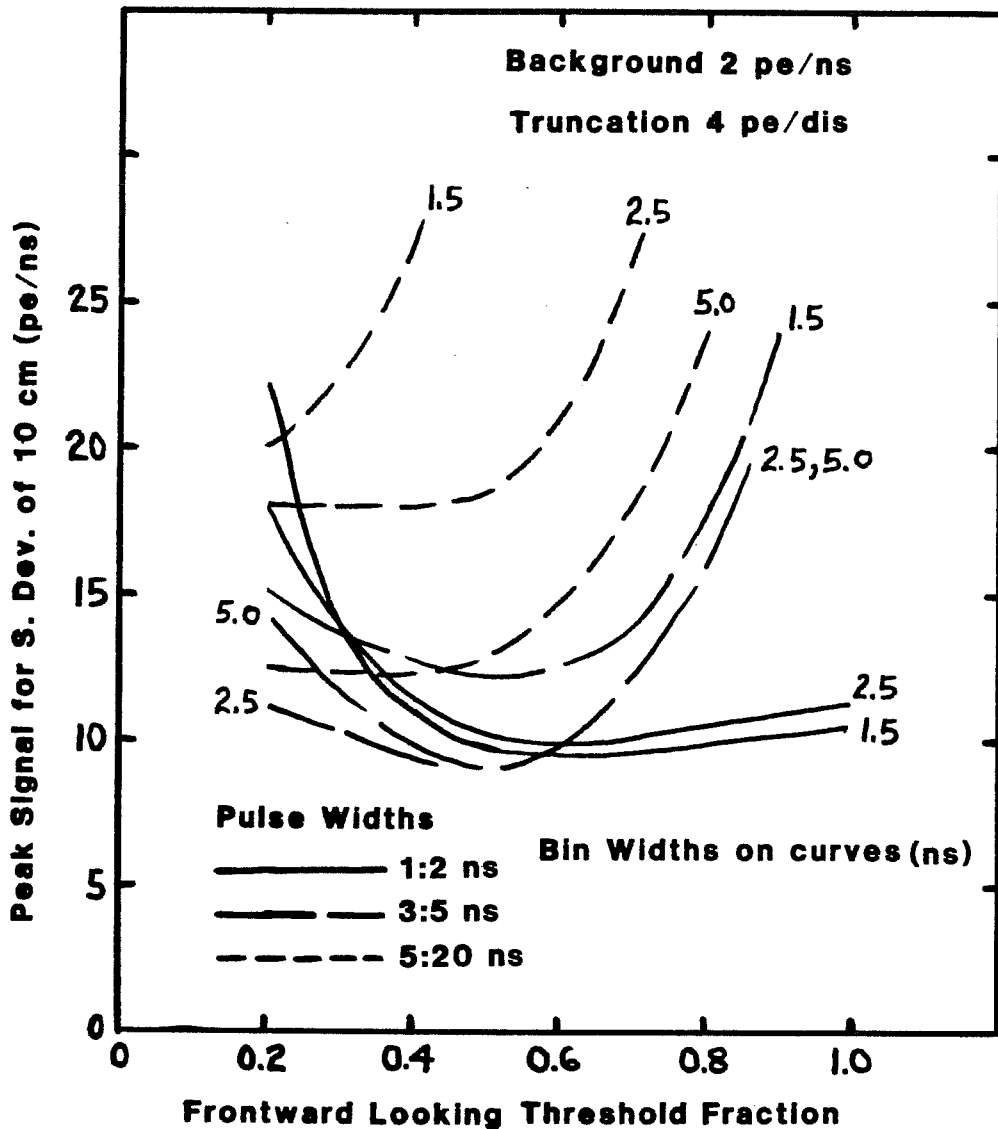


Figure 9-52. Effect of Threshold Fraction on Signal Required for 10 cm Precision

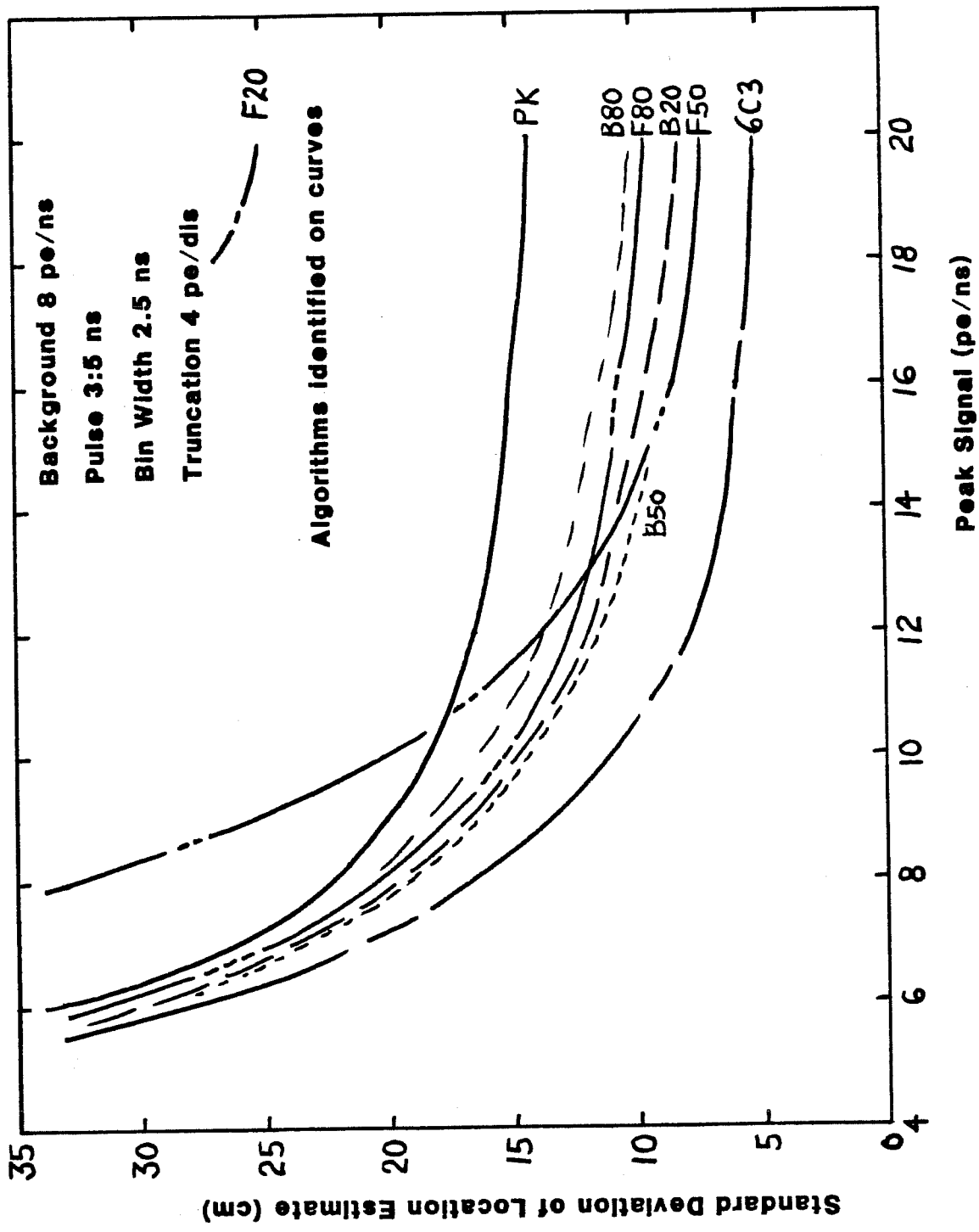


Figure 9-53. Precision for Nominal Pulse in Daylight

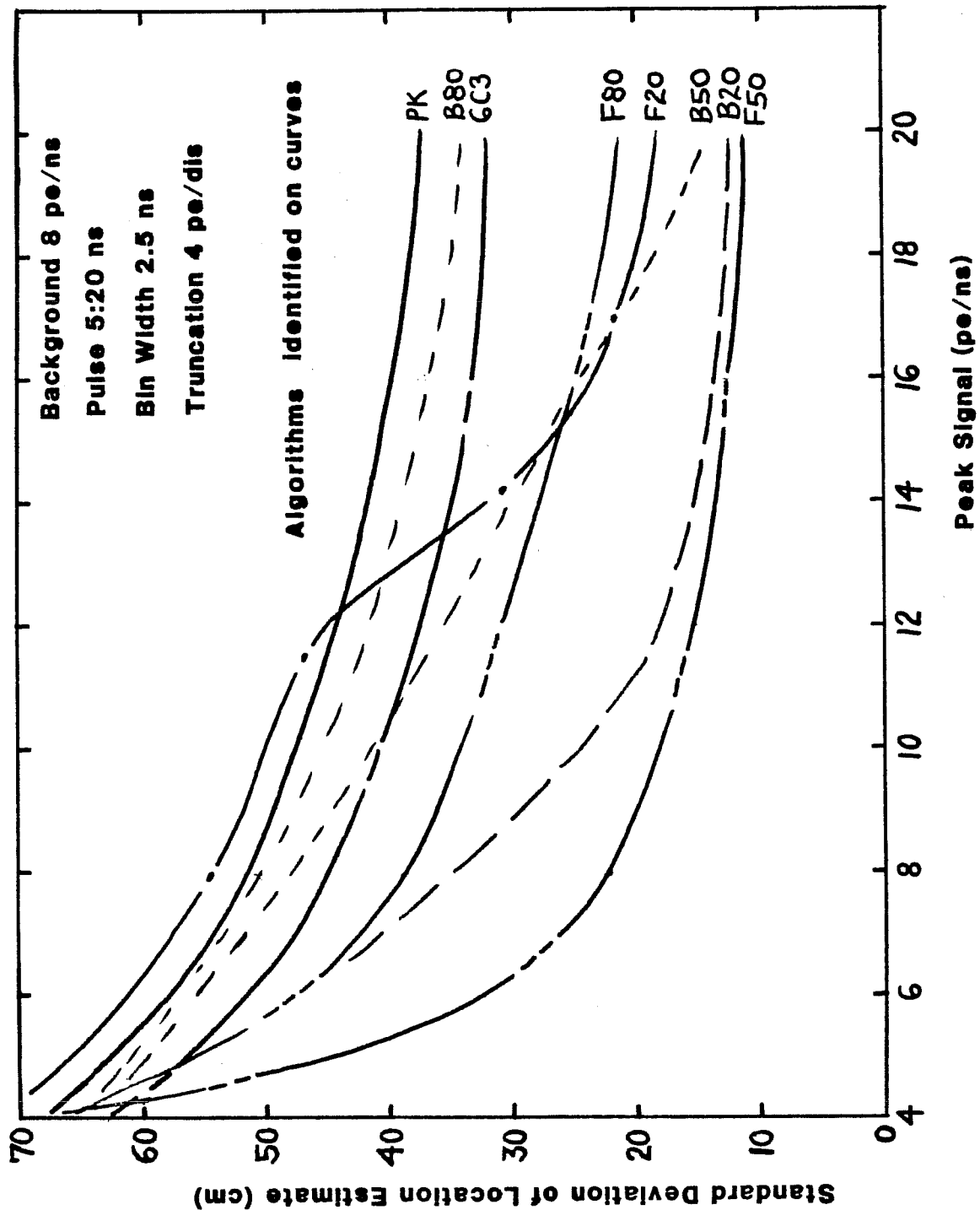


Figure 9-54. Precision for Stretched Pulse In Daylight

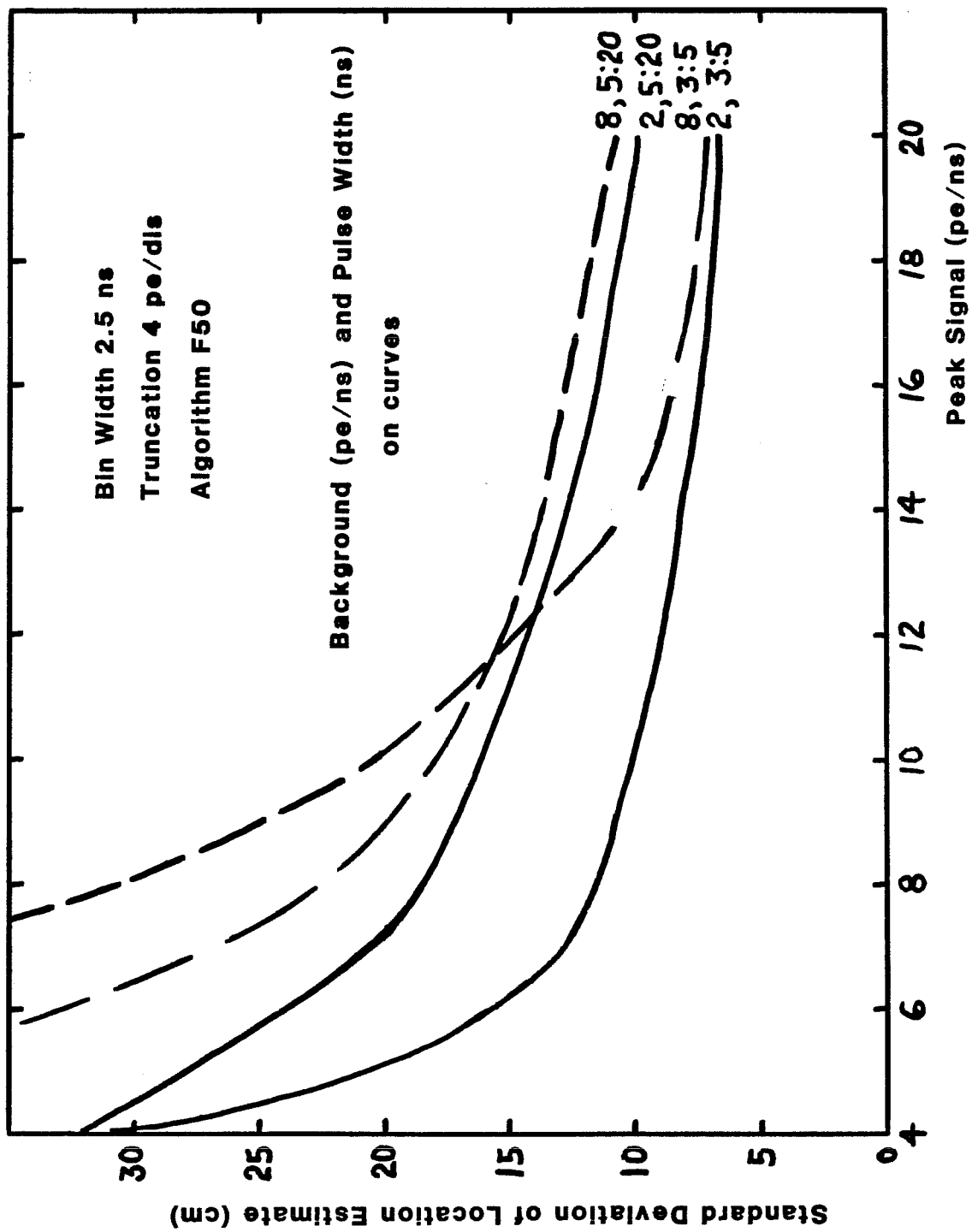


Figure 9-55. Day vs. Night Effect

Because of its demonstrated superior performance, the F50 algorithm will be used as a standard for the remaining sensitivity analyses.

The effect of truncation of counts by the digitizer is demonstrated in Fig. 9-56 for the F50 algorithm. It is clear that this effect is small compared to many others, and the "standard" value of 4 pe/ns which has been used in previous comparisons will be continued.

The effect of bin size for an F50 algorithm applied to nominal and stretched pulses is seen in Figs. 9-57 and 9-58 to be quite small and not worth discussing except to note that for a wide pulse, decreasing the bin width causes a slight increase (rather than decrease) in the random pulse location error -- due to the previously mentioned effect of counting statistics.

The effect of pulse width for three bin widths is presented in Figs. 9-59 through 9-61. It can be noted that for an F50 algorithm, the reduction in precision due to moderate pulse stretching is only about 3 cm and is not significant.

High Signal Rates

Sample results are illustrated in Figs. 9-62 through 9-65. The effect of pulse location algorithm on the behavior of the means and standard deviations of the estimated pulse location is qualitatively similar to that for low signal rates. Specifically, the measurement bias and precision from peak detectors depend strongly on both bin width and pulse width, and the precision is poor (compared to fractional threshold detectors) for either wide bins or wide pulses). For narrow pulses, i.e., 3:5 or less, the precision depends on the bin width due to the discrete nature of the detection locations. For a wide (5:20 ns) pulse, the random error dominates due to the high probability of detection along the broad trailing edge, and the standard deviation is thus large and fairly independent of bin widths up to 5.0 ns. A considerable deep bias is also associated with this effect as seen in Fig. 9-64. Centroid detectors with a fixed number of bins locked to the peak vary considerably in performance depending on relative bin and pulse width and provide tremendous

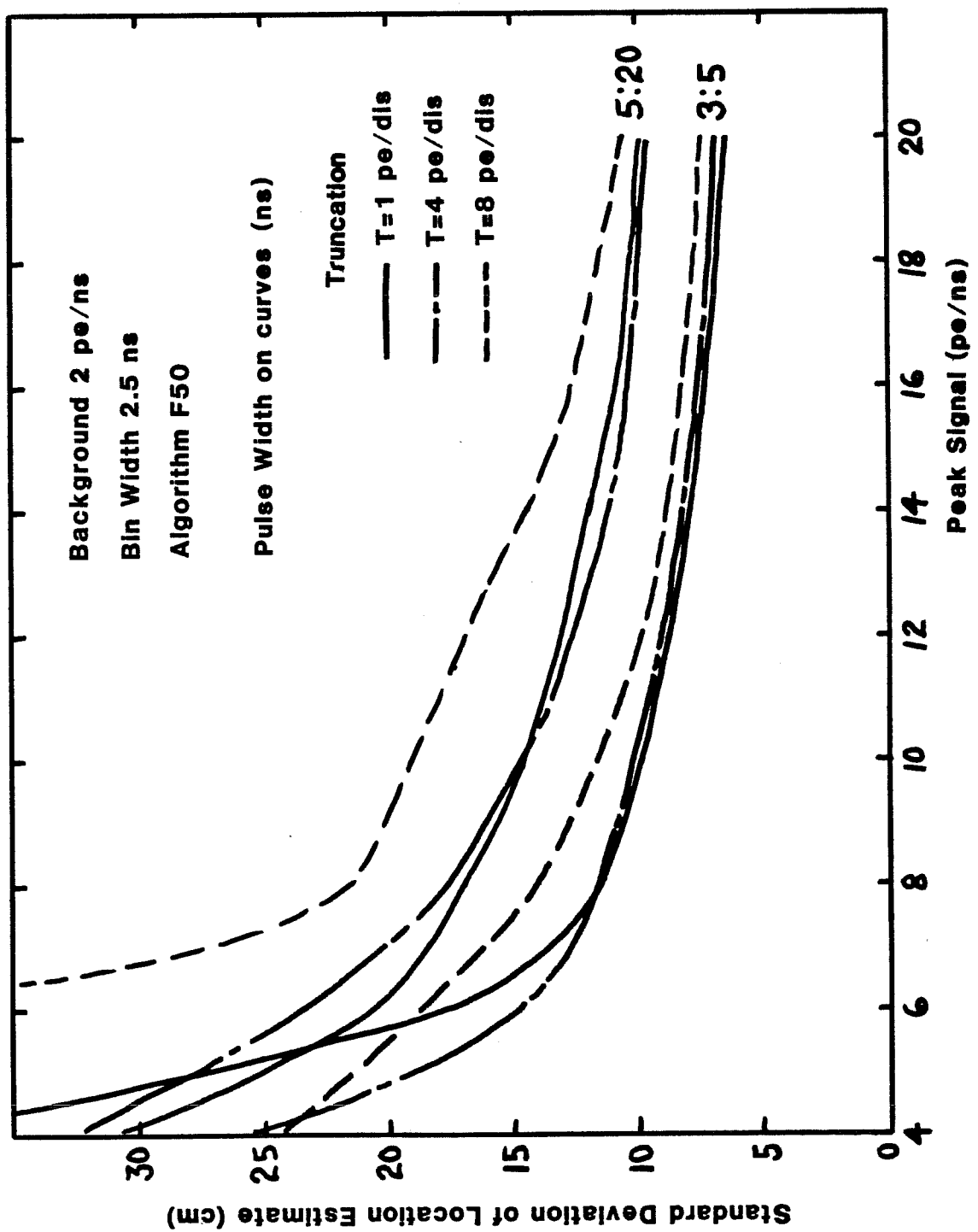


Figure 9-56. Truncation Effect

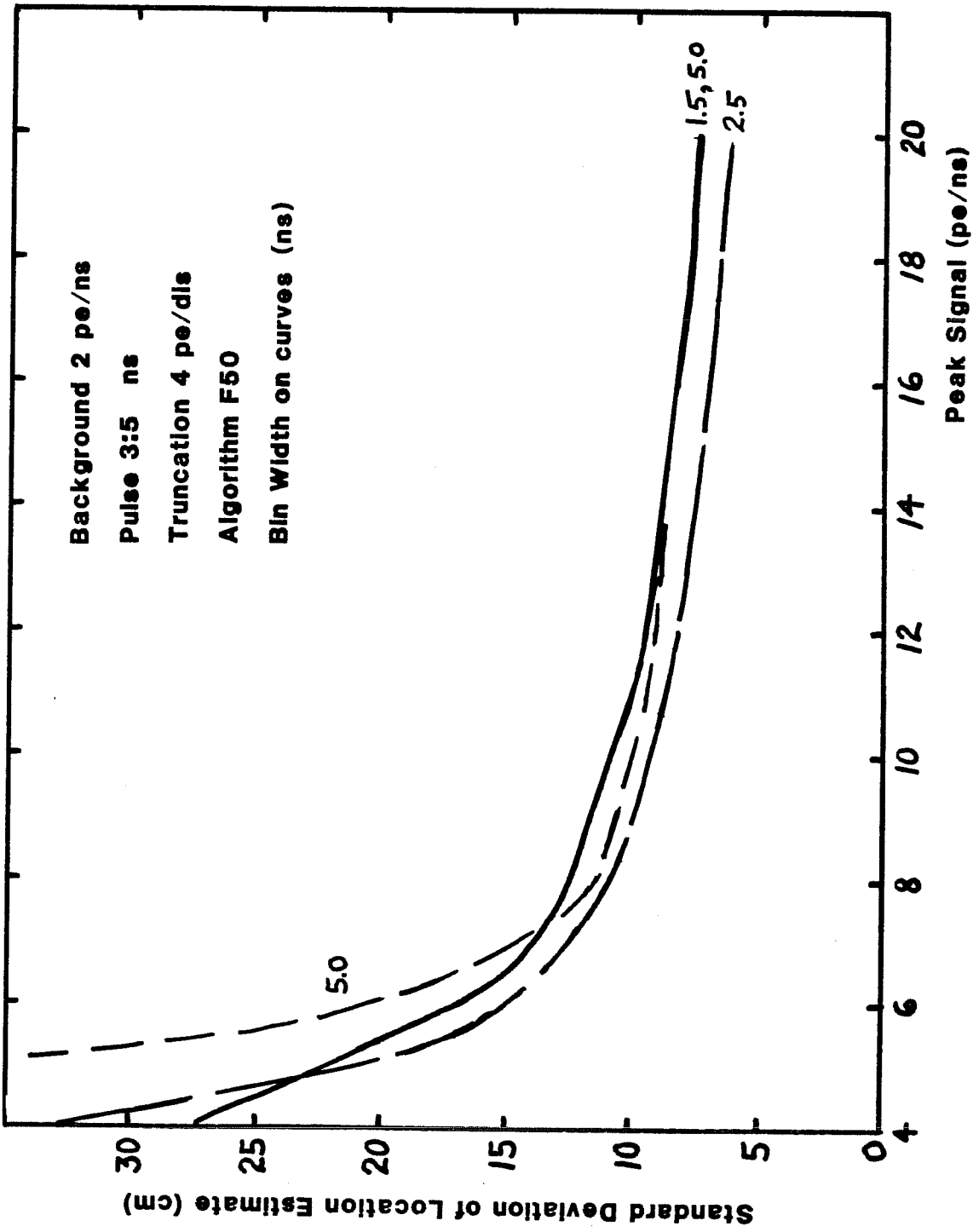


Figure 9-57. Bin Width Effect for Nominal Pulse

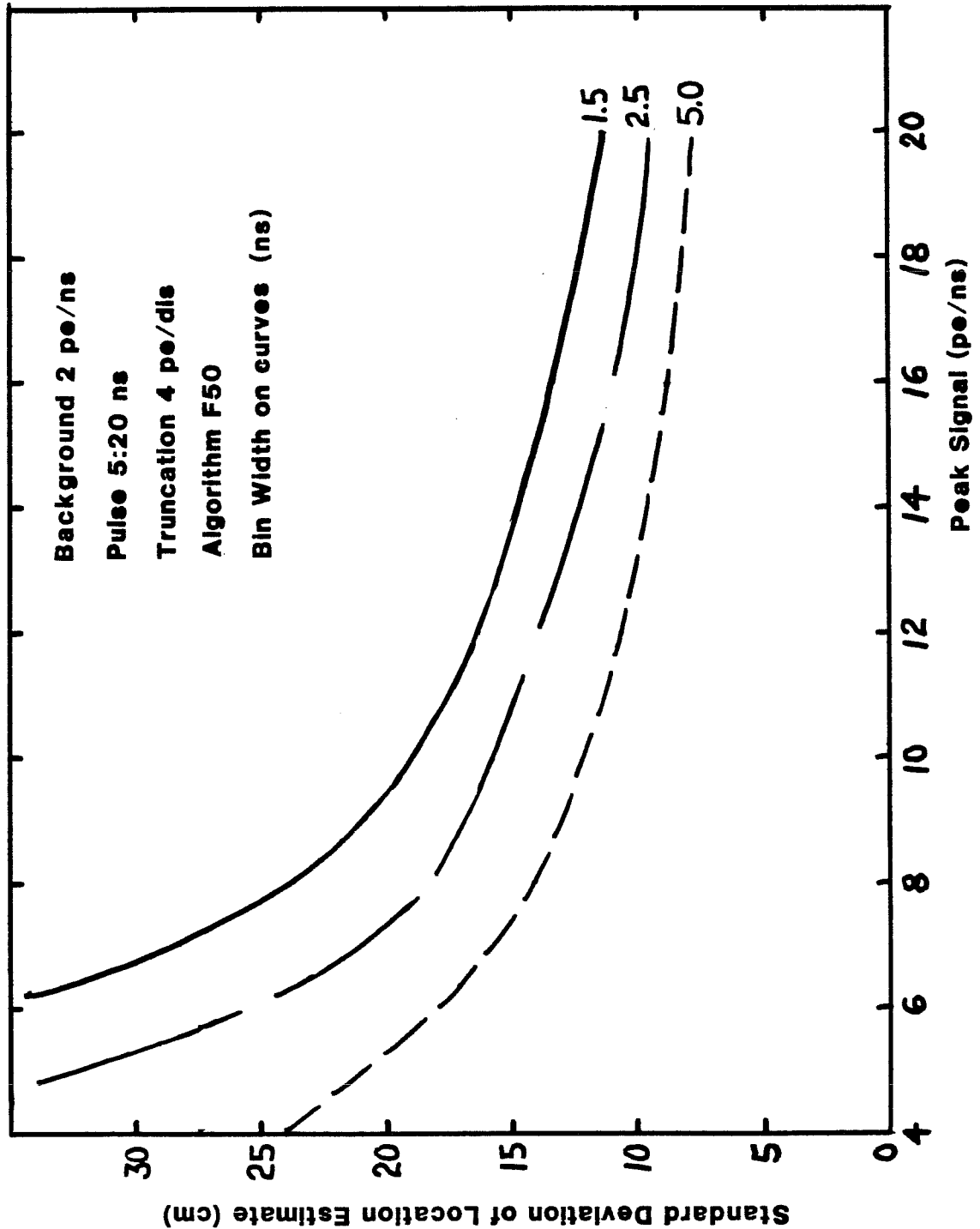


Figure 9-58. Bin Width Effect for Stretched Pulse

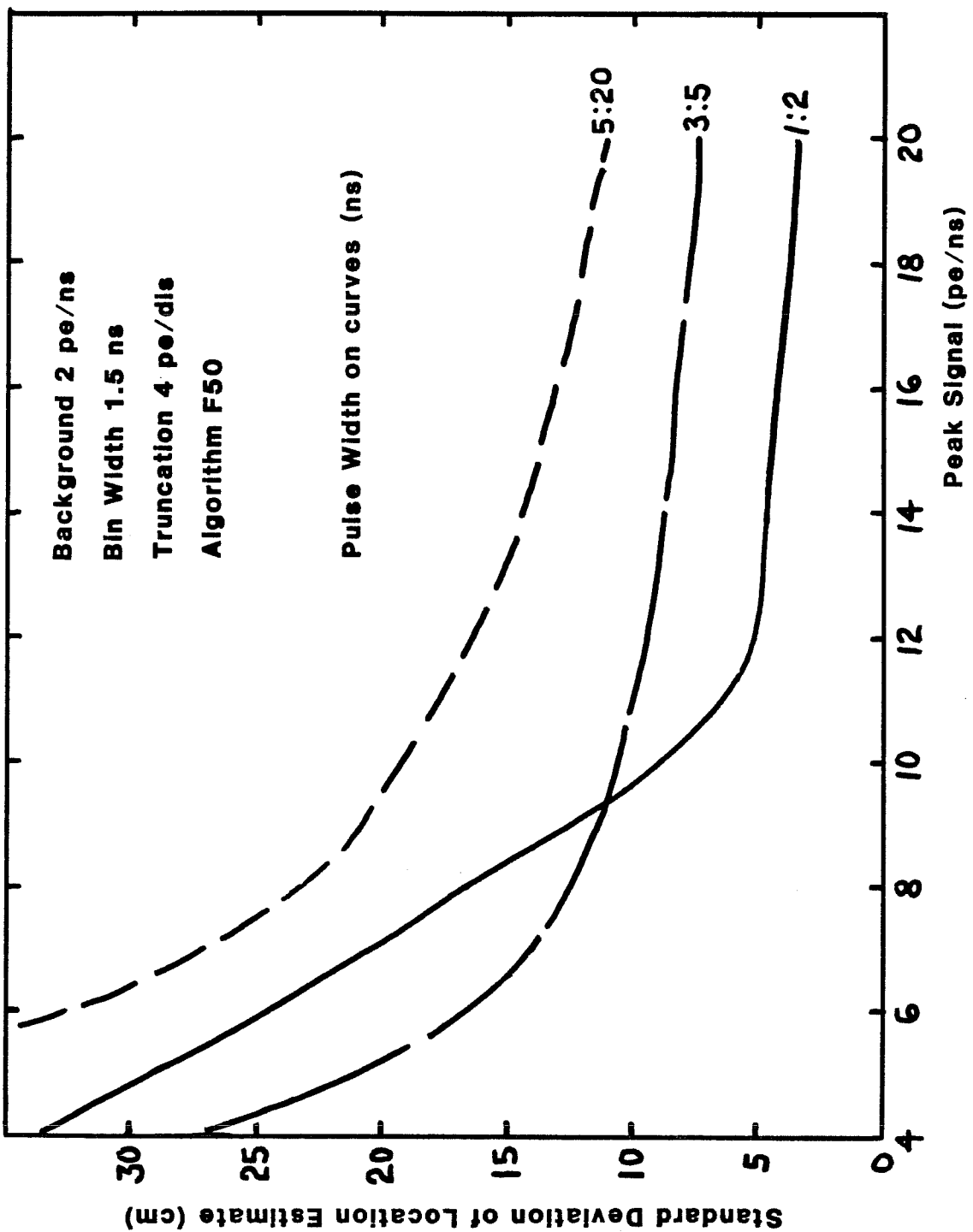


Figure 2-59. Pulse Width Effect for Small Bin

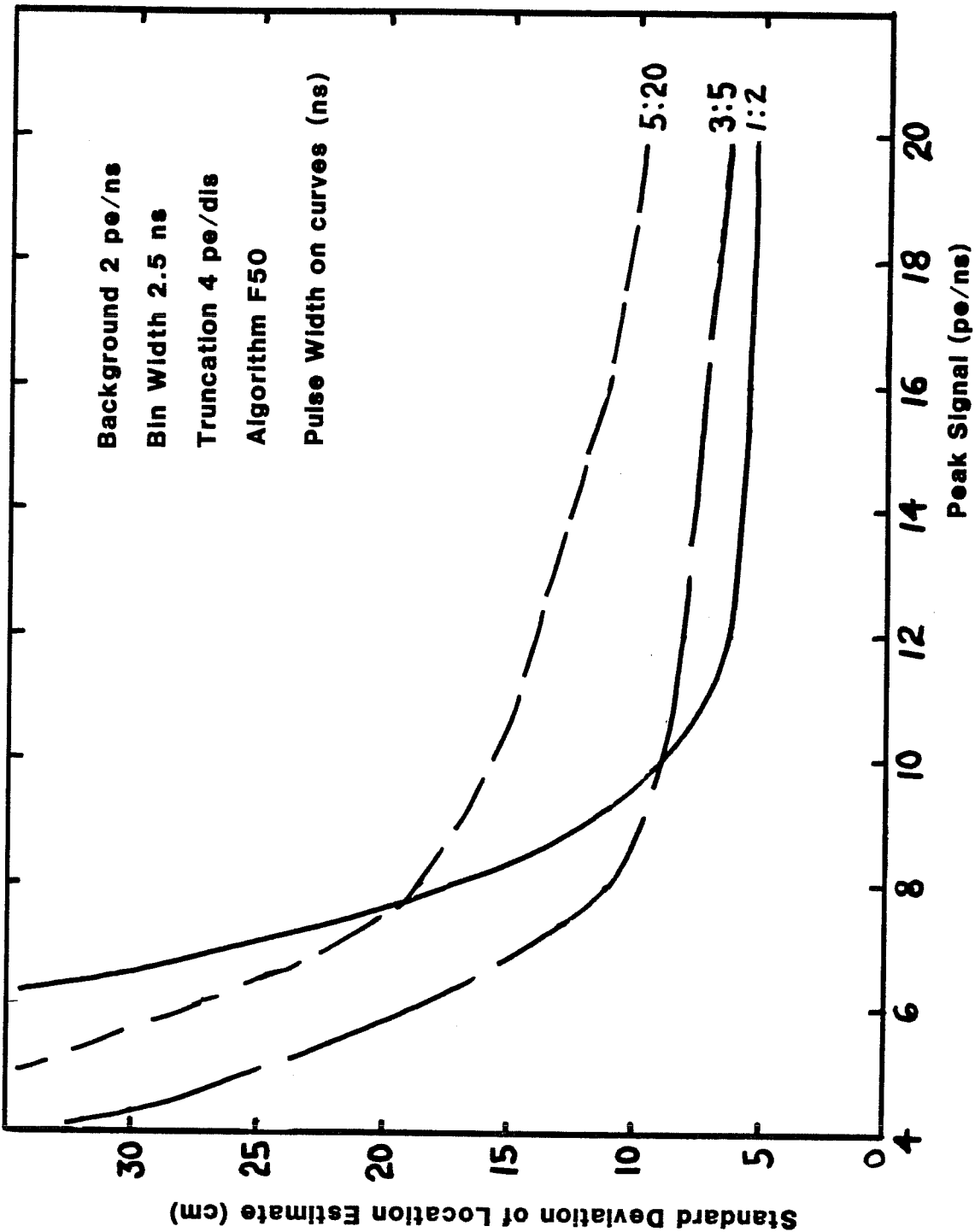


Figure 9-6a. Pulse Width Effect for Nominal Bin

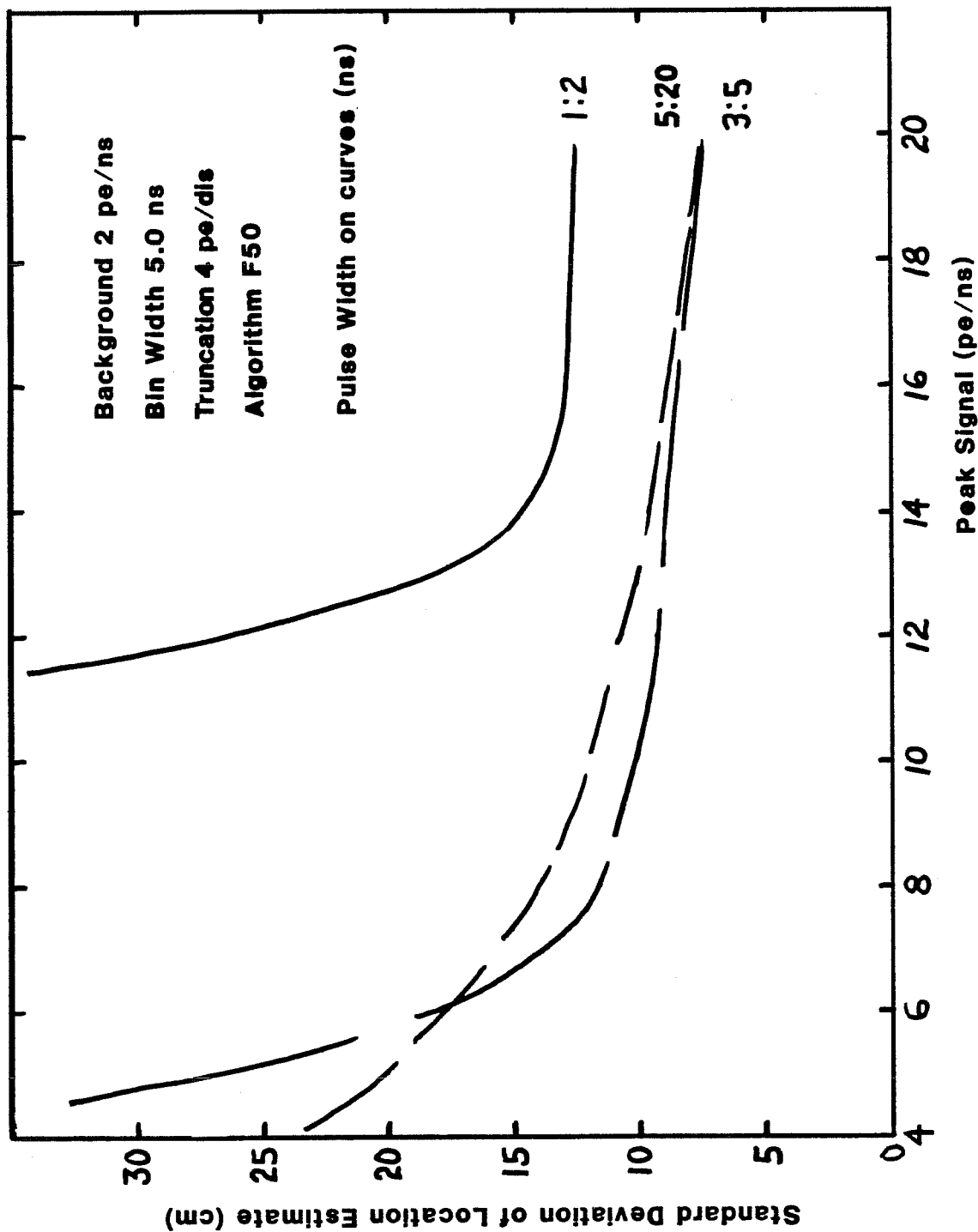


Figure 9-6: Pulse Width Effect for Wide Bin

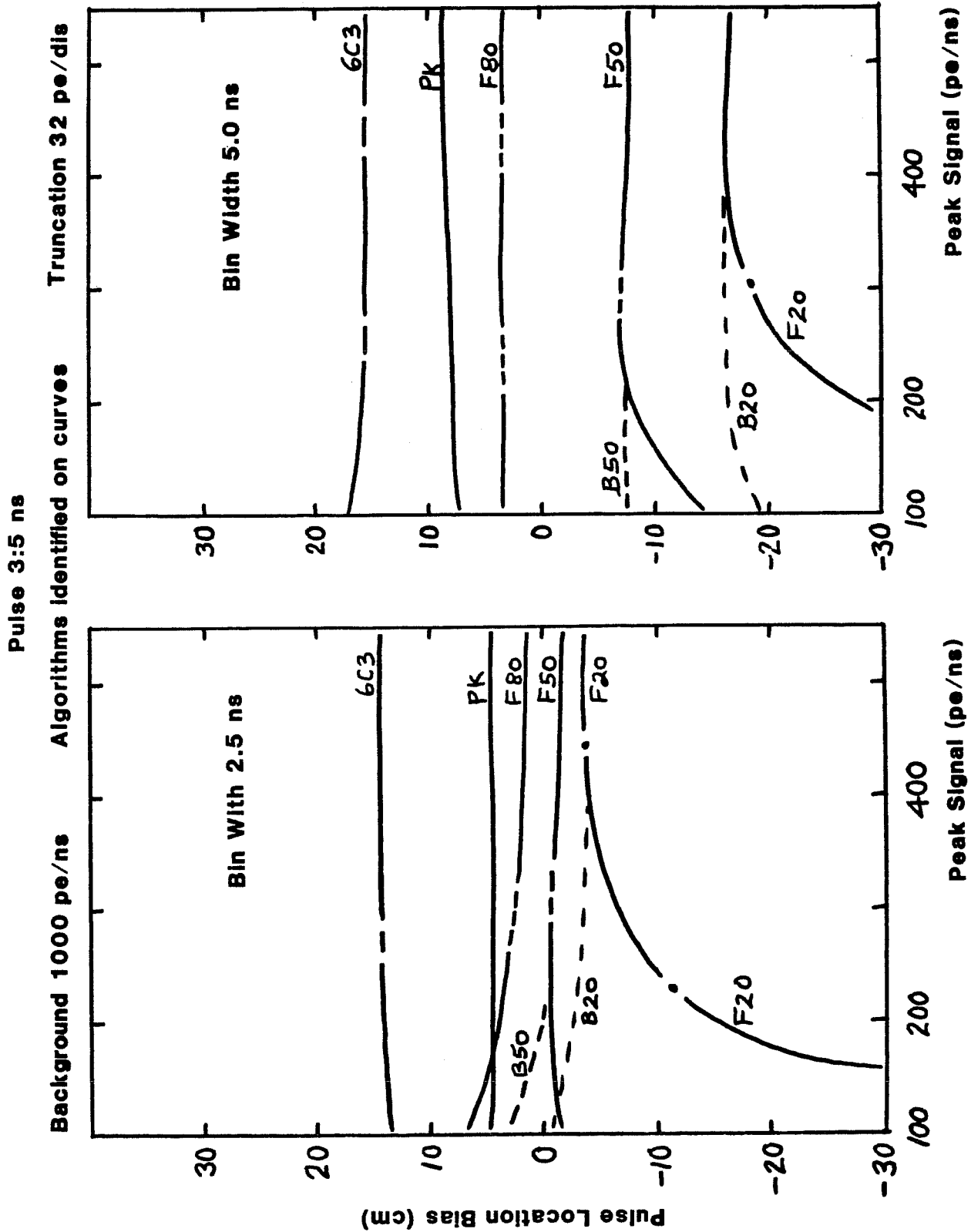


Figure 9-62. Biases for Nominal Pulse in Daylight

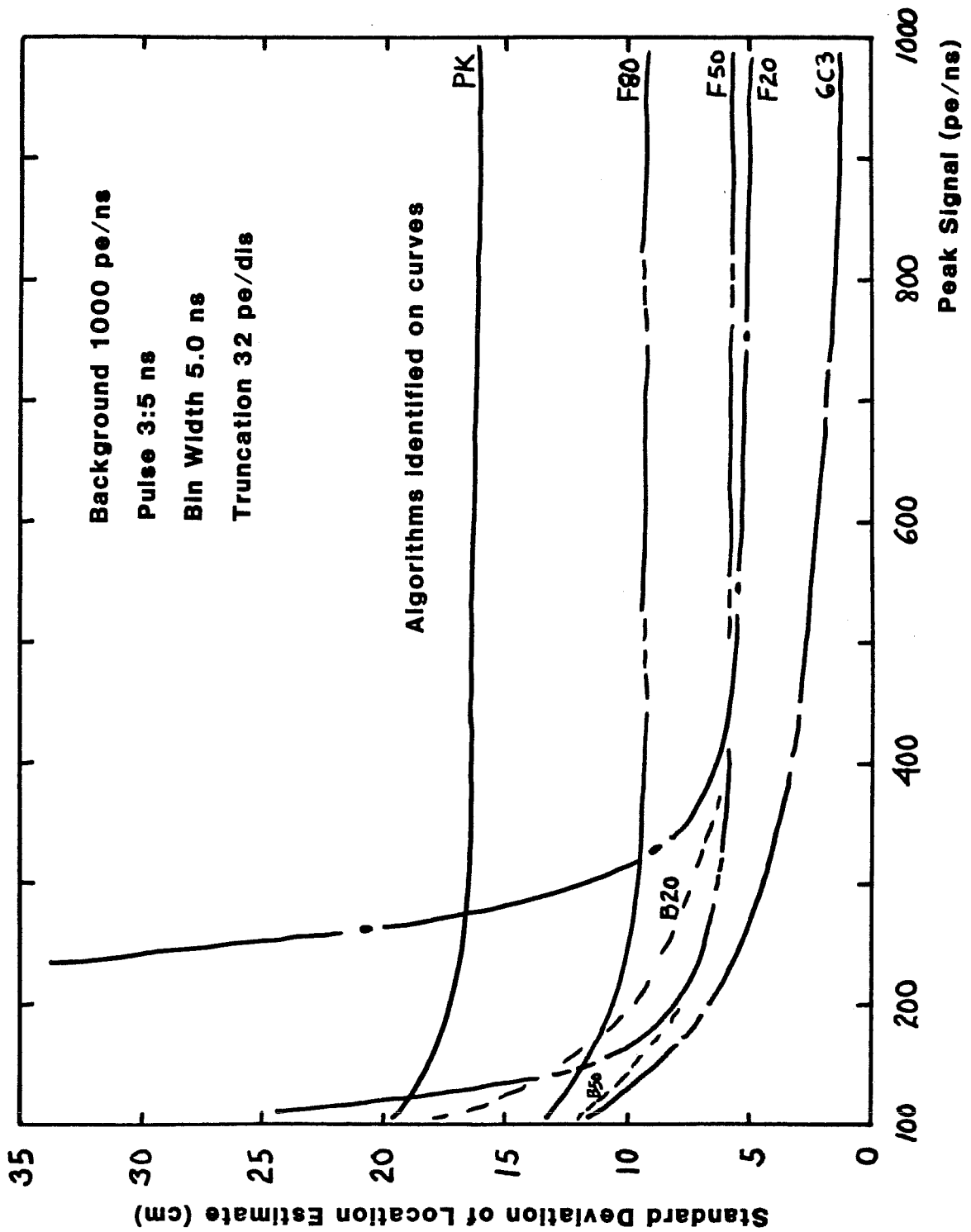


Figure 9-63. Precision for Nominal Pulse In Daylight

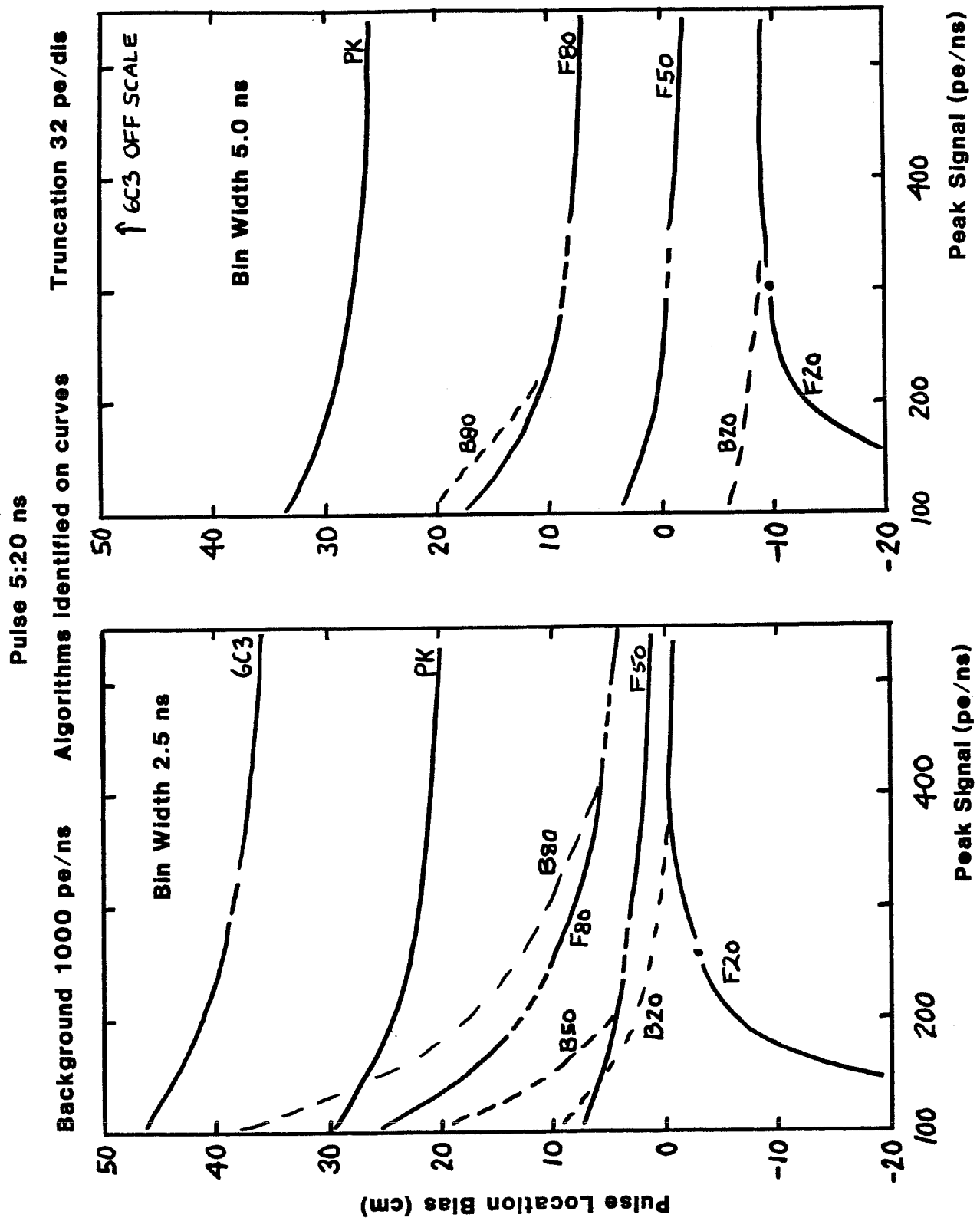


Figure 9-64. Biases for Stretched Pulse in Daylight

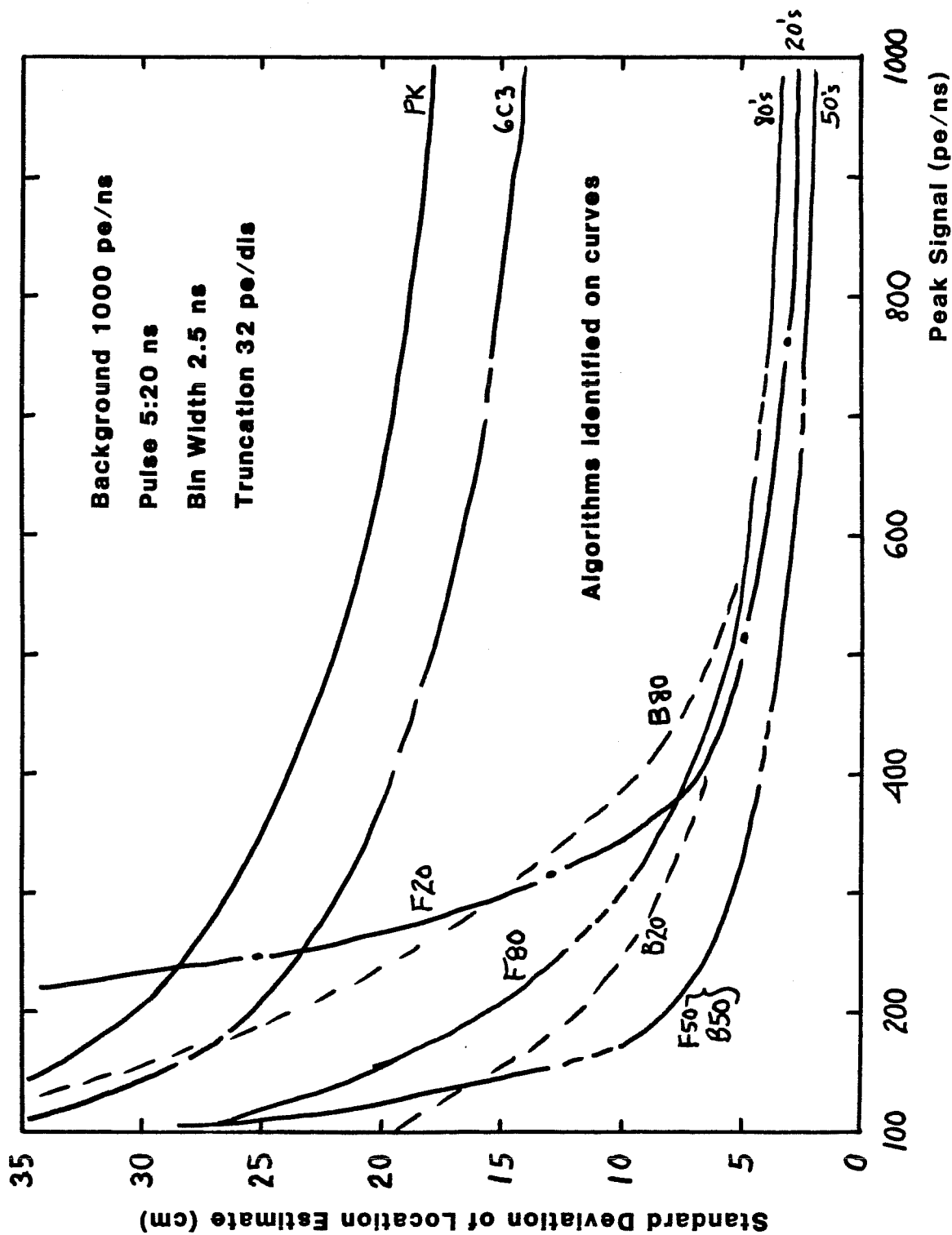


Figure 9-65. Precision for Stretched Pulse in Daylight

biases for asymmetric stretched pulses (Fig. 9-64). Both of these detectors are consequently unacceptable.

Fractional threshold pulse locators utilizing linear interpolation between bin centers based on amplitude tend to be well behaved in that most biases and standard deviations are relatively small and exhibit only moderate dependence on bin width and pulse width. As seen in Figs. 9-62 and 9-64, 5.0 ns bins can produce fairly large shallow biases for 20 percent threshold fractions. Biases for 50 percent and 80 percent thresholds are typically less than ± 8 cm. The narrow bins are least prone to bias and for most algorithms are biased slightly deep; wide bins tend to result in slightly shallow biases. Although the asymptotic standard deviations for all thresholds are reasonably small (Figs. 9-63 and 9-65), F50, B50, and B20 provide the best results. F80 and B80 tend to be noisier due to detection at a lower slope (particularly on wide pulses), and F20 is the first to lose precision under low signal-to-noise ratio conditions. B20 performs to low signal rates if a small threshold is desired. For F50, B50, and B20, the bin width effect on precision is quite small.

The most important feature of the precision plots is the signal strength at which the standard deviation rises above some preselected maximum permissible value such as, say, 10 cm. The knees in these high signal rate plots tend to be much sharper than those seen earlier for low rates. It can be seen in Figs. 9-63 and 9-65 that for F50 the 10-cm mark is passed at a rate of about 150 pe/ns or S/B=0.15. This is a considerably lower ratio than for low rates due to the relatively smaller effect of random noise.

9.3.1.4 Conclusions

The effects of pulse shape and duration, integration time, pulse location algorithm, signal level, background level, and digitizer truncation on the pulse location estimation accuracy for quantum limited returns have been studied via a Poisson count simulator utilizing Monte Carlo techniques. Experimental pulse-to-pulse precision data obtained with the NASA/AVCO Airborne Oceanographic Lidar system were consistent with predictions for that specific configuration.

The pulse location algorithm is very important in determining both the limiting precision at high signal rates and the signal rate at which the random error drops to an acceptable level. (The latter is most strongly influenced by the absolute peak signal and background rates and must be examined individually for each specific case of interest.) Centroid-type pulse locators require interactive decisions on window size and placement and nevertheless result in large unacceptable biases on stretched pulses. Correlation or matched-filter locators are not appropriate for application to propagation stretched pulses. Peak detectors are inherently noisy due to both their discrete nature and detection in a zero slope region. They exhibit disastrous loss of precision with increasing pulse width and are also prone to a deep bias for asymmetric pulses. Fixed level thresholds produce large signal strength dependent biases and are unacceptable. Fractional threshold detectors with interpolation between adjacent time bin amplitudes offer the best overall performance. The optimum threshold fraction (of peak height) depends to a certain extent on the other parameters, but of all algorithms examined, the one preferred was the forward-looking 50 percent threshold (F50) which offers low bias, low limiting standard deviation, and a rapid approach to limiting standard deviation with increasing signal rates. The backward-looking 20 percent threshold (B20) is acceptable as long as bin width is maintained below about 3 ns.

For well-chosen fractional threshold pulse locators, such as F50, the effects on precision of digitizer truncation and integration time (bin width) are minimal. The effects of pulse width and shape are small for F50 and, for the simulated parameters, fall within the desired error budget. Specifically, a system with an 8-ns wide laser pulse and integration time between 2.5 and 5.0 ns has the theoretical potential to provide biases and precisions below 10 cm -- even though the pulses may be stretched by propagation to 25-ns wide -- for reasonable signal to background ratios (which depend strongly on the absolute level of the background). This is advantageous because it implies that there is no need to struggle with state-of-the-art hardware to seek out the last possible nanosecond of performance from either the laser or receiver electronics.

9.3.1.5 Acknowledgements

I wish to thank Lowell R. Goodman who inspired the original study, Bob Thomas who wrote the simulation code, and Rodney McJimpsey who patiently performed the tedious data reduction necessary for the presentation of these results.

9.3.2 Non-Linear Processing Effect on Detection Time

9.3.2.1 Background

Airborne laser bathymetry signals characteristically exhibit very large amplitude dynamic range between the strong interface (or volume backscatter) returns and the generally much weaker bottom returns. This dynamic range cannot be accommodated by typical system electronics without some form of compression. Customary approaches involve the use of gain-controlled photomultiplier tubes, polarizers, partial optical blocks, and the insertion of a logarithmic amplifier. The latter linearizes the volume backscatter exponential temporal decay which can be used for the estimation of certain optical properties of the water, rather than destroying the information as the others do, but the accuracy of these estimates is probably not sufficient to permit their use as an input to "active" bias correction procedures.

An additional problem for a real-time depth determining system such as HALS is the fact that the bottom return follows on the steeply sloping backscatter decay. This makes it difficult to perform the threshold-type pulse location algorithms which are preferred. Avco Everett Research Laboratories, Inc., in their design of HALS, came up with an electronic circuit design which has some interesting properties. A wide-range logarithmic amplifier is followed by a finite difference circuit with a delay roughly equal to the unstretched risetime of the incident pulse. This reduces the slope of the log backscatter to a constant negative level preceding the bottom return which can then be detected and located by standard techniques such as fractional thresholds or, as in the case of HALS, a so-called "constant fraction discriminator" (CFD) circuit.

A problem with logarithmic compression is the fact that such non-linear processing seriously distorts pulse shapes and can lead to potentially significant signal strength dependent bias errors in depth measurements. The exact value of the bias depends on the specific return pulse shape, the type of pulse locator, and the relative signal-to-background ratios of the surface and bottom return pulses. An analysis has been conducted to determine whether such bias errors can be constrained within the permissible system error bounds. Two significantly different pulse location algorithms applied to the log-difference signal -- fractional amplitude threshold and CFD -- have been examined. The results for a realistic (gamma function) waveform are very similar for both schemes, although the CFD biases were slightly smaller. This subsection is a condensation of a more detailed study reported in Guenther (1982).

9.3.2.2. Formalism

A typical return waveform is seen in Fig. 4-10; the bottom return is isolated in Fig. 9-66 where P_m , B , and t_p are illustrated. Define a typical bottom return signal in linear space as $P'(t) = P_m P_N(t)$, where P_m is the peak signal amplitude, and $P_N(t)$ is a typical return pulse shape normalized such that its peak amplitude is unity at a time, t_p , from the start of the pulse. Elevate $P'(t)$ on a background signal of amplitude B at the start of the return; then $P(t) \approx P_m P_N(t) + B$ as diagrammed in Fig. 9-66.

The non-linear processing procedure being investigated first performs a logarithmic operation and then a differencing operation with a time delay, d , which will be roughly equal to the pulse rise time. The output of this processing step on $P(t)$ is a signal

$$S(t) = \ln P(t) - \ln P(t - d) \quad (9-13)$$

For moderately "clean" water, the risetime of the bottom return pulse is short compared to the volume backscatter decay time, and thus $P(t - d) \approx B$ for $t \leq t_p$. From Eq. (9-13) this leads to

$$S(t) = \ln \left[\frac{P_m P_N(t) + B}{B} \right] = \ln \left[\frac{P_m P_N(t)}{B} + 1 \right]. \quad (9-14)$$

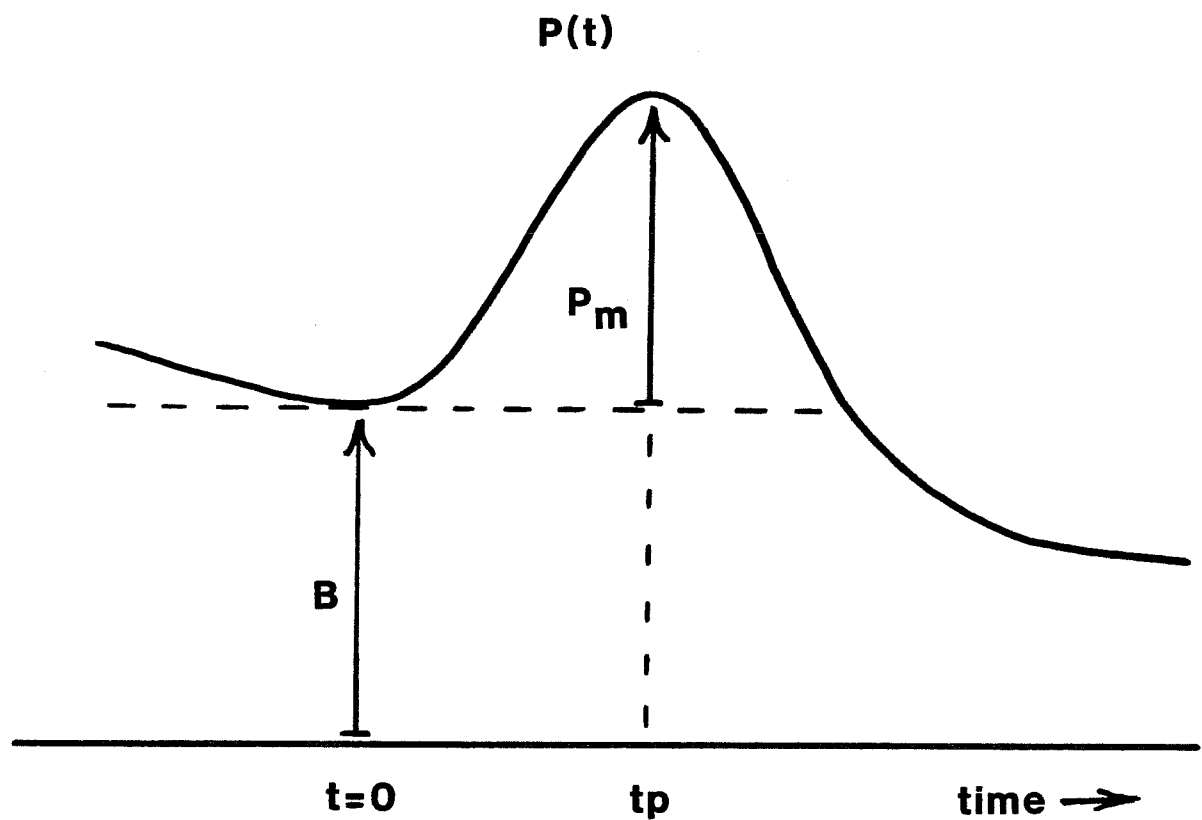


Figure 9-66. Pulse Geometry $P(t)$

At the peak,

$$S(t_p) = \ln (P_m + B) - \ln B = \ln \left(\frac{P_m}{B} + 1 \right).$$

If a constant fraction threshold, "e", is applied to $S(t)$, the threshold will be reached at a time, t_e , where

$$S(t_e) = e S(t_p)$$

or

$$\ln \left[\frac{P_m P_N(t_e)}{B} + 1 \right] = e \ln \left(\frac{P_m}{B} + 1 \right) = \ln \left(\frac{P_m}{B} + 1 \right)^e.$$

The general expression is then

$$\frac{P_m P_N(t_e)}{B} + 1 = \left(\frac{P_m}{B} + 1 \right)^e \quad (9-15)$$

for a constant fraction threshold applied to any waveform $P_N(t)$.

From an analytic approach to propagation theory (Thomas and Guenther 1979), it was determined that the impulse response of the round trip path to the bottom may be described roughly as a gamma function of the form

$$P_N(t) = \left(\frac{t}{t_p} \right)^k e^{k(1 - t/t_p)}, \quad (9-16)$$

where the suggested value of k was unity. Subsequent Monte Carlo calculations (Guenther and Thomas 1981b, 1984b) have shown that typical bottom return pulses are better described by k 's between 4 and 6, as seen in Fig. 9-67. Substituting Eq. (9-16) into Eq. (9-15) with $R \equiv P_m/B$ yields

$$\left(\frac{t_e}{t_p} \right)^k e^{k(1 - t_e/t_p)} = \frac{(R + 1)^e - 1}{R}, \quad (9-17)$$

which if of the form $T^k e^{k(1 - T)} = \text{constant} \equiv A$, or

$$T = \ln T + 1 - \frac{1}{k} \ln A,$$

where $T \equiv t_e/t_p$.

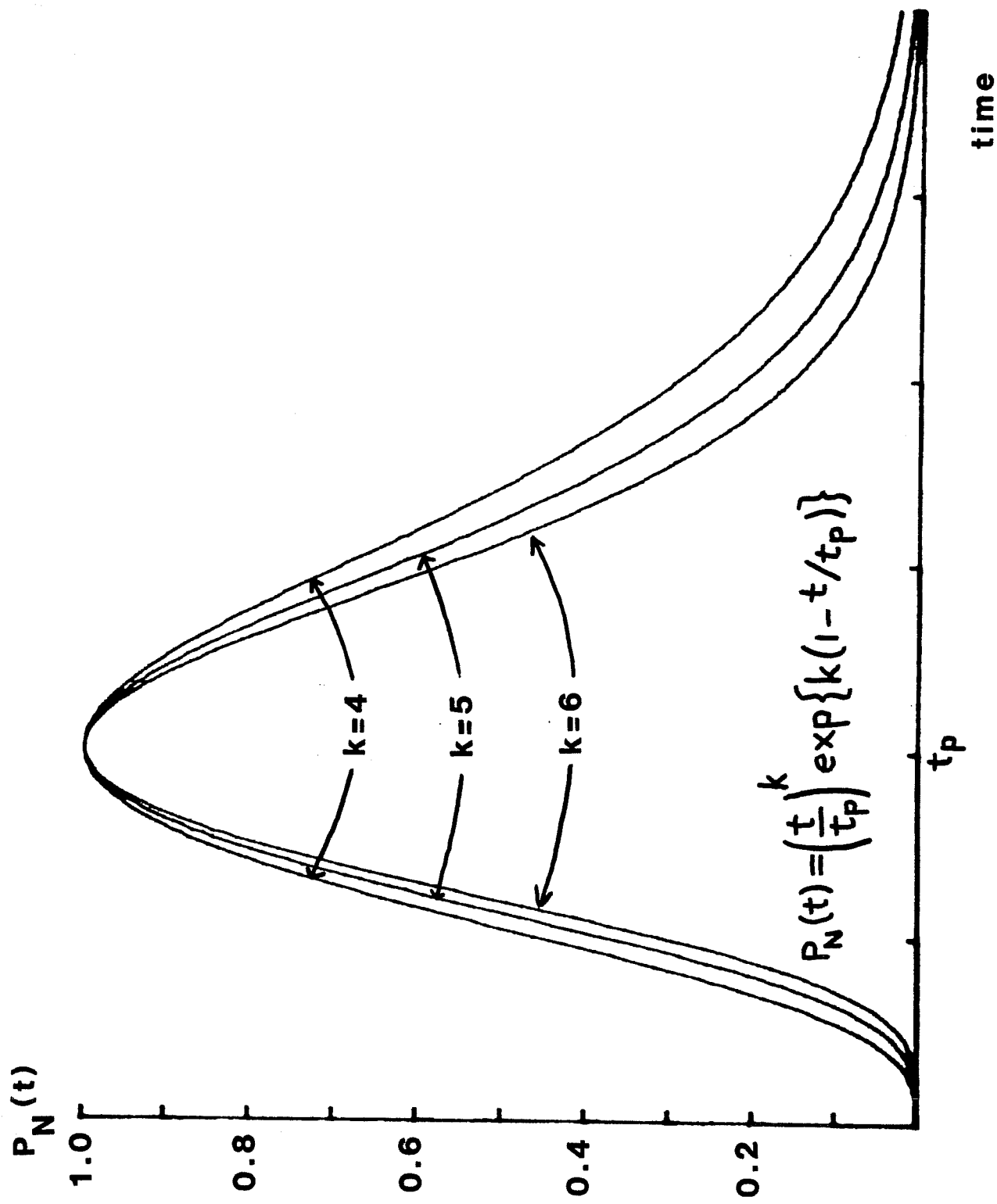


Figure 9-67. Gamma Function for $4 \leq k \leq 6$

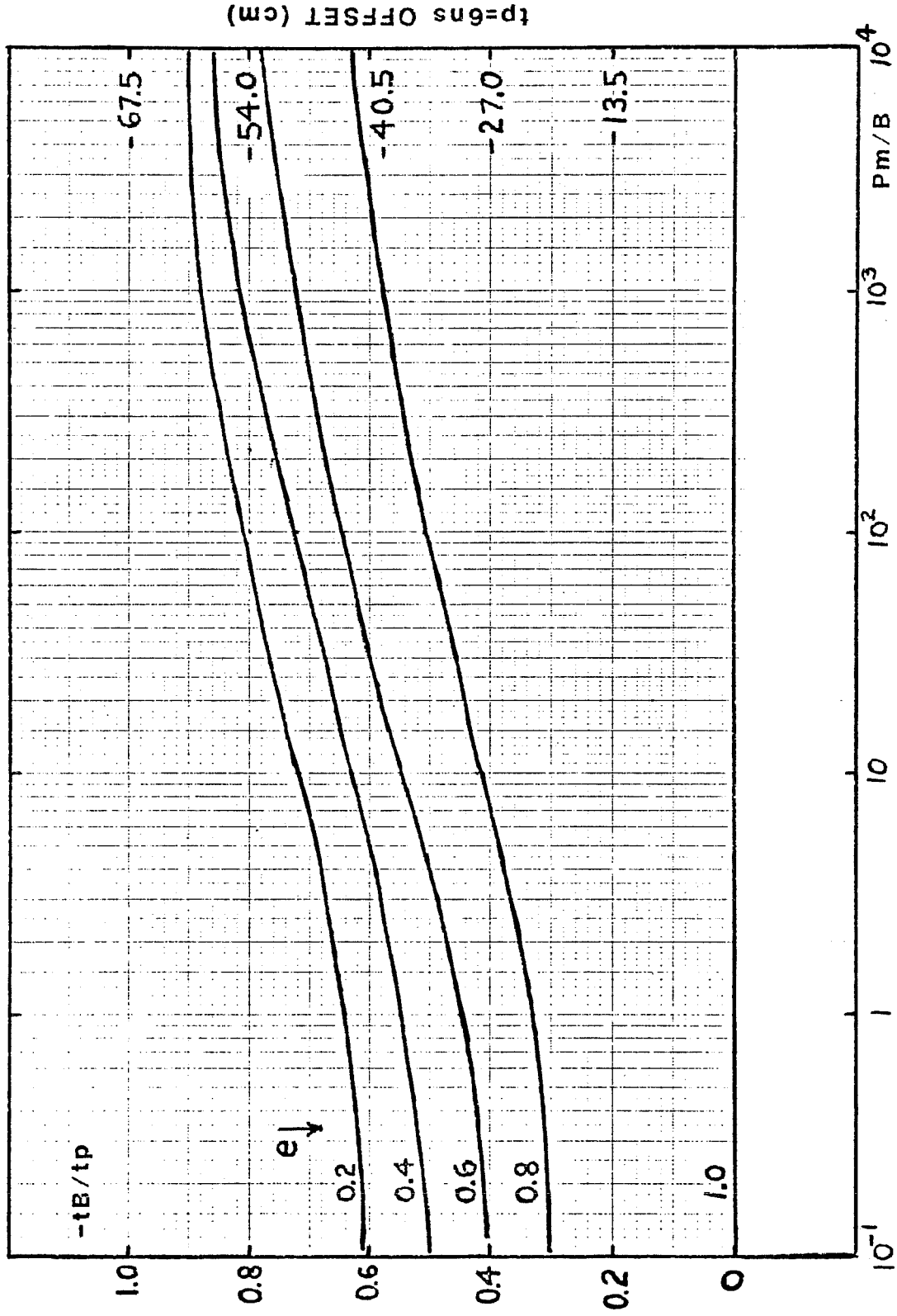
9.3.2.3 Results

The attempted solution of this transcendental equation by an iterative technique would not converge to the desired leading edge result, so a brute-force technique was utilized. Let the "offset" for a single pulse location measurement be defined as the time difference of the threshold time from the peak time: $t_B \equiv t_e - t_p$. (With this definition, all offsets will have a negative sign.) The use of the peak as a reference location is arbitrary, and no connotation of the peak being the "true" location is implied. The "fractional offset" is then $t_B/t_p = t_e/t_p - 1 \equiv T - 1$ which is plotted in Fig. 9-68 as a function of $R \equiv P_m/B$. Absolute offsets, plotted on the right-hand axis for $t_p = 6$ ns, are calculated as $ct_B/2 = ct_p(T - 1)/2$, where c is the speed of light in water. The large variation in T with R will cause a large signal-to-background ratio dependent bias error for constant amplitude fraction threshold detection applied to the logarithmically compressed pulse. The curves approach an asymptotic limit for large R because this waveform has a definite starting point (zero at $t = 0$). The offsets for large thresholds saturate at high values of R (offscale, $> 10^4$), and hence the variation in offset with R is seen to be nearly independent of threshold fractions.

The actual depth measurement bias is the difference between the t_B values for R_S and R_B (the surface and bottom returns, respectively). The optimum offset curve is thus the one exhibiting not the smallest absolute offset (since the offsets are defined from an arbitrary reference), but the smallest variation in offset across the required range of R .

The maximum (i.e., peak to peak) offset variations over the $10^{-1} < R < 10^4$ and $1 < R < 10^3$ ranges as a function of threshold fraction are shown in Fig. 9-69 for a t_p of 6 ns. Note that modifying the bounding R values slightly has only a small effect on the results, because the offset curves are relatively flat in those regions. Biases for the gamma function are nearly independent of threshold fraction and are just slightly larger than

Figure 9-68. Offset vs. Peak Signal to Background Ratio
Gamma Function Input ($k=5$)



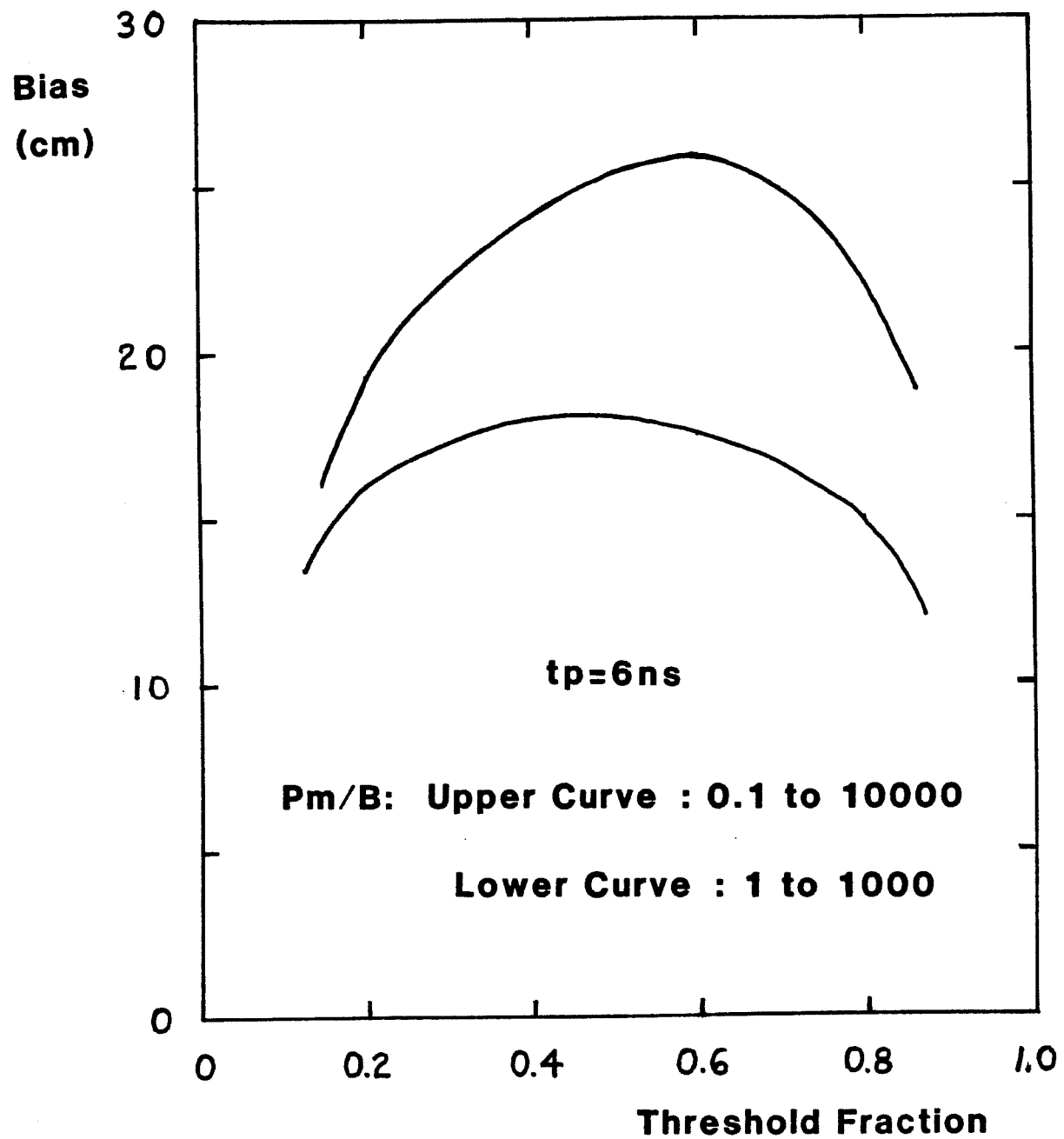


Figure 9-69. Non-linear Processing Bias vs. Threshold Fraction

the 10-15 cm one would perform as an uncorrected component of a ± 30 cm total error budget.

Because this pulse-to-pulse processing "bias" will vary with the signal-to-background ratios of the surface and bottom returns, it will obey the same statistics: i.e., if the R's are fairly constant, a fairly constant bias will result; but if the R's were to vary widely in a random fashion, then the biases would appear to be random errors and would add to the random error component. For realistic returns, the former case applies, and distinct biases will be observed.

The biases could be significantly reduced by measuring R_S and R_B (for the surface and bottom returns, respectively) for each pulse and calculating a bias corrector from computerized tables of Fig. 9-68 data. In practice, however, this will not be necessary. Theoretically, the biases could be positive or negative depending on the relative magnitudes of the R's, and the error contribution would need to be significantly less than the one-sided system accuracy requirement of 30 cm. Actual waveform simulations indicate that R_S is generally quite large ($50 - 10^6$), and R_B is moderately small ($10^{-1} - 20$) for typical systems. This means that the bias is always "deep". Under these circumstances, a mean expected bias of, say 15 cm, could be applied to all measurements, and the residual errors become bipolar around this value and roughly halved in magnitude.

The net results of this investigation of fractional amplitude threshold pulse locators is that biases introduced by non-linear processing are not insignificant compared to a ± 30 cm RMS error budget. They are reasonably well-behaved and predictable and can be compensated for by the application of simple depth correctors or within other correction procedures such as those for propagation-induced biases.

A similar protocol has been followed for the derivation of biases for a CFD pulse locator (Guenther, 1982). The results, plotted in Fig. 9-70, are seen to be similar to those in Fig. 9-69, but slightly smaller. For typically expected P_m/B 's (with weak bottom returns) there will be an 18-cm deep bias across a wide range of delay (for unstretched 6-ns wide pulses) as seen in

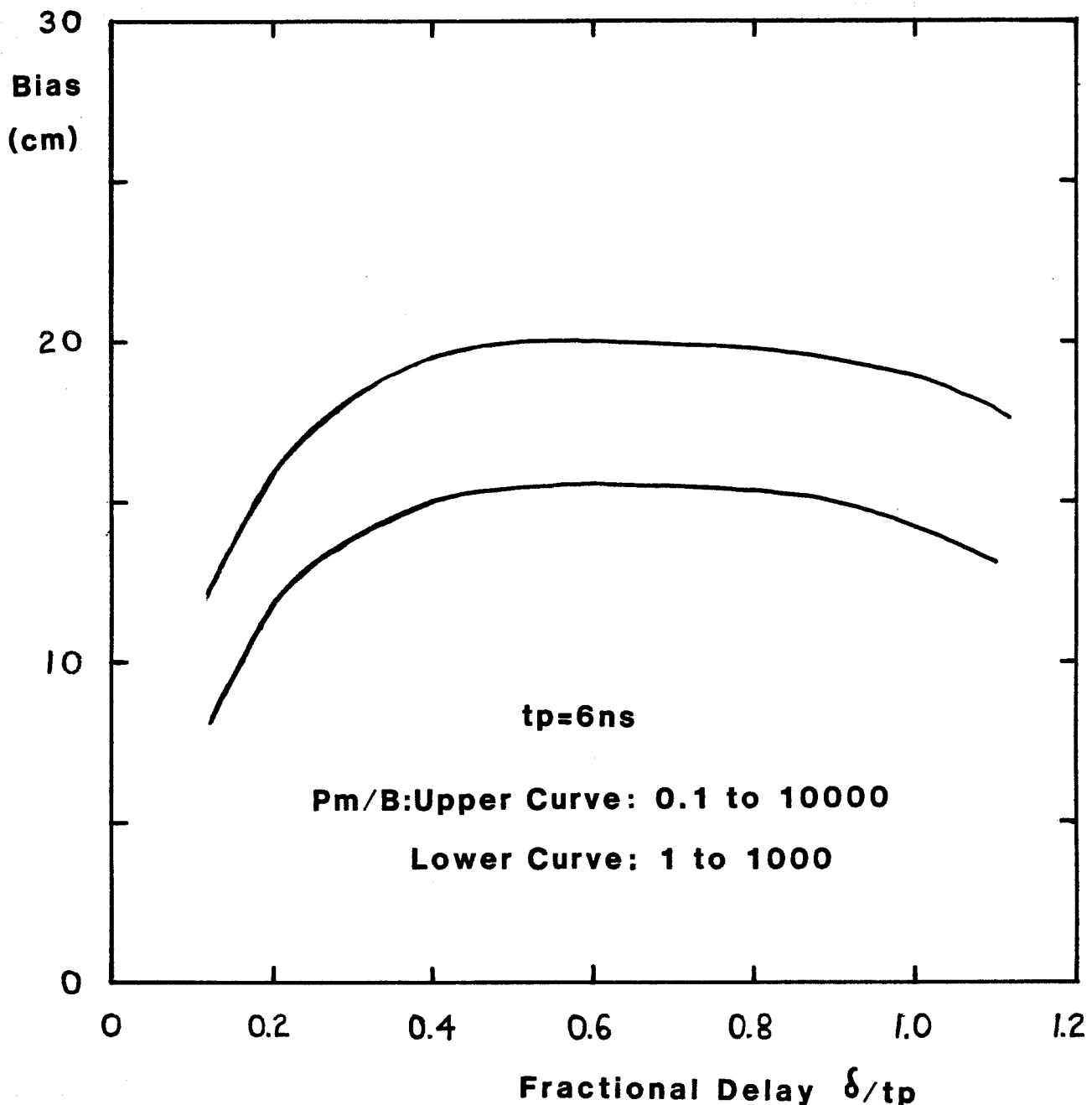


Figure 9-70. Non-linear Processing Bias vs. CFD Delay Fraction

Fig. 9-70. For a higher bottom P_m/B , the bias would be somewhat less, but propagation-induced pulse stretching (which needs to be accounted for separately) will cause it to be somewhat greater. Arbitrarily compensating all depth measurements for an 18-cm deep bias would thus be a reasonable ad hoc solution to the problem of non-linear processing bias for HALS raw hydrographic measurements.

9.3.2.4 Conclusions

It has been demonstrated that non-linear processing can introduce moderately large signal strength dependent depth measurement errors and that these errors will typically appear in the form of deep biases. The magnitude of the error depends, to some extent, on pulse location algorithm, being less for a CFD (roughly 18 cm) than for a fractional amplitude threshold (roughly 24 cm), but is fairly independent of the threshold fraction or the fractional delay over a reasonable range of values.

Knowledge of the functionalities of these errors permits their estimation and removal in post-flight data processing. In reality, however, propagation-induced pulse stretching will result in larger bias effects (Guenther and Thomas 1984b), and the depth corrections for the non-linear processing biases calculated here can best be determined implicitly by applying the desired pulse location algorithm to the stretched pulses calculated by Monte Carlo techniques and calculating the resulting net overall biases, as was done in the cited reference.

In short, logarithmic and difference processing do not appear to contribute excessive or unrecoverable depth measurement errors.

9.3.2.5 Acknowledgement

The author wishes to thank Merlin Miller at Avco Everett for developing the analytic framework for the HALS processing scheme.

9.3.3. Miscellaneous Errors

9.3.3.1 Timing

Airborne laser hydrography requires electronics with bandwidths in the hundreds of megahertz. A timing error of 1 ns produces a depth error of 11.25 cm which is the maximum that can be tolerated. It is critical therefore that all electronic components have a very large bandwidth, be accurately and frequently calibrated, have excellent long and short term stability, and be insensitive to temperature effects. This is not an easy specification to meet, but the design and construction of the hardware must meet these exacting standards. Errors due to drifts, instabilities, temperature sensitivity, limited bandwidth, and all forms of timing jitter must be limited so that neither biases nor random errors exceed roughly 10 cm.

9.3.3.2 Other Non-Linear Processing Effects (HALS)

Non-linear processing presents numerous dangers. The bias errors associated with the detection points for log/difference processed signals were seen in the previous subsection. These are not, however, the only errors associated with the HALS processing scheme. The use of a fixed delay in the difference circuit will introduce some timing biases when dealing with a variety of propagation-stretched bottom return pulses of differing rise times. The magnitude of this error has not been modeled.

The detection point of the CFD is very sensitive to the exact shape of the leading edge of the bottom return. The results quoted in the previous subsection were for a gamma function with a parameter between four and six. As was noted in section 9.2.1, the leading edge power law for the calculated ERFs varies between 1.5 and 8.0 depending on αD , D , θ , and w_0 . This will cause parameter dependent biases of unspecified magnitudes.

The CFD circuit was designed to operate with a zero level input datum. The output of the difference circuit is a negative level whose magnitude is proportional to the slope of the volume backscatter, which is in turn proportional roughly to the diffuse attenuation coefficient. The negative

input levels move the detection point and hence add a bias which depends on the water clarity. For K's exceeding a certain value, the error will be accurately modeled and predicted, but the signal level may become unacceptable in the hardware. To forestall this, a second difference circuit was suggested by Avco to raise the negative level to zero. This further distorts the input signal and results in another pulse risetime dependent bias of uncertain size.

It is clear that once non-linear processes are invoked, a plethora of errors are generated whose magnitudes are very difficult to assess in advance and which will provide confusing results in the field. In general, the fewer non-linear operators used, the better.

9.3.3.3 Spurious Responses

The strong surface returns can generate "after pulses" in the PMT. These can be mistaken for the actual bottom or can add enough energy to seriously affect the estimated pulse location. These spurious signals must be neutralized by some technique. It is also likely that some false bottom returns will be received from schools of fish. These will have to be recognized and edited as statistical outliers.

9.4 Summary

The errors sources discussed in sections 9.2 and 9.3 can now be classified as either "random" or as "variable biases".

9.4.1 Random Errors

The three major random errors which have been identified are beam steering, residual wave heights, and pulse location estimation uncertainties. These errors are kept within bounds by limiting the beam nadir angle and receiver integration time, by measuring system timing and aircraft attitude to very high precision, and by selecting the pulse detection and location algorithms with great care.

9.4.2 Variable Biases

Variable biases discussed in this section have been propagation-induced pulse stretching residuals, uncertainty in the origin of the "surface" return (flip-flop), surface geometry, non-linear processing, and system timing, calibration, and stability. The factors required to minimize each error have been discussed in context. They include tightly constraining the beam nadir angle, devising an unambiguous surface detection technique, minimizing laser pulse width, utilizing sufficient beam divergence, minimizing the number of non-linear operators, and designing for low drift and frequent calibration.

Because of their large number, care must be taken to minimize the magnitudes of these error sources by studious attention to detail in the design phase. Each should be limited to no more than 10 cm if possible.

9.5 References

- Cox, G. and Munk, W., 1954: Measurement of the Roughness of the Sea Surface from Photographs of the Sun's Glitter. JOSA, 44, 11, 838-850.
- Gordon, H.R., Brown, O.B., and Jacobs, M.M., 1975: Computed Relationships Between the Inherent and Apparent Optical Properties of a Flat Homogeneous Ocean. Appl. Opt., 14, 2, 417-427.
- Gordon, H.R., 1982: Interpretation of Airborne Oceanic Lidar: Effects of Multiple Scattering. Appl. Opt., 21, 2996-3001.
- Guenther, G.C. and Thomas, R.W.L., 1981a: Monte Carlo Simulations of the Effects of Underwater Propagation on the Penetration and Depth Measurement Bias of an Airborne Laser Bathymeter. NOAA Technical Memorandum OTES 01, National Oceanic and Atmospheric Administration, U.S. Department of Commerce, Washington, D.C., 144 pp.
- Guenther, G.C. and Thomas, R.W.L., 1981b: Bias Correction Procedures for Airborne Laser Hydrography. NOAA Technical Report OTES 03, National Oceanic and Atmospheric Administration, U.S. Department of Commerce, Washington, D.C., 104 pp.

Guenther, G.C. and Thomas, R.W.L., 1981c: Simulations of the Impact of Inhomogeneous Water Columns on the Temporal Stretching of Laser Bathymeter Pulses. NOAA Technical Report OTES 02, National Oceanic and Atmospheric Administration, U.S. Department of Commerce, Washington, D.C., 39 pp.

Guenther, G.C. and Thomas, R.W.L., 1981d: Error Analysis of Pulse Location Estimates for Simulated Bathymetric Lidar Returns. NOAA Technical Report OTES 01, National Oceanic and Atmospheric Administration, U.S. Department of Commerce, Washington, D.C., 51 pp.

Guenther, G.C., 1982: Effects of Detection Algorithm on Accuracy Degradation from Logarithmic and Difference Processing for Airborne Laser Bathymetry Returns. NOAA Technical Report OTES 06, National Oceanic and Atmospheric Administration, U.S. Department of Commerce, Washington, D.C., 37 pp.

Guenther, G.C. and Thomas, R.W.L., 1984a: Effects of Propagation-Induced Pulse Stretching in Airborne Laser Hydrography. Proceedings SPIE Ocean Optics VII, Vol. 489, June 25-27, 1984, Monterey, Calif., 287-296.

Guenther, G.C. and Thomas, R.W.L., 1984b: Propagation-Induced Depth Measurement Biases and Peak Bottom Return Power Relationships for Airborne Laser Hydrography. NOAA Technical Report NOS 106 CGS 2, National Oceanic and Atmospheric Administration, U.S. Department of Commerce, Washington, D.C., 121 pp.

Kinsman, B., 1965: Wind Waves: Their Generation and Propagation on the Ocean Surface. Prentice-Hall, Englewood Cliffs, N.J., 676 pp.

Moniteq Ltd., 1983: Determination of Parameters of Significance for Accuracy Optimization of a Scanning Lidar Bathymeter. Final Report, Canadian Hydrographic Service Contract, Concord, Ontario, Canada, 129 pp.

Petzold, T.J., 1972: Volume Scattering Functions for Selected Ocean Waters. SIO Ref. 72-78, Scripps Institution of Oceanography, Visibility Laboratory, San Diego, Calif., 79 pp.

Phillips, D.M. and Koerber, B.W., 1984: A Theoretical Study of an Airborne Laser Technique for Determining Sea Water Turbidity. Australian J. Phys., 37, 1, 75-90.

Thomas, R.W.L. and Guenther G.C., 1979: Theoretical Characterization of Bottom Returns for Bathymetric Lidar. Proceedings of the International Conference on Lasers '78, December 11-15, 1978, Orlando, Fla., Society for Optical and Quantum Electronics, McLean, Va., 48-59.

Timofeyeva, V.A. and Gorobets, F.I., 1967: On the Relationship Between the Attenuation Coefficients of Collimated and Diffuse Light Fluxes. Isv., Atmospheric and Oceanic Physics (Acad. of Sci., USSR, 3, 291-296 (166-169 in translation).

Wilson, W.H., 1979: Spreading of Light Beams in Ocean Water. Proc. SPIE Ocean Optics VI, October 23-25, 1979, Monterey Calif., Society of Photo-optical Instrumentation Engineers, Bellingham, Wash., Vol. 208, 64-72.

APPENDIX 9A. Bias Tabulation

Note: The mean biases presented here are averaged between NAVY and NOS phase functions as well as over various αD and ω_0 combinations. Single-scattering values of 0.8 and 0.6 were associated with NAVY, and 0.9 and 0.8 with NOS.

MEAN BIAS TABLES

Algorithm LFT; Air nadir angle 0°

Depth (m)	Threshold (%)	FOV(R/D)	Scattering Optical Depth ($\omega_0 \alpha D$)			
			2	6	10	14
5	20	0.25	2	7	12	18
5	20	0.50	4	11	19	27
5	50	0.25	1	6	11	18
5	50	0.50	3	11	19	26
5	80	0.25	0	4	8	14
5	80	0.50	1	8	15	22
10	20	0.25	2	11	20	29
10	20	0.50	5	15	28	41
10	50	0.25	2	10	19	29
10	50	0.50	4	16	29	43
10	80	0.25	0	7	15	26
10	80	0.50	1	15	28	41
20	20	0.25	3	13	26	38
20	20	0.50	4	19	36	53
20	50	0.25	3	15	28	41
20	50	0.50	4	21	40	60
20	80	0.25	0	11	25	40
20	80	0.50	1	20	42	66
40	20	0.25	1	14	30	55
40	20	0.50	2	17	39	68
40	50	0.25	1	16	35	62
40	50	0.50	1	20	48	82
40	80	0.25	0	15	37	66
40	80	0.50	0	21	52	98

All biases in centimeters

MEAN BIAS TABLES

Algorithm LFT ; Air nadir angle 10°

Depth (m)	Threshold (%)	FOV(R/D)	Scattering Optical Depth ($\omega_0 \propto D$)			
			2	6	10	14
5	20	0.25	1	6	11	17
5	20	0.50	3	9	15	22
5	50	0.25	0	4	11	18
5	50	0.50	2	8	16	23
5	80	0.25	-2	2	7	13
5	80	0.50	-1	6	13	20
10	20	0.25	1	8	17	26
10	20	0.50	2	12	23	33
10	50	0.25	-1	8	16	26
10	50	0.50	2	13	23	37
10	80	0.25	-3	5	13	23
10	80	0.50	-1	10	23	37
20	20	0.25	-2	8	18	28
20	20	0.50	-2	11	24	38
20	50	0.25	-3	8	21	34
20	50	0.50	-2	14	30	49
20	80	0.25	-6	7	20	35
20	80	0.50	-5	13	34	58
40	20	0.25	-13	-3	11	27
40	20	0.50	-12	-1	17	39
40	50	0.25	-12	2	21	40
40	50	0.50	-11	7	30	58
40	80	0.25	-14	5	30	56
40	80	0.50	-14	11	45	85

All biases in centimeters

MEAN BIAS TABLES

Algorithm LFT ; Air nadir angle 15°

Depth (m)	Threshold (%)	FOV(R/D)	Scattering Optical Depth ($\omega_0 \propto D$)			
			2	6	10	14
5	20	0.25	1	4	9	14
5	20	0.50	2	8	13	19
5	50	0.25	0	4	8	13
5	50	0.50	1	7	14	20
5	80	0.25	-2	1	5	11
5	80	0.50	-1	4	10	16
10	20	0.25	-1	5	11	20
10	20	0.50	0	7	16	24
10	50	0.25	-1	5	13	21
10	50	0.50	0	8	18	28
10	80	0.25	-3	2	11	20
10	80	0.50	-2	7	18	28
20	20	0.25	-6	-2	5	13
20	20	0.50	-6	-2	6	15
20	50	0.25	-6	1	9	18
20	50	0.50	-6	1	11	22
20	80	0.25	-8	0	11	22
20	80	0.50	-7	4	18	32
40	20	0.25	-19	-24	-16	-2
40	20	0.50	-21	-31	-22	-8
40	50	0.25	-16	-11	2	17
40	50	0.50	-16	-12	2	24
40	80	0.25	-16	-5	14	37
40	80	0.50	-17	-4	18	43

All biases in centimeters

MEAN BIAS TABLES

Algorithm LFT; Air nadir angle 20°

Depth (m)	Threshold (%)	FOV(R/D)	Scattering Optical Depth ($\omega_0 \propto D$)			
			2	6	10	14
5	20	0.25	0	3	5	8
5	20	0.50	1	4	8	12
5	50	0.25	-1	2	4	8
5	50	0.50	0	4	8	13
5	80	0.25	-3	-1	1	4
5	80	0.50	-2	2	6	11
10	20	0.25	-2	0	3	7
10	20	0.50	-2	0	4	9
10	50	0.25	-3	1	4	9
10	50	0.50	-2	2	7	13
10	80	0.25	-4	-2	2	6
10	80	0.50	-4	1	8	15
20	20	0.25	-8	-15	-13	-5
20	20	0.50	-11	-21	-18	-10
20	50	0.25	-8	-8	-5	-1
20	50	0.50	-9	-11	-7	3
20	80	0.25	-9	-5	-1	3
20	80	0.50	-8	-6	1	8
40	20	0.25	-24	-60	-58	-41
40	20	0.50	-27	-76	-74	-57
40	50	0.25	-17	-26	-30	-25
40	50	0.50	-18	-32	-35	-27
40	80	0.25	-16	-16	-14	-10
40	80	0.50	-17	-14	-5	3

All biases in centimeters

MEAN BIAS TABLES

Algorithm LFT; Air nadir angle 25°

Depth (m)	Threshold (%)	FOV(R/D)	Scattering Optical Depth ($\omega_0 \alpha D$)			
			2	6	10	14
5	20	0.25	-1	1	3	5
5	20	0.50	0	2	4	6
5	50	0.25	-2	0	2	4
5	50	0.50	-1	1	4	6
5	80	0.25	-4	-3	-1	2
5	80	0.50	-3	-1	2	5
10	20	0.25	-4	-5	-5	-5
10	20	0.50	-5	-9	-9	-8
10	50	0.25	-5	-4	-1	2
10	50	0.50	-5	-5	-2	3
10	80	0.25	-5	-5	-1	3
10	80	0.50	-5	-3	1	8
20	20	0.25	-12	-28	-32	-35
20	20	0.50	-15	-42	-48	-50
20	50	0.25	-10	-15	-18	-19
20	50	0.50	-11	-21	-21	-18
20	80	0.25	-10	-11	-10	-9
20	80	0.50	-10	-11	-7	-3
40	20	0.25	-32	-87	-98	-104
40	20	0.50	-35	-118	-140	-143
40	50	0.25	-18	-46	-61	-71
40	50	0.50	-23	-48	-57	-64
40	80	0.25	-13	-29	-41	-47
40	80	0.50	-19	-25	-19	-10

All biases in centimeters

MEAN BIAS TABLES

Algorithm: log / difference ($\Delta = 6\text{ns}$) / CFD ($\delta = 6\text{ns}$)

Air nadir angle 0°

Depth (m)	Pm/B	FOV(R/D)	Scattering Optical Depth ($\omega_0 \alpha D$)			
			2	6	10	14
5	1	0.25	21	35	46	52
5	1	0.50	21	40	49	55
5	10	0.25	7	16	23	30
5	10	0.50	8	19	27	35
10	1	0.25	18	32	43	51
10	1	0.50	20	37	49	57
10	10	0.25	6	14	23	30
10	10	0.50	7	18	27	37
20	1	0.25	15	30	43	54
20	1	0.50	16	34	48	60
20	10	0.25	5	13	23	34
20	10	0.50	6	15	28	41
40	1	0.25	11	25	41	57
40	1	0.50	11	26	45	65
40	10	0.25	2	7	20	40
40	10	0.50	2	7	21	43

All biases in centimeters

MEAN BIAS TABLES

Algorithm: log / difference ($\Delta = 6\text{ns}$) / CFD ($\delta = 6\text{ns}$)

Air nadir angle 10°

Depth (m)	Pm/B	FOV(R/D)	Scattering Optical Depth ($\omega_0 \alpha D$)			
			2	6	10	14
5	1	0.25	18	33	42	48
5	1	0.50	21	36	45	51
5	10	0.25	6	14	22	29
5	10	0.50	7	17	26	32
10	1	0.25	15	28	37	44
10	1	0.50	17	32	41	46
10	10	0.25	4	11	19	26
10	10	0.50	4	14	22	30
20	1	0.25	9	21	29	35
20	1	0.50	9	22	31	37
20	10	0.25	-2	5	12	19
20	10	0.50	-2	6	15	23
40	1	0.25	-6	0	9	21
40	1	0.50	-6	1	11	22
40	10	0.25	-20	-19	-9	1
40	10	0.50	-20	-18	-9	2

All biases in centimeters

MEAN BIAS TABLES

Algorithm: log / difference ($\Delta = 6\text{ns}$) / CFD ($\delta = 6\text{ns}$)

Air nadir angle 15°

Depth (m)	Pm/B	FOV(R/D)	Scattering Optical Depth ($\omega_0 \alpha D$)			
			2	6	10	14
5	1	0.25	17	29	36	41
5	1	0.50	19	31	38	42
5	10	0.25	5	12	17	22
5	10	0.50	6	14	20	25
10	1	0.25	12	21	28	32
10	1	0.50	12	21	28	32
10	10	0.25	1	6	11	16
10	10	0.50	1	5	10	16
20	1	0.25	1	4	8	16
20	1	0.50	0	1	4	9
20	10	0.25	-9	-10	-7	0
20	10	0.50	-12	-16	-11	-4
40	1	0.25	-22	-42	-40	-32
40	1	0.50	-36	-54	-46	-39
40	10	0.25	-50	-63	-59	-44
40	10	0.50	-72	-77	-67	-57

All biases in centimeters

MEAN BIAS TABLES

Algorithm: log / difference ($\Delta = 6\text{ns}$) / CFD ($\delta = 6\text{ns}$)

Air nadir angle 20°

Depth (m)	Pm/B	FOV(R/D)	Scattering Optical Depth ($\omega_0 \alpha D$)			
			2	6	10	14
5	1	0.25	15	23	29	32
5	1	0.50	15	25	30	33
5	10	0.25	4	9	13	16
5	10	0.50	4	10	14	18
10	1	0.25	7	10	13	16
10	1	0.50	6	9	12	14
10	10	0.25	-1	-3	0	4
10	10	0.50	-3	-5	-1	4
20	1	0.25	-3	-18	-17	-6
20	1	0.50	-7	-29	-27	-20
20	10	0.25	-19	-36	-34	-21
20	10	0.50	-37	-49	-45	-38
40	1	0.25	-105	-108	-98	-85
40	1	0.50	-152	-143	-135	-134
40	10	0.25	-121	-121	-118	-114
40	10	0.50	-168	-162	-157	-151

All biases in centimeters

10.0 SYSTEM DESIGN TRADEOFFS

10.1 Background

It has been demonstrated in this text that the major system variables influence performance through numerous, complex relationships and are hence highly interdependent in nature. Altering the value of one variable can have a domino effect which requires changes in other variables and which can cause unexpected consequences if the intricate interrelationships are not clearly understood. It is necessary to carefully examine the many changes in system performance which can result from the alteration of a single variable and to determine what other variables must be changed in concert. Ultimately, all design features and variables must be derived from one or both of two areas: absolute requirements and cost-effectiveness. Table 10-1 lists the major items falling within these categories (in no particular order).

Table 10-1. Design Driving Considerations

A. Absolute Requirements

1. Aircraft Safety
2. Eye Safety
3. Depth Measurement Accuracy
4. Positioning Accuracy
5. Sounding Density

B. Cost-Effectiveness

1. Aircraft Costs
2. Surveyable Area (Penetration)
3. Environmental Constraints
4. Coverage Rate

Of these, by far the most important, the most complicated, and the most difficult to meet are depth measurement accuracy and surveyable area (penetration).

Table 10-2 breaks each of these items down further into the specific hardware features or environmental parameters which directly influence those particular requirements. (Note: "RX" = receiver; "TX" = transmitter.)

Table 10-2. Implementation Variables and Parameters Affecting Design

- A1. Aircraft Safety - minimum flight altitude
 - maximum wind speed
 - system size/weight
- A2. Eye Safety - laser energy (peak power, pulse duration)
 - laser beam divergence
 - aircraft altitude
- A3. Depth Measurement Accuracy - beam nadir angle
 - laser pulse width
 - calibration
 - RX integration time
 - RX non-linear processing
 - pulse location algorithm
 - laser beam divergence
 - spurious responses
 - wind speed
 - RX dynamic range reduction techniques
- A4. Positioning Accuracy - beam nadir angle
 - positioning system
 - wind speed
 - optical system alignment calibration
 - aircraft altitude
- A5. Sounding Density - scanner pattern
 - laser pulse repetition rate
 - aircraft speed
 - scanner nadir angle
 - aircraft altitude
- B1. Aircraft Costs - system size/weight/power requirements
 - RX optical aperture diameter
 - laser average power output
 - RX field of view
 - RX optical bandwidth
 - electronics concept

- B2. Surveyable Area (Penetration) -
- laser wavelength
 - laser peak output power
 - aircraft altitude
 - beam nadir angle
 - RX optical bandwidth (day only)
 - laser beam divergence
 - RX field of view
 - RX optical aperture diameter
 - RX, TX efficiency
 - RX noise level
 - PMT dark current (night only)
 - RX dynamic range
 - pulse location algorithm
 - RX non-linear processing
 - RX spurious responses

- B3. Environmental Constraints - day/night operation
- solar (or lunar) zenith angle
 - wind speed/wave height
 - water clarity/depth

- B4. Coverage Rate - maximum scanner nadir angle
- aircraft altitude
 - aircraft speed
 - laser pulse repetition rate
-

It can be seen from Table 10-2 that several of the key system design variables influence performance in numerous ways. A large number of important cause-and-effect relationships among the variables and parameters have been discussed in context which lead to constraints in system design and parameterization. It is necessary to compile a cross-reference of sets of constraints for individual variables from the various design considerations to determine acceptable operating regions. The remainder of this section is that cross reference. Its purpose is to summarize the requirements and restrictions on all major design variables, to trace these requirements back to their origin, and to elucidate and attempt to compromise sometimes conflicting dependencies.

10.2 Scanner Nadir Angle, Aircraft Altitude, and Pulse Repetition Rate

As seen in Table 10-2, the scanner nadir angle affects five of the nine critical categories. The scanner nadir angle and aircraft altitude of an

airborne hydrographic lidar system determine the width of the swath sampled on the surface and hence, for a given aircraft speed, the coverage rate. Because the coverage rate is one of the factors which has been found (Enabnit et al. 1978) to most strongly affect the cost/benefit ratio for the system, a scanner angle as large as possible is important. The choice of the scanner angle is also important from the point of view of system design, because the size and weight of the hardware increase somewhat with the scanner nadir angle requirement. As seen in section 8.2.6, penetration is not a driving factor because the bottom return peak power for any selected constant swath width increases with increasing nadir angle up to angles of at least 30 degrees. The critical factor is that depth measurement accuracy degrades rapidly with increasing nadir angle due to beam steering, residual propagation-induced biases, surface uncertainty, and geometric effects. It can be seen from the combined results in sections 9.2.3, 9.2.1, and 9.2.4 that the limiting angle for ± 30 -cm RMS total system error depends on signal processing procedures but is expected to be about 25 degrees.

The nadir angle strongly affects the surface identification uncertainty or "flip-flop" problem described in sections 7.4 and 9.2.2. The possibility of mistaking volume backscatter returns for interface reflections is a potentially serious problem which can lead to large and unacceptable depth measurement errors. It has been seen in sections 5 and 7 that the interface and volume return peak powers depend in a complex way on the beam nadir angle and wind speed. Except for systems operating with nadir angles under about 15 degrees, it is not practical for surface returns to be restricted, in general, to either interface-only or volume-only by selection of a particular beam nadir angle within the desired operating range. The flip-flop error will have to be limited in some other way.

The most important restraint on nadir angle is the minimization and correction of propagation-induced depth measurement bias errors. It has been seen in section 9.2.1 that small as well as large beam nadir angles lead to large propagation-induced biases. The optimum nadir angle for minimizing propagation-induced biases varies with signal processing and detection procedures, but typical requirements fall in the 15 - 25 degree range. For a given procedure, the range of desirable angles can be quite small,

particularly in the "passive" bias correction mode where actively sensed water clarity parameters are not estimated from the air. It may thus be preferable to utilize a scanner pattern which maintains a nearly constant nadir angle rather than a nutating scan (such as used on the AOL and planned for HALS) whose nadir angle varies by $\sqrt{2}$ from major to minor axis. A scanner design of interest is a flat mirror gimballed in two perpendicular directions by servos. This arrangement is advantageous both because any desired scan pattern (such as a constant nadir angle circle) can be programmed into the servo controllers and because feedback from the attitude measurement subsystem can be used to interactively correct for aircraft roll and pitch in real time. The disadvantage is that they are mechanically unstable and require frequent maintenance. Oscillatory scanners with large variations in nadir angle are undesirable and will inevitably lead to scan angle dependent errors.

Given a scan angle, the flight altitude is then selected, within bounds dictated by safety and signal-to-noise ratio, to produce the necessary swath width, the magnitude of which will depend on economic or operational factors. It was determined in a cost/benefit study (Enabnit et al. 1978) that in shallow water, airborne laser hydrography enjoys a significant advantage in cost and manpower savings over traditional sonar techniques for a swath width on the order of 210 m (with a small allowance for overlap). This can be achieved, for example, with a ± 20 degree nadir angle from an altitude of just under 300 m.

Coincidentally, 300 m is roughly the minimum "safe" flight altitude (depending somewhat on the aircraft and visibility) for operations conducted at night with fixed-wing aircraft. If lower altitudes were desired, aircraft safety would be a limiting factor. Lower altitudes could be safely flown during the day (ignoring swath width and cost-effectiveness), but for a fixed receiver surface image, the added penetration potential provided by inverse-square gains in the bottom return peak power are at least partially compromised, as seen in sections 8.3.1 and 8.2.5.1, by correspondingly increased solar background noise. Furthermore, maintaining a fixed receiver surface image requires an increased receiver field of view which would probably be difficult to attain due to a simultaneous and conflicting need for very narrow interference filter bandwidth (as seen in section 8.2.5.3). When

all of these factors are considered, one can see that the optimum altitude for safe and cost-effective airborne laser hydrography flight operations, day or night, is at or slightly under 300 m.

If a narrower swath width with higher sounding density is desired for a detailed look at a smaller area (to investigate high relief features such as rocks, cliffs, or coral reefs), it could be achieved with either lower altitude or lower scanner nadir angle. In the daytime, a lower altitude would lead to stronger bottom returns (assuming that eye safety is not violated) and similarly stronger solar background. This results in a somewhat improved signal-to-noise ratio (SNR) (particularly if the receiver field of view can be increased to maintain a fixed receiver surface spot size -- which is, however, unlikely) since the noise varies as the square root of the solar background level. A lower nadir angle, on the other hand, would yield only marginally increased bottom signal strength and SNR. The effect of lower nadir angle on accuracy is complex and depends on the bias-correction procedure. With passive bias correction, reducing the nadir angle would be undesirable, even though the beam-steering error might be reduced slightly. Lowering the altitude is thus preferred, if practical. With active bias correction, the nadir angle could also be reduced. At night, the altitude cannot be reduced due to safety limitations. If passive bias correction is used, the nadir angle must remain fixed, and no high density mode is possible.

For a given swath width, the average sounding density is determined by the aircraft speed and the laser repetition rate. For a 210-m swath width and a 75 m/sec aircraft speed, a pulse repetition rate of 650/sec would yield an average spot density of about 1 per 25 m^2 or 5 m between centers. In all but quite shallow depths, scattering-induced beam spreading (section 8.2.5.1) would cause heavy overlapping of irradiated areas on the bottom such that the entire bottom would be irradiated. Such extremely dense coverage is probably unwarranted. Backing off to, say, a 65/sec rate would yield an average density of 1 per 250 m^2 or 16 m between spots. This seems to be a more reasonable situation; a large fraction of the entire bottom is still irradiated, but the demands on laser design are significantly reduced. Laser lifetime would be extended, or higher pulse energies could be achieved which would improve penetration (within the bounds of eye safety as seen in section

10.3. Lower rates would also ease the significant data processing burden. A realistic, desirable sounding density should be established in consultation with the user hydrographers before system design so that a reasonable pulse repetition rate can be specified. Care must be taken to insure that for the scanner pattern selected, the minimum spot density, not the average, is as required.

10.3 Transmitter Beam Divergence, Pulse Energy, Pulse Width, and Peak Power

Transmitter beam divergence has direct effects on both penetration and accuracy via eye-safety limitations and the wave correction technique, respectively. The critically important consideration is a viable wave correction technique. If wave correction required an extremely narrow (i.e., 1 mr) beam width for profiling small waves, eye-safety restrictions would cause severely reduced permissible pulse energy and unacceptably limited penetration potential. As noted in section 9.2.5, it is believed that wave correction is best accomplished with a broader (10-15 mr) beam which is also preferred to maximize penetration within eye-safety considerations (since the acceptable pulse energy increases as the square of the beam divergence). Spatial resolution at the bottom is not seriously degraded by such beam divergences since scattering in the water column will dominate for all but very shallow depths. With such large beam divergences, however, care must be taken to insure that the depth measurement bias caused by distortion of the surface return pulse by the resulting geometry (as seen in section 9.2.4) remains acceptably small. This depends primarily on the divergence, the nadir angle, and the altitude; it could cause problems at 15 mr/30 degrees/300 m, for example.

Of all technologies affecting system performance, laser development is probably the area of most rapid change. Within this category, the area of least potential improvement is average output power -- i.e., pulse energy times pulse repetition rates. For a compact system destined for a light aircraft, the average transmitted power is limited by the available input power, laser efficiency, the laser thermal damage threshold, and the size and weight of the laser cooler. It is clear that the pulse repetition rate should be as low as possible (while providing a satisfactory density of soundings for

the hydrographer) in order to maximize the pulse energy and the lifetime of laser components, such as the flash tubes in a solid state laser which need to be replaced after a certain number of firings.

Eye-safety limited pulse energies are desired in order to maximize penetration which is an extremely important factor in the areal coverage potential and cost-effectiveness of the system. As seen in section 8.2.4, relatively large beam divergences permit eye-safe operation for laser pulse energies in excess of those commercially available at the present time given the required narrow pulse widths (< 7 ns) and high repetition rates (60 - 400/sec). For a 300-m altitude, for example, pulse energies in the range from 35 mJ for a 10-mr divergence to 80 mJ for a 15-mr divergence are the limits of eye-safety.

Because propagation-induced pulse stretching results in bottom return impulse response functions which can be significantly wider than the incident pulse, no penetration gain can be achieved at fixed pulse energies by going to very narrow, high peak power laser pulses. A reduction in typical pulse width to about 2 ns FWHM would, however, be highly desirable as the most straightforward solution to the surface identification uncertainty or "flip-flop" problem for which the error is linearly proportional to pulse width. A corresponding increase in receiver bandwidth and decrease in integration time or digitizer "bin width" would also be required, according to the principles developed in section 9.3.1.

Typical laser pulses tend to exhibit a slow trailing edge decay characteristic which, if not suppressed, could be the dominant penetration limiting noise source, as seen in section 8.3. The trailing edge decay rate determines the poorest water clarity for which the system can be used. In order to provide coverage in moderately turbid areas, the decay should be faster than an exponential with a time constant of 7 ns. A separate "tail-biter" Pockels cell may be needed to accomplish this.

10.4 Receiver Field of View, Optical Bandwidth, and Receiver Aperture

The spatial and temporal aspects of beam spreading in the water which determine the maximum receiver field-of-view (FOV) requirement have been discussed at length in section 8.2.5. The FOV requirement for optimum bottom return peak power has been determined to be that which is large enough from the flight altitude to encompass a diameter at the surface equal to roughly seventy percent of the water depth. For a 35-m depth, for example, a 300-m altitude would require an 80-mr FOV to maximize the return signal. Nighttime operation is clearly preferred. If only nighttime operation were required (which is a management decision) an optical system could be built to meet the resulting specifications without a great deal of trouble.

For daytime operation, however, a very narrow bandwidth optical filter of the grating or the "interference" type, centered on the laser wavelength, is required to attenuate the majority of the solar background reflected into the receiver from scattering in the water column. This background level, or the shot noise associated with it, is the dominant noise source and determines the maximum penetration depth of the system for given water clarity: the narrower the filter bandwidth, the greater the penetration potential. The problems associated with such filters are, first, that they are extremely temperature sensitive and generally need to be stabilized in temperature-controlled ovens. More importantly, they highly attenuate radiation entering at off-axis angles. Large fields of view have large off-axis components, and in order to keep the resulting angles small at the filter, the length of the optical train must be increased. This also requires a correspondingly larger filter diameter, but the filters are readily available only up to certain physical sizes.

If the size of the system or individual optical components is limited, a large receiver FOV and a very narrow filter bandwidth will be mutually exclusive. Maximizing bottom return signal power for daytime operation thus requires compromising one or both of these to sub-optimal levels. A somewhat limited FOV is less damaging during the daytime than an excessively wide filter bandwidth. Bandwidths no larger than 5-10 Å are considered to be highly desirable, with the smallest possible bandwidth preferred as long as

the FOV reduction is not excessive. During operations, the FOV should be set at the value required for the deepest expected depth. There is a greater penalty in signal-to-noise ratio caused by too small a FOV than for too large a FOV. For nighttime operation, however, the filter should be bypassed or removed (because insertion losses are significant), and the FOV should be expanded to a fully optimized value.

The telescope aperture should be as large as possible within the constraints of size, weight, and reasonable interference filter diameter. This maximizes the intercepted radiation and hence the penetration potential. Larger apertures are not proportionally more effective during daylight because they also intercept more solar background; but at night the return signal increases as the square of the aperture with no increase in noise. The aperture should have an effective area of at least 500 cm^2 , and $700 - 800 \text{ cm}^2$ is preferable.

10.5 Receiver Resolution and Pulse Location Algorithm

The bandwidth, resolution, and digitizing capabilities of the receiver/processor must be appropriate for the received pulse widths. Typical accuracy estimates for various pulse widths, digitizer bin widths or integration times, and signal and noise rates were described in detail in section 9.3.1. Optimum bin widths depend on the received pulse widths and signal levels, but for relatively weak signals from deep water, between four and eight bins per pulse width provided the lowest random error.

The pulse-location algorithm is very important and must be tailored to the specific system design because the signal processing procedures -- particularly non-linear operators -- have a strong effect on resulting accuracy. Two pulse-location algorithms have been studied in great detail: "fractional" thresholds proportional to peak power for linear signal processing (section 9.3.1), and constant fraction discriminators (CFD) applied to signals processed by logarithmic amplification and first-order differencing (section 9.3.2).

The selection of a pulse-location algorithm and its parameters is complex and difficult because the choice has direct effects on the error magnitudes from a number of diverse sources such as random noise, pulse location bias, non-linear processing biases, propagation-induced pulse stretching biases, surface uncertainty bias, and beam steering errors. The algorithm must be selected not just to minimize one or two of these errors, but all of the errors simultaneously. Problems arise with conflicting dependencies -- some errors are smaller for small thresholds or CFD delays, and others are smaller for large thresholds or delays. For example, large CFD delays are desirable for best penetration and low pulse stretching bias, but small delays are better for low non-linear processing bias.

For linear processing it was found that thresholds at half the peak height searching forward in time provide the lowest random errors and least sensitivity to varying return pulse widths (which occur due to propagation-induced pulse stretching). Smaller threshold fractions or "early" detection algorithms yield marginally smaller surface uncertainty biases, beam steering errors, and log/difference processing biases, but most of these biases are moderately insensitive across a wide range of detection points, and the negative aspects of added random noise and pulse width sensitivity are probably overriding. A more important aspect may be the need to operate at as high an off-nadir angle as possible with a "passive" propagation-induced bias corrector. It was seen in section 9.2.1.3 that for given procedures, this error is fairly sensitive to the threshold fraction or CFD delay, and operation at larger nadir angles is possible with algorithms which detect later on the bottom return pulse.

Bottom return detection and location procedures and algorithms for weak signals at night are fairly straight-forward, but they can be more difficult for daytime operation due to the fact that returns with reasonable signal-to-noise ratios will have extremely low signal-to-background ratios because of the high solar background ambient level. Gains in maximum penetration depth can be made if sophisticated techniques are utilized to detect and locate the bottom returns.

10.6 Receiver Dynamic Range Limitation

It is very important for maximum nighttime penetration that the receiver be so sensitive that it is shot-noise limited. This requirement dictates the lower end of the receiver dynamic range scale. The upper end is dictated by the maximum surface return amplitude. The problem with airborne laser hydrography returns is not only that the waveform amplitudes vary over such a wide dynamic range -- as much as six decades for a 250-kW peak pulse power transmitter -- but that they do so over a very short period of time, i.e., in a few tens or hundreds of nanoseconds. This can cause spurious responses in the PMT which must be identified and reduced to the greatest possible extent. The most straight-forward approaches for dynamic range reduction are techniques such as receiver polarization, partial optical blocks, and PMT gain control to reduce the magnitude of the interface and near-surface volume backscatter returns. The remainder of the dynamic range can then be compressed, if necessary, by a logarithmic amplifier.

While these techniques may resolve the spurious response problem they also seriously distort the volume backscatter return which contains the information on the optical properties of the water column. It has been seen in section 9.2.1 that propagation-induced scattering and geometry effects for off-nadir beam entry lead to potentially disastrous depth measurement bias errors. These errors could be estimated and largely corrected if sufficiently accurate water clarity information were available from the soundings themselves. If this information is lost, as by the above dynamic range reduction techniques, then the system can only be operated within acceptable accuracy bounds if the scanner nadir angle is restricted to a small range of angles for which the errors are small for that particular receiver/processor configuration. The specific nadir angles for which this occurs depend on the signal processing procedures and pulse location algorithms. It is important, therefore, that if volume backscatter information must be lost to reduce the spurious responses and dynamic range, or is too inaccurate, then the signal processing and pulse location procedures must be designed in such a way as to optimize the nadir angle for which the passive bias correction errors remain within the desired bounds.

Dynamic range reduction and spurious response suppression are serious problems, and I would recommend that the contractor 1) be required to demonstrate in the laboratory the capability of operating a receiver over the required dynamic range without significant spurious responses and 2) prove by simulation and modeling techniques that the nadir angle dictated by the selected receiver/processor (to yield small depth measurement biases) is large enough to provide economically viable swath widths from an altitude no greater than 300 m.

10.7 Summary

System design and development for airborne laser hydrography are complex and difficult because many of the problems requiring solution are at the cutting edge of state-of-the-art technologies and analytic techniques. This volume describes many of these problems and areas of concern in detail and offers either solutions or guidance for their approach. The two major general concerns are penetration and accuracy. Every indication is that performance in both of these areas can be made acceptable if strict attention is paid to the many complex effects and interactions described herein and if appropriate solutions are carefully designed into the hardware at its inception. Nothing can be taken for granted. The tasks ahead are difficult but will be richly rewarding.

EPILOG

This volume presents a set of compelling technical problems with accompanying solutions and discusses a number of additional areas of concern. Analytical and computer simulation modeling of various physical phenomena are documented, complex interrelationships of the key variables and parameters are extensively described, and guidance is provided where decisions are required. This is the most comprehensive description of the physics of airborne laser hydrography to date.

No treatise, however extensive, can contain a complete set of solutions for all associated problems. Detailed results are frequently dependent on the specific system design and implementation; these are, to a greater or lesser extent, the responsibility of the contractor. Advances in technology in the next decade could conceivably provoke alterations in design concepts. The four following examples are problem areas in which specific solutions will need to be carefully developed: propagation-induced bias correction, surface uncertainty, signal processing, and spurious responses. All are related to a single primary concern -- depth measurement accuracy.

1) The complex scattering and absorption processes which affect underwater light propagation, combined with the geometric effects of off-nadir beam entry angles, lead to serious depth measurement biases which must be constrained and removed. Although the biases are caused by environmental effects and thus depend on water clarity parameters, their magnitudes also depend strongly on the system variables, on the signal processing hardware, and on the pulse location algorithms utilized in the system or in post-flight data reduction. The basic impulse response functions of the water have been derived via Monte Carlo computer simulation as described in section 6. Resulting depth measurement biases for two specific hardware configurations are reported in section 9.2.1.

System-specific bias correctors for other than these two examples must be developed for each instrument. This can be accomplished by using the aforementioned impulse response functions (or the associated environmental response functions derived for a 7-ns source pulse) as a starting point. These signals

must be processed in a system simulator and the resulting depth measurement biases used as predictor/correctors. The biggest problem is the lack of availability of the necessary input parameters from the flight data. Potential bias correction procedures are discussed in section 9.2.1.

2) A potentially serious problem is the depth measurement bias caused by the uncertainty of whether the "surface" return originates chiefly from the interface reflection, the volume backscatter below the interface, or a combination of both. The incidence of this "flip-flop" problem is seen in section 7.4 to fall within the desired operational window of wind speed and beam nadir angle constraints. The magnitude of the error for a green surface return is seen in section 9.2.2 to be too large to go uncorrected, and the problem will have to be solved before a system meeting international accuracy standards can be fielded. Section 9.2.2 contains some thoughts on the subject and identifies potential solutions.

3) Signal processing is a wide-open area with serious ramifications on precision, accuracy, and maximum penetration depth. An important preliminary operation is reduction of the amplitude dynamic range between the surface and bottom returns. Techniques include polarization, optical blocks, variable-gain photomultiplier tubes, and logarithmic amplifiers. The problem that these non-linear techniques have in common is that they distort the various components of the returning signal and cause biases or loss of information content. Of primary importance are pulse detection and location algorithms. It has been seen from the two examples presented that this phase of signal processing plays a critical role in both system design and performance. Associated with this is the major decision to calculate depths in real time or to return recorded waveforms for later off-line processing. Algorithm selection is particularly crucial for systems which calculate depths in real time, because the waveforms are lost forever. The system designer must consider many interactions among all these factors in arriving at an approach which maintains both accuracy and system effectiveness.

4) The dynamic range of returning signal amplitudes is very large due to the relatively strong surface return and the rapid attenuation of the bottom signal by the absorption in the water column. Photomultiplier tubes, in

general, have the capacity to accept extremely high ranges of input signal amplitude, and to perform well as long as the large amplitude changes are not too rapid. The airborne laser bathymetry situation poses an extremely difficult problem because a five or six decade change in signal amplitude can occur in under 100 ns. The relatively huge surface return causes, by several different mechanisms, the generation of small but significant secondary pulses or "ringing" which can seriously interfere with bottom return recognition and pulse location as well as with estimation of water optical parameters. These interfering signals which have posed severe problems in existing systems will be present at some level in all systems and must be carefully handled in system design and operation. Techniques for reducing the input dynamic range to ameliorate this situation also affect the estimation of water optical parameters.

These problems must be properly addressed and solved for each individual system if international hydrographic accuracy standards are to be met. Prospective contractors should be directed to provide detailed solutions in their proposals.

Recommendations for two changes of emphasis are made in the text. The first is that daytime operation be relegated to a secondary status due to the simplified system design constraints and distinctly superior performance for night surveys. The second is that the previously specified high sounding density of one pulse every $25-50\text{ m}^2$ which leads to pulse-to-pulse overlap be reconsidered in favor of a lower value. The potential reduction in laser pulse repetition rate would ease laser design and maintenance problems and could permit slightly increased penetration depth for the system.